

cy.1

**ARCHIVE COPY  
DO NOT LOAN**



**DOMINANCE OF RADIATED AERODYNAMIC NOISE  
ON BOUNDARY-LAYER TRANSITION  
IN SUPERSONIC-HYPERSONIC WIND TUNNELS  
Theory and Application**

**Samuel R. Pate  
ARO, Inc., a Sverdrup Corporation Company**

**VON KÁRMÁN GAS DYNAMICS FACILITY  
ARNOLD ENGINEERING DEVELOPMENT CENTER  
AIR FORCE SYSTEMS COMMAND  
ARNOLD AIR FORCE STATION, TENNESSEE 37389**

**March 1978**

**Final Report for Period September 1975 – March 1977**

Approved for public release; distribution unlimited.

Property of U. S. Air Force  
AEDC LIBRARY  
F40500-77-C-0003

**Prepared for**

**ARNOLD ENGINEERING DEVELOPMENT CENTER/DOTR  
ARNOLD AIR FORCE STATION, TENNESSEE 37389**

AEDC TECHNICAL LIBRARY



REF ID: A6000 0210 5  
5 0720 00034 1638

## NOTICES

When U. S. Government drawings, specifications, or other data are used for any purpose other than a definitely related Government procurement operation, the Government thereby incurs no responsibility nor any obligation whatsoever, and the fact that the Government may have formulated, furnished, or in any way supplied the said drawings, specifications, or other data, is not to be regarded by implication or otherwise, or in any manner licensing the holder or any other person or corporation, or conveying any rights or permission to manufacture, use, or sell any patented invention that may in any way be related thereto.

Qualified users may obtain copies of this report from the Defense Documentation Center.

References to named commercial products in this report are not to be considered in any sense as an indorsement of the product by the United States Air Force or the Government.

This report has been reviewed by the Information Office (OI) and is releasable to the National Technical Information Service (NTIS). At NTIS, it will be available to the general public, including foreign nations.

## APPROVAL STATEMENT

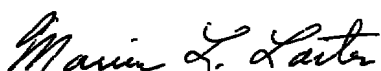
This report has been reviewed and approved.



ELTON R. THOMPSON  
Project Manager, Research Division  
Directorate of Test Engineering

Approved for publication:

FOR THE COMMANDER



MARION L. LASTER  
Director of Test Engineering  
Deputy for Operations

# UNCLASSIFIED

REPORT DOCUMENTATION PAGE		READ INSTRUCTIONS BEFORE COMPLETING FORM
1 REPORT NUMBER <b>AEDC-TR-77-107</b>	2 GOVT ACCESSION NO.	3. RECIPIENT'S CATALOG NUMBER
4 TITLE (and Subtitle) <b>DOMINANCE OF RADIATED AERODYNAMIC NOISE ON BOUNDARY-LAYER TRANSITION IN SUPERSONIC- HYPERSONIC WIND TUNNELS Theory and Application</b>		5 TYPE OF REPORT & PERIOD COVERED <b>Final Report - September 1975 - March 1977</b>
		6 PERFORMING ORG. REPORT NUMBER
7 AUTHOR(s)  <b>Samuel R. Pate - ARO, Inc.</b>		8 CONTRACT OR GRANT NUMBER(s)
9 PERFORMING ORGANIZATION NAME AND ADDRESS <b>Arnold Engineering Development Center/DOTR Air Force Systems Command Arnold Air Force Station, Tennessee 37389</b>		10. PROGRAM ELEMENT, PROJECT, TASK AREA & WORK UNIT NUMBERS  <b>Program Element 65807F</b>
11 CONTROLLING OFFICE NAME AND ADDRESS <b>Arnold Engineering Development Center/DOS Arnold Air Force Station Tennessee 37389</b>		12. REPORT DATE <b>March 1978</b>
		13. NUMBER OF PAGES <b>412</b>
14 MONITORING AGENCY NAME & ADDRESS (if different from Controlling Office)		15. SECURITY CLASS. (of this report)  <b>UNCLASSIFIED</b>
		15a DECLASSIFICATION/DOWNGRADING SCHEDULE <b>N/A</b>
16 DISTRIBUTION STATEMENT (of this Report)  <b>Approved for public release; distribution unlimited.</b>		
17 DISTRIBUTION STATEMENT (of the abstract entered in Block 20, if different from Report)  <i>2. Boundary layer transition - Noise effects</i> <i>3. Noise - Effects</i>		
18 SUPPLEMENTARY NOTES  <b>Available in DDC</b>		
19 KEY WORDS (Continue on reverse side if necessary and identify by block number) <div style="display: flex; justify-content: space-between;"> <div> <b>boundary-layer transition</b>  <b>aerodynamic noise</b>  <b>supersonic flow</b>  <b>hypersonic flow</b>  <b>theory</b> </div> <div> <b>conical body</b>  <b>flat plates</b>  <b>boundary layer</b>  <b>research management</b>  <b>correlation techniques</b> </div> <div> <b>Reynolds number</b>  <b>Mach number</b>  <b>computer program</b> </div> </div>		
20 ABSTRACT (Continue on reverse side if necessary and identify by block number) <p>An experimental investigation was conducted to determine the effects of radiated aerodynamic-noise on boundary-layer transition in supersonic-hypersonic wind tunnels. It is conclusively shown that the aerodynamic noise (pressure fluctuations associated with sound waves), which radiate from the tunnel wall, turbulent boundary layer, will dominate the transition process on sharp flat places and sharp slender cones at zero incidence. Transition data measured</p>		

# UNCLASSIFIED

# UNCLASSIFIED

## 20. ABSTRACT (Continued)

in supersonic tunnels ( $M_\infty \geq 3$ ) varying in test section heights from 1 to 16 ft have demonstrated a significant and monotonic increase in transition Reynolds numbers with increasing tunnel size. It has also been shown that the measured root-mean-square pressure fluctuations in the tunnel test section decrease with increasing tunnel size. A unique set of "shroud" experiments enabled the wall boundary layer to be directly controlled (either laminar or turbulent) and allowed transition Reynolds numbers to be correlated with the root-mean-square of the pressure fluctuations. Correlations of transition Reynolds numbers as a function of the radiated noise parameters [tunnel wall  $C_f$  and  $\delta^*$  values and tunnel test section circumference ( $c$ )] have been developed. These correlations were based on sharp-flat-plate transition Reynolds number data from 13 wind tunnels having test section heights ranging from 7.9 in. to 16 ft, for Mach numbers from 3 to 8, and a unit Reynolds number per inch range from  $0.1 \times 10^6$  to  $1.9 \times 10^6$ , and sharp-slender-cone transition Reynolds number data from 17 wind tunnels varying in size from 9 to 54 in. for a Mach number range from 3 to 14 and a unit Reynolds number range from  $0.1 \times 10^6$  to  $2.75 \times 10^6$ . A FORTRAN IV computer code has been developed using the aerodynamic-noise-transition correlations. This code will accurately predict transition locations on sharp flat plates and sharp slender cones in all sizes of conventional supersonic-hypersonic wind tunnels for the Mach number range  $3 \leq M_\infty \leq 15$ . The effect of aerodynamic noise on transition Reynolds numbers must be considered when supersonic-hypersonic wind tunnel data are used to (a) develop transition correlations, (b) evaluate theoretical stability-transition math models, and (c) analyze transition-sensitive aerodynamic data. The radiated aerodynamic-noise transition dominance theory as presented in this research provides an explanation for the unit Reynolds number effect in conventional supersonic-hypersonic wind tunnels. If a true Mach number effect exists, it is doubtful that it can be determined from data obtained in conventional supersonic-hypersonic wind tunnels because of the adverse effect of radiated noise. It has been shown that the ratio of cone transition Reynolds numbers to flat-plate values does not have a constant value of three, as often assumed. The ratio will vary from a value of near three at  $M_\infty = 3$  to near one at  $M_\infty = 8$ . The exact value is unit Reynolds number and tunnel size dependent. The aerodynamic-noise-transition empirical equations developed in this research correctly predict this trend. The boundary-layer trip correlation developed by van Driest and Blumer has been shown to be valid for different sizes of wind tunnels and not dependent on the free-stream radiated noise levels. The trip correlation developed by Potter and Whitfield remains valid if the effect of tunnel size on the smooth body transition location is taken into account. Wind tunnel transition Reynolds numbers have also been shown to be significantly higher than ballistic range values.

## PREFACE

The research reported herein was conducted by the Arnold Engineering Development Center (AEDC), Air Force Systems Command (AFSC), under Program Element 65807F. The results were obtained by ARO, Inc., AEDC Division (a Sverdrup Corporation Company), operating contractor for AEDC, AFSC, Arnold Air Force Station, Tennessee, under ARO Projects Numbers VT5717 and VT8049. The manuscript was submitted for publication on October 21, 1977.

This report was initially published as a doctoral dissertation at The University of Tennessee, Knoxville, Tennessee, in March 1977.

## CONTENTS

CHAPTER	PAGE
I. INTRODUCTION . . . . .	17
Background Information . . . . .	17
Wind Tunnel Free-Stream Disturbances . . . . .	24
Objective and Approach . . . . .	32
II. METHODS COMMONLY USED FOR PREDICTING BOUNDARY-LAYER TRANSITION . . . . .	34
Introduction . . . . .	34
Linear Stability Theory. . . . .	35
Kinetic Energy of Turbulence . . . . .	37
Correlations Based on Physical Concepts. . . . .	41
Data Correlations. . . . .	48
Tripped flows. . . . .	48
Smooth body flows. . . . .	52
Summary. . . . .	57
III. RADIATED AERODYNAMIC NOISE IN SUPERSONIC WIND TUNNELS. . .	59
Introduction . . . . .	59
Origins of Disturbance Modes . . . . .	60
Experimental Confirmation . . . . .	64
IV. EXPERIMENTAL APPARATUS . . . . .	88
Wind Tunnels . . . . .	88
AEDC-VKF Supersonic Tunnel A . . . . .	88
AEDC-VKF Hypersonic Tunnel B . . . . .	91
AEDC-VKF Supersonic Tunnel D . . . . .	91
AEDC-VKF Hypersonic Tunnel E . . . . .	94
AEDC-VKF Hypervelocity Tunnel F (Hotshot). . . . .	94
AEDC-PWT Supersonic Tunnel 16S . . . . .	97
Transition Models. . . . .	97
AEDC-VKF hollow-cylinder model (Tunnels A, D, and E) . . .	99
AEDC-PWT hollow-cylinder model (Tunnel 16S). . . . .	102
AEDC-VKF flat-plate model (Tunnel F) . . . . .	108
AEDC-VKF sharp-cone model (Tunnels A and D). . . . .	111
AEDC-VKF sharp-cone model (Tunnel F) . . . . .	116
V. EXPERIMENTAL TECHNIQUES AND BASIC TRANSITION DATA. . . . .	118
Basic Transition Data. . . . .	118
Pitot probe data . . . . .	126
Heat-transfer data . . . . .	127
Application of a Surface Microphone. . . . .	127
Dynamic pressure instrumentation . . . . .	127
Recording and analyzing equipment. . . . .	129
Calibration procedure. . . . .	133
Transition detection . . . . .	133
Induced errors . . . . .	141
Summary. . . . .	143

CHAPTER	PAGE
VI. SUPPORTING STUDIES . . . . .	144
Effects of Small Amounts of Leading-Edge Bluntness . . . . .	144
Investigation of Possible Leading-Edge Bevel Angle Effects. . . . .	150
Investigation of Possible Probe Tip Size Effects . . . . .	152
Investigation of Possible Adverse Effects of Hollow-Cylinder Internal Flow on External Surface Transition Measurements . . . . .	153
Methods for Detecting the Location of Transition and a Correlation of Results . . . . .	153
VII. SUMMARY OF BASIC TRANSITION REYNOLDS NUMBER DATA OBTAINED IN AEDC WIND TUNNELS ON PLANAR AND SHARP-CONE MODELS . . . . .	168
VIII. EXPERIMENTAL DEMONSTRATION OF AERODYNAMIC NOISE DOMINANCE ON BOUNDARY-LAYER TRANSITION . . . . .	180
Introduction . . . . .	180
AEDC Shroud Experiments. . . . .	181
Approach . . . . .	181
Shroud models. . . . .	185
Free-stream static pressure measurements . . . . .	185
Long-shroud wall boundary-layer characteristics. . . . .	190
Transition results . . . . .	194
Aerodynamic noise measurements . . . . .	199
Noise Measurements in Two AEDC Supersonic Wind Tunnels. . . . .	207
Transition Measurements in Different Sizes of AEDC Supersonic Tunnels . . . . .	215
NASA Activities. . . . .	218
European and USSR Studies. . . . .	226
IX. DEVELOPMENT OF AN AERODYNAMIC-NOISE-TRANSITION CORRELATION FOR PLANAR AND SHARP-CONE MODELS . . . . .	233
X. EFFECTS OF TUNNEL SIZE, UNIT REYNOLDS NUMBER, AND MACH NUMBER: COMPARISONS BETWEEN THEORY AND EXPERIMENTAL DATA . . . . .	256
Introduction . . . . .	256
Effect of Tunnel Size. . . . .	256
Variation of $Re_t$ with Model Position . . . . .	260
$Re_t$ Trends with Mach Number and Unit Reynolds Number . . . . .	264
Comparison of Tunnel and Ballistic Range $Re_t$ Data. . . . .	282
XI. COMPARISONS OF PLANAR AND SHARP CONE TRANSITION REYNOLDS NUMBERS. . . . .	286
XII. CONCLUSIONS. . . . .	295
REFERENCES . . . . .	299

## ILLUSTRATIONS

FIGURE	PAGE
I-1. Schematic Illustration of a Laminar, Transitional, and Turbulent Boundary Layer . . . . .	18
I-2. An Attempt to Picture the Capability for Analyzing and Predicting Boundary Layers and Laminar-Turbulent Transition. Chart considers only steady two-dimensional and axisymmetric, attached flow for Mach numbers less than 6 [from Reference (30)] . . . . .	22
I-3. Flow Disturbances in Supersonic and Hypersonic Tunnels . .	27
II-1. Correlation and Prediction of Incompressible Flow Transition Reynolds Numbers [from Reference (68)] . . . . .	38
II-2. Application of Laminar Stability Theory to Predicting Boundary-Layer Transition. . . . .	39
II-3. Comparison between Measured and Predicted Transitional Heat Transfer with Transition Triggered from Pressure-Velocity Fluctuation [from Reference (24)] . . . . .	40
II-4. Data on the Effect of Free-Stream Turbulence on Boundary-Layer Transition, Compared with Data of Other Investigators and Theory of van Driest and Blumer [from References (39) and (76)] . . . . .	43
II-5. Comparisons of Benek-High Method for Predicting Transition with Experimental Sharp Cone Data, $M_\infty \approx 0.4-1.3$ . . .	45
II-6. Three-Dimensional Boundary-Layer Velocity Profile and Cross-Flow Reynolds Number Criteria. . . . .	46
II-7. Critical Cross-Flow Influence on the Boundary-Layer Transition Profile . . . . .	47
II-8. Correlation of Transition and Cross-Flow Reynolds Number . . . . .	49
II-9. Ratio of Transition Reynolds Number of Rough Plate to That of Smooth Plate and Ratio of Height of Roughness Element to Boundary-Layer Displacement Thickness at Element, Single Cylindrical (Circle and Square Symbols) and Flat-Strip Elements (Triangular Symbols) [from Reference (78)] . . . . .	51



FIGURE	PAGE
II-10. Comparison of Measured and Predicted Transition Reynolds Numbers [from Reference (63)] . . . . .	54
II-11. Correlation of Sharp Cone Transition Reynolds Numbers at Supersonic-Hypersonic Conditions and Zero Angle of Attack [from Reference (81)] . . . . .	55
II-12. Correlation of Space Shuttle Wind Surface Centerline Transition Reynolds Number Data [from Reference (8)] . .	58
III-1. Comparison of Fluctuation Diagram for Three Modes [from Reference (43)] . . . . .	62
III-2. Mode Diagrams . . . . .	66
III-3. Pressure Fluctuation from a Supersonic Turbulent Boundary Layer [from Reference (93)] . . . . .	71
III-4. Correlation of Pressure Fluctuation Levels. . . . .	73
III-5. Comparison of Measured and Predicted Radiated Pressure Levels [from Reference (96)] . . . . .	74
III-6. Spectra of Free-Stream Fluctuation at $M_\infty = 4.5$ with and without Turbulence Generated Sound [from Reference (4)] .	77
III-7. Free-Stream Radiated Noise Fluctuations, Directionality, and Intensity, $M_\infty = 4.5$ [from Reference (74)] . . . . .	79
III-8. Energy Spectra [from Reference (74)] . . . . .	80
III-9. Mode Diagrams from AEDC-VKF Tunnel D at $M_\infty = 4.0$ [from Reference (88)] . . . . .	82
III-10. Variation of Flow Fluctuations with Unit Reynolds Number [from Reference (88)] . . . . .	83
III-11. Variation of RMS Pressure Fluctuations (Normalized by Dynamic Pressure) with Unit Reynolds Number [from Reference (88)]. . . . .	84
III-12. Variation of RMS Pressure Fluctuations (Normalized by Wall Shearing Stress) with Unit Reynolds Number [from Reference (88)] . . . . .	86
III-13. Hot-Wire Signal Spectra for Wire Overheat of $a_w^* = 0.4$ [from Reference (88)] . . . . .	87

FIGURE	PAGE
IV-1. AEDC-VKF Tunnel A . . . . .	90
IV-2. AEDC-VKF Tunnel B . . . . .	92
IV-3. AEDC-VKF Tunnel D . . . . .	93
IV-4. AEDC-VKF Tunnel E . . . . .	95
IV-5. AEDC-VKF Tunnel F (Hotshot) Facility ( $M_\infty \approx 7$ to 15) . .	96
IV-6. AEDC-PWT Tunnel 16S Supersonic Wind Tunnel Facility (16-ft x 16-ft Test Section). . . . .	98
IV-7. 3.0-in.-Diam Hollow-Cylinder Transition Model (AEDC-VKF Tunnels A, D, and E). . . . .	100
IV-8. Hollow-Cylinder Model Installed in AEDC-VKF Tunnel E. .	103
IV-9. AEDC-PWT 16S Transition Model Installation. . . . .	104
IV-10. 12-in.-Diam Hollow-Cylinder Transition Model Details - AEDC-PWT 16S. . . . .	105
IV-11. Sketch of AEDC-PWT 16-ft Supersonic Tunnel Test Section Area. . . . .	106
IV-12. AEDC-VKF Tunnel F Flat-Plate Transition Model . . . . .	109
IV-13. Transition Model Installed in the Tunnel F Test Section . . . . .	110
IV-14. AEDC-VKF Sharp-Cone Model Geometry. . . . .	112
IV-15. Photograph of Sharp-Cone Model Components . . . . .	113
IV-16. Installation of the 5-deg Cone Transition Model in the AEDC-VKF Tunnel A . . . . .	114
IV-17. Probe Details and Installation Sketch of the 5-deg Transition Cone in the AEDC-VKF Tunnel D . . . . .	115
IV-18. AEDC-VKF Tunnel F 10-deg Cone Transition Model. . . . .	117
V-1. Basic Transition Data from the Hollow-Cylinder Model, AEDC-VKF Tunnel A, $M_\infty = 4.0$ . . . . .	119

FIGURE	PAGE
V-2. Probe Pressure Data Showing the Location of Boundary-Layer Transition on the 12-in.-Diam Hollow-Cylinder Model in the AEDC-PWT 16S Tunnel for $M_\infty = 2.0, 2.5, \text{ and } 3.0$ , Probe No. 1, $\bar{b} = 0.0012 \text{ in.}$ , $\theta_{LE} = 6.5 \text{ deg}$ . . . . .	120
V-3. Comparison of Probe Pressure Transition Traces in the AEDC-VKF Tunnels A and D and AEDC-PWT 16S for $M_\infty = 3.0$ . . . . .	121
V-4. Examples of Surface Probe Transition Profile Traces on the 5-deg Half-Angle Sharp-Cone Model. . . . .	122
V-5. AEDC-VKF Tunnel F Flat-Plate Transition Data . . . . .	124
V-6. Heat-Transfer Rate Distributions on a 10-deg Half-Angle, Sharp Cone at Zero Incidence in the $M_\infty \approx 7.5$ Contoured Nozzle . . . . .	125
V-7. Cut-a-Way View Illustrating Microphone Installation. . . . .	128
V-8. Microphone Frequency Response. . . . .	130
V-9. Ambient Pressure Effects on Microphone Frequency Response, $M_\infty = 3$ . . . . .	131
V-10. Microphone System Used in the AEDC-VKF Tunnel A Aerodynamic-Noise-Transition Study . . . . .	132
V-11. Detection of Transition from Microphone RMS Pressure Fluctuations, $M_\infty = 3.0$ and $4.0$ (AEDC-VKF Tunnel A) . . . . .	134
V-12. Microphone Results, $M_\infty = 3$ . . . . .	136
V-13. Variation of Acoustic Spectra with Boundary-Layer State, $M_\infty = 3$ . . . . .	137
V-14. Oscilloscope Record of Microphone Output (Pressure Fluctuation) with Laminar, Transitional, and Turbulent Flow, $M_\infty = 3.0$ . . . . .	139
V-15. Comparison of Pressure Fluctuation Spectra for Planar and Axisymmetric Flow. . . . .	140
VI-1. Basic Transition Reynolds Number Data from the AEDC-VKF Tunnel D for $M_\infty = 3, 4, \text{ and } 5$ with Variable $\bar{b}$ , $\theta_{LE}$ , and $Re/in.$ . . . . .	145

FIGURE	PAGE
VI-2. AEDC-VKF Tunnel A $Re_t$ Values versus $\bar{b}$ for $M_\infty = 3, 4,$ and 5 . . . . .	146
VI-3. Circumferential Transition Locations on the AEDC-PWT Tunnel 16S Hollow-Cylinder Model . . . . .	147
VI-4. AEDC-PWT Tunnel 16S Transition Results, $Re_t$ versus $\bar{b}$ for $M_\infty = 2.0, 2.5,$ and $3.0$ . . . . .	148
VI-5. Absence of Effects from Bevel Angle and Probe Tip Size on Transition Location Hollow-Cylinder Model, $M_\infty = 3.0$ . . . . .	151
VI-6. Effectiveness of Serrated Fiber-Glass Tape Boundary-Layer Trip at $M_\infty = 3.0$ . . . . .	154
VI-7. Absence of Effect of Internal Flow Quality on Hollow- Cylinder Transition Data . . . . .	155
VI-8. Comparison of Transition Location for Various Detection Methods, $M_\infty = 5$ , $Re/in. = 0.28 \times 10^6$ , $b = 0.003$ in. [from Reference (37)]. . . . .	158
VI-9. Typical Data Showing Location of Boundary-Layer Transition on Hollow Cylinder at $M_\infty = 8$ [from Reference (108)]. . . . .	160
VI-10. Reynolds Number of Transition on Hollow Cylinder at $M_\infty = 5$ and $8$ . . . . .	161
VI-11. Illustration of Transition Location Variation with Methods of Detection . . . . .	163
VI-12. Correlations of Transition Detection Methods . . . . .	165
VII-1. Basic Transition Reynolds Number Data from AEDC-VKF Tun- nels D and E, $M_\infty = 3.0$ and $5.0$ , Hollow-Cylinder Model. . . . .	169
VII-2. Basic Transition Reynolds Number Data from the AEDC-VKF Tunnel A for $M_\infty = 3, 4,$ and $5$ and Variable $\bar{b}$ and $\theta_{LE}$ , Hollow-Cylinder Model . . . . .	170
VII-3. Basic Transition Reynolds Number Data from the 12-in.- Diam Hollow-Cylinder Model in the AEDC-PWT Tunnel 16S for $M_\infty = 2.0, 2.5,$ and $3.0$ and $\bar{b} = 0.0015, 0.0050,$ and $0.0090$ in. . . . .	171

FIGURE	PAGE
VII-4. Basic Transition Reynolds Number Data from the AEDC-VKF 12-in. Tunnel D, 40-in. Tunnel A and the AEDC-PWT 16-ft Supersonic Tunnel for $M_\infty = 3.0$ , Hollow-Cylinder Models . . . . .	172
VII-5. Transition Reynolds Number Data from AEDC-VKF Tunnel D, Sharp-Cone and Planar Models . . . . .	173
VII-6. Transition Reynolds Number Data from AEDC-VKF Tunnel A, Sharp-Cone and Planar Models . . . . .	175
VII-7. AEDC-VKF Tunnel F (Hotshot) Transition Data. . . . .	177
VIII-1. Long Shroud Installation in the AEDC-VKF Tunnel A. . . . .	183
VIII-2. AEDC-VKF Tunnel A Long- and Short-Shroud Configurations . . . . .	184
VIII-3. Inviscid Pressure Distribution Inside Long Shroud. . . . .	186
VIII-4. Free-Stream Flat-Plate Pressure Data, $M_\infty = 3.0$ , AEDC-VKF Tunnel A Centerline. . . . .	189
VIII-5. Long-Shroud Boundary-Layer Rake. . . . .	191
VIII-6. Boundary-Layer Profiles on Inner Wall of Long Shroud . . . . .	192
VIII-7. Long-Shroud Boundary-Layer Characteristics . . . . .	193
VIII-8. Transition Data Measured with and without Long Shroud, $M_\infty = 3.0$ , AEDC-VKF Tunnel A. . . . .	195
VIII-9. Surface Pitot Probe Pressure Traces on 3.0-in.-Diam Model, Short-Shroud Configuration, $M_\infty = 4$ and 5 . . . . .	197
VIII-10. Transition Reynolds Numbers Measured with and without Long and Short Shroud, $M_\infty = 4.0$ and 5.0 . . . . .	198
VIII-11. Flat-Plate Microphone Model. . . . .	200
VIII-12. AEDC-VKF Tunnel A Microphone-Flat-Plate Installation . . . . .	201
VIII-13. Comparisons of Transition Reynolds Numbers and Root-Mean-Square Radiated Pressure Fluctuations at $M_\infty = 3.0$ . . . . .	203
VIII-14. Comparisons of Transition Reynolds Numbers and Root-Mean-Square Radiated Pressure Fluctuations at $M_\infty = 5.0$ . . . . .	206
VIII-15. Fourier Analysis of Selected Data Points from Figure VIII-13c . . . . .	208

FIGURE	PAGE
VIII-16. Free-Stream Pressure Fluctuation Measurements, AEDC-VKF Tunnels A and D . . . . .	209
VIII-17. Power Spectral Density Analysis of Microphone Output Recorded at $Re/in. = 0.24 \times 10^6$ [from Reference (88)] . . . . .	211
VIII-18. Comparison of Power Spectra of Microphone Output for Various Unit Reynolds Numbers [from Reference (88)] . .	212
VIII-19. Measurements of Fluctuating Pressures under Laminar and Turbulent Boundary Layers on a Sharp Cone in Mach 6 High Reynolds Number Tunnel at NASA Langley . . . . .	214
VIII-20. Variation of Transition Reynolds Numbers with Tunnel Size . . . . .	216
VIII-21. Effect of Tunnel Size on Transition Reynolds Numbers at $M_\infty \approx 3.0$ , Flat Plates and Sharp Cones . . . . .	217
VIII-22. Effect of Free-Stream Disturbances on Wedge Model Transition, $M_\infty \approx 20$ [from Reference (89)] . . . . .	220
VIII-23. Correlation of Transition Reynolds Numbers with RMS Disturbance Levels [from Reference (81)]. . . . .	222
VIII-24. NASA-Langley $M_\infty = 5$ Quiet Tunnel Concept [from Reference (28)]. . . . .	225
VIII-25. Hollow-Cylinder Transition Data [from Reference (57)]. .	228
VIII-26. Effect of Tunnel Size on $Re_t$ Data from Netherland Tunnels [from Reference (60)]. . . . .	230
VIII-27. Effect of Tunnel Size on Flat-Plate Transition Reynolds Numbers - USSR Studies. . . . .	232
IX-1. Influence of Tunnel Size on the Boundary-Layer Transition Reynolds Number Correlation [from Reference (10)] . . . . .	237
IX-2. Tunnel Size Parameter . . . . .	239
IX-3. Initial Correlation of Transition Reynolds Numbers on Sharp Flat Plates with Aerodynamic Noise Parameters [from Reference (10)] . . . . .	240

FIGURE	PAGE
IX-4. Initial Correlations of Planar and Sharp-Cone Transition Reynolds Numbers [from Reference (11)] . . . . .	241
IX-5. Tunnel Size Normalizing Parameters. . . . .	243
IX-6. Correlation of Transition Reynolds Numbers on Sharp Cones with Aerodynamic Noise Parameters [from Reference (11)] . . . . .	244
IX-7. Transition Reynolds Number Correlation. . . . .	247
IX-8. Correlation of Planar Model Transition Reynolds Numbers . . . . .	249
IX-9. Correlation of Sharp-Cone Transition Reynolds Numbers . . . . .	251
X-1. Effect of Wind Tunnel Size on Planar Model Transition Reynolds Numbers for Various Mach Numbers . . . . .	257
X-2. Effect of Wind Tunnel Size on Sharp-Cone Transition Reynolds Numbers for Various Mach Numbers . . . . .	258
X-3. Variation of Transition Reynolds Numbers with Tunnel Size and $M_\infty = 3.0$ , Sharp-Leading-Edge Flat-Plate/Hollow-Cylinder Models . . . . .	261
X-4. Variation of Sharp-Cone Transition Reynolds Numbers with Tunnel Size at $M_\infty \approx 8$ . . . . .	262
X-5. AEDC-VKF Tunnel E Transition Model Locations. . . . .	263
X-6. Effect of Model Axial Locations on $Re_t$ Data (Hollow-Cylinder Model) . . . . .	265
X-7. Computed Values of $Re_t$ with Varying Model ( $x_m$ ) Locations (Planar Models) . . . . .	266
X-8. Effect of Mach Number and Unit Reynolds Number on Planar Model Transition Data . . . . .	267
X-9. Effect of Mach Number and Unit Reynolds Number on Sharp-Cone Transition Data . . . . .	270
X-10. Variation of Planar Model Transition Reynolds Numbers with Tunnel Size and Mach Number. . . . .	274
X-11. Variation of Sharp-Cone Transition Reynolds Numbers with Tunnel Size and Mach Number . . . . .	275

FIGURE	PAGE
X-12. Transition Reynolds Numbers as a Function of Local Mach Number for Sharp Cones, $M_\infty = 8$ . . . . .	276
X-13. Comparisons of Predicted and Measured $(Re_t)_\delta$ Values on Sharp Cones for Various Local Mach Numbers, $M_\infty = 8$ . . . . .	278
X-14. Comparison of Predicted and Measured Transition Reynolds Number from Current Method (Eqs. (10) and (11) and the Fortran Computer Program, Appendix C) . . . . .	280
X-15. Variation of Transition Reynolds Numbers with Tunnel Mach Number . . . . .	281
X-16. Comparison of Sharp-Cone Transition Reynolds Numbers from Wind Tunnels and an Aeroballistic Range . . . . .	283
XI-1. Correlation of Axisymmetric and Planar Transition Reynolds Number Ratios . . . . .	288
XI-2. Comparison of Predicted and Measured Cone Planar Transition Ratios. . . . .	290
A-1. Adiabatic, Mean Turbulent Skin-Friction Coefficients as a Function of Mach Number and Length Reynolds Number . . . . .	321
A-2. Mean, Turbulent Skin-Friction Coefficient Computed Using the Method of van Driest-II. . . . .	323
B-1. AEDC-PWT Tunnel 16S Boundary-Layer Characteristics . . . . .	328
B-2. Boundary-Layer Rakes Used in the AEDC-PWT 16S Tunnel and the AEDC-VKF Tunnel A to measure Tunnel Wall Boundary-Layer Profiles . . . . .	329
B-3. AEDC-VKF Tunnel A Boundary-Layer Characteristics . . . . .	330
B-4. Pilot Pressure Profiles from AEDC-VKF Tunnel E, $M_\infty = 5.0$ . . . . .	333
B-5. AEDC-VKF Tunnel E Turbulent Boundary-Layer Displacement Thickness ( $\delta^*$ ) for $M_\infty = 5.0$ . . . . .	335
B-6. Turbulent Boundary-Layer Characteristics at $M_\infty = 3.0$ for AEDC Tunnels PWT-16S, VKF-A and VKF-D. . . . .	337
B-7. Flexible Plate Displacement Thickness Correlations for $M_\infty = 1$ to 10 . . . . .	339



FIGURE	PAGE
B-8. Correlation of Hypersonic Wind Tunnel Wall Displacement Thickness ( $\delta^*$ ) . . . . .	341
C-1. Comparisons of Approximate and Exact Cone Surface Reynolds Number Ratios . . . . .	355
D-1. Sensitivity of the Reynolds Number Ratio to Various Viscosity Laws . . . . .	375
D-2. Variation of Reynolds Number Ratio with Cone Half-Angle, Mach Number, and Temperature . . . . .	376
E-1. Boundary-Layer Trip Geometry . . . . .	379
E-2. Methods of Transition Detection, $M_\infty = 3.0$ , AEDC-VKF Tunnel D . . . . .	382
E-3. Surface Probe Transition Profiles, $M_\infty = 3.0$ , AEDC-VKF Tunnel A . . . . .	383
E-4. Effect of Spherical Roughness on Transition Location, $M_\delta = 2.89$ , AEDC-VKF Tunnel D . . . . .	384
E-5. Effect of Spherical Roughness on Transition Location, $M_\delta = 2.89$ , AEDC-VKF Tunnel A . . . . .	385
E-6. Effect of Spherical Roughness on Transition Location, $M_\delta = 3.82$ , AEDC-VKF Tunnel D . . . . .	386
E-7. Variation of Transition Reynolds Numbers with Trip Reynolds Number for $M_\delta = 2.89$ and $3.82$ , AEDC-VKF Tunnels D and A. . . . .	388
E-8. Correlation of Tripped Results Using the Methods of Van Driest-Blumer. . . . .	390
E-9. Correlation of Tripped Results Using the Method of Potter-Whitfield . . . . .	393
E-10. Comparisons of Correlation Predictions with Experimental Results. . . . .	395

## TABLES

TABLE	PAGE
1. AEDC Supersonic-Hypersonic Wind Tunnels . . . . .	89
2. Methods for Measuring the Location of Transition . . . . .	157
3. Methods Used for Correlating Transition Detection Techniques (See Figures VI-11 and VI-12). . . . .	162
4. European Transition Test Facilities [From Reference (57)]. .	227
5. Source and Range of Data Used in the Planar Model Transition Reynolds Number Correlation (See Figure IX-8). . . . .	250
6. Source and Range of Data Used in the Sharp Cone Transition Reynolds Number Correlation (See Figure IX-9) . . . . .	253
7. Estimated Cone-Planar Transition Ratios . . . . .	293
F-1. AEDC-VKF Tunnel D Transition Reynolds Number Data, 3.0-in.-Diam Hollow Cylinder. . . . .	399
F-2. AEDC-VKF Tunnel E 3.0-in.-Diam Hollow-Cylinder Transition Data. . . . .	400
F-3. AEDC-VKF Tunnel A Transition Reynolds Number Data, 3.0-in.-Diam Hollow Cylinder. . . . .	401
F-4. AEDC-PWT-16S Tunnel Basic Transition Reynolds Number Data, 12.0-in.-Diam Hollow Cylinder . . . . .	402
F-5. AEDC-VKF Tunnel D Transition Reynolds Number, 10-Deg Total-Angle Sharp Cone. . . . .	403
F-6. AEDC-VKF Tunnel A Transition Reynolds Number, 10-Deg Total-Angle Sharp Cone. . . . .	404
F-7. AEDC-VKF Tunnel A Long- and Short-Shroud Transition Results . . . . .	405
F-8. AEDC-VKF Tunnel F Transition Reynolds Number Data . . . . .	406

## APPENDIXES

APPENDIX A. TURBULENT BOUNDARY-LAYER SKIN FRICTION . . . . .	315
Review of Theoretical Methods . . . . .	315
Method of van Driest-II . . . . .	320
APPENDIX B. TUNNEL WALL BOUNDARY-LAYER CHARACTERISTICS . . . . .	324
Data Reduction Procedures . . . . .	324
AEDC-PWT Tunnel 16S Data. . . . .	327
AEDC-VKF Tunnel A Data. . . . .	327
AEDC-VKF Tunnel E Data. . . . .	332
Correlations of Boundary-Layer Displacement Thickness . . . . .	336
APPENDIX C. DEVELOPMENT OF FORTRAN IV COMPUTER PROGRAM FOR PREDICTING TRANSITION LOCATIONS USING THE AERODYNAMIC-NOISE- TRANSITION CORRELATION. . . . .	343
Method of Approach. . . . .	343
Basic Equations . . . . .	345
Computer Code Nomenclature. . . . .	356
Computer Program Listing. . . . .	361
Input Data Format and Check Problems... . . . .	369
Flow Chart for Fortran Computer Program . . . . .	372
APPENDIX D. EFFECTS OF DIFFERENT VISCOSITY LAWS ON INVISCID FLOW CONE SURFACE REYNOLDS NUMBER RATIOS . . . . .	373
APPENDIX E. COMBINED EFFECTS OF AERODYNAMIC NOISE AND SURFACE ROUGHNESS ON TRANSITION . . . . .	377
Transition Models and Apparatus . . . . .	378
Transition Dependency on Tunnel Size . . . . .	380
Transition Detection and Identification . . . . .	381
Basic Results . . . . .	381
Van Driest, et al. Trip Correlation . . . . .	389
Potter and Whitfield Trip Correlation . . . . .	391
APPENDIX F. TABULATIONS OF BASIC EXPERIMENTAL TRANSITION DATA FROM THE AEDC SUPERSONIC-HYPERSONIC WIND TUNNELS . . . . .	399
NOMENCLATURE . . . . .	407

## CHAPTER I

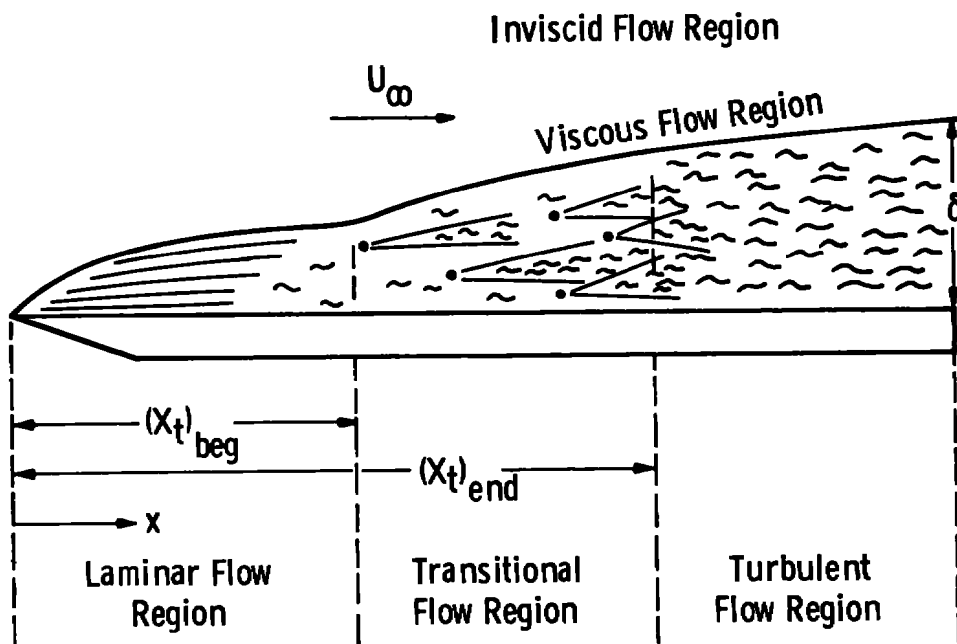
## INTRODUCTION

## I. BACKGROUND INFORMATION

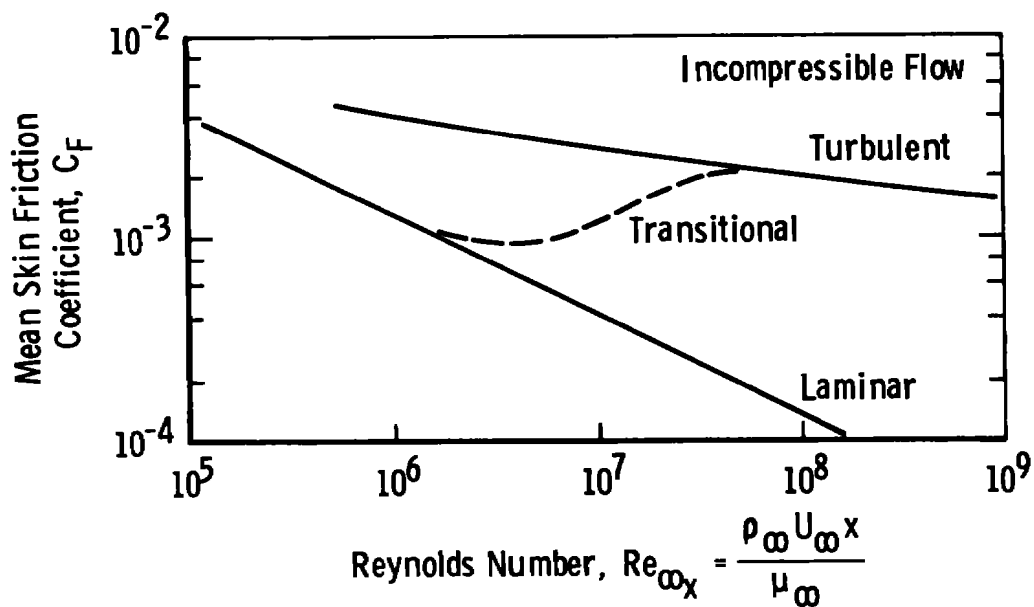
The growth of a boundary layer (viscous flow region) on the surface of a flat plate is illustrated in the diagram presented in Figure I-1. Initially, the boundary layer is laminar and can be characterized by an infinite number of viscous flow stream tubes arranged in laminated layers. The flow quantities are defined by steady-state properties, i.e., random fluctuations are not present. As the axial distance increases, the boundary layer becomes unstable and disturbances become amplified (1,2). Further downstream, the appearance of turbulent spots (bursts) will occur as reported by Emmons (3), and finally the boundary layer will become fully turbulent. Turbulent boundary-layer properties are defined as the sum of time averaged<sup>1</sup> mean flow quantities plus the fluctuating quantity (i.e.,  $p = \bar{p} + p'$ ,  $\rho = \bar{\rho} + \rho'$ ,  $u = \bar{u} + u'$ , etc.). The transition region is defined as the region connecting fully laminar and fully turbulent flow as shown in Figure I-1. This is a very simplified explanation and the reader is referred to the report by Morkovin (4) for an indepth discussion. White (2) also provides interesting reading on the historical background of instability-transition concepts, a summary of the classical studies, and a good concise summary on the transition process as generally accepted today.

---

<sup>1</sup>Time averaged quantities,  $\bar{Q} = \frac{1}{T} \int_0^T Q dt$ ;  $T \equiv$  time.



a. Boundary-Layer Development



b. Skin-Friction Coefficient

Figure I-1. Schematic illustration of a laminar, transitional, and turbulent boundary layer.

The importance of knowing the body station where the boundary layer changes from a laminar to a turbulent state (boundary-layer transition location) is well documented and can be briefly illustrated by a few examples:

1. The skin-friction drag of a flight vehicle (subsonic to hypersonic) increases about a factor of ten when the boundary layer changes from laminar to turbulent, as illustrated in Figure I-1. Since skin friction can comprise as much as 80 to 90% of the total vehicle drag at subsonic speeds and up to 50% of the total drag at hypersonic speeds, then the importance of knowing the location of transition is obvious.
2. Similarly, surface heat-transfer rates<sup>2</sup> can vary a factor of ten between a laminar and turbulent boundary layer, and this difference must be considered in vehicle design and selection of thermal protection system (ablation materials) for hypersonic vehicles.
3. Effectiveness of control surfaces can be strongly influenced because of the sensitivity of flow separation and the resulting surface pressure distributions to the location of transition and the state of the boundary layer.
4. Vehicle stability and control can be affected by the location of transition (5,6,7).

---

<sup>2</sup>From Reynolds analog  $C_h = \frac{C_f}{2(Pr)^{2/3}}$  [(see (1,2))]

5. Conducting successful experiments in ground test facilities (wind tunnels, ballistic ranges, engine test facilities, etc.) often requires knowledge of the location of transition on the subscale test model to ensure proper simulation of the flight conditions and/or to ensure that transition is occurring at the desired or expected location on the test article (8,9). A knowledge of the location of transition can be particularly significant when data for a particular test model geometry are obtained in several different facilities and where comparisons and/or analysis and evaluations of transition sensitive data are made (10,11).

The study of boundary-layer transition, particularly at high speeds, is still very much an area of active research, as illustrated by the wide diversity of publications appearing in the last ten years. Recent studies into the basic mechanisms contributing to boundary-layer instability and transition have been reported in References (4) and (12) through (15). Experimental studies of transition Reynolds numbers at supersonic-hypersonic Mach numbers have been reported in References (8) through (11) and (16) through (23). Correlation and semi-empirical methods for predicting the occurrence of transition have been reported in References (8) through (12) and (16) through (22), and theoretical studies on predicting transition have been reported in References (13), (15), and (24). In particular, the effects of free-stream disturbances on boundary-layer transition at supersonic-hypersonic Mach numbers have received much interest in recent years, as reported in References (4), (10) through (14), (19), and (24) through (29).

In a recent article, A. M. O. Smith (30) commented on the current state of being able to predict, in general, the occurrence of boundary-layer transition. Presented in Figure I-2 is Smith's qualitative assessment of the percentage of time that a prediction would be about 90 to 95% correct. Note that even today (after 90 years of transition research), the understanding of the transition process rates about only a 15% on predictability as compared to the laminar-turbulent boundary-layer understanding level of about 85 to 90%. Figure I-2 provides some appreciation for the complexity of the transition process.

The complexity of the transition process and the many contributing factors that can be a significant influence have been discussed in detail by Morkovin (4). Morkovin provides a critical review of high-speed boundary-layer transition and provides an indepth discussion on the many factors that can contribute to the transition process, the departure of the nonlinear transition process from the linear stability, and how the many factors can interrelate depending on the flow conditions, body surface conditions and free-stream disturbances. Morkovin devotes considerable space to a discussion of the adverse effects of free-stream disturbance on the transition process.

The American Institute of Aeronautics and Astronautics (AIAA) has also produced a nine-hour lecture series on "High-Speed Boundary-Layer Stability and Transition" (31). These lectures were prepared by Morkovin (4) and Mack (13) and based on their recent, but now well-known, work.

In general, the boundary-layer transition process can be associated with four different types of disturbance mechanisms:



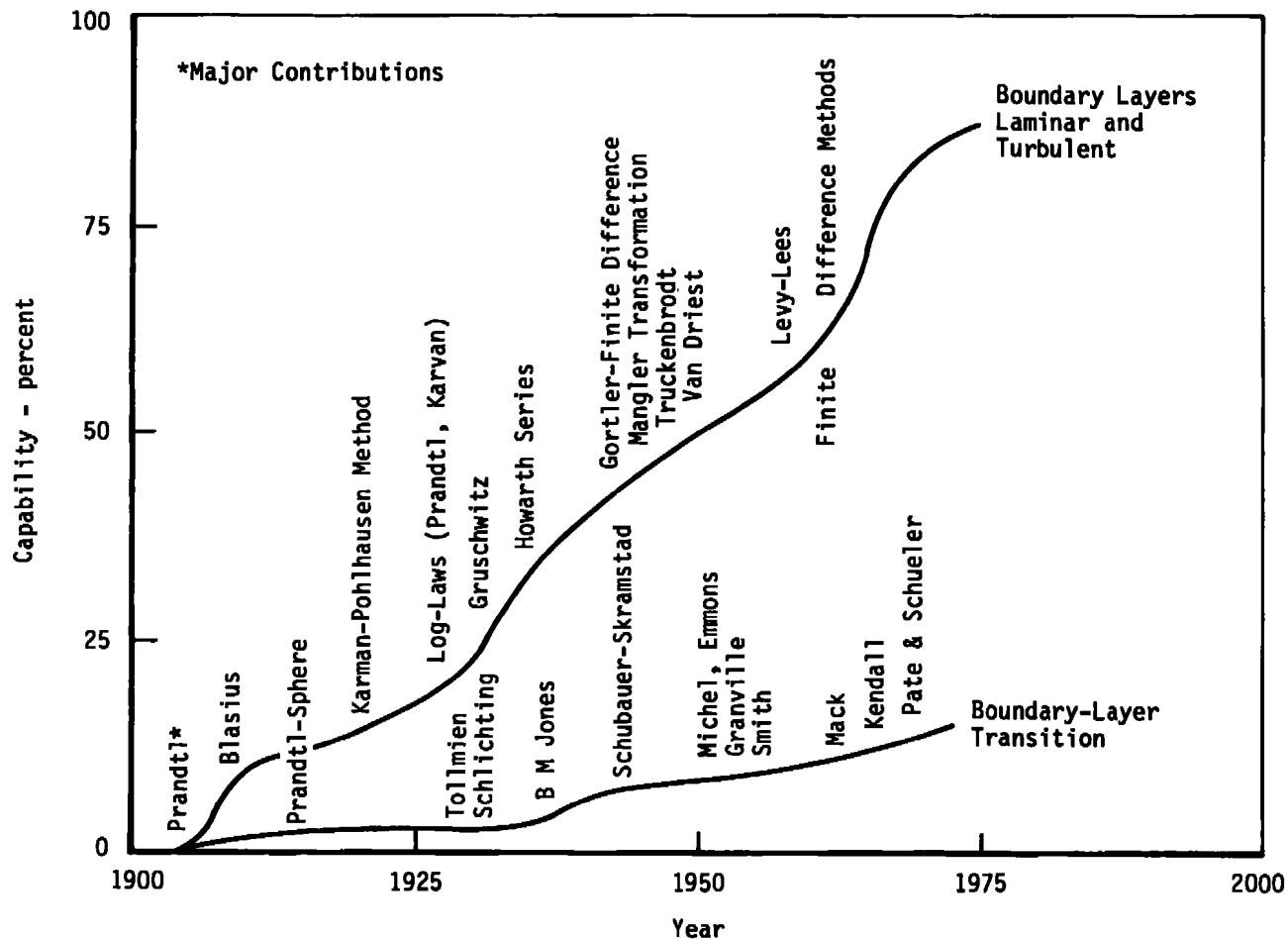


Figure I-2. An attempt to picture the capability for analyzing and predicting boundary layers and laminar-turbulent transition. Chart considers only steady two-dimensional and axisymmetric, attached flow for Mach numbers less than 6 [from Reference (30)].

1. Tollmien-Schlichting Type Instability: In an inviscid or viscous fluid, an inflection point in the velocity profile, can, in general, be sufficient to cause instability. However, in a viscous fluid an inflection point is not a necessary requirement since viscosity can also be destabilizing for certain wave numbers (wave frequency/wave velocity) and Reynolds numbers. Viscous instabilities were successfully predicted theoretically by Tollmien and Schlichting (1) using linear stability theory. Experimental verification was provided by Schubauer and Skramstad (32). Tollmien-Schlichting instabilities are characterized by small finite disturbances becoming amplified into sinusoidal oscillations at some critical frequency.
2. Crossflow or Dynamic Instability: This type instability is associated with three-dimensional boundary-layer flow with the instability being the result of a component of flow (crossflow) that is normal to the outer flow streamline and which develops from a spanwise pressure gradient. This crossflow profile inherently has a maximum point and a basically unstable inflection point. Crossflow instability was first investigated by Owen and Randall (33) on subsonic swept wings and later by Chapman (34), Pate (18), and Adams, et al. (35), (36) at supersonic and hypersonic speeds.
3. Roughness-Dominated Transition: This type of instability occurs when two- or three-dimensional disturbances are generated by isolated roughness elements which produce a wake-type turbulence. Van Driest (16,17), Potter and Whitfield (37), Whitehead (20), and Whitfield and Iannuzzi (21) have

experimentally studied isolated spherical roughness effects at supersonic-hypersonic Mach numbers.

4. Influence of Free-Stream Disturbance Levels (i.e., spectra and intensity levels): Schubauer and Skramstad (32) showed free-stream velocity fluctuations affected transition locations in subsonic wind tunnels. Pate and Schueler (10) and Pate (11) have shown that free-stream pressure fluctuations (aerodynamic noise) in supersonic-hypersonic wind tunnels can dominate the transition process. Morkovin (4) discusses the effects of free-stream disturbances in promoting transition and Mack (13) recently used linear stability theory in conjunction with free-stream pressure fluctuations (aerodynamic noise) as measured by Laufer (38) to predict the onset of transition.

The bulk of the transition data published to date has been obtained in wind tunnels. Consequently, most of the experimental data used in the development of essentially all correlations of transition Reynolds numbers and for verification of transition theories have been obtained in wind tunnels. Unfortunately, the location of transition on test models can be strongly affected by wind tunnel free-stream disturbances. The next section provides a brief summary of the various types of wind tunnel disturbances.

## II. WIND TUNNEL FREE-STREAM DISTURBANCES

It has been known for many years that disturbances present in the free-stream of subsonic wind tunnels can have a dominating effect on

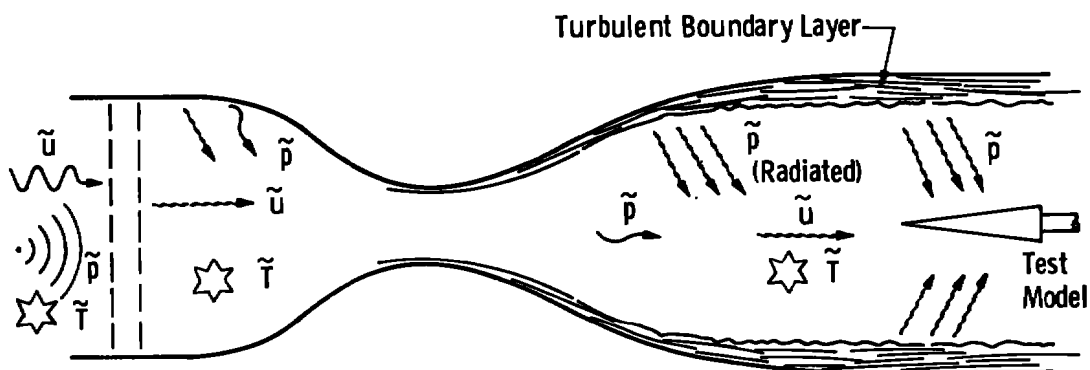
the boundary-layer instability and transition process. The incompressible stability theory developed by Tollmien and Schlichting in the 1920's, see Reference (1), had to wait about 20 years for experimental confirmation by Schubauer and Skramstad (32) because of the high level of turbulence (velocity fluctuations) present in most conventional subsonic wind tunnels. The classical experiments of Schubauer and Skramstad (conducted in the early 1940's) not only showed that the infinitesimally small Tollmien-Schlichting type disturbance waves could be amplified as predicted by theory (provided the tunnel velocity fluctuations were sufficiently small), but they also showed that the location of transition was dependent on the tunnel turbulence level. The low turbulence, subsonic transition Reynolds number data ( $Re_t = 2.9 \times 10^6$ ) of Schubauer-Skramstad were the maximum values obtained for many years and consequently were the values used in many data correlations and data comparisons. Van Driest and Blumer (39) used the data of Schubauer-Skramstad (32) in studying the effects of subsonic disturbances on the location of transition. Recent data (1968) obtained by Spangler and Wells (40) have shown that the subsonic transition Reynolds number could be increased to  $Re_t = 5.2 \times 10^6$  by reducing the background noise levels and by changing the frequency distribution from fans, diffuser, etc. Thus it has been shown that the disturbance level (intensity) as well as the type of disturbance are major contributing factors to the transition process at subsonic speeds. Consequently, it has been accepted that  $Re_t$  data obtained in subsonic wind tunnels can vary between facilities. Correlations that have been developed to predict transition on subsonic, smooth wall models

have usually been based on data from low turbulence wind tunnels. One well-known correlation was developed by Michel in 1951 (41).

Experiments conducted at supersonic speeds by NACA personnel (42) in the early 1950's also showed significant differences in transition locations measured on a 10-deg cone for similar test conditions but different wind tunnels. Differences exhibited in these data were found to decrease sharply as the Mach number increased to about 3 or 4. The differences in the  $Re_t$  values were believed to be directly related to the free-stream turbulence levels (velocity fluctuations  $(\tilde{u}/U_\infty)$  present at low supersonic speeds.

Kovaszny in 1953 (43) theoretically identified three possible disturbance sources in wind tunnels: (a) vorticity fluctuations (turbulence), (b) entropy fluctuations (or temperature spottiness), and (c) sound waves. Morkovin discussed these three possible modes of disturbance in 1957 (44) and 1959 (45) and speculated on where their origins could originate in a supersonic wind tunnel. The vorticity and entropy fluctuations were essentially convected along streamlines and were traceable to conditions in the settling chamber. Sound disturbances could travel across streamlines, and they could originate in the stilling chamber and from the boundaries of the test section. Morkovin identified the turbulent boundary layer (shear layer) on the tunnel wall as a potential source for radiating a sound disturbance. Figure I-3 illustrates the origins of these disturbances.

Vorticity (turbulence) fluctuations were investigated at Mach numbers from 1.7 to 4 by Laufer and Marte (46) by varying the turbulence level in the stilling chamber from 0.6 to 7%. In the low Mach



Mach Number Range	Type Disturbance	Effect on Transition
$M_\infty = 1.5$ to 3	Vorticity (Turbulence) ( $\tilde{u}$ )	← Usually Dominant
	Noise ( $\tilde{p}$ )	- May Be Dominant
	Entropy (Temp. Spots) ( $\tilde{T}$ )	- Negligible
$M_\infty = 3$ to 15 20 (Cold Flow)	Radiated Noise ( $\tilde{p}$ )	← Usually Dominant
$M_\infty > 10$ Arc Tunnels Shock Tunnels MHD Tunnels	Entropy ( $\tilde{T}$ )	- ?
	Radiated Noise ( $\tilde{p}$ )	- May Be Dominant

Figure I-3. Flow disturbances in supersonic and hypersonic tunnels.

number flow,  $M_\infty < 2.5$ , the stilling chamber turbulence level was found to have a strong effect on sharp cone boundary-layer transition Reynolds numbers; however, no significant effect was noted for  $M_\infty > 2.5$ . Similar experiments were conducted at Mach 1.76 by Morkovin (44), and no measurable shift in flat-plate transition Reynolds number resulted when the settling chamber turbulence was raised from 0.7 to 4.6%. Van Driest and Boison (47) also showed that for  $M_\infty \gtrsim 2.5$  the stilling chamber turbulence level had no significant effect on sharp cone transition Reynolds numbers. Therefore, it is concluded that for  $M_\infty \gtrsim 2.5$  to 3 velocity fluctuations have a negligible effect on wind tunnel transition data.

Sources of the entropy fluctuations (temperature spottiness) are traceable to the settling chamber and farther upstream. In the test section, the temperature fluctuations are related isentropically to those in the stilling chamber. Effective means such as the use of mixing sections and screens in the supply passage are used to reduce temperature fluctuations to small levels in supersonic tunnels and consequently their influence on transition in well-designed tunnels is thought to be insignificant. Limited studies of the effects of temperature fluctuations on transition locations have been conducted by Brinich (48) and Ross (49). Brinich (48) changed  $T_0$  from 52 to 176°F at  $M_\infty = 3.1$  and found that the transition location on a flat plate was essentially unchanged. Transition measurements were conducted by Ross (49) at  $M_\infty = 4$  where  $T_0$  was varied from 295 to 434°K, keeping the unit Reynolds number constant, and he found no appreciable change in  $Re_t$  data obtained with a hollow-cylinder model. Thus, it is concluded that in well-designed supersonic wind

tunnels (i.e., a stilling chamber equipped with proper mixing screens), entropy fluctuations will have a negligible effect on transition data.

The third type of unsteady disturbances, the radiated sound (or pressure fluctuations) (43) generated by the turbulent boundary layer on the walls of the test section, remain as a possible major factor affecting transition in supersonic and hypersonic wind tunnels for  $M_\infty > 2.5$ .

In 1952, AGARD established a series of calibration models with somewhat the same general objective as the NACA (42) had in testing a 10-deg cone in several wind tunnels. One of the calibration models was a high fineness ratio, parabolic body (AGARD Calibration Model A) which had been tested extensively by the NACA to compare zero lift drag measurements made in many different wind tunnels. Tests of the same model in the Arnold Engineering Development Center, von Kármán Facility (AEDC-VKF) 12-in. and 40-in. supersonic tunnels (Gas Dynamic Wind Tunnels, Supersonic (D) and (A)) revealed discrepancies in base pressure and drag data that could be explained by differences in transition Reynolds numbers in these tunnels (50). These tests were followed by tests of a hollow-cylinder model to obtain transition locations for a range of Mach numbers and unit Reynolds numbers. Schueler (51) showed from these tests that transition Reynolds numbers obtained in the AEDC-VKF 40-in. supersonic tunnel were significantly larger than those from the AEDC-VKF 12-in. supersonic tunnel. Aerodynamic noise generated in the tunnel boundary layers was suggested as being responsible for the variations in transition Reynolds numbers.

By the early 1960's, primarily as a result of Laufer's research (38), radiated noise had been identified as a significant source of wind



tunnel test section free-stream disturbances at supersonic Mach numbers ( $M_\infty \gtrsim 2$ ). However, there were no data available that demonstrated directly the effect that radiated sound (noise) disturbances might have on supersonic-hypersonic transition data taken in wind tunnels. Consequently, all of the transition experiments and resulting data correlations that were developed in the 1950's and '60's in an attempt to predict the behavior of flight transition Reynolds numbers at supersonic and hypersonic Mach numbers did not consider (include) the effects of free-stream disturbances (radiated noise).

Research by Pate and Schueler (10) and Pate (11) presented the first data showing the dominating effect of wind tunnel "aerodynamic noise" on boundary-layer transition. This research was undertaken after the first author (10) developed a correlation of transition Reynolds numbers as a function of the free-stream aerodynamic noise parameters ( $C_F$ ,  $\delta^*$ , and  $C$ ). This correlation was based on existing flat-plate and hollow-cylinder  $Re_t$  data published from eight wind tunnels covering the Mach number range from 3 to 8 with test section heights varying from 1 to 4 ft. The correlation was independent of unit Reynolds number and Mach number. To confirm the validity of the correlation and to establish that  $Re_t$  values increased monotonically with increasing tunnel (test section) size as predicted by the correlation, an extensive experimental program was formulated. This program provided for hollow-cylinder transition data to be obtained in the largest supersonic tunnels in the world, with test sections ranging from 1 to 16 ft, and the initial results were reported in Reference (10). Transition experimental studies were also

conducted using a sharp, slender 5-deg half-angle cone model to determine if the correlation held for an axisymmetric configuration, and these results were reported in Reference (11). This initial research also included a series of unique experiments that allowed the radiation of the free-stream aerodynamic noise to be controlled and measured and thus provided direct confirmation of the dominance of noise on transition.

Since the late 1960's, considerable research has been conducted by NASA on the effects of aerodynamic noise on transition [i.e., see References (26), (28), and (29)]. Currently, a new type of supersonic ( $M_\infty = 5$ ) wind tunnel, designed to eliminate the turbulent boundary layer on the tunnel wall and thus provide a test environment free of radiated noise disturbances, is being constructed at NASA-Langley Research Center as reported by Beckwith (28). Extensive studies of the effects of wind tunnel free-stream disturbances on transition at transonic and low supersonic speeds are also being conducted at the USAF AEDC<sup>3</sup> facilities (52). Transition measurements using different sizes of wind tunnels, similar to those conducted by Pate (10,11), have also been carried out in the USSR (53) and (54) and in several European countries (55 through 60). All of these studies have supported the findings of Pate and Schueler (10,11) and have provided additional and independent verification that the noise that radiates from a turbulent boundary on the wall of a supersonic-hypersonic wind tunnel can dominate the transition process on smooth wall planar and sharp cone models at zero angle of attack.

---

<sup>3</sup>Arnold Engineering Development Center (AEDC), Air Force Systems Command (AFSC), Arnold Air Force Station, Tennessee.

Wind tunnel disturbances, particularly turbulence ( $\tilde{u}/U_\infty$ ) and radiated aerodynamic noise ( $\tilde{p}/q_\infty$ ), primarily influence boundary-layer transition. However, free-stream disturbances can also affect aerodynamic data such as buffet onset and stability of wind tunnel models as recently discussed by Michel (61).

### III. OBJECTIVE AND APPROACH

The objective of the present research is to extend the study of the effects of radiated aerodynamic noise on the location of boundary-layer transition on test models in supersonic-hypersonic wind tunnels.

Hollow-cylinder (planar model) and sharp-cone geometries were selected as the transition models because they represent two basic configurations used in the design of supersonic-hypersonic vehicles. These configurations also allow leading-edge bluntness effects, surface roughness, and surface pressure gradients to be eliminated as variables, and at zero angle of attack the flow field is two-dimensional in nature. Also, a considerable amount of transition data from various wind tunnels on these configurations already existed. These configurations are also used as wind tunnel calibration models.

To present as complete a picture as possible, the initial investigations that identified aerodynamic noise as a major disturbance source are reviewed. The author's previous work showing that radiated noise dominates the transition process in supersonic-hypersonic wind tunnels is discussed in detail. New transition data obtained by the author on a flat plate at  $M_\infty = 8$  and  $(Re/ft)_\infty \lesssim 15 \times 10^6$  and a 10-deg half-angle sharp cone at  $M_\infty \approx 7.5$   $(Re/ft)_\infty \lesssim 30 \times 10^6$  are presented. Additionally, recent

research of aerodynamic noise effects on transition conducted in the USSR, the European countries, and by the NASA are reviewed and evaluated.

The aerodynamic-noise-transition correlations developed by the author for sharp-leading-edge flat plate and sharp slender cones are re-examined in light of this new data. A FORTRAN computer program has been developed which allows the location of transition on sharp-leading-edge planar models (flat plates and hollow cylinders) and sharp slender cones to be accurately predicted in all size wind tunnels for  $3 \lesssim M_\infty \lesssim 15$ .

The variations of transition Reynolds numbers with tunnel size, unit Reynolds number, and Mach number are discussed in detail. Extensive comparisons are made between the experimental data and results from the FORTRAN computer program.

A detailed evaluation and comparison of planar and sharp cone transition Reynolds numbers over the Mach number range from 3 to 10 is also made.

The possible effect of aerodynamic noise on the effectiveness of spherical boundary-layer trips was investigated and these results are presented.

The following supporting studies were also conducted and are included: (a) a review of methods currently used to predict transition locations, (b) correlations of transition locations determined using various detection methods, and (c) the influence of various viscosity laws on the calculation of Reynolds number.

## CHAPTER II

## METHODS COMMONLY USED FOR PREDICTING BOUNDARY-LAYER TRANSITION

## I. INTRODUCTION

Methods that have been used for predicting boundary-layer transition can be grouped into four general classifications:

1. Linear stability theory
2. Kinetic energy of turbulence approach
3. Semi-empirical methods and correlations based on physical ideas
4. Data correlations based on observed trends in experimental data.

Linear stability theory and the kinetic energy of turbulence approach offers perhaps the best possibility of eventually modeling and predicting the onset of the boundary-layer transition, even though to date they have not yet been very successful. However, these methods will probably not be widely used (at least not for many years) by the design engineer, wind tunnel experimentalists, or the aeronautical engineer involved in trying to predict the occurrence of transition on his aircraft or missile of interest. The linear stability and kinetic energy theories are very sophisticated, both in the concepts involved and the numerical and analytical mathematics required. Years of experience are required in developing and using the complicated computer programs. Vehicle configurations, particularly in the preliminary design stage, often change faster than the theory can be modified and/or the geometry is too complicated to be modeled.

Because of the absence of a readily available, easily used, and successful theoretical transition model, researchers, from necessity, have pursued the traditional path of attempting to develop data correlations that allow reasonable estimates to be made. These correlations have been and still are the basis on which most transition locations on aircraft and missiles are estimated and wind tunnel test programs are planned.

Reviews of smooth body transition prediction methods have been given by Gazley (62), Deem et al. (63), Morkovin (4), Granville (64), Kistler (65), Shamroth and McDonald (24), Tetervain (66), Hairstrom (67), Smith and Bamberoni (68), Reshotko (69), and Hanner and Schmitt (70). White (2) also gives a good review of many of the older well-known methods and some of the more recent methods. Of course, the interested person will want to read the sections on stability and transition by Schlichting (1).

Since it is not the purpose of this paper to present a critical review of the many published papers and methods, only a few of the more well-known techniques will be presented to illustrate types of methods, the correlation parameters used, and some of the typical results obtained.

## II. LINEAR STABILITY THEORY

The stability of fluid flow was first considered by Raleigh for incompressible, inviscid flows (1,2). He found that an inflection point in the velocity profile was a necessary requirement for instabilities to occur. Prandtl extended linear stability theory to include the destabilizing effects of the fluid viscosity (1,2). A detailed theory of

stability for incompressible, viscous flows was developed by Tollmien and Schlichting (1). The confirmation of the existence of the Tollmien-Schlichting type waves was provided by the classical experiments of Schubauer and Skramstad (32). Extension of the linear stability theory to compressible flows was accomplished by Lees and Lin (71). Experimental verification of this theory was provided by Laufer and Vrebalovich (72). Mach (13,73) extended linear stability theory to higher Mach numbers, identified and studied the presence of higher modes<sup>4</sup> of disturbance, and showed that the destabilizing effects of viscosity begin to decrease above  $M_\infty \approx 3$ . Kendall (14,74) provided experimental verification for many of Mack's theoretical predictions. One particularly significant finding of the Mack-Kendall research at JPL was the prediction and experimental confirmation that free-stream aerodynamic noise disturbance, regardless of frequency, are amplified by the laminar-boundary layer and this amplification begins at the leading edge of a flat plate and continues downstream until transition occurs. Mack-Kendall showed that a laminar boundary layer at  $M_\infty = 3$  to 4 can amplify the free-stream disturbance by an order of magnitude (73,74). The fact that all free-stream disturbances are amplified and can be an order of magnitude higher in the laminar-boundary layer than in the free stream is discussed later with regard to surface microphone measurements.

The use of linear stability theory to predict the onset of boundary-layer transition as opposed to just predicting the onset of amplification of small disturbance waves has been studied by Smith (68),

---

<sup>4</sup>The Tollmien-Schlichting type were defined as the primary mode.

Jaffe, Okamura, and Smith (15), Mack (13), and Reshotko (12). This approach is based on the observation by Michel (41) that the location of transition occurred at a constant value ( $\approx e^9$ ) of the amplification of the Tollmien-Schlichting type sinusoidal disturbances. Presented in Figures II-1 and II-2 are results computed by Smith (68), Jaffe, Okamura, and Smith (15), and Mack (13), respectively, and comparisons are made with experimental data.

The theoretical results presented in Figures II-1 and II-2 have limited application because of the following reasons. The theory of Smith, et al. (15) and (68) is applicable only to incompressible, low turbulence flows. The subsonic data presented in Figures II-2 were obtained in very low turbulence wind tunnels where the free-stream disturbance levels were negligible. Mack (13) made the assumptions that: (a) the initial disturbance amplitude ( $A_0$ ), at a reference Mach number ( $M_\infty = 1.3$ ), varied as the square of the Mach number ratio, (b) the disturbances in the boundary layer are proportional in amplitude to the free-stream radiated sound, and (c) the disturbance spectrum in the boundary layer is flat with respect to frequency and independent of axial location.

### III. KINETIC ENERGY OF TURBULENCE

More recently, kinetic energy of turbulence model equations, as investigated by Shramroth and McDonald (24) have been used to investigate transition as shown in Figure II-3. This method considers a particular type of free-stream disturbance which is introduced into the laminar boundary layer and follows the disturbance until transition occurs. One



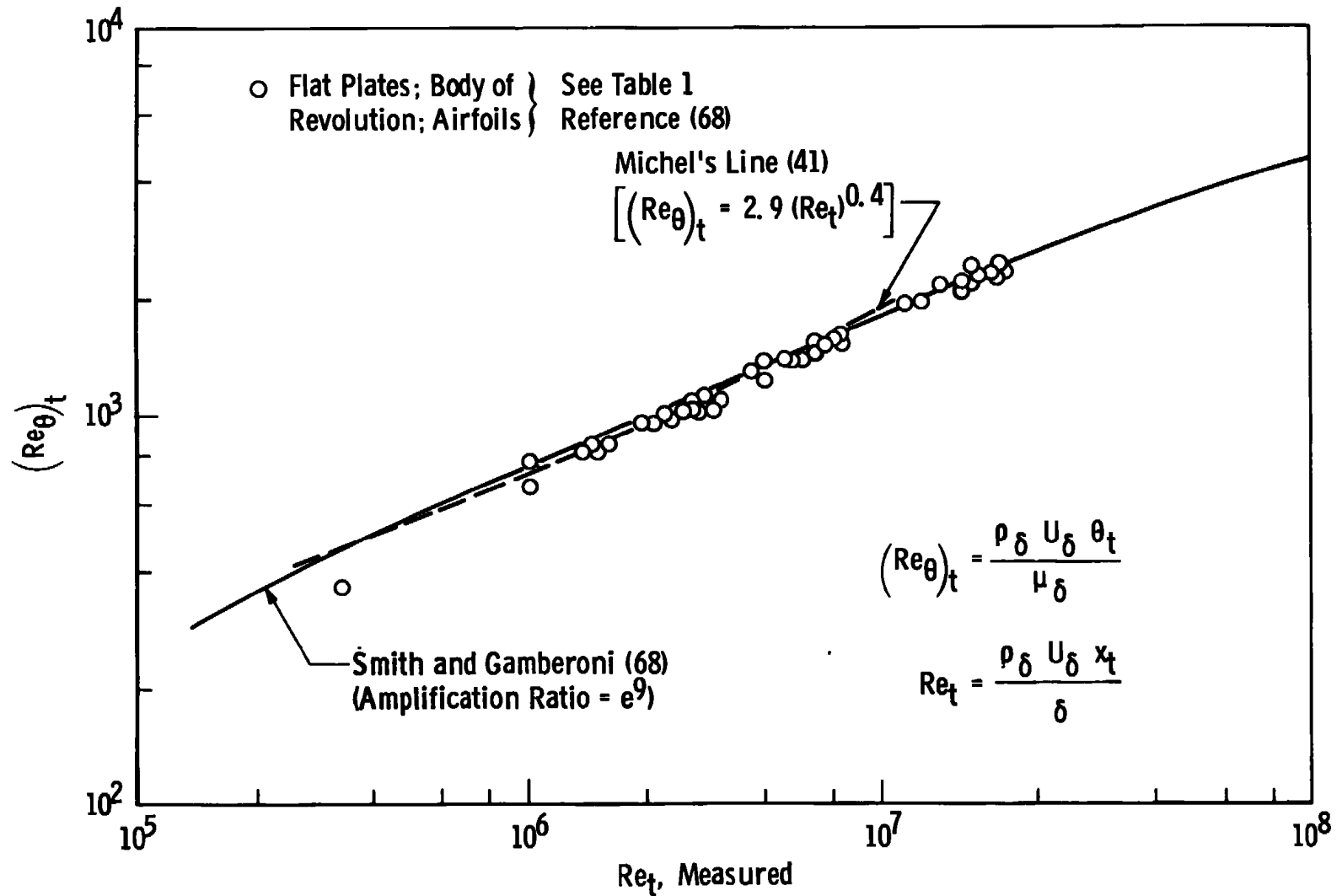
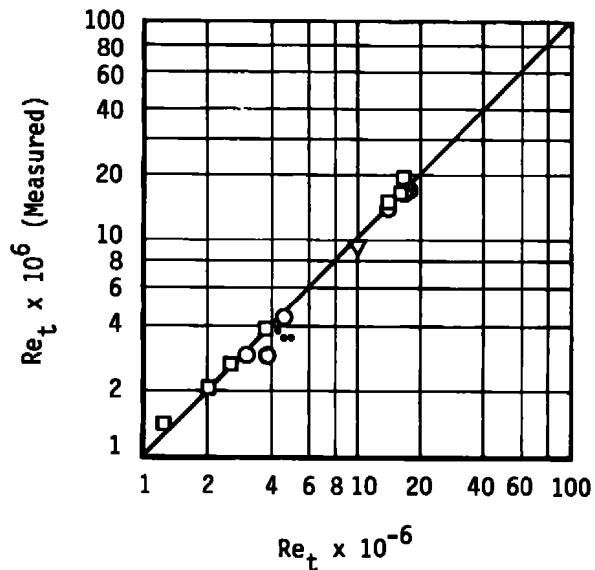


Figure II-1. Correlation and prediction of incompressible flow transition Reynolds numbers [from Reference (68)].

Data Represent Incompressible Flow  
over Flat Plates, Airfoils, and  
Bodies of Revolution as Specified  
in Ref. 15.

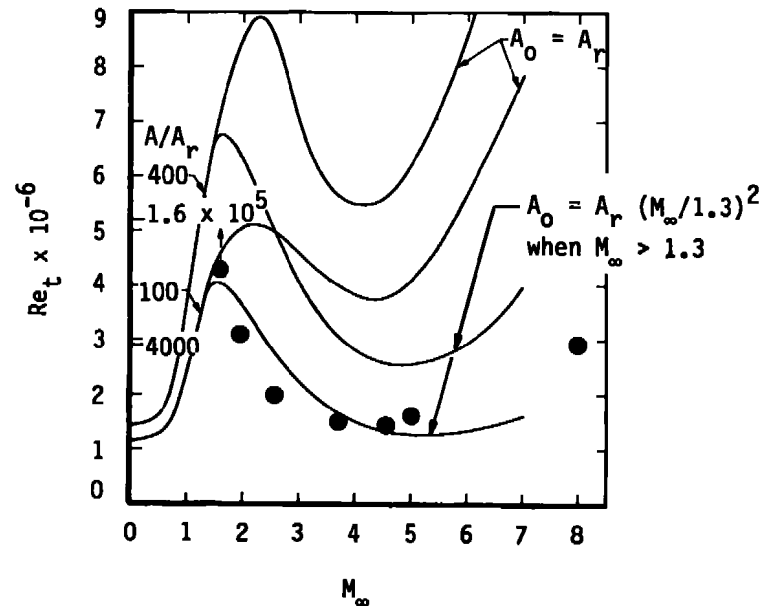
Calculated at Amplification Ratio =  $e^{10}$



a. Overall Correlation of Transition  
Data [from Reference (15)]

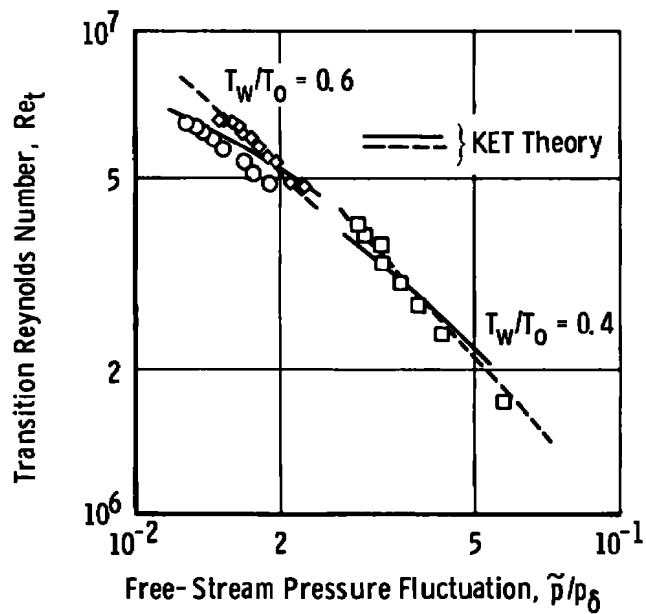
● Experimental Data (Flat Plate,  
 $\alpha = 0$ ),  $T_w = T_{Aw}$

— Calculated

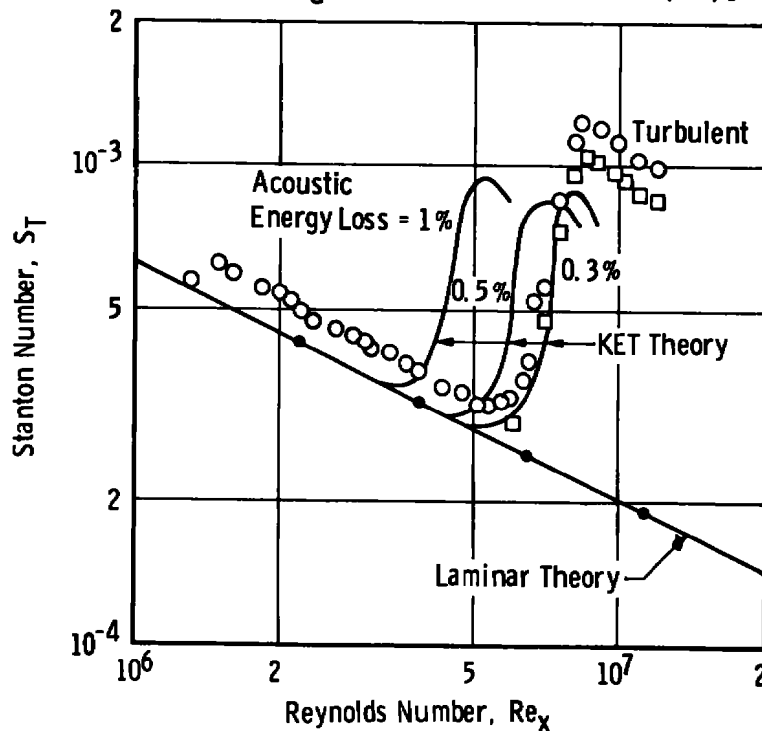


b. Theoretical Calculations of Effect  
of Mach Number on Transition for  
Two  $A/A_r$  and Two Assumptions About  
Initial Disturbance Amplitude [from  
Reference (13)]

Figure II-2. Application of laminar stability theory to predicting boundary-layer transition.



a. Effect of Free-Stream Fluctuating Pressure on Boundary-Layer Transition Location on Sharp Cones at  $M_e = 5$  [from Reference (24)]



b. Heat-Transfer Distributions

Figure II-3. Comparison between measured and predicted transitional heat transfer with transition triggered from pressure-velocity fluctuation [from Reference (24)].

objection to this approach, at least by the proponents of linear stability theory, is the absence of a critical frequency in the theory and only a requirement that the free-stream disturbance amplitude (or energy) be specified.

This technique has been used with some success in predicting the occurrence of transition and of relaminarization of turbulent boundary layers subjected to strong favorable pressure gradients.

Of particular significance to the present research is the fact that pressure fluctuations (aerodynamic noise) as presented in this thesis are considered by Shamroth and McDonald (24) as the primary source of the free-stream disturbances which they incorporate into their kinetic energy of turbulence formulation. Shamroth and McDonald (24) reported that only a small amount ( $\approx 1\%$ ) of acoustic energy absorption is required to trigger transition. Presented in Figure II-3 are computed results of Shamroth and McDonald (24) compared with experimental heat-transfer data. It is important to note that the acoustic energy loss (absorbed) must be specified. Therefore, for the data presented in Figure II-3 it is not known a priori which disturbance level should be used to predict the location of transition.

#### IV. CORRELATIONS BASED ON PHYSICAL CONCEPTS

Several examples of this type prediction technique will be briefly discussed:

1. Michel (41) was successful in correlating low turbulence wind tunnel transition Reynolds number data obtained on smooth surface wings having varying pressure gradients in

subsonic incompressible flow. Michel used the momentum thickness Reynolds number ( $Re_\theta$ ) as the correlating parameter. His correlation is shown in Figure II-1, Granville (64) using Michel's hypothesis that the transition Reynolds number ( $Re_t$ ) was related to a momentum thickness Reynolds number ( $Re_\theta$ ) [just as there is a minimum critical Reynolds number ( $Re_{cr}$ ) stability theory] successfully correlated low speed flows using the parameter ( $Re_t - Re_{cr}$ ) with  $Re_\theta$ . (Below  $Re_{cr}$ , all small disturbances are damped).

2. van Driest, et al. (39) used Liepman's hypothesis (75) that transition will occur at a critical Reynolds number ( $Re_{cr}$ ) that is equal to the ratio of the turbulent shear stress (Reynolds stress)  $\rho \overline{u'v'}$  and the viscous stress  $\mu du/dy$ , i.e.,  $Re_{cr} = \rho \overline{u'v'} / [\mu (du/dy)]$ . By evaluating the Reynolds stress using Prandtl's mixing length hypothesis and using the Pohlhausen velocity profile to determine  $du/dy$ , van Driest developed a semi-empirical equation for transition Reynolds number in incompressible flow that accounts for the effect of free-stream turbulence through the effect of the pressure fluctuation on the pressure gradient and consequently the velocity profile through the Pohlhausen shape factor. Presented in Figure II-4 are some of the classical subsonic data plotted versus free-stream vorticity disturbance (or velocity fluctuation). Included in Figure II-4 is van Driest's semi-empirical equation with the constants adjusted to match the older data. Note that the more recent data of Spangler and

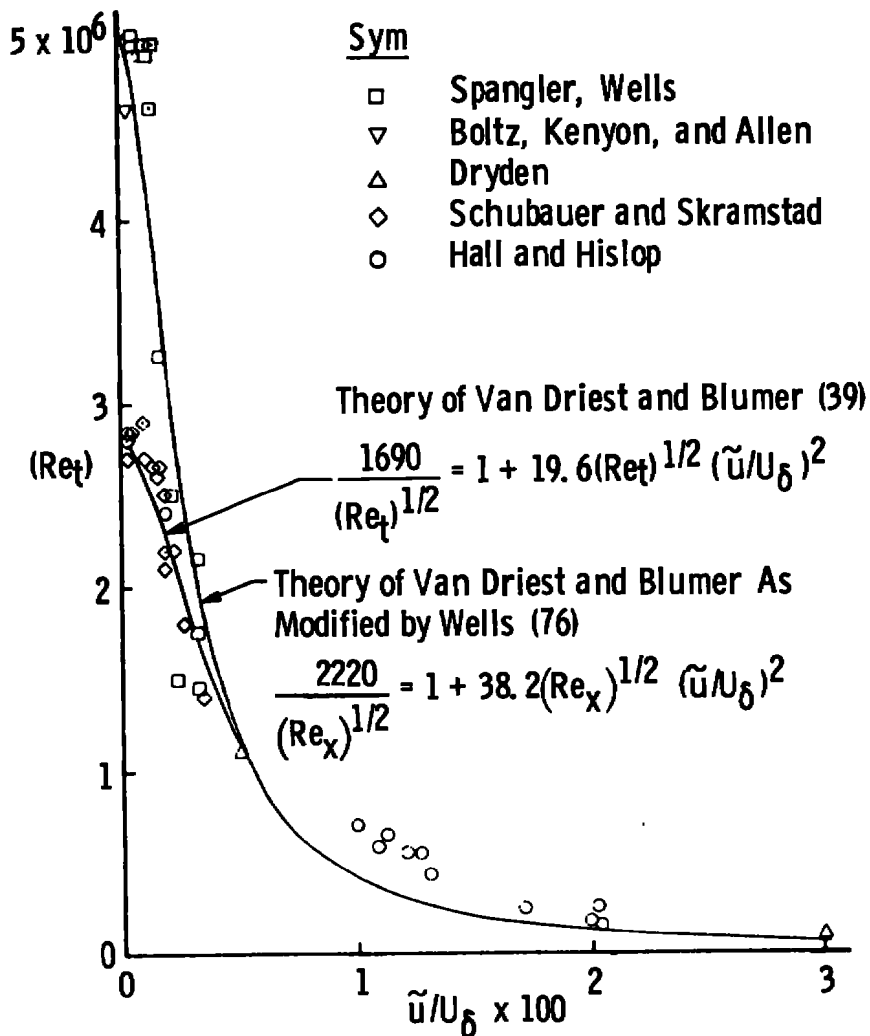
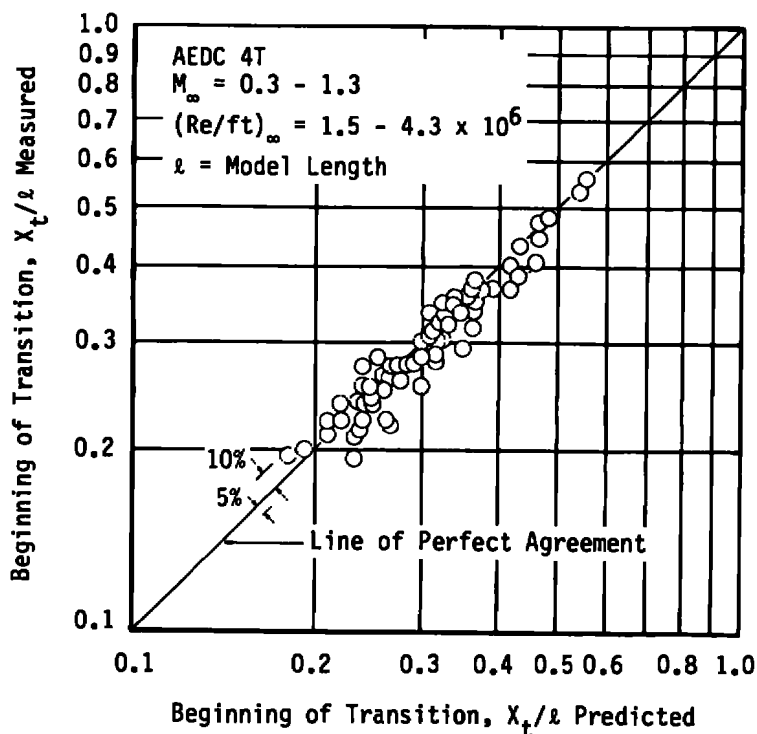


Figure II-4. Data on the effect of free-stream turbulence on boundary-layer transition, compared with data of other investigators and theory of van Driest and Blumer [from References (39) and (76)].

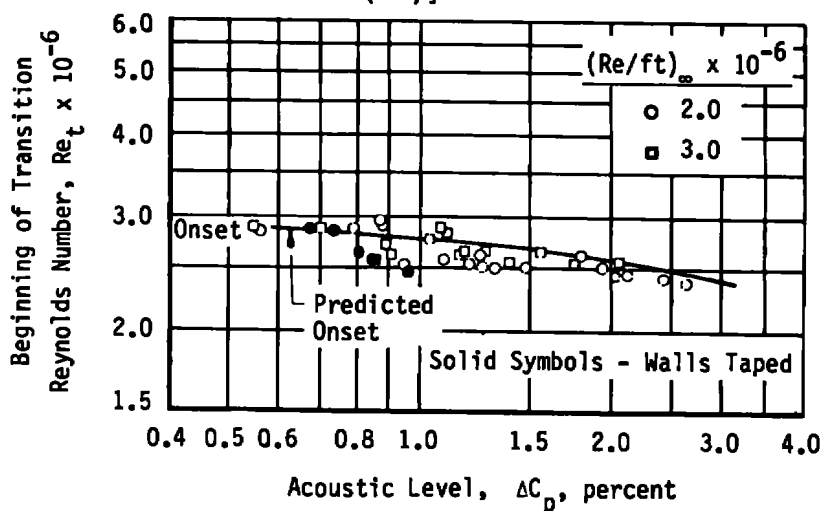
Wells (40) are much higher than the older Schubauer-Skramstad data (32). Wells (76) developed a new expression using the new data, and this equation is also shown in Figure II-4.

3. Benek and High (77) followed the approach used by van Driest et al. and successfully developed a semi-empirical expression for compressible transonic and low supersonic flow that successfully predicts transition on sharp slender cones. Typical results are shown in Figure II-5.
4. The laminar boundary-layer profile in a three-dimensional viscous flow such as a swept wing or cylinder will have a twisted profile that can be resolved into tangential ( $u$ ) and normal ( $w$ ) velocity components as illustrated in Figure II-6. Owen and Randall (33) found that the instantaneous jump of transition from the trailing edge to near the leading edge of subsonic swept wings could be correlated with a critical crossflow Reynolds number. This phenomenon is illustrated in Figure II-7. This critical crossflow Reynolds number is a function of the maximum crossflow velocity (normal component) and a thickness defined as nine-tenths the boundary-layer thickness as shown in Figure II-6. This type of transition process can be related physically to the instability of the boundary layer as a result of the inflection point in the crossflow profile.

The crossflow concept was investigated initially at subsonic speeds by Owen and Randall (33) and at supersonic conditions by Chapman (34) using swept cylinders and by Pate (18) using supersonic swept wings.



a. Comparison of Predicted and Measured Transition Locations [from Reference (77)]



b. Transition Reynolds Number as a Function of Acoustic Level in the AEDC-PWT 16T. Comparison with Prediction [from Reference (77)]

Figure II-5. Comparisons of Benek-High method for predicting transition with experimental sharp cone data,  $M_\infty \approx 0.4-1.3$ .



### Local Crossflow Reynolds Number

$$\chi = \frac{(\rho_e)(w_{\max})(0.9)(\delta)}{\mu_e}$$

### Crossflow-Dominated Transition Criteria

- $\chi < 100 \rightarrow$  Laminar Boundary Layer  
 $100 \leq \chi \leq 200 \rightarrow$  Vortex Formation and Transitional Boundary Layer  
 $\chi > 200 \rightarrow$  Turbulent Boundary Layer

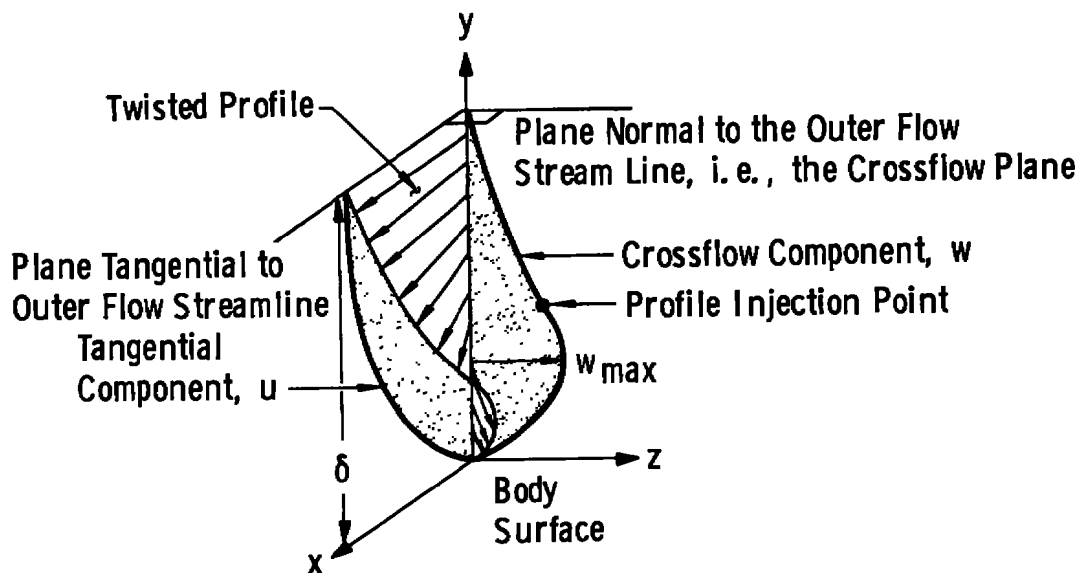


Figure II-6. Three-dimensional boundary-layer velocity profile and cross-flow Reynolds number criteria.

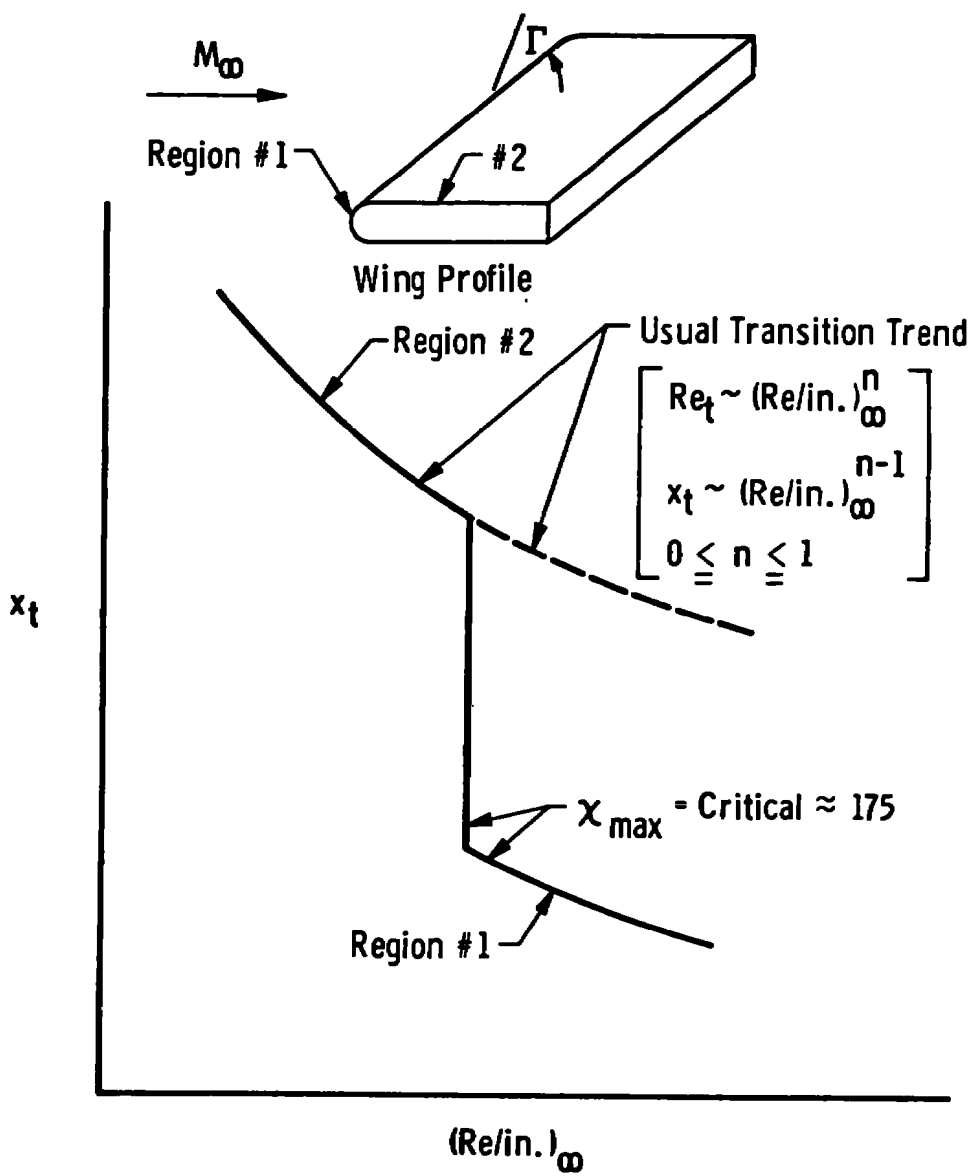


Figure II-7. Critical cross-flow influence on the boundary-layer transition profile.

More recently, Adams (35) extended this concept to supersonic sharp cones at incidence. Adams, et al. (36) explained high heating rates on the NASA space shuttle at incidence using the crossflow concept.

This technique is classified as semi-empirical since it requires a theoretical solution of the three-dimensional laminar boundary, and transition is then predicted to occur when the crossflow Reynolds ( $\chi$ ) number reaches a value of  $\approx 150$  to 175 as first reported by Owen and Randall. This empirical constant appears to hold for subsonic and supersonic flow regimes and for all types of geometries as shown by the correlation presented in Figure II-8.






## V. DATA CORRELATIONS

By far the largest effort to provide methods for predicting boundary-layer transition has been devoted to conducting experimental studies and attempting to develop useful correlations based on the observed trends and variations in transition with certain parameters and variables. These correlations can be divided into two general areas:

1. Tripped flows
2. Smooth body flows.

### Tripped Flows

Since surface roughness is present, more or less, on all vehicles, its effect on the location of transition has received much attention at both subsonic and supersonic speeds. Also the necessity for simulating fully developed turbulent flow on wind tunnel models has prompted many trip-effectiveness studies. If one knows the local flow conditions,

	Sym	Source	Configuration	Method of Detecting $X_t$
$X_{\max}$ Computed at Experimentally Determined Transition Location		Reference (33)	Subsonic Swept Wings	Flow Visualization
		Reference (34)	Yawed Cylinders	Heat-Transfer
		Reference (18)	Supersonic Swept Wing	Surface Pitot Probe
		Reference (36)	Space Shuttle ( $M_\infty = 8$ )	Heat Transfer ( $\alpha = 30$ and $50$ deg)
		Reference (35)	Sharp Cone ( $M_\infty = 7.4$ )	Flow Visualization ( $\alpha = 5$ deg)

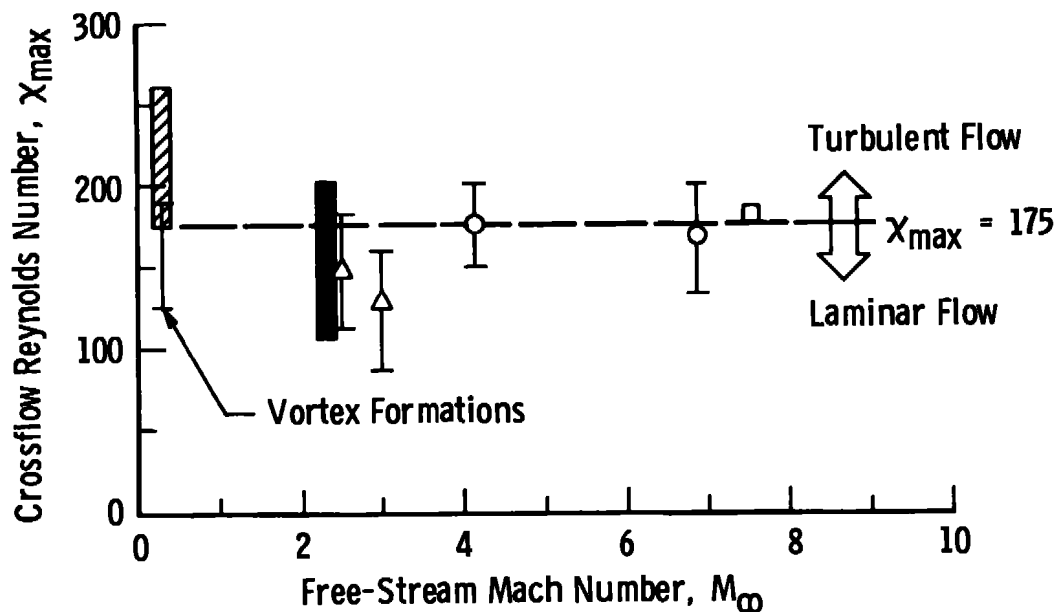


Figure II-8. Correlation of transition and cross-flow Reynolds number.

trip geometry, and certain boundary-layer properties (i.e.,  $\delta$ ,  $\delta^*$ ) at the trip location, then, in general, reasonable estimates of the location of transition can be made using existing methods. Results from three of these methods are briefly discussed to illustrate the correlation parameters used.

At subsonic speeds, Dryden (78) successfully correlated the effectiveness of two-dimensional elements (wires) and cylindrical roughness elements in promoting early boundary-layer transition. This correlation is shown in Figure II-9.

Van Driest et al. (16,17,79) conducted a systematic experimental and analytical program and successfully correlated the location of the "effective" transition location for spherical roughness heights, and the effects of roughness in conjunction with wall cooling and Mach number ( $0 < M_\infty < 4$ ) on flat plates, sharp cones, and hemispherical blunt bodies.

The trip correlation developed by Potter and Whitfield (37) for flat plates and sharp cones is, to this author's knowledge, the most comprehensive of any published to date and incorporates the effects of trip size, wall cooling, and local Mach number ( $0 < M_\delta < 10$ ). This correlation also predicts the trip size required to move transition from its smooth body location to the trip location or any point in between.

A portion of the research presented in this dissertation is directed toward determining if the radiated noise disturbance present in the free stream of supersonic wind tunnels and the resulting large variation in smooth body transition on flat plates and cones with tunnel size invalidates the correlations of van Driest and Potter-Whitfield. These results are presented in Appendix E.

$k$  = Roughness Height

$\delta_k^*$  = Boundary-Layer Displacement Thickness at  $x_k$  Location

$Re_t$  = Tripped Transition Reynolds Number

$Re_0$  = Smooth Body Transition Reynolds Number

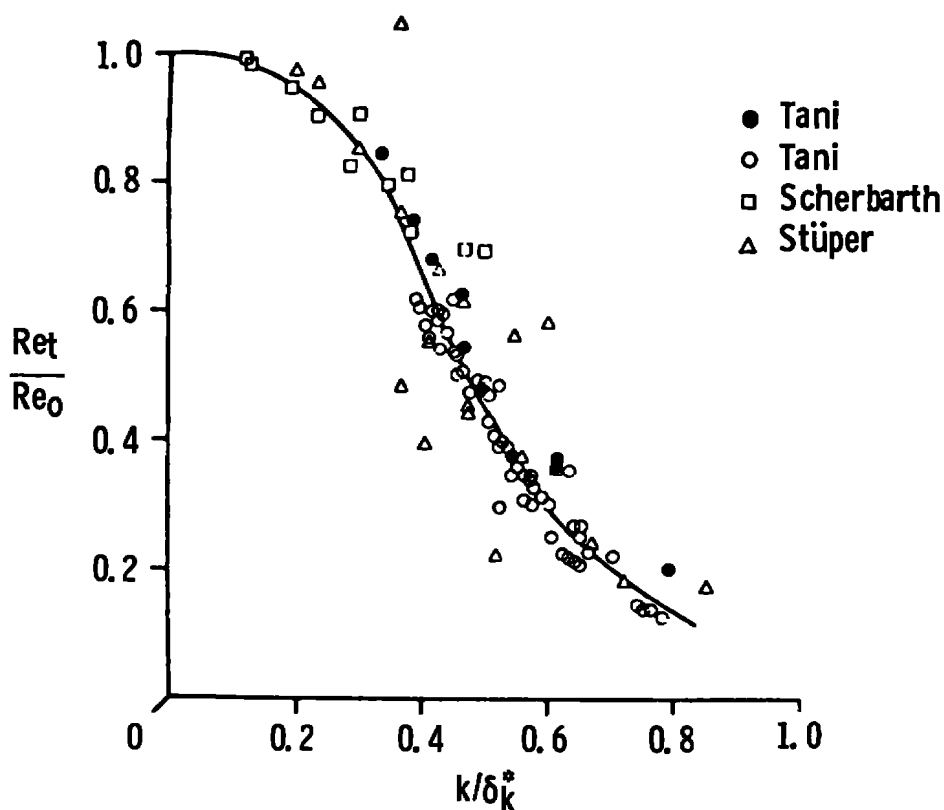


Figure II-9. Ratio of transition Reynolds number of rough plate to that of smooth plate and ratio of height of roughness element to boundary-layer displacement thickness at element, single cylindrical (circle and square symbols) and flat-strip elements (triangular symbols) [from Reference (78)].

Other extensive experimental studies using different trip geometries at hypersonic conditions have been performed and reported in Reference (20).

The problem of roughness effects on transition is always a current problem<sup>5</sup> as illustrated by recent wind tunnel tests conducted to establish the effective roughness of the thermal insulating tiles on the space shuttle orbiter (80).

### Smooth Body Flows

In correlations of transition Reynolds numbers on smooth wall, two-dimensional models (flat plates or hollow cylinders) at supersonic speeds the effects of Mach number, leading-edge bluntness, wall cooling, unit Reynolds number, and leading-edge sweep have been considered. The studies by Deem et al. (63) were perhaps the most extensive in scope of these types of correlations.

Deem et al. (63) considered all five of the above parameters and variables, and their research included both extensive experimental and analytical efforts. Their objective was to place in the hands of the design and test engineer a tool in the form of an analytical expression that would give reasonable prediction of the location of transition on a flat plate at zero incidence and at supersonic-hypersonic Mach numbers.

---

<sup>5</sup>Aircraft companies have very tight fabrication tolerances for rivet heads, joints, etc. on aircraft to ensure maximum lengths of laminar flow is maintained.

Their correlation did not include the effects of free-stream disturbance<sup>6</sup> and consequently often provides only qualitative predictions. Nevertheless, there is still considerable interest in these types of correlations as evidenced by the report by Hopkins and Jillie (22) and Hairstrom (67). In References (22) and (67) the analytical expressions developed by Deem et al. have been presented in graphical form for rapidly estimating the transition location for flat-plate wind tunnel models with supersonic leading edges at zero angle of attack. Deem et al. also compared the estimated  $Re_t$  for each data point used in developing their correlation, and the result is shown in Figure II-10. The standard deviation was 33%.

Beckwith and Bertram (81) developed supersonic-hypersonic transition correlations using boundary-layer parameters such as  $Re_{\delta^*}$  and local flow conditions  $M_e$  and  $h_e$  and the wall parameter  $h_w$ . Their correlations were developed using a digital computer to define functional relationships and corresponding coefficients that produced the smallest standard deviation ( $\delta_x$ ). An example of one correlation developed for wind tunnel data is presented in Figure II-11. Correlations for ballistic range and free-flight data were also developed and published in Reference (81).

$$F_2 = \sum_{i=0}^m \left[ \left( \sum_{j=0}^k a_{ij} M_e^j \right) \left( \frac{h_w}{h_e} \right)^i \right] \quad (1)$$

---

<sup>6</sup>In conventional supersonic wind tunnels, the transition location is dominated by aerodynamic noise and can vary as much as a factor of three between small (1-ft) and large (16-ft) wind tunnels as discussed in Chapters VII through XI.



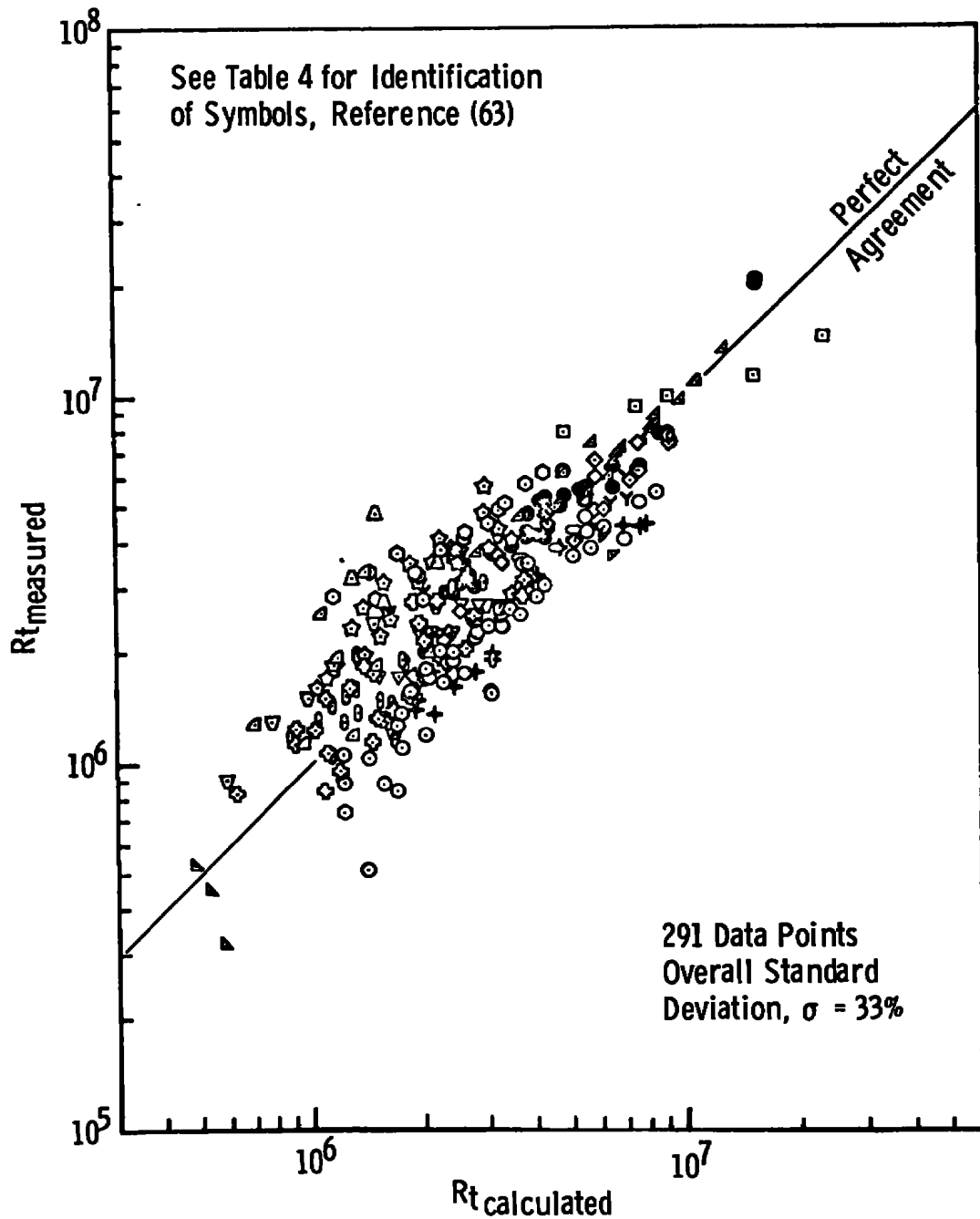


Figure II-10. Comparison of measured and predicted transition Reynolds numbers [from Reference (63)].

$$\text{General Eq. } F_2 = \sum_{i=0}^k \left[ \left( \sum_{j=0}^k a_{ij} M_e^j \right) \left( \frac{h_w}{h_e} \right)^i \right]$$

For Wind Tunnel Data:

$$F_2 = 1.6002 + 0.14207 M_e + 0.27641 \left( \frac{h_w}{h_e} \right) - 0.032828 M_e \left( \frac{h_w}{h_e} \right) \\ - 0.042888 \left( \frac{h_w}{h_e} \right)^2 + 0.0054027 M_e \left( \frac{h_w}{h_e} \right)^2$$

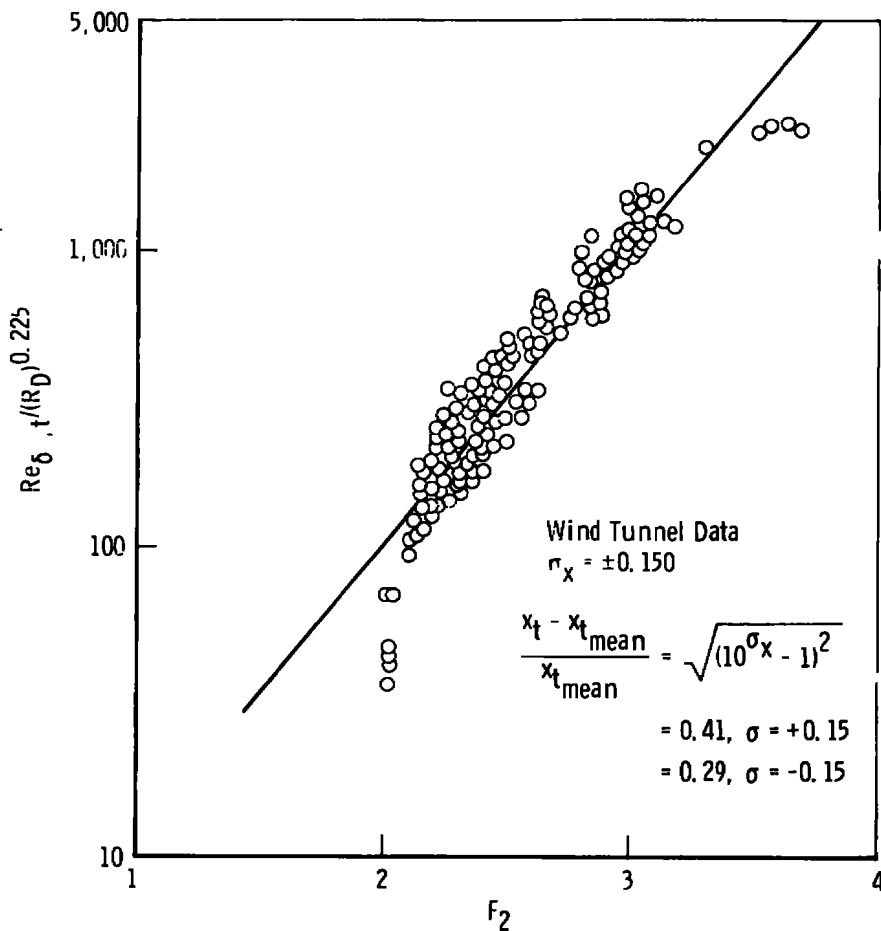


Figure II-11. Correlation of sharp cone transition Reynolds numbers at supersonic-hypersonic conditions and zero angle of attack [from Reference (81)].

For wind tunnel sharp-cone transition data, Beckwith and Bertram determined the  $F_2$  parameter to be

$$\begin{aligned}
 F_2 = & 1.6002 + 0.14207 M_e + 0.27641 \left( \frac{h_w}{h_e} \right) \\
 & - 0.032828 M_e \left( \frac{h_w}{h_e} \right) - 0.042888 \left( \frac{h_w}{h_e} \right)^2 \\
 & + 0.0054027 M_e \left( \frac{h_w}{h_e} \right)^2
 \end{aligned} \tag{2}$$

The location of transition can be determined using the  $F_2$  parameter in conjunction with Eq. (3) as determined from Figure II-11.

$$\log_{10} \left[ \frac{R_{\delta^*,t}}{(R_D)^n} \right] = A + B F_2 \tag{3}$$

where A and B are constants. From Reference (81) for sharp cones

$$n = 0.225$$

$$A = 0.11168$$

$$B = 0.94935$$

and

$Re_{\delta^*,t}$  = Reynolds number based on the boundary-layer displacement thickness at the transition location,  $x_t$ .

$R_D$  = Reynolds number based on model base diameter.

From Figure II-11 and Eqs. (1), (2), and (3), it is seen that the transition correlation becomes quite complicated. The results presented in Figure II-4 and the additional correlations presented in Reference (81) are the most comprehensive published to date and represent several years of effort by researchers at the NASA Langley Research Center. The

standard deviation for wind tunnel sharp-cone transition data is between 29% and 41% as illustrated in Figure II-11. These correlations can only be judged to be fair in their ability to provide reasonable predictions of transition Reynolds numbers.

Recently, Kipp and Masek (82) and Fehrman and Masek (8) attempted to correlate high Mach number transition Reynolds numbers measured on the windward centerline of the NASA orbiter at angle of attack using  $Re_\theta$ ,  $M_\theta$ , and the local unit Reynolds number ( $Re_\theta/ft$ ) as the correlating parameters. The correlation from Reference (8) is shown in Figure II-12, and the scatter in the correlation of the data is seen to be quite large.

### Summary

In concluding this section, it seems that past history indicates that the transition correlations and prediction methods for smooth bodies that are based on physical concepts seems to withstand the test of time and give more acceptable results than correlations based on observing trends and variations in experimental data.

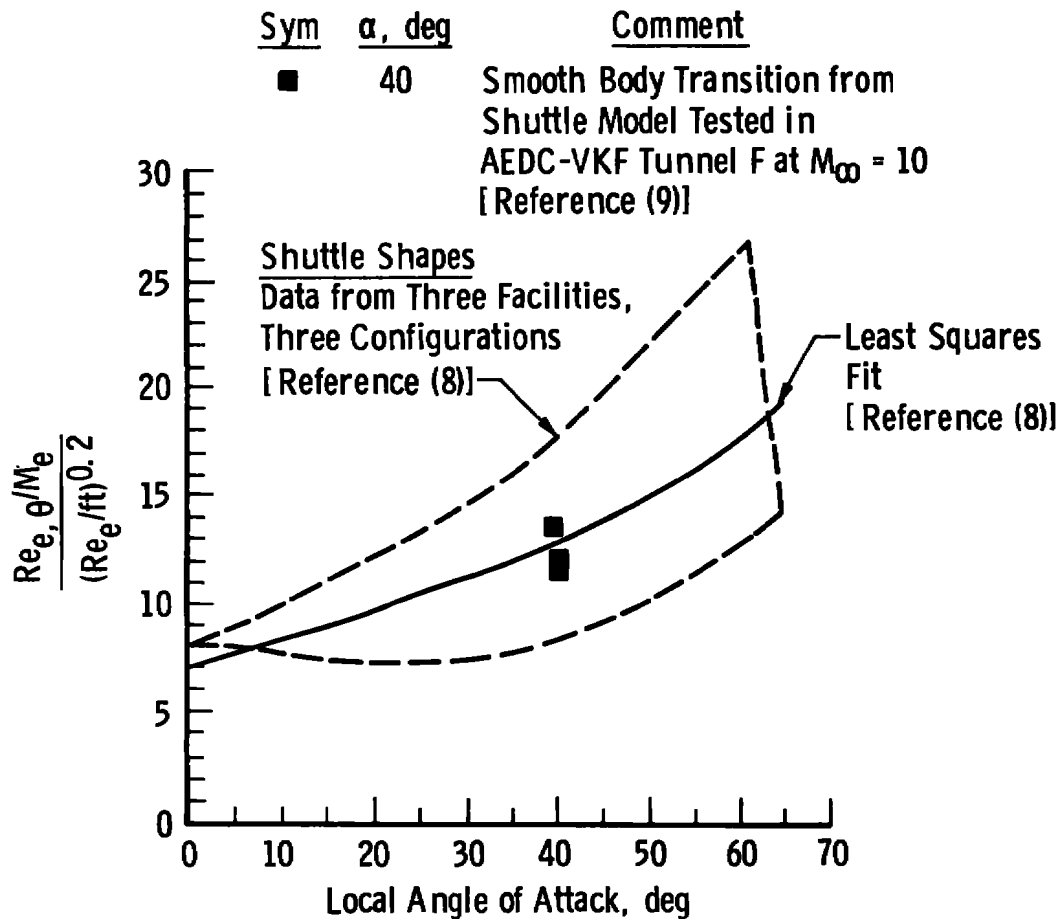


Figure II-12. Correlation of space shuttle wind surface centerline transition Reynolds number data [from Reference (8)].

## CHAPTER III

## RADIATED AERODYNAMIC NOISE IN SUPERSONIC WIND TUNNELS

## I. INTRODUCTION

In Chapter I, the various types of test section free-stream disturbances present in wind tunnels were discussed. The origins of these disturbances (both steady and unsteady) were identified along with their relative intensity and their effect, or probable effect, on boundary-layer transition.

This chapter is devoted exclusively to discussing the dominant source of disturbance present in well-designed supersonic wind tunnels, i.e., radiated aerodynamic noise from the tunnel wall turbulent boundary layer. The major literature references dealing with wind tunnel generated aerodynamic noise are reviewed and the significant contributions from these publications are discussed. The mechanism that generates the aerodynamic noise, the intensity and spectra of these unsteady isentropic pressure waves, and the wind tunnel parameters that affect the radiated pressure rms value ( $\hat{p}_{rms}$ ) are identified. Emphasis is placed primarily on presenting and discussing experimental pressure fluctuating intensity and spectra data obtained in the tunnel free-stream using the hot-wire anemometer. The theory (83,84,85) is not presented here; however, analytical expressions as required in discussing the experimental data are presented. Extensive discussions of the application of the technique to measure aerodynamic noise has been presented in detail in References (38) and (85) through (91).

## II. ORIGINS OF DISTURBANCE MODES

Kovaszny (43) identified three major types of disturbance fields in compressible flow wind tunnels: (a) vorticity (velocity fluctuations), (b) entropy fluctuations (temperature spottiness), and (c) sound (pressure fluctuations). Starting with the Navier-Stokes equation for a flat plate (three momentum equations) plus the energy equation, the continuity equation, and the perfect gas equation of state, Kovaszny introduced the small perturbation concept, i.e.,  $p = \bar{p} + p'$ ,  $T = \bar{T} + T'$ ,  $\rho = \bar{\rho} + \rho'$ , into the equations of motion. Dropping higher order terms, he obtained a set of linear, partial differential equations. By taking the curl of the momentum equation, Kovaszny obtained a separate, second order partial differential equation for vorticity ( $\omega = \text{curl } V$ ) that was uncoupled from pressure and entropy and which was similar to the classical heat equation. By combining the continuity equation and the divergence of the momentum equation, he then obtained an uncoupled second order partial differential equation for pressure. This equation was similar to the wave equation, and consequently Kovaszny defined the pressure that obeyed this equation as a sound wave. Using further manipulation, he developed a second order, partial differential equation for entropy that was also similar to the classical heat conduction equation but uncoupled from pressure and vorticity. Since the resulting equations were linear, then the different modes did not interact (uncoupled); however, if strong gradients exist such as a shock wave then small perturbation theory no longer is valid, the resulting equations are nonlinear, and there is a coupling between the three modes.

Kovaszny (43) then showed that the hot-wire anemometer could be operated in a supersonic flow and the three disturbance modes (vorticity, entropy, and sound) could be represented by the rms output of a hot wire operated at different temperatures. Figure III-1 illustrates the characteristics exhibited by these three modes.

Kovaszny conducted hot-wire experiments and showed that all three disturbances could be present in wind tunnels. The presence of entropy fluctuations (temperature spottiness) was confirmed from stilling chamber measurements and free-stream measurements using various types of stilling chamber arrangements and tunnel air heating apparatus. Free-stream hot-wire data produced a mode diagram similar to Figure III-1c. A fluctuating pressure field (sound waves) was generated using a weak shock emanating from the leading edge of a sharp flat plate. The mode diagram of a hot wire placed in an oscillating flow field generated by a weak wave produced a mode diagram similar to Figure III-1a. Thus Kovaszny developed the analytical models and produced some experimental data at  $M_\infty = 1.7$  to support his three-mode theory.

In 1955, Laufer and Marte (46) presented results of a systematic investigation of factors affecting the location of transition on adiabatic cones and flat plates at  $M_\infty$  between 1.5 to 4.5. They investigated various methods for detecting transition and predicting the effects of the stilling chamber turbulence level, surface roughness, Mach number, and unit Reynolds number on transition. Following the earlier work of Kovaszny (43) Laufer and Marte showed that even though significant levels of stilling chamber turbulence could be present, above about  $M_\infty = 2.5$  the effects on cone transition Reynolds numbers were negligible



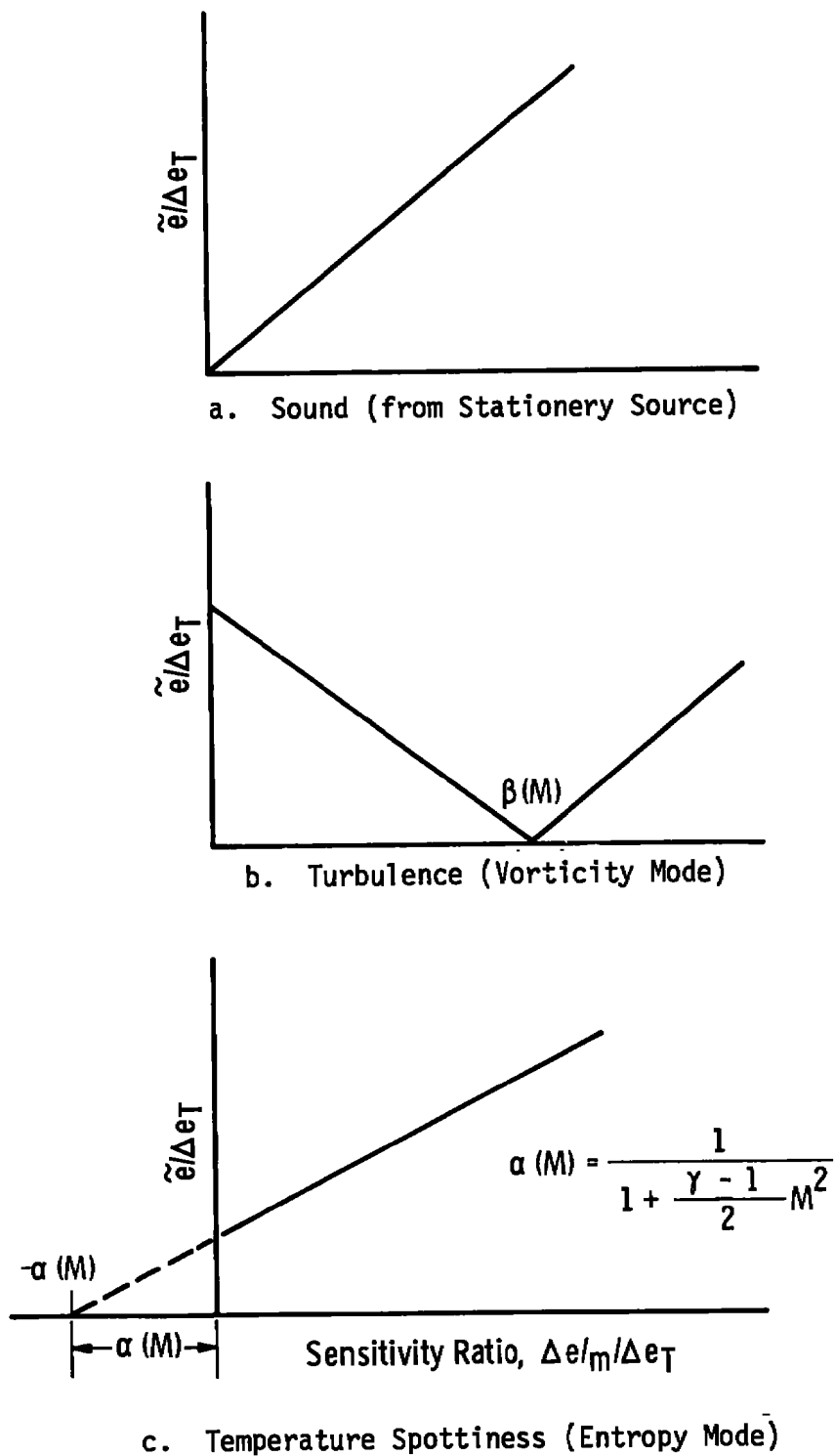


Figure III-1. Comparison of fluctuation diagram for three modes [from Reference (43)].

(as discussed in Chapter II). They also speculated that the pressure disturbance turbulence field generated by the tunnel wall turbulent boundary might influence transition. They commented on operating the JPL supersonic tunnel with a laminar and turbulent boundary layer on the tunnel walls to check this possibility, but the tunnel could not be operated at a low enough pressure to produce the laminar flow condition. As an alternate approach, they tried shielding a hollow-cylinder transition model from the radiated noise by using a larger protective hollow-cylinder shield model. The idea was to isolate the transition model from the turbulence field emanating from the tunnel walls. However, disturbances generated by the larger outer shield model impinged on the inner transition model and caused the transition point to move forward; thus the experiments were invalidated. However, Laufer and Marte were the first to focus attention directly on radiated aerodynamic noise as a possible source of significance disturbances in supersonic wind tunnels. They further speculated that the effects of tunnel pressure level (i.e., unit Reynolds number) on transition Reynolds numbers might be explained as an effect caused by acoustic disturbances.

Morkovin in 1957 (44) discussed the possible sources of free-stream disturbance in supersonic wind tunnels. Following Kovasznay (43) he discussed the sources that could produce free-stream turbulence: (1) vorticity fluctuations, (2) entropy fluctuations, and (3) sound waves. He further classified sound waves as; (1) radiation from the wall turbulent boundary layer, (2) shimmering Mach waves from wall roughness or waviness, (3) wall vibrations, and (4) diffraction and scattering of otherwise steady pressure gradients. Morkovin further stated that any

of the three principle modes or any of the four specific sound sources could promote early transition if the disturbance levels were high enough. In conclusion, Morkovin stated that transition studies must be conducted with care, all experimental transition data evaluated with care, and all inferences drawn with caution.

Morkovin in 1959 (45) commented further on wind tunnel disturbances. He discussed ways to effectively reduce vorticity fluctuations and entropy fluctuations by proper stilling chamber design. However, he stated that the sound from the turbulent boundary layer would probably be the major disturbance. Morkovin stated that this type of disturbance was very difficult to measure or to predict theoretically. Furthermore he stated that seemingly little could be done to appreciably reduce its intensity level.

### III. EXPERIMENTAL CONFIRMATION

Laufer (38) reported in 1959 on an investigation using a hot wire to study free-stream disturbances in supersonic wind tunnels. The experiments were conducted in connection with boundary-layer stability experiments and the knowledge that Tollmien-Schlichting oscillations could not be detected if free-stream disturbance levels were high (32). Starting with the basic hot-wire equation

$$e' = \Delta e_T T_T' / \bar{T}_T - \Delta e_m m' / \bar{m} \quad (4)$$

the time averaged, mean-square of the measured voltage fluctuation ( $\tilde{e}^2$ ) can be written as

$$\frac{(\tilde{e})^2}{(\Delta e_T)^2} = \frac{(\tilde{e}')^2}{\Delta e_T^2} = \frac{(\tilde{T}_T')^2}{\bar{T}_T^2} - 2r R_{mT} \frac{\tilde{m} \tilde{T}_T}{\bar{m} \bar{T}_T} + r^2 \frac{(\tilde{m}')^2}{\bar{m}^2} \quad (4a)$$

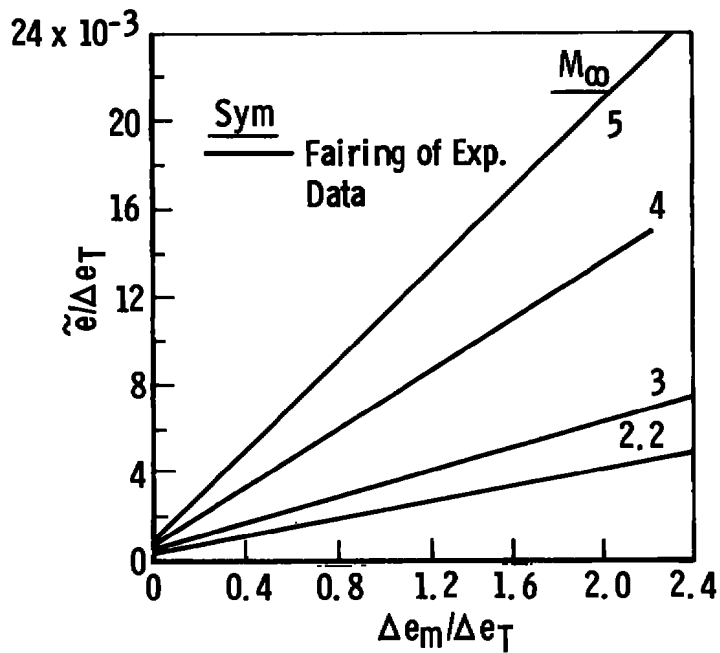
where

$$r = \frac{\Delta e_m}{\Delta e_T} \text{ and } R_{m_T} = \frac{\overline{(m')(\tau'_T)}}{\tilde{m} \tilde{\tau}_T}$$

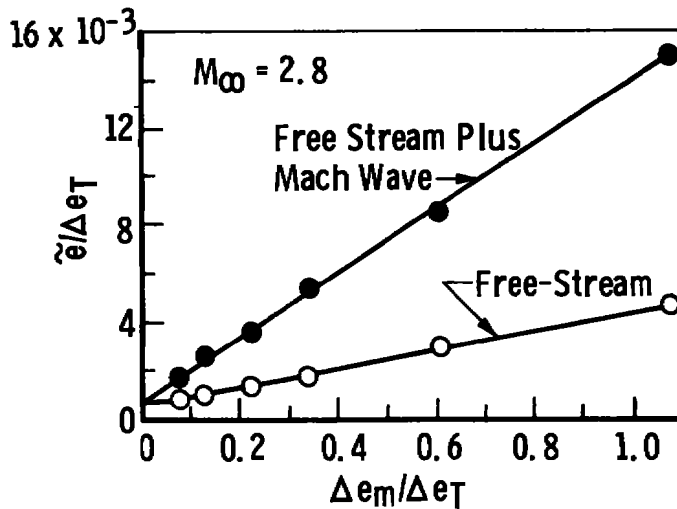
$\Delta e_T$  and  $\Delta e_m$  are sensitivity coefficients that are determined by mean flow conditions and the mean temperature of the hot wire (38).

The values of  $\overline{(\tau'_T)^2} = (\tilde{\tau}_T)^2$ ,  $\overline{(m')^2} = (\tilde{m})^2$  and  $R_{m_T}$  can be calculated when  $\overline{(e')^2}$  is measured for three different values of  $r$  (i.e., three different mean wire temperatures. Typical results measured by Laufer are presented in Figure III-2.

Laufer pointed out the startling fact that fluctuations at the high Mach numbers were 50 times greater than fluctuations measured in a low turbulence subsonic wind tunnel. Laufer also found that the correlation coefficient ( $R_{m_T}$ ) had a value of -1 (within measurement accuracy) for all conditions. This means that the mass flow and total temperature fluctuations are perfectly anticorrelated. Laufer then pointed out that no further information could be obtained directly from the hot-wire measurements; however, he showed analytically that if it were assumed that the fluctuations were pure vorticity (velocity fluctuations) then it could be shown that  $R_{m_T} = +1$ ; but  $R_{m_T} = +1$  contradicts the experimental data. Consequently, vorticity as the cause was eliminated. Laufer then assumed pure entropy fluctuations (temperature fluctuations) to exist and he obtained the correct slope. However, the computed value of  $r$  at  $\tilde{e}/\Delta e_T = 0$  was not consistent with the measurements. As shown by Kovasznay (43) at  $\tilde{e}/\Delta e_T = 0$  then  $r = -\alpha$ . For  $M_\infty = 2.2$ , one has (43)  $r = -\alpha = -(1 + \frac{\gamma - 1}{2} M^2)^{-1} = -0.508$  and for  $M_\infty = 5$ ,  $r = -\alpha = -0.167$ . From inspection of Figure III-2, one sees that the experimental data does not



a. Mode Diagrams for Free-Stream Radiated Noise Fluctuations [from Reference (38)]



b. Mode Diagram for a Fluctuating Mach Wave Superimposed on Free-Stream Fluctuations [from Reference (38)]

Figure III-2. Mode diagrams.

agree with these values. Thus, Laufer ruled out entropy fluctuations as the cause of the measured hot-wire fluctuations. Laufer also argued on physical grounds that vorticity and entropy could be ruled out. Since no temperature fluctuations had been measured in the stilling chamber and since temperature fluctuations are convected along streamlines, then if they are negligible in the stilling chamber they will be negligible in the test section. He also argued that the large contraction ratio in the JPL tunnel (40 at  $M_\infty = 1.6$  and 1,500 at  $M_\infty = 5$ ) diminished the stilling chamber velocity fluctuations to such a low value that they could not be the source of the disturbance. Following Kovasznay (43) Laufer then postulated that the only other simple fluctuating field would be a pure sound field in which the isentropic relationships between the fluctuating quantities hold. Inserting the small disturbance isentropic relationships

$$\frac{p}{\bar{p}} = \gamma \frac{p'}{\bar{p}} = \frac{\gamma}{\gamma - 1} \frac{T'}{\bar{T}}, \quad \frac{m'}{\bar{m}} = \frac{u'}{\bar{u}} + \frac{1}{\gamma} \frac{p'}{\bar{p}}, \quad \frac{T'}{\bar{T}} = \alpha(M)(\gamma - 1) \left[ \frac{p'}{\gamma \bar{p}} + M^2 \frac{u'}{\bar{u}} \right]$$

into the hot-wire equation (Eq. 4), Laufer (38) showed that the following root-mean-square voltage equation could be obtained when the condition  $R_{mT} = -1$  was applied.

$$\frac{\tilde{e}}{\Delta e_T} = \alpha(M)(\gamma - 1) \left[ M^2 \frac{\tilde{u}}{\bar{u}} - \frac{\tilde{p}}{\gamma \bar{p}} \right] + \left[ \frac{\tilde{p}}{\gamma \bar{p}} - \frac{u}{\bar{u}} \right] \frac{\Delta e_m}{\Delta e_T} \quad (4b)$$

where

$$\alpha(M) = \left( 1 + \frac{\gamma - 1}{2} M^2 \right)^{-1} \quad \text{and} \quad \frac{\tilde{p}}{\gamma \bar{p}} = \frac{\tilde{\rho}}{\bar{\rho}} = \frac{1}{\gamma - 1} \frac{\tilde{T}}{\bar{T}}$$

Equation (4b) is a linear equation and is consistent with the hot-wire data presented in Figure III-2a. The fluctuating pressure ( $\tilde{p}/\bar{p}$ ) and velocity ( $\tilde{u}/\bar{u}$ ) ratios can be determined from Eq. (4b) by solving two equations for two unknowns ( $\tilde{p}/\bar{p}$  and  $\tilde{u}/\bar{u}$ ) and by realizing the first term is

the ordinate intercept and the coefficient of  $\Delta e_m / \Delta e_T$  is the slope of the faired data presented in Figure III-2a.

Laufer, therefore, concluded that the measured free-stream disturbance was a fluctuating isentropic pressure field that emanated from the tunnel wall turbulent boundary. Laufer also presented other evidence to confirm his hypothesis.

1. A flat-plate shield that protected the hot wire from one tunnel wall caused a 25% drop in the mean-square voltage output.
2. He showed analytically, as did Kovasznay (43), that a fluctuating Mach wave (weak shock) would produce a straight line on the mode diagram and pass through the origin as illustrated in Figure III-1, page 46. By placing tape on the tunnel wall at exactly the right location, he showed that at  $r = 0$  the measured value of  $\tilde{e} / \Delta e_T$  equaled the no shock data and was a linear line but had a steeper slope. Thus he ruled out shimmering Mach waves as a possible source.
3. He also produced free-flight Schlieren photographs showing a sound field emanating from the turbulent boundary layer on a model.

Based on the results from his very thorough experimental investigation and supporting analytical analysis, Laufer concluded that the source of free-stream disturbances was the sound field (aerodynamic noise) emanating from the tunnel wall turbulent boundary layer. Laufer pointed out, however, that direct measurements of the sound field were

not yet available. Laufer further cautioned that stability and transition studies in supersonic wind tunnels would be handicapped by the presence of the sound field.

Vrebalovich (92) commented on Morkovin's paper on free-stream disturbances (45) and stated that hot-wire measurements made in the test section of the JPL tunnels showed that when the wall boundary-layer was turbulent, the free-stream mass-flow fluctuations not only increased with Mach number but were higher at the lower unit Reynolds number. Vrebalovich further stated that experiments (early 1960's) in the JPL 12-in. supersonic tunnel with either laminar, transitional, or fully turbulent boundary-layer flow on the tunnel wall produced the following results: (a) free-stream pressure fluctuation levels were smallest when the boundary layer was laminar and (b) tripping the boundary layer introduced less fluctuations in the free stream than when transition from laminar to turbulent flow occurred naturally between the nozzle throat and test section. These experiments in which the only change was in the nature of the tunnel wall boundary layer showed that a dominant source of free-stream disturbances at the higher Mach numbers was the aerodynamic sound radiated from the wall boundary layers.

During continuing studies conducted in the JPL wind tunnels, aerodynamic noise radiated by supersonic turbulent boundary layers was reported in January 1961 (93). In Reference (93) it was pointed out that previous JPL studies (38) had shown that: (a) the amplitude of pressure fluctuations increased with Mach number, (b) the intensity was uniform in the flow field, and (c) the pressure field manifested a certain directionality. Reference (93) presented results of investigations designed to establish if a correlation between the measured free-stream



pressure fluctuation and certain boundary-layer characteristics could be found. Figure III-3 presents the results of this effort. Figure III-3 is of particular interest since it was developed following the argument of Liepmann that pressure fluctuations are produced by displacement-thickness fluctuations.

The correlation shown in Figure III-3 is of special interest to the present study since in Chapter IX an aerodynamic noise transition Reynolds number correlation will be developed and the displacement thickness ( $\delta^*$ ) appears as one of the correlating parameters.

Phillips (94) proposed a theory to describe the generation of sound by turbulence at high Mach numbers. Laufer (86) in commenting on Phillips' theory, noted that it is based on the premise that the sound-generating mechanism consists of a moving, spacially random, virtually wavy wall formed by an eddy pattern that is convected supersonically with respect to the free-stream and is consistent with the principal features of the sound field found in experiments. Using this view, Laufer derived an expression for the pressure fluctuation intensity which is shown to be a function of the mean skin-friction coefficient, the wall boundary-layer thickness, lengths which scale with the boundary-layer thickness, convection speed, angle of the radiated disturbance, and free-stream Mach number. This theory was found to be in partial agreement with experimental data at Mach numbers from 1.5 to 3.5 and considerably below experimental data at Mach 5.

From Reference (86)

$$\frac{\tilde{p}}{\bar{p}_\infty \sqrt{C_F}} = \frac{\gamma}{\sqrt{2}} \frac{\tilde{u}}{U_\tau} \frac{L}{\delta} \sqrt{\frac{\tau}{\delta} \frac{U_\infty}{U_c}} \frac{M_\infty}{\sin \theta} \quad (5)$$

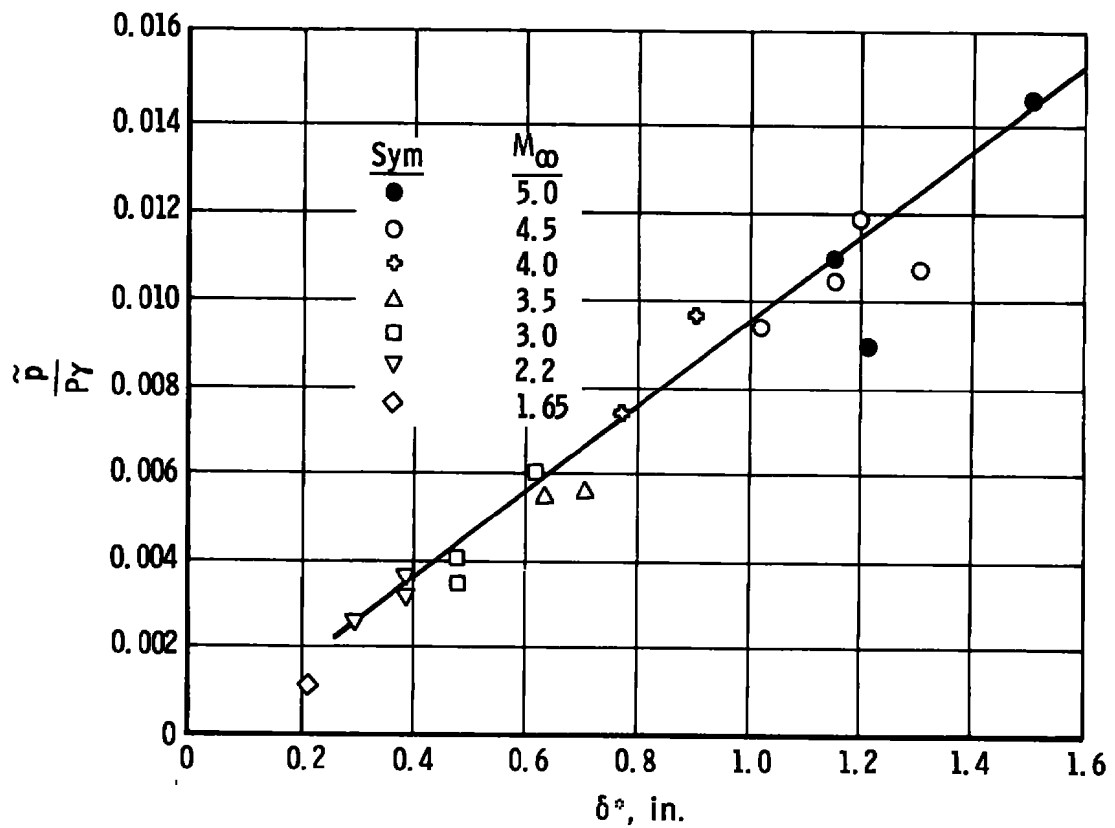


Figure III-3. Pressure fluctuation from a supersonic turbulent boundary layer [from Reference (93)].

where

$$\frac{U_c}{U_\infty} \approx 0.5; \quad U_\tau^2 = C_F/2U_\infty^2; \quad \tau = \text{time constant}; \quad U_c = \text{convection velocity} \quad (5a)$$

$$\cos \theta = \frac{1}{M_\infty \left[ 1 - \frac{U_c}{U_\infty} \right]} \quad (5b)$$

An important point to note from Eq. (5) is that the mean boundary-layer characteristics  $C_F$  and  $\delta$  and certain lengths appear as parameters in the free-stream pressure fluctuation equation. This fact is relevant to the analysis presented in Chapter IX.

Kistler and Chen (95) reported on pressure fluctuations that were made under a turbulent boundary layer on the sidewalls of the JPL 18- by 20-in. supersonic wind tunnel at  $M_\infty = 1.3$  to 5.0. Two findings of particular importance were:

1. The normalized pressure fluctuation ( $\tilde{p}/\tau_w$ ) on the surface of a flat plate was found to correlate with  $Re_\delta^*$ , and
2. The tunnel wall root-mean-square ( $\tilde{p}$ ) of the pressure fluctuation was found to be proportional to the tunnel wall turbulent skin friction as shown in Figure III-4.

Laufer (87) discussed the radiation field generated by a supersonic turbulent boundary layer at Mach numbers from 1.5 to 5 and compared the hot-wire results with those obtained by Kistler and Chen (93) using microphones positioned in the tunnel wall. In each of these tests, the wall and free-stream pressure fluctuations were found to scale with the mean wall shear for all Mach numbers as shown in Figure III-5, which was taken from References (87) and (96). In addition, it was noted that

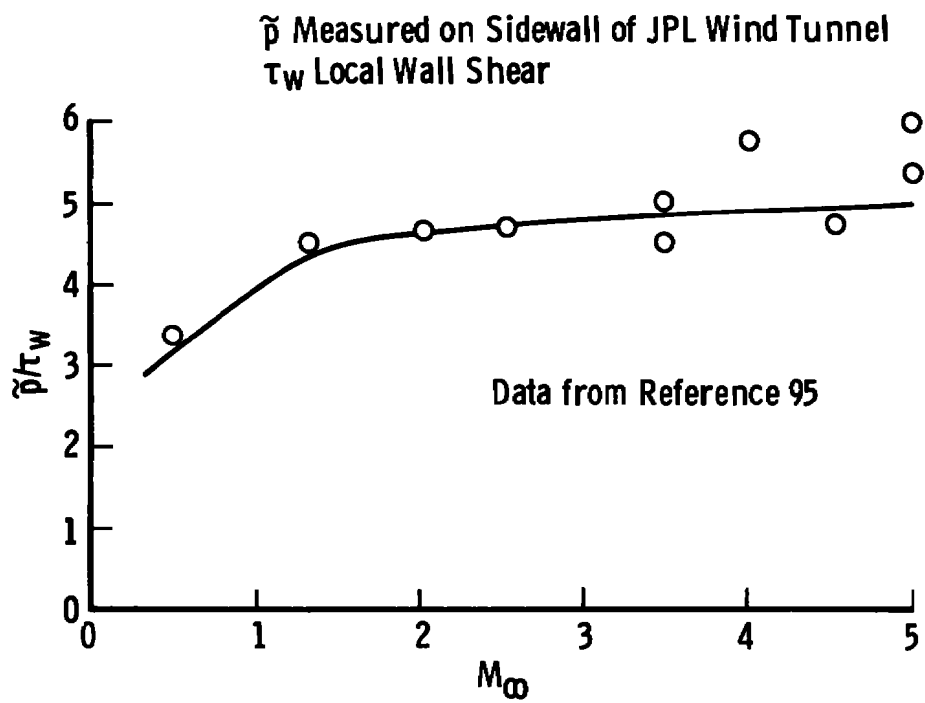


Figure III-4. Correlation of pressure fluctuation levels.

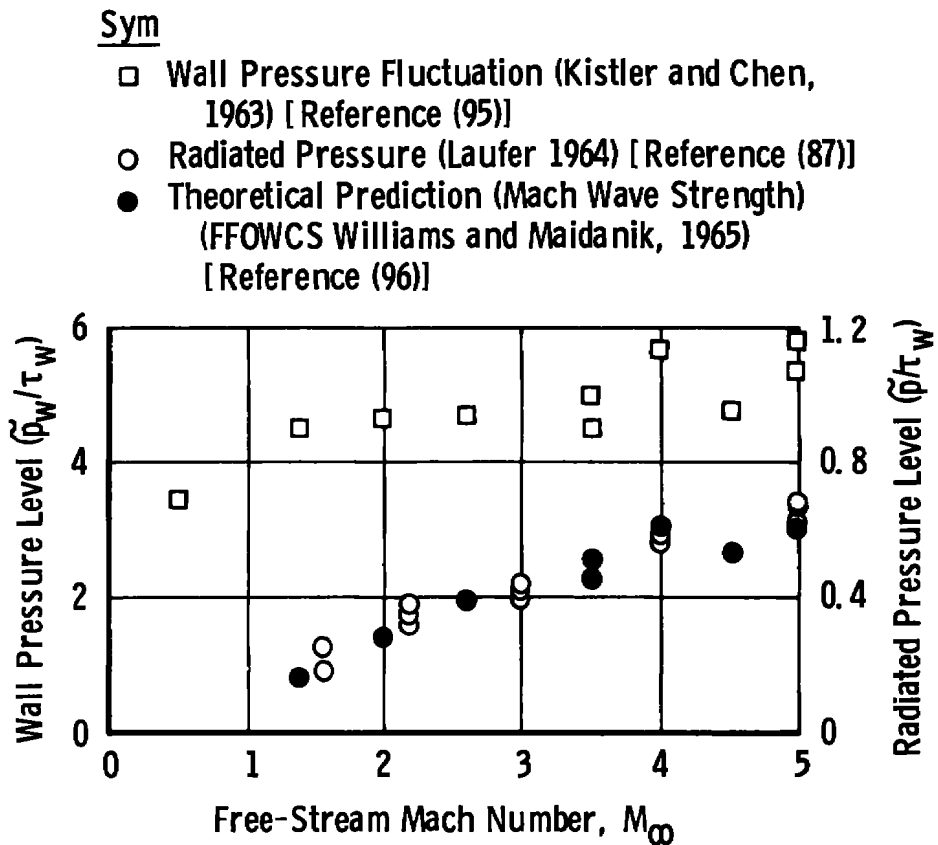


Figure III-5. Comparison of measured and predicted radiated pressure levels [from Reference (96)].

the intensity of the radiated pressure fluctuations was an order of magnitude less than the pressure fluctuations on the wall. By operating the JPL 18- x 20-in. supersonic tunnel at low pressures, the boundary layer was maintained laminar on all four walls. Then by tripping the boundary layer on one wall, Laufer showed that the intensity of the radiated pressure fluctuations was proportional to the size of the test section. For example, radiation from one wall was approximately equal to one-fourth the radiation measured from four walls. Also the measured values were constant across the test section, once the hot wire was one to two boundary-layer thicknesses away from the wall.

Williams reported in 1965 (96) that the sound field in supersonic flows would be dominated by eddy Mach waves. He stated that the efficiency of radiation increases with Mach number as a result of the turbulent "eddies" moving supersonically with respect to the mean flow and creating Mach waves. Also the waves were highly directional and had their fronts aligned near the Mach angle as pointed out by Phillips (94).

Williams commented that Phillips in 1960 (94) was the first to make a thorough theoretical attack on the supersonic shear-radiated wave problem. Williams (96) developed an analytical equation, Eq. (6), for estimating the Mach wave radiation from a supersonic turbulent shear layer based on a description of the pressure fluctuation in the boundary layer. Basic in his derivation was the assumption that turbulent pressures scale with the boundary-layer thickness.

$$\frac{\tilde{p}}{\tau_w} = \frac{\tilde{p}_w}{\tau_w} \left\{ \frac{5\epsilon}{24\pi^2} \int_1^{M_\infty} \frac{(M^2 - 1)^{\frac{1}{2}} dM}{M^m \{1 + 0.2 M^2\}^2} \right\}^{\frac{1}{2}} \quad (6)$$

$$\epsilon = 0.2$$

$$\tau_w = \text{Wall local shear}$$

$$\gamma = 1.4$$

$$m = 0$$

$$M = \text{Mach number}$$

The results from Eq. (6) as computed by Williams using the measured wall  $\tilde{p}_w$  of Kistler are shown in Figure III-5. Excellent agreement between the computed values of Williams and the free-stream measurements of Laufer are seen to exist.

It should be remembered that the data of Kistler can be used since they were obtained on the wall of the same tunnel (the JPL 18- by 20-in. tunnel) as were Laufer's free-stream data.

Kendall (74) continued the outstanding work begun by Laufer at JPL and in 1970 published additional experimental hot-wire data on wind tunnel free-stream disturbances. Before beginning his flat-plate boundary-layer stability-transition studies [which were directed toward providing experimental confirmation of Mack's stability theory (73)], Kendall demonstrated that the fluctuations picked up by the hot wire located in the laminar boundary layer on the flat plate were the result of forcing by the tunnel free-stream sound field which emanated from the tunnel wall boundary. Data taken by Kendall and published by Morkovin (4) are shown in Figure III-6. These data represent free-stream hot-wire measurements obtained when the JPL tunnel wall boundary layer was laminar and then turbulent. By operating the JPL tunnel at low pressures, a laminar boundary layer could be maintained on all four walls. Then by tripping the flow on one wall and then rotating the flat plate, Kendall showed the hot-wire response was greatest when facing the turbulent wall,

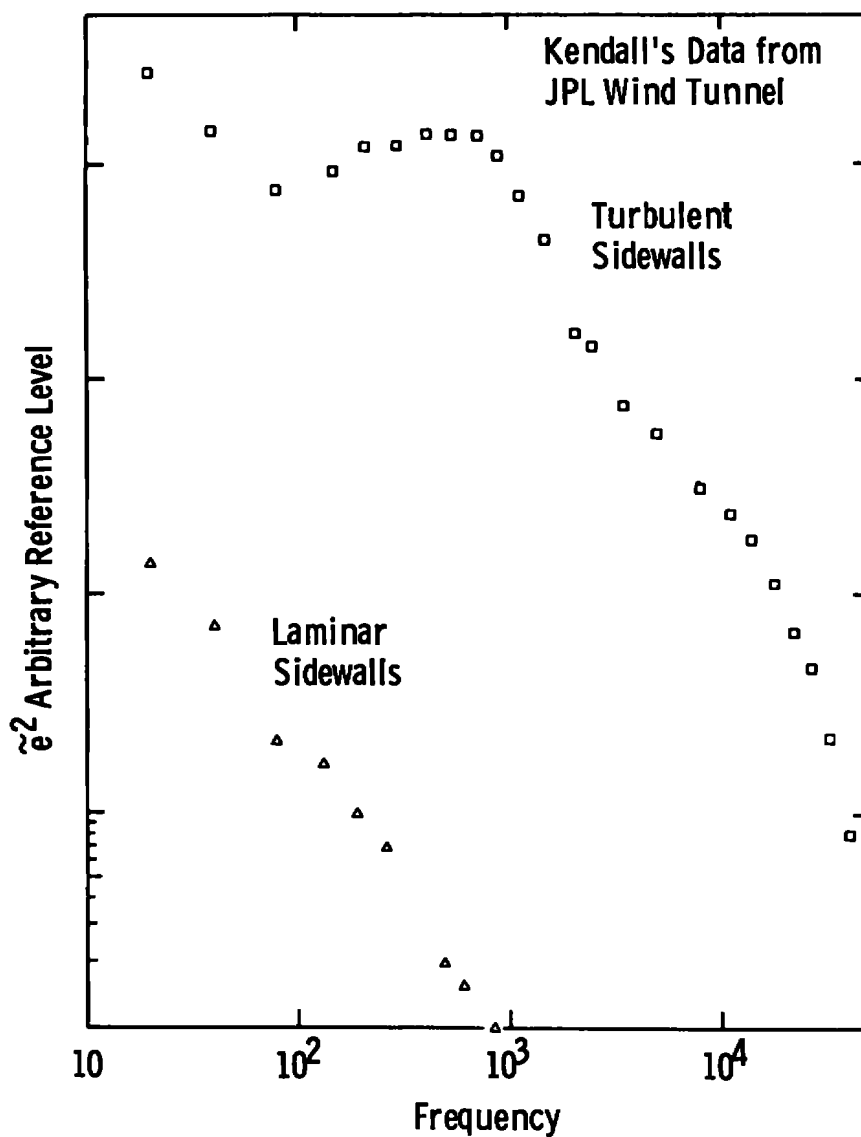


Figure III-6. Spectra of free-stream fluctuation at  $M_\infty = 4.5$  with and without turbulence generated sound [from Reference (4)].



as shown in Figure III-7. The data shown in Figures III-6 and III-7 remove any doubts as to the intensity of the radiated aerodynamic noise.

Kendall (94) also found that the free-stream pressure fluctuations were amplified one to two orders of magnitude by the laminar boundary layer on a flat plate as shown in Figure III-8. This amplification has significance when comparing surface microphone ( $\tilde{p}$ ) and free-stream hot-wire ( $\tilde{p}$ ) measurements as will be discussed in Chapter V.

In 1969, Wagner, Maddalon, Weinstein, and Henderson (89) reported on the first of a long series of investigations conducted at NASA/LRC<sup>7</sup> on the influence of free-stream disturbances on boundary-layer transition at hypersonic speeds. Using an approach similar to Laufer's (38), they found that the mode diagrams were linear with a positive slope for all pressure levels investigated in the  $M_\infty = 20$ , 22-in.-diam helium tunnel. They found that when the tunnel flow was laminar, the free-stream fluctuations were lowest and when the nozzle flow was transitional, they were highest. Analysis of the mode diagrams led to the conclusion that the disturbance was radiated noise as described by Laufer (38).

Fischer and Wagner (90) reported on hot-wire measurements conducted in the NASA-LRC 22-in.-diam and 60-in.-diam helium tunnels at  $M_\infty = 20$  and 18, respectively. Using the mode diagram method of analysis, they found the free-stream fluctuation disturbances to be consistent with the radiated noise hypothesis.

---

<sup>7</sup>National Aeronautics and Space Administration (NASA) Langley Research Center (LRC), Hampton, Virginia.

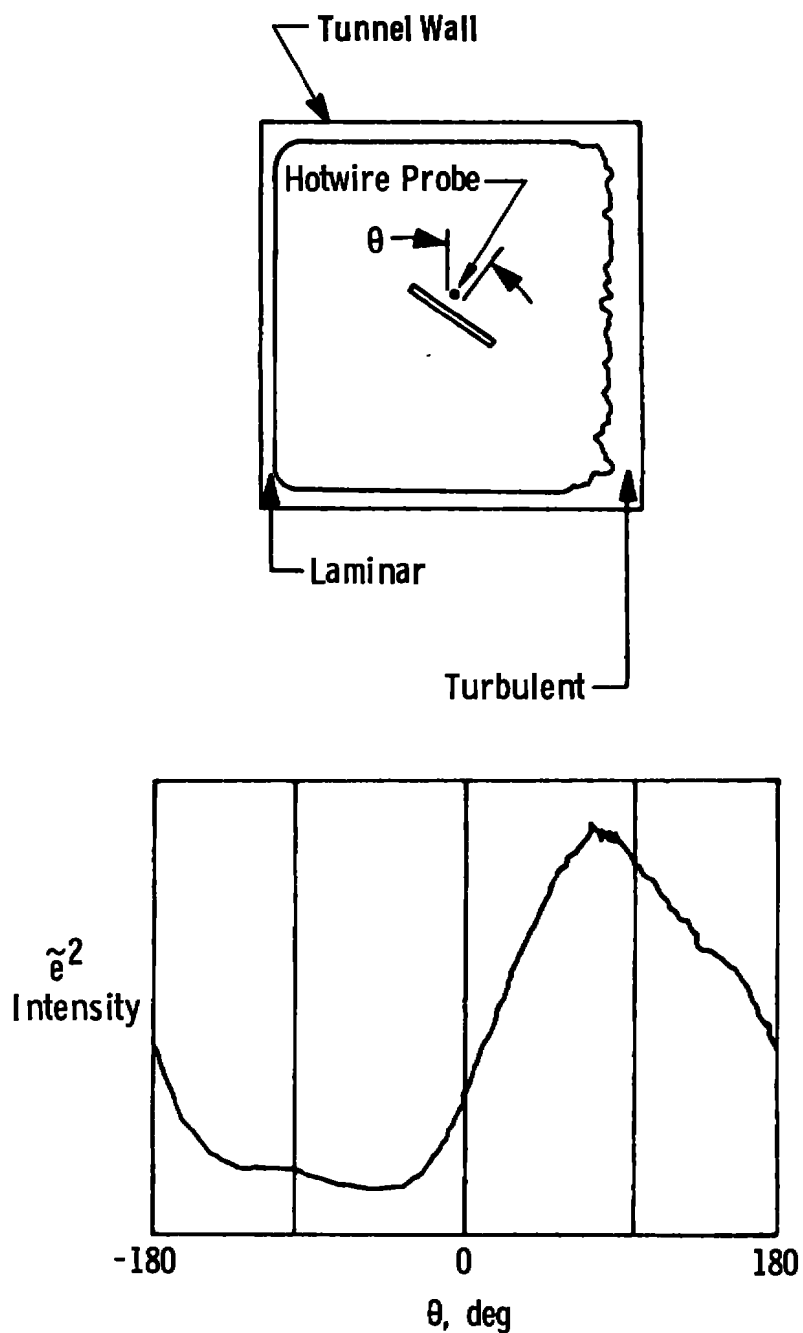


Figure III-7. Free-stream radiated noise fluctuations, directionality, and intensity,  $M_\infty = 4.5$  [from Reference (74)].

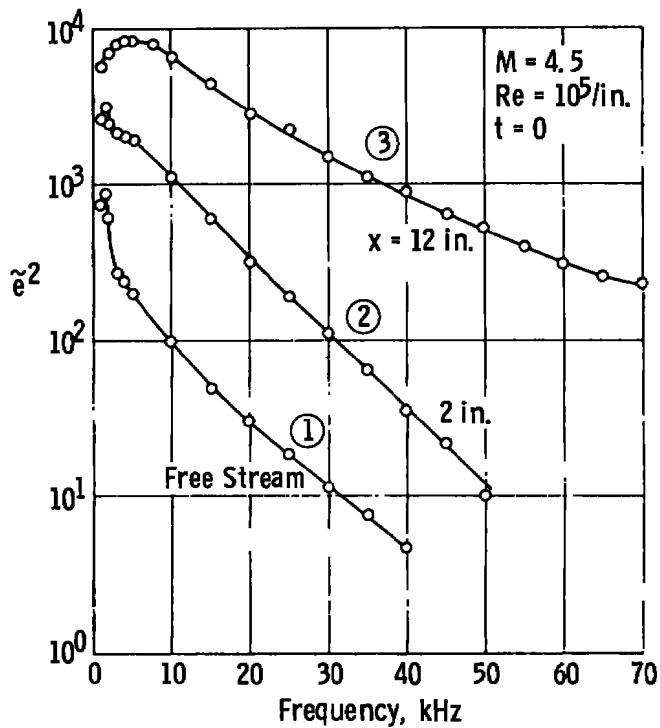
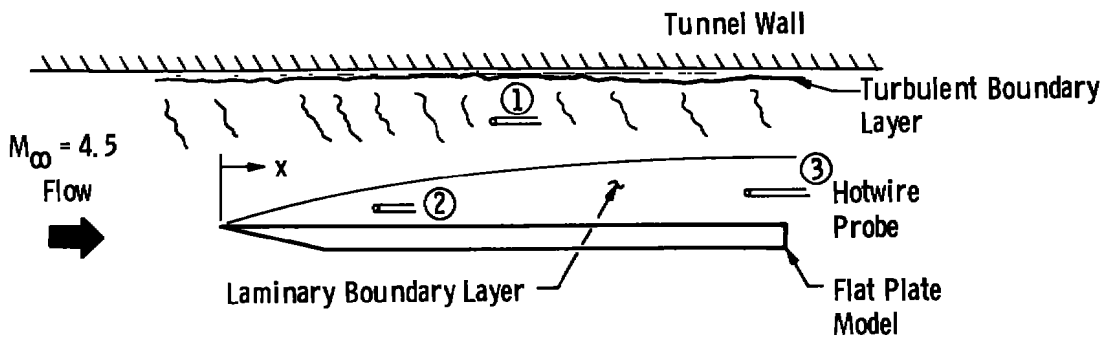


Figure III-8. Energy spectra [from Reference (74)].

Further measurements by Stainback and Wagner (91) showed that a pitot probe instrumented with a flush-mounted pressure transducer could be used to measure the free-stream pressure fluctuations in hypersonic wind tunnels.

Donaldson and Wallace (88) in 1971 reported on hot-wire anemometry measurements made in the AEDC-VKF 12-in. supersonic wind tunnel to determine the level of flow fluctuations in the test section free stream. They also obtained supplementary acoustic measurements made using a microphone mounted flush with the surface of a flat plate. The flat-plate model was the one designed and used by Pate (10). The mode diagram for several free-stream unit Reynolds numbers are shown in Figure III-9. Donaldson and Wallace analyzed the hot-wire data using the mode diagram concept of Kovasznay (43) and the data reduction technique of Morkovin (84) following the assumption used by Laufer (38). Their results supported the hypothesis of Laufer that the disturbance was a fluctuating pressure field (aerodynamic noise) that radiated from the tunnel wall boundary layer. Using the mode diagrams shown in Figure III-9, along with the assumption that the fluctuating field was a pure sound field, then the hot-wire rms voltage equation [Eq. (4b), page 57] was used to estimate the fluctuating quantities of pressure, mass flow density, temperature, velocity, and total temperature. Results of these calculations as taken from Reference (88) are shown in Figure III-10. The rms pressure fluctuation data measured by Donaldson and Wallace are presented in Figure III-11 and compared with Laufer's data (38). Note that both sets of data have been divided by four to correspond to the radiation from one wall only. By normalizing  $\tilde{p}$  with the wall shear

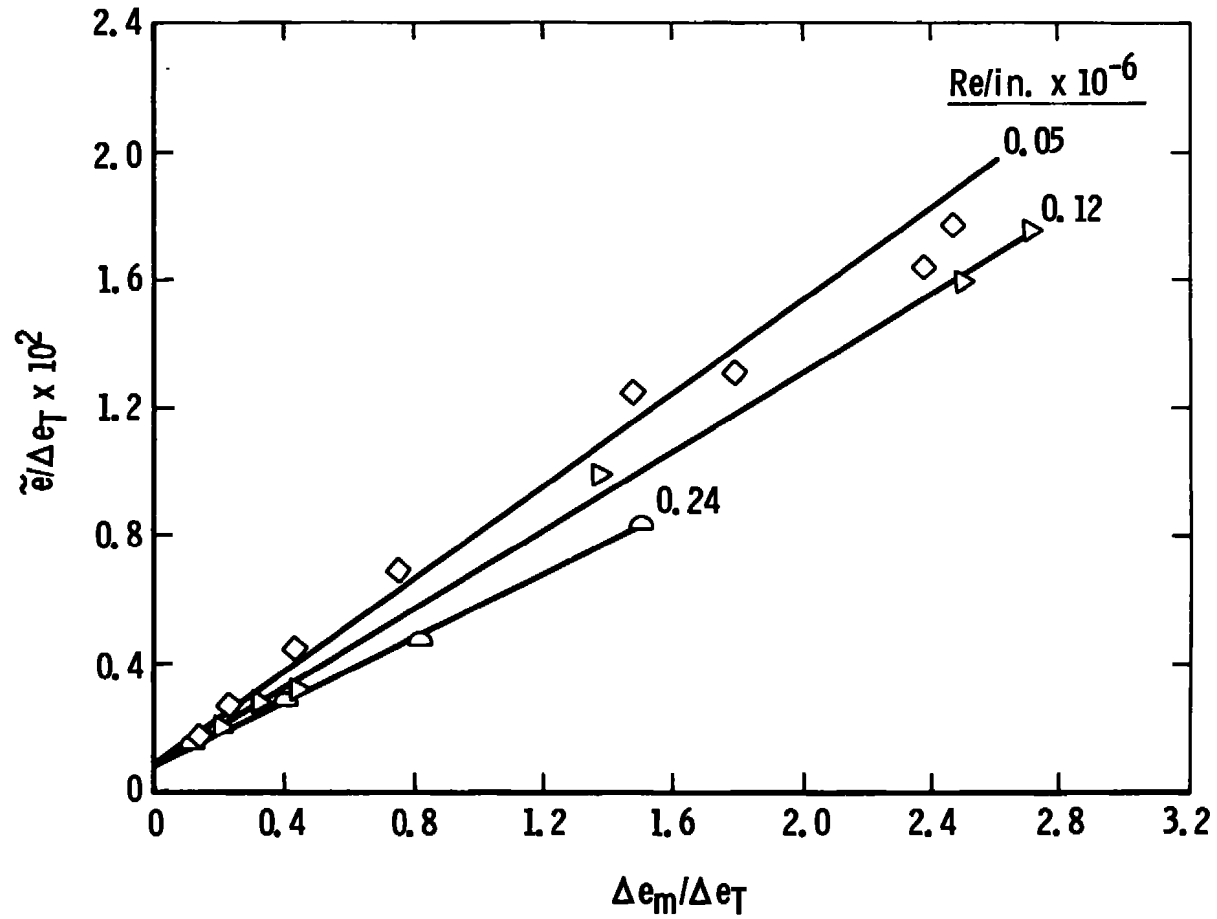


Figure III-9. Mode diagrams from AEDC-VKF Tunnel D at  $M_\infty = 4.0$  [from Reference (88)].

- Notes: 1. Bars indicate data spread possible with alternate fairings of mode diagram for each unit Reynolds number.
2. Absence of bars indicates data spread is within symbol.

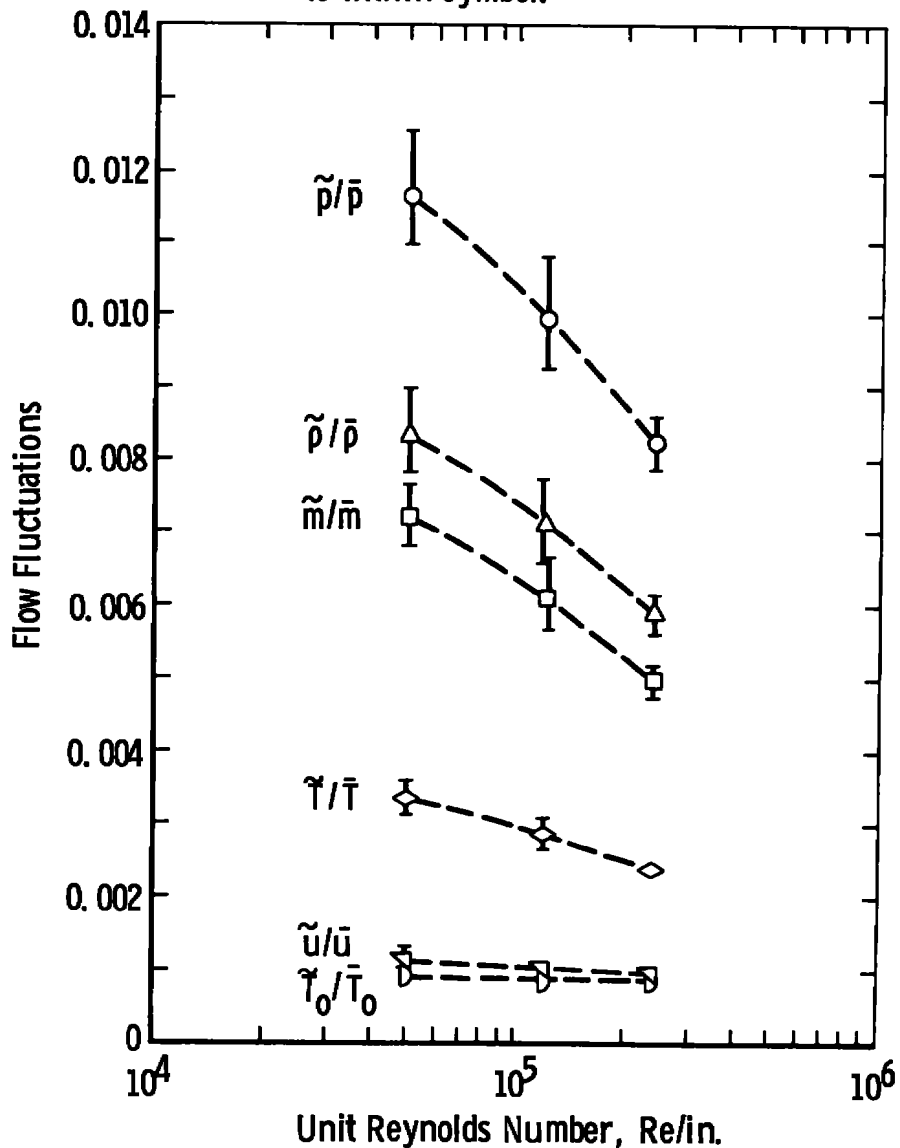


Figure III-10. Variation of flow fluctuations with unit Reynolds number [from Reference (88)].

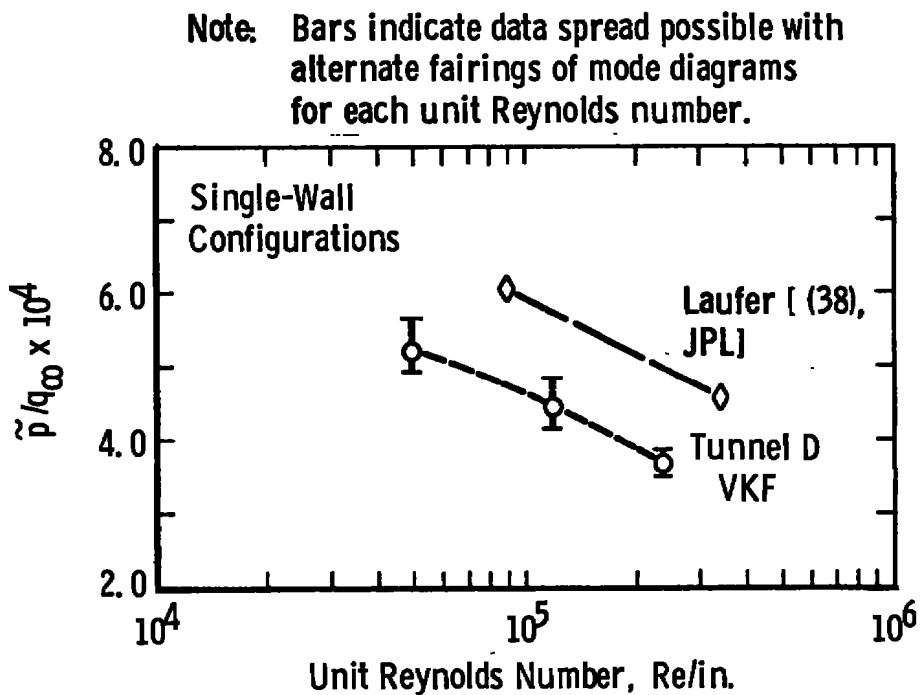


Figure III-11. Variation of RMS pressure fluctuations (normalized by dynamic pressure) with unit Reynolds number [from Reference (88)].

stress as done by Laufer and computing  $\tau_w$  from  $\tau_w = \frac{1}{2} \rho_\infty U_\infty^2 C_f$  where  $C_f$  was determined from the method of van Driest, then the dependence of  $\hat{p}$  on the unit Reynolds number is almost completely removed as shown in Figure III-12. The power spectral density for the three unit Reynolds numbers are shown in Figure III-13 as taken from Reference (88) where the experimental boundary-layer thickness ( $\delta$ ) obtained from Reference (97) was used to normalize the data.

Recently, hypersonic free-stream disturbance measurements have been reported by Demetriades (98). Donaldson (99) provided information on equipment and techniques used in the hot-wire experiments conducted at  $M_\infty = 6$  and 8 (99).

From the now classical experimental work of Laufer (38,86) and the follow-on work of Kendall (14,74), Wagner, et al. (89) and Donaldson and Wallace (88) and the theoretical work of Kovasznay (43), Phillips (94), and Williams (96), it is definitely concluded that the dominant source of free-stream disturbance in a well-designed supersonic-hypersonic wind tunnel will be the pressure fluctuating field (radiated noise) emanating from the tunnel wall turbulent boundary layer.



Note: Bars indicate data spread possible with alternate fairings of mode diagrams for each unit Reynolds number.

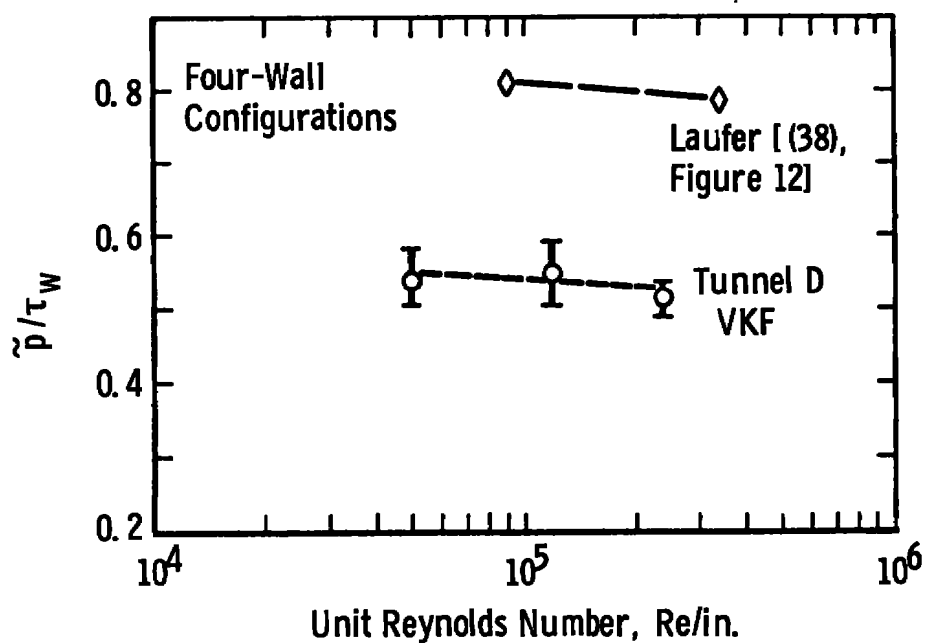


Figure III-12. Variation of RMS pressure fluctuations (normalized by wall shearing stress) with unit Reynolds number [from Reference (88)].

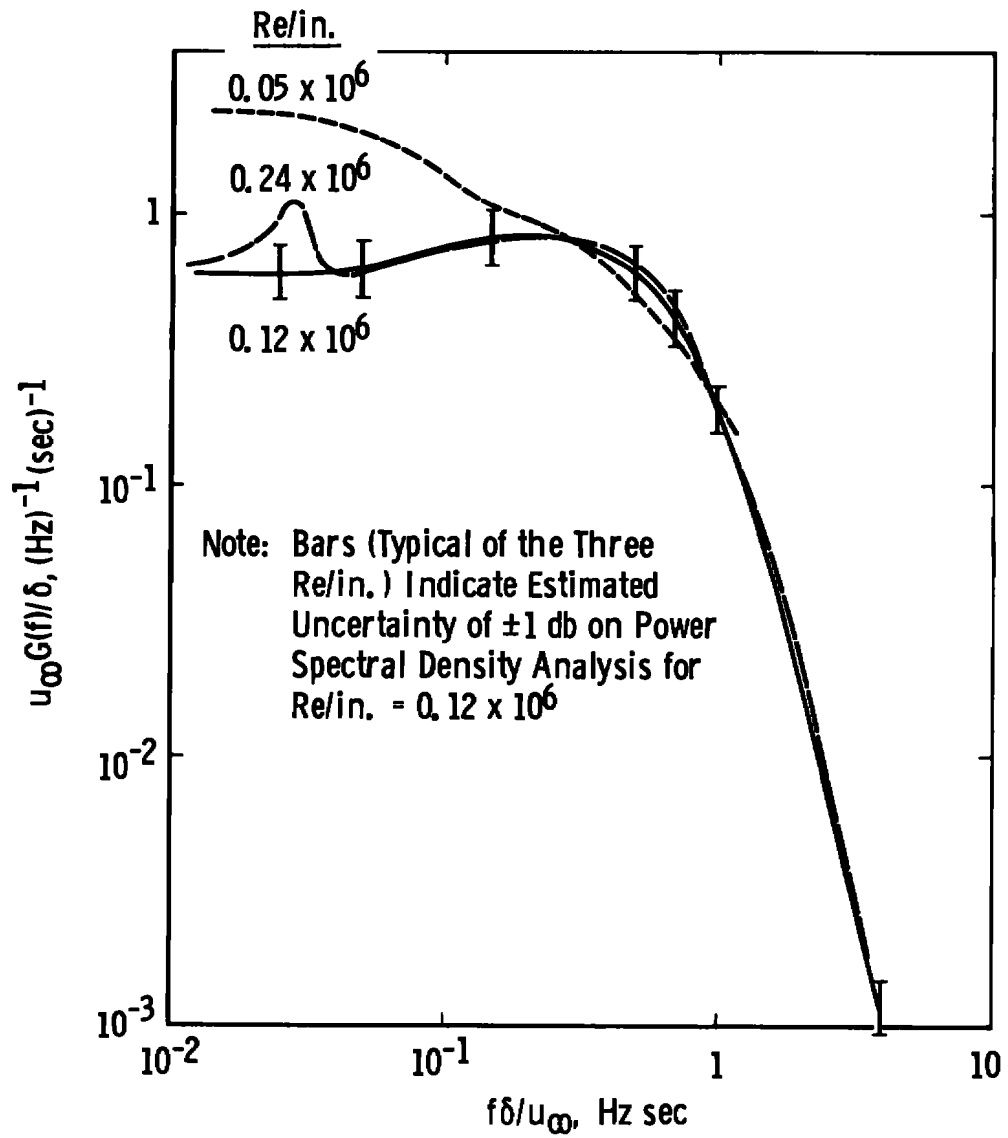


Figure III-13. Hot-wire signal spectra for wire overheat of  $a_w' = 0.4$  [from Reference (88)].

## CHAPTER IV

## EXPERIMENTAL APPARATUS

## I. WIND TUNNELS

The primary boundary-layer transition data and pressure fluctuation data used in support of the present research effort were obtained in the wind tunnels located at the Arnold Engineering Development Center, AEDC, AFSC. This section describes the wind tunnel facilities, experimental apparatus, instrumentation and the flat-plate, hollow-cylinder, and sharp-cone transition models used to supply these basic data. The facilities in which the author conducted transition experiments (!), included five wind tunnels located in the von Kármán Facility (VKF) and one in the Propulsion Wind Tunnel Facility (PWT), as listed in Table 1. Brief descriptions of these wind tunnel facilities are presented in the following sections.

AEDC-VKF Supersonic Tunnel A

Tunnel A<sup>8</sup> (Figure IV-1) is a continuous, closed-circuit, variable-density wind tunnel with an automatically driven, flexible-plate-type nozzle and a 40- by 40-in. test section. The tunnel can be operated at Mach numbers from 1.5 to 6.0 at maximum stagnation pressures from 29 to 200 psia, respectively, and stagnation temperatures up to 300°F ( $M_\infty = 6$ ). Minimum operating pressures range from about one-tenth to one-twentieth

---

<sup>8</sup>AEDC-VKF Tunnels A, B, and C are equipped with a model injection system which allows removal of the model from the test section while the tunnel remains in operation.

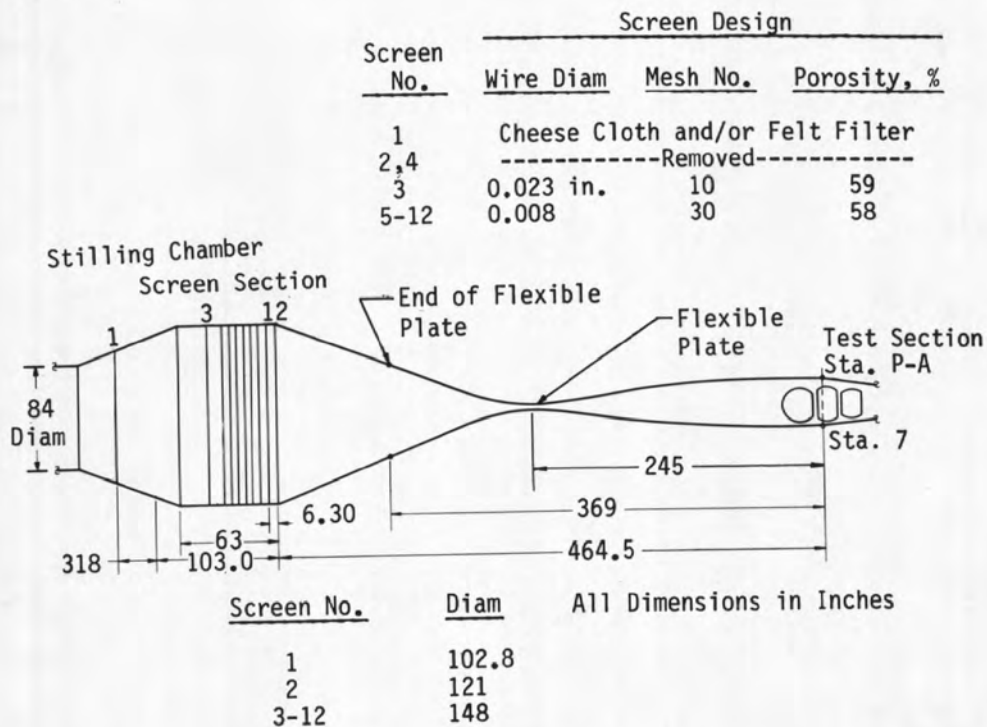
Table 1. AEDC supersonic-hypersonic wind tunnels.

Tunnel	Test Section	Type	$M_{\infty}$
! AEDC-VKF Tunnel A	*40 in. x 40 in.	Supersonic	1.5 to 6.0
AEDC-VKF Tunnel B	*50-in. Diam	Hypersonic	6, 8
! AEDC-VKF Tunnel D	*12 in. x 12 in.	Supersonic	1.5 to 5.0
! AEDC-VKF Tunnel E	*12 in. x 12 in.	Hypersonic	5 to 8
! AEDC-VKF Tunnel F	*25-in. Diam	Hypersonic	7.5
! AEDC-VKF Tunnel F	*40-in. Diam	Hypersonic	10, 12
AEDC-VKF Tunnel F	**54-in. Diam	Hypersonic	10, 14
! AEDC-PWT 16S	16 ft x 16 ft	Supersonic	1.6 to 4.0

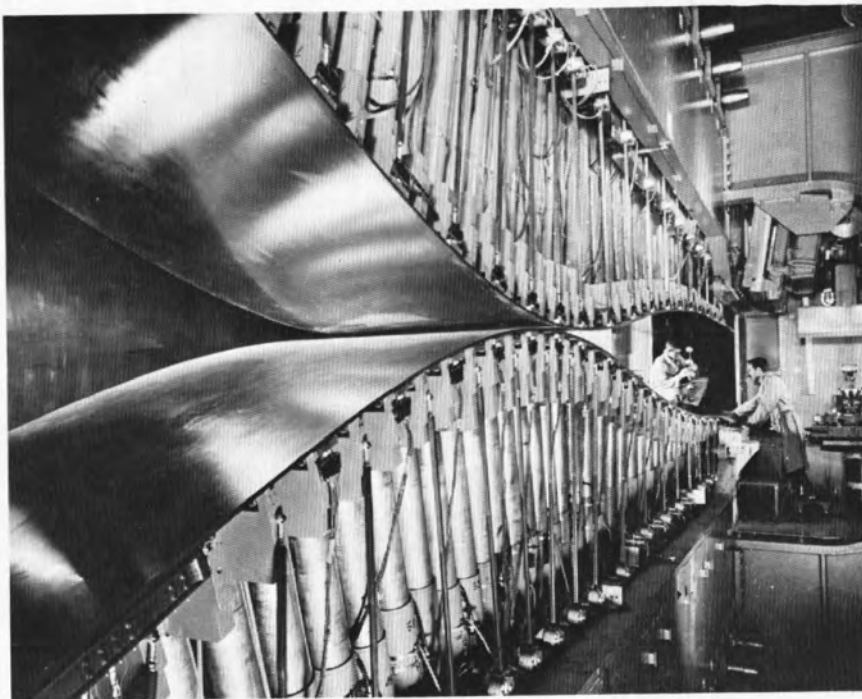
\*Contoured Nozzles

\*\*Conical Nozzles

!Tunnels used by the author in direct support of the present research.



a. Assembly



b. Nozzle and Test Section (40 in. by 40 in.)

Figure IV-1. AEDC-VKF Tunnel A.

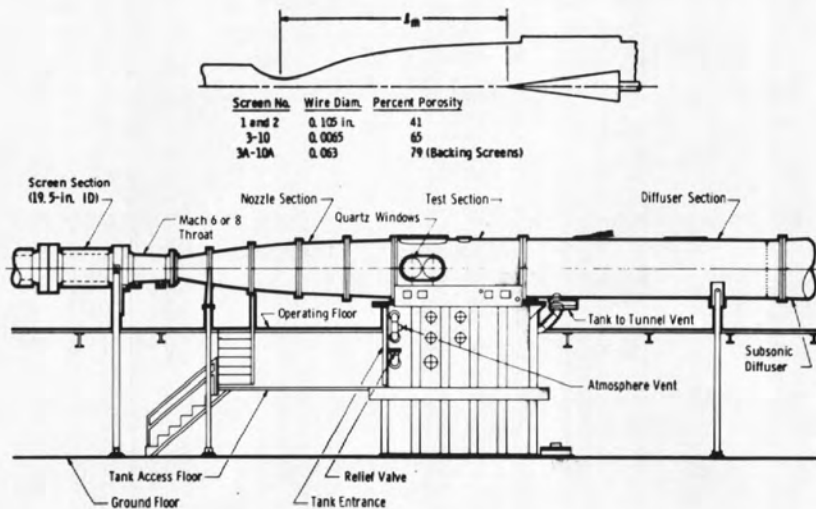
of the maximum pressures. A description of the tunnel and airflow calibration information can be found in Reference (100). Additional information on the tunnel wall boundary-layer characteristics can be found in Appendix B.

#### AEDC-VKF Hypersonic Tunnel B

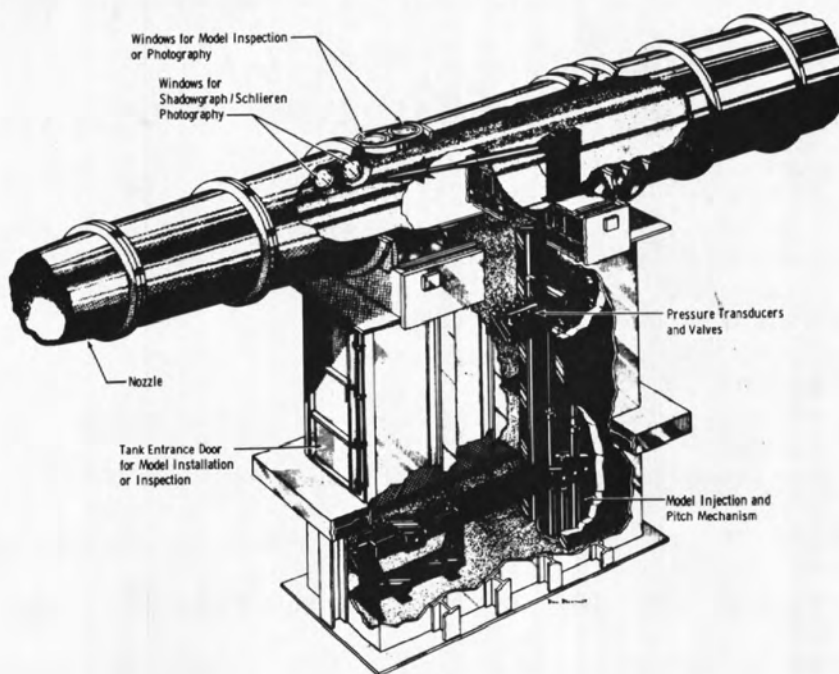
Tunnel B (Figure IV-2) has a 50-in.-diam test section and two interchangeable axisymmetric contoured nozzles to provide Mach numbers of 6 and 8. The tunnel can be operated continuously over a range of pressure levels from 20 to 300 psia at  $M_\infty = 6$ , and 50 to 900 psia at  $M_\infty = 8$ , with air supplied by the AEDC-VKF main compressor plant. Stagnation temperatures sufficient to avoid air liquefaction in the test section (up to 1,350°R) are obtained through the use of a natural-gas-fired combustion heater. The entire tunnel (throat, nozzle, test section, and diffuser) is cooled by integral, external water jackets. A description of the tunnel and initial calibration can be found in Reference (101). Information on the tunnel wall boundary-layer characteristics is presented in Appendix B.

#### AEDC-VKF Supersonic Tunnel D

Tunnel D is an intermittent, variable density wind tunnel with a manually adjusted, flexible-plate-type nozzle and a 12- by 12-in. test section. The tunnel can be operated at Mach numbers from 1.5 to 5.0 at stagnation pressures from about 5 to 60 psia and at average stagnation temperatures of about 70°F. A description of the tunnel and airflow calibration information can be found in Reference (97). An illustration showing the pertinent Tunnel D geometry is presented in Figure IV-3.

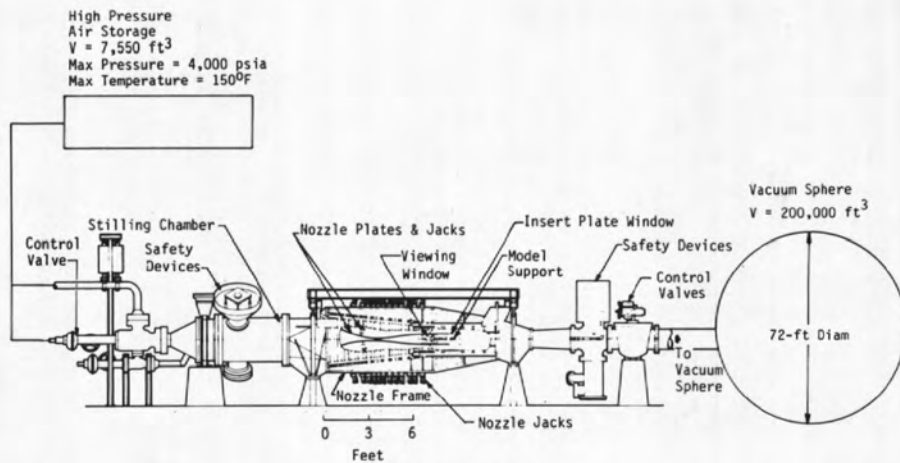


a. Tunnel Assembly

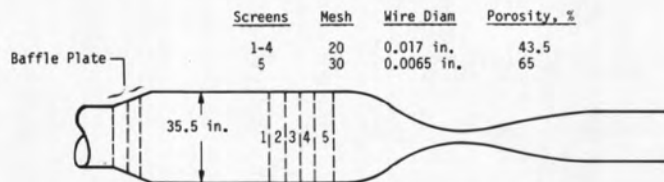


b. Tunnel Test Section (50-in. Diam)

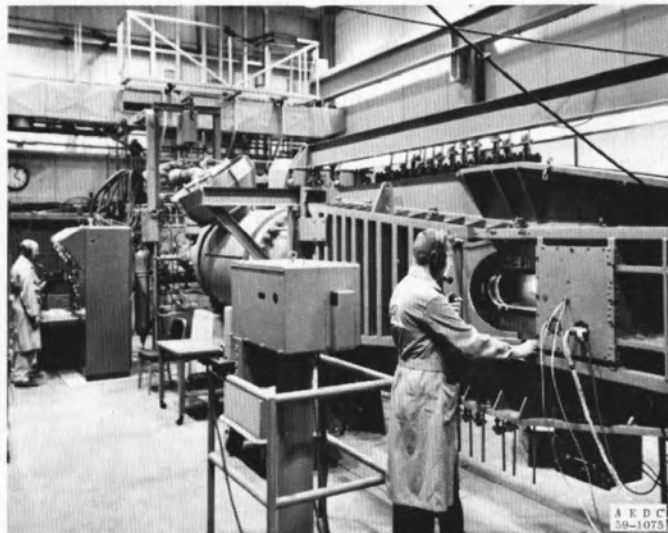
Figure IV-2. AEDC-VKF Tunnel B.



a. Assembly



b. Stilling Chamber Screen Geometry



c. Nozzle and Test Section (12 in. by 12 in.)

Figure IV-3. AEDC-VKF Tunnel D.



AEDC-VKF Hypersonic Tunnel E

Tunnel E<sup>9</sup> (Figure IV-4) is an intermittent, variable-density wind tunnel having a contoured throat block and a flexible-plate-type nozzle with a 12- by 12-in. test section. The tunnel operates at Mach numbers from 5 to 8 at maximum stagnation pressures from 400 to 1,600 psia, respectively, and stagnation temperatures up to 1,400°R (102). Minimum stagnation pressures for normal operation are one quarter of the maximum at each Mach number.

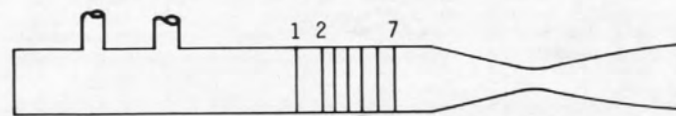
For the present investigation at Mach number 5, the maximum stagnation pressures were approximately 400 psia and 690°R, respectively. A minimum operating pressure of 50 psia was obtained by removing a second throat-block located in the diffuser section which had been used to provide improved operating conditions at  $M_\infty = 8$ .

AEDC-VKF Hypervelocity Tunnel F (Hotshot)

The Hypervelocity Wind Tunnel (F) is an impulsively arc-driven wind tunnel of the hotshot type and provides a Mach number range from 7.5 to  $\approx 15$  over a Reynolds number per foot range from  $0.05 \times 10^6$  to  $50 \times 10^6$ . The facility is equipped with three axisymmetric contoured nozzles ( $M_\infty = 8$ ,  $d = 25$  in.;  $M_\infty = 12$ ,  $d = 40$  in.; and  $M_\infty = 16$ ,  $d = 48$  in.) which connect to a 54-in.-diam test section as shown in Figure IV-5. Nitrogen is the test gas used for aerodynamic testing. Air is used for combustion tests. The test gas is confined in either a 1.0-, 2.5-, or a 4.0-ft<sup>3</sup>

---

<sup>9</sup>The Tunnel E flexible plate nozzle was removed from service in 1969 and replaced by a  $M_\infty = 8$ , axisymmetric contoured nozzle having a 13.25-in.-diam test section and equipped with a magnetic model suspension system.



Screen Section (10.0 in. ID)

Stilling Chamber Baffle Geometry

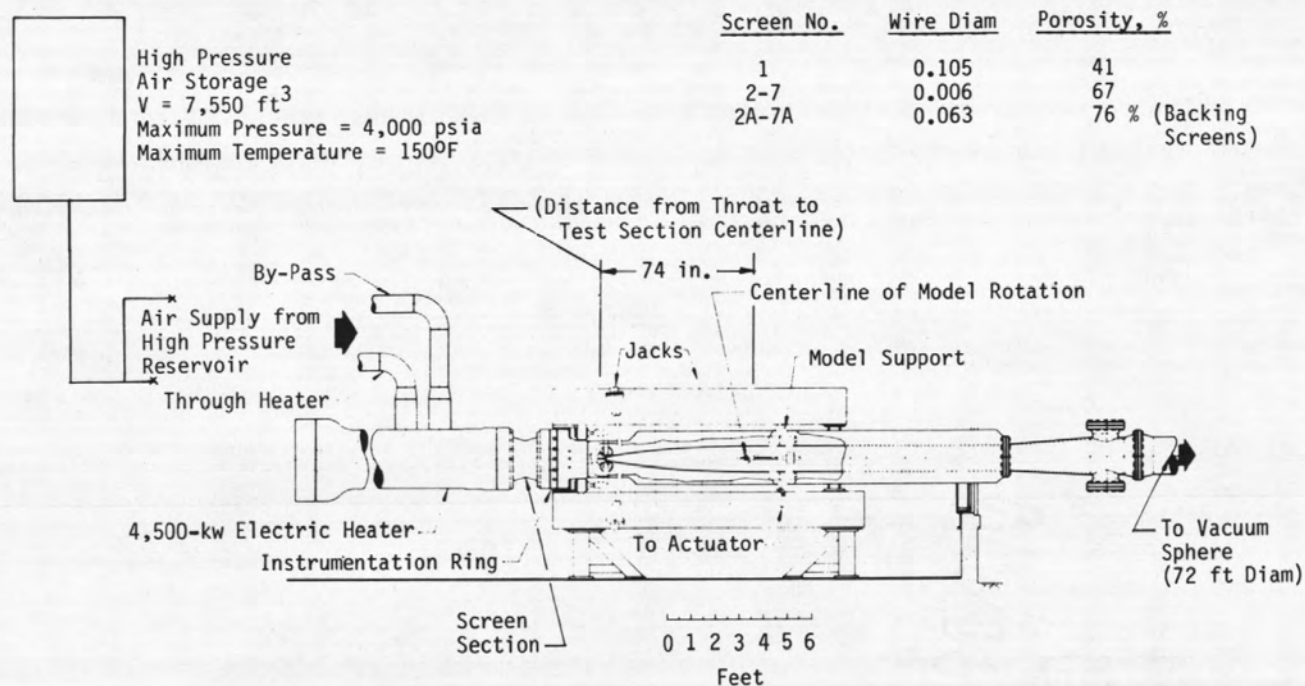


Figure IV-4. AEDC-VKF Tunnel E

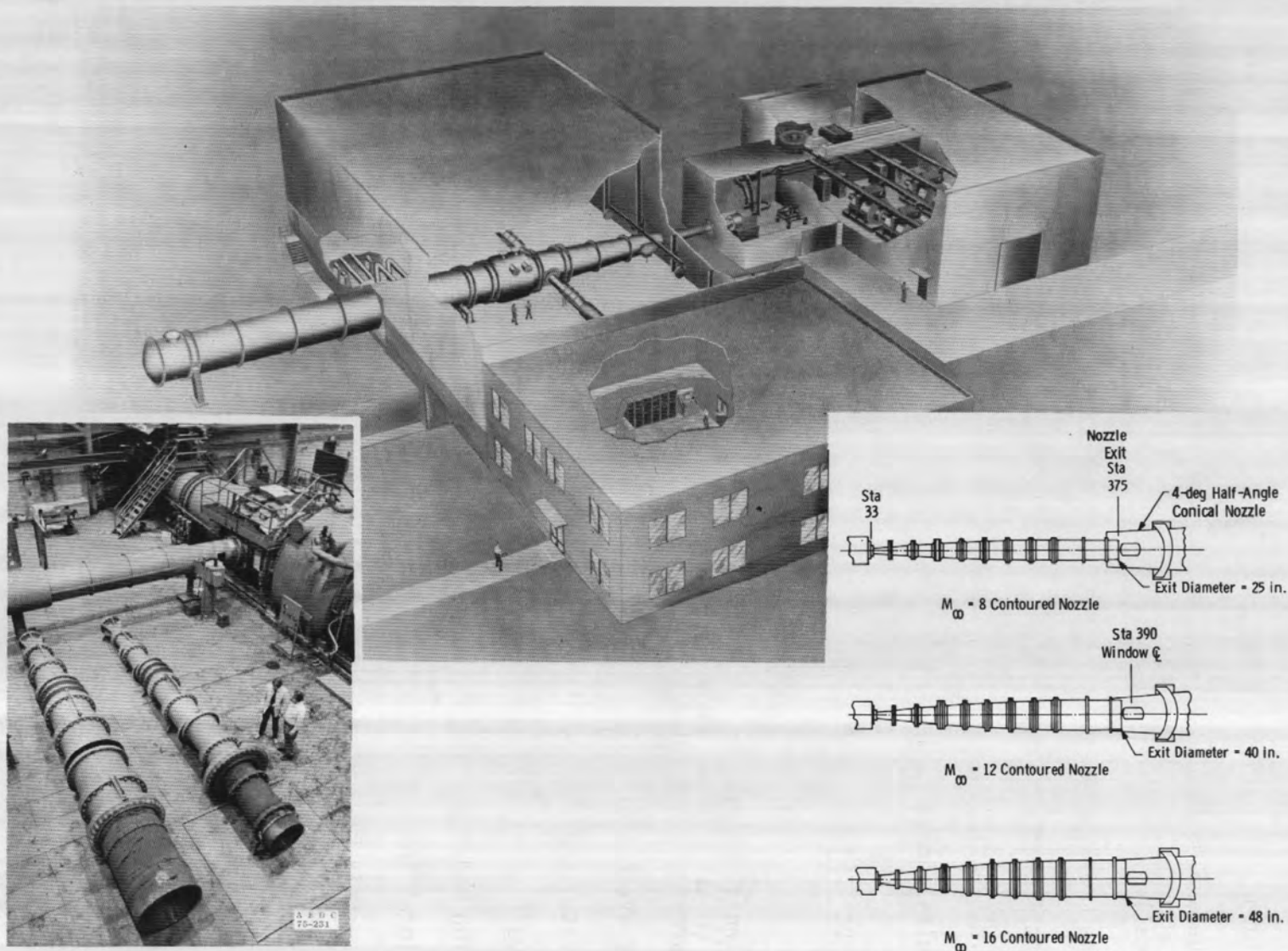


Figure IV-5. AEDC-VKF Tunnel F (Hotshot) Facility ( $M_\infty \approx 7$  to 15).

arc chamber where it is heated and compressed by an electric arc discharge. The increase in pressure results in a diaphragm rupture with the subsequent flow expansion through the nozzle. Test times are typically from 50 to 200 msec. Because of the relatively short test times, the model wall (and tunnel wall) temperature remains essentially invariant from the initial value of approximately 300°K; thus  $T_w/T_0 \approx 0.1$  to 0.3. Additional details, test capabilities, and flow calibrations results can be found in References (103) through (105).

#### AEDC -PWT Supersonic Tunnel 16S

Tunnel 16S (Figure IV-6) is a closed-circuit, variable-density wind tunnel with an automatically controlled, flexible-plate-type nozzle. Current test capabilities include a Mach number range from 1.65 to 4.5 at stagnation pressures from approximately 0.7 to 11 psia. For these tests, the stagnation temperature was held constant at approximately 200°F. The test section is 16 ft square by 40 ft long, and the transition model was located in the first 10 ft of the test section. Additional information on the tunnel may be found in Reference (106) and in Appendix B.

## II. TRANSITION MODELS

Flat-plate, hollow-cylinder, and slender-cone models were selected as the basic transition models for this research. These configurations were selected for the following reasons:

1. Planar and sharp-cone geometries are basic configurations used in many supersonic-hypersonic designs.

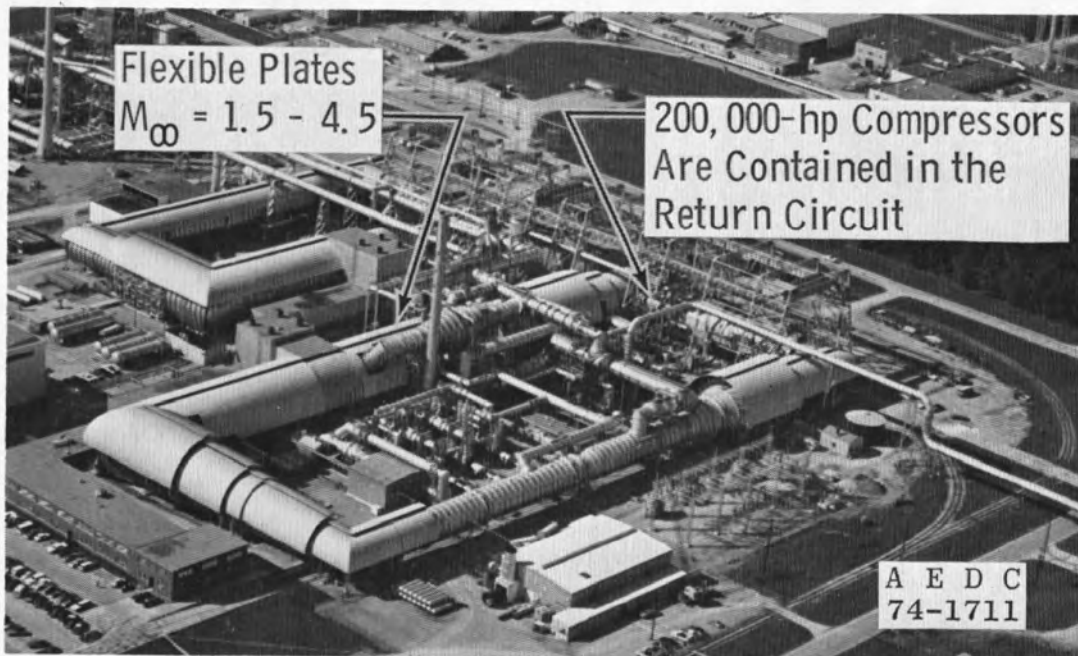
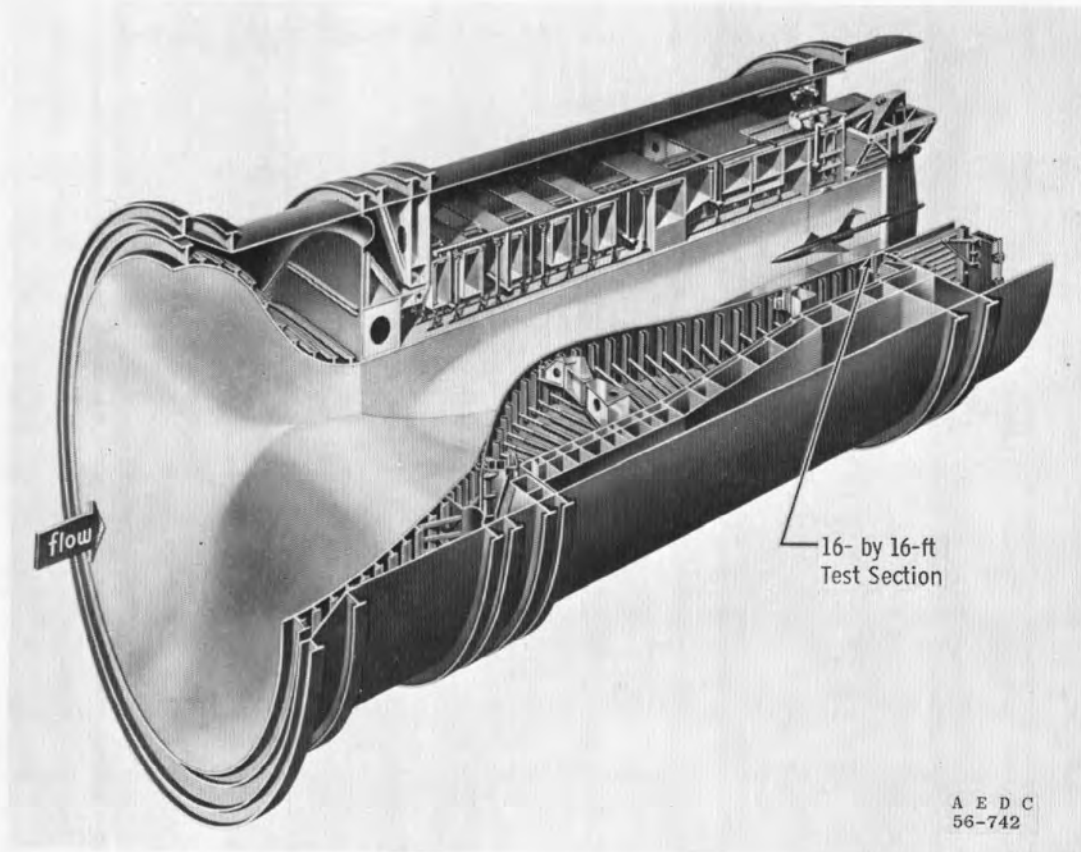


Figure IV-6. AEDC-PWT Tunnel 16S Supersonic Wind Tunnel Facility (16-ft x 16-ft test section).

2. Leading-edge bluntness effects could be systematically eliminated as a variable.
3. Surface Mach number (and pressure) gradients are absent and therefore do not enter as variables.
4. These configurations produce two-dimensional flow fields at zero angle of attack.
5. There are no spanwise or axial pressure gradients, flow expansion or compression fields, or surface areas with flow separation.
6. Surface roughness can be eliminated as a variable.
7. Fairly large amounts of transition data already exist on these configurations.
8. Sharp-cone and flat-plate models are often used as standard wind tunnel calibration geometries.

The models used in this research and which provided transition data from the AEDC wind tunnels are described in this section.

#### AEDC-VKF Hollow-Cylinder Model (Tunnels A, D, and E)

The basic transition model was a 3.0-in.-diam by 32-in.-long hollow cylinder having a surface finish of 15 microinches ( $\mu\text{in.}$ ) as shown in Figure IV-7. This transition model was used in the AEDC-VKF Tunnels A, D, and E. The same basic model was used in the previous investigations of Potter and Whitfield (37) and Schueler (51). Four new interchangeable nose sections having leading-edge, internal bevel angles of 6 and 12 deg and leading-edge bluntnesses ( $\bar{b}$ ) of 0.0013, 0.0021, 0.0030, and 0.0036 in. were designed and fabricated for use in the present

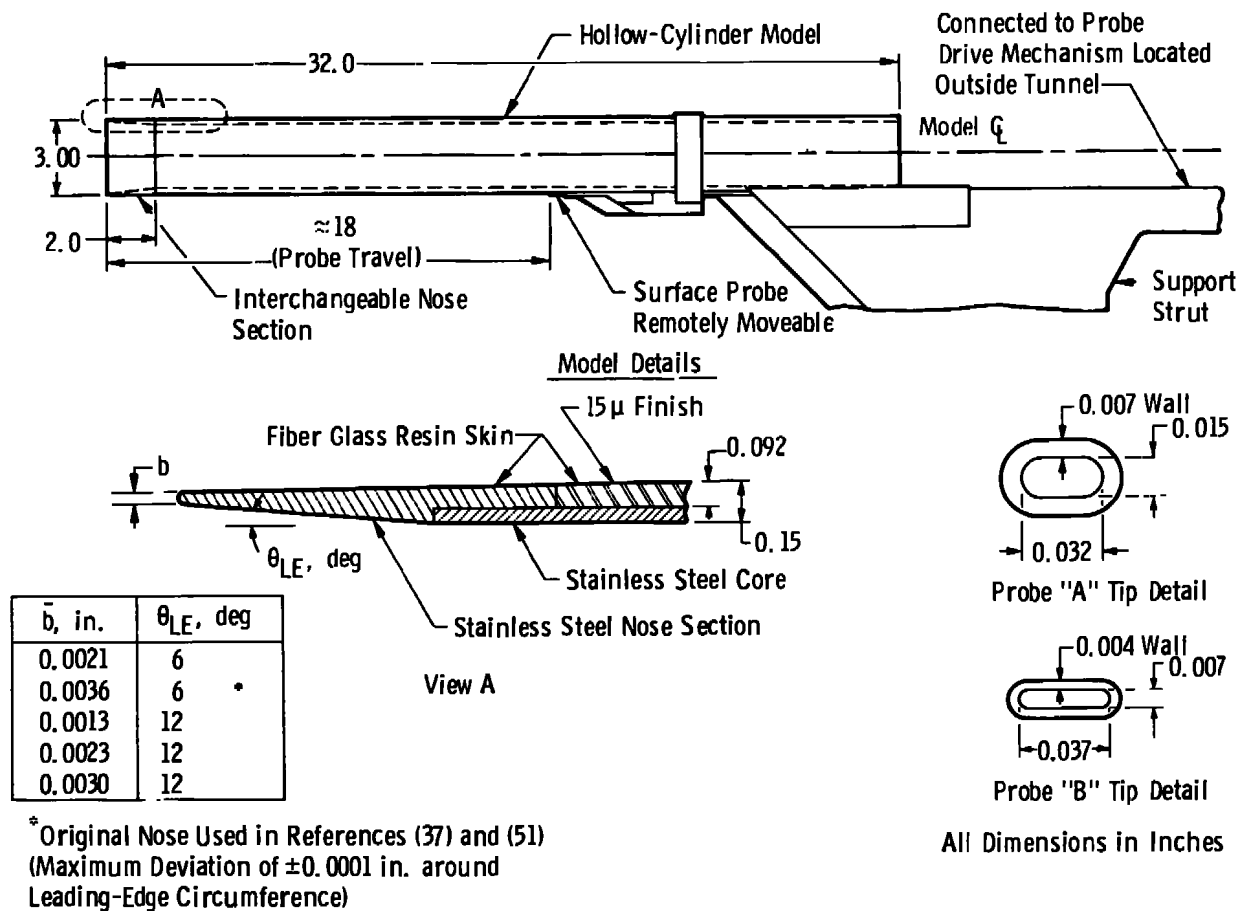


Figure IV-7. 3.0-in.-diam hollow-cylinder transition model (AEDC-VKF Tunnels A, D, and E).

research. A remotely controlled, electrically driven, surface pitot probe provided a continuous trace of the probe pressure on an X-Y plotter from which the location of transition was determined. Details of the 3.0-in.-diam hollow-cylinder transition model are given in Figure IV-7.

Several techniques were investigated to determine the best method for determining the bluntness of sharp-leading-edge flat plates and included: (a) wax impressions that were sliced into thin strips and then examined with a comparator, (b) direct measurement with a micrometer, (c) impressions made using a rubber compound, and (d) impressions made in sharpened lead sheet. Method (d) eventually proved to be the method most often used because of its simplicity and ability to produce repeatable impressions. Methods (a) and (b) produced unacceptable results.

The model leading-edge nose bluntness quoted in this report was determined from impressions (depth equal to approximately two to four times the bluntness value made in thin (sharpened) soft lead sheet and from rubber molds made from General Electric Company RVT 60<sup>®</sup> silicone rubber compound. Both methods were nondestructive to the model leading edge. Profiles of the lead impressions and the rubber slices (approximately 0.04-in. in width) cut from the rubber mold were then read on a 100-power comparator to determine the leading-edge bluntness. Several lead impressions and several cuts from each of the rubber molds were averaged to obtain the bluntness value at each of several circumferential stations around each of the leading-edge sections. The maximum difference between average bluntness values obtained using lead impressions and rubber molds was  $\pm 0.0002$  in. Measurements with the lead impressions were repeatable to within  $\pm 0.0002$  in. and measurements with the rubber molds were



repeatable to within  $\pm 0.0001$  in. The circumferential variation in bluntness around the model leading edge was typically  $\pm 0.0001$  in.

It should be noted that the 3.0-in.-diam hollow-cylinder model, surface probe, and all related apparatus used in Tunnels A, D, and E were identical. A photograph of the hollow-cylinder model installed in Tunnel E for testing at  $M_\infty = 5$  is shown in Figure IV-8.

#### AEDC-PWT Hollow-Cylinder Model (Tunnel 16S)

A photograph of the hollow-cylinder model installed in the AEDC-PWT 16-ft test section is shown in Figure IV-9. A sketch of the model is presented in Figure IV-10. The position of the hollow-cylinder transition model and the locations of the two wall boundary-layer rakes relative to the test section and the tunnel throat are shown in Figure IV-11. This transition model was designed<sup>10</sup> specifically for this research program and consisted of a 12-in.-diam by 115-in.-long steel hollow cylinder having an external surface finish of 15  $\mu$ in. The location of transition was determined from pressure data obtained from four equally spaced, external surface pitot probes (0.016- by 0.032-in. tip geometry) as shown in Figure IV-10.

---

<sup>10</sup>A major factor to be considered in the design of a hollow-cylinder transition model is the assurance that the internal flow remains supersonic. The length ( $l$ ) to internal diameter ( $d$ ) ratio ( $l/d$ ) for the AEDC-PWT model was  $l/d = 9.6$ . To ensure that the internal flow remained supersonic for  $M_\infty \gtrsim 2.5$ , the shock wave generated by the leading-edge internal bevel angle was evaluated considering the shock waves and expansion fields generated inside the cylinder. The method of A. H. Shapiro (177) was also used as a guide in the design of the AEDC-PWT hollow cylinder. This method accounts for friction losses which can drive supersonic flow to the sonic condition.

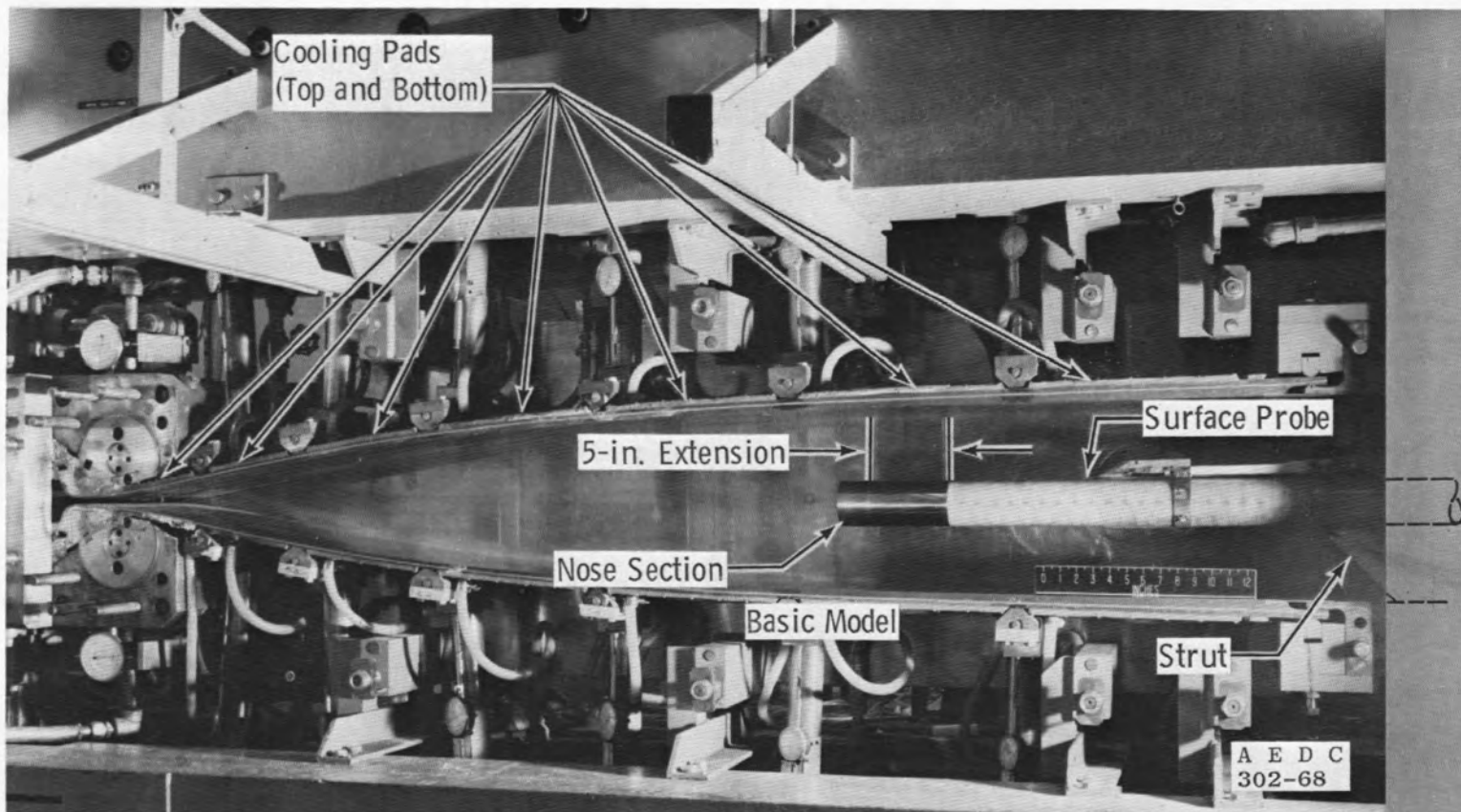


Figure IV-8. Hollow-cylinder model installed in AEDC-VKF Tunnel E.



Figure IV-9. AEDC-PWT 16S transition model installation.

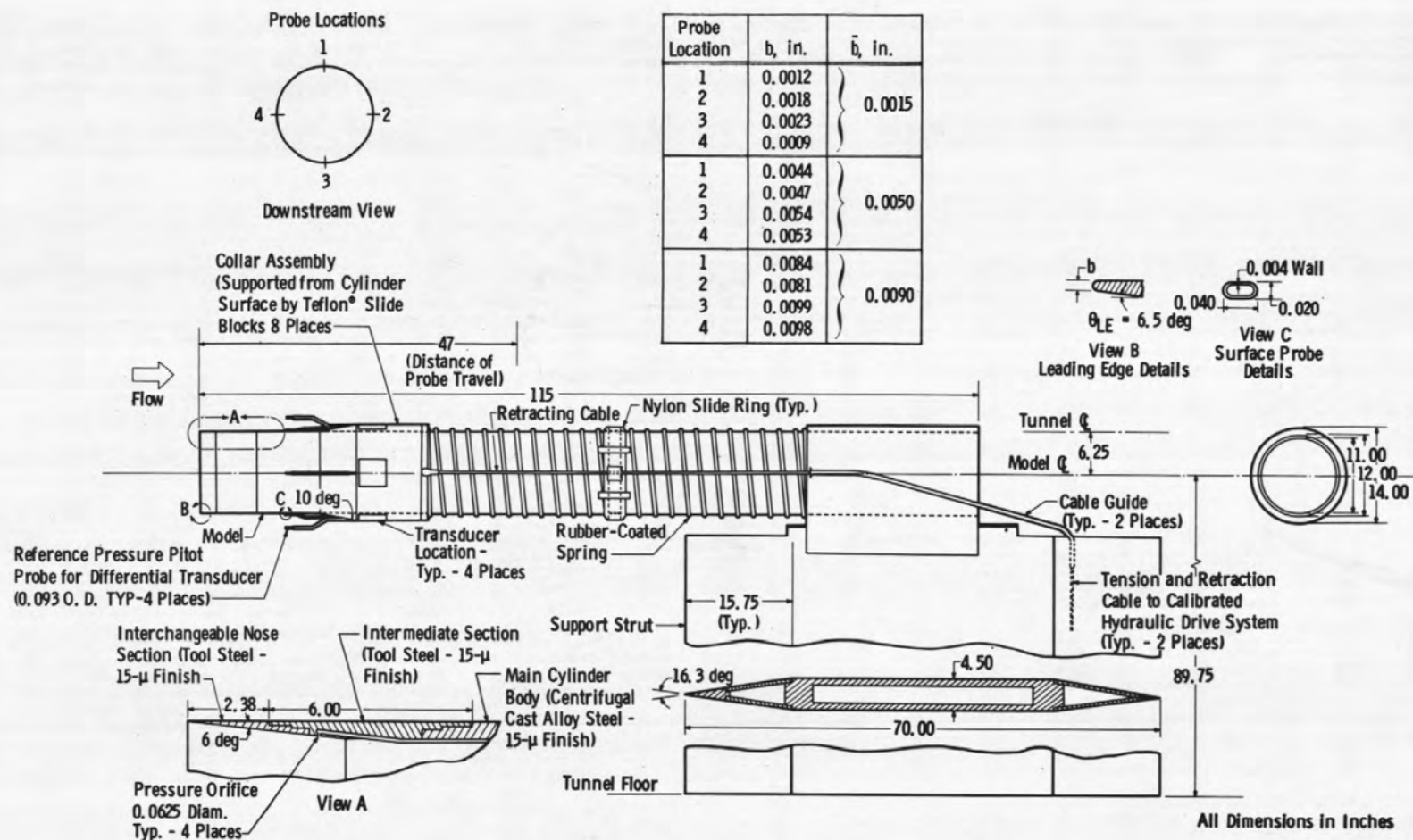
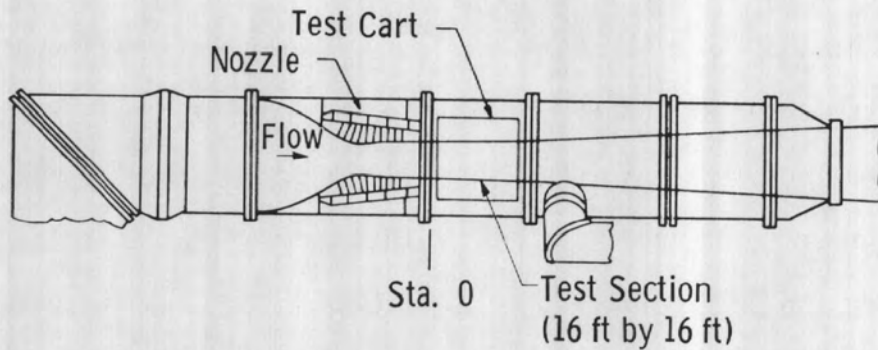
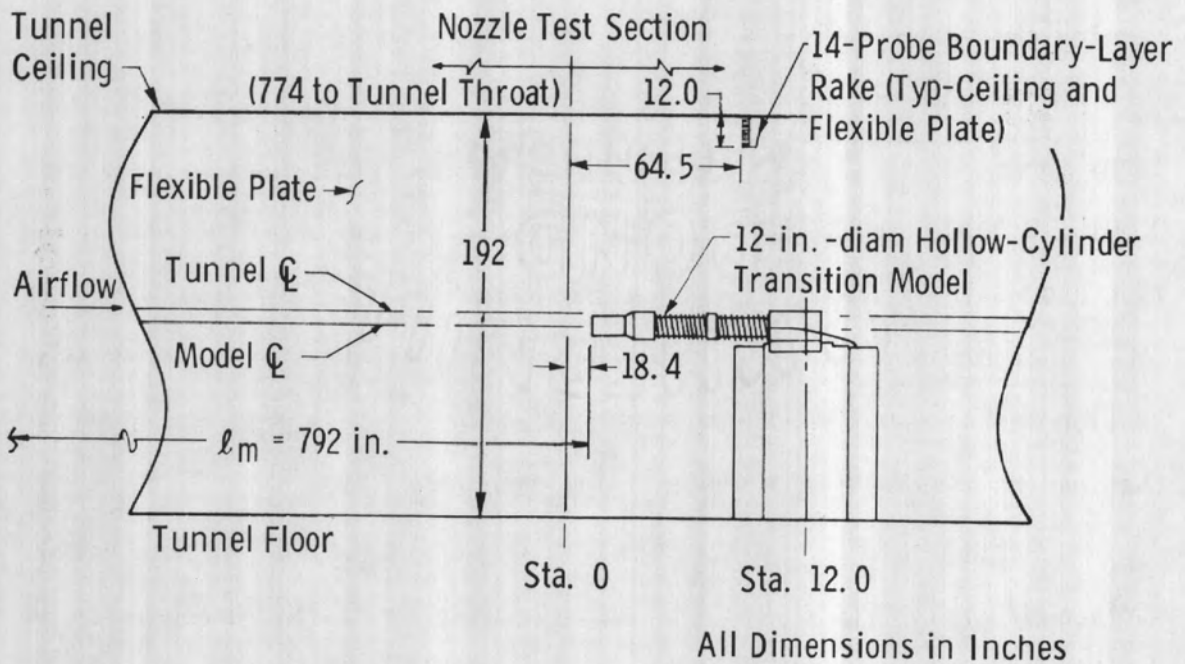


Figure IV-10. 12-in.-diam hollow-cylinder transition model details - AEDC-PWT 16S.



a. Plan View.



b. Test Section

Figure IV-11. Sketch of AEDC-PWT 16-ft supersonic tunnel test section area.

Details of the hollow-cylinder model, model support, and probe drive mechanism are shown in Figure IV-10. Small variations in the model leading-edge thickness existed, and these bluntness values are tabulated in the table included in Figure IV-10 as a function of the model circumferential location. The leading-edge bluntness was determined by making bluntness impressions (impressions depth approximately two to four times bluntness value) in thin (sharpened) soft lead sheet and viewing the profile on a 100-power comparator. The individual bluntness values (b) listed in Figure IV-10 for each model leading-edge location are the average of several impressions. Additional comments concerning the accuracy of this method were given in the previous section.

Three interchangeable, leading-edge, nose sections with an internal bevel angle of 6.5 deg and average leading-edge bluntness ( $\bar{b}$ ) of 0.0015, 0.0050, and 0.0090 in. were tested. The maximum bluntness deviation around the leading edge was approximately  $\pm 0.0005$  in.

In order to maintain absolutely smooth joints, each leading-edge section was hand polished after each attachment. This produced a joint that had no measurable (or detectable) discontinuity.

A sliding collar arrangement which was separated from the model surface by eight Teflon<sup>®</sup> inserts supported the four pitot probes and housed four differential pressure transducers. An actuating apparatus consisting of a coil spring and a hydraulic cylinder (used for compressing the spring) provided the means for automatically positioning the pitot probes along the surface. Probe pressure data were recorded at small intervals of probe travel at discrete model axial locations.

Profiles of the boundary layer on the tunnel straight wall and flexible plate at the model location were measured with two 14-probe rakes to determine the characteristics of the wall turbulent boundary layer. The experimental boundary-layer characteristics obtained on the tunnel walls can be found in Appendix B.

#### AEDC-VKF Flat-Plate Model (Tunnel F)

The flat-plate model used in Tunnel F is shown in Figure IV-12. The model was 18 in. long and 12 in. wide and had a leading-edge bevel angle of 30 deg and a leading-edge radius of 0.00025 in. (total bluntness  $b = 0.005$  in.). The model was equipped with side plates to minimize edge effects resulting from outflow from beneath the model.

The model upper surface (transition surface) was instrumented with 45 flush-mounted heat-transfer gages and nine pressure ports. The surface pressures were measured with on-board fast-response transducers (103). The pressure orifices were positioned 2.0-in. off centerline to eliminate any possible roughness effects<sup>11</sup> on the transition location. The surface thermocouples were sanded absolutely flush with the model surface using emery paper. A discussion of this type of heat-transfer gage is given in References (103) and (107). The model surface finish was 10  $\mu$ in. as measured with a profilometer. The model leading edge was located at  $x_m = 381$  as shown in Figure IV-13.

---

<sup>11</sup>Effects of pressure orifices promoting premature transition has been reported in Reference (9).

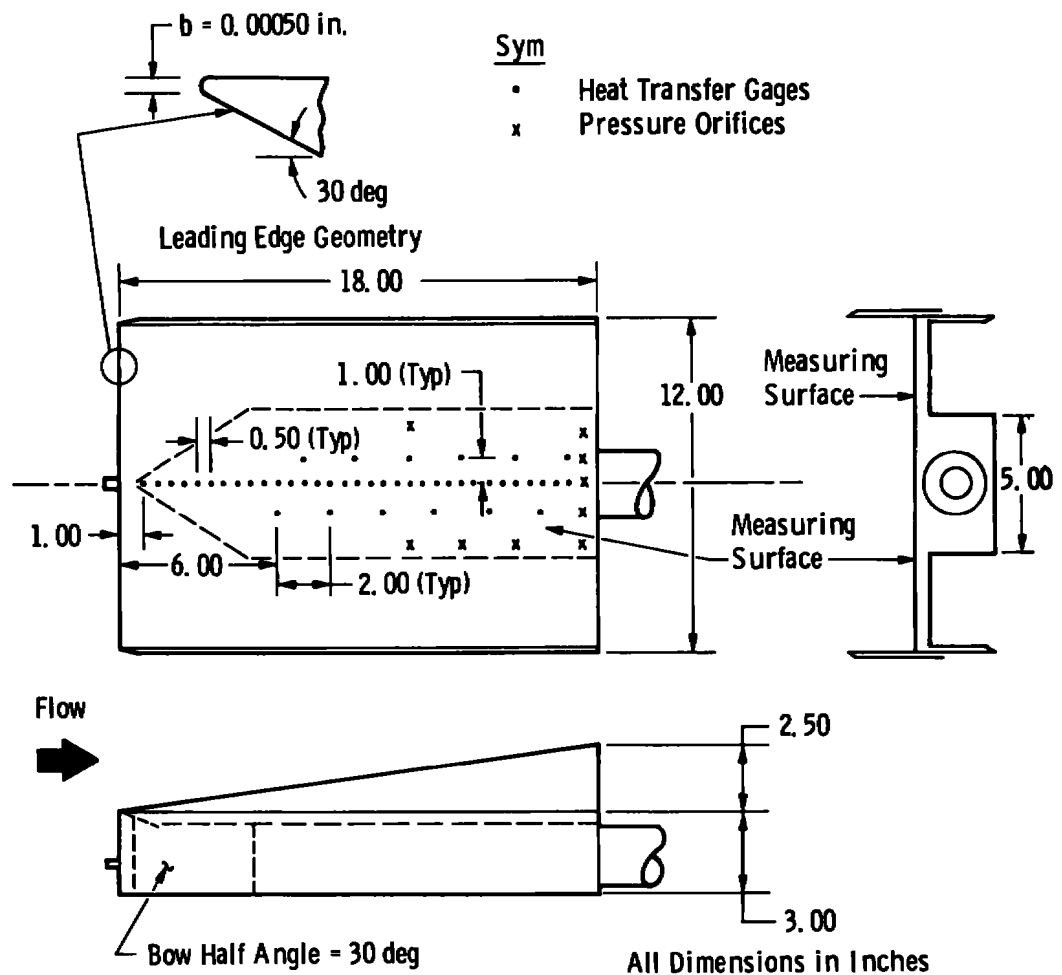


Figure IV-12. AEDC-VKF Tunnel F flat-plate transition model.



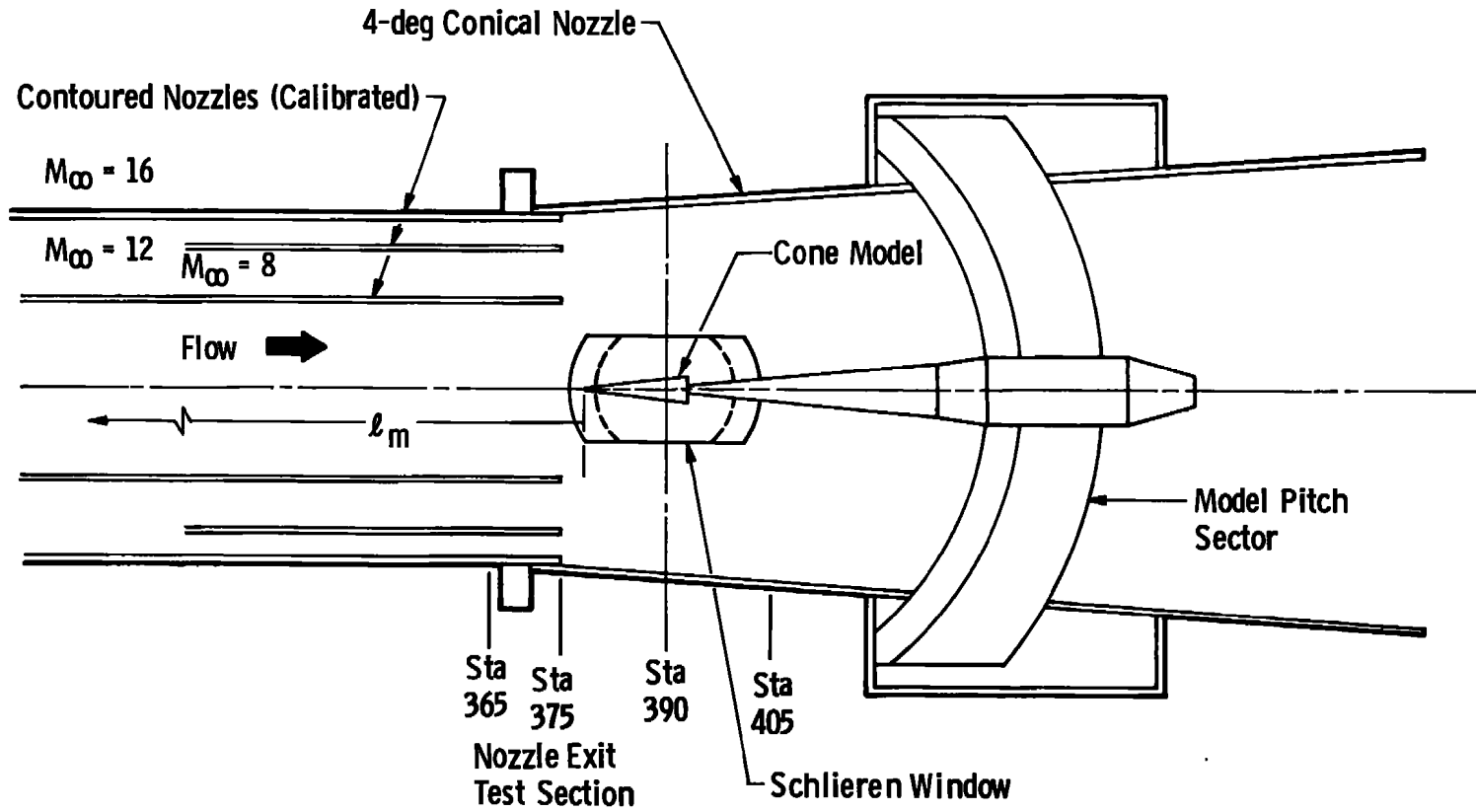


Figure IV-13. Transition model installed in the Tunnel F test section.

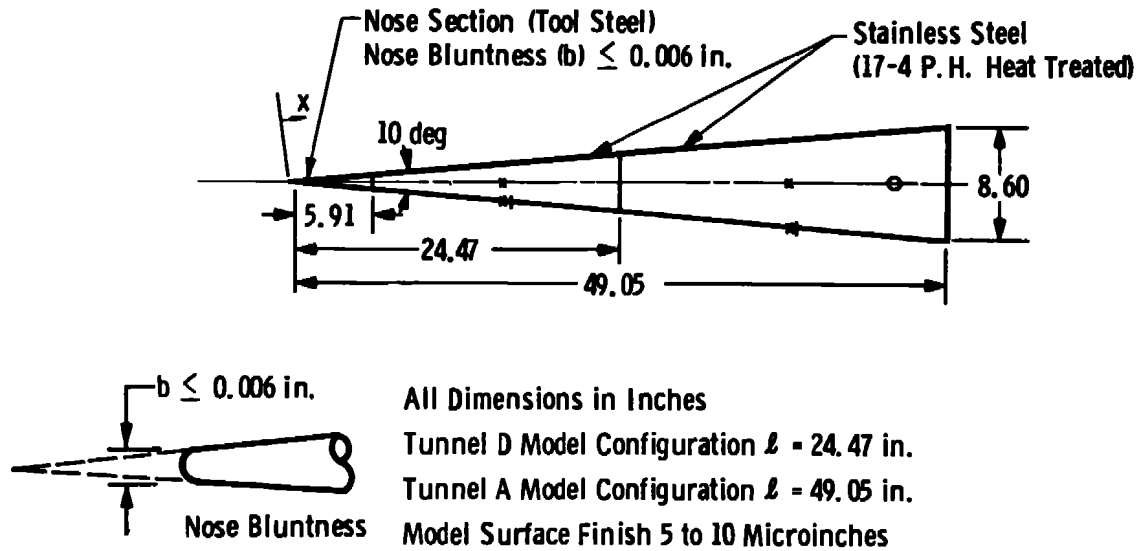
AEDC-VKF Sharp-Cone Model (Tunnels A and D)

The cone model used in the AEDC-VKF Supersonic Tunnels A and D (Figures IV-14 and IV-15) was a 10-deg total-angle, right circular, stainless-steel cone equipped with a tool steel nose section. The model had a surface finish of approximately 10  $\mu$ in. and a tip bluntness ( $\bar{b}$ ) between 0.005 and 0.006 in. The Tunnel D model consisted of the nose and center section as shown in Figures IV-14 and IV-15. The Tunnel A model was obtained by adding an aft section as shown in Figure IV-15. In order to maintain a near-perfect joint between the sections, the model surface was refinished after attaching each model section. A photograph of the model installed in Tunnel A is shown in Figure IV-16a. Sketches illustrating the position of the models in Tunnels A and D are presented in Figures IV-16 and IV-17.

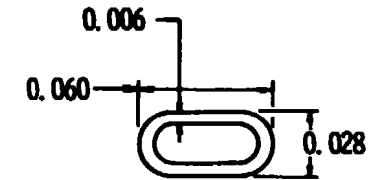
A remotely controlled, electrically driven, surface pitot probe as shown in Figures IV-16 and IV-17 provided a continuous trace of the probe pressure on an X-Y plotter from which the location of transition was determined. Details of the surface probe design are given in Figure IV-17b. It should be noted that a spring apparatus (Figure IV-17) was used to keep the probe tip in contact with the cone surface.

Schlieren and shadowgraph photographic systems were used as a secondary method for detecting the location of transition in Tunnels D and A, respectively.

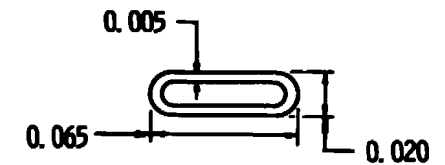
A  $\frac{1}{8}$ -in.-diam. flush-mounted surface microphone having a frequency response from 0 to 30 kHz and a dynamic response from 70 to 180 db was also used to measure the model surface pressure fluctuations in the laminar, transitional, and turbulent flow regimes and to determine the



Model Instrumentation			
Sym	Type	Quantity	Surface Location $x$ , in.
x	Pressure Orifice, (0.020-in. -diam)	4	15.59, 37.26 (90 deg Apart)
I	Thermocouple	2	16.08, 37.76
o	Microphone	1	45.51



Probe A  
(Used in Tunnels D and A)



Probe B  
(Used in Tunnel A Only)

#### PROBE DETAILS

Figure IV-14. AEDC-VKF sharp-cone model geometry.

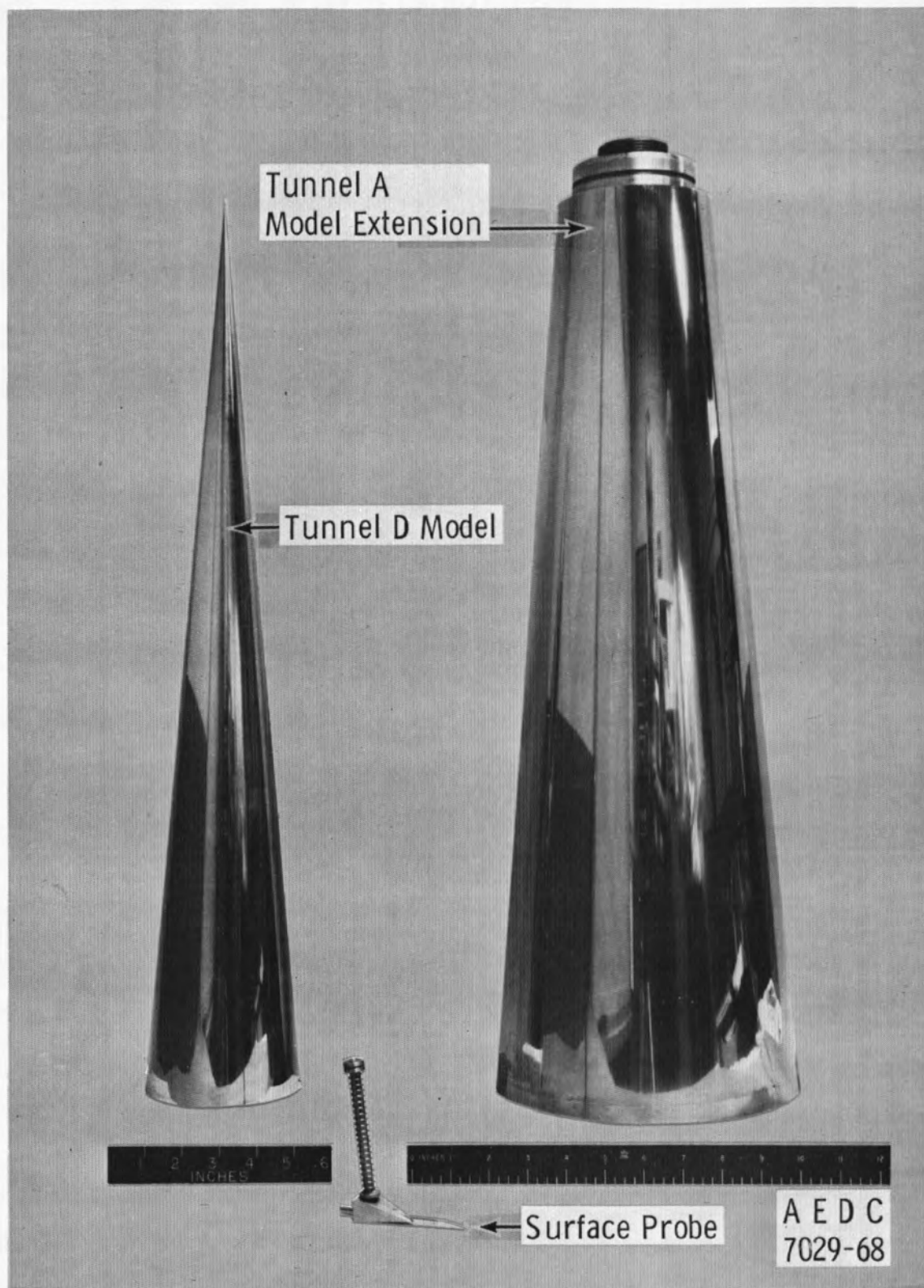
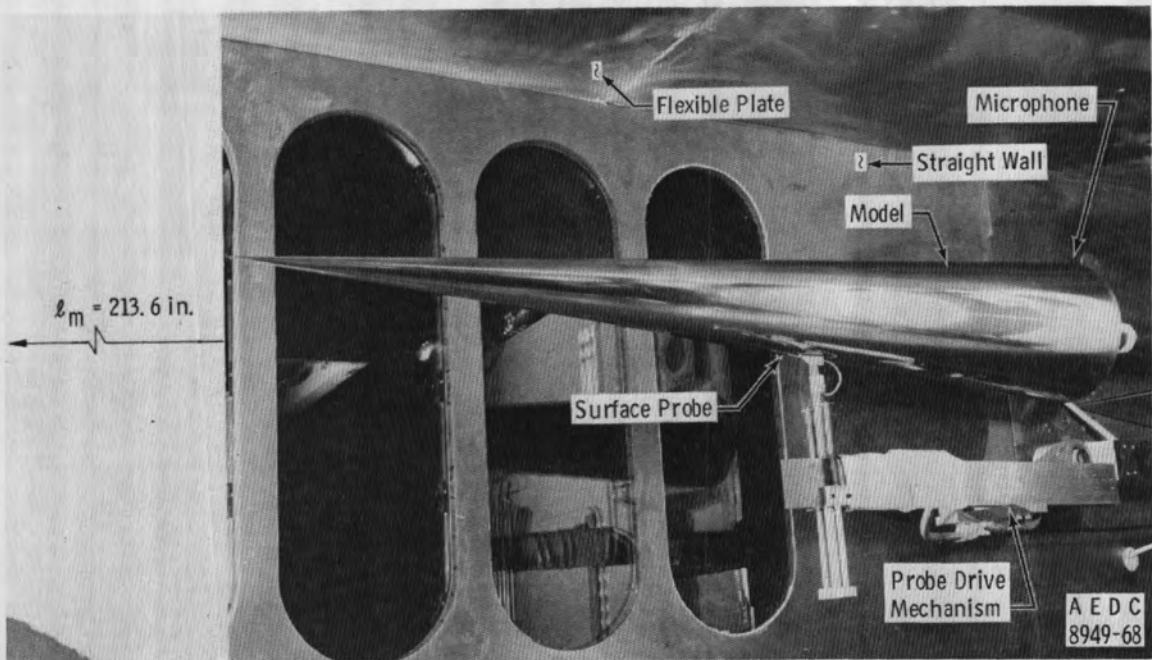
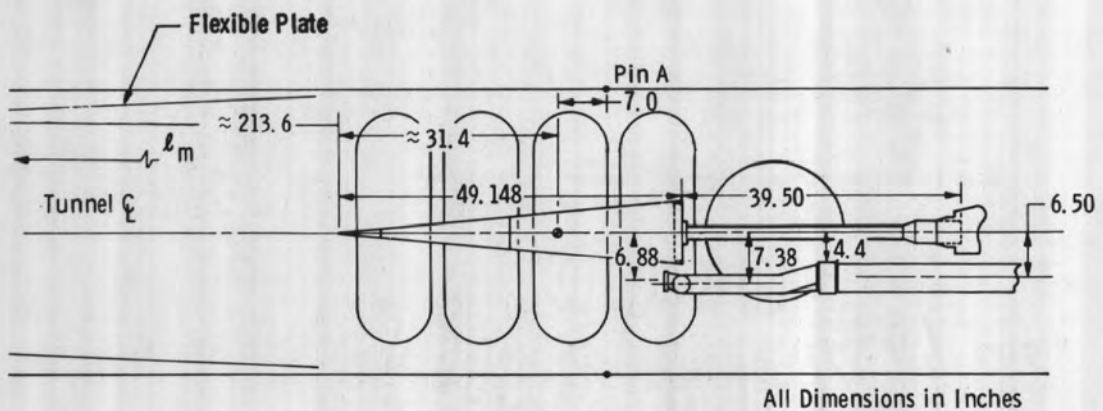


Figure IV-15. Photograph of sharp-cone model components.

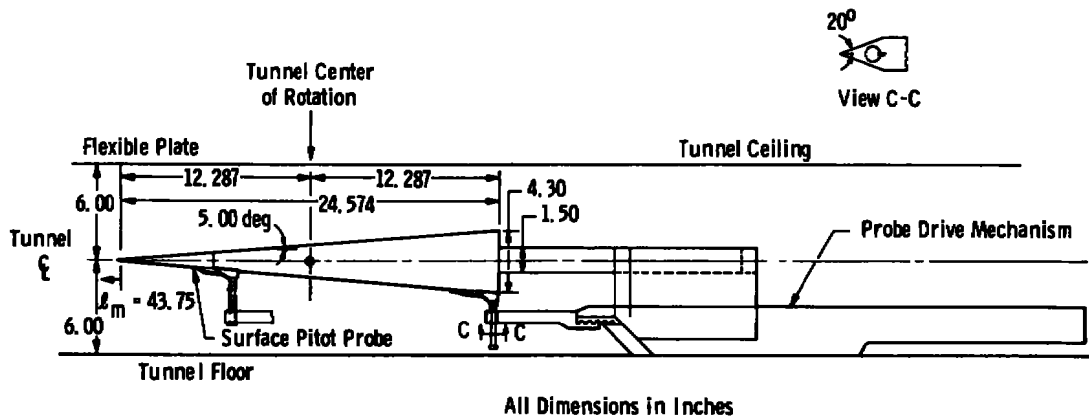


a. Model Installation Photograph

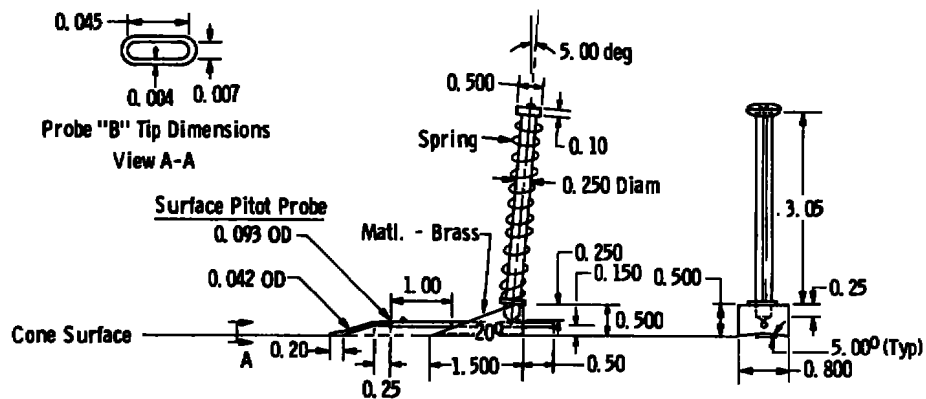


b. Model Installation Sketch

Figure IV-16. Installation of the 5-deg cone transition model in the AEDC-VKF Tunnel A.



a. Model Installation Sketch



b. Details of Surface Probe

Figure IV-17. Probe details and installation sketch of the 5-deg transition cone in the AEDC-VKF Tunnel D.

location of transition. A description of the microphone installation is given in the next chapter.

#### AEDC-VKF Sharp-Cone Model (Tunnel F)

The 10-deg half-angle sharp-cone model used in AEDC-VKF Tunnel F is shown in Figure IV-18. The cone was 17.01 in. in length (base diameter = 6.0 in.) and was instrumented to measure heat-transfer rates at 34 locations and surface pressures at 25 locations. Surface static pressures were measured using on-board transducers, and surface thermocouple data were used to compute the heat-transfer rates. The heat-transfer gages were filed and sanded (using emery paper) flush with the model surface as discussed in Reference (103). The model surface finish was 15  $\mu$ in. and the nose bluntness was less than 0.005 in. Figure IV-13, page 94, shows the position of the cone models in the Tunnel F test section.

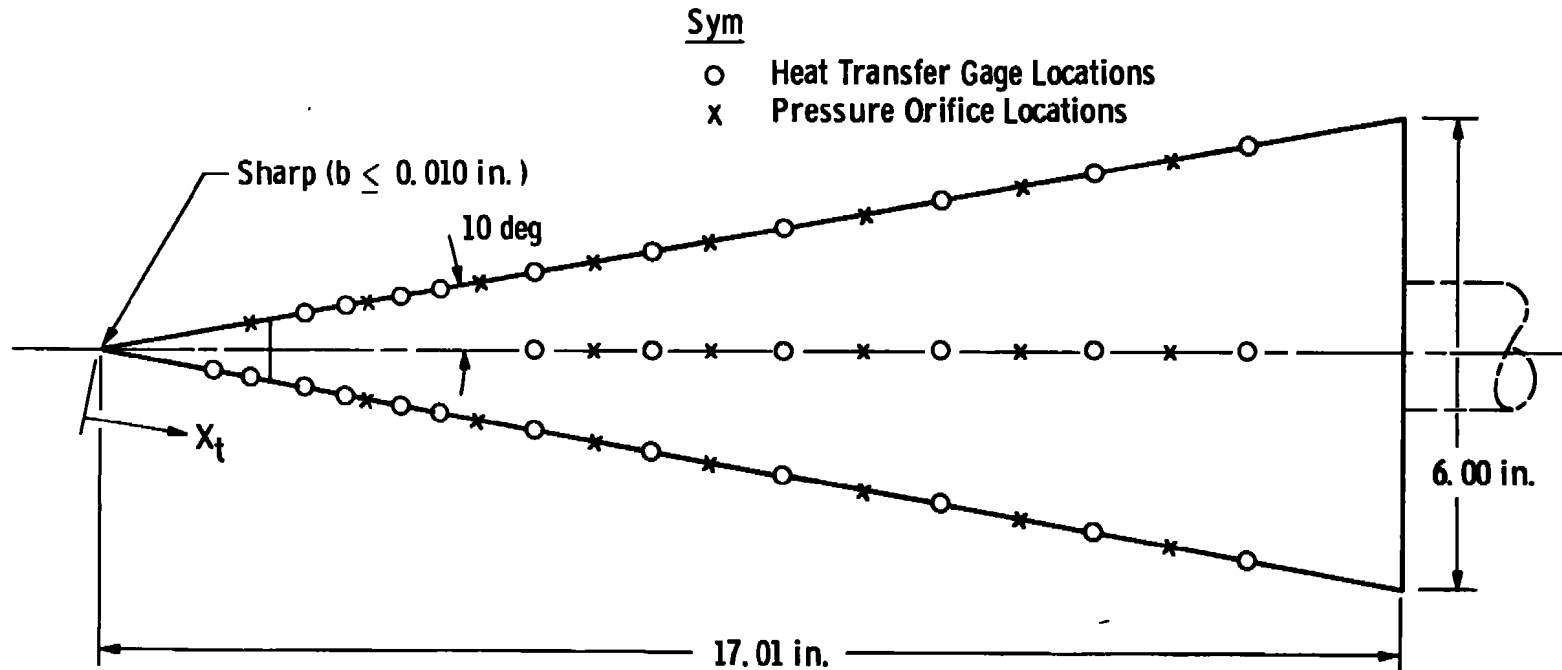


Figure IV-18. AEDC-VKF Tunnel F 10-deg cone transition model.



## CHAPTER V

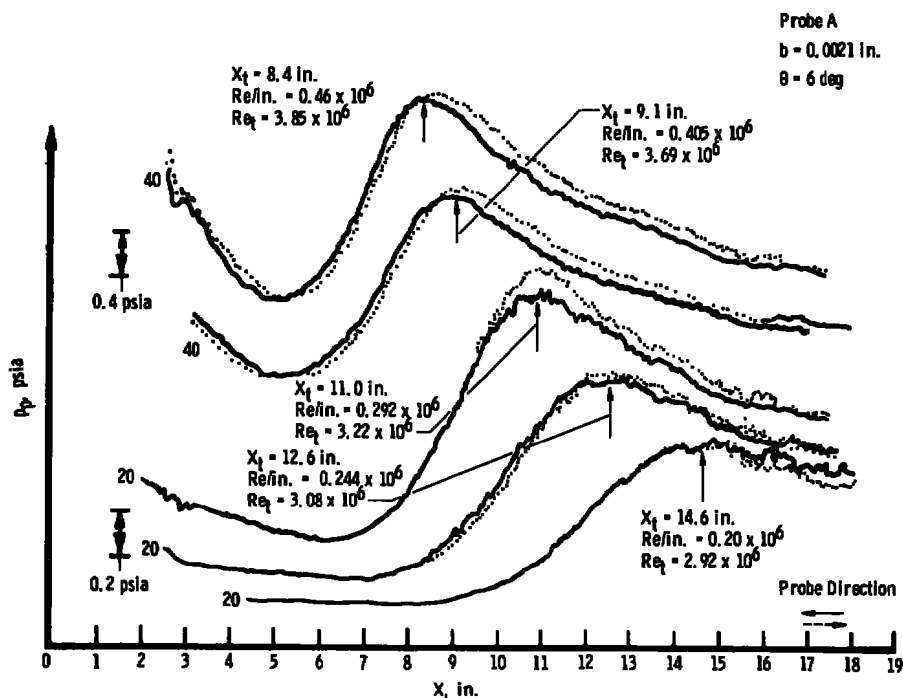
## EXPERIMENTAL TECHNIQUES AND BASIC TRANSITION DATA

## I. BASIC TRANSITION DATA

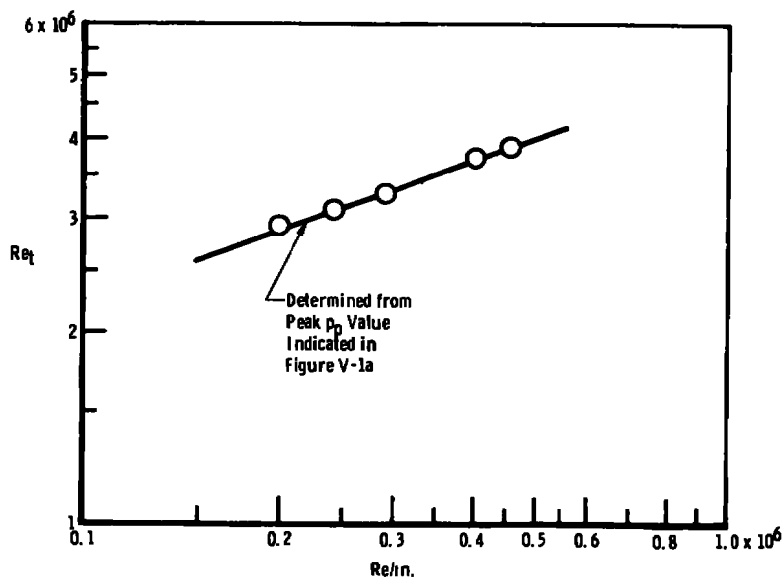
Many techniques have been used and reported in the literature on ways to determine the location of boundary-layer transition on the surface of wind tunnel models. The basic methods used in this research were the surface probe method for  $M_\infty \lesssim 6$  and measurement of surface heat-transfer rates for  $M_\infty \gtrsim 6$ . Some data were obtained using optical techniques (schlieren and shadowgraph) and a surface microphone for  $M_\infty \lesssim 6$ . Further discussion on these methods and other techniques and a correlation of the location of transition as determined by the different techniques are presented in Chapter VI.

The location of transition used in this report is defined as the peak in the pitot pressure profile as indicated in Figures V-1 through V-4 or the peak in the heat-transfer rate as shown in Figures V-5 and V-6. These methods of transition detection are generally accepted as being near the end of the transition process (region) and have been established as some of the more repeatable and reliable methods of selecting a particular and finite location for transition. The location of the peak in the surface heat-transfer-rate value for  $M_\infty \gtrsim 8$  is approximately equal to the location of the peak in the surface probe pressure ( $p_p$ ) value as shown in Chapter VI.

The surface pitot probe is particularly well suited for detecting transition at subsonic and supersonic speeds, whereas heat-transfer-rate data provide the better method at hypersonic Mach numbers.



a. Surface Pitot Probe Pressure Traces



b. Transition Reynolds Numbers

Figure V-1. Basic transition data from the hollow-cylinder model, AEDC-VKF Tunnel A,  $M_\infty = 4.0$ .

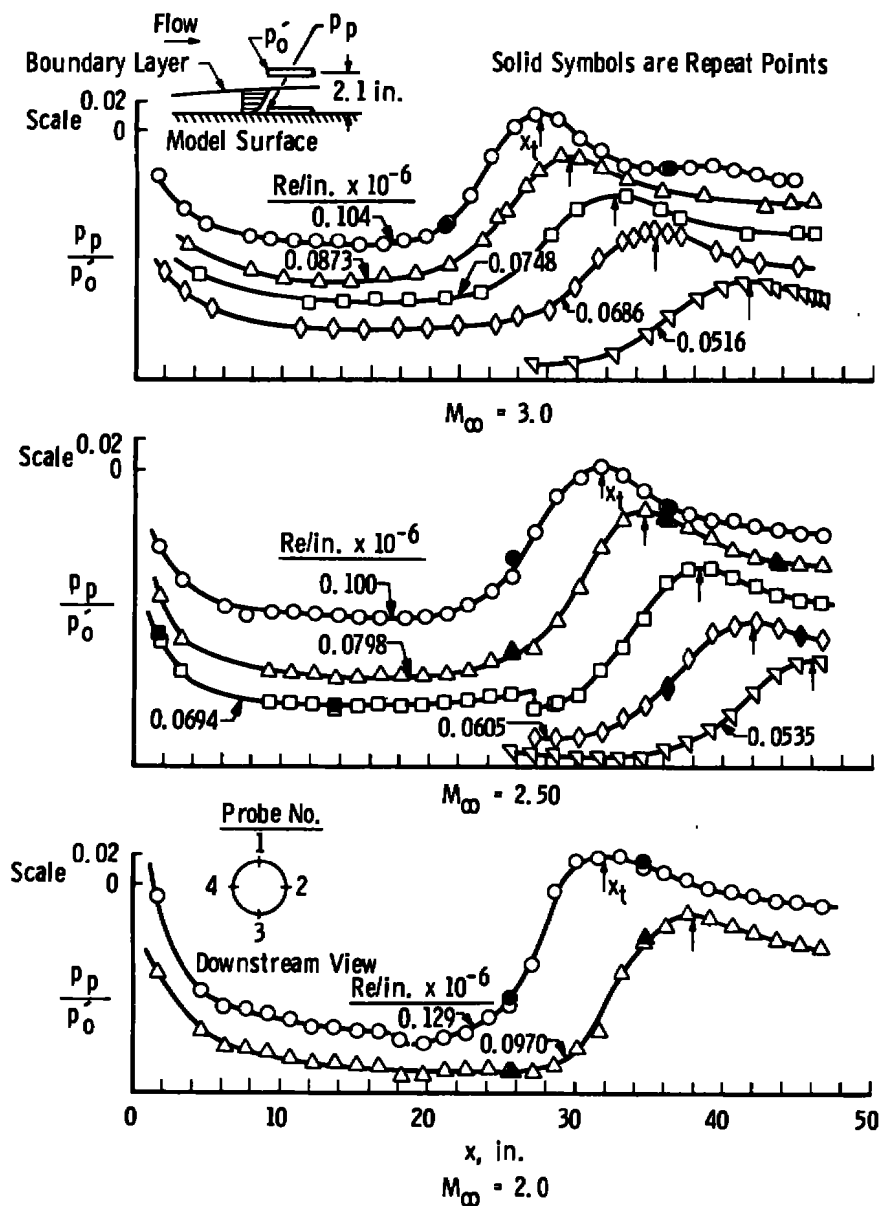


Figure V-2. Probe pressure data showing the location of boundary-layer transition on the 12-in.-diam hollow-cylinder model in the AEDC-PWT 16S Tunnel for  $M_\infty = 2.0, 2.5$ , and  $3.0$ , probe No. 1,  $\bar{b} = 0.0012$  in.,  $\theta_{LE} = 6.5$  deg.

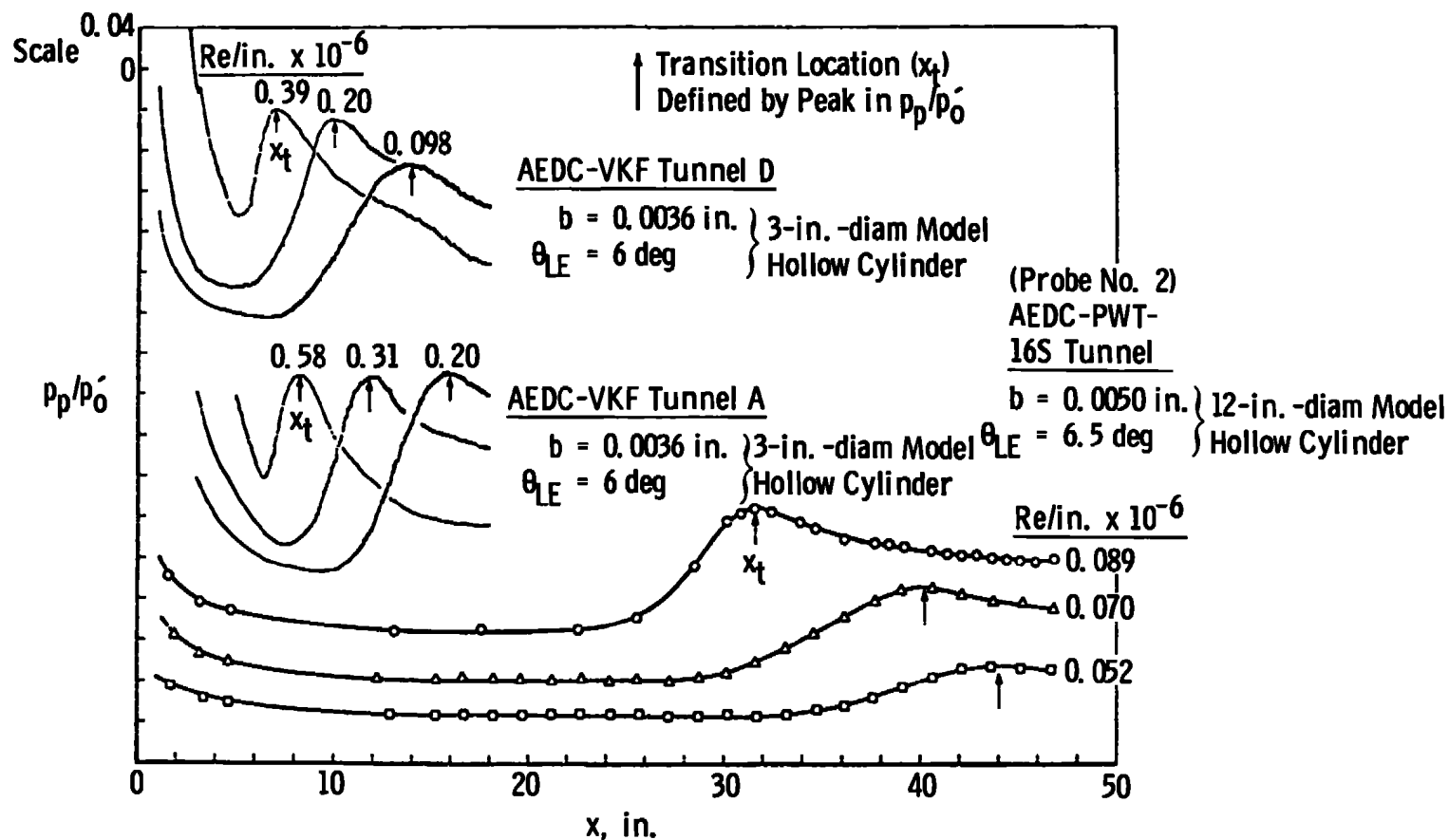
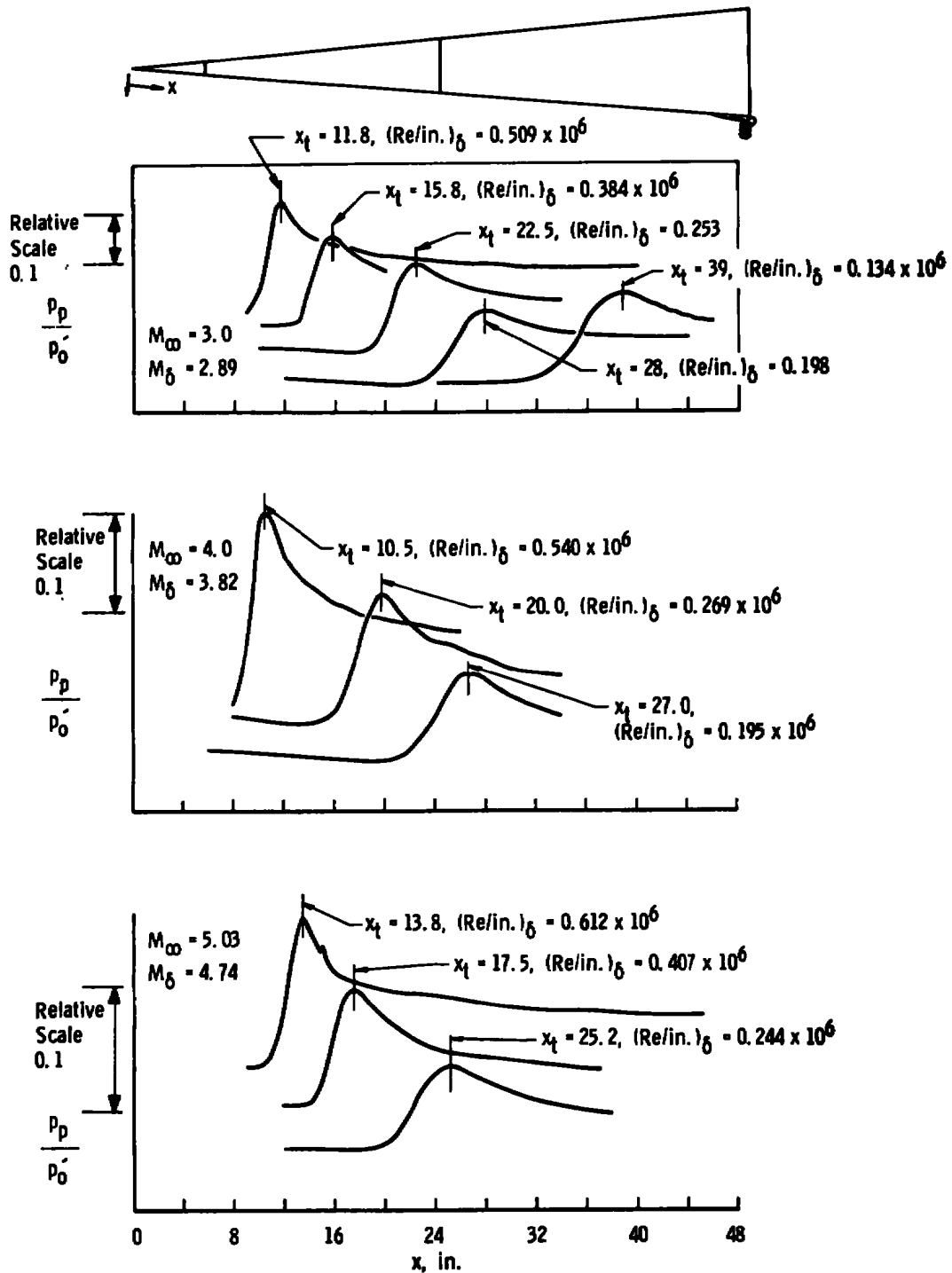
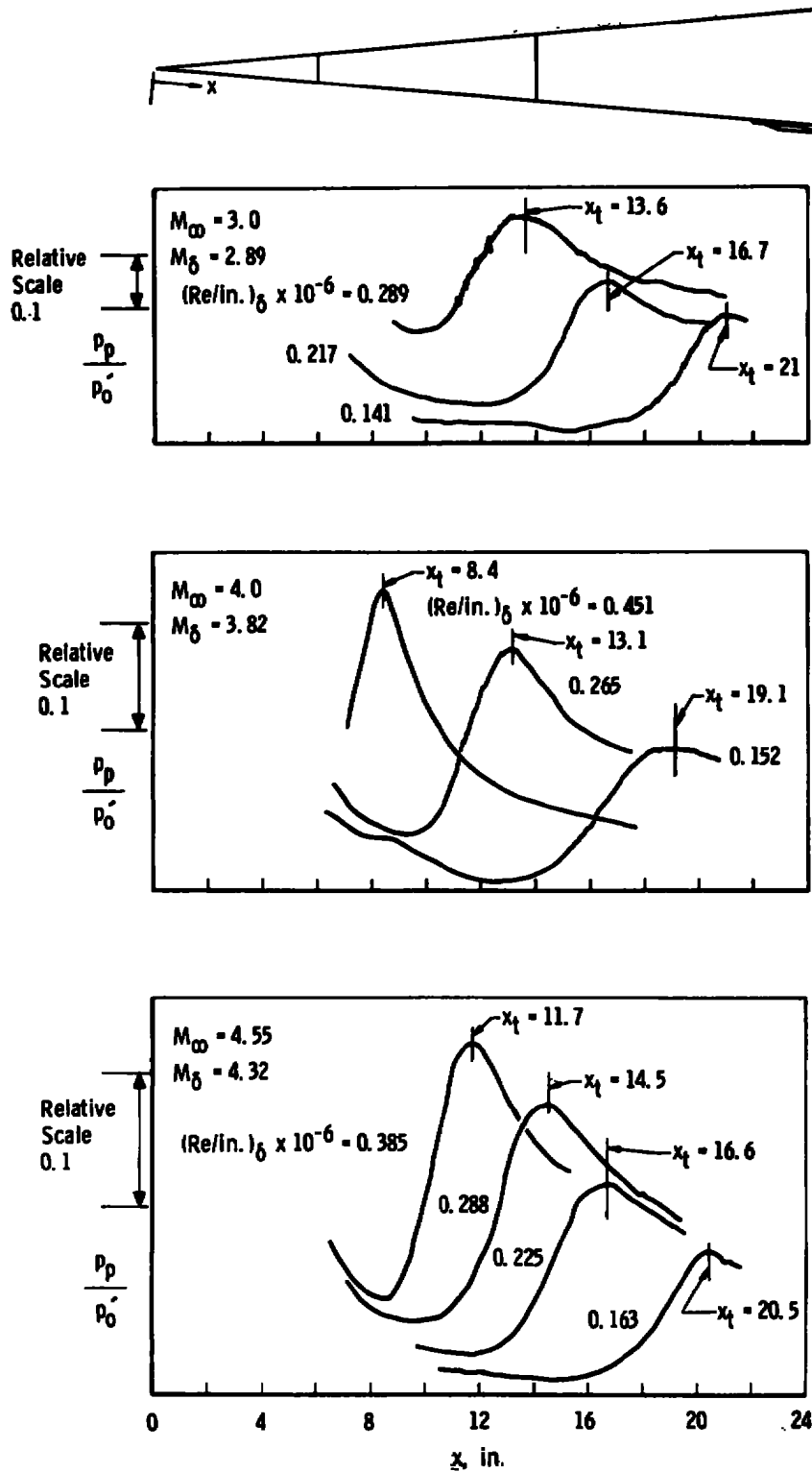


Figure V-3. Comparison of probe pressure transition traces in the AEDC-VKF Tunnels A and D and AEDC-PWT 16S for  $M_\infty = 3.0$ .



## a. AEDC-VKF Tunnel A

Figure V-4. Examples of surface probe transition profile traces on the 5-deg half-angle sharp-cone model.



b. AEDC-VKF Tunnel D  
Figure V-4. (Continued)

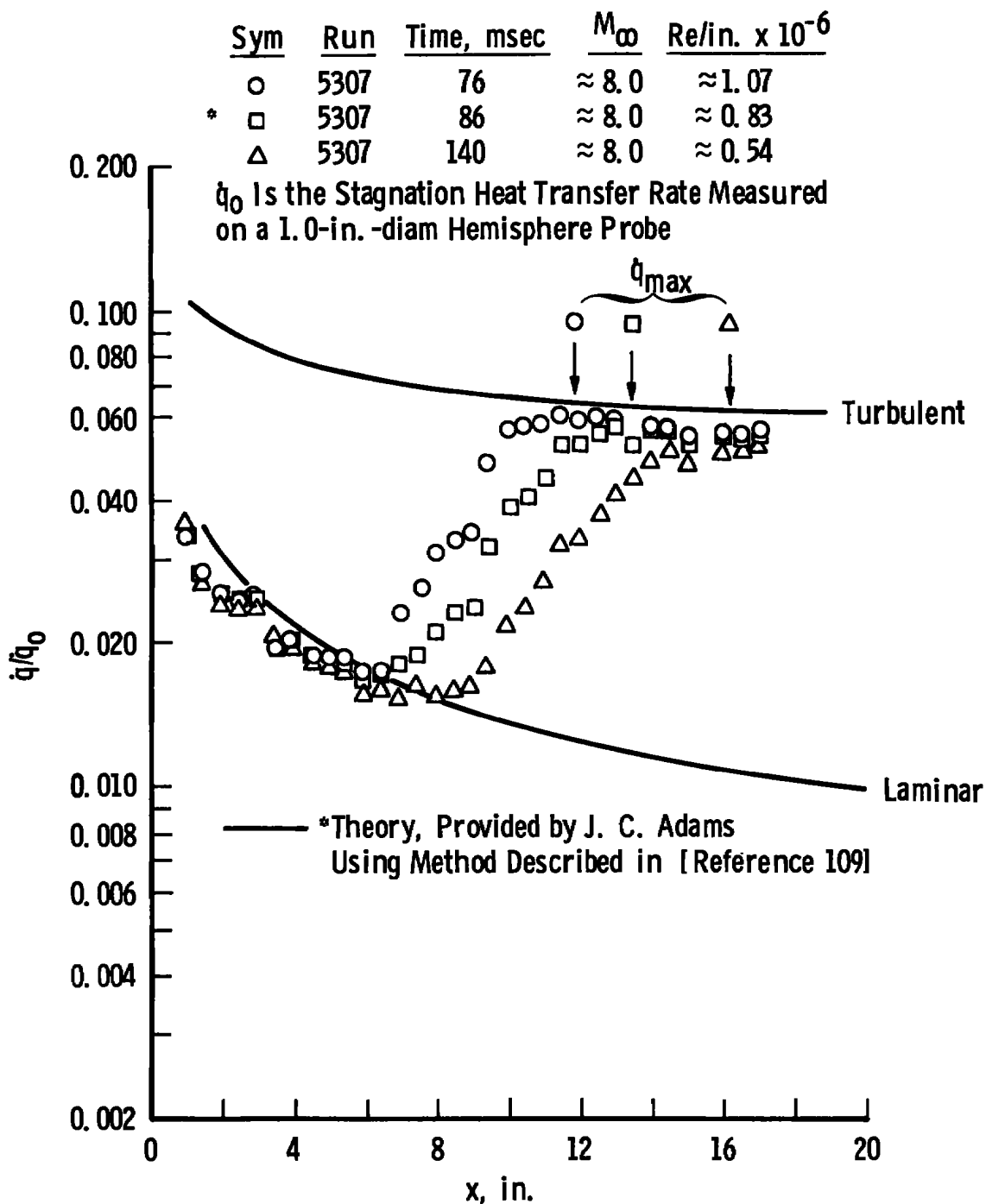
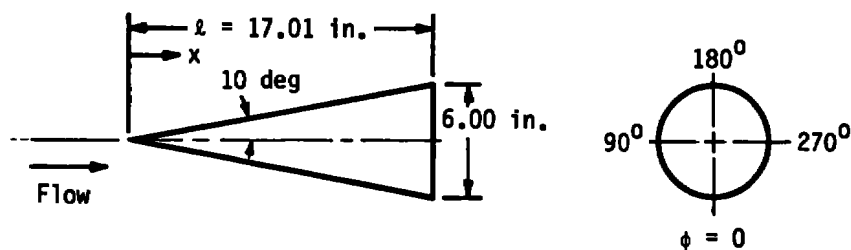
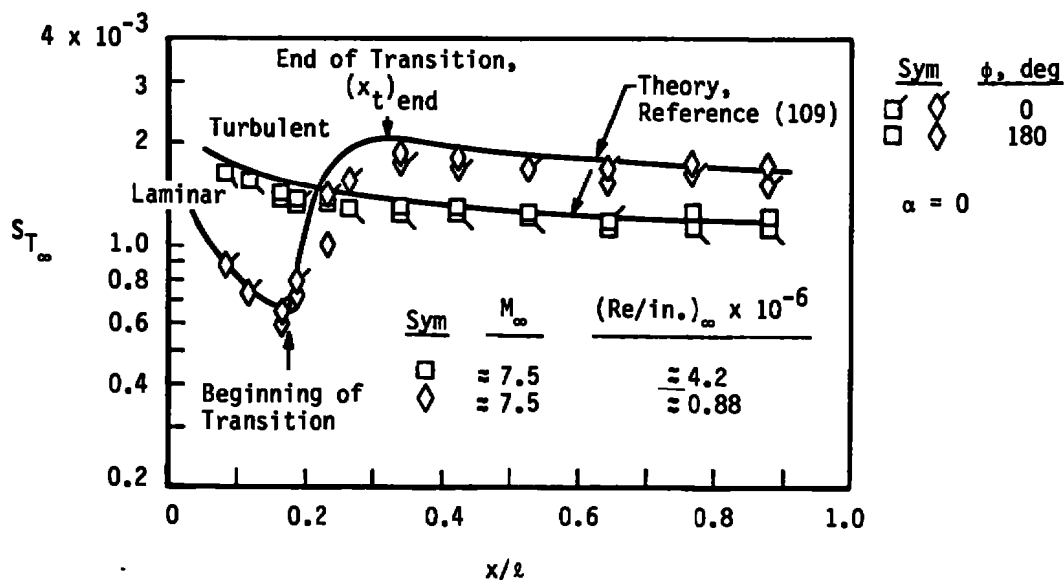


Figure V-5. AEDC-VKF Tunnel F flat-plate transition data.



a. Model Geometry

$$S_{T_\infty} = \dot{q} / \rho_\infty U_\infty (H_o - H_w)$$



b. Surface Heating Rates

Figure V-6. Heat-transfer rate distributions on a 10-deg half-angle, sharp cone at zero incidence in the  $M_\infty \approx 7.5$  contoured nozzle.



### Pitot Probe Data

Examples of the basic transition data obtained using the surface pitot probe on the hollow-cylinder models at supersonic Mach numbers in the AEDC-VKF Tunnel A are shown in Figure V-1. Note that the peak pitot pressure is well defined, and this was typical of all the probe data. The beginning of transition (defined as the minimum  $p_p$  value) is usually less well defined as observed from Figures V-1 through V-4. Also plotted in Figure V-1 are the  $(Re_t)_{end}$  values determined from the probe peak value. The trend of  $Re_t$  with the unit Reynolds number is a well-documented variation. The unit Reynolds number effect has been extensively studied by Potter and Whitfield (37,108) and by Potter (23,27).

Pitot traces obtained on the hollow-cylinder model in the AEDC-PWT Tunnel 16S at  $M_\infty = 2.0, 2.5,$  and  $3.0$  are shown in Figure V-2.

A comparison of the surface probe profile data obtained in the AEDC-VKF Tunnels A and D and the AEDC-PWT Tunnel 16S is presented in Figure V-3 to illustrate the consistency and quality of the probe data obtained. It should be noted that the location of transition moved aft as the tunnel size increased. This behavior is the direct result of free-stream radiated noise disturbance and will be explained in Chapters VIII and IX.

Examples of the surface probe data obtained on the 5-deg half-angle cone at several Mach numbers in the AEDC-VKF Tunnels A and D are shown in Figure V-4. Again the consistency and good quality of the data and the distinctive location of the peak  $p_p/p'_0$  value are exhibited.

## Heat-Transfer Data

Typical heat-transfer-rate distributions obtained in the AEDC-VKF Tunnel F on the flat-plate model at  $M_\infty \approx 8$  and the 10-deg angle sharp cone at  $M_\infty \approx 7.5$  are presented in Figures V-5 and V-6, respectively. The peak values of the  $\dot{q}/q_0$  ratio are indicated. Theoretical<sup>12</sup> laminar and turbulent heating rates are included as reference values and for comparative purposes. The well-defined minimum-maximum values in the  $\dot{q}$  distribution should be noted. The surface heat-transfer distribution is an excellent method for defining the beginning and the end of transition region.

## II. APPLICATION OF A SURFACE MICROPHONE

### Dynamic Pressure Instrumentation

The transducer used to measure the cone surface pressure fluctuations was a Bruel and Kjar, Model No. 4136,  $\frac{1}{4}$ -in.-diam condenser microphone mounted as illustrated in Figure V-7. The microphone cartridge, when connected to Bruel and Kjar types UA0122 flexible adapter and 2615 cathode follower, and powered by a Bruel and Kjar type 2801 power supply, has an atmospheric pressure frequency response of 30 Hz to 70 kHz and a dynamic pressure range of 70 to 180 db, referenced pressure = 0.0002 microbars.

Since the air mass inside the cartridge is used to provide critical damping for a flat frequency response at one atmosphere of pressure, the microphone has a resonant peak in its frequency response curve

---

<sup>12</sup>These theoretical values were supplied by Dr. J. C. Adams, Jr., AEDC-VKF and were obtained using the method reported in Reference (109).

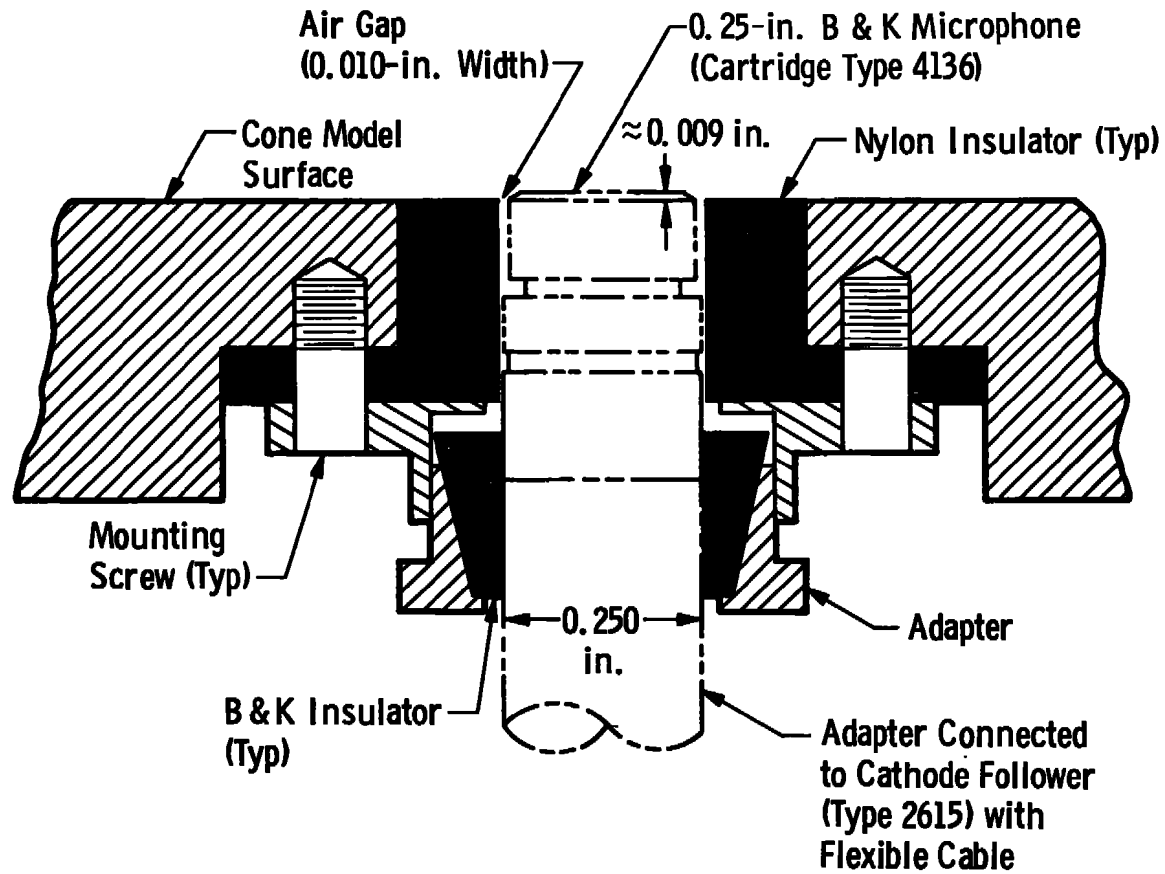


Figure V-7. Cut-a-way view illustrating microphone installation.

when operated at ambient pressures lower than one atmosphere. Figure V-8 shows the change in sensitivity versus frequency at a pressure of 300 mm Hg. This curve was obtained using Bruel and Kjar type 4142 calibration apparatus. A Fourier analysis of tunnel data (Figure V-9) shows the effect of the microphone's resonance when operated at a low pressure and exposed to wideband fluctuating pressures. The output signals centered about the resonant frequency will cause errors in the rms values of the fluctuating pressure. To reduce these errors, frequencies above 25 kHz were filtered out of selected tunnel data with a filter having a 12 db per octave rolloff.

#### Recording and Analyzing Equipment

The output of the microphone was fed through a Spencer-Kennedy Laboratories, Inc. Model 302 variable electronic low pass filter to a Bruel and Kjar type 2409 voltmeter. The rms values of pressure fluctuations were read directly on-line from the voltmeter, and the time varying pressure fluctuations, using the voltmeter's amplifier as a preamplifier, were recorded on an Ampex Model FR1300 analog tape recorder for post-test data analysis and for verification of the on-line rms values. The data were recorded simultaneously on a direct and an FM channel having frequency responses of 300 Hz to 300 kHz and 30 to 20 kHz, respectively.

For analysis, loops were made from the data tapes and the recorded signals were played back into a Technical Products Model TP-625 spectrum analyzer. Power spectral density analyses were made from the recorded data using a 10-Hz bandwidth filter and covering a frequency range from 10 Hz to 20 kHz. Figure V-10 shows a calibration curve and

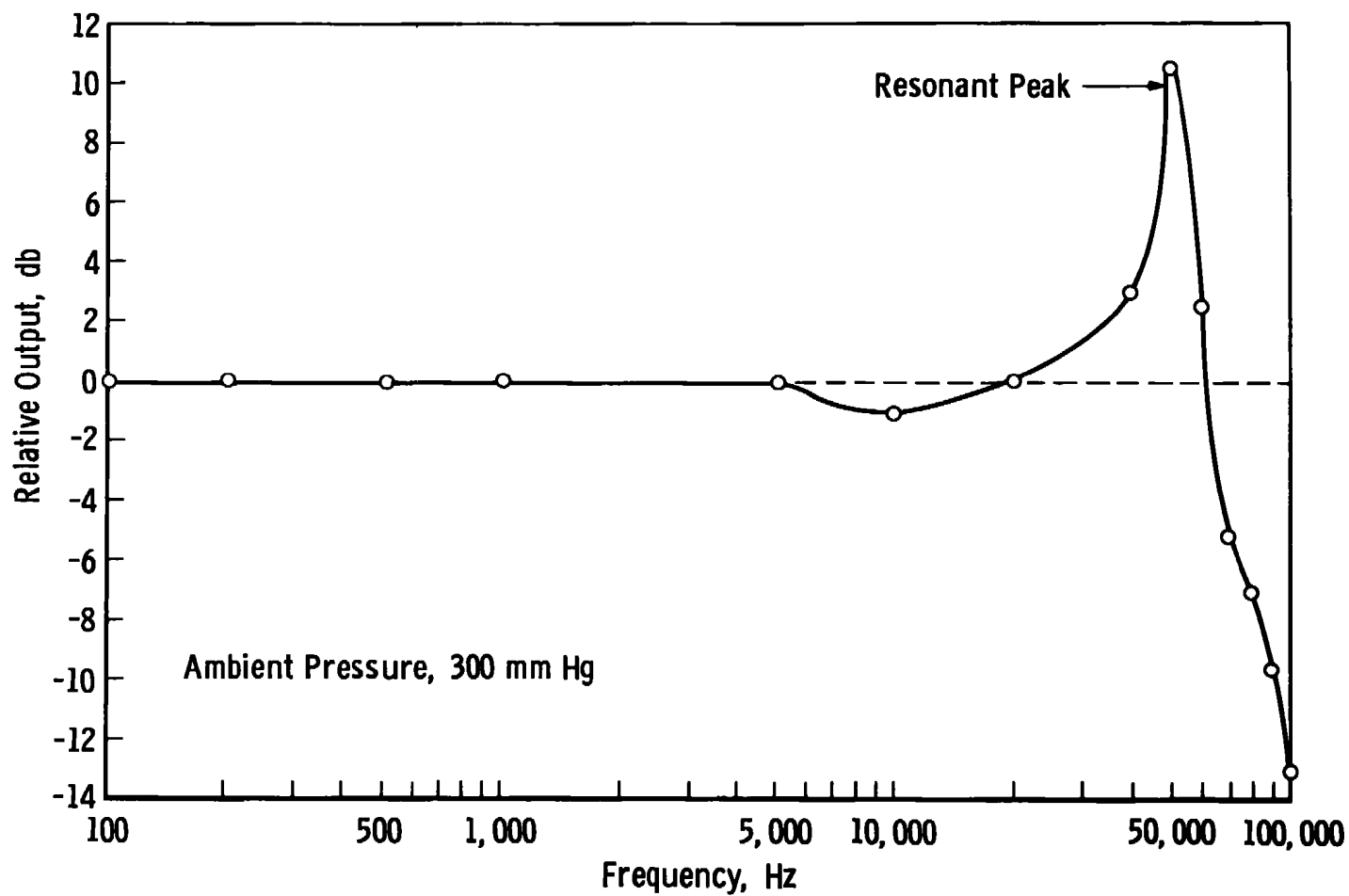


Figure V-8. Microphone frequency response.

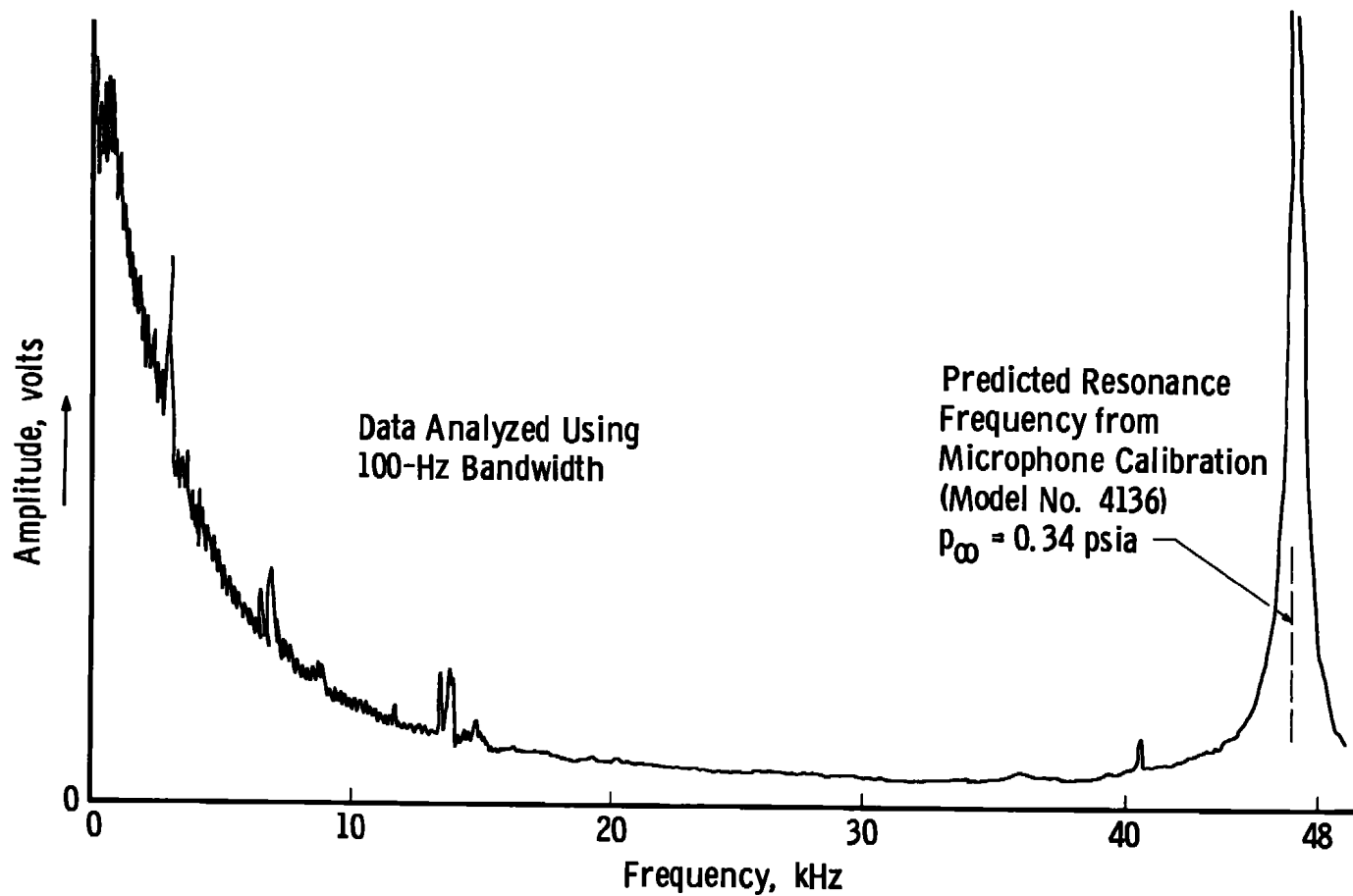
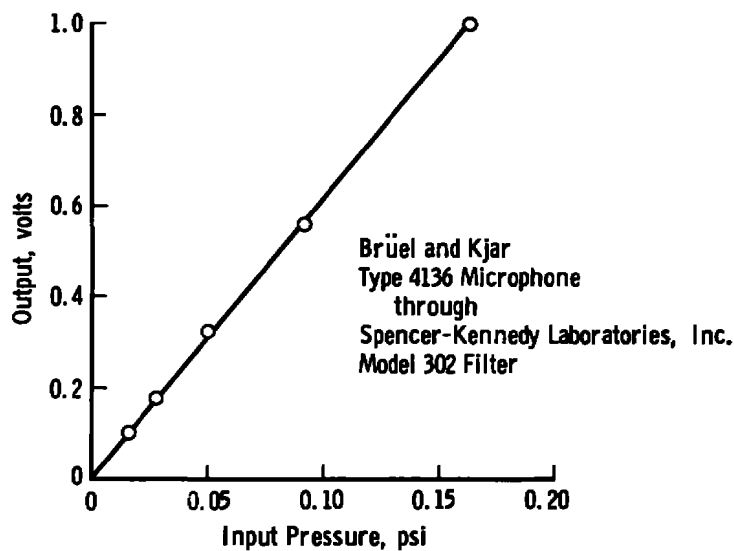
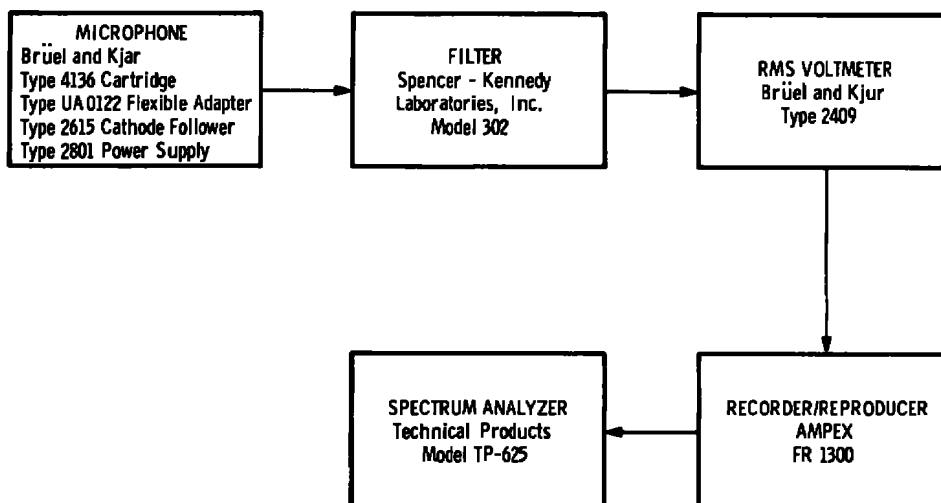


Figure V-9. Ambient pressure effects on microphone frequency response,  $M_\infty = 3$ .



a. Microphone Transfer Characteristics



b. Dynamic Pressure Recording and Analyzing System

Figure V-10. Microphone system used in the AEDC-VKF Tunnel A aerodynamic-noise-transition study.

the block diagram for the dynamic pressure recording and analyzing system.

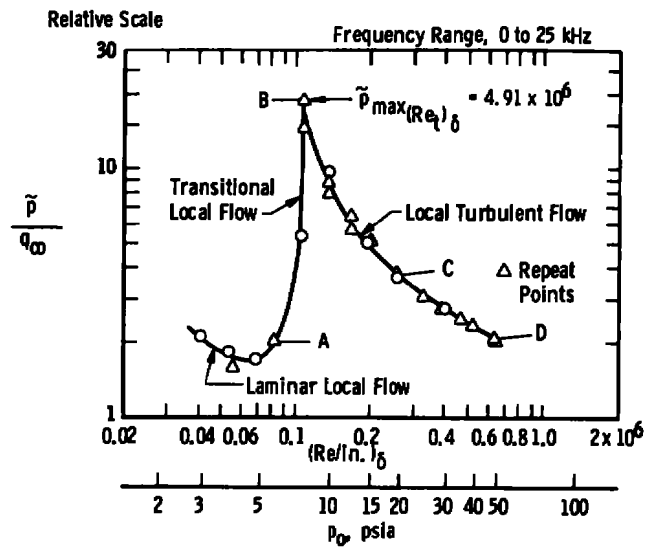
### Calibration Procedure

The voltage versus pressure characteristics of the microphone were obtained by applying known pressure levels to the microphone and recording the voltage output from the filter. This calibrates the filter and microphone as a single unit. Known pressure levels were generated using an oscillator, a power amplifier, a horn driver, and a standard microphone. Using a frequency of 250 Hz, the pressure levels were set with the standard microphone and then transferred to the working microphone. The resulting calibration curve is shown in Figure V-10. Since the sensitivity of a microphone is usually listed in decibels, appropriate scale factors were used to convert the sound pressure levels to psi.

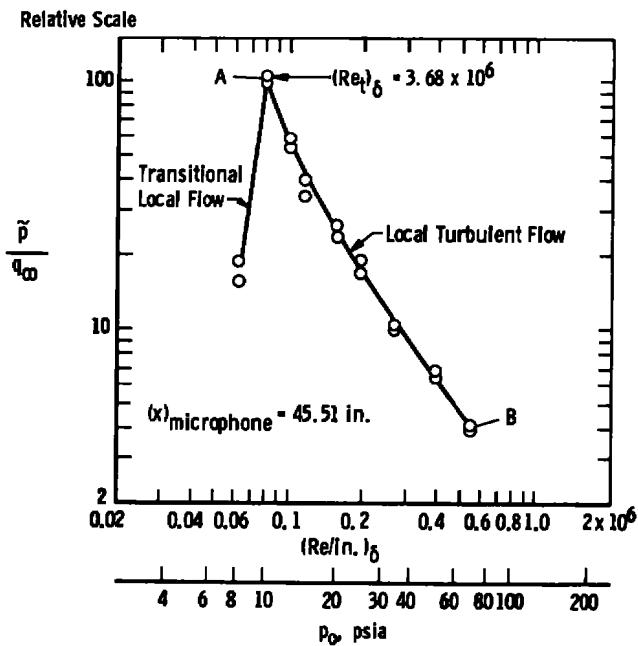
### Transition Detection

Presented in Figure V-11 are the surface pressure fluctuations ( $\tilde{p}/q_\infty$ ) measured with the  $\frac{1}{4}$ -in. microphone on the surface of the 10-deg sharp-cone model at station 45.5 in. (see Figure IV-14, page 112). These data were measured in the AEDC-VKF Tunnel A at Mach numbers 3 and 4. The data show a low  $\tilde{p}/q_\infty$  value existing when the boundary layer was laminar over the entire model surface followed by a very sharp peak and then rapid decay with increasing  $p_0$  or  $(Re/in.)_\delta$ , as transition moved forward and the sensor was exposed to fully developed turbulent flow. The finite  $\tilde{p}/q_\infty$  levels that existed when the flow was laminar is the direct result of the noise level that radiates from the tunnel walls turbulent boundary as discussed in Chapter III.





a.  $M_\infty = 3.0$

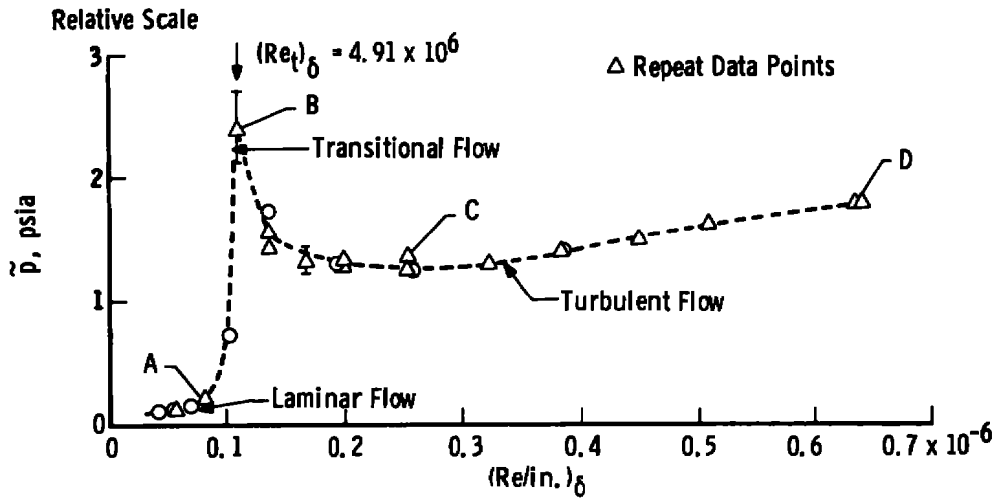
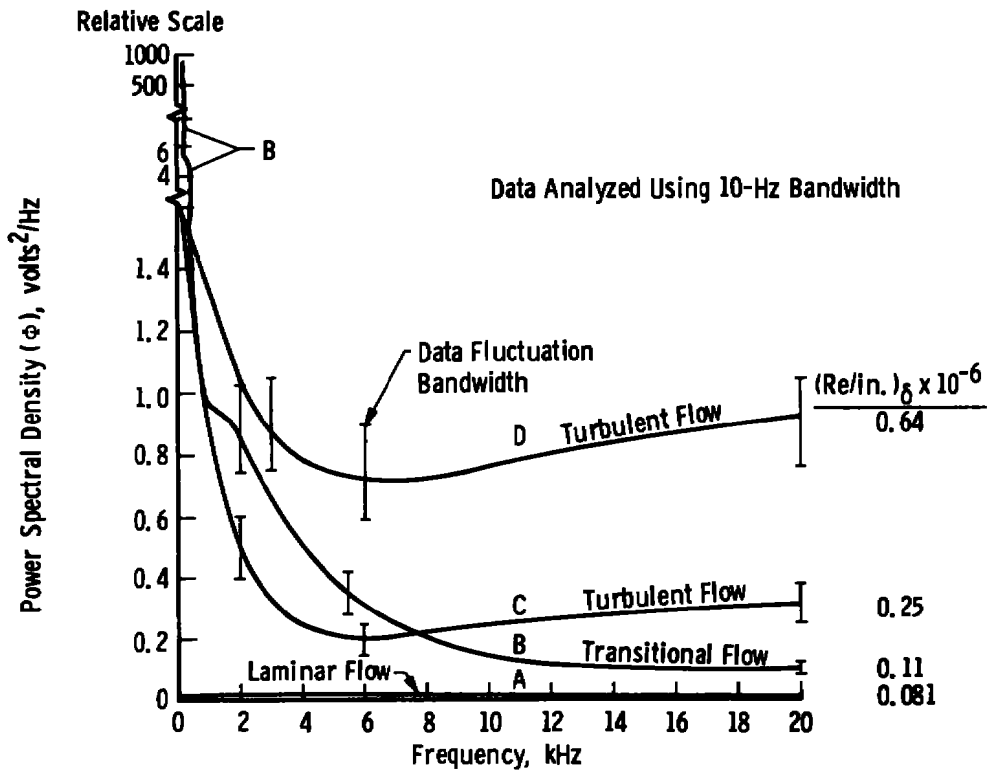


b.  $M_\infty = 4.0$

Figure V-11. Detection of transition from microphone rms pressure fluctuations,  $M_\infty = 3.0$  and  $4.0$  (AEDC-VKF Tunnel A).

Data as presented in Figure V-11 in terms of rms alone can be misleading, as has sometimes occurred in the literature, when one is not aware of the limitations imposed by the microphone or data-recording system frequency range. The absolute values of the fluctuating pressure profile expressed as  $\tilde{p}$  are presented in Figure V-12a for  $M_\infty = 3$ . These data clearly indicate the relation of the absolute levels of the pressure fluctuation when the flow was laminar, transitional, or turbulent. Four selected data points, designated points A, B, C, and D, have been analyzed, and their spectral distributions are shown in Figure V-12b. As discussed in the preceding section, a 25-kHz filter was installed to eliminate the microphone resonance effects at frequencies above 25 kHz. The spectral distributions presented in Figure V-12b show that a significant amount of the overall rms data in Figures V-11 and V-12a were not recorded for test points C and D. Based on the results of References (110) and (111), it can be estimated that frequencies up to approximately 200 to 300 kHz are present in the cone turbulent flow. Consequently, the turbulent  $\tilde{p}$  data for  $(Re/in.)_\delta \approx 0.15 \times 10^6$  presented in Figures V-11 and V-12a are significantly lower than a true total overall rms would indicate.

Figure V-13 presents a replot of the spectral data in Figure V-12b to more clearly show certain pertinent features. The spectra of the laminar flow profile (A) (which is related to the tunnel radiated aerodynamic noise levels) are more clearly illustrated. Also evident is the concentration of energy present in the transition profile (B) at the lower frequencies of ( $f < 1000$ ). The exact source of the low frequencies associated with the transition process is not completely understood, but

a. RMS Pressure Fluctuations ( $\bar{p}$ )

b. Spectral Distribution

Figure V-12. Microphone Results,  $M_\infty = 3$ .

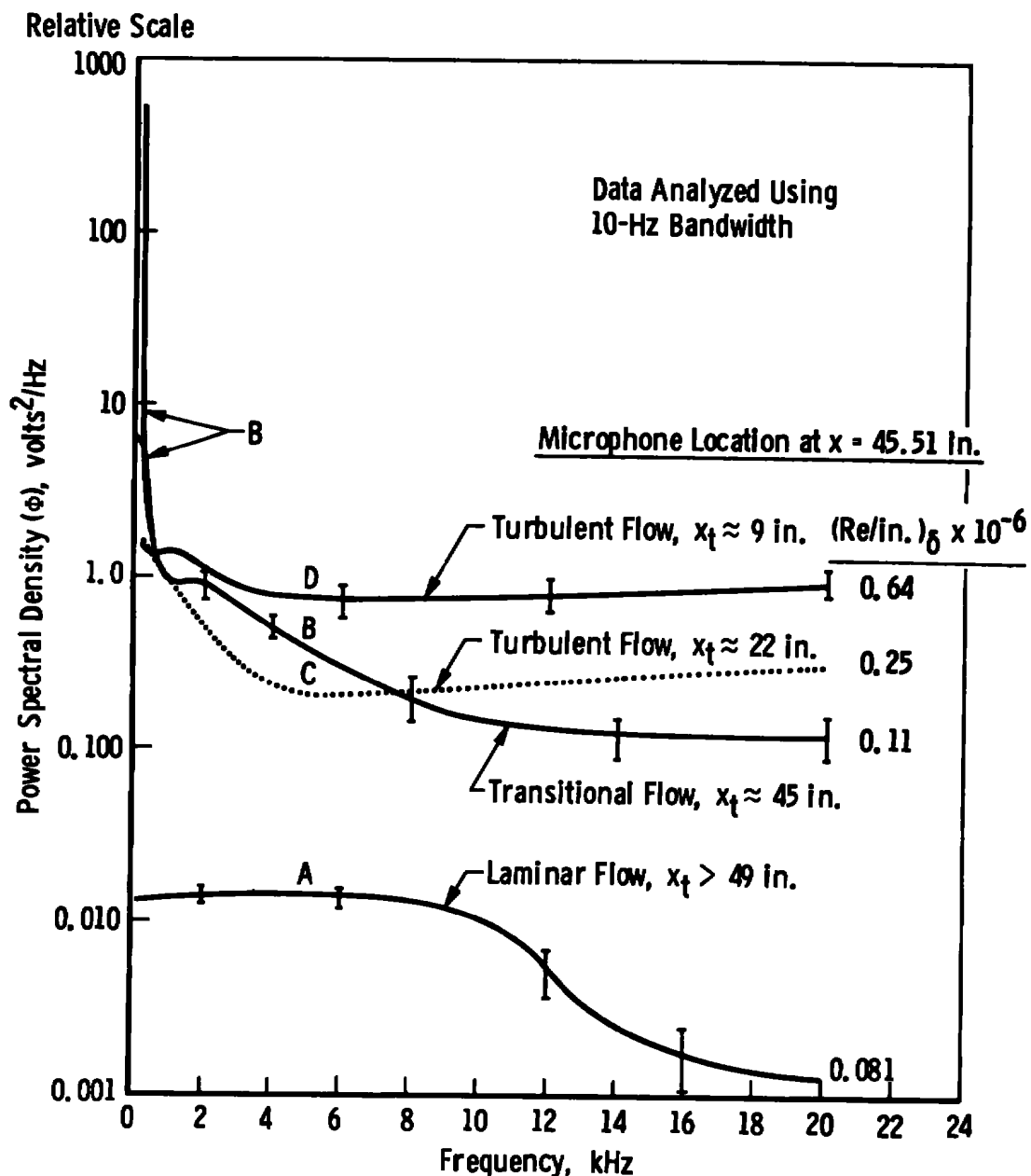


Figure V-13. Variation of acoustic spectra with boundary-layer state,  
 $M_\infty = 3$ .

they are tentatively believed to be aerodynamic and not structurally generated. Figure V-14 presents photographs of the oscilloscope record showing the time-dependent microphone pressure fluctuation output for the selected data points A, B, C, and D plus a fully laminar point  $(Re/in.)_\delta = 0.054 \times 10^6$ .

The sharp peak in the rms profiles or  $\tilde{p}/q_\infty$  profiles indicates that the microphone is an excellent indicator of transition. This conclusion is also consistent with recently published data obtained with a thin film (112). The peak in the  $\tilde{p}/q_\infty$  data is more pronounced than the pitot probe trace data as seen by comparing Figures V-11, page 118, and V-4, page 106. The peak point in the rms pressure fluctuation was selected to define the point of transition. This definition is consistent with the peak probe pressure obtained using the traversing surface probe. It should now be clear to the reader that the transition process occurs over a finite length rather than instantaneously at a specific location. Transition Reynolds numbers for  $M_\infty = 3$  and 4, as defined by the peak locations in the rms pressure fluctuation profile and the surface probe pressure trace, will be discussed in Chapter VII and compared with results from other methods. These data will show that the location of transition as determined by a surface microphone is consistent with pitot and shadowgraph data and is an excellent indicator of transition at supersonic speeds.

Presented in Figure V-15 are the spectra data obtained when the boundary layer on the cone surface was fully turbulent. The power spectra density is correlated with the Strouhal number  $\omega\delta^*/u_\delta$ . Several

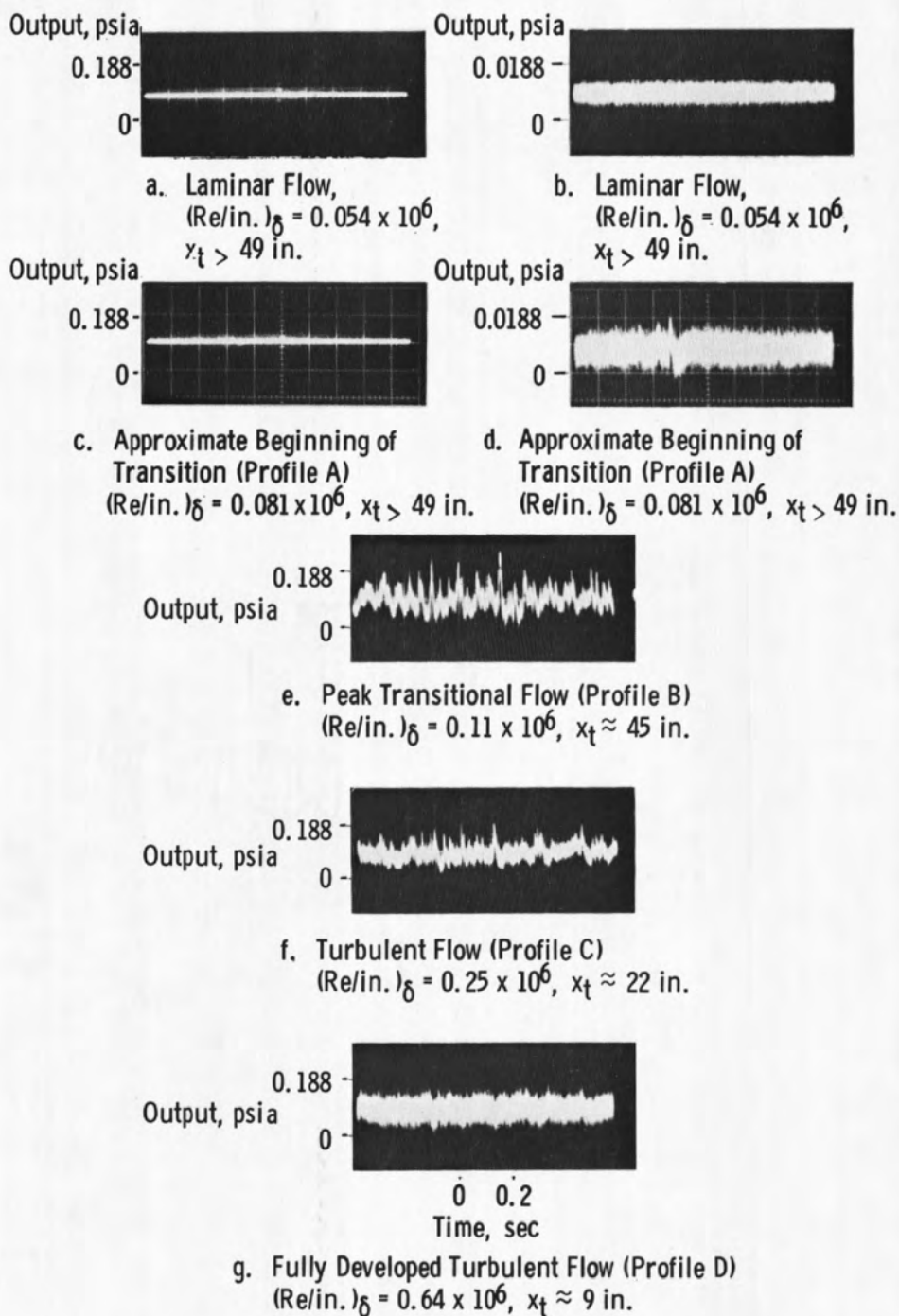


Figure V-14. Oscilloscope record of microphone output (pressure fluctuation) with laminar, transitional, and turbulent flow,  $M_{\infty} = 3.0$ .

Sym	$M_\delta$	$x_{\text{eff}}$ , in.	$\delta^*$ , in.	$\delta$ , in.	$(\text{Re}/\text{in.})_\delta \times 10^{-6}$	Ref.	Config
$\triangle$	2.52	$l_t + 2.0$	0.179	--	0.78	111	Flat Plate
$\diamond$	2.52	$l_t + 6.5$	0.194	--	0.78	111	Flat Plate
$\bullet$	2.89	40.5	0.14	0.43	0.64	Present Study	Cone

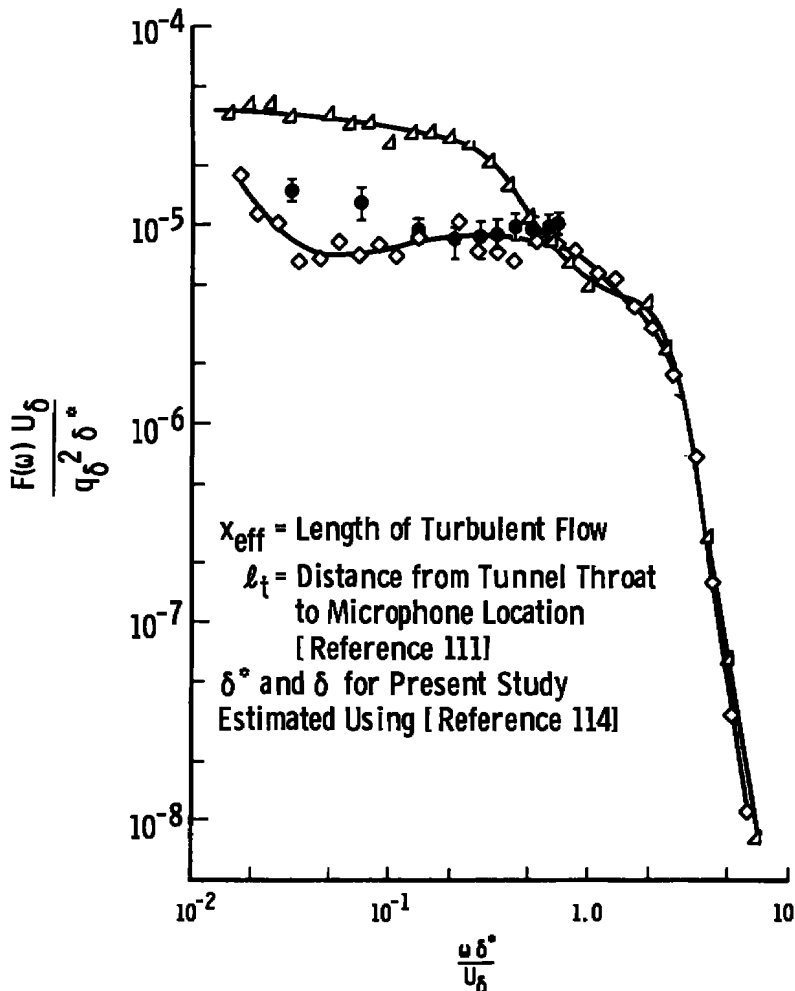


Figure V-15. Comparison of pressure fluctuation spectra for planar and axisymmetric flow.

other sets of data are included in Figure V-15, and there is good agreement exhibited between the cone data and the previously published data.

The ability of the flush-mounted microphone to measure the intensity and spectra of the fluctuating pressure associated with the transition process and to detect the location of transition at supersonic speeds is clearly illustrated in Figures V-11 through V-15. These results indicate the utility of the microphone to provide valuable information on the transition process at supersonic Mach numbers. Additional information relating to these experiments can be found in Reference (113).

It is of interest to note that the present data (113) were used as a guide in evaluating transition data obtained on the X-15 aircraft as reported in 1971 (115).

### Induced Errors

Microphone resonance was shown in a previous section to be a source of possible error at high frequencies and subatmospheric mean pressures. Errors in overall rms values and spectra distributions as a result of microphone size and microphone flushness will be discussed in this section.

Errors associated with transducer size and surface flushness should always be considered. Unfortunately, the available information for supersonic flows is rather scarce. As a part of the present investigation, the  $\frac{1}{8}$ -in.-diam surface microphone as installed in the flat-plate model (Figure V-7) was displaced upward about  $\pm 0.010$  in. above the model surface to establish if surface flushness was a critical factor. This



was done at  $M_\infty = 3$  for laminar flow over the microphone with no significant change occurring in the on-line rms reading.

A recent publication by Hanley (116) showed that if the microphone protusion ( $y$ ) ratioed to the boundary-layer thickness ( $\delta$ ) is greater than about  $y/\delta \gtrsim \pm 0.002$  for  $M_\infty = 2.5$  then the effect on the fluctuating pressure coefficient ( $C_{p_{rms}} = \bar{p}/q_\infty$ ) and the power spectral density distribution will be significant. The microphone data presented in Figures V-11 through V-15 were obtained with the microphone diaphragm extruding about 0.009 in. above the cone model surface as shown in Figure V-7. From Figure V-15, one sees that the computed value of the turbulent boundary-layer thickness was  $\delta = 0.43$  in. for  $M_\delta = 2.89$  and  $(Re/in.)_\delta = 0.64 \times 10^6$ . Thus one has  $y/\delta = 0.009/0.43 = 0.021$ . The results from Reference (116) indicate that the data presented in Figures V-11 through V-15 may be significantly higher than those which would have been obtained with a perfectly flush microphone.

However, note that the various data presented in Figure V-15 show reasonable agreement. It is of interest to point out that a 0.001 extension would have given for the present tests  $y/\delta = 0.001/0.43 = 0.0023$ . Also, note that a model length of 45 in. (Figure IV-14, page 112) was required to produce  $\delta = 0.43$  in. Hanley (116) used 1/8-in.-diam microphones with boundary layers up to 4-in. thick (Tunnel Wall NASA Ames 9-ft x 7-ft supersonic wind tunnel). Hanley also reported that a microphone submerged below the surface ( $y/\delta \lesssim -0.012$ ) had negligible effects on the measured data. Also he showed that increasing the Mach number significantly decreased the effects of microphone extrusion.

The ability of a microphone to measure high-frequency turbulence is limited by the size of the microphone. That is, a microphone cannot measure wavelengths smaller than the microphone diameter. Considerable error will result if  $\omega R/U_\infty > \pi/2$  [see White (117)]. For the present data, one has  $\omega < \pi U_\delta/2R \approx [\pi(2000)/(2)(0.25)/(2)12] \approx 300,000$  rad/sec. Since all frequencies above 25 kHz were filtered out, the transducer diameter did not introduce a significant error.

Fellows (118) also investigated the effect of microphone extrusion on the overall rms value ( $\tilde{p}_{rms}/q_\infty$ ) measured in the transition region. She found that the  $\tilde{p}_{rms}$  value was very sensitive to a protruding microphone ( $y \geq 0.0078$  in.) and a recessed microphone had negligible effects as compared to an exactly flush microphone. However, it is significant to note that Fellows also found that the location of transition as determined by a microphone was not significantly affected by the degree of flushness.

### Summary

In summary, it is concluded that the surface microphone can be used successfully on supersonic wind tunnel models to measure the location of transition. However, microphone flushness is a critical factor, and the microphone should be intentionally recessed a very slight amount when quantitative overall rms and spectral data are to be measured.

## CHAPTER VI

## SUPPORTING STUDIES

## I. EFFECTS OF SMALL AMOUNTS OF LEADING-EDGE BLUNTNESS

Results reported by Brinich (48,119) and Potter and Whitfield (37,108) and Deem et al. (63) have established that small amounts of leading-edge bluntness on two-dimensional planar models (hollow cylinders and flat plates) have a strong effect on the location of transition in the Mach number range  $M_\infty = 3$  to 8. Consequently, in order to eliminate as many variables as possible in the present research, it was necessary to establish an effective zero bluntness for the data to be used in evaluating the effects of aerodynamic noise on transition. This was accomplished by obtaining transition data at several leading-edge thickness values and then extrapolating the transition data to zero bluntness.

The basic transition Reynolds number data obtained in the AEDC-VKF Tunnels A and D and the AEDC-PWT Tunnel 16S for several bluntness ratios are presented in Figures VI-1 through VI-4 as a function of the leading-edge bluntness. The strong effect of small amounts of bluntness is obvious. To be noted is the good agreement in Figure VI-1 between the present data and the previously published Tunnel D data obtained by Potter and Whitfield (37). Good agreement also existed between the present data and previous Tunnel A data published by Schueler (51) as shown in Figure VI-2.

There was a slight variation in leading-edge bluntness that existed around the circumference of the AEDC-PWT hollow-cylinder model

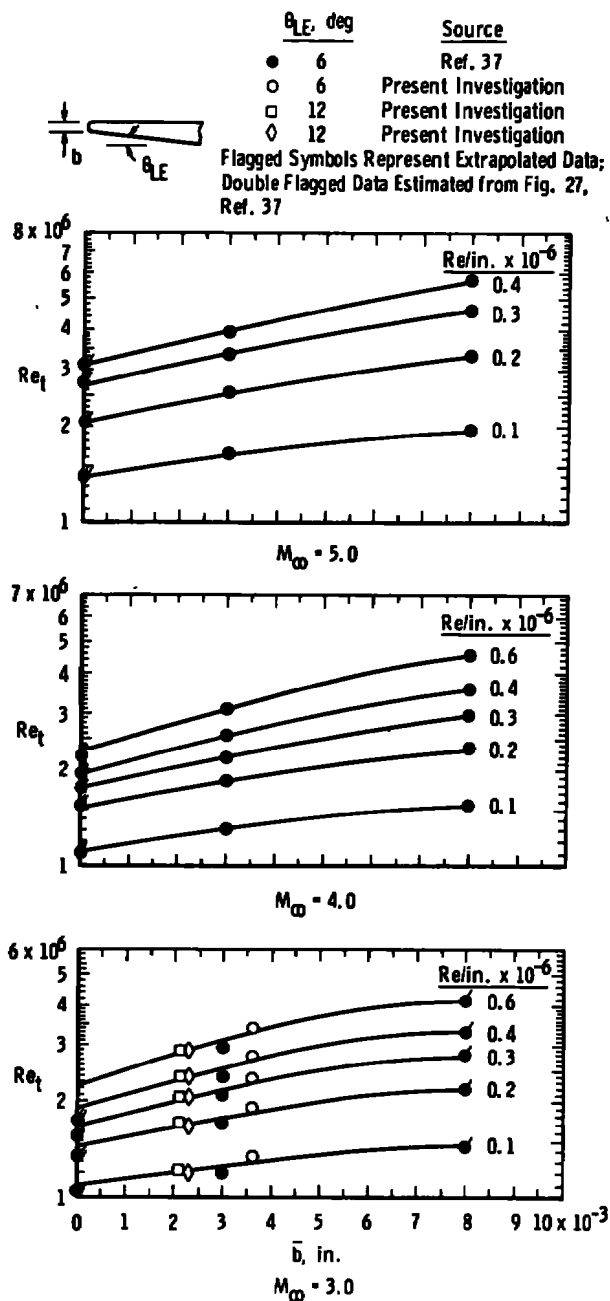


Figure VI-1. Basic transition Reynolds number data from the AEDC-VKF Tunnel D for  $M_\infty = 3, 4$ , and 5 with variable  $\bar{b}$ ,  $\theta_{LE}$ , and  $Re/in.$

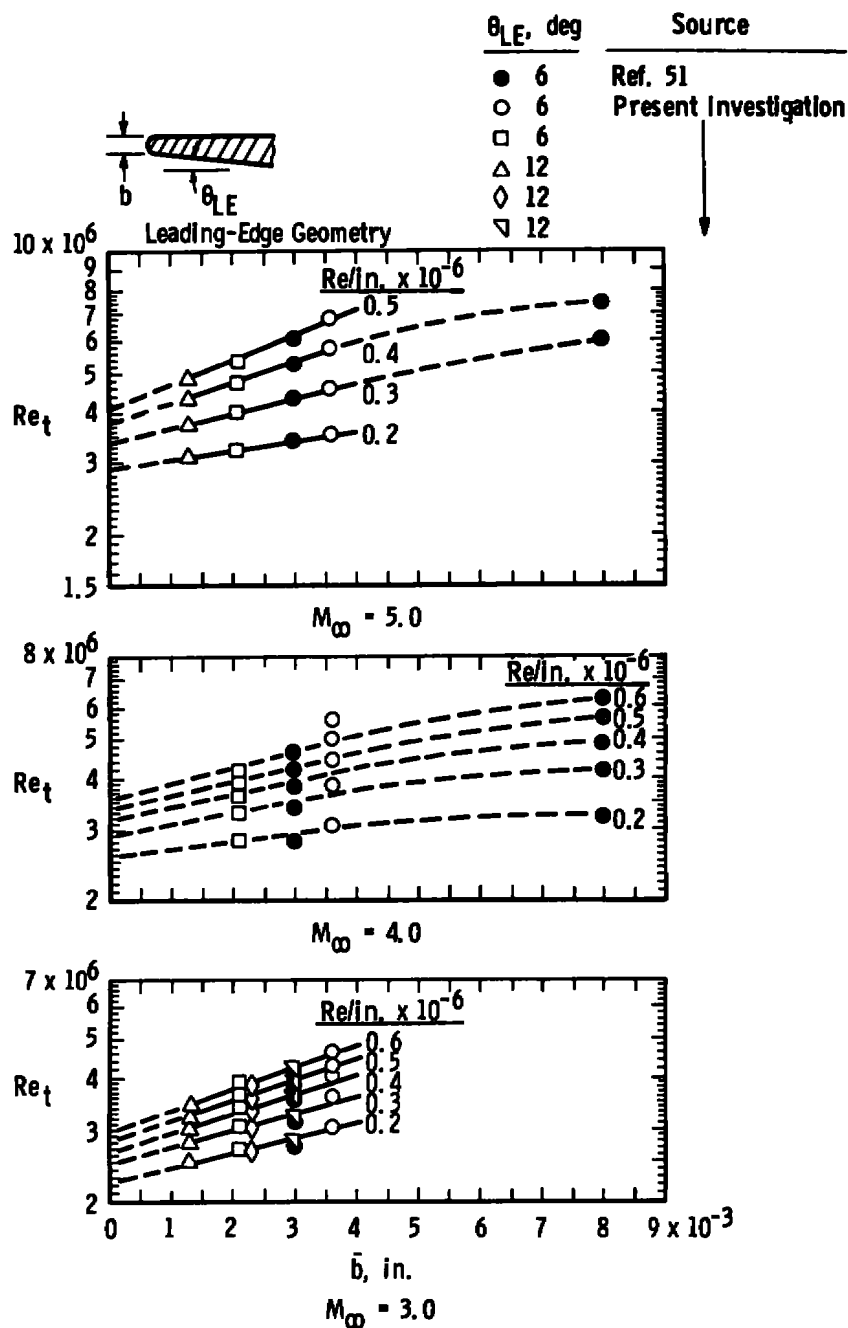
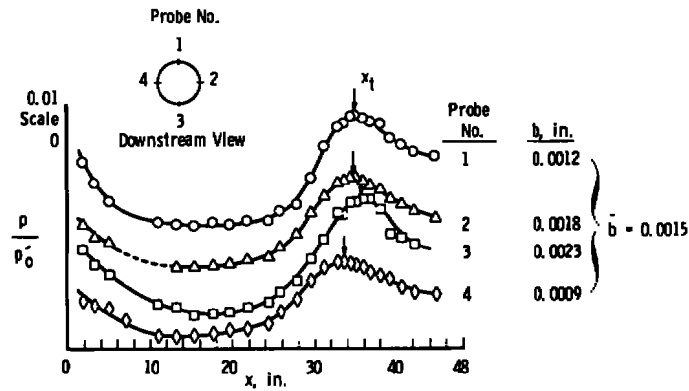
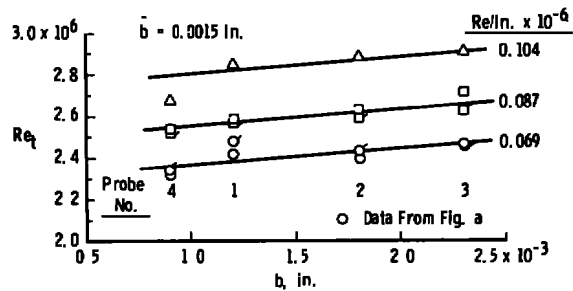


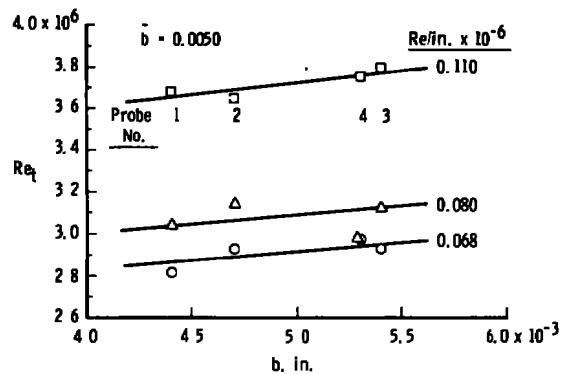
Figure VI-2. AEDC-VKF Tunnel A  $Re_t$  values versus  $\bar{b}$  for  $M_\infty = 3, 4$ , and  $5$ .



a. Surface Probe Pressure Trace,  $M_\infty = 3$ ,  $Re = 0.069 \times 10^6/\text{in.}$



b. Circumferential Transition Reynolds Number Distribution,  $M_\infty = 3.0$



c. Circumferential Transition Reynolds Number Distribution,  $M_\infty = 2.5$

Figure VI-3. Circumferential transition locations on the AEDC-PWT Tunnel 16S hollow-cylinder model.

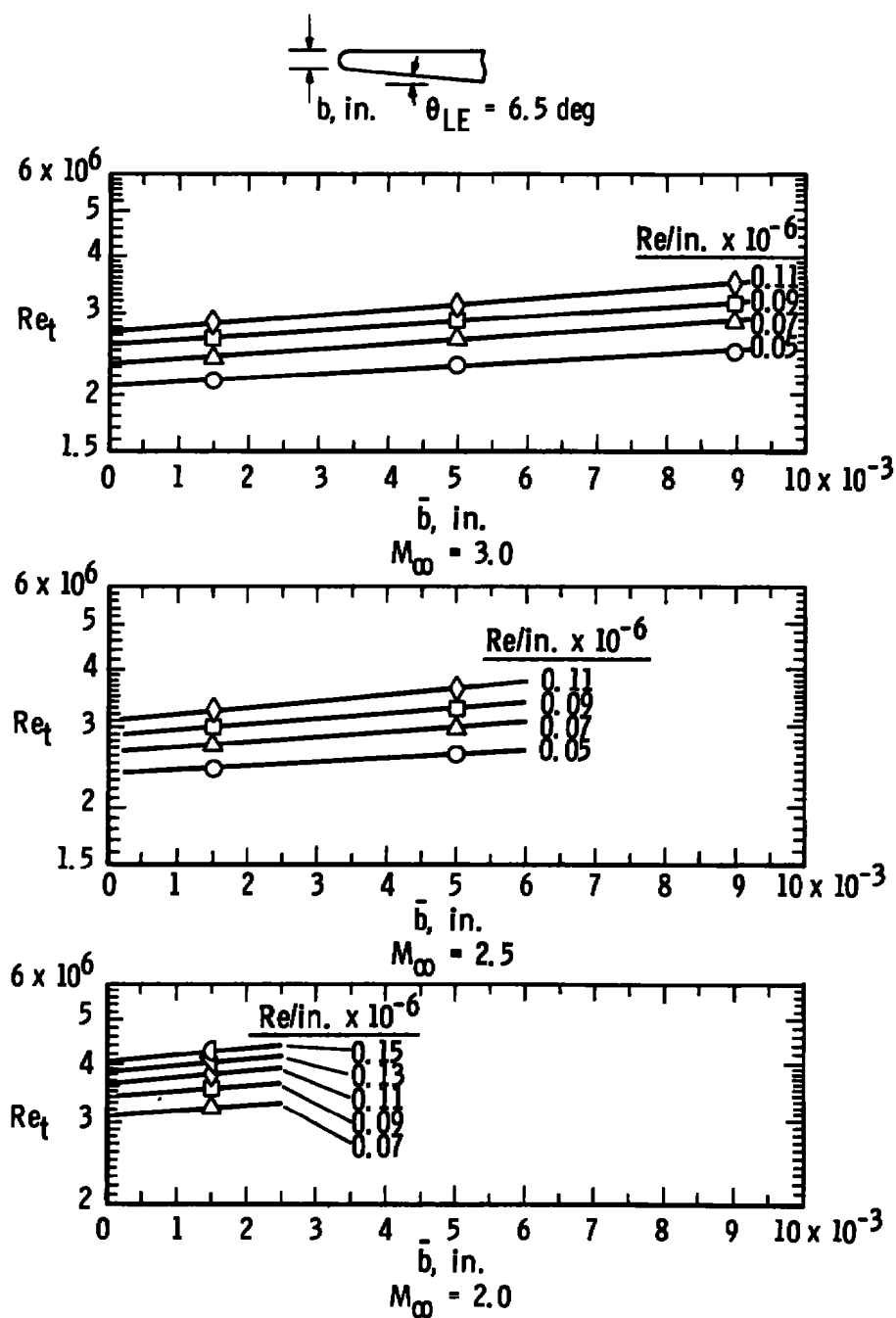


Figure VI-4. AEDC-PWT Tunnel 16S transition results,  $Re_t$  versus  $\bar{b}$  for  $M_\infty = 2.0, 2.5$ , and  $3.0$ .

(see Figure IV-10, page 105) that was sufficient to influence the location of transition. Figure VI-3a shows the pitot pressure traces obtained with the sharpest nose section installed ( $\bar{b} = 0.0015$  in.). Measurements from the four surface probes clearly show variations in the  $x_t$  values. Figures VI-3b and VI-3c show a systematic variation of  $Re_t$  with the local leading-edge bluntness value ( $b$ ), and the slope is in general agreement with the slope of the data presented in Figures VI-1 and VI-2. This indicates that the small variation in  $Re_t$  that existed between the four pitot probes is traceable to variations in the model leading-edge bluntness rather than to individual probe effects or from any tunnel flow angularity. The internal lip pressures measured on the AEDC-PWT model indicated that a free-stream flow angle less than approximately  $\pm 0.1$  deg existed, and this is in general agreement with Reference (106). The AEDC-PWT transition data presented in Figure VI-4 represent the average value of  $Re_t$  determined from the four independent pitot probes. The average leading-edge bluntness ( $\bar{b}$ ) is the average of the four bluntness values that existed at the leading-edge upstream of each individual probe. The transition Reynolds numbers for each probe location are tabulated in Appendix F, page 381. Agreement between the four sets of  $Re_t$  values for a given test condition was good and in general agreement with the leading-edge thickness variation of approximately  $\pm 0.0005$  in. around the leading-edge circumference. The standard deviation of  $Re_t$  determined using each individual probe  $Re_t$  value and the mean  $Re_t$  curves presented in Figure VI-4 for  $\bar{b} = 0.0015, 0.0050, \text{ and } 0.0090$  in. was  $Re_t = \pm 0.011 \times 10^6$ .

All of the planar transition data using the aerodynamic noise transition correlation developed in Section IX are for zero bluntness

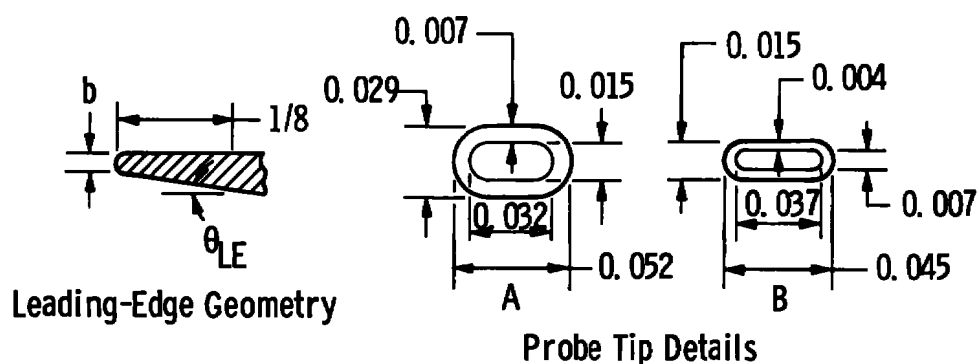


( $b = 0$ ) and were obtained by extrapolating to zero bluntness as shown in Figures VI-1 through VI-4.

Cones are not nearly so sensitive to small amounts of trip bluntness as are planar models as reported by Brinich (120), Stainback (121), and Fischer (122). For tip bluntness values less than about 0.010 in., cones can be considered to be effectively sharp.

## II. INVESTIGATION OF POSSIBLE LEADING-EDGE BEVEL ANGLE EFFECTS

Brinich (48) reported that the effect of leading-edge bevel ( $\theta_{LE} = 5$  and 30 deg) on boundary-layer transition was negligible at  $M_\infty = 3$ . However, Potter and Whitfield (37) correlated three sets of  $M_\infty = 3$  transition data using the bevel angle as a parameter. Unfortunately, the three sets of data were from three different wind tunnels. Later experiments by Whitfield and Potter (108) at a Mach number of eight showed no bevel angle effect. Therefore, in order to use transition data in this research from various sources, it was felt necessary to determine conclusively if the leading-edge bevel angle has an influence on transition at supersonic speeds. The data presented in Figure VI-5 (see also Figure VI-1, page 145) from the AEDC-VKF Tunnel D for bevel angles of 6 and 12 deg clearly show no bevel angle effect at  $M_\infty = 3$ . Similar results were also obtained at  $M_\infty = 5$  in Tunnel A (see Figure VI-2, page 146). Therefore, it was concluded that there is no leading-edge bevel-angle effect on transition Reynolds numbers from sharp-leading edge models at supersonic and hypersonic speeds.



All Dimensions in Inches

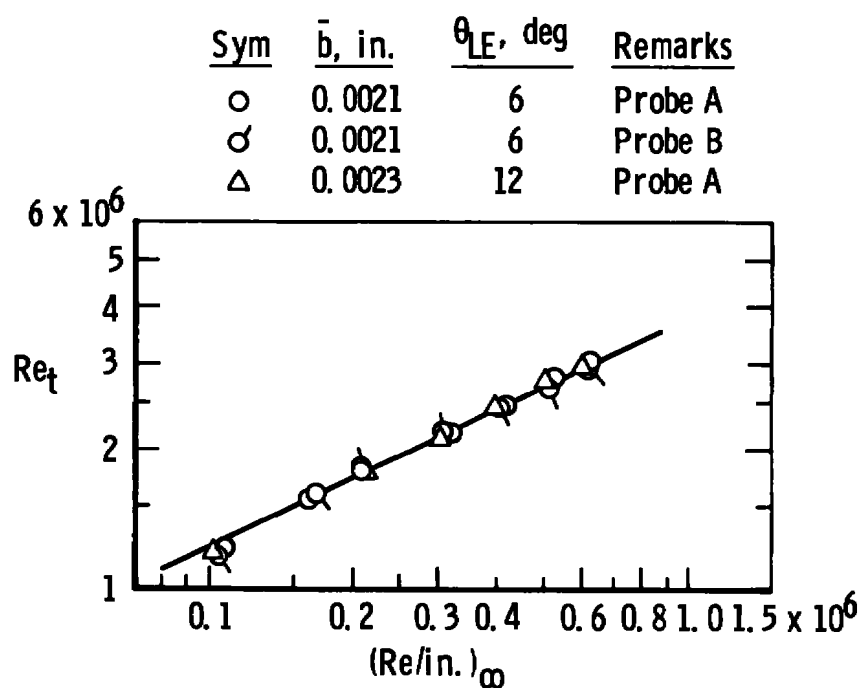


Figure VI-5. Absence of effects from bevel angle and probe tip size on transition location hollow-cylinder model,  $M_{\infty} = 3.0$ .

### III. INVESTIGATION OF POSSIBLE PROBE TIP SIZE EFFECTS

The possible effect of the probe tip size on the location of transition was investigated using two probes with different tip geometry as shown in Figure VI-5. The data presented in Figure VI-5 establish that there was no adverse effect from the probe tip geometry. In addition to size effects, there is the possibility of pressure lag in continuously moving probes having small tip openings. This possible adverse effect was checked at all Mach numbers and tunnel pressure levels by comparing the forward and rearward traverse of the probe as shown in Figure V-1, page 103. The data presented in Figure V-1 are typical of the hollow-cylinder and sharp-cone pitch traces obtained in the AEDC-VKF Tunnels A and D. If a small difference happened to exist (i.e.,  $\Delta X_t \lesssim 0.25$  in.) in any particular sequence, then the two values were averaged.

Fellows (118) reported that at  $M_\infty = 1.8$  and 3.0, the transition Reynolds numbers measured on the surface of a 7.13-deg total-angle sharp cone using a surface pitot probe were adversely affected if the probe tip size was significantly larger than 0.027-in. in height. These results give confirmation to the conclusions reached in tip effect studies conducted in the present research. For probe tip sizes of 0.029-in. in height and 0.015-in. in height, no difference in  $Re_t$  values was measured at  $M_\infty = 3$  on the hollow-cylinder model as shown in Figure VI-5.

It is of interest to point out that Fellows (118) suspected a probe tip effect only after the probe  $Re_t$  data disagreed significantly from  $Re_t$  values determined on a subsequent experiment using a surface

microphone. These findings emphasize the necessity for always using two independent methods for measuring the transition location.

#### IV. INVESTIGATION OF POSSIBLE ADVERSE EFFECTS OF HOLLOW-CYLINDER INTERNAL FLOW ON EXTERNAL SURFACE TRANSITION MEASUREMENTS

A brief experiment was conducted at  $M_\infty = 3.0$  to determine if the state of the boundary layer on the inside of the hollow-cylinder model could adversely affect the transition location on the outside surface. There was the possibility that the pressure fluctuations associated with the turbulent boundary layer on the inside wall of the model might generate a mechanical vibration disturbance within the model wall which would adversely affect the transition location on the outside surface.

A boundary-layer trip consisting of serrated glass tape was used to trip the flow inside the hollow cylinder. The effectiveness of this type of trip was established by first placing the trip on the outside surface and recording the location of transition downstream of the trip. These results are presented in Figure VI-6 and show that the trip was effective above a unit Reynolds number of about  $0.2 \times 10^6$  per inch.

Transition data obtained on the outside surface with and without the trip placed on the inside surface are shown in Figure IV-7. As evident from these data, the state of either the laminar or turbulent boundary layer did not affect the transition location on the outside surface.

#### V. METHODS FOR DETECTING THE LOCATION OF TRANSITION AND A CORRELATION OF RESULTS

The primary methods used to determine the location of transition in this research were the surface pitot probe for  $M_\infty \lesssim 6$  and surface

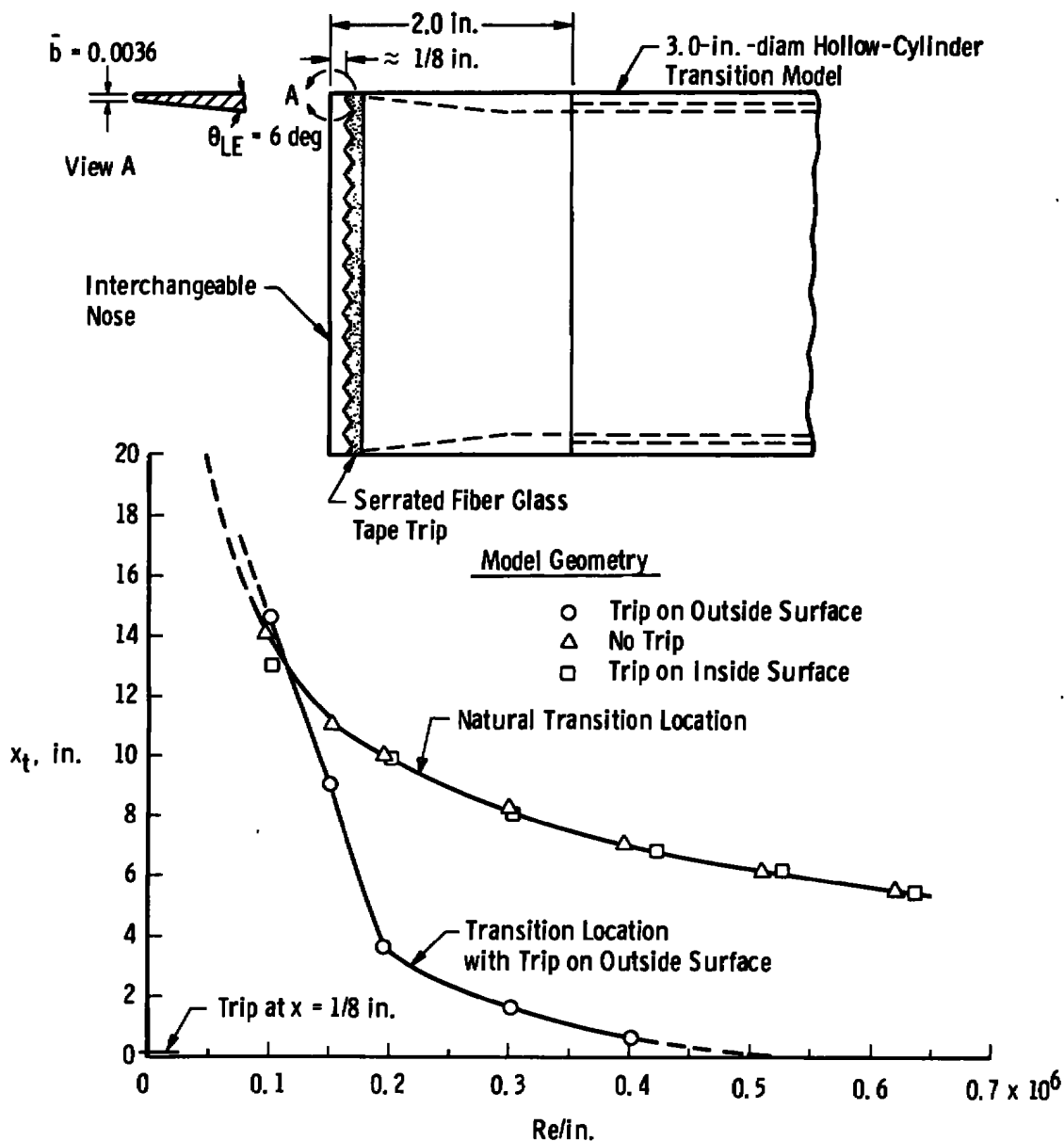


Figure VI-6. Effectiveness of serrated fiber-glass tape boundary-layer trip at  $M_\infty = 3.0$ .

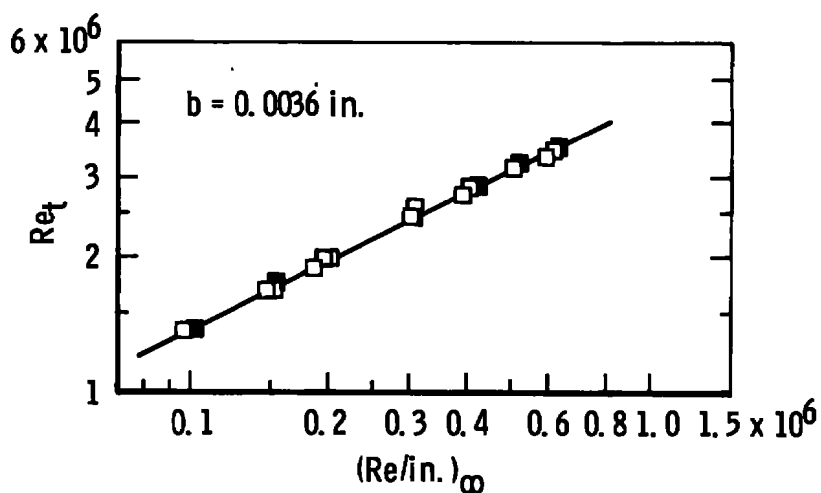
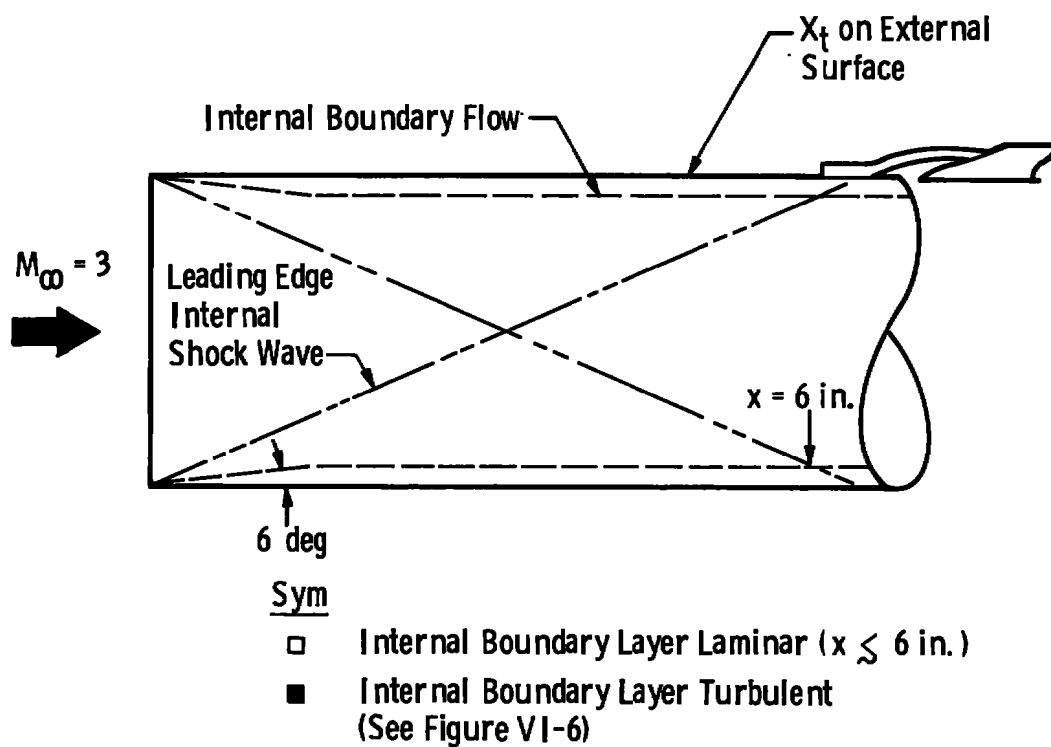


Figure VI-7. Absence of effect of internal flow quality on hollow-cylinder transition data.

heat-transfer rates for  $M_\infty \gtrsim 6$ . However, many other methods are commonly used and, unfortunately, the different methods do not provide a consistent location of transition. For example, there is a significant difference in the location of transition defined by the minimum value of a surface pitot probe and the maximum value (see Figure V-1, page 119). Either location can be used to define the location. The same is true for heat-transfer rate distributions (see Figure V-5, page 124). The transition location determined by a schlieren photograph usually lies in the middle of the transition region. In general, no one method is applicable to all types of flow conditions and body geometries. Table 2 provides a summary of the techniques that have been used.

Transition data obtained from many different sources will be used in the aerodynamic noise transition correlation developed in Chapter IX. Since different methods were often used to measure the location of transition in the various sources, it was necessary to establish a correlation between the different methods used. This correlation then allowed all the data to be adjusted to the location corresponding to one common technique. The maximum value of the surface pitot probe trace was the method to which all data presented in this study have been adjusted.

Potter and Whitfield conducted extensive experimental studies at  $M_\infty = 3$  to 5 (37) and  $M_\infty = 8$  (108) using several different techniques to measure the location of transition and define the transition region. Their work is the cornerstone in allowing some sort of systematic correlation between the various methods to be developed.

Presented in Figure VI-8 are comparisons of the basic data published in Reference (37) using five different techniques (schlieren,

Table 2. Methods for measuring the location of transition.

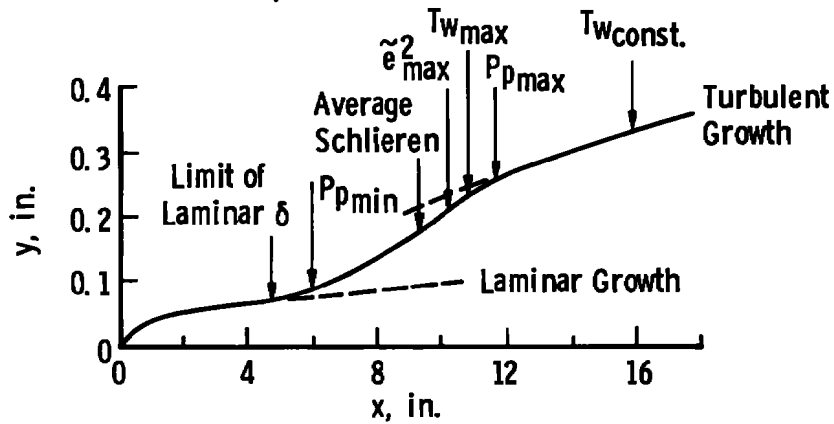
- 
- |      |   |
|------|---|
| 131. | Boundary-layer profile and edge measurements.<br>References (37), (45), (62), (98), and (108).  |
| 142. | Surface pitot probe.<br>References (10), (11), (18), (19), (32), (37), (44), through (60), (63), (108), (113), and (118).   |
| 3.   | Surface skin-friction measurements.<br>Reference (123).   |
| 4.   | Hot-wire and hot-film probing.<br>Reference (3), (26), (37), (45), (74), and (112).   |
| 5.   | Surface temperature distribution.<br>References (17), (26), (37), (39), (46), (47), (79), (89) through (91), (98), and (108).   |
| 136. | Surface heat-transfer-rate distributions (gages, paints, phosphorous).<br>References (6), (7), (9), (21), (26), (28), (29), (36), (98), (103), (107), (122), (124), (126), (127). |
| 137. | Sublimation and oil-flow patterns.<br>References (17), (18), (33), (35), and (63).  |
| 138. | Schlieren and shadowgraph photographs.<br>References (10), (11), (23), (27), (37), (46), (79), and (98).  |
| 139. | Surface microphones (acoustic-pressure fluctuations).<br>References (11), (76), (113), (115), and (118).  |
| 10.  | Static pressure distribution.<br>References (46) and (123).   |
- 

13 Methods used by the author.

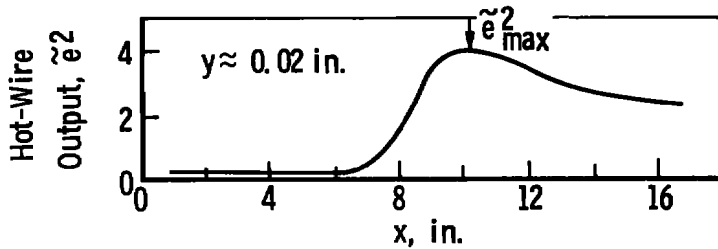
14 All data used in this report correspond to the end of transition as defined as the maximum value in the surface pitot probe trace (see Figures V-1 through V-4, pages 119 through 123).



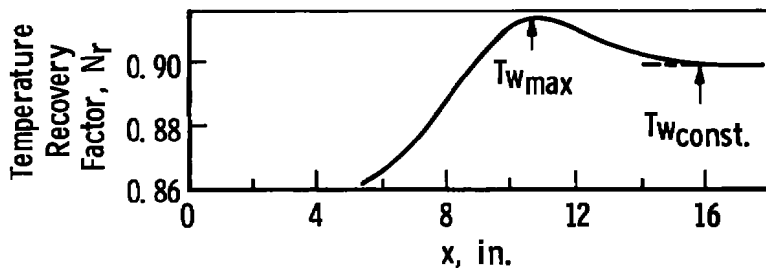
Data Compiled from [Reference (37)]



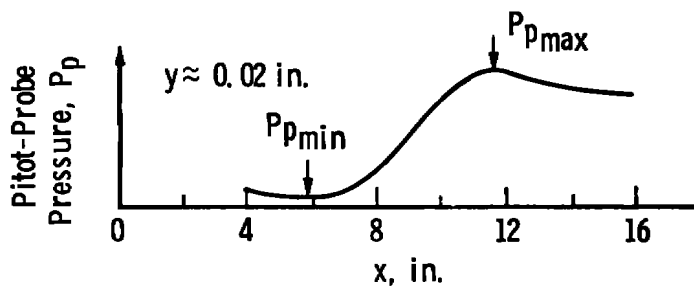
a. Thickness Profile



b. Hot-Wire Trace



c. Surface Temperature Distribution



d. Surface Pitot Probe Pressure Distribution

Figure VI-8. Comparison of transition location for various detection methods,  $M_\infty = 5$ ,  $Re/in. = 0.28 \times 10^6$ ,  $b = 0.003$  in. [from Reference (37)].

boundary-layer profile thickness, hot-wire, surface temperature, surface pitot probe) at  $M_\infty = 5$  on a hollow-cylinder model. The beginning of transition can be defined at the locations given by: (a) limit of laminar  $\delta \sim x^{1/2}$ , (b) minimum hot-wire output, or (c) minimum pitot pressure ( $p_{p_{min}}$ ). Likewise, the end of transition can be defined using: (a) turbulent growth  $\delta \sim x^{4/5}$ , (b) maximum hot-wire output, or (c) maximum probe pressure ( $p_{p_{max}}$ ). Figures VI-8b, c, and d show the individual data traces (variations) and Figure VI-8a provides a direct comparison of the different location. It is obvious that a considerable and significant difference in the transition location can exist depending on the technique and method of definition. Figure VI-9 is a similar type of plot for  $M_\infty = 8$  as determined by Whitfield and Potter (108). Presented in Figure VI-10 is a comparison of the different techniques as a function of unit Reynolds number. Fortunately, the locations relative to each other appear to remain constant for a given Mach number over a wide unit Reynolds number (or range of tunnel pressure levels). Similar comparisons between the surface pitot probe, schlieren, and sublimation techniques at  $M_\infty = 2.5$  to 5.0 have been published by Pate (18).

Table 3 provides a listing of transition data taken from eight different sources plus the present investigation, that have been used to develop a correlation of methods of detection. These data are presented in Figure VI-11 for Mach numbers 2.5 to 8.0. The variation in the data at a given Mach number for a given technique and reference include the variation with unit Reynolds number. Although there are many data included in Figure VI-11, the data when normalized by  $(Re_t)_{p_{p_{max}}}$  and

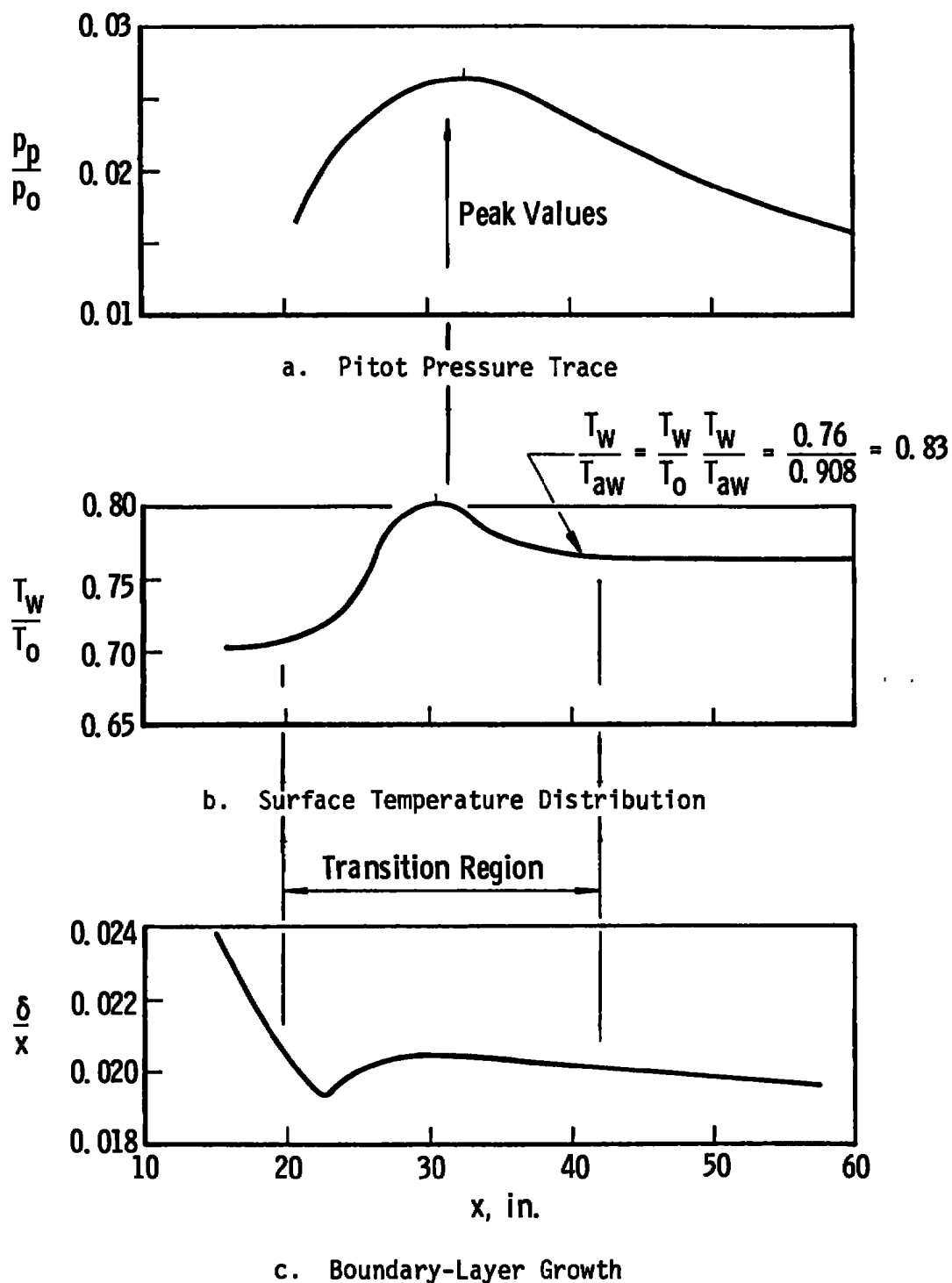
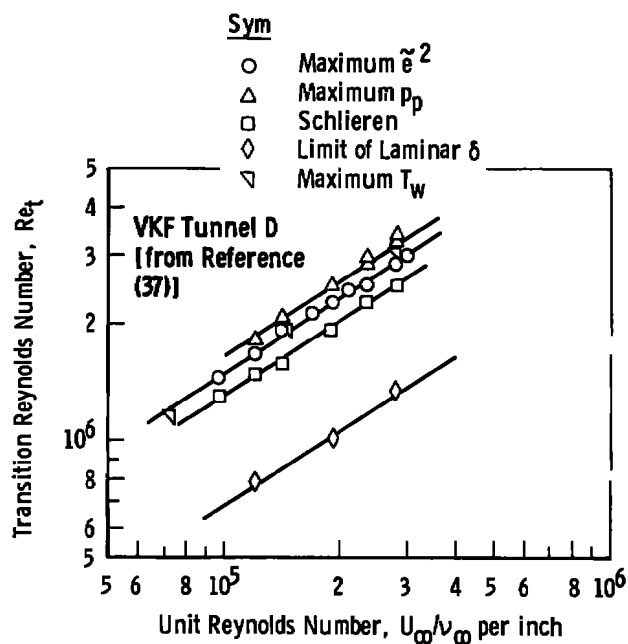
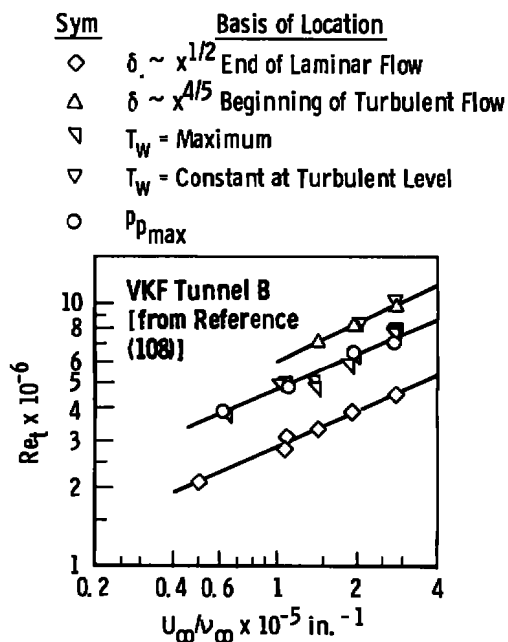


Figure VI-9. Typical data showing location of boundary-layer transition on hollow cylinder at  $M_\infty = 8$  [from Reference (108)].














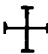





a.  $M_\infty = 5$ ,  $\bar{b} = 0.003$  in.



b.  $M_\infty = 8$ ,  $\bar{b} = 0.0006$  in.

Figure VI-10. Reynolds number of transition on hollow cylinder at  $M_\infty = 5$  and 8.

Table 3. Methods used for correlating transition detection techniques (see Figures VI-11 and VI-12).

Symbol	Reference	Model Configuration	Method $X_L$ Detection
	(18)	Sharp Swept Wing	Minimum $P_p$ Value
	(123)	Sharp Flat Plate	Minimum Shear Stress ( $\tau_{min}$ )
	(37) (108)	Sharp Hollow Cylinder	End of Laminar Growth Rate ( $\delta \sim x^{1/2}$ )
	(63)	Sharp Flat Plate	Minimum $p_p$ Value
	(37)	Sharp Hollow Cylinder	Minimum $p_p$ Value
	(126)	Sharp Flat Plate	Minimum Surface Heat Transfer ( $\dot{q}_{min}$ )
	Present Study	Sharp Hollow Cylinder	Minimum $p_p$
	Present Study	Sharp Cone	Minimum $p_p$
	(37) (108)	Sharp Hollow Cylinder	Average Schlieren
	(63)	Sharp Flat Plate	Sublimation
	(18)	Sharp Swept Wing	Sublimation
X	Present Study	Sharp Cone	Surface Microphone Maximum ( $\bar{P}_{rms}$ ) rms Pressure Fluctuation
	(118)	Sharp Cone	Surface Microphone Maximum ( $\bar{P}_{rms}$ ) rms Pressure Fluctuation
	(112)	Sharp Flat Plate	Hot Film Maximum rms Voltage ( $V_{rms}$ )
	(37) (108)	Sharp Hollow Cylinder	Maximum Surface Temperature ( $T_{wmax}$ ) and Maximum Hot Wire Output ( $\epsilon^2$ )
II	Present Study	Sharp Cone	Average Schlieren
	(37) (108)	Sharp Hollow Cylinder	Constant Maximum Surface Temperature ( $T_{wconst}$ ) and Beginning of Turbulent Growth Rate ( $\delta \sim x^{4/5}$ )
	(63)	Flat Plate	$P_p$ Inflection Point
	(123)	Flat Plate	Maximum Surface Static Pressure

I Indicates Data Spread Over Reported Re/n. Range

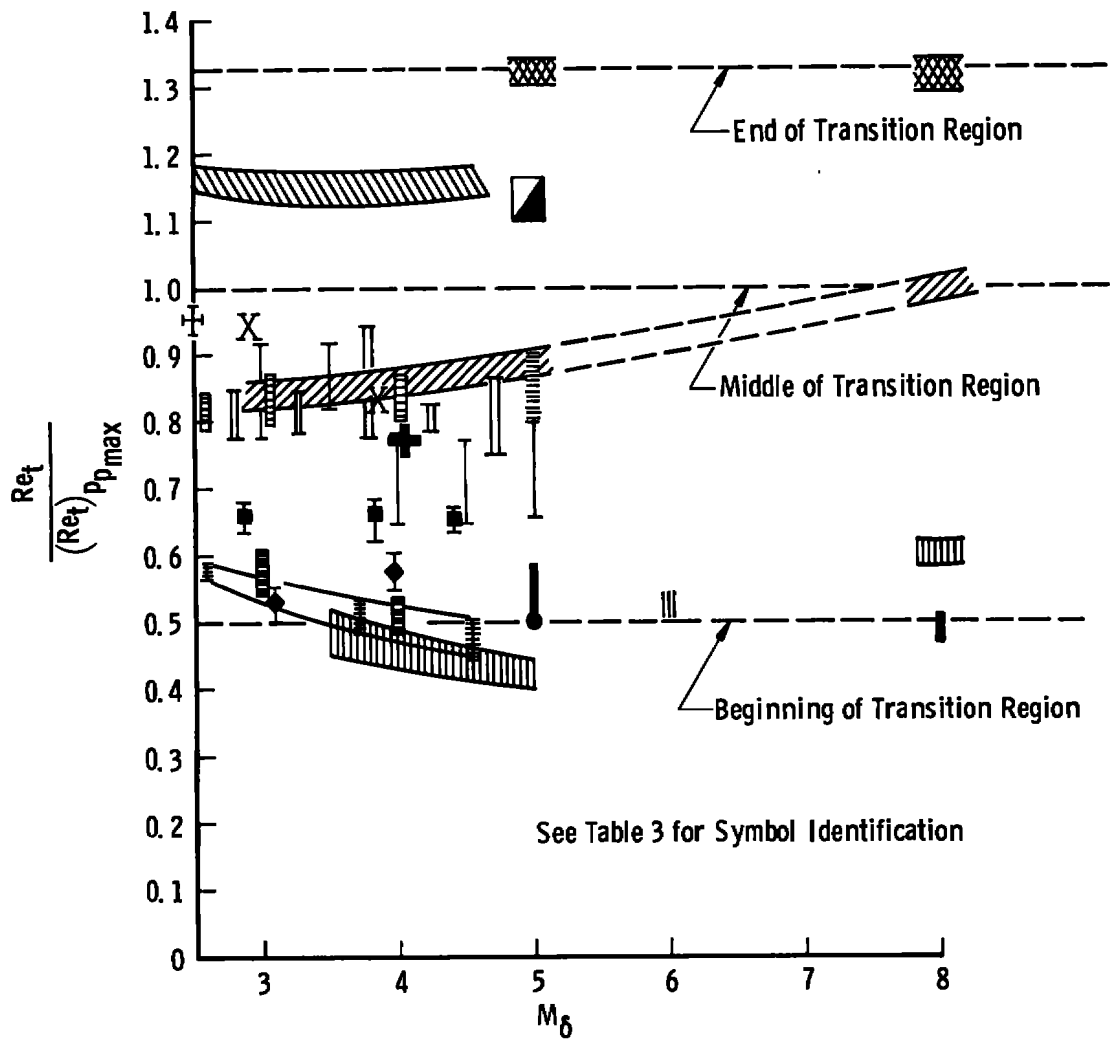


Figure VI-11. Illustration of transition location variation with methods of detection.

grouped according to similar techniques form systematic patterns, as shown in Figure VI-12. The correlations and recommended lines of adjustment shown in Figure VI-12 can be used to adjust transition data from various techniques to an equivalent  $(p_o)_{\max}$  location. The justification for doing this should be obvious, i.e., a 20-percent error is better than a 50-percent error.

Several assumptions were made in developing and applying the results shown in Figure VI-12. First, note that in Figure VI-12 for  $M_\infty = 8$ , the maximum wall temperature  $Re_t$  value normalized by the probe peak pressure  $(Re_t)_{p_{p_{\max}}}$  value is equal to one. It is assumed they are also equal for  $M_\infty > 8$ . Second, it is assumed that the location of transition given by  $(T_w)_{\max}$  and  $(\dot{q})_{\max}$  are equal. This assumption is supported by  $(T_w)_{\max}$  and  $(\dot{q})_{\max}$  data published in Reference (98) and which was obtained on a sharp cone at  $M_\infty = 8$ . Thus for  $M_\infty > 8$ , it is assumed that the location of transition given by  $(\dot{q})_{\max}$  equals the value determined from  $(p_p)_{\max}$ . Third, most of the data presented in Figure VI-12 are from planar models with small amounts of leading-edge bluntness ( $b < 0.01$  in.) and sharp slender cones at zero angle of attack. It is assumed that the relative ratios are not strongly dependent on small amounts of bluntness. This assumption is supported by the data presented in Reference (37).

There are several significant features to note in Figure VI-12. The beginning of transition is about one-half the end of transition location. It is interesting to note that this is in agreement with the results presented by Masaki and Yahura (125) which was based on a correlation of transition data taken from several sets of sharp cone and flat plate data. The data from sharp slender cones also seem to have the same

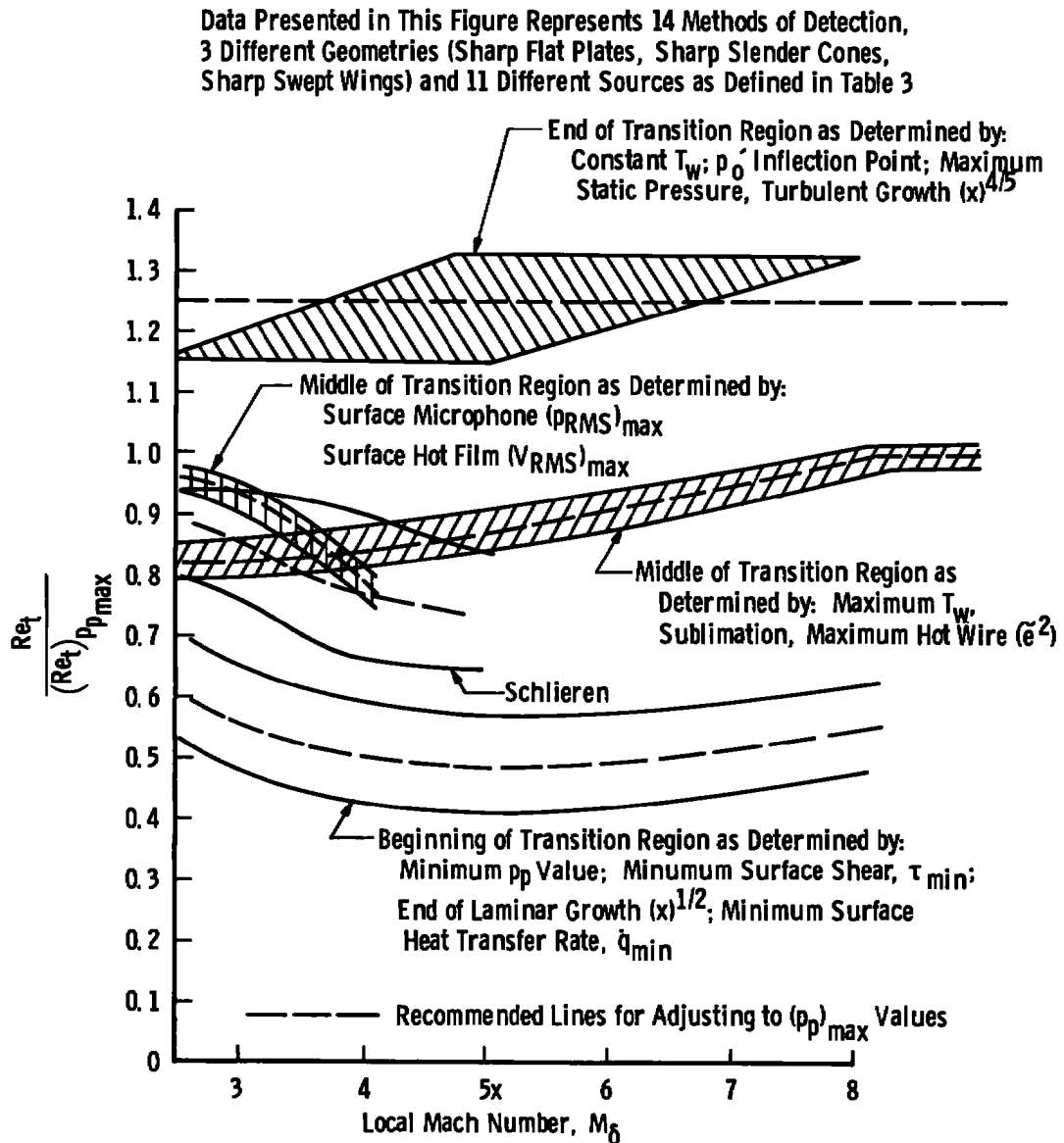


Figure VI-12. Correlations of transition detection methods.



correlation as the planar models (flat plates, hollow cylinder). Optical techniques give a location of transition at about the middle of the transition region.

The data presented in Figure VI-12 show that flat-plate transition locations determined at  $(T_w)_{\max}$  and from schlieren photographs should be the same in the range  $2.5 \lesssim M_\infty \lesssim 3.5$ . Transition results obtained by van Driest and Boison (47) using a magnified schlieren concept and surface temperature measurements also show that schlieren  $x_t$  data are essentially equal to  $(T_w)_{\max}$  locations on a sharp cone for  $M_\infty = 1.8$ , 2.7, and 3.7.

Transition data published by Mateer (127) on a 5-deg half-angle cone at  $M_\infty = 7.4$  has shown that thermographic paint and thermocouples give the same results. Similar results have been shown by Matthews et al. (124) on a space shuttle configuration.

Based on the author's experience, the surface pitot probe is the easiest and most dependable method for determining the location of transition for  $0 < M_\infty \lesssim 6$  and surface heat-transfer ratio is recommended for  $M_\infty > 6$ .<sup>15</sup> When conducting transition studies at least two methods should always be used. Optical methods (schlieren, shadowgraph) often provide a satisfactory second technique.

Unless indicated otherwise all the boundary-layer transition Reynolds numbers presented in this thesis correspond to the location determined by the peak in a surface pitot probe pressure trace ( $p_{p_{\max}}$ ).

---

<sup>15</sup>Surface skin-friction measurements, detailed hot-wire data, and surface temperature or surface heat rates probably provide data best suited to support theoretical studies. Unfortunately, these methods are also the most difficult to apply.

Transition locations obtained from references wherein other methods of detection were used have been adjusted in accordance with Figure VI-12, e.g., see data on pages 250 and 253.

## CHAPTER VII

SUMMARY OF BASIC TRANSITION REYNOLDS NUMBER DATA OBTAINED  
IN AEDC WIND TUNNELS ON PLANAR AND SHARP-CONE MODELS

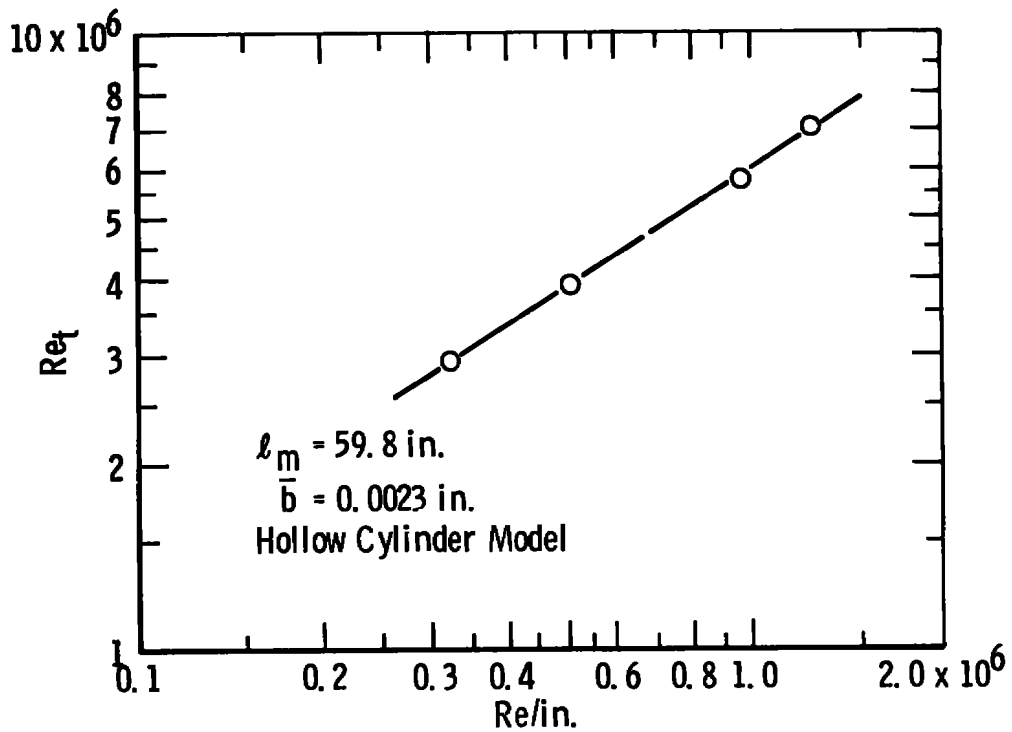
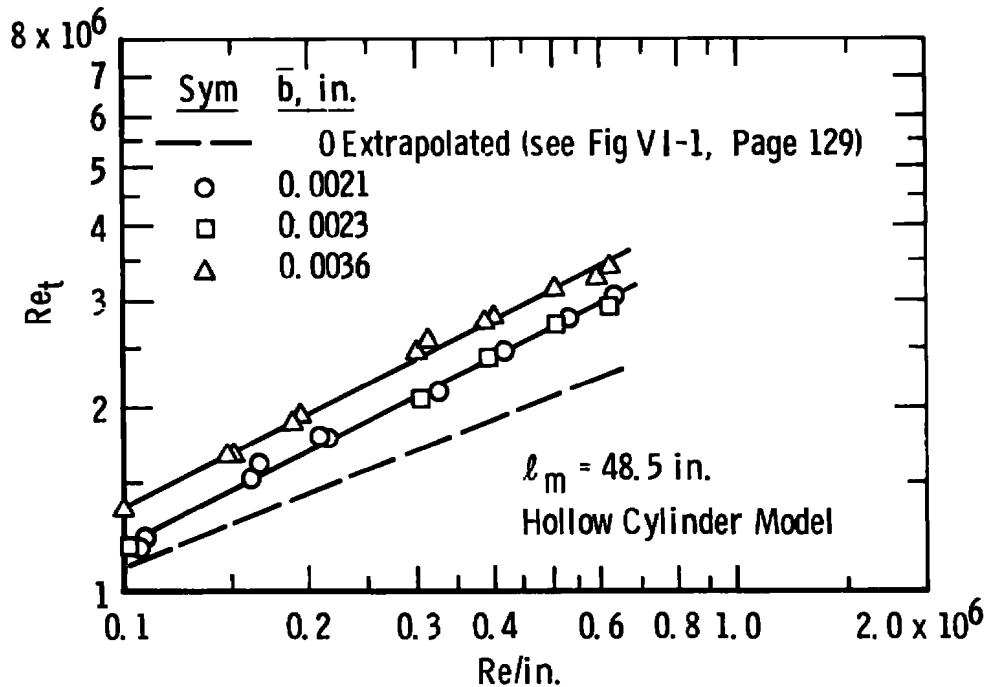
The basic planar (hollow-cylinder and flat-plate) and sharp-cone transition Reynolds number data obtained at AEDC in support of this research are presented in Figures VII-1 through VII-7. Tabulated data are also provided in Appendix F, page 381.

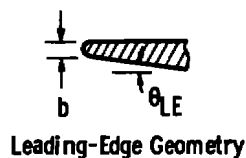
To maintain as nearly identical free-stream flow disturbances as possible, the cone model was positioned in Tunnels A and D very near the hollow-cylinder locations (see Figures IV-16, page 98, and IV-17, page 99).

<u>Tunnel A</u>	<u>Tunnel D</u>
$(\ell_m)_{\text{cone}} = 215 \text{ in.}$	$(\ell_m)_{\text{cone}} = 44 \text{ in.}$
$(\ell_m)_{\text{hollow cylinder}} = 231 \text{ in.}$	$(\ell_m)_{\text{hollow cylinder}} = 48.5 \text{ in.}$

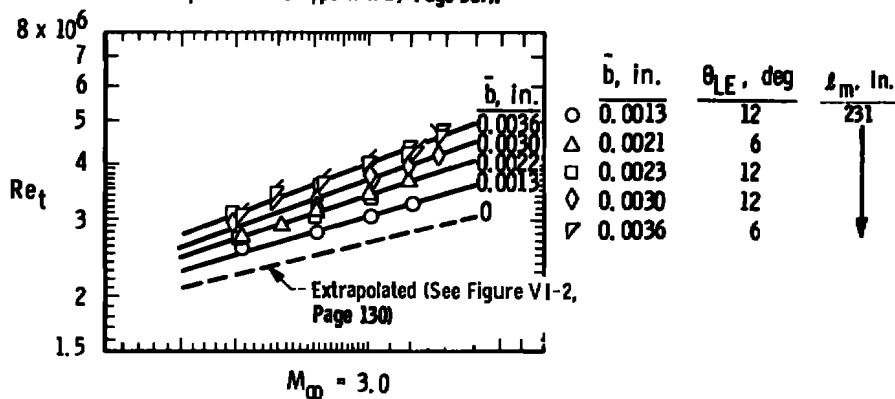
The experiments were also conducted at equivalent free-stream Mach number and unit Reynolds number values.

The hollow-cylinder data measured in the AEDC-VKF Tunnels A, D, and E and AEDC-PWT Tunnel 16S using a surface probe are presented in Figures VII-1 through VII-4. Figure VII-4 presents a composite plot of all the hollow-cylinder transition Reynolds number data obtained at  $M_\infty = 3$  in the AEDC-VKF Tunnels A and D and the AEDC-PWT Tunnel 16S. The difference in the  $Re_t$  data from these three wind tunnels is the result of radiated aerodynamic noise effects as discussed in Chapters VIII and IX.

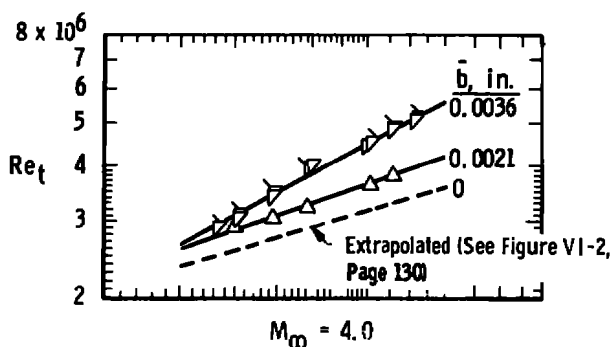
a. AEDC-VKF Tunnel E,  $M_\infty = 5.0$ b. AEDC-VKF Tunnel D,  $M_\infty = 3.0$ Figure VII-1. Basic transition Reynolds number data from AEDC-VKF Tunnels D and E,  $M_\infty = 3.0$  and  $5.0$ , hollow-cylinder model.



Flagged Symbols Represent Data Obtained with Duplicate Set of Rubber Bolt Heads on Top Plate (See Appendix B, Page 307).



a.  $M_\infty = 3$



b.  $M_\infty = 4$

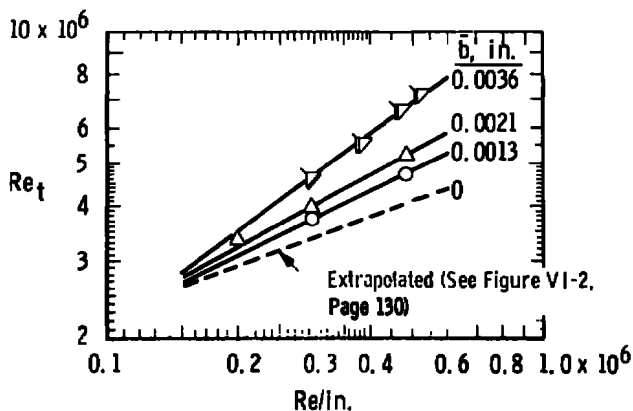
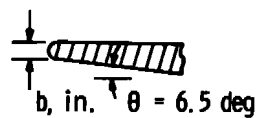


Figure VII-2. Basic transition Reynolds number data from the AEDC-VKF Tunnel A for  $M_\infty = 3, 4$ , and  $5$  and Variable  $\bar{b}$  and  $\theta_{LE}$ , hollow-cylinder model.



$l_m = 792$  in.

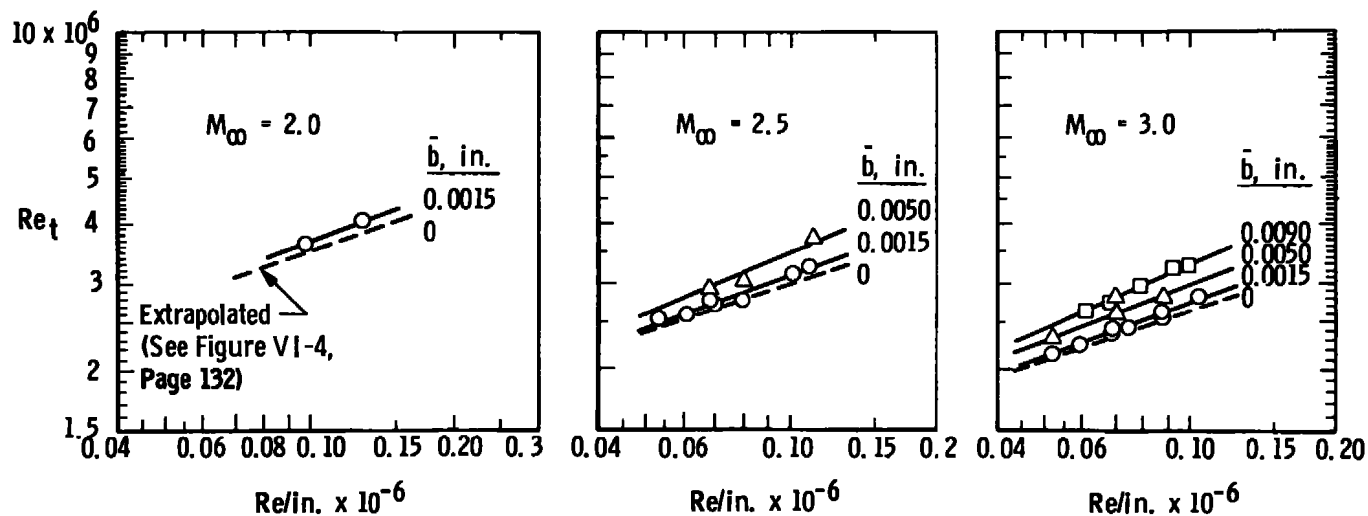
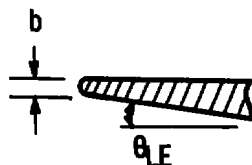


Figure VII-3. Basic transition Reynolds number data from the 12-in.-diam hollow-cylinder model in the AEDC-PWT Tunnel 16S for  $M_\infty = 2.0, 2.5$ , and  $3.0$  and  $b = 0.0015, 0.0050$ , and  $0.0090$  in.



Hollow-Cylinder Leading-Edge Geometry

AEDC-PWT			AEDC-VKF			Tunnel	$l_m$ , in.
	$\bar{b}$ , in.	$\theta_{LE}$ , deg		$\bar{b}$ , in.	$\theta_{LE}$ , deg		
---	0	6.5	---	0	---	16S	792
○	0.0015	↓	○	0.0013	6	A	231
◇	0.0050	↓	△	0.0021	6	D	48.5
◇	0.0090	↓	□	0.0023	12		
			◇	0.0030	12		
			▽	0.0036	6		

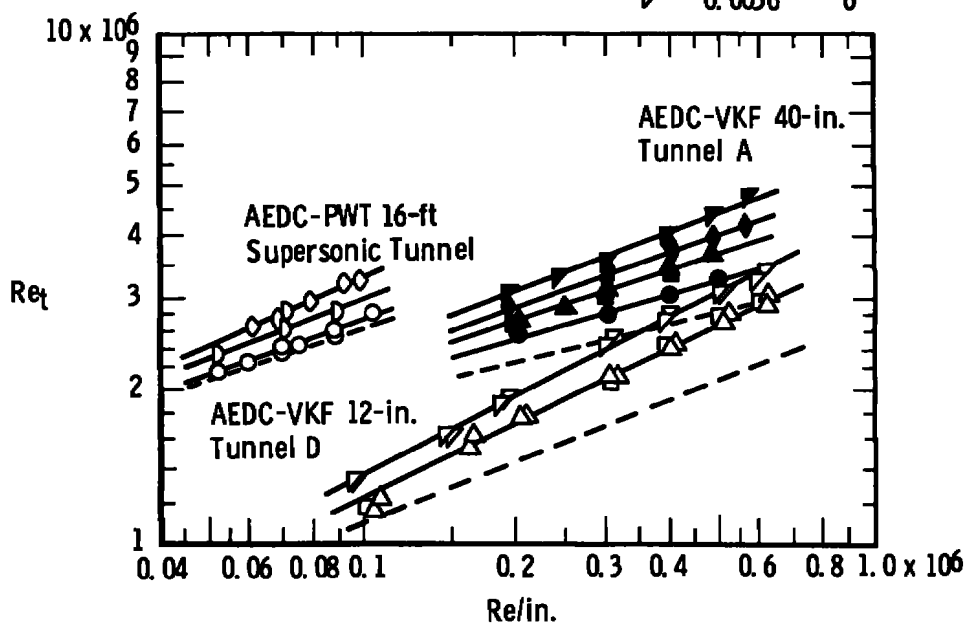
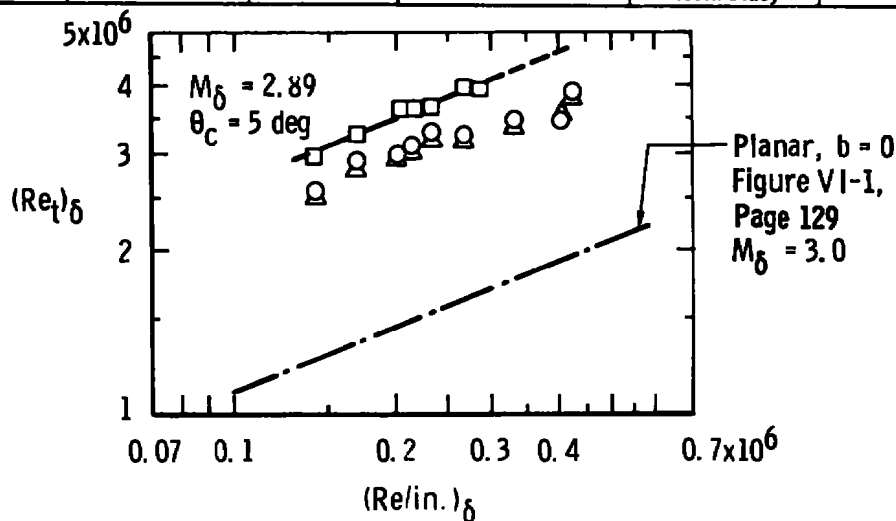
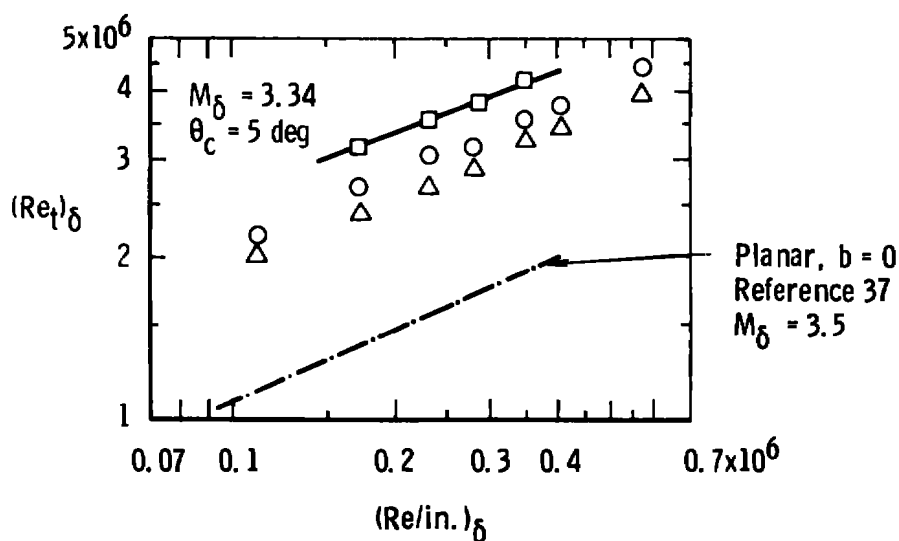


Figure VII-4. Basic transition Reynolds number data from the AEDC-VKF 12-in. Tunnel D, 40-in. Tunnel A and the AEDC-PWT 16-ft Supersonic Tunnel for  $M_\infty = 3.0$ , hollow-cylinder models.

Sym	Configuration	Surface Ray	Method of Detection	Source	$l_m$ , in.
$\Delta$	5-deg Cone	Top	Schlieren	Present Study	44
$\circ$	5-deg Cone	Bottom	Schlieren	Present Study	44
$\square$	5-deg Cone	Bottom	Surface Probe ( $p_{max}$ )	Present Study	44
---	Hollow Cylinder	Bottom	Surface Probe ( $p_{max}$ )	Reference 37 and Present Study	48



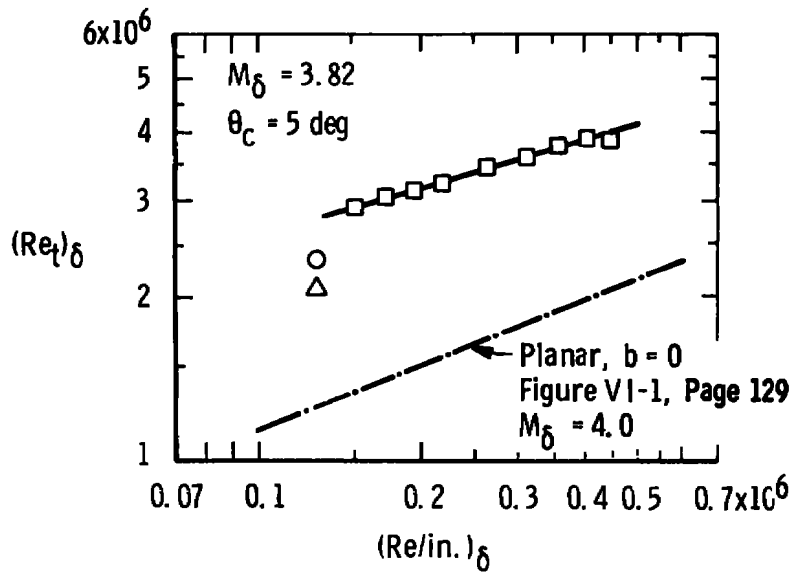
a.  $M_\infty = 3.0$



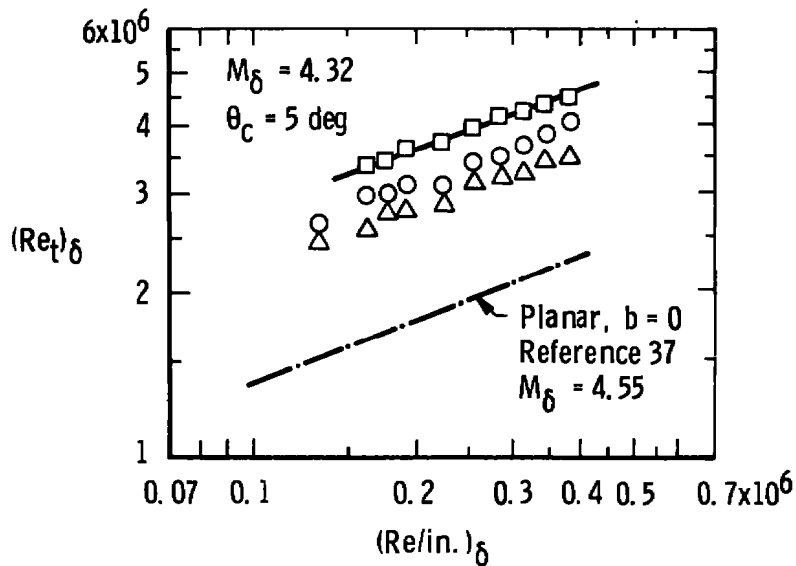
b.  $M_\infty = 3.48$

Figure VII-5. Transition Reynolds number data from AEDC-VKF Tunnel D, sharp-cone and planar models.





c.  $M_\infty = 4.0$



d.  $M_\infty = 4.55$

Figure VII-5. (Continued).

Sym	Configuration	Surface Ray	Method of Detection	Source	$l_m$ , in.
$\triangle$	5-deg Cone	Top	Shadowgraph	Present Study	215
$\circ$	5-deg Cone	Bottom	Shadowgraph	Present Study	215
$\square$	5-deg Cone	Bottom	Surface Probe( $p_{max}$ )	Present Study	215
---	Hollow Cylinder	Side	Surface Probe( $p_{max}$ )	Present Study	231
$\times$	5-deg Cone	Top	Microphone( $\tilde{p}_{max}$ )	Present Study	215

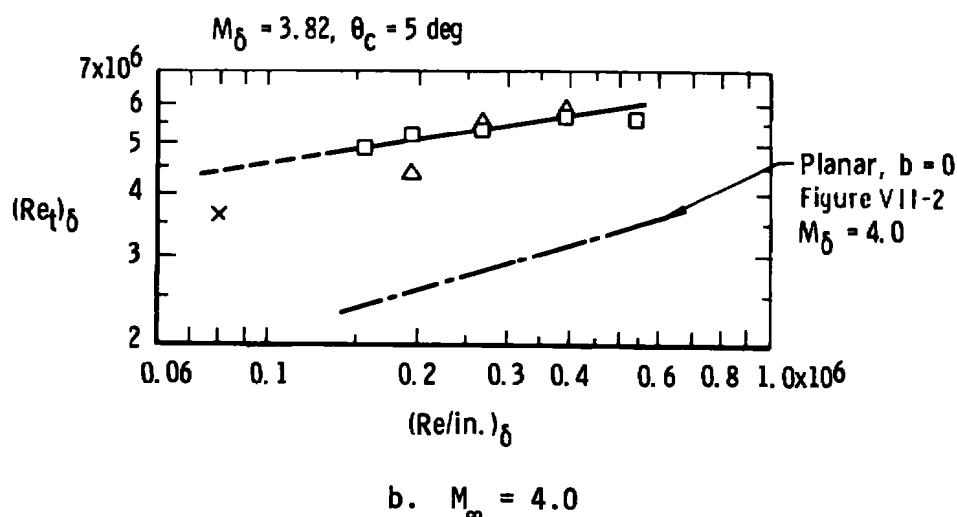
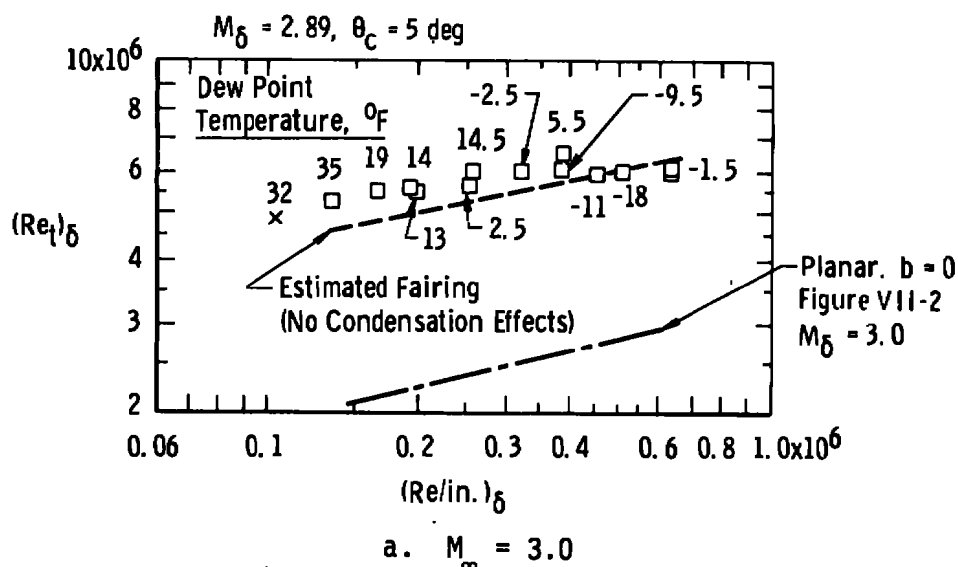
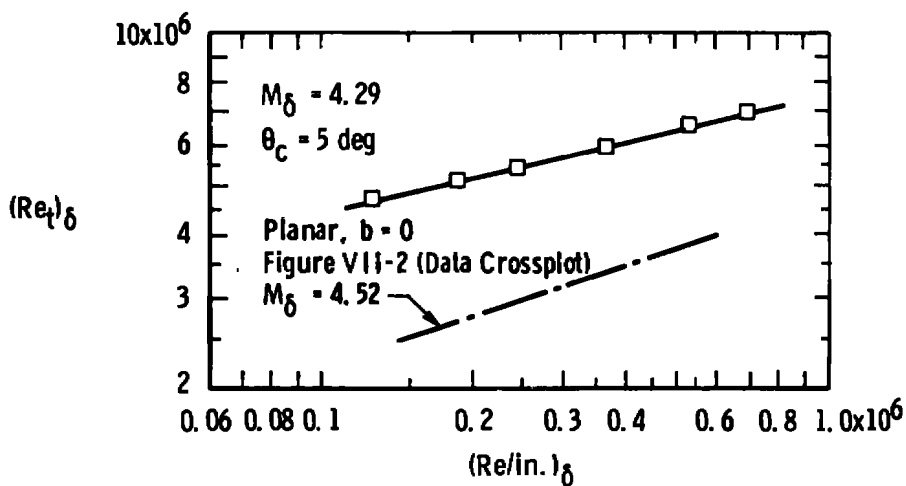
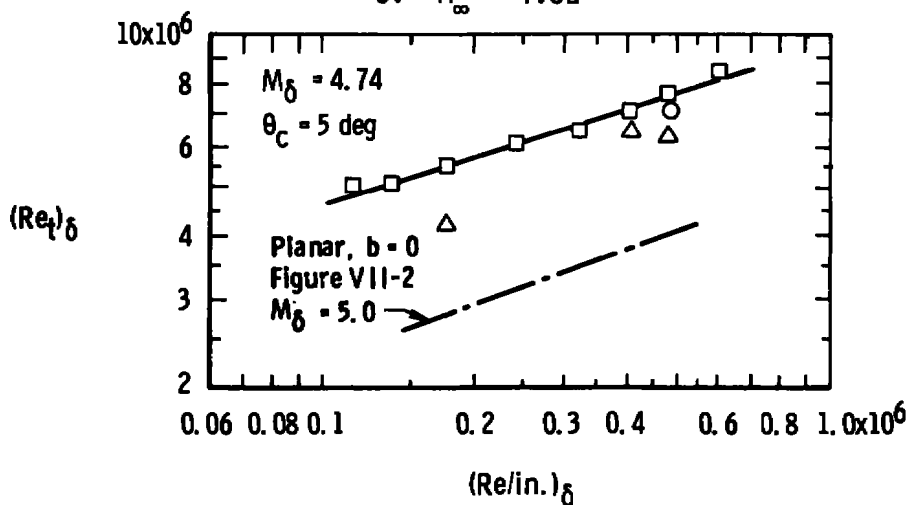


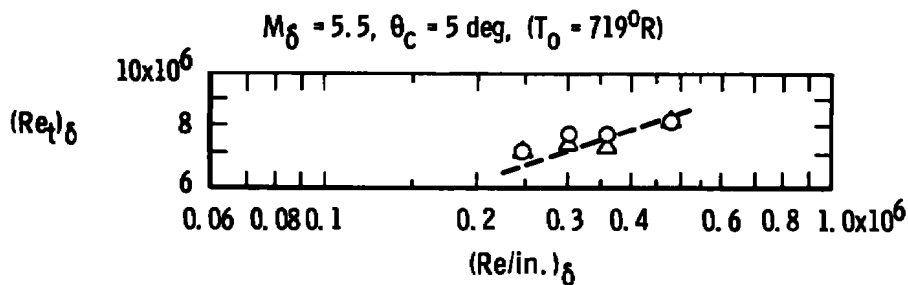
Figure VII-6. Transition Reynolds number data from AEDC-VKF Tunnel A, sharp-cone and planar models.



c.  $M_\infty = 4.52$



d.  $M_\infty = 5.03$



e.  $M_\infty = 5.94$

Figure VII-6. (Continued).

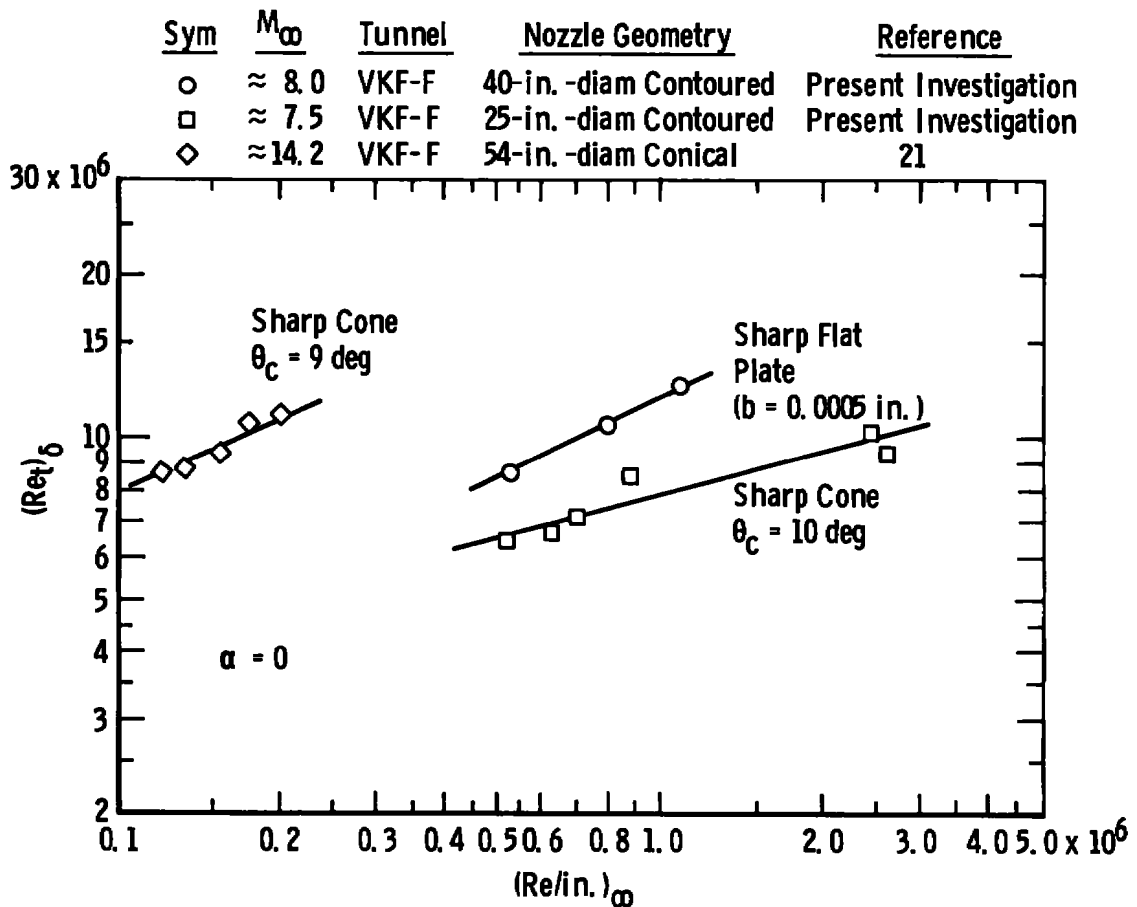


Figure VII-7. AEDC-VKF Tunnel F (Hotshot) transition data.

The sharp-cone data obtained in Tunnels A and D are presented in Figures VII-5 and VII-6. The location of transition was determined using the surface probe, schlieren photographs, and a flush-mounted surface microphone. The data presented in Figures VII-1 through VII-7 appear quite normal in that they exhibit the usual increase in  $(Re_t)_\delta$  with increasing  $(Re/in.)_\delta$  and increases in  $Re_t$  with increasing small amounts of bluntness (Figures VII-2 and VII-3). Although the microphone results were limited to two data points (Figure VII-6), the peak in the pressure fluctuation profile provided  $(Re_t)_\delta$  values consistent with the surface probe and photographic values.

One of the known (but sometimes forgotten) variables that can affect the transition location is the dewpoint (temperature at which water condensation occurs) as discussed in Reference (46). In Tunnel D, the dewpoint was sufficiently low ( $<0^\circ\text{F}$ ) at all Mach numbers not to affect the  $x_t$  locations. Also, in Tunnel A, the dewpoint was sufficiently low<sup>16</sup> at all Mach numbers except for the lower unit Reynolds numbers (subatmospheric pressure levels) at  $M_\infty = 3$ , as illustrated in Figure VII-6a. Therefore, a recommended  $(Re_t)_\delta$  trend as indicated by the dashed line has been included in Figure VII-6a for  $M_\infty = 3$ .

The location of transition as determined from schlieren and shadowgraph photographs was selected at the body station where the boundary layer had developed into what appeared visually to be fully turbulent flow. This location of transition provided  $(Re_t)_\delta$  values, in

---

<sup>16</sup>The relatively high dewpoint existing in the  $M_\infty = 3$  data reflects facility limitations existing on that particular date and does not necessarily represent standard test conditions.

general, about 10 to 20 percent lower than  $(Re_t)_\delta$  results obtained from the surface probe peak pressure locations. Any burst, ripple, or rope [see References (14) and (128)] effects that were observable upstream of the fully developed turbulent location were ignored in the selection of  $x_t$ . The transition values presented represent an average of  $x_t$  value determined from approximately four different photographs.

Flat-plate transition Reynolds number data obtained in the AEDC-VKF Tunnel F at  $M_\infty \approx 8$  are presented in Figure VII-7. Sharp-cone data obtained at  $M_\infty \approx 7.5$  and 14.2 are also included in Figure VII-7. It should be noted that the transition Reynolds number continued to increase with increasing unit Reynolds number for all Mach numbers and unit Reynolds numbers investigated. To the author's knowledge, the transition data obtained in Tunnel F at  $M_\infty = 8$  and 7.5 are at the highest unit Reynolds number reported to date from hypersonic wind tunnels.

## CHAPTER VIII

EXPERIMENTAL DEMONSTRATION OF AERODYNAMIC NOISE DOMINANCE  
ON BOUNDARY-LAYER TRANSITION

## I. INTRODUCTION

Primarily as a result of the research by Laufer (38), it has been established, as discussed in Chapter III, that the only significant source of free-stream disturbance in a well-designed supersonic wind tunnel is the aerodynamic noise that radiates from the tunnel wall turbulent boundary layer. Although these early experiments investigated the intensity and spectra of the free-stream aerodynamic noise disturbance, there were no experiments conducted that showed what effect radiated noise would have on transition locations on test models. Laufer and Marte (46) attempted one such experiment but the effort was unsuccessful, as discussed in Chapter III. The present research produced the first experimental data that showed conclusively the dominating effect that aerodynamic noise has on the location of transition on flat plates and cone model tested in supersonic-hypersonic wind tunnels.

There have been subsequent aerodynamic-noise-transition experiments conducted by NASA and in several European countries including Russia. Results from all of these studies have supported the conclusions published in the present research and have provided additional confirmation of the dominance of aerodynamic noise on transition. This chapter includes results from the present study and results from other experimental studies that have been published in recent years.

## II. AEDC SHROUD EXPERIMENTS

### Approach

To determine if radiated noise significantly affected the location of transition, it was necessary to create a test environment where a transition model could be exposed to various levels of aerodynamic noise intensity. One obvious approach would be to try to keep the boundary layer on the tunnel walls laminar. This approach is possible [see References (14), (74), and (92)] but at the very low tunnel pressure level (or unit Reynolds number), low enough to obtain laminar flow on the tunnel walls, transition will not occur on a test model. A second approach could be to try and shield a test model from the tunnel-wall-generated aerodynamic noise. Previous experiments using two concentric hollow cylinders with the outer cylinder serving as a shield to protect the small hollow cylinder from the tunnel radiated aerodynamic noise were reported in Reference (46). The idea was to measure the transition point on the inside of the small shroud using a pitot probe and, thereby, provide some measure of the effect that a radiated pressure field had on transition. Unfortunately, the presence of the outer cylinder introduced disturbances in the flow, and the results were inconclusive.

Based on the negative results of the experiments reported in Reference (46), a somewhat different approach was used in the present research. Results of these studies are reported in this section. The experimental apparatus employed to demonstrate the effects of radiated aerodynamic noise generated by a turbulent boundary layer consisted of



a 12-in.-diam shroud model placed concentrically around the 3.0-in.-diam hollow-cylinder transition model (Figure IV-7, page 100). This design was selected because it allowed a controlled boundary-layer environment to be maintained on the shroud inner wall upstream of the transition model. The specific design (shown in Figure VIII-1) resulted from a detailed engineering study that evaluated: (a) shroud lip shock locations, (b) optimum position of the transition model and microphone model inside the shroud, (c) aerodynamic choking inside the shroud from model blockage, (d) tunnel choking, (e) shroud lip bluntness effect on the shroud inner wall boundary-layer transition location, (f) utilization of the hardware at  $M_\infty = 3, 4, \text{ and } 5$ , (g) aerodynamic loads, and (h) the ability to control and provide laminar, transitional, and turbulent flow as desired on the shroud inner wall. The 12.0-diam shroud model, as shown in Figures VIII-1 and VIII-2, was the result of this study. The shroud also provided some protection from the noise radiating from the turbulent boundary layer on the wall of the 40-in. Tunnel A. The basic procedure was to measure the location of transition on the 3.0-in.-diam model and pressure fluctuations on a microphone flat-plate model as the boundary layer on the shroud inner wall upstream of the transition model changed from laminar to turbulent.

From the earlier experiments of Laufer (38,86,87) and Morkovin (44,45), it was anticipated that when the shroud wall boundary layer changed from laminar through transitional to fully turbulent, then the radiated aerodynamic noise would increase and adversely influence the location of transition on the internal 3.0-in.-diam transition model.

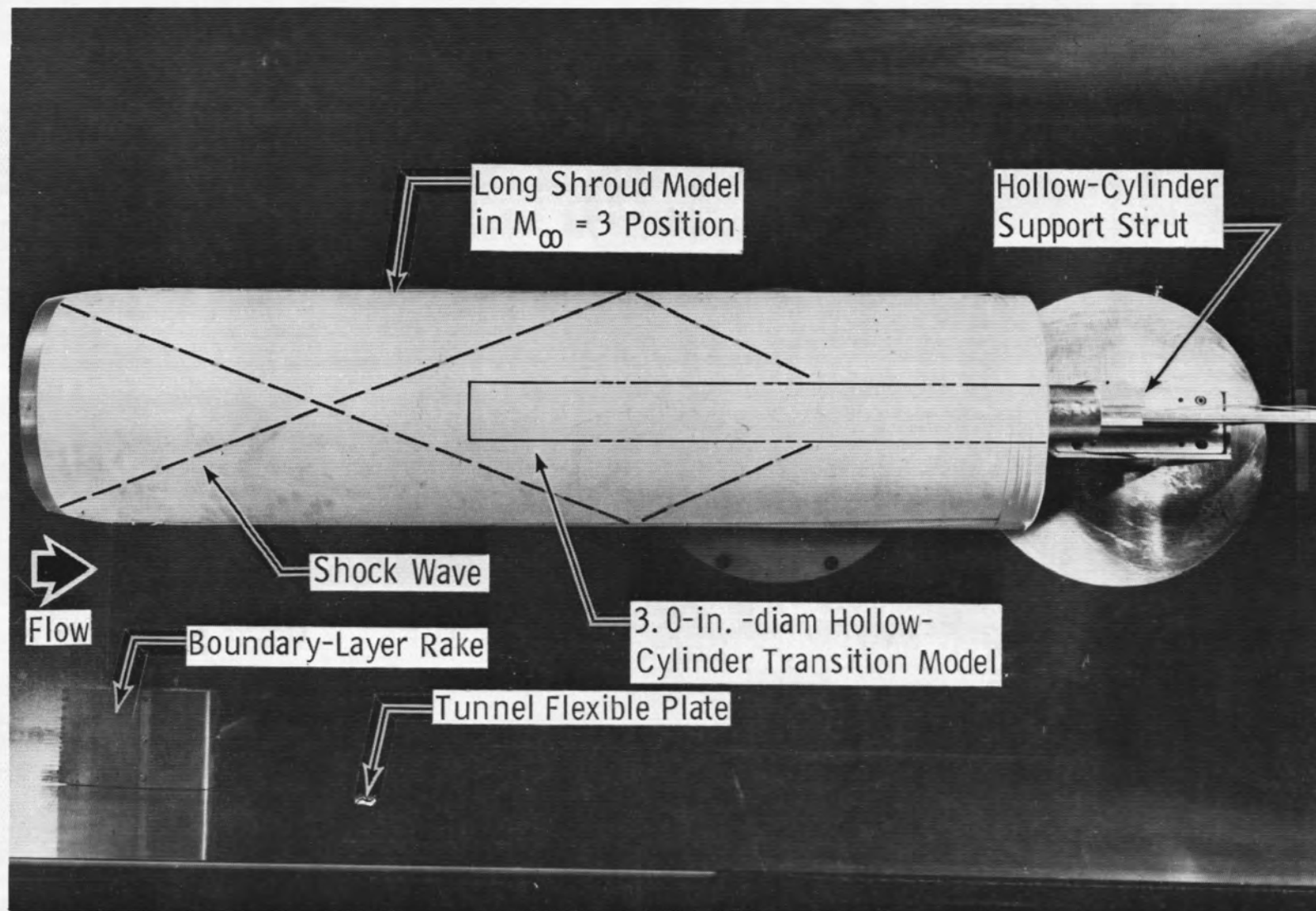


Figure VIII-1. Long shroud installation in the AEDC-VKF Tunnel A.

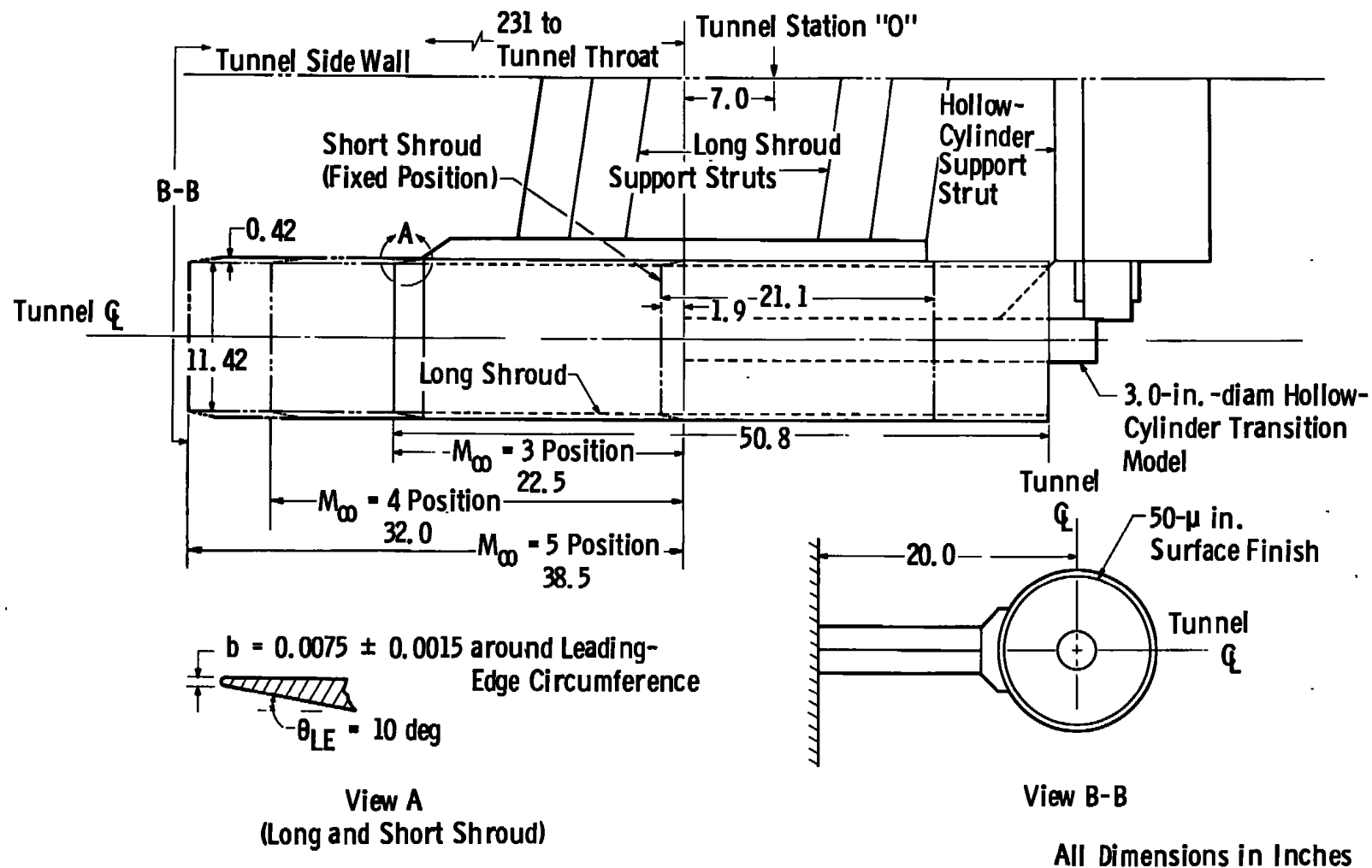


Figure VIII-2. AEDC-VKF Tunnel A long- and short-shroud configurations.

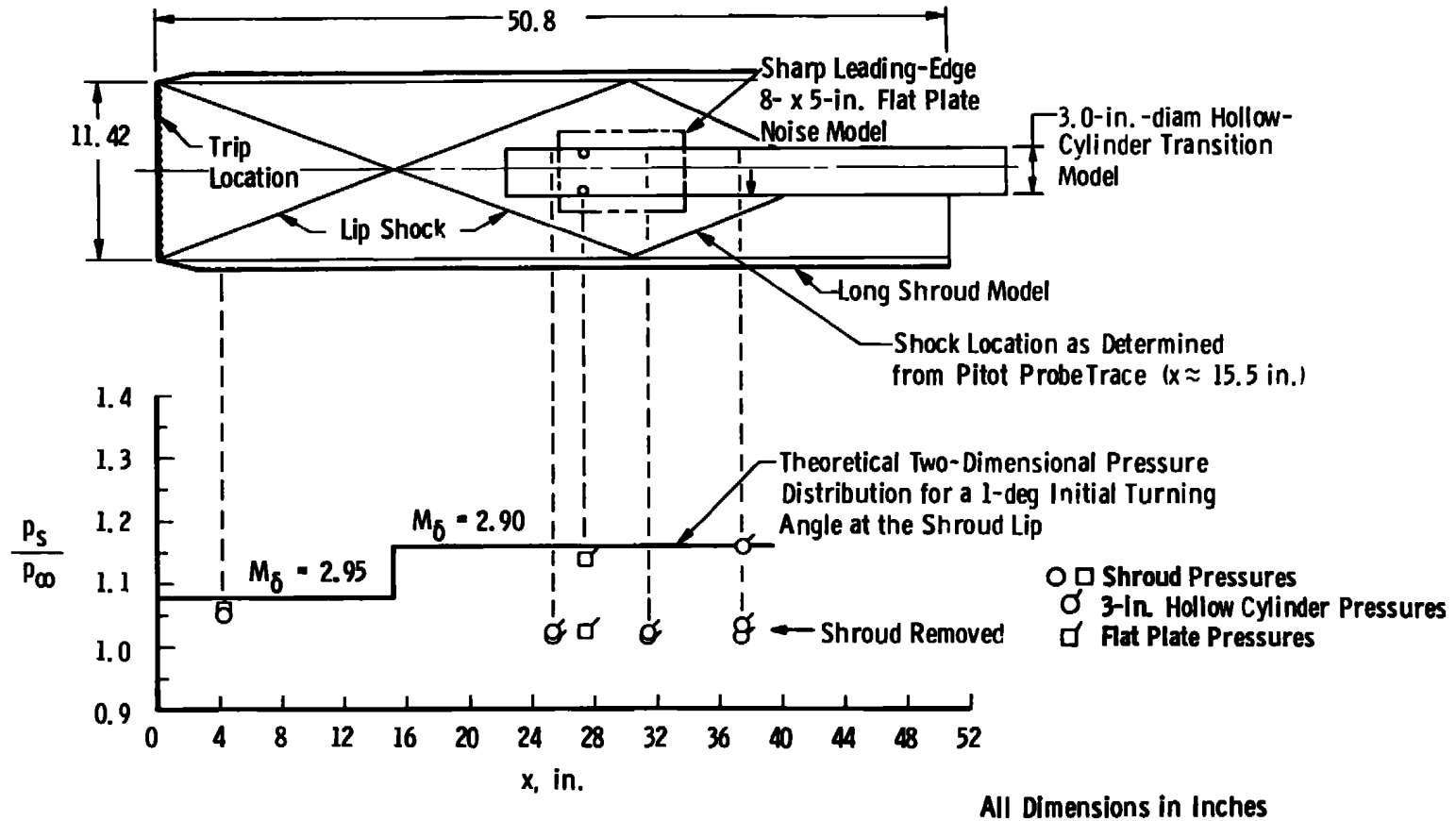
### Shroud Models

Long and short shrouds (Figure VIII-2) were used to shield the 3.0-in.-diam hollow-cylinder transition model and a flat-plate microphone model. The 12-in.-diam shroud model installation in the AEDC-VKF Tunnel A is shown in Figure VIII-1. The short shroud (Figure VIII-2) was maintained at a fixed position, and the long shroud was repositioned axially to prevent shroud leading-edge shock interference in the region of transition measurements on the transition and microphone models, as shown in Figures VIII-1 and VIII-3. The state of the boundary layer (laminar or turbulent) on the shroud inner wall was controlled by varying the tunnel pressure level and/or by using a boundary-layer trip. The steel shroud had an external, leading-edge bevel angle of 10 deg and a leading-edge bluntness value of approximately 0.007 in. with an internal surface finish of 50  $\mu$ in. The shroud design was such that the weak shock waves emanating from the shroud leading edge did not impinge on the test area of the 3.0-in.-diam transition model, as illustrated in Figure VIII-3.

### Free-Stream Static Pressure Measurements

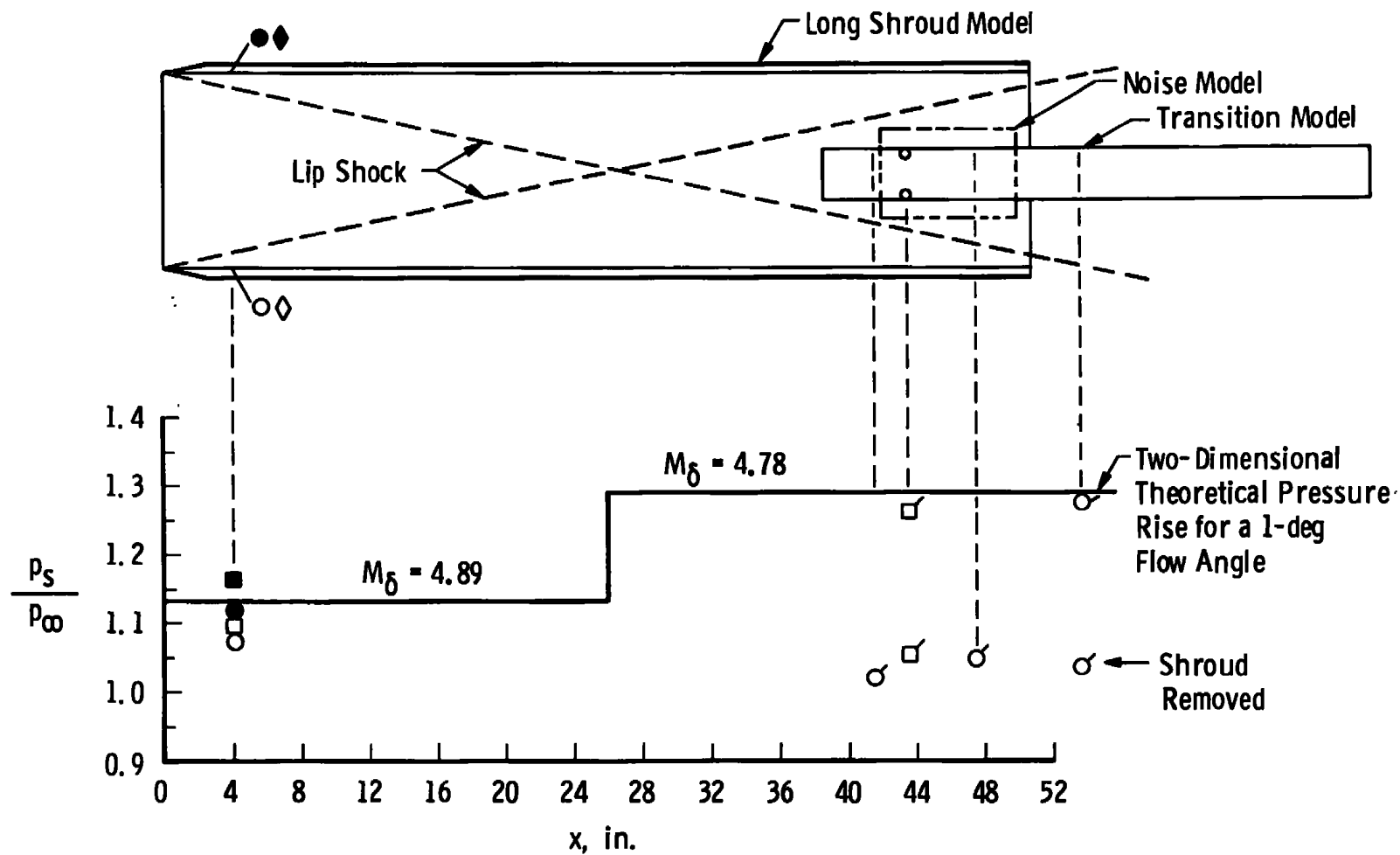
Static pressures were measured on the surface of the 3.0-in.-diam hollow-cylinder transition model and the flat-plate microphone model during all experiments. The purpose of these measurements was two-fold:

1. to ensure that the internal flow inside the shroud was supersonic as required; that the lip shock location was in the desired location; and there were no other shock waves or compression or expansion fields impinging on the models, and



a.  $M_\infty = 3.0$ ,  $Re/in. = 0.30 \times 10^6$

Figure VIII-3. Inviscid pressure distribution inside long shroud.



b.  $M_\infty = 5.0$ ,  $Re/in. = 0.48 \times 10^6$

Figure VIII-3. (Continued).

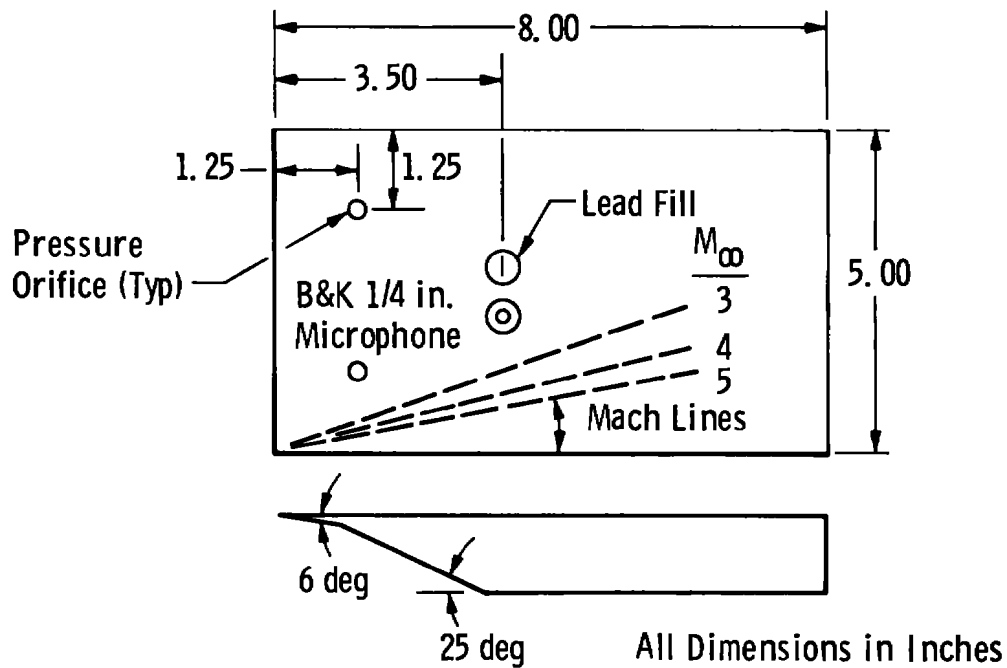
2. to ensure that the free-stream flow field in the AEDC-VKF Tunnels A, D, and E were free from shock waves, compression or expansion waves, and the static pressures were in agreement with the tunnel calibration data.

Flow inside the shroud remained supersonic at all times as confirmed by static pressures measured inside the shroud at all test conditions. Figure VIII-3 presents the static pressure data measured inside the long shroud for  $M_\infty = 3$  and 5 as determined from static pressure orifices located on the shroud inner surface near the shroud leading edge, from orifices on the 3.0-in.-diam hollow-cylinder transition model, and from orifices on the flat-plate microphone model. These data confirm that the shroud internal flow was supersonic at all times. A fairly good theoretical estimate of the static pressure distribution inside the shroud was obtained assuming that a 1-deg, two-dimensional shroud lip shock existed.

Presented in Figure VIII-4 are the static pressure data measured on the flat plate at  $M_\infty = 3$  and a large range of unit Reynolds numbers. For comparative purposes, the Tunnel A centerline calibration data<sup>17</sup> are also included in Figure VIII-4, and good agreement is seen to exist. These types of data were obtained at all test conditions using the flat-plate model and/or the 3.0-in.-diam hollow-cylinder model to establish that uniform flow existed over the model at all test conditions. Additional free-stream measurements (shroud removed) are also included in Figure VIII-3.

---

<sup>17</sup>The bar I shown in Figure VIII-4 indicates the spread of the experimental data.



- Tunnel A Calibrated  
 Centerline Mach Number  
 (Determined from Pitot Rake)
- Flat Plate Static Pressure  
 (Shroud Removed)
- Present Investigation

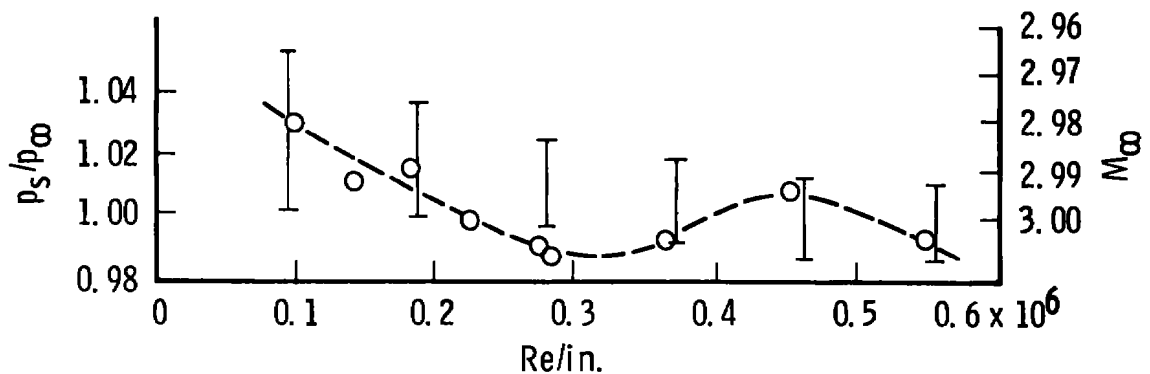


Figure VIII-4. Free-stream flat-plate pressure data,  $M_\infty = 3.0$ , AEDC-VKF Tunnel A centerline.



### Long-Shroud Wall Boundary-Layer Characteristics

A pitot rake having fifteen probes (Figure VIII-5) was used to determine the long shroud inner-wall boundary-layer characteristics. From these data, the condition of the boundary layer, whether turbulent or laminar, along with other boundary-layer characteristics was determined.

The local boundary-layer velocity ( $u$ ) was determined using the pitot probe total pressure and the shroud static pressure. The static pressure (measured shroud static) and total temperature was assumed to remain constant through the boundary layer. The local flow velocity ( $U_L$ ) outside the shroud boundary layer was calculated using  $T_0$  with the measured shroud static and the pitot pressure from the outermost probe on the rake which was outside the shroud boundary layer.

The shroud inner-wall boundary-layer displacement ( $\delta^*$ ) and momentum thicknesses ( $\theta$ ) were evaluated using the following equations:

$$\delta^* = \int_0^{\delta} \left(1 - \frac{\rho u}{\rho_L U_L}\right) \left(1 - \frac{y}{r}\right) dy \quad (7a)$$

$$\theta = \int_0^{\delta} \frac{\rho u}{\rho_L U_L} \left(1 - \frac{u}{U_L}\right) \left(1 - \frac{y}{r}\right) dy \quad (7b)$$

Detailed data reduction equations are presented in Appendix B. Typical velocity profiles, momentum thickness profiles, and displacement thickness profiles are presented in Figure VIII-6. These data were integrated graphically (using a planimeter) to produce the values of  $\theta$  and  $\delta^*$  presented in Figure VIII-7.

At  $M_\infty = 3.0$  and  $5.0$ , the boundary layer (no trip) was fully turbulent at the rake location for  $Re/in. \gtrsim 0.2 \times 10^6$ , as shown in

Probe No.	y, in.
15	1.940
14	1.690
13	1.525
12	1.330
11	1.100
10	0.970
9	0.815
8	0.700
7	0.630
6	0.525
5	0.390
4	0.310
3	0.160
2	0.070
1	0.037

Note: y Is Distance to Centerline of Probe  
Tube Size: 0.031 O.D. x 0.023 I.D.

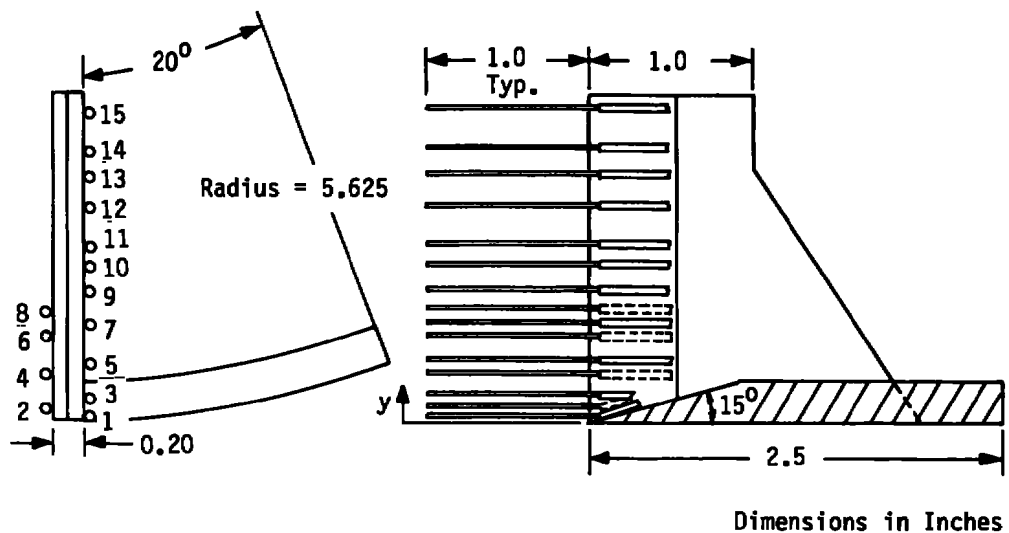
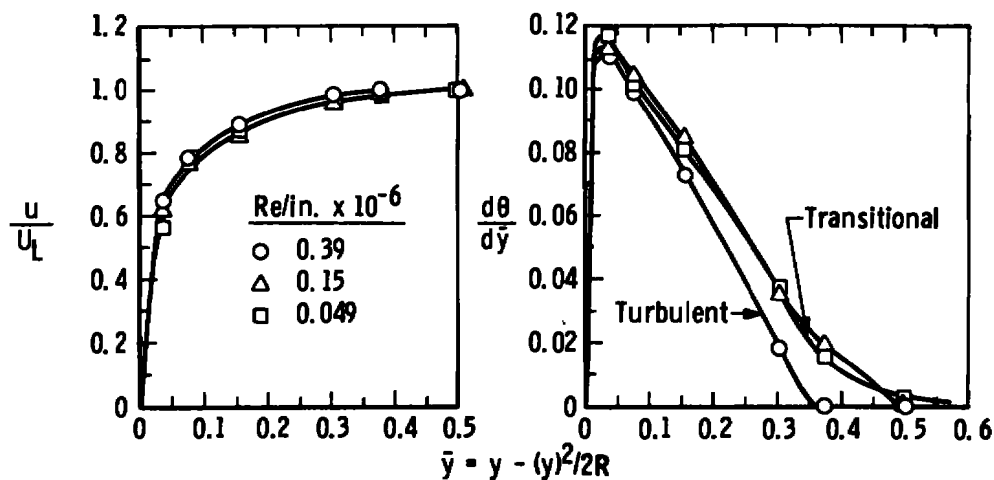
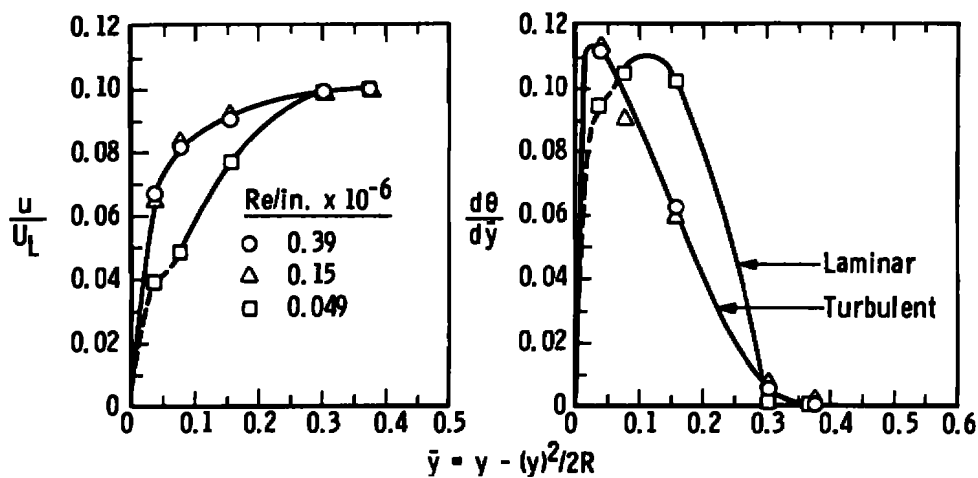
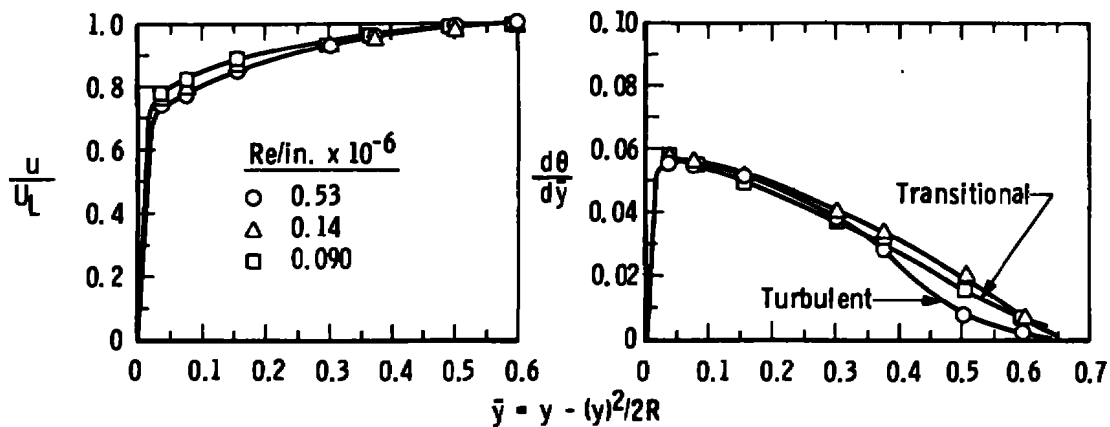


Figure VIII-5. Long-shroud boundary-layer rake.

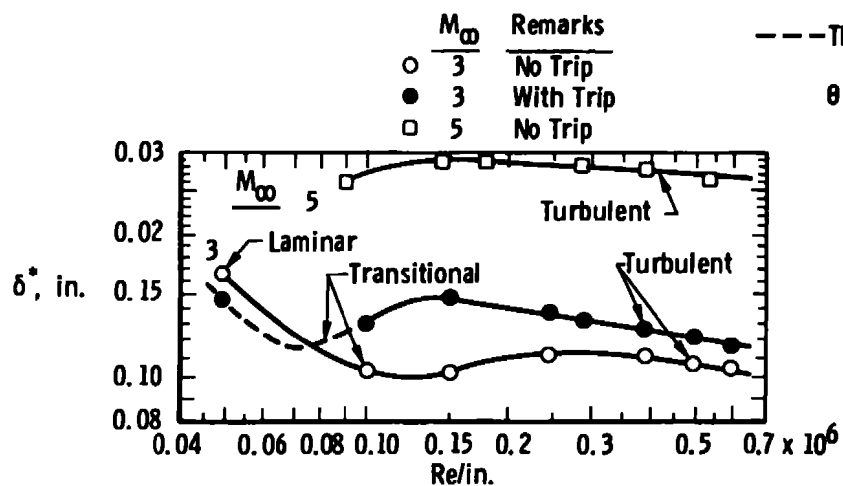
a.  $M_\infty = 3.0$ , with Trip on Shroudb.  $M_\infty = 3.0$ , No Trip on Shroud

Velocity Profiles

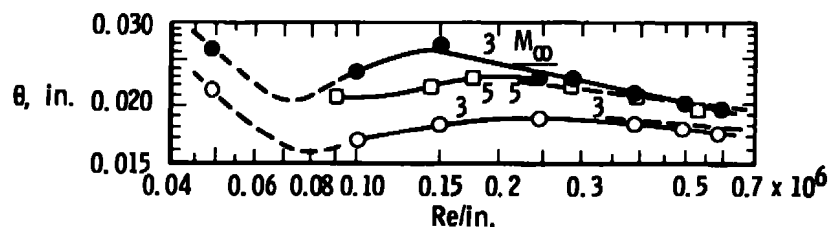
Momentum Thickness Profiles

c.  $M_\infty = 5.0$ , No Trip on Shroud

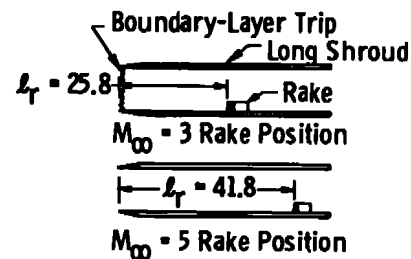
Figure VIII-6. Boundary-layer profiles on inner wall of long shroud.



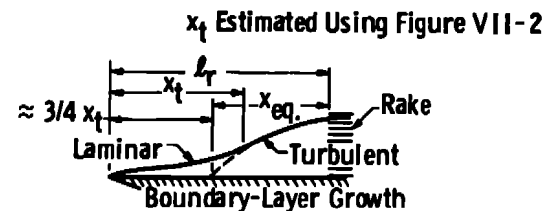
a. Displacement Thickness



b. Momentum Thickness



c. Rake Locations



d. Sketch of Boundary-Layer Growth

All Dimensions in Inches

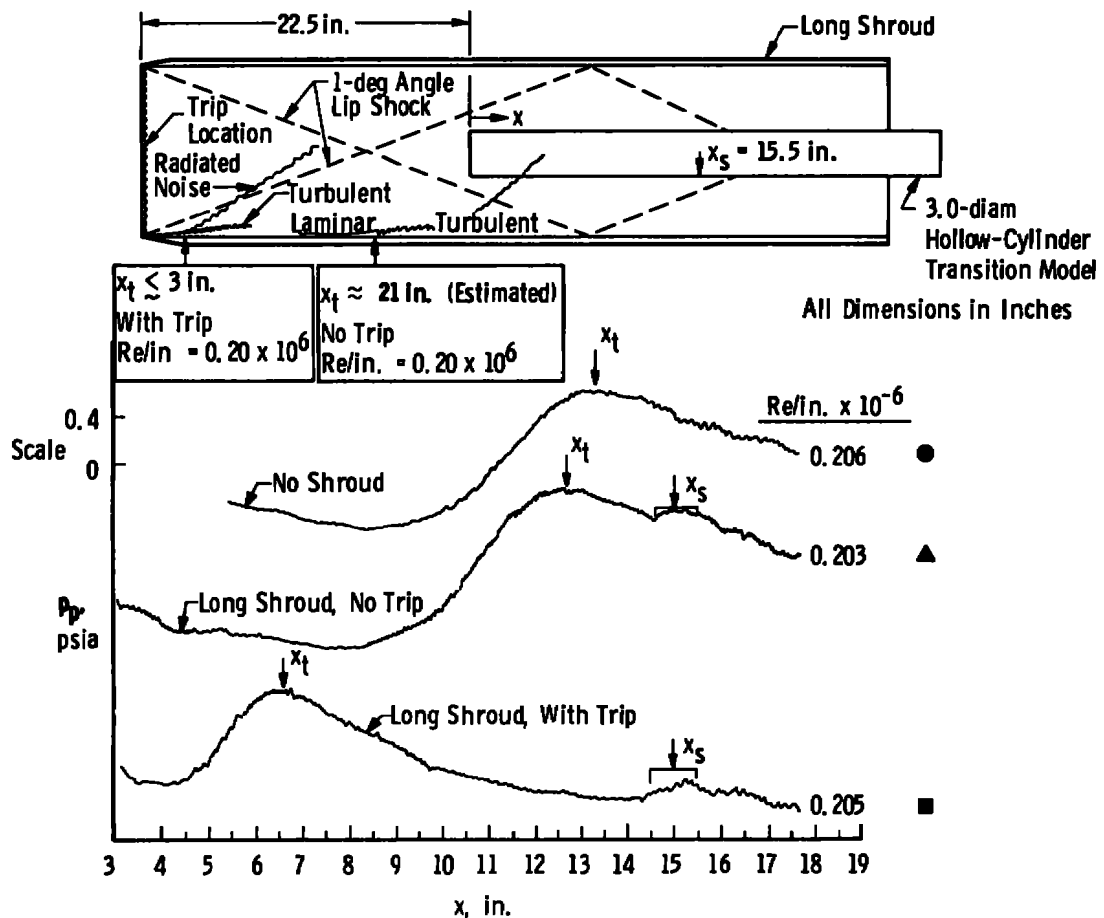
Figure VIII-7. Long-shroud boundary-layer characteristics.

Figures VIII-6a and b. For  $M_\infty = 3.0$  and  $Re/in. = 0.05 \times 10^6$ , the boundary layer was laminar at the rake for the no-trip condition. When an equivalent length concept ( $x_{eq.}$ ) was used as outlined in Figure VIII-7d, the experimentally no-trip, momentum thickness ( $\theta$ ) data were in good agreement with the theoretical calculations, as shown in Figure VIII-7b. With the trip installed, the boundary layer became fully turbulent at the rake location for  $Re/in. \gtrsim 0.12 \times 10^6$ . This result is as expected since the serrated fiber-glass tape had been demonstrated to be an effective trip at  $M_\infty = 3$  and  $Re/in. \gtrsim 0.15 \times 10^6$  as shown in Figure VI-6, page 138. The trip was ineffective at  $M_\infty = 5$ .

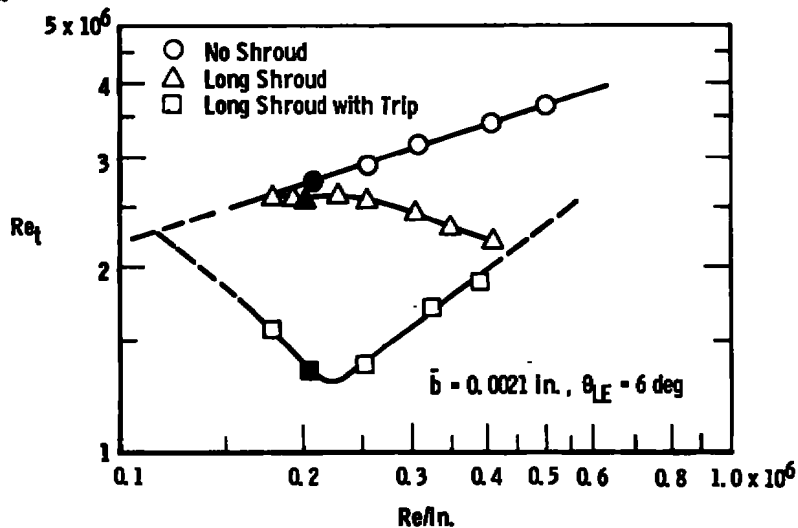
### Transition Results

Surface pitot pressure traces obtained on the 3.0-in.-diam hollow cylinder, with and without the long shroud in position, are presented in Figure VIII-8a for  $M_\infty = 3$ . The pitot probe was remotely controlled, and a continuous pitot pressure trace was provided by an X-Y plotter, as discussed in Chapter IV. As previously discussed, the location of transition was defined as the peak in the pitot pressure trace. The impingement location of the long shroud lip shock ( $x_s$ ) on the 3.0-in.-diam hollow-cylinder model was clearly visible on the probe pressure trace and was near the anticipated station.

The locations of turbulent flow on the shroud inner wall for two conditions of particular interest are shown in Figure VIII-8a. The no-trip location was estimated using the data presented in Figure VII-2, page 154, and the tripped location was determined using Figure VI-6, page 138. The probe traces presented in Figure VIII-8b show a large forward



a. Surface Pitot Probe Pressure Traces for 3.0-in.-Diam Model,  $M_\infty = 3.0$ , Long



b. Transition Reynolds Numbers

Figure VIII-8. Transition data measured with and without long shroud,  $M_\infty = 3.0$ , AEDC-VKF Tunnel A.

movement of the location of transition on the 3.0-diam model when turbulent flow occurred near the shroud leading edge (tripped case). Based on the estimated location of turbulent flow on the shroud inner wall, it was anticipated that for the no-trip long shroud case, transition on the 3.0-in.-diam model would be affected near  $Re/in. \approx 0.15 \times 10^6$  to  $0.2 \times 10^6$ . This is indeed the case as seen in Figures VIII-8a and b. All of the transition Reynolds number data obtained at  $M_\infty = 3$  are presented in Figure VIII-8b. These data provide conclusive evidence that the transition location on the 3.0-in.-diam model is adversely affected by the presence of a turbulent boundary on the shroud inner wall. This effect is shown in the next section to be the result of radiated aerodynamic noise.

In addition to the long shroud, a short configuration was also tested, as shown in Figure VIII-9. The purpose of this configuration was to maintain laminar flow on the inner wall and attempt to shield some of the radiated aerodynamic noise from the walls of the 40-in. Tunnel A from the 3.0-in.-diam transition model. However, it was suspected that this short shroud configuration would not shield an appreciable amount of radiation since the radiated pressure fluctuations travel along incline rays similar to, but somewhat steeper than, Mach waves [see Reference (86)]. Again, the leading-edge shock impingement ( $x_s$ ) was clearly visible on the probe pressure traces presented in Figure VIII-9 and occurred on the 3.0-in.-diam model near the anticipated location.

Figure VIII-10 presents the transition Reynolds number results obtained without the shroud configuration and with the short and long shroud configurations placed concentrically around the 3.0-in.-diam

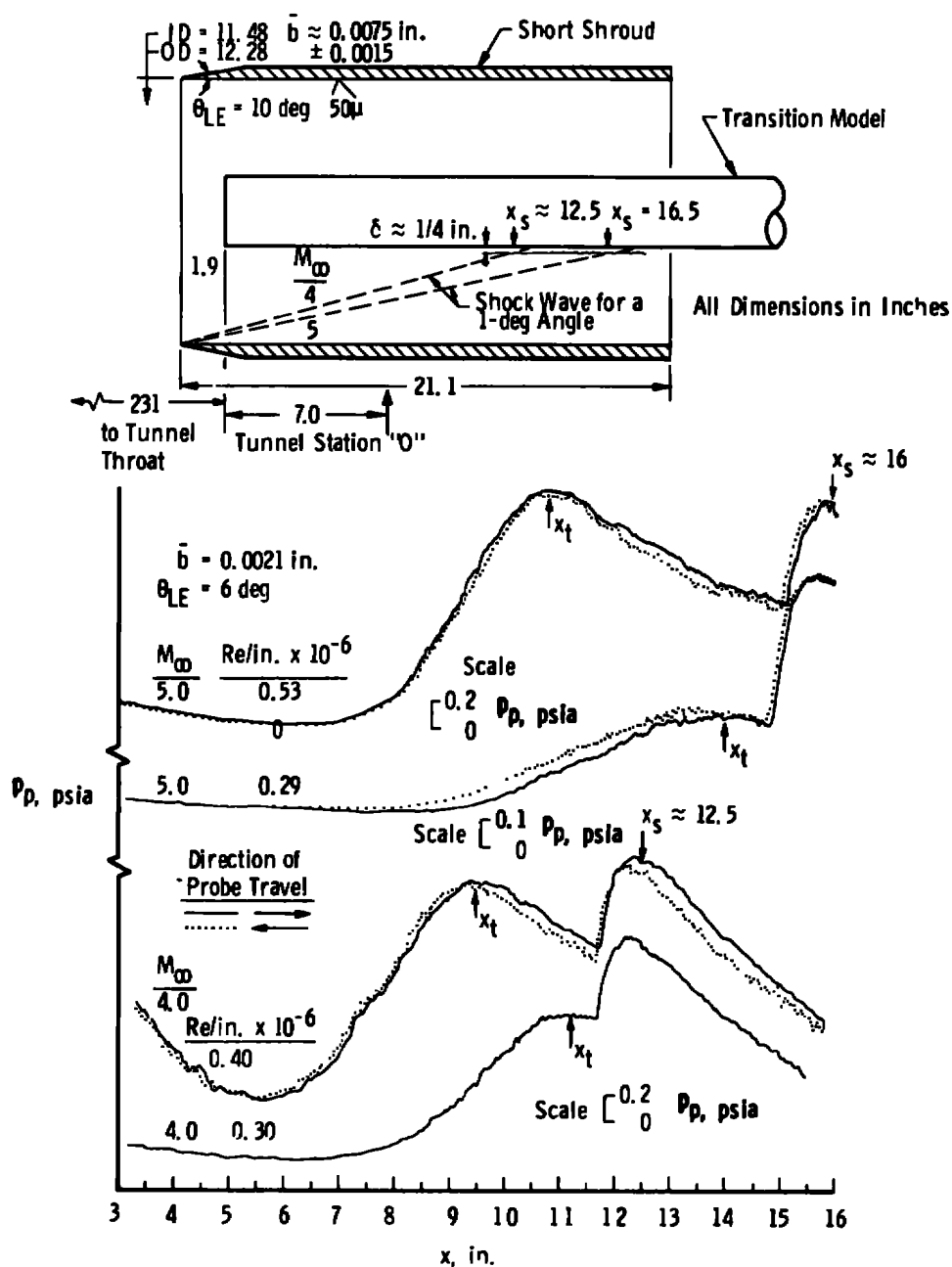
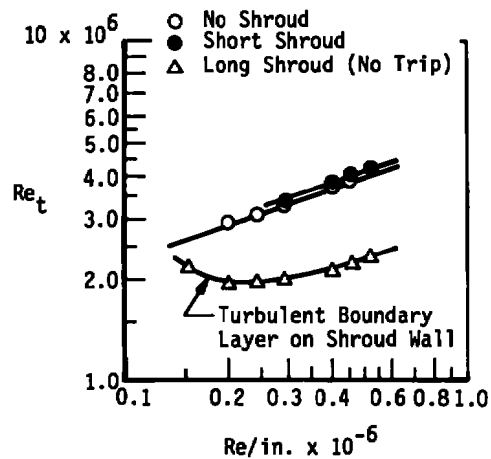
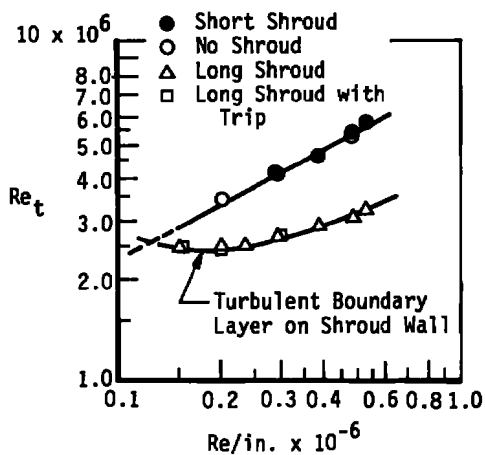


Figure VIII-9. Surface pitot probe pressure traces on 3.0-in.-diam model, short-shroud configuration,  $M_\infty = 4$  and 5.

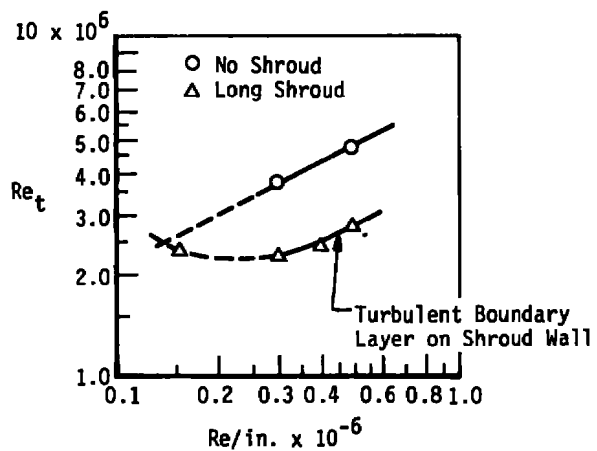




a.  $M_\infty = 4$ ,  $\bar{b} = 0.0021$  in.,  $\theta_{LE} = 6$  deg



b.  $M_\infty = 5$ ,  $\bar{b} = 0.0021$  in.,  
 $\theta_{LE} = 6$  Deg



c.  $M_\infty = 5$ ,  $\bar{b} = 0.0013$  in.,  
 $\theta_{LE} = 12$  Deg

Figure VIII-10. Transition Reynolds numbers measured with and without long and short shroud,  $M_\infty = 4.0$  and  $5.0$ .

hollow-cylinder model for  $M_\infty = 4$  and 5. These data were taken with and without the boundary-layer trip on the long shroud inner surface at  $M_\infty = 5$ . The trip was not effective at  $M_\infty = 5$ , which was not unexpected. The transition Reynolds number decreased at  $M_\infty = 4$  and 5 as the shroud inner wall boundary layer became turbulent.

These results are discussed in more detail in the next section. All of the transition results obtained in this investigation are tabulated in Appendix F, page 399.

### Aerodynamic Noise Measurements

A flat-plate model (Figure VIII-11) instrumented with a surface microphone was used to measure the free-stream aerodynamic noise levels inside the long shroud as the boundary layer on the shroud inner wall was changed from laminar to turbulent. The flat-plate microphone model was also positioned inside the long shroud, as shown in Figure VIII-12. The microphone model was an 8- by 5-in., sharp-leading-edge flat-plate instrumented with two  $\frac{1}{4}$ -in.-diam microphones and two static orifices, as shown in Figure VIII-11. One microphone was mounted flush with the model surface and the other mounted internally to record model vibrations. The microphone model locations inside the long shroud were similar to the 3.0-in.-diam transition model locations and were repositioned with changes in free-stream Mach number to prevent the shroud leading-edge generated shock wave from impinging on the model surface, as shown in Figure VIII-3, pages 186 and 187.

The rms pressure fluctuations were read directly from two on-line rms voltmeters during test operation. The microphone output was also

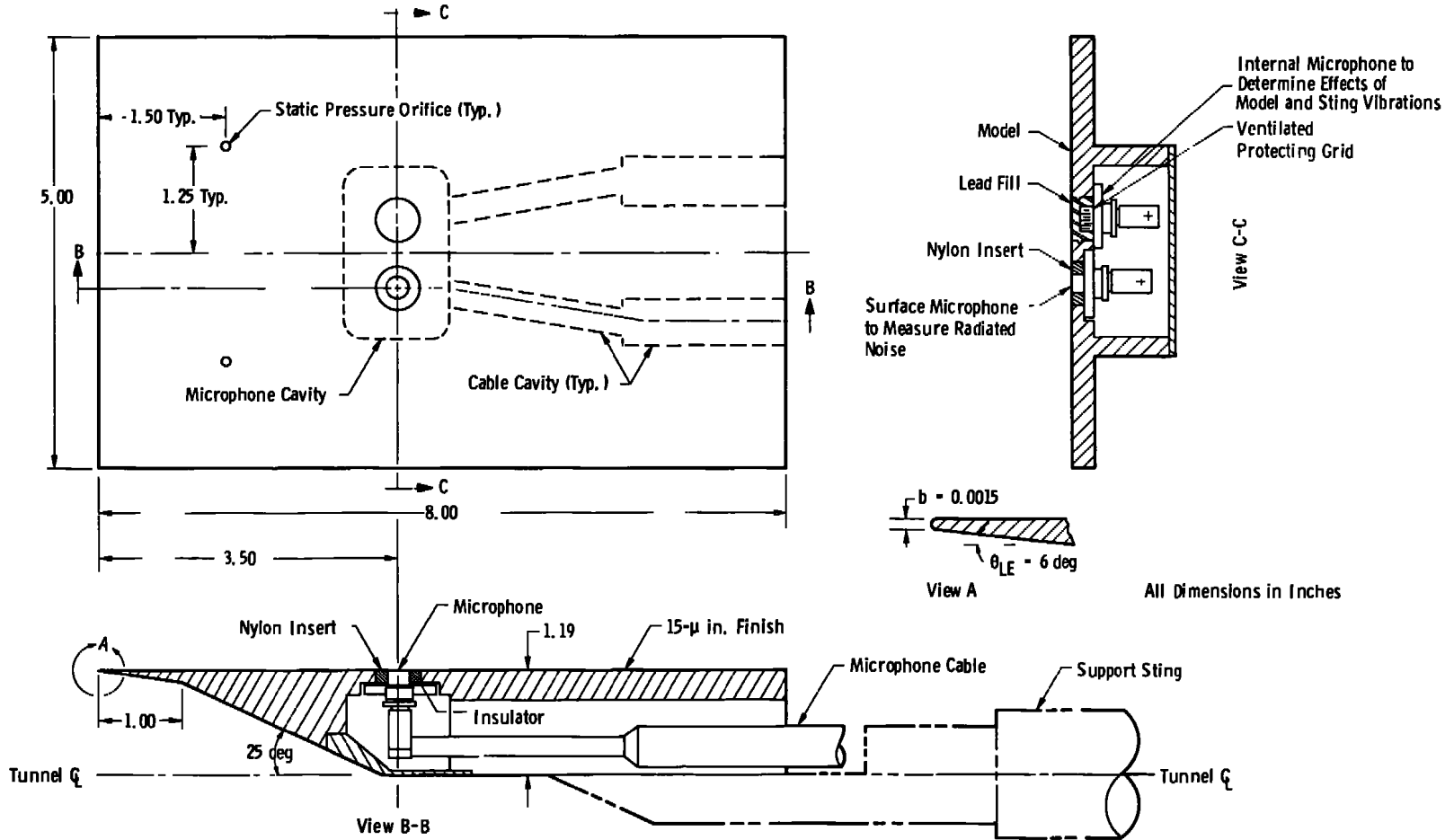


Figure VIII-11. Flat-plate microphone model.

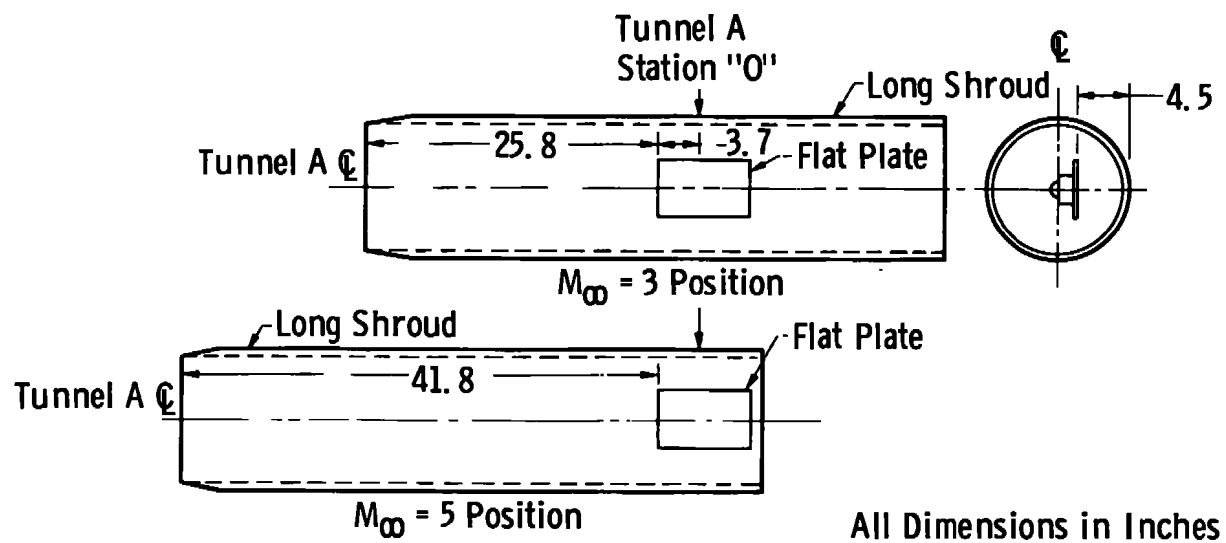
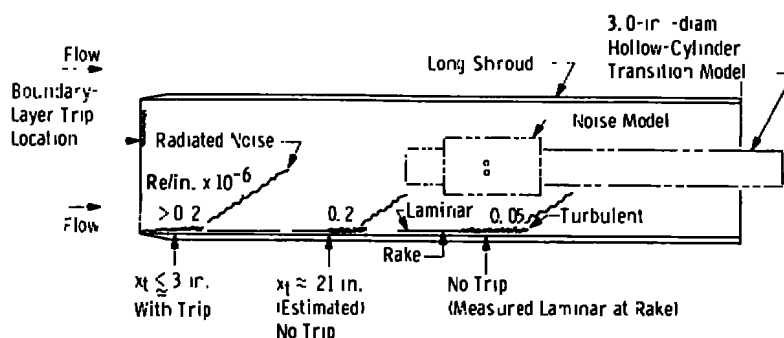


Figure VIII-12. AEDC-VKF Tunnel A microphone-flat-plate installation.

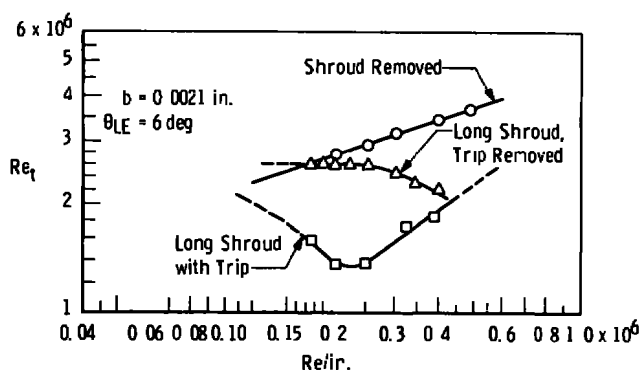
recorded on an Ampex® data tape system and later checked for verification of the on-line rms values. Microphone interference from model vibration was minimized by providing a nylon insert around the surface microphone, using insulator strips on the mounting plate, and filling the microphone cable cavity with cotton. Model vibrations as determined from the internally mounted microphone were found to be negligible. See Chapter V for additional details on data-recording procedures. The microphone model was also tested in the free-stream of the AEDC-VKF Tunnels A and D.

Pressure fluctuations data measured on the flat-plate model with and without the long shroud in position are presented in Figure VIII-13. Significant results to be concluded from this figure are:

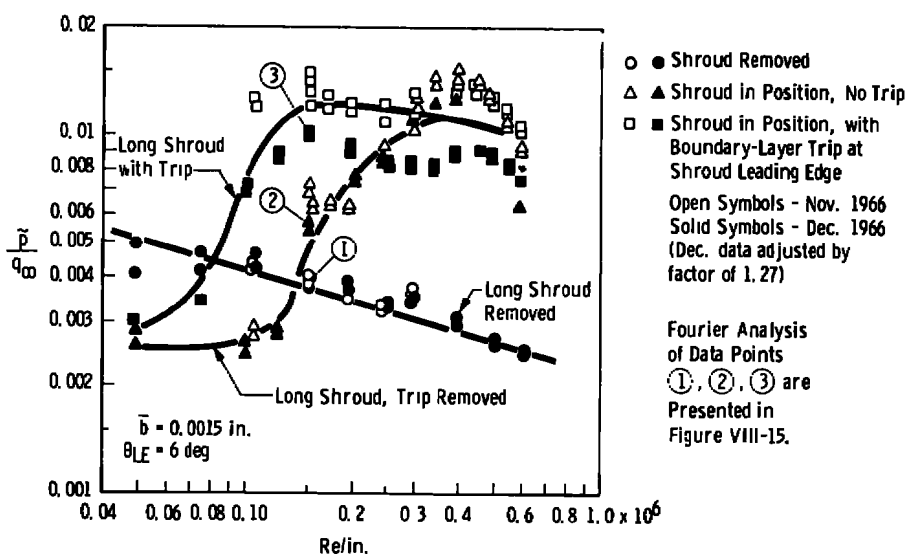
1. The no shroud data exhibited a monotonic decrease in the  $\tilde{p}/q_\infty$  data with increasing unit Reynolds number. Note that the  $Re_t$  data (taken from Figure VIII-8b) show just the opposite trend, i.e., an increase in  $Re_t$  values with increasing unit Reynolds number.
2. For  $Re/in. \lesssim 0.05 \times 10^6$ , the boundary-layer flow on the shroud inner wall was definitely laminar past the flat-plate model location. This was established from the boundary-layer rake data obtained at position  $x = 25.8$  in., as shown in Figure VIII-7, page 177. At  $Re/in. \leq 0.05 \times 10^6$  the  $\tilde{p}/q_\infty$  data shown in Figure VIII-13 have a lower value than the no-shroud condition. This means that the long shroud shielded the flat-plate model from the tunnel wall radiated pressures.



a. Boundary-Layer Development Inside Long Shroud



b. Transition Reynolds Numbers on the 3.0-in.-Diam Hollow-Cylinder Model



c. Root-Mean-Square Radiated Pressure Fluctuations

Figure VIII-13. Comparisons of transition Reynolds numbers and root-mean-square radiated pressure fluctuations at  $M_\infty = 3.0$ .

3. As the unit Reynolds number was increased, the transition on the shroud inner wall moved forward and transition occurred at the rake station ( $x = 25.8$  in.) at approximately  $Re/in. \approx 0.10 \times 10^6$  (see Figure VIII-7, page 193). Radiated pressure waves strike the microphone model when  $Re/in. \approx 0.15 \times 10^6$ . The  $\tilde{p}/q_\infty$  data presented in Figure VIII-18c confirm this expected result. As transition moved closer to the shroud leading edge and the flow became fully turbulent, the  $\tilde{p}/q_\infty$  data increased to a maximum value that is approximately three times higher than the no-shroud data.
4. With the boundary-layer trip placed on the shroud inner wall, it was expected that the boundary layer would be fully turbulent for  $x > 3$  in. and  $Re/in. \approx 0.2 \times 10^6$  (see Figure VI-6, page 138). Also the trip was shown to be ineffective for  $Re/in. \lesssim 0.1 \times 10^6$ . The  $\tilde{p}/q_\infty$  data (obtained with long shroud and with the trip) presented in Figure VIII-13c show that the pressure fluctuations reached a maximum value at  $Re/in. \approx 0.15 \times 10^6$  and remained essentially constant for  $0.15 < Re/in. < 0.6 \times 10^6$ . This trend is in agreement with the expected behavior of the tripped boundary layer on the shroud inner wall.
5. The pressure fluctuation data ( $\tilde{p}/q_\infty$ ) presented in Figure VIII-13c are essentially a reverse image of the hollow-cylinder transition data presented in Figure VIII-13b. For example, the  $Re_t$  data increased with decreasing noise ( $\tilde{p}/q_\infty$ ) levels, or vice versa. Also the points of intersection present in

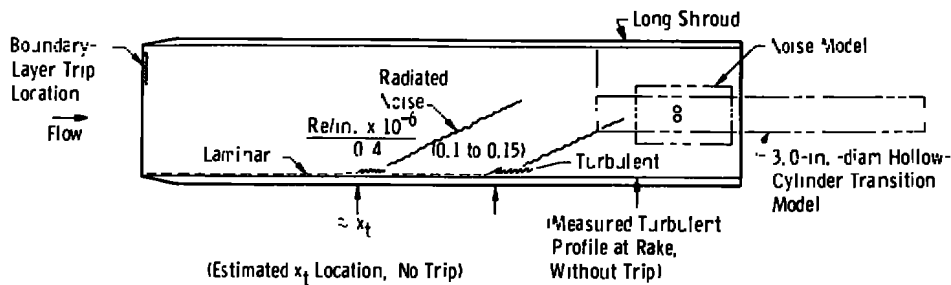
the  $Re_t$  data are in close agreement with the  $\tilde{p}/q_\infty$  points of intersection. Furthermore, the minimum  $Re_t$  value corresponds to the peak  $\tilde{p}/q_\infty$  value.

6. Confirmation of the data presented in Figure VIII-13c was obtained by conducting a second complete set of measurements as indicated in the figure.

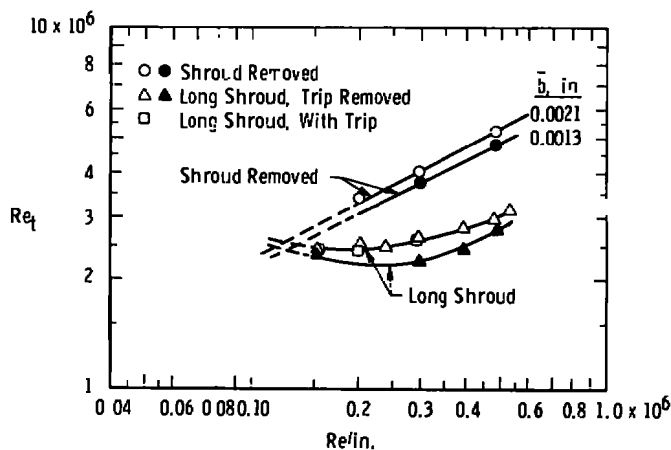
Presented in Figure VIII-14 are the pressure fluctuation data and  $Re_t$  data measured at  $M_\infty = 5$  with and without the long shroud in position. The  $M_\infty = 5$  data exhibit characteristics similar to the  $M_\infty = 3$  results:

1. For the no-shroud condition,  $Re_t$  increases monotonically with decreasing  $\tilde{p}/q_\infty$  values.
2. The  $\tilde{p}/q_\infty$  values are initially low, which would be characteristic of laminar flow on the shroud wall. The  $\tilde{p}/q_\infty$  data then increase with increasing  $Re/in.$  until the flow becomes fully turbulent on the shroud inner wall for the  $Re/in. \gtrsim 0.2 \times 10^6$  (see Figure VIII-7, page 193).
3. The  $Re_t$  data are a reverse image of the  $\tilde{p}/q_\infty$  data and exhibit similar points of intersection.
4. It is of interest to note that the  $M_\infty = 5$  transition Reynolds number results shown in Figure VIII-14b exhibited the characteristic decrease in  $Re_t$  with a decrease in leading-edge bluntness ( $b$ ) even when exposed to the intensified field of radiated noise.

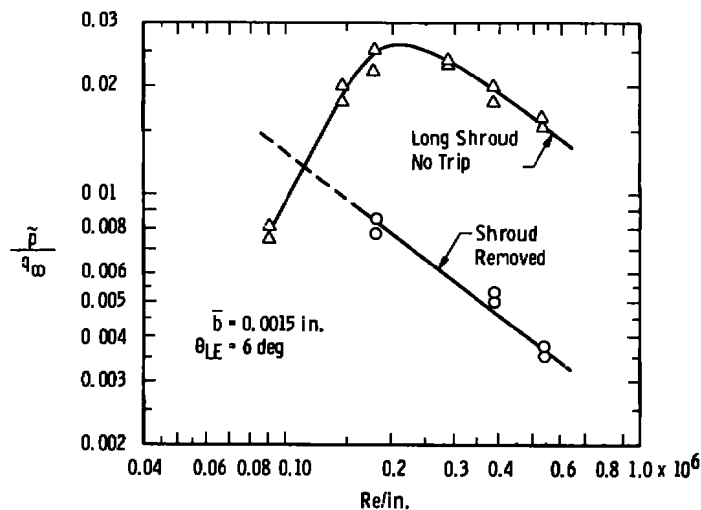




### a. Boundary-Layer Development Inside Long Shroud



### b. Transition Reynolds Numbers on the 3.0-in.-Diam Hollow-Cylinder Model



### c. Root-Mean-Square Radiated Pressure Fluctuations

Figure VIII-14. Comparisons of transition Reynolds numbers and root-mean-square radiated pressure fluctuations at  $M_\infty = 5.0$ .

The long shroud data presented in Figures VIII-13 and VIII-14 show that the boundary layer on a model can be dominated by the presence of aerodynamic noise in the free stream.

Presented in Figure VIII-15 are the Fourier analysis of the three data points identified in Figure VIII-13c as ① , ② , and ③ . The spectra data follow the same qualitative trend as exhibited by the overall rms ( $\tilde{p}/q_\infty$ ) data presented in Figure VIII-13c. The pressure fluctuations at low frequencies were quite large. Two spikes appeared in all three sets of data at approximately 7 kHz and 14 kHz. These were probably mechanically induced vibrational effects.

## II. NOISE MEASUREMENTS IN TWO AEDC SUPERSONIC WIND TUNNELS

Pressure fluctuation data measured on the flat plate positioned in the free stream of the AEDC-VKF Tunnels D and A are presented in Figure VIII-16. The present data obtained at  $M_\infty = 3$  and 4 are compared with data taken at  $M_\infty = 4$  by Donaldson and Wallace (88) using the same model. There are several points to note in this figure:

1. At  $Re/in. = 0.025 \times 10^6$ , the Tunnel D  $\tilde{p}/q_\infty$  values were very low. This corresponds to a laminar boundary layer on the tunnel wall as determined from boundary-layer data published in Reference (97).
2. At  $Re/in. \approx 0.05 \times 10^6$ , the wall boundary layer was estimated to be transitional and the measured high peak is in agreement with the findings of Vrebalovich (92), Laufer (38), and Wagner, et al. (89).

See	}	①	No Shroud
Figure		②	Long Shroud, No Trip
VIII-136		③	Long Shroud, With Trip

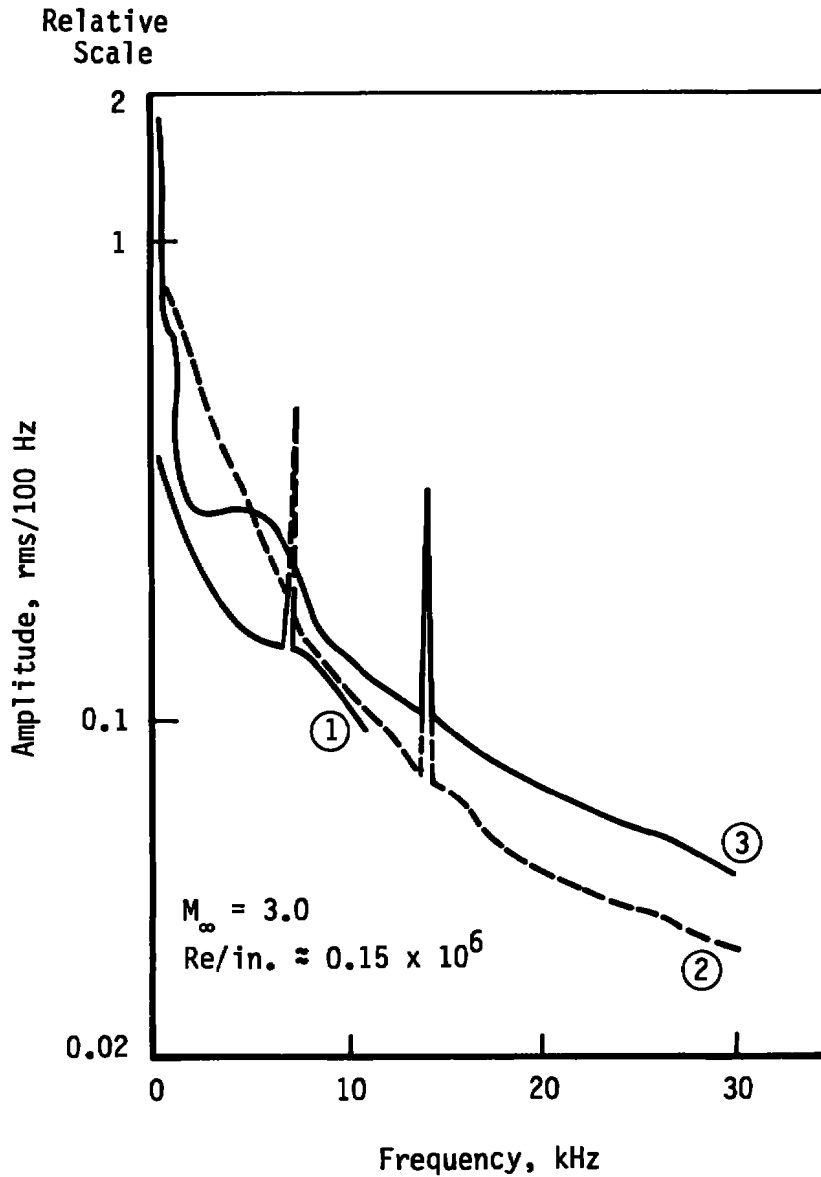


Figure VIII-15. Fourier analysis of selected data points from Figure VIII-13c.

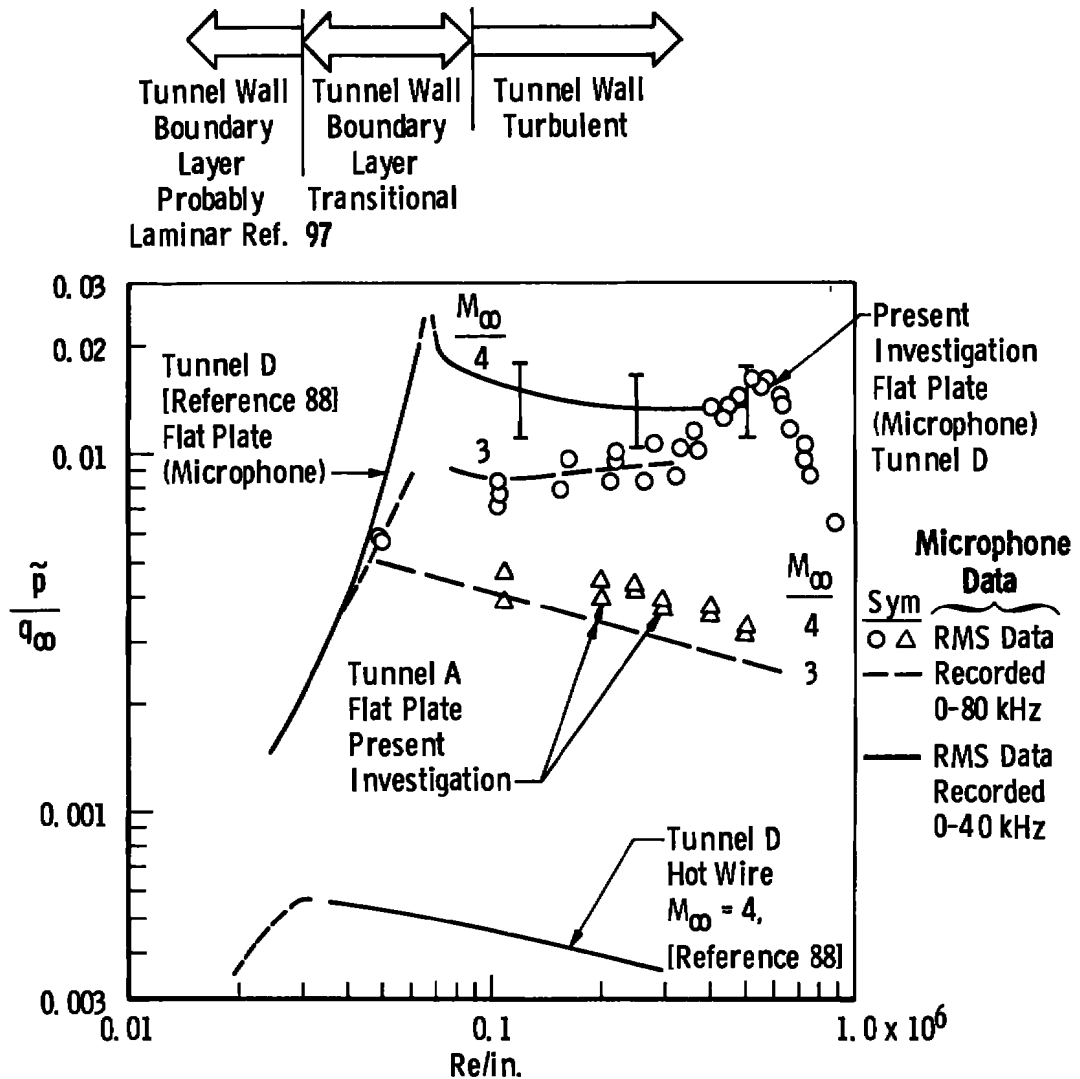
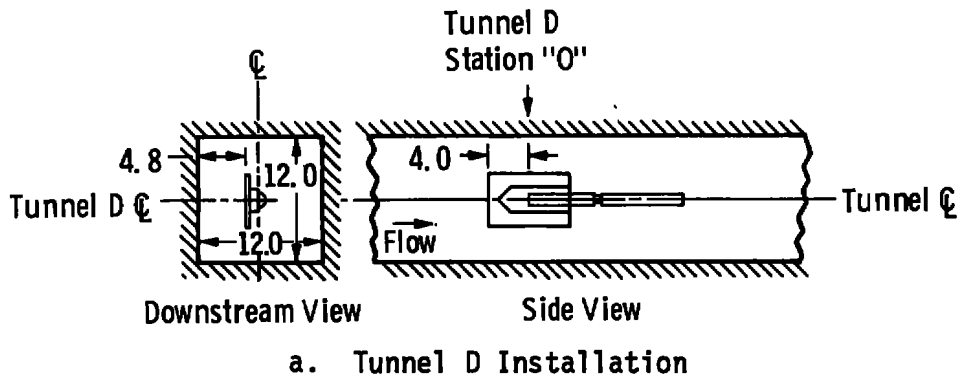


Figure VIII-16. Free-stream pressure fluctuation measurements, AEDC-VKF Tunnels A and D.

3. The microphone  $\tilde{p}/q_\infty$  measurements in Tunnel D were significantly higher than the free-stream hot-wire data. These results are as expected, if the findings of Kendall (74) are considered. Using a hot wire, Kendall found that the free-stream disturbance ( $\tilde{p}$ ) was amplified by the laminar boundary layer on a flat plate by as much as a factor of one to two orders of magnitude, as previously shown in Figure III-8, page 64. The data presented in Figure VIII-16 are consistent with the results of Kendall.

The most significant result obtained from Figure VIII-16 is that the Tunnel D  $\tilde{p}/q_\infty$  data are significantly higher than the Tunnel A data. Referring back to Figure VII-4, page 172, it is noted that the Tunnel D  $Re_t$  data are significantly lower than the Tunnel A data. These results are in agreement with the aerodynamic noise theory, i.e., the higher the noise intensity, the lower the transition Reynolds number.

Power spectral density plots as measured in Tunnel D by Donaldson and Wallace (88) are shown in Figures VIII-17 and VIII-18. The peak at 45 kHz evident in Figure VIII-17 is the microphone resonance frequency. Donaldson and Wallace concluded that the other peaks must be mechanically introduced by the microphone or mounting system since no such peaks appeared in the free-stream hot-wire data.

Recent data published by Beckwith (28) supports the assumption that a microphone mounted on the surface of a model will measure significantly higher pressure fluctuation intensities than a hot-wire or flush-mounted microphone-pitot tube positioned in the free stream at certain

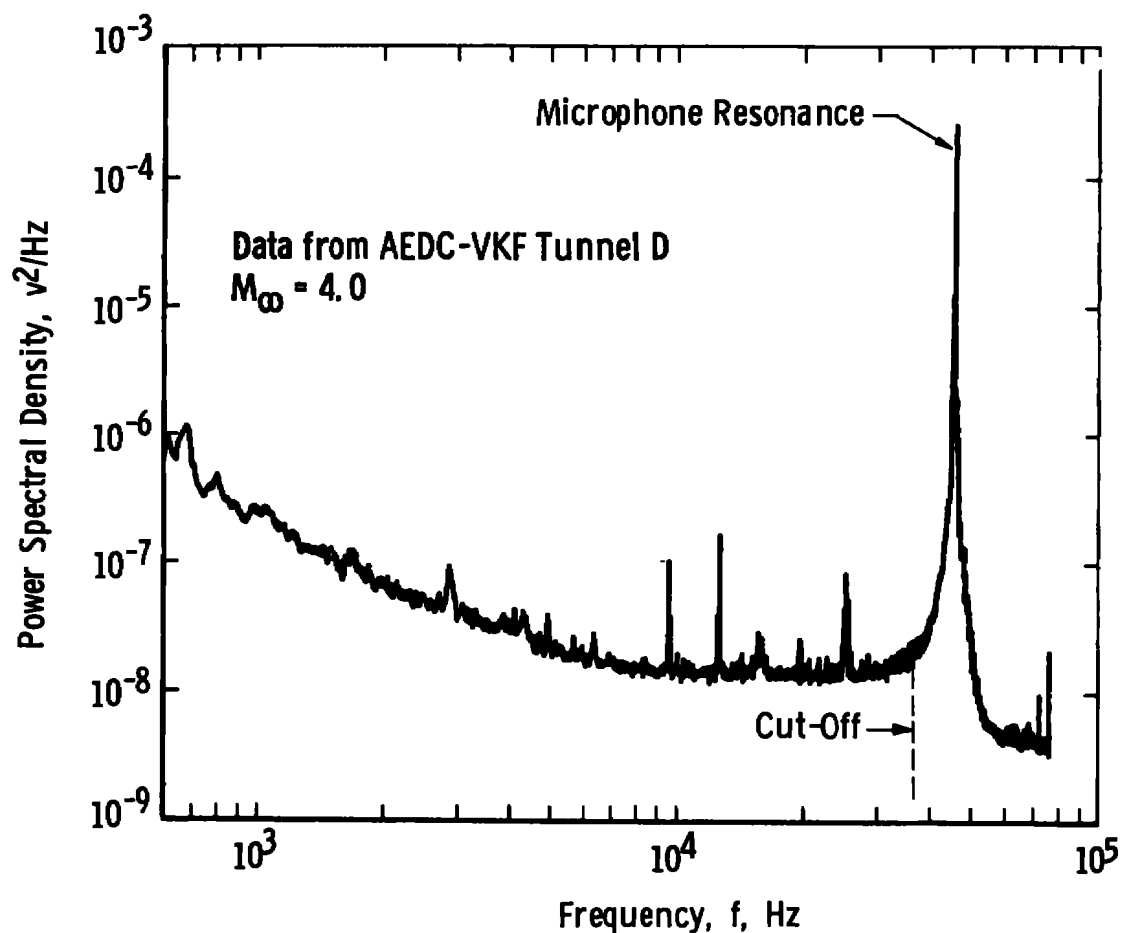


Figure VIII-17. Power spectral density analysis of microphone output recorded at  $Re/in. = 0.24 \times 10^6$  [from Reference (88)].

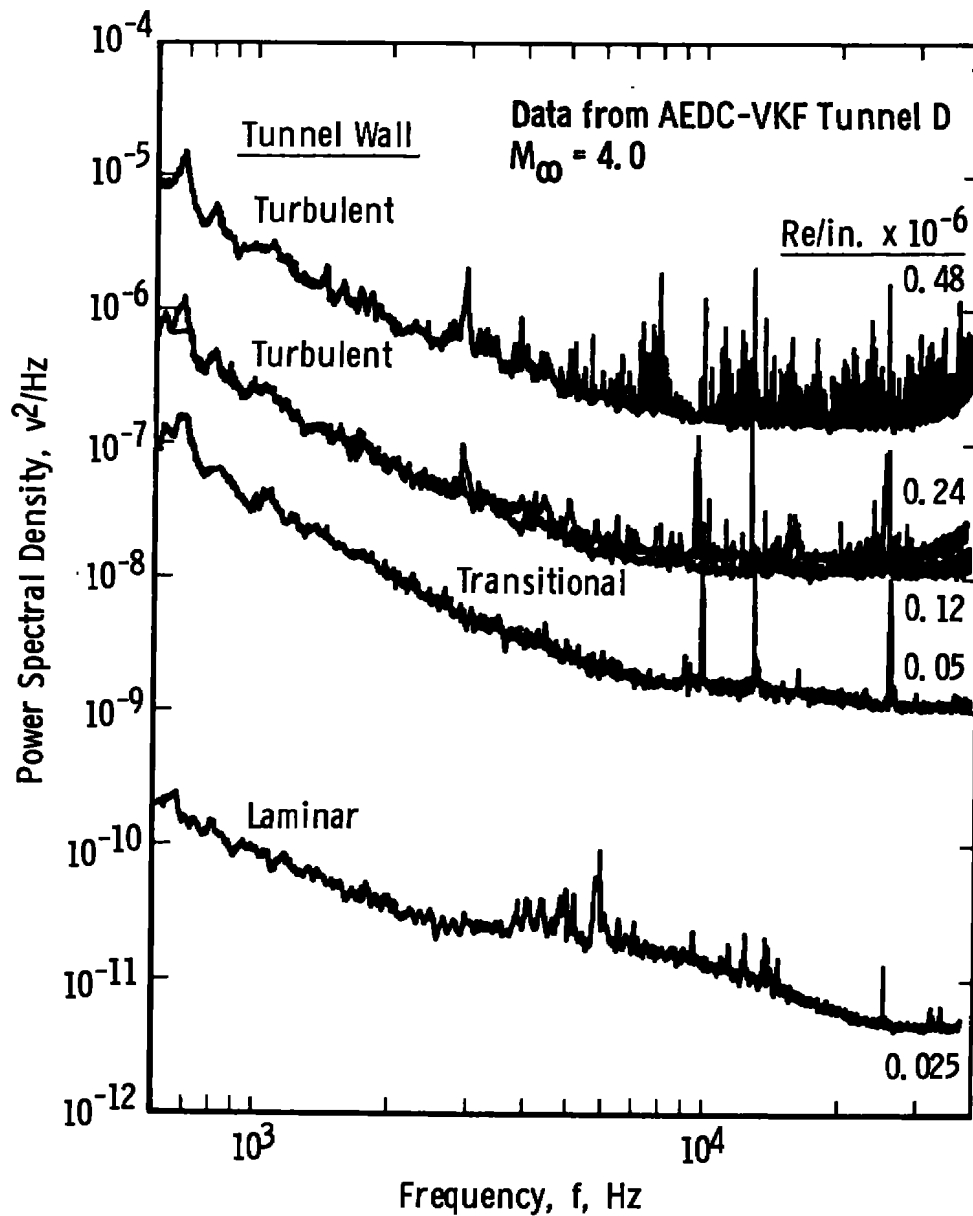


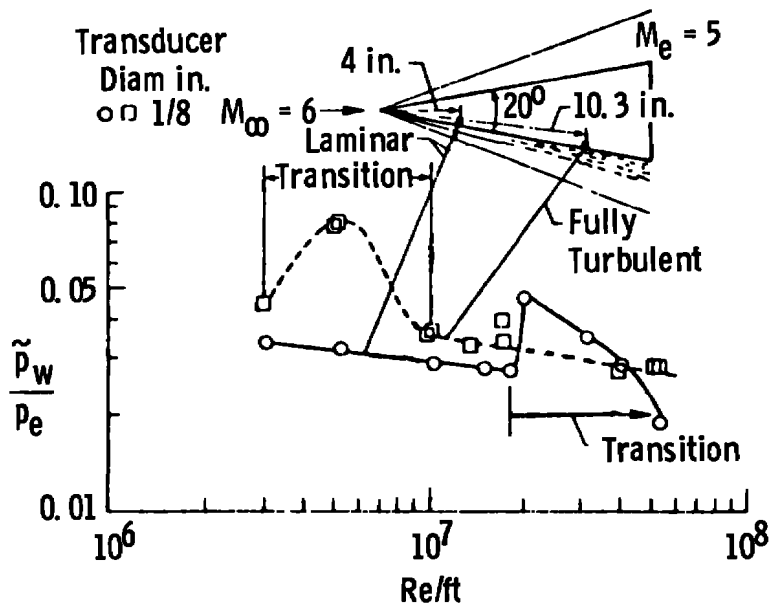
Figure VIII-18. Comparison of power spectra of microphone output for various unit Reynolds numbers [from Reference (88)].

supersonic-hypersonic Mach numbers. Presented in Figure VIII-19 are Beckwith's data taken from Reference (28). There are two significant factors to note:

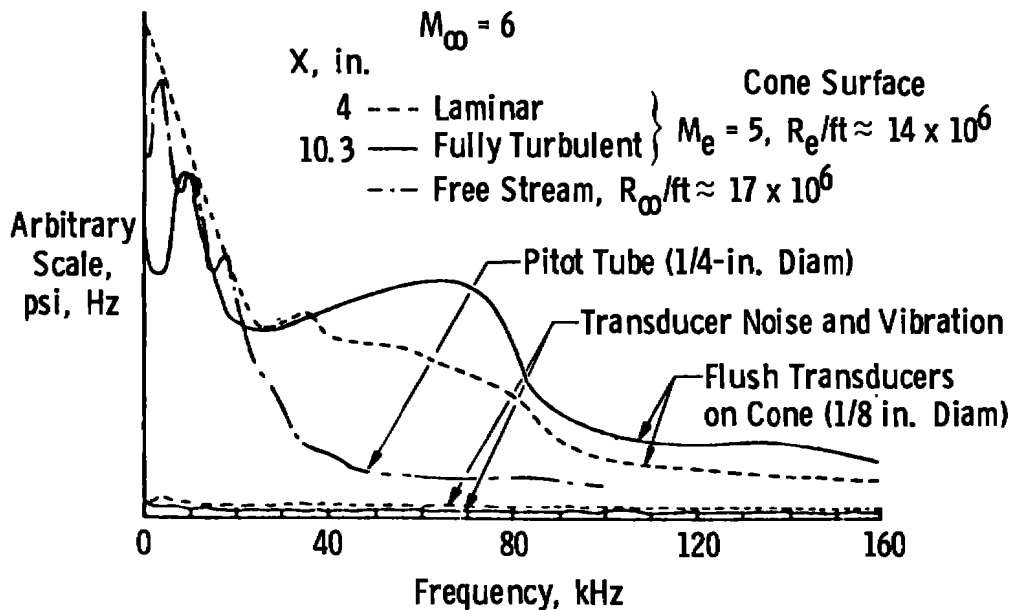
1. Pressure-fluctuating rms levels measured on the surface of a model may not be strongly dependent on the model boundary layer provided the model boundary layer is fully turbulent or fully laminar, as shown in Figure VIII-19a. This conclusion was also reached by Dougherty (52) for low supersonic and transonic test conditions.
2. The model microphones measured a significantly higher pressure fluctuation intensity, Figure VIII-19b. This result supports statement three above. Beckwith also concluded that the amplification of the free-stream radiated noise by the laminar boundary layer as reported by Mack (73) and Kendall (74) might be the reason.

A recent paper by Bergstrom (59) compared wind tunnel free-stream disturbance measurements from several sources and commented on the large scatter in the data. The data used for the comparison included free-stream hot-wire and model surface microphone data. Bergstrom noted that the model surface microphone data were significantly higher than the hot-wire data and concluded that additional studies need to be directed toward resolving this apparent discrepancy. It is proposed that a significant part of the differences in the data are the result of the free-stream radiated noise disturbance being amplified by the model laminar boundary layer and producing the higher microphone rms levels.





a. Variation of Overall RMS Pressure with Unit Reynolds Number



b. Spectra of Pressure Fluctuations with  $\Delta F = 200$  Hz

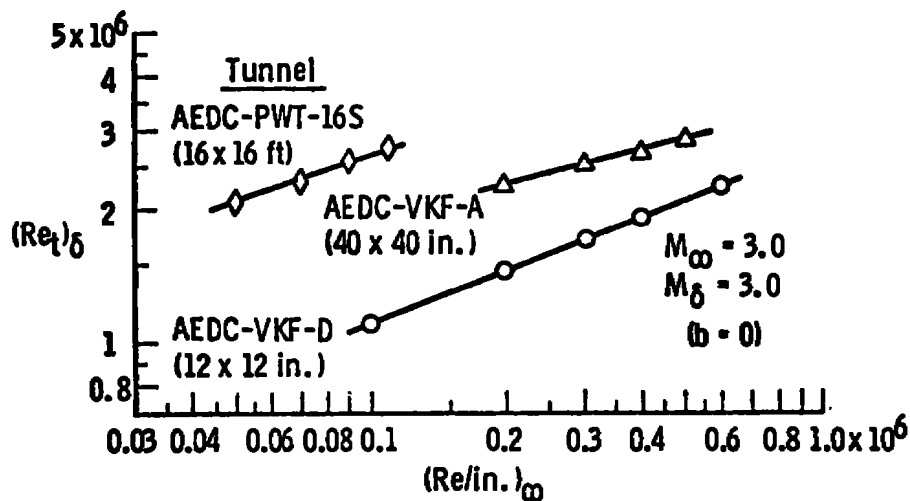
Figure VIII-19. Measurements of fluctuating pressures under laminar and turbulent boundary layers on a sharp cone in Mach 6 high Reynolds number tunnel at NASA Langley.

### III. TRANSITION MEASUREMENTS IN DIFFERENT SIZES OF AEDC SUPERSONIC TUNNELS

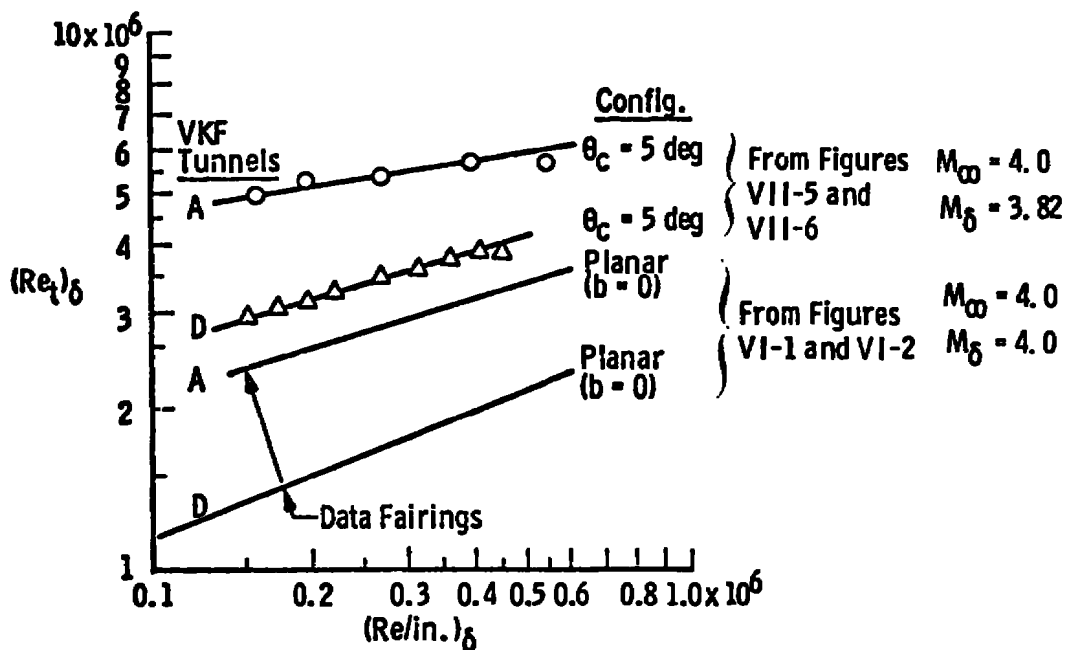
Results obtained in this research and presented in Figures VIII-13 and VIII-14 (the shroud experiments), pages 203 and 206, have provided conclusive evidence that radiated noise can dominate the transition process. The free-stream pressure fluctuation data measured in the AEDC-VKF Tunnel A (40- by 40-in. test section) and the AEDC-VKF Tunnel D (12- by 12-in. test section) presented in Figure VIII-16, page 193, have shown that higher noise levels are associated with smaller tunnels.

To verify that the transition location is dependent on tunnel size (or radiated noise levels) an extensive experimental transition program was conducted. The location of transition was measured in five different AEDC supersonic-hypersonic wind tunnels using planar (flat-plate and hollow-cylinder) and sharp-cone models as described in Chapter IV. The basic data from these studies were presented in Chapter VII.

Transition Reynolds numbers measured at  $M_\infty = 3.0$  on hollow-cylinder models in three AEDC wind tunnels having test sections ranging in size from 1 to 16 ft are presented in Figure VIII-20a. Sharp-cone transition data obtained at  $M_\infty = 4.0$  in two different sizes of AEDC wind tunnels are presented in Figure VIII-20b. The large increase in transition Reynolds numbers with increasing tunnel size is attributed to the decrease in radiated aerodynamic noise levels as discussed in Chapter III and the previous sections. The monotonic increase in transition Reynolds numbers with increasing tunnel size is illustrated in Figure VIII-21 for  $M_\infty = 3.0$ .



a. Planar (Hollow Cylinder) Model



b. Cone Model

Figure VIII-20. Variation of transition Reynolds numbers with tunnel size.

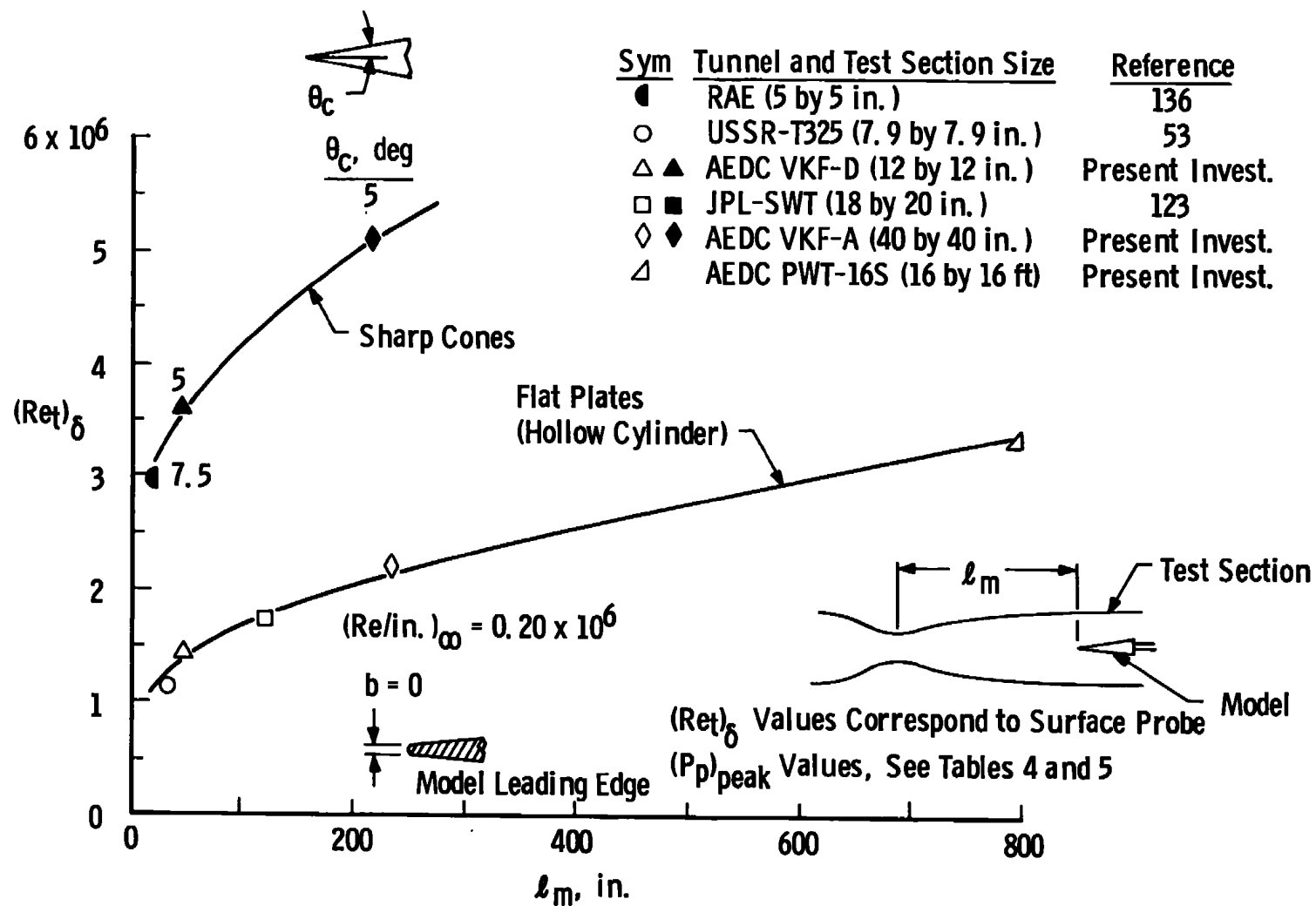


Figure VIII-21. Effect of tunnel size on transition Reynolds numbers at  $M_\infty \approx 3.0$ , flat plates and sharp cones.

The data presented in Figures VIII-20 and VIII-21 show conclusively that transition data obtained in supersonic tunnels is strongly dependent on the size of the tunnel. The increase in  $Re_t$  values with increasing tunnel size is attributed to a decrease in the radiated noise levels.

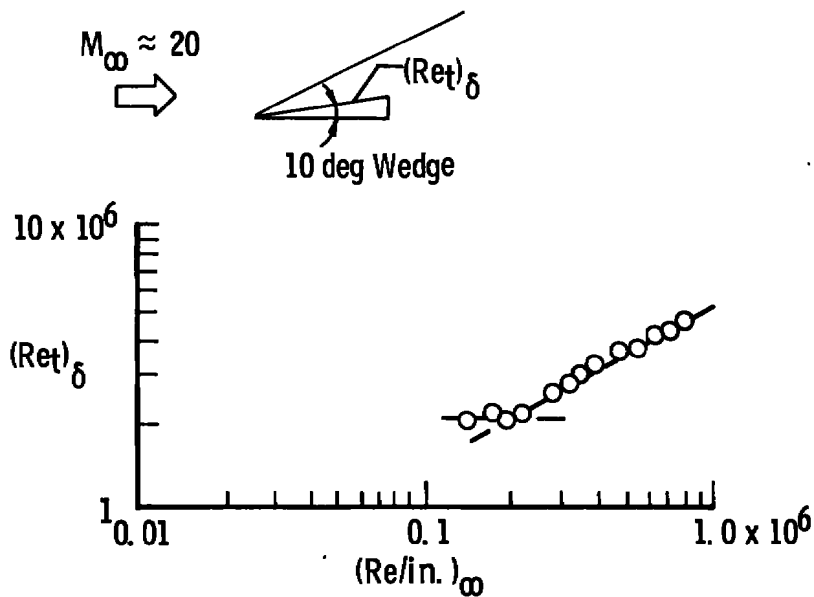
#### IV. NASA ACTIVITIES

In the late 1960's, the National Aeronautics and Space Administration (NASA) at the Langley Research Center (LRC) began a series of detailed and very extensive experimental research programs to investigate the effects of radiated pressure fluctuations on the location of boundary-layer transition on wind tunnel models. These studies were confined primarily to the hypersonic Mach number range  $5 \lesssim M_\infty \lesssim 20$  and included conventional continuous-flow and intermittent air and nitrogen tunnels as well as their  $M_\infty \approx 20$  helium tunnels. These research efforts have been underway continuously since 1969 and have progressed to the point where NASA-LRC is currently involved in defining the criteria for a "quiet" hypersonic,  $M_\infty = 5$  wind tunnel that will incorporate unique mechanical and aerodynamic design features. These features will enable a laminar boundary layer to be maintained on the tunnel walls and thereby eliminate the radiated aerodynamic noise disturbance that is now known to dominate the transition process in conventional supersonic wind tunnels.

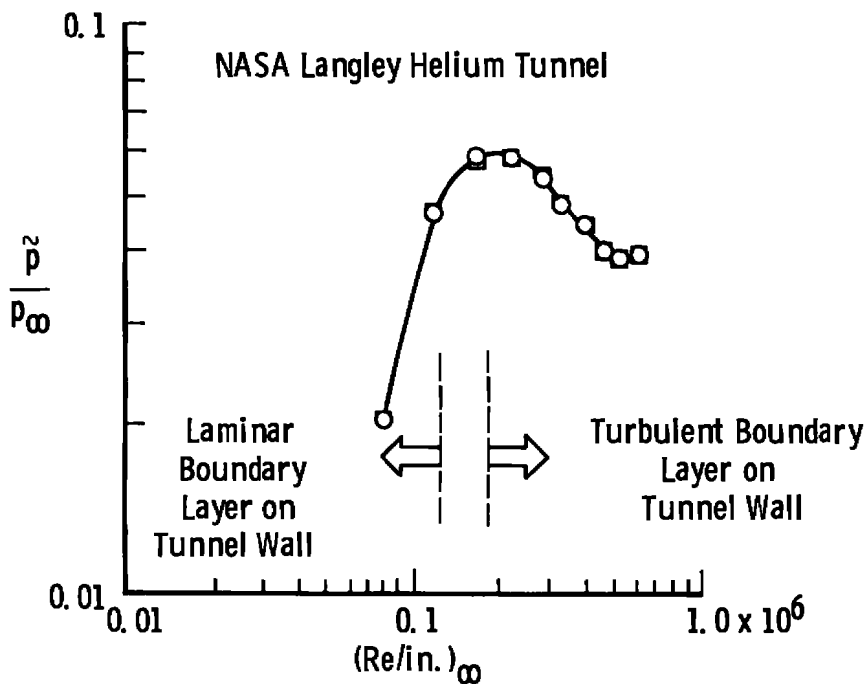
Wagner, Maddalon, and Weinstein (89) reported in 1970 on one of the most fundamental and informative of the NASA-LRC transition studies. They used a  $M_\infty = 20$  helium flow tunnel (test section diameter = 20 in.)

to investigate radiated aerodynamic noise disturbances in the tunnel free stream when the tunnel wall boundary changed from laminar to turbulent. They used a hot wire positioned in the free stream to determine the type and magnitude of the free-stream disturbances using the Kovasznay-type model diagram and the analysis developed by Laufer as discussed in Chapter III. Presented in Figure VIII-22 are the rms pressure fluctuations measured in the test section free stream (Station 139) of the  $M_\infty = 20$  helium tunnel. Note that below a unit Reynolds number of  $0.15 \times 10^6$ , there was a sharp drop in the  $\tilde{p}/p_\infty$  data, and this was the result of a laminar boundary developing on the tunnel wall (89). Boundary-layer transition Reynolds numbers were measured on a sharp-leading-edge, 10-deg inclined wedge positioned in the test section as shown in Figure VIII-22a. Included in Figure VIII-22b are the measured free-stream radiated pressure fluctuation data. Although, there were no transition data obtained below  $(Re/in.) \approx 0.15 \times 10^6$  (transition off the back of the model), it can be seen that the changes in  $Re_t$  data varied inversely with the  $\tilde{p}/q_\infty$  values. The results presented in Figure VIII-22 provide direct confirmation to the results obtained in this research and presented previously in Figures VIII-13 and VIII-14, pages 203 and 206.

The shroud results obtained in the present investigation and presented in the previous section (Figures VIII-13, page 203, and VIII-14, page 206) and the NASA studies, Figure VIII-22, have produced essentially the same results using completely independent methods. The NASA studies provide additional verification of the present research that was first published (10) in 1968.



a. 10-Deg Wedge Transition Reynolds Numbers



b. Free-Stream Pressure Fluctuations

Figure VIII-22. Effect of free-stream disturbances on wedge model transition,  $M_\infty \approx 20$  [from Reference (89)].

Fischer and Wagner (90) extended the NASA-LRC transition studies to include the study of transition on sharp cones and the measurement of the free-stream radiated noise levels in two helium tunnels<sup>18</sup> ( $M_\infty = 20$ , 22-in.-diam tunnel and the  $M_\infty = 18$ , 60-in.-diam tunnel). The found transition Reynolds numbers varied inversely with the measured noise levels as reported earlier in Reference (89). They also compared their  $(Re_t)_\delta$  data with the sharp-cone  $Re_t$ -noise correlation developed by Pate (11). These data are presented later in Chapter IX.

NASA personnel have attempted to correlate  $Re_t$  data directly with the measured  $\tilde{p}/q_\infty$  values and found fair correlation provided the free-stream Mach number remained constant, as illustrated by the data presented in Figure VIII-23 taken from Reference (81).

Fischer (122) conducted an experimental study of boundary-layer transition on a 10-deg half-angle sharp cone at  $M_\infty = 7$ . He compared his  $Re_t$  data with the flat-plate aerodynamic noise correlation published by Pate and Schueler (10) and found good agreement after giving consideration to the fact that sharp-cone  $Re_t$  data should be higher than flat-plate  $Re_t$  data at comparable test conditions.

Stainback (130) studied the effects of roughness and bluntness (variable entropy) on cone transition in Reynolds numbers. One major result from these studies was the finding that  $(Re_t)_\delta$  data were insensitive to Mach number variations obtained by changing the cone angle while

---

<sup>18</sup>In Appendix D, page 355, a discussion of the significant effects of using inappropriate viscosity laws when computing transition Reynolds numbers will be discussed. It is of interest to note that similar problems have occurred in helium tunnels as discussed in Reference (129).



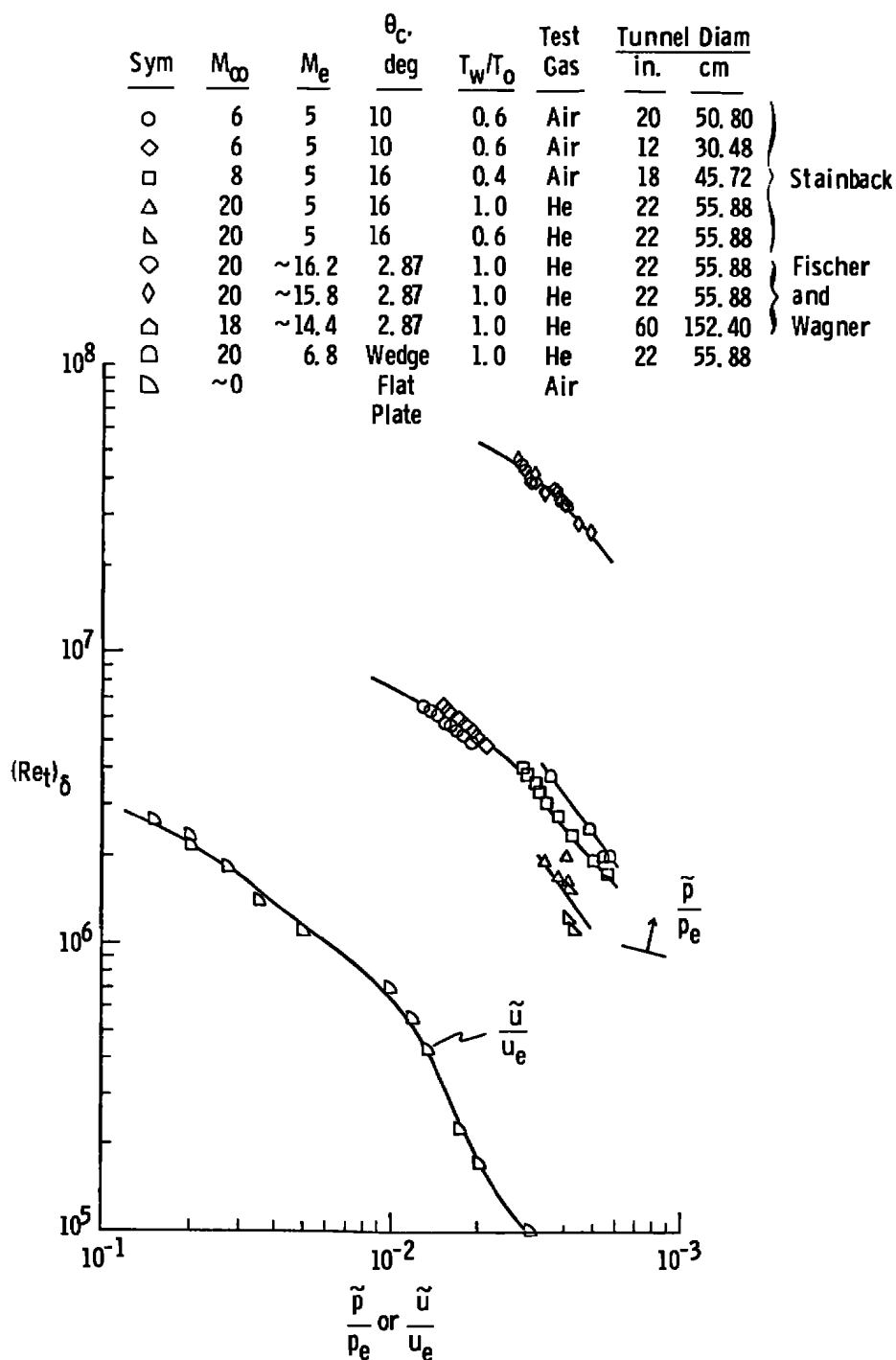


Figure VIII-23. Correlation of transition Reynolds numbers with rms disturbance levels [from Reference (81)].

maintaining a constant  $(Re/in.)_\delta$  value. These data were discussed in Reference (10) and it was pointed out that the aerodynamic-noise-dominance theory could explain this anomaly. Stainback (121) published the data as presented in Reference (10) and commented on the absence of a variation of  $(Re_t)_\delta$  with Mach number. Stainback mentioned the fact that the aerodynamic noise correlation as published in Reference (10) offered an explanation of this unusual result.

Measurements of free-stream pressure fluctuations using a pitot pressure probe instrumented with a flush-mounted transducer was investigated and reported by Stainback and Wagner (91). They also investigated the effect of changing the tunnel stilling chamber screen configurations and found a significant effect on the  $Re_t$  data measured on a 5-deg half-angle sharp cone. Also the transition data did not correlate very well with the rms pressure fluctuation levels measured with the pitot probe at  $M_\infty = 5$ .

As a result of unusual transition data reported by Mateer and Larson (131) in 1969 and because of considerable differences in the  $(Re_t)_\delta$  data measured in the NASA Ames 3.5-ft hypersonic tunnel and the NASA Langley  $M_\infty = 8$  variable density tunnel on sharp slender cones, an indepth review and remeasure of transition data in these two facilities were conducted by NASA personnel (26,132).

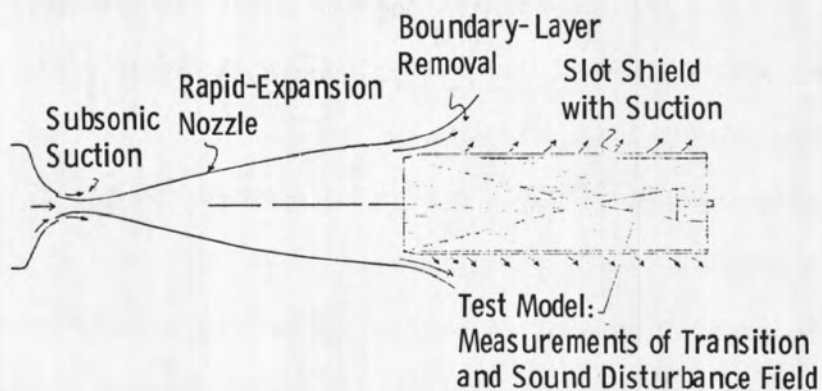
These very exhaustive studies and reviews (including sending research engineers to Ames to make measurements and vice versa) finally established that, when certain tunnel modifications were made which included heater changes at Ames and injecting air into the tunnel wall boundary layer for cooling [instead of helium as used in Reference (131)]

and making changes in upstream values and tunnel settling chamber screen design, then similar  $Re_t$  results were obtained. Similar free-stream rms pressure fluctuations were measured in each facility using flush-mounted transducers on the cone surface. However, free-stream rms pressure fluctuating data measured using the pitot probe technique (132) gave results that were about 30% different. The cone  $Re_t$  data were found to correlate with the cone surface rms data.

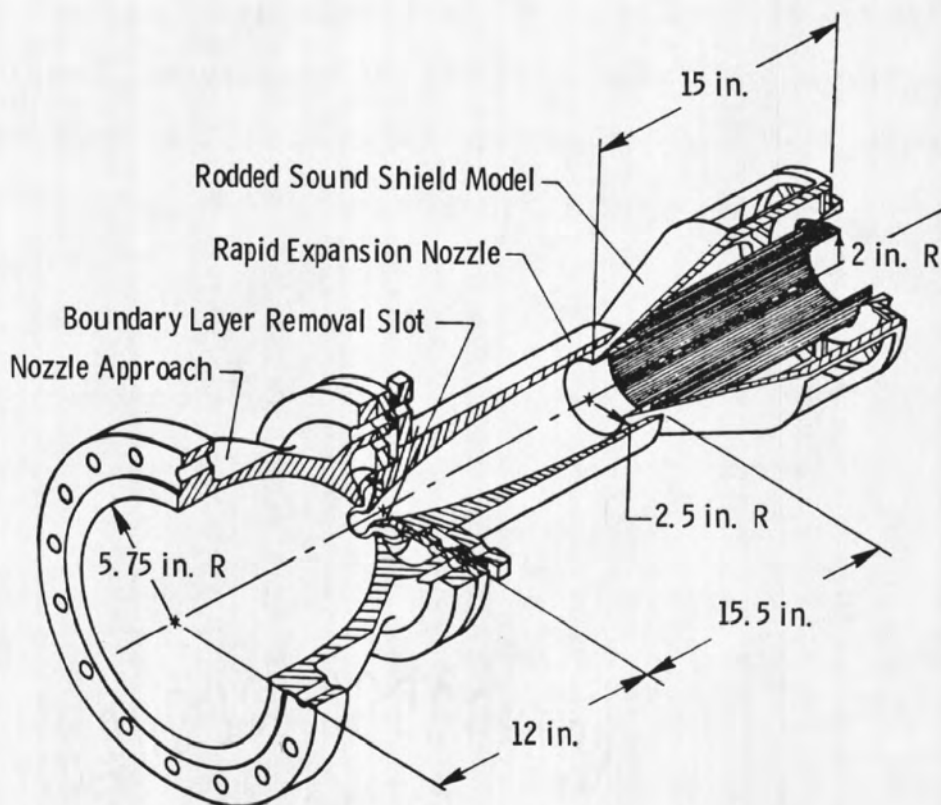
The high Reynolds number "quiet" tunnel currently being investigated by NASA-LRC is shown in Figure VIII-24 and described by Beckwith in Reference (28). Some of the basic studies conducted in support of the tunnel conceptional design have been reported by Harvey, Stainback, Anders, and Cary (29). The proposed facility will utilize a combination of unique mechanical and aerodynamic design features to try and maintain a laminar boundary layer on the tunnel interior walls as illustrated in Figure VIII-24. The objective will be to maintain a laminar boundary layer over the most of the initial conventional nozzle (29). The rod wall\*

---

\*The concept of rod wall application to supersonic wind tunnel design can be attributed to Spangenberg and Klebanoff, National Bureau of Standards, Washington, D.C. Initial work conducted at the NBS in the mid and late 1960's demonstrated the feasibility of using rod walls to maintain laminar flow on supersonic tunnel walls. This technique provided a means for eliminating "aerodynamic noise" disturbances which radiate from the turbulent boundary layer that exists on conventional solid surface walls. Fundamental research work is currently continuing at NBS under sponsorship and funding by the USAF Arnold Engineering Division (AEDC), AFSC, Arnold AFS, Tennessee.



a. Sound Shield Concept



b. Nozzle Details

Figure VIII-24. NASA-Langley  $M_\infty = 5$  quiet tunnel concept [from Reference (28)].

section shield will allow the turbulent boundary layer to bypass the test section. A pressure drop across the rod walls sound shield will then serve the two-fold purpose of maintaining a laminar flow along the inside of the rods and preventing any background noise from radiating back into the test section. Noise cannot be transmitted across the sonic line that will exist in the rod gaps.

Successful completion of the "quiet" tunnel will not only allow transition Reynolds numbers at high Reynolds number, hypersonic conditions ( $M_\infty = 5$ ) to be obtained in a "quiet" test environment, but will also provide for the first time a test condition that will allow microscopic studies and evaluation of eddy viscosity models, turbulent shear stresses, etc. in hypersonic turbulent boundary layers that are free from free-stream disturbance effects.

## V. EUROPEAN AND USSR STUDIES

LaGraff (57) reported on a series of supersonic transition studies conducted using a hollow-cylinder model. He stated that as a result of the paper by Pate and Schueler (10) a test program was initiated at Oxford University, England to further investigate the dependence of transition on facility-generated disturbances. The model was a 3-in.-diam hollow-cylinder model having a leading-edge diameter of 0.0003 in. The location of transition was measured using a sliding pitot probe adjacent to the model surface. Four research groups participated in the study as listed in Table 4 taken from Reference (57). The two sets of data that can be compared directly are the Oxford University data for  $M_\infty = 6.95$  and the Aerodynamic Research Institute of Sweden data for

Table 4. European transition test facilities [from Reference (57)].

Organization	Facility	Research Personnel	Mach No. ( $M_\infty$ )	Reynolds No. /in. $\times 10^{-5}$ ( $Re/in.$ ) $_\infty$	$T_w/T_o$	Working Section Diameter (in.)
Oxford University Dept. Eng. Science (O.U.)	Gun Tunnel	J.E. LaGraff D.L. Schultz	6.95	4.45 - 8.7	0.410	Open Jet (6.1)
Imperial College Aero Dept. (I.C.)	Gun Tunnel	A. Hunter J.L. Stollery	8.2	3.82 - 6.81	0.378	Open Jet (7.5)
Rolls Royce Bristol Engines (R.R.)	Gun Tunnel	E. Charlton R. Hawkins	7.75	3.78 - 7.10	0.369	Open Jet (11.1)
Aero Research Inst. of Sweden (F.F.A)	Hyp. 500 Blowdown Tunnel	Bo Lemcke	7.15	10.5	0.454	Open Jet (19.7)

$M_\infty = 7.15$ . These gun tunnel data are presented in Figure VIII-25 and show the effects of tunnel size similar to the findings found in the present research (see Figure VIII-20, page 216). The results presented in Figure VIII-25 provide added confirmation of the increase in  $Re_t$  with increasing tunnel size.

Ross (60) conducted an experimental transition program in two supersonic blowdown wind tunnels (Netherlands):

<u>Tunnel</u>	<u><math>M_\infty</math></u>	<u>Size, m</u>	<u>Nozzle Length, m</u>
SST	3.6	1.2 x 1.2	5.42
GSST	3.6	0.27 x 0.27	1.22

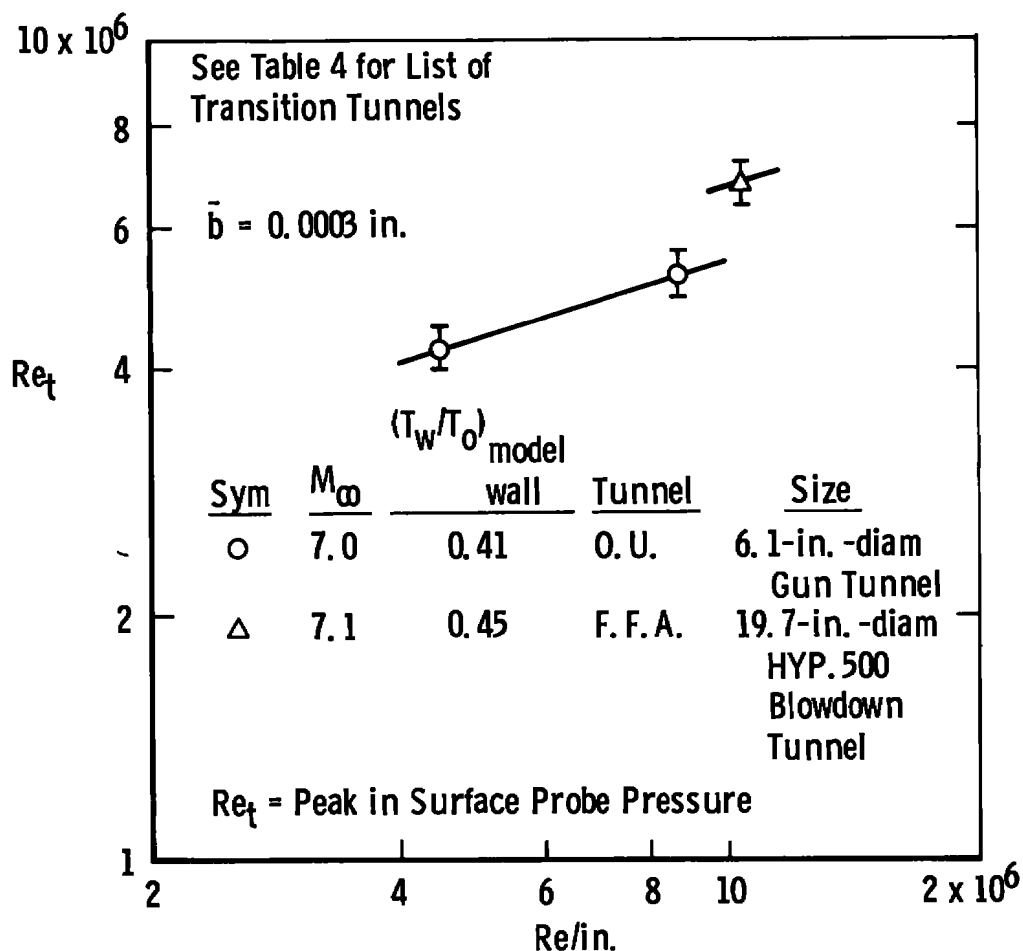


Figure VIII-25. Hollow-cylinder transition data [from Reference (57)].

The transition model was the 3-in.-diam hollow-cylinder model ( $d = 0.0003$  in.) used by LaGraff (57). The transition location was determined using a surface pitot probe. Ross found a large variation in  $Re_t$  with tunnel size as shown in Figure VIII-26. These results are in agreement with the present findings and provide independent confirmation of the strong variation of  $Re_t$  data with tunnel size.

Bergstrom, et al. (55) analyzed three sets of gun tunnel flat-plate transition data (56,57,133) in addition to his transition studies conducted at  $M_\infty = 7.0$  in the Loughborough University of Technology gun tunnel. Using the Pate-Schueler aerodynamic noise correlation (10) developed for conventional wind tunnels, he correlated gun tunnel  $Re_t$  data and concluded that transition data obtained in hypersonic gun tunnels were influenced essentially by the aerodynamic noise present in the test section. He further concluded that many of the discrepancies in gun tunnel transition data could be explained on this basis. The transition data from the four gun tunnels displayed good overall correlation with aerodynamic noise and tunnel size parameters according to the method of Pate and Schueler (10). For a given Mach number, Bergstrom et al. (55) also found that transition Reynolds numbers correlated very well against the free-stream rms pressure fluctuations ratioed to free-stream static ( $\tilde{p}_{rms}/p_\infty$ ) as calculated using the method of Williams and Maidanik (96) [Eq. (6), page 59] for a wide range of tunnel sizes.

Studies were conducted in the USSR by Struminskiy, Kharitonov, and Chernykh (53) in the early 1970's to establish if unit Reynolds number effects and tunnel size effects as reported in Reference (10) existed at higher unit Reynolds numbers at  $M_\infty = 3$  and 4. Two wind tunnels were



<u>Sym</u>	<u><math>M_\infty</math></u>	<u>Tunnel</u>	<u>Test Section Size</u>	<u><math>l_m</math>, in.</u>
○	3.6	CSST	10.6 x 10.6 in.	48
△	3.6	SST	47.2 x 47.2 in.	213

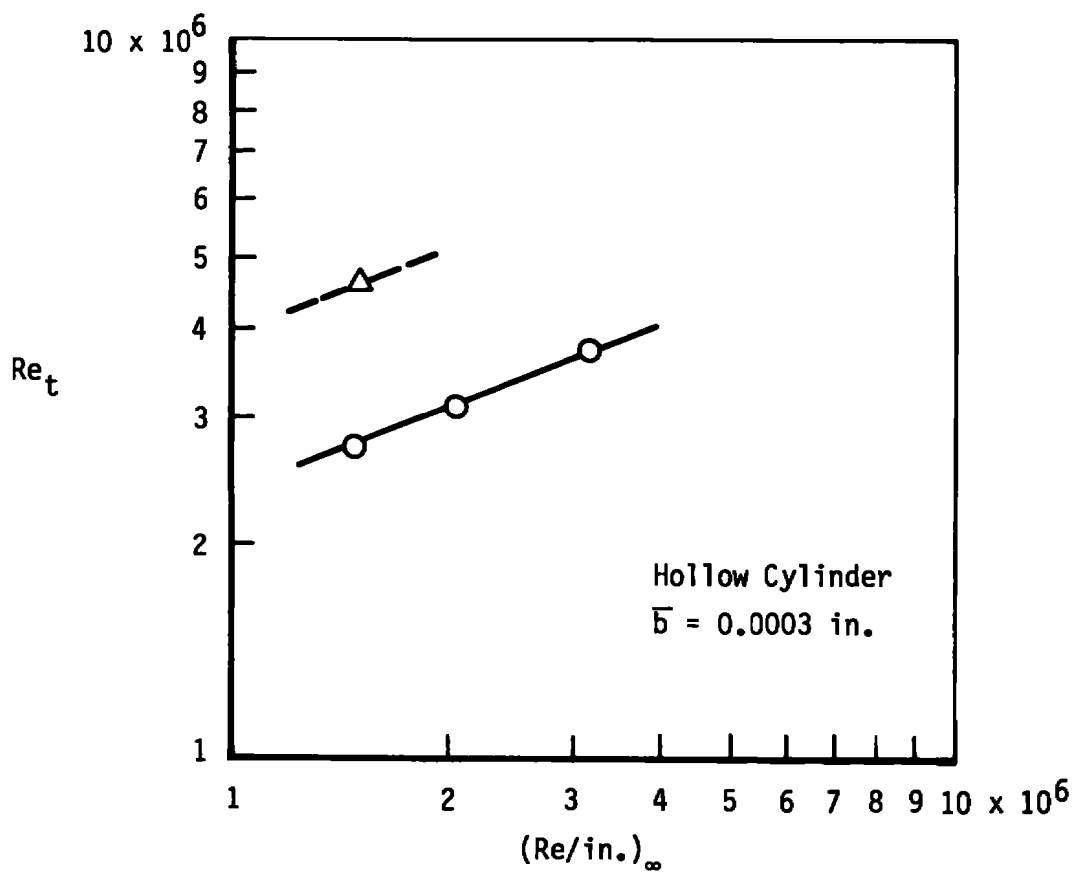


Figure VIII-26. Effect of tunnel size on  $Re_t$  data from Netherland Tunnels [from Reference (60)].

used (Tunnel T-313, 0.6 by 0.6 in. and Tunnel T-325, 0.2 in. by 0.2 in.). The test model was a sharp flat plate having a surface finish of 2  $\mu\text{m}$  and positioned at zero angle of attack. Transition locations were determined using the surface pitot probe technique. Values of  $Re_t$  for an effective zero leading-edge bluntness was obtained by extrapolation (see Section VI). Presented in Figure VIII-27 are the basic transition data from Reference (53). An attempt was made in Reference (53) to correlate the  $Re_t$  data for a given Mach number using a Reynolds number based on the test section diameter. For the  $M_\infty = 3$  data, fair agreement was obtained by correlating  $Re_t$  with  $Re_{\infty, D}$ .

In 1975 Kharitonov and Chernykh (54) extended their research to include pressure fluctuation measurements on the walls of Tunnels T-325 and T-313 at  $M_\infty = 3$  and 4. Their studies established a change in  $Re_t$  levels with a change in acoustic levels. They concluded that the change in  $Re_t$  with a change in unit Reynolds number ( $\text{Re/in.}$ ) was the result of the acoustic perturbations (aerodynamic noise) present in the test section. They reasoned that the scale of turbulence was related to the tunnel wall turbulent boundary-layer displacement thickness. Using a theory proposed by Taylor (134) that related  $Re_t$  to the intensity ( $\tilde{u}/u$ ), the scale of turbulence ( $\ell = \delta^*$ ), and a characteristic length ( $L = d$ ), they obtained a correlation of  $Re_t = F[(\tilde{u}/u)(L/\ell)^{1/n}]$  for  $n = 0.25$  and  $M_\infty = 2.5$  to 6. The scatter for flat-plate transition data obtained in six wind tunnels was  $\pm 15\%$ . They included data from AEDC-Tunnels VKF A and D and AEDC-PWT Tunnel 16S as taken from Reference (10). They concluded that by correlating the experimental transition Reynolds numbers with the tunnel wall boundary-layer characteristics then it was possible to explain the nature of the unit Reynolds number effect in conventional wind tunnels.

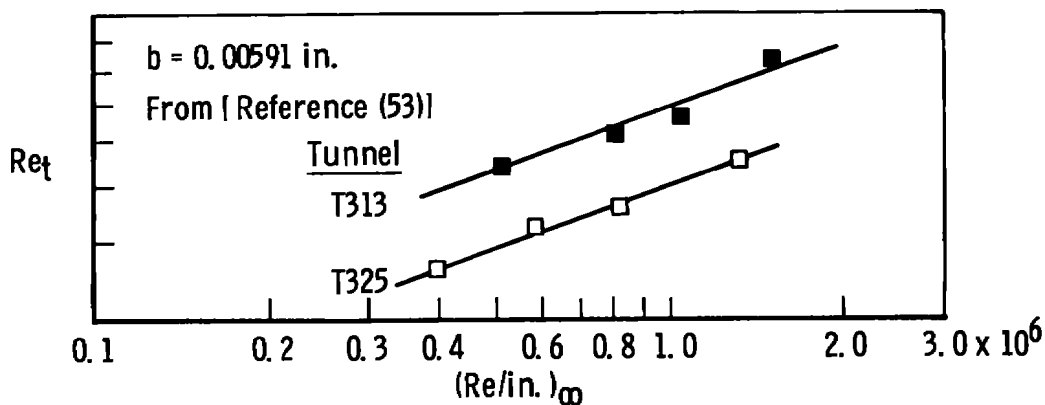
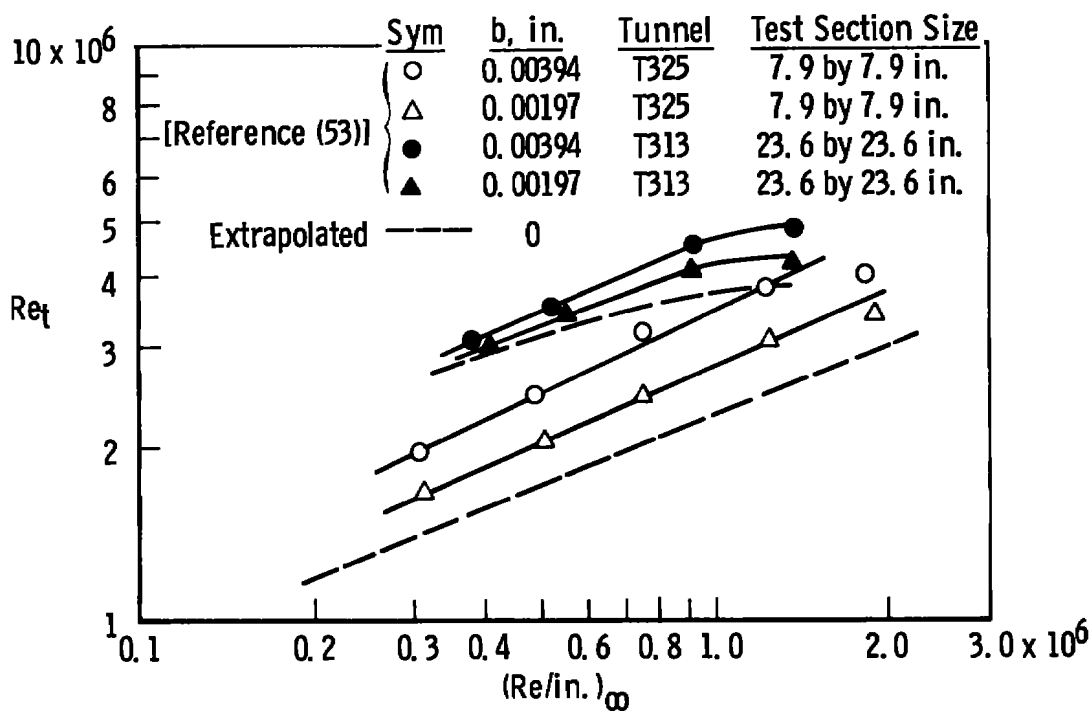
a.  $M_\infty = 4.0$ b.  $M_\infty = 3.0$ 

Figure VIII-27. Effect of tunnel size on flat-plate transition Reynolds numbers - USSR studies.

## CHAPTER IX

DEVELOPMENT OF AN AERODYNAMIC-NOISE-TRANSITION CORRELATION  
FOR PLANAR AND SHARP-CONE MODELS

Theoretical and experimental studies contributing to the basic understanding of the radiated pressure field (aerodynamic noise) generated by a turbulent boundary layer were reviewed in Chapter III. Results were presented which identified the tunnel wall turbulent boundary layer mean shear and displacement thickness as major parameters influencing the radiated pressure fluctuations ( $\tilde{p}/q_\infty$ ).

The experimental results obtained in this research using the long shroud apparatus (Chapter VIII) demonstrated that aerodynamic noise could have a dominating effect on the location of transition. The shroud experiments demonstrated, conclusively, that the radiated noise dominated the transition process on models with simple geometry such as flat-plate and slender sharp-cone models in supersonic-hypersonic wind tunnels ( $M_\infty \gtrsim 3$ ). The shroud experiments also showed that  $Re_t$  data could be correlated directly with rms pressure fluctuations.

Subsequent studies by NASA-LRC at  $M_\infty = 20$  have provided independent confirmation of the dominance of radiated noise on transition and that  $Re_t$  data can be correlated with radiated noise intensities, i.e.,  $\tilde{p}/q_\infty$  data. Attempts at correlating  $Re_t$  data directly with measured  $\tilde{p}/q_\infty$  data are still hampered by inconsistencies in the measured  $\tilde{p}/q_\infty$  data. Experimental scatter (nonrepeatable) in pressure fluctuation data was illustrated in Figure VIII-13, page 203, of the present research. References (28) and (132) provide additional information on differences in

measured  $\tilde{p}/q_\infty$  data. There are also basic differences in the absolute levels of intensity measured using a flat plate equipped with microphones and hot-wire anemometers positioned in the free stream as discussed in Chapter VIII.

During the initial efforts of the present research the only wind tunnel free-stream pressure fluctuation data available before about 1970 were the data of Laufer (1960) published in Reference (38). Since transition data from many different wind tunnels existed at the beginning of this research and essentially no pressure fluctuation data existed (except Laufer's), an effort was made to correlate  $Re_t$  data with the parameters that could be identified as related to the radiated aerodynamic noise intensity, i.e., the tunnel wall shear stress, displacement thickness and a characteristic length.

From Figure III-4, page 57, one sees that

$$\tilde{p}/\tau_w = f(M) \approx \text{constant}$$

since

$$C_f = \frac{\tau_w}{\frac{1}{2} \rho_\infty U_\infty^2} = \frac{\tau_w}{q_\infty}$$

then

$$\frac{\tilde{p}}{q_\infty} = f(M_\infty, C_f)$$

From Reference (135) one knows that for turbulent flow

$$C_F \approx 1.2 C_f$$

Then

$$\frac{\tilde{p}}{q_w} = f(C_F, M_\infty) \quad (8a)$$

From Figure III-3, page 71,

$$\frac{\tilde{p}}{p_\infty} \sim \delta^* \left( \frac{1}{\text{length scale}} \right) \sim \frac{\delta^*}{\ell} \quad (8b)$$

Since

$$q_\infty = \frac{\gamma}{2} p_\infty M_\infty^2$$

then

$$\frac{\tilde{p}}{q_\infty} \sim M_\infty^2 \frac{\delta^*}{\ell} ;$$

Combining Eqs. (8a) and (8b), one obtains the functional relationship

$$\frac{\tilde{p}}{q_\infty} = f(M, C_F, \delta^*, \ell) \quad (8c)$$

Assuming

$$Re_t = f\left(\frac{\tilde{p}}{q_\infty}\right)$$

Then one has

$$Re_t = f(M_\infty, C_F, \delta^*, \ell) \quad (8d)$$

The use of  $\delta^*$  as a correlating parameter in an aerodynamic-noise-transition correlation is not only suggested by Figure III-3, page 71, but also from physical reasoning. Weak (isentropic) waves can be related to a supersonic wavy wall analogy where the turbulence eddies "globs" that create the turbulence are related to the boundary thickness (or displacement thickness) as discussed in References (87), (93), (94), and (96). It is also reasoned that  $\delta^*$  could enter into the correlation because of a frequency dependency related to the physical size, i.e., scale effects as shown in Figure V-15, page 140, where  $\delta^*$  appears in the frequency correlating parameter (Strouhal number).

Attempts were made to correlate  $Re_t$  data directly with  $C_F$ , but these efforts were unsuccessful. If a plot of  $Re_t$  versus  $C_F$  were made, it would be shown that the Mach number and tunnel size would appear as additional parameters.

Presented in Figure IX-1 is a successful correlation of  $Re_t \sqrt{\delta^*/C}$  as a function of the tunnel wall mean skin-friction coefficient ( $C_{F1}$ ) with the tunnel size appearing as a parameter. This correlation evolved from a series of trial and error efforts and was first published in Reference (10). The data included in Figure IX-1 represent sharp-flat-plate and hollow-cylinder model transition data obtained in nine wind tunnels covering a Mach number range from 3 to 8, unit Reynolds number per inch range from  $0.05 \times 10^6$  to  $1.1 \times 10^6$ , and tunnel test section sizes from 1.0 to 16 ft.

Values of the transition Reynolds number used in the correlations correspond to the transition location determined from the peak in the surface pitot probe pressure trace and are for a zero bluntness leading-edge thickness. Transition data from other sources which were not obtained using a pitot probe were adjusted as listed in Table 5, page 234, as determined from Figure VI-12, page 165. The zero bluntness  $Re_t$  data were obtained by extrapolating the transition values from sharp, but finite, leading-edge models (see Chapter VI) to  $b = 0$ . It is desirable to correlate  $Re_t$  data for  $b = 0$  since this in effect removes any model leading-edge geometric influences.

It is seen from Figure IX-1 that Mach number does not appear as a parameter. Also, the systematic variation with the tunnel size

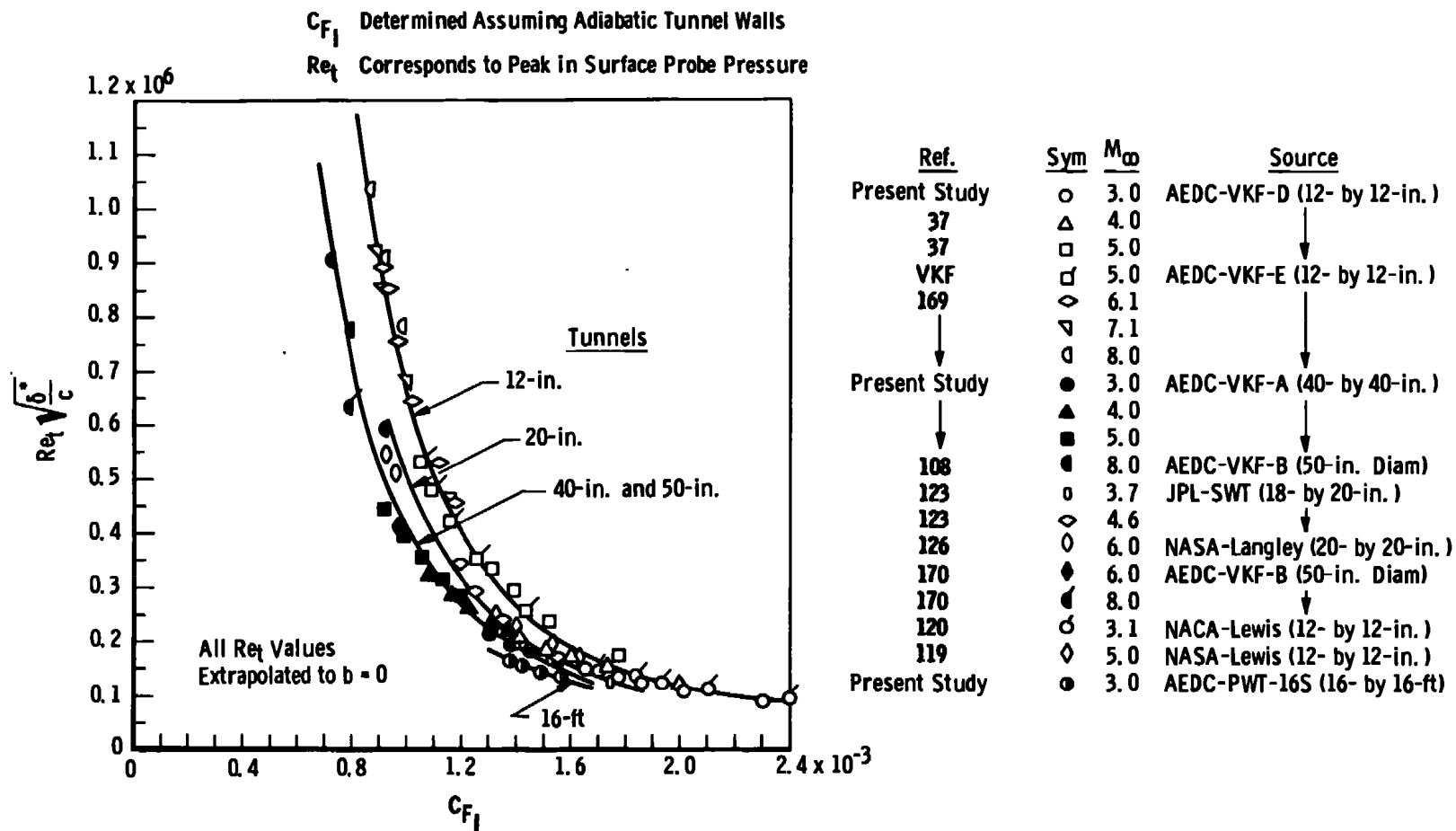


Figure IX-1. Influence of tunnel size on the boundary-layer transition Reynolds number correlation [from Reference (10)].



suggests that the data can be collapsed into a single curve if the tunnel test section size is incorporated into the correlation as a normalizing parameter.

The normalizing parameter

$$Re_t \sqrt{\frac{\delta^*}{C}} / \left( Re_t \sqrt{\frac{\delta^*}{C}} \right)_{C_1=48 \text{ in.}}$$

is a function of the tunnel test section circumference as shown in Figure IX-2. A linear fairing of these data provides a method for collapsing all of the  $Re_t$  data presented in Figure IX-1 onto a single correlation curve, as shown in Figure IX-3.

The empirical equation presented in Figure IX-3 for sharp flat plates was modified by Ross (58) into a simple analytical expression. Defining  $C_F = (d)(Re_{\ell_m})^e$  where  $d = 0.0276 M_\infty^{0.22}$  and  $e = -0.146 - 0.011 M_\infty$  and  $\delta^* = (0.0194)(M_\infty)(\ell_m)(Re_{\ell_m})^{-1/7}$ , Ross expressed Eq. (1) in Figure IX-3 as

$$Re_t = \frac{1006}{(M_\infty)^{1.06}} \left[ 0.56 + 0.44 \frac{C_1}{C} \right] \sqrt{C} (\ell_m)^{0.028 M_\infty - 0.057} (Re/m)^{0.443 + 0.028 M_\infty} \quad (9)$$

Equation (8) gives reasonable results over the Mach number range  $3 \leq M_\infty \lesssim 6$  for adiabatic wall wind tunnel and adiabatic wall models.

A similar correlation for sharp slender cones has also been developed. The initial correlation of cone  $Re_t$  data obtained using the planar correlation parameters is presented in Figure IX-4. Although the sharp-cone data correlated fairly well using the planar correlating parameters, the correlation exhibited two systematic inconsistencies. First, the slope of a linear fairing of the data is somewhat steeper than

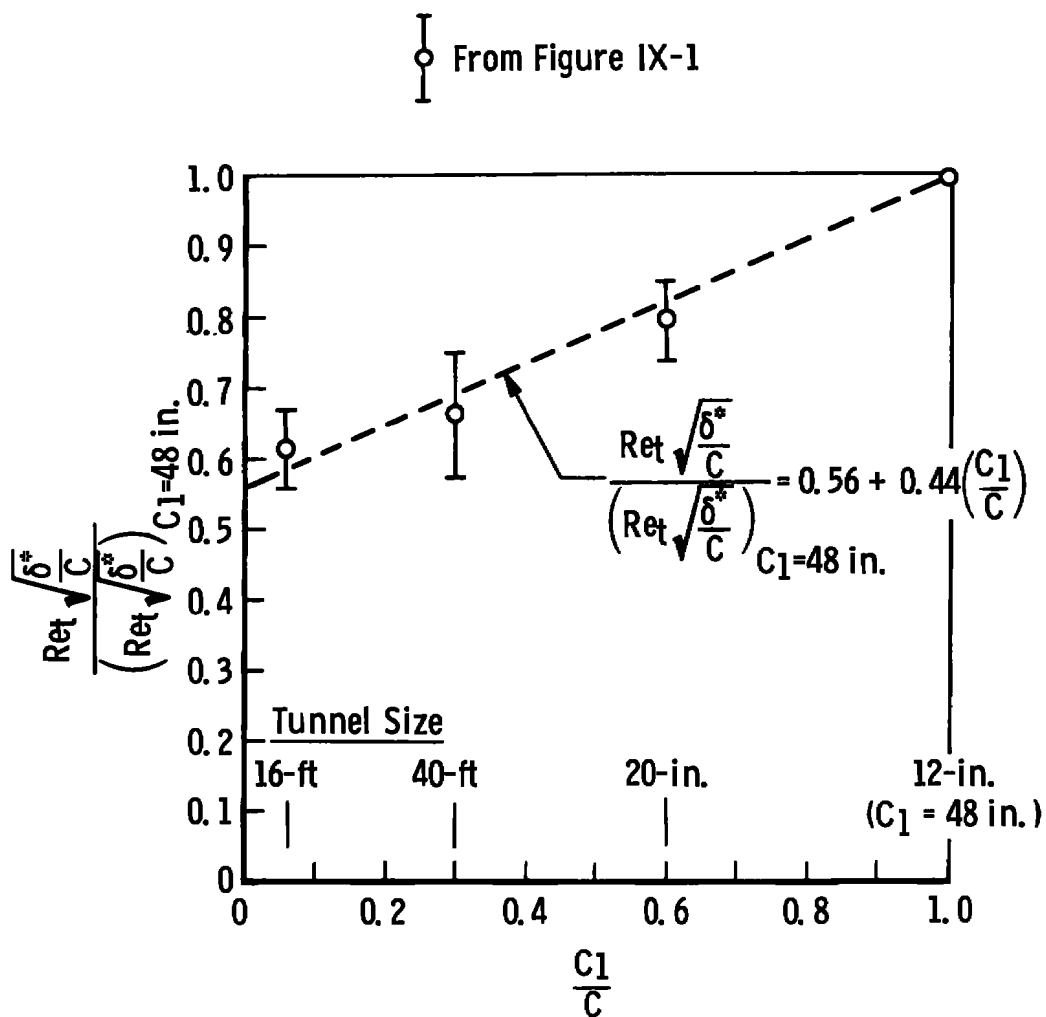


Figure IX-2. Tunnel size parameter.

$$\text{Eq. (A) from Ref. 10, } Re_t = \frac{0.0141 C_F^{-2.55} (0.56 + 0.44 C_1/C)}{\sqrt{\delta^*/C}}$$

Based on data from Nine Facilities varying in size from 1 to 16 ft, Mach number range from 3 to 8 and  $(Re/ft)_\infty$  range from  $0.6 \times 10^6$  to  $13.2 \times 10^6$ .

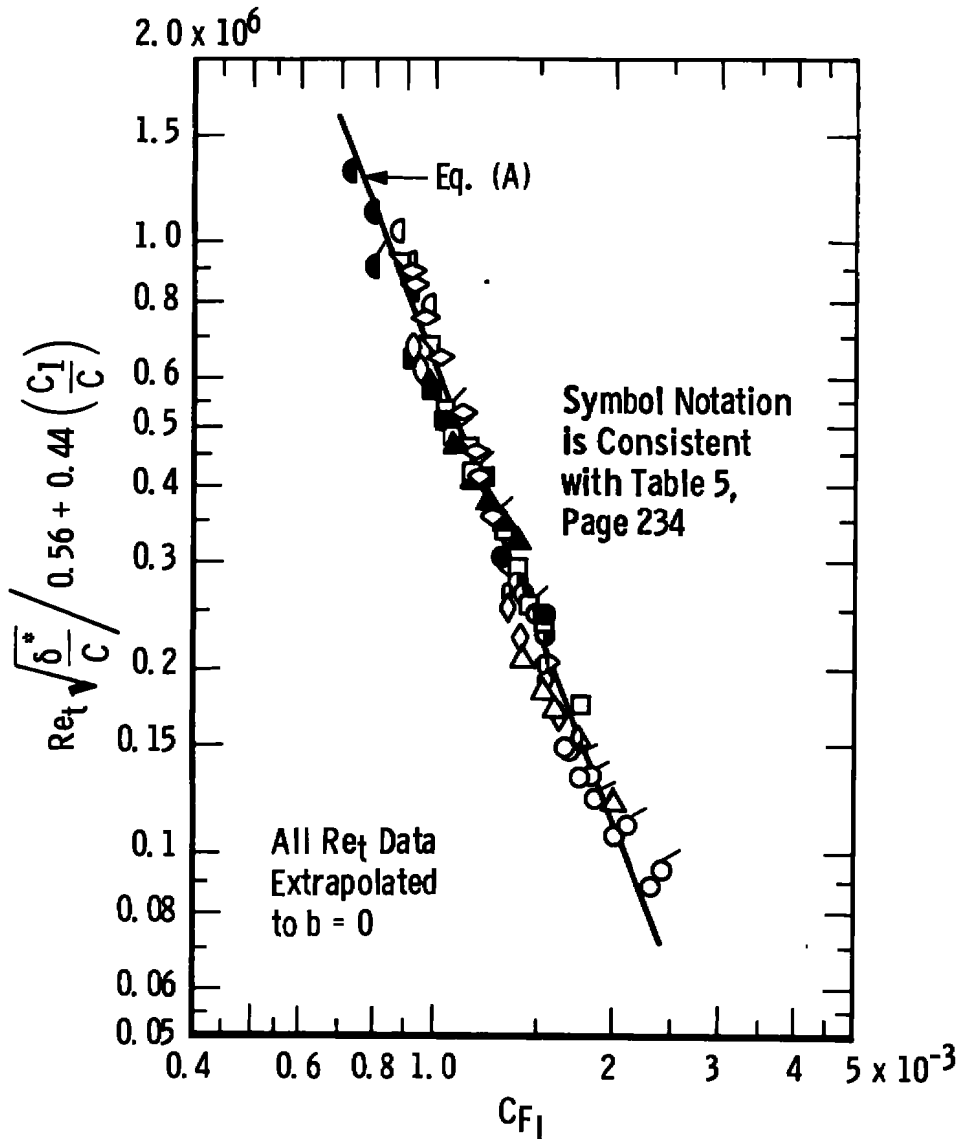


Figure IX-3. Initial correlation of transition Reynolds numbers on sharp flat plates with aerodynamic noise parameters [from Reference (10)].

Planar Data Consistent with Data Presented in Figure IX-3  
 Sharp-Cone Data from Eleven Facilities Varying in Size  
 from 1 to 4.5 ft in Test Section Diameter. Mach Number  
 Range from 3 to 14, and  $(Re/ft)_\infty$  Range from  $1.2 \times 10^6$   
 to  $14.4 \times 10^6$

Symbol Notation for Cone Data is Consistent with Table III  
 in Reference 11.

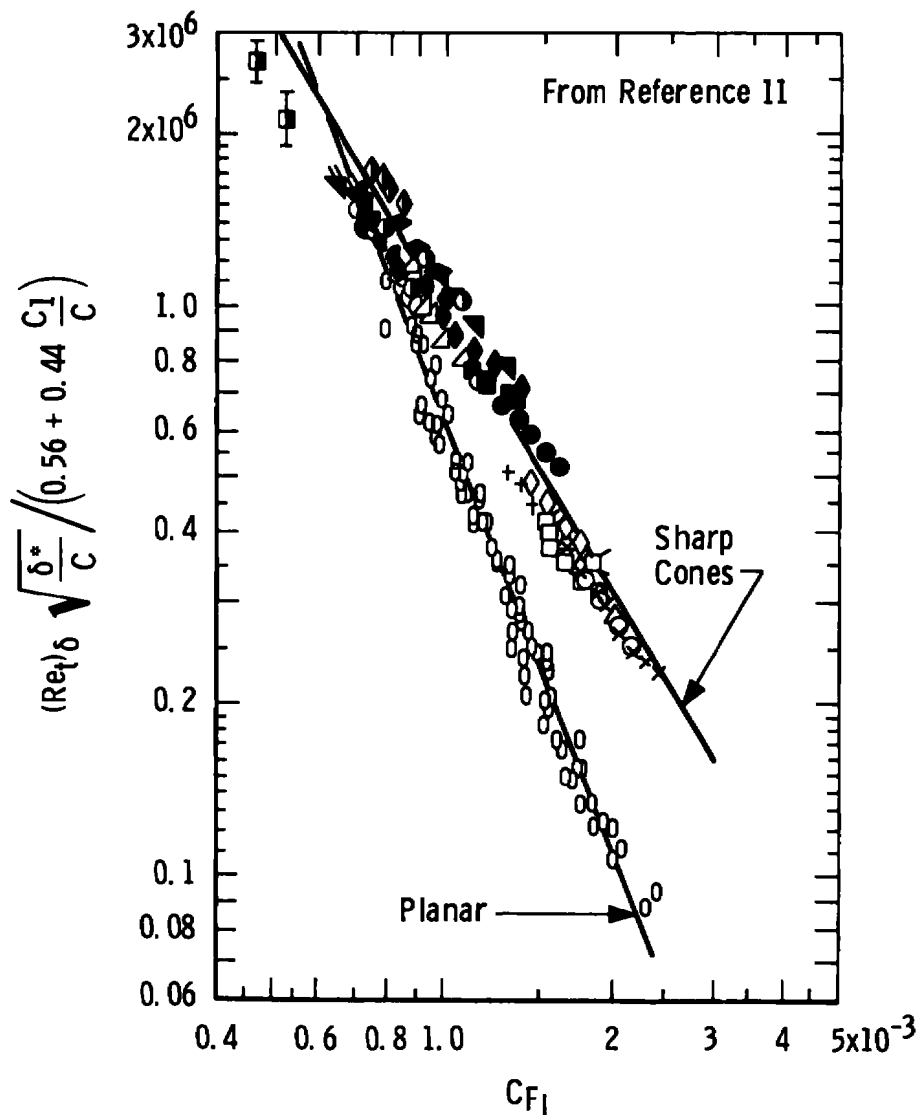


Figure IX-4. Initial correlations of planar and sharp-cone transition Reynolds numbers [from Reference (11)].

the slopes of most of the individual data sets. Second, the data from the larger tunnels show a systematic grouping somewhat higher than the smaller tunnels. Systematic differences of this type and magnitude were not apparent in the correlation of the planar data. These two inconsistencies were eliminated by establishing a different tunnel size normalizing parameter for the sharp-cone data. A plot similar to Figure IX-1, page 221, was made for the sharp-cone data. The new normalizing parameter for sharp slender cones was determined to be  $0.8 + 0.2 (C_1/C)$  for  $C_1/C < 1.0$  as shown in Figure IX-5.

Presented in Figure IX-6 is the correlation of the cone  $(Re_t)_\delta$  data using the slender-cone normalizing parameter. A significantly improved correlation of the data was accomplished.

One factor that must be recognized in the correlation of cone data is the absence of a one-to-one relationship or even a constant ratio between the free-stream and cone surface unit Reynolds number (see Appendix D, page 373). If a series of cone angles had been selected that would have allowed a constant ratio of certain cone to free-stream parameters -- say, the unit Reynolds number ratio to have been maintained -- then any relationship that might have existed between the strength of the cone bow shock wave and the influence of the radiated noise levels on the cone laminar flow after passage through the bow shock might possibly have remained more constant. Future investigation in these areas would, of course, be desirable.

Since the correlation only included  $(Re_t)_\delta$  from sharp slender cones ( $\theta_c \leq 10$  deg), caution should be exercised when using the correlation to predict transition locations on large angle cones with a strong bow shock.

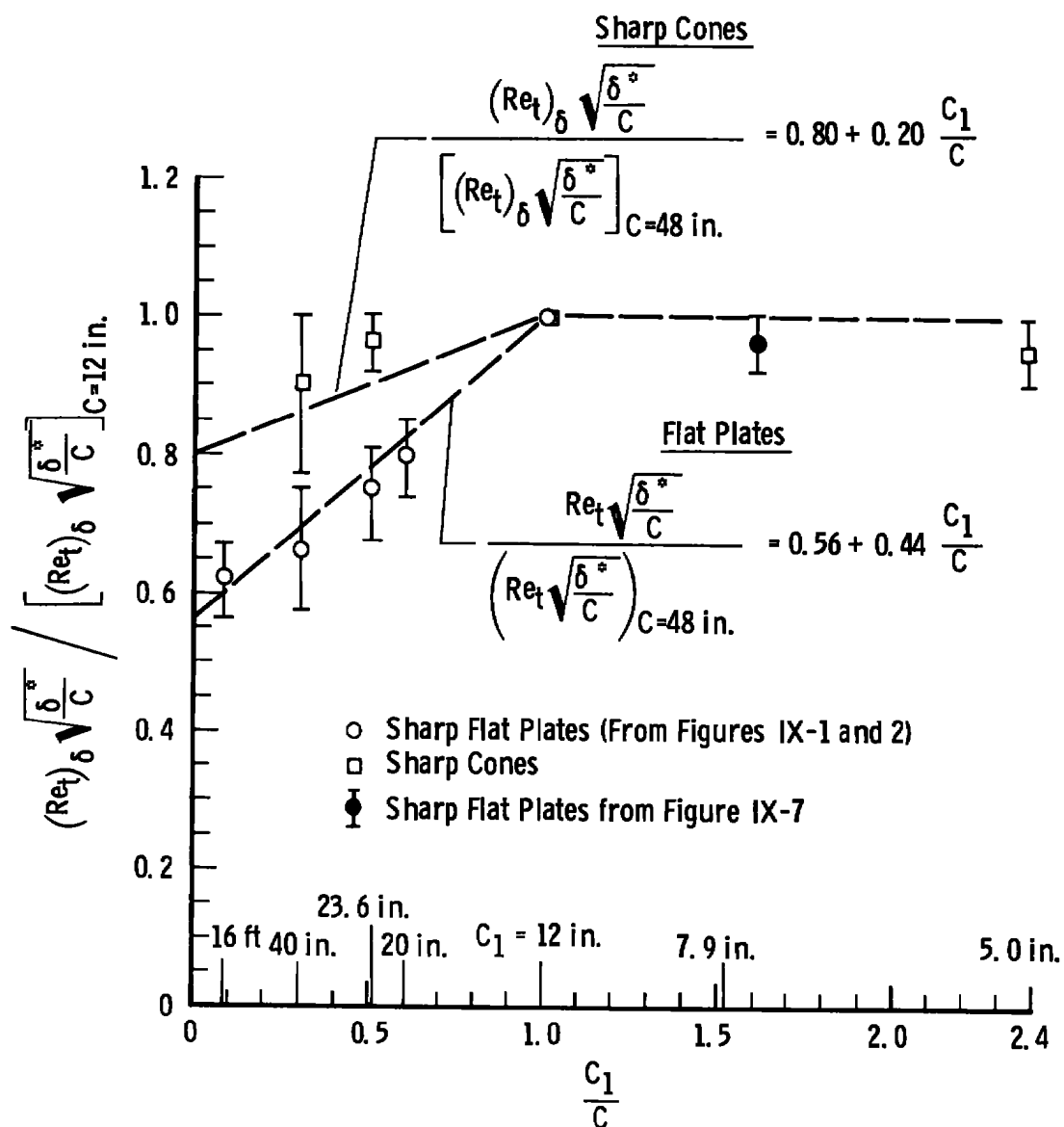


Figure IX-5. Tunnel size normalizing parameters.

$$\text{Eq. (B) from Ref. 11, } (Re_t)_\delta = \frac{48.5 C_F^{-1.40} (0.8 + 0.2 C_1/C)}{\sqrt{\delta^*/C}}$$

Based on Data from Eleven Facilities Varying in size from 1 to 4.5 ft in diameter, Mach number range from 3 to 14, and  $(Re_\infty/ft)_\infty$  range from  $1.2 \times 10^6$  to  $14.4 \times 10^6$ .

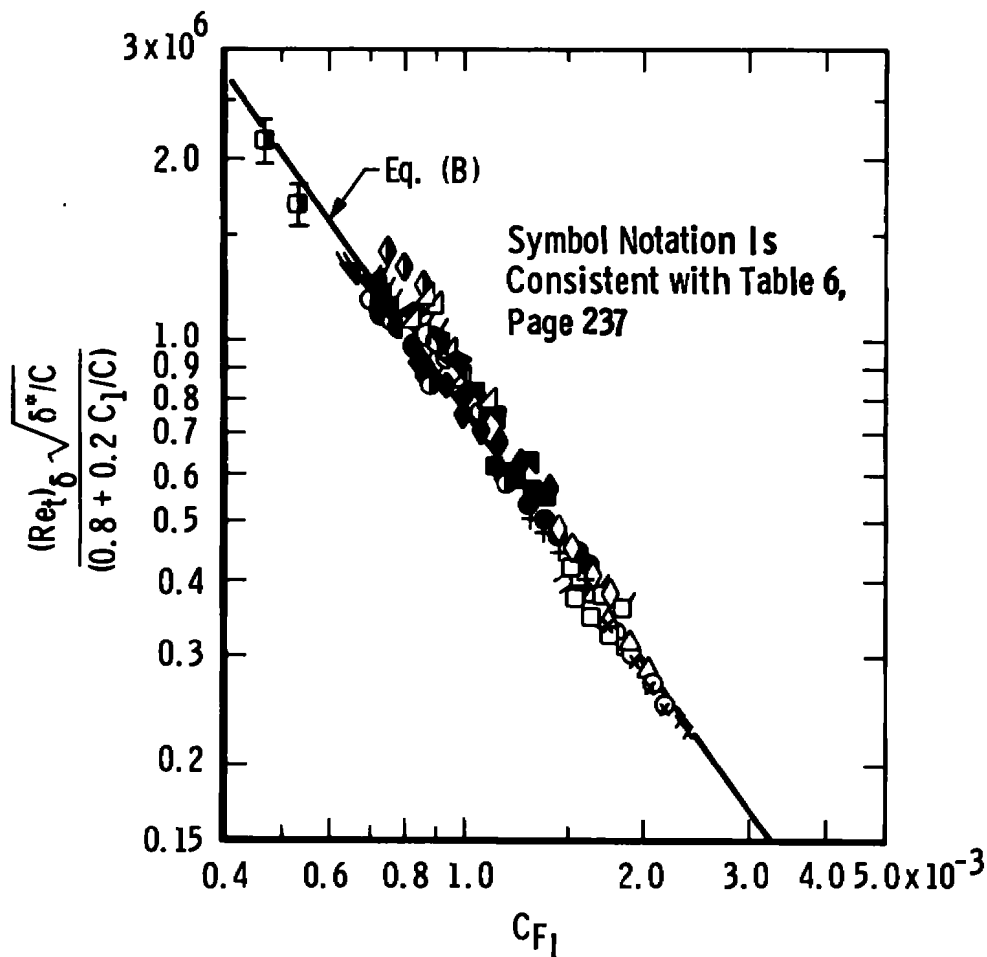


Figure IX-6. Correlation of transition Reynolds numbers on sharp cones with aerodynamic noise parameters [from Reference (11)].

The average turbulent skin-friction coefficient ( $C_{F_I}$ ) used in the correlations presented in Figures IX-1 through IX-6 was determined using the method of van Driest (van Driest - I) as published in Reference (135). The values of the tunnel wall turbulent boundary-layer displacement thickness ( $\delta^*$ ) used in the correlations were the experimentally measured data or computed values as indicated in the data presented on pages 250 and 253 and discussed in Appendix B, page 324.

Since the original aerodynamic-noise-transition correlations were published (Figures IX-3, page 224 and IX-6, page 229, there has been a great deal of world-wide attention devoted to studying aerodynamic-noise-transition correlations as discussed in Chapter VII. Consequently, there have been new transition data published from a number of different wind tunnels on which data were not previously available.

New and unpublished transition data have also been obtained at AEDC-VKF. These data have been obtained primarily in the AEDC-VKF Tunnel F (hotshot) hypersonic wind tunnel (see Chapter IV) on a sharp slender cone and flat plate for  $M_\infty \approx 7.5$  and 8, respectively. The Tunnel F facility has been undergoing a major modification program, including the addition of a family of contoured nozzles [see Reference (103)]. Sharp slender cones and the flat-plate models described in Chapter IV were the standard flow calibration models. These models have provided new transition data which allow the aerodynamic-noise-transition correlations presented in Figures IX-3, page 240, and IX-6, page 244, to be extended to higher Reynolds numbers.

The data published by NASA, the European countries, and the USSR plus the new hypersonic tunnel data obtained by the author has prompted



a re-evaluation of the aerodynamic-noise-transition correlations presented in Figures IX-3 and IX-6. Specifically:

1. the tunnel normalizing parameter will be re-evaluated using new data from very small tunnels (test section height less than 12 in.) and
2. the tunnel wall skin-friction coefficient will be computed using the method of van Driest-II (see Appendix A, page 315) including nonadiabatic wall effects. In References (10) and (11) (and Figures IX-1 through IX-6), an adiabatic wall temperature was assumed. This was a valid approach since most of the transition data were from supersonic tunnels having essentially adiabatic walls. However, there can be a significant effect of wall temperature on  $C_F$  at the higher Mach numbers and high Reynolds numbers as discussed in Appendix A, page 315. Also the method of van Driest-II is now generally accepted to be better than van Driest-I as discussed in Appendix A, page 315.

Presented in Figure IX-7 are new transition data (53) compared with the transition correlation curves from Figure IX-1, page 237. Note that the data from the medium size tunnel (T313) correlates as would be expected but the data from the very small tunnel (T325) does not establish a new tunnel size correlation curve, but follows the 12-in. tunnel data fairing closely. Results from these data were included in Figure IX-5, page 243, and it is seen that the normalizing parameter for  $C_1/C_\infty$  1.0 should be held at a constant value of 1.0. Data obtained on a sharp-cone model (136) have also been evaluated, and the results are included

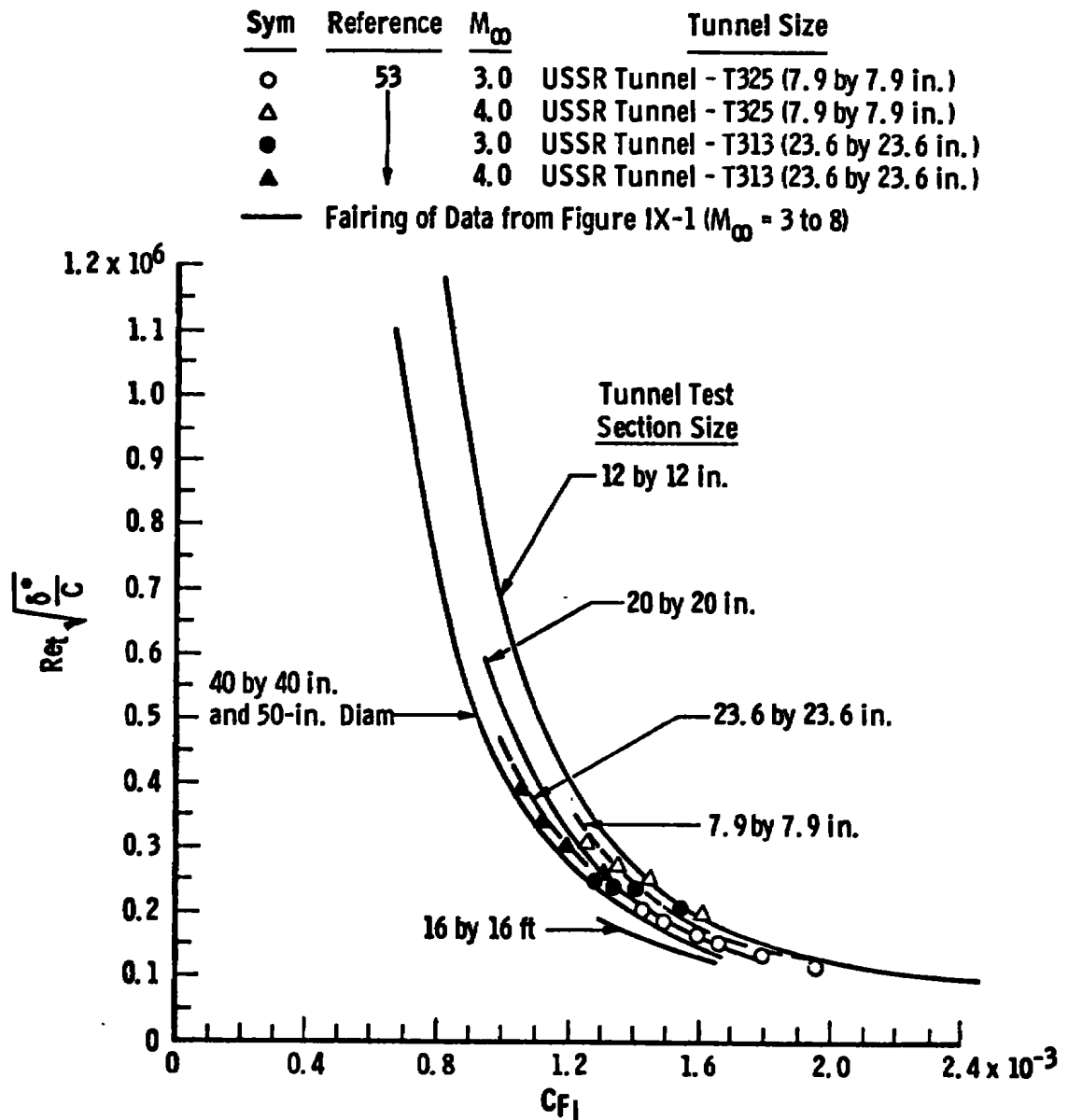


Figure IX-7. Transition Reynolds number correlation.

in Figure IX-5. These data also indicate that for  $C_1/C \approx 1.0$ , the cone normalizing parameter should also be 1.0.

Presented in Figure IX-8 is the new correlation of planar model transition data obtained using transition Reynolds number data from 13 wind tunnels covering the Mach number range from 3 to 8 and tunnel sizes from 7.9-in. to 16-ft test sections. The tunnel wall turbulent skin friction was computed using the method of van Driest II. The value of  $C_{FII}$  includes nonadiabatic tunnel wall effects. Table 5 lists the values of the tunnel wall temperature ratios ( $T_w/T_{aw}$ ) used in these computations. Table 5 provides additional information on test conditions, tunnel size, method of transition measurement, amounts of adjustment in  $Re_t$  values, etc., and identifies the sources for all the data presented in Figure IX-8. It should be noted that the slope of the correlation shown in Figure IX-8 is identical to the initial results presented in Figure IX-3, page 240.

The correlation presented in Figure IX-8 is recommended for use in estimating  $Re_t$  values on sharp flat plates in wind tunnels. Equation (9) has been programmed in FORTRAN for digital computer application as discussed in Appendix C, page 343:

$$(Re_{t_\delta})_{\text{flat plates}} = \frac{0.0126 (C_{FII})^{-2.55} (\bar{C})}{\sqrt{\frac{\delta^*}{C}}} \quad (10)$$

The new correlation of sharp-cone transition Reynolds number obtained from 16 supersonic-hypersonic facilities is presented in Figure IX-9. These data cover the Mach number range from 3 to 20 and tunnel

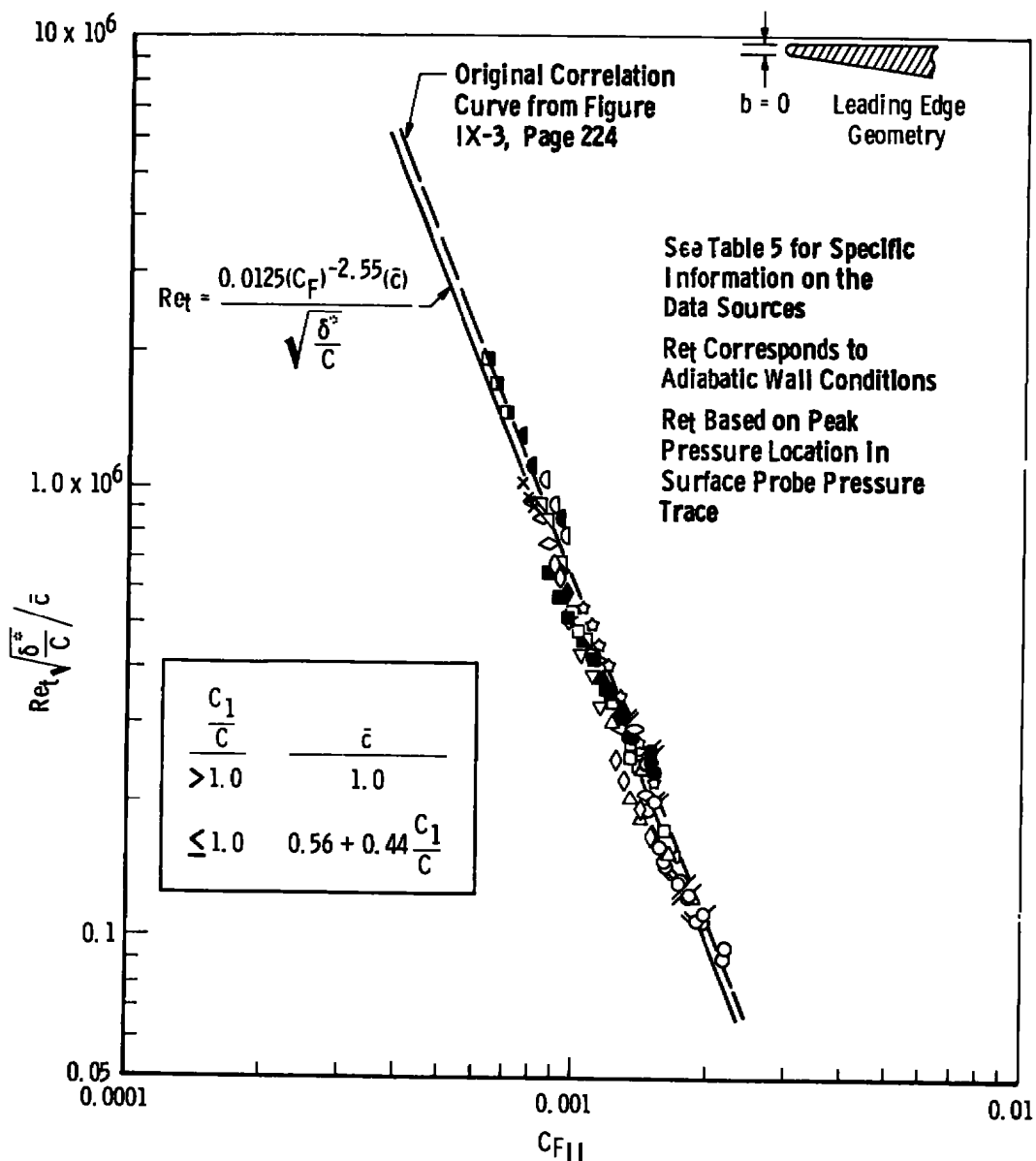


Figure IX-8. Correlation of planar model transition Reynolds numbers.

Table 5. Source and range of data used in the planar model transition Reynolds number correlation (see Figure IX-8).

Source	Symbol	$M_\infty$	$x \times 10^3$ , in.	$\theta$ LE, deg	(Ref. $Re_\infty \times 10^{-6}$ )	Model Configuration	Tunnel	Test Section Size	Method of Transition Detection	Amount of Adjustment	$L$ , in.	Method of Determination	Tunnel Wall $T_w/T_\infty$	
Present Study (see Figure V-1)	$\circ$	3.0	1.3, 2.1, 2.3, 3.0, 3.6	6, 12	0.1 to 0.6	HC ↓	AEDC-VKF D	12 by 12 in.	Peak $p_p$	None	48.5	Flexible Plate Wake Profiles ( $L_p = 56$ in.) Reference (97)	1.0	
	$\triangle$	4.0	3.8	6	0.1 to 0.6		↓	↓	↓	↓	↓			↓
	$\square$	5.0	3.8	6	0.1 to 0.4									
Present Study (Figure VII-1)	$\square$	5.0	1	10	0.2 to 1.0	FP	AEDC-VKF E	12 by 12 in.	Peak $p_p$		64	$\delta^*$ Correlation ( $L_p = 64$ in.) see Figure B-7, Appendix B	1.0 0.8 0.7 0.6	
Reference (169)	$\circ$	6.1	1.1, 2.4	15	0.3 to 1.1	FP ↓	↓	↓	↓	↓	60			↓
	$\nabla$	7.1	1.1, 2.4	↓	0.2 to 0.7									
	$\square$	8.0	1.1, 2	↓	0.3 to 0.5									
Present Study (see Figure VI-2)	$\bullet$	3.0	1.3, 2.1, 2.3, 3.0, 3.6, 8	6, 12	0.15 to 0.6	HC ↓	AEDC-VKF A	40 by 40 in.	Peak $p_p$		231 and 213	Flexible Plate Wake Profiles ( $L_p = 208$ in.) see Figure B-7, Appendix B	1.0	
	$\triangle$	4.0	2.1, 3.3, 6, 8	6	0.15 to 0.6		↓	↓	↓	↓	↓			↓
	$\blacksquare$	5.0	1.3, 2.1, 3.3, 6, 8	6, 12										
Reference (37) (see Figure VI-10)	$\bullet$	8.0	0.6 to 9.4	5.6, 12.5	0.1 to 0.3	HC	AEDC-VKF B	50-in. diam	Peak $p_p$		232	Rake Profile ( $L_p = 244$ in.) Exp. Data, Figure B-8	0.5	
Reference (123)	$\circ$	3.7	<1	15	0.1 to 0.4	FP	JPL 20-in. SWT	18 by 20 in.	Maximum $T_w$		$\approx 118$	Flexible Plate Wake Profiles ( $L_p = 117$ in.) Reference (93)	1.0	
	$\circ$	4.6	<1	15	0.1 to 0.4	FP	JPL 20-in. SWT	18 by 20 in.	Maximum $T_w$		$\approx 118$			
Reference (126)	$\circ$	6.0	<2	20	0.59, 0.69	FP	NASA-Langley	20 by 20 in.	Peak $p_p$	1.1	$\approx 90$	$\delta^*$ Correlation Figure B-7, Appendix B	0.8	
Reference (170)	$\nabla$	6.0	1	20	0.14, 0.27	FP	AEDC-VKF B	50-in. diam	Peak $p_p$	None	$\approx 232$	Rake Profile ( $L_p = 244$ in.) Exp. Data, Figure B-8	0.7 0.5	
	$\nabla$	8.0	1	20	0.2	FP	AEDC-VKF B	50-in. diam	Peak $p_p$	None	$\approx 232$			
Reference (120)	$\square$	3.1	0.8 to 8.0	5	0.1 to 0.6	HC	NACA-Lewis	12 by 12 in.	Maximum $T_w$	1.2	40.5	$\delta^*$ Correlation Figure B-7, Appendix B	1.0	
Reference (119)	$\square$	5.0	1.5, 10	15	0.15 to 0.4	HC	NASA-Lewis	12 by 12 in.	Maximum $T_w$	1.15	47			
Present Study	$\bullet$	3.0	1.5, 5, 9	6.5	0.05 to 0.11	HC	AEDC-PWT 16S	16 by 16 ft.	Peak $p_p$	None	792	Flexible Plate Wake Profiles ( $L_p = 839$ in.) see Figure B-1, Appendix B	1.0	
Present Study	$\square$	$\approx 8$	0.5	30	0.53 to 1.06	FP	AEDC-VKF F	42-in. diam	Maximum $q$	None	381	$\delta^*$ Correlation Figure B-8, Appendix B	0.3	
Present Study	$\nabla$	5	2.3	12	0.3 to 1.3	HC	AEDC-VKF E	12 by 12 in.	Peak $p_p$	None	39.6 56.8	Flexible Plate Meas. Figure B-5, Appendix B	1.0	
Reference (53)	$\square$	3	2.4	14.5	0.3 to 1.85	FP	USSR-T325	7.9 by 7.9	Peak $p_p$	None	36	$\delta^*$ Correlation Figure B-7, Appendix B	1.0	
	$\square$	4	6		0.4 to 1.5		USSR-T325	7.9 by 7.9			36			
	$\square$	3	2.4		0.4 to 1.35		USSR-T313	23.6 by 23.6			106			
	$\square$	4	6		0.4 to 1.5		USSR-T313	23.6 by 23.6			106			
Reference (63)	$+$	5	2	10	0.2 to 0.6	FP	AEDC-VKF A	40 by 40	Peak $p_p$	None	231	Experimental Data, see Figures B-7 and B-8, Appendix B	1.0	
	$\times$	8			0.2, 0.3		AEDC-VKF B	50-in. diam			232			
	$\times$	10			0.2		AEDC-VKF C	50-in. diam			300			

HC - Hollow Cylinder

FP - Flat Plate

\*\*Adjustment based on results from Figure VI-12, page

 $T_w$  - Surface Shear Stress $q$  - Heat Transfer $p_p$  - Peak in Surface Pitot Probe Pressure $T_w$  - Maximum Surface Temperature

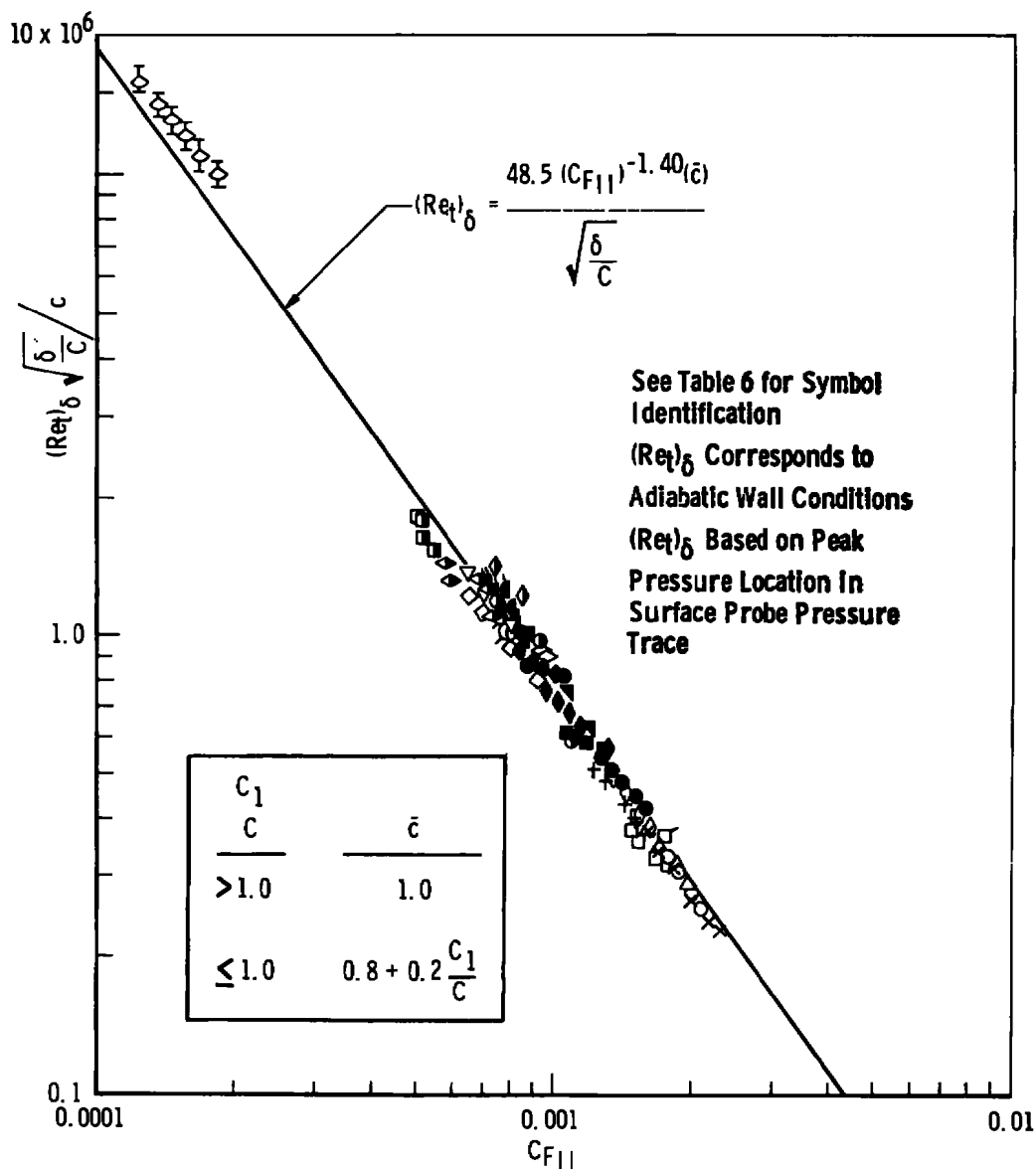


Figure IX-9. Correlation of sharp-cone transition Reynolds numbers.

sizes from 5- to 54-in.-diam test sections (see Table 6). The use of  $C_{FII}$  did not change the correlation. The linear fairing of the cone correlation in Figure IX-9 matches the data correlation previously developed (Figure IX-6, page 244) exactly. Equation (10) represents the analytical expression for the correlation curve:

$$(Re_{t_\delta})_{\text{cone}} = \frac{48.5 (C_{FII})^{-1.40} (\bar{C})}{\sqrt{\frac{\delta^*}{C}}} \quad (11)$$

Of particular interest is the recent transition data obtained in the NASA-LRC 22-in.-diam helium tunnel at  $M_\infty \approx 21$  as reported by Fischer and Wagner (90). Included in Figure IX-9 are the Langley data from Reference (90), and good agreement with the correlation is shown to exist. It should be noted that the Langley data lie about an order of magnitude outside the range of the original correlation. The total skin-friction coefficient ( $C_F$ ) and the parameter  $(Re_t)_\delta \sqrt{\delta^*/C}$  used for the Langley data are the values reported in Reference (90).

The sharp-cone  $Re_t$  correlation shown in Figure IX-9 [Eq. (11)] has been programmed in FORTRAN IV digital computer application as discussed in Appendix C, page 326, for predicting transition Reynolds numbers and locations in conventional supersonic-hypersonic wind tunnels.

Tunnel wall turbulent boundary-layer displacement thickness ( $\delta^*$ ) values used in the correlations presented in Figures IX-8 and IX-9 represent experimentally determined values or estimates using the theoretical or empirical methods as discussed in Appendix B, page 324. See Tables 5 and 6 for additional information on how  $\delta^*$  was determined for specific data sets.

Table 6. Source and range of data used in the sharp cone transition Reynolds number correlation (see Figure IX-9).

Source	Symbol	$M_\infty$	$M_\delta$	$b \times 10^3$	$\theta_c$ , deg	$(Re/\eta)_\infty \times 10^5$	Tunnel	Test Section Size	Method of Transition Detection	Amount of Adjustment	$L$ , in.	Model $T_w/T_\infty$ $T_w/T_0$	Method of $\delta$ Determination	Tunnel Wall $T_w/T_\infty$
Present Study (see Figure VII-5)	$\circ$ $\Delta$ $\square$ $\diamond$	3 3.5 4 4.55	2.9 3.4 3.8 4.3	5 (Sharp)	5	0.15 to 0.4	AEDC-VKF D	12 by 12 in.	Peak Probe Pressure ( $p_p$ )	None	44	$\approx 1.0$ $\approx 0.9$	Experimental Data ( $L_T = 56$ in.) Reference (97)	1.0
Present Study (see Figure VII-6)	$\bullet$ $\blacksquare$ $\blacktriangledown$ $\blacklozenge$ $\blacktriangleleft$	3 4 4.5 5 5.9	2.9 3.8 4.3 4.7 5.5	5 (Sharp)	5	0.15 to 0.6	AEDC-VKF A	40 by 40 in.	Peak Probe Pressure ( $p_p$ ) Shadowgraph	None	215	$\approx 1.0$ $\approx 0.9$	Experimental Data, ( $L_T = 208$ in.), Present Investigation, see Figure B-7	1.0  0.9
Reference (137) and VKF	$\blacktriangle$ $\blacksquare$ $\blacktriangledown$	6 8 8	5.5 7.0 6.4	Sharp	6 6 9	0.16 to 0.43 0.16 to 0.29 0.12 to 0.29	AEDC-VKF B	50-in. Diam	Maximum $\dot{q}$ Maximum $\dot{q}$ Shadowgraph	1.08 None	245	0.72 0.48 $\approx 0.93$	VKF Experimental and Reference (101) ( $L_T = 244$ in.) see Figure B-8	0.8 0.5 0.5
Reference (165) VKF	$\nabla$ $\nabla$	10 10	8.5 7.5	Sharp	6 9	0.13 0.17	AEDC-VKF C		Maximum $\dot{q}$ Shadowgraph		$\approx 300$	$\approx 0.29$ $\approx 0.25$ $\approx 0.77$	VKF Experimental Data ( $L_T \approx 300$ in.), see Figure B-7	0.35 0.35
*Reference (21)	$\blacksquare$	14.2	9.3	4	9	0.12, 0.2	AEDC-VKF F (Hotshot)	54-in. Diam	Maximum $\dot{q}$	None	350	$\approx 0.22$ $\approx 0.19$	Reference (158), ( $L_T = 384$ in.), see Figure B-8	0.2
Reference (137)	$\delta$ $\delta$	6 8	5.0 6.2	Sharp	10 10	0.34 to 1.2 0.35 to 0.54	AEDC-VKF E	12 by 12 in.	Shadowgraph	1.1 1.1	$\approx 64$ $\approx 64$	$\approx 0.86$ $\approx 0.75$ $\approx 0.6$ $\approx 0.5$	Estimated Using $\delta$ Correlation Figure B-7	$L_T = 64$ in. 0.8 0.6
Reference (171)	$\phi$	10.2	9.2	4 to 10	3.75	0.10 to 0.19	NASA-Langley	31 by 31 in.	Maximum $\dot{q}$	None	158	0.43 to 0.63 0.37 to 0.54		$L_T = 158$ in. 0.35
Reference (120)	$\times$	3.1	3.0	$< 6$ (Sharp)	5	0.1 to 0.67	NACA-Lewis	12 by 12 in.	Maximum $T_w$	1.19	$\approx 40$	$\approx 1.0$ $\approx 0.9$		$L_T = 47$ in. 1.0
Reference (119)	$+$	5.0	4.9	3 (Sharp)	2.5	0.16 to 0.47	NASA-Lewis			1.13	$\approx 47$	$\approx 1.0$		$L_T = 55$ in.
Reference (79)	$\nabla$	3.84	3.67	$< 1$ (Sharp)	5	0.18 to 0.46	JPL-SiWT	9 by 12 in.	Maximum $\dot{q}$	1.19	$\approx 49$	$\approx 1.0$	Experimental Data Reference (168), ( $L_T = 49$ in.)	
Reference (172)	$\bullet$	$\approx 11.3$ $\approx 10.1$		1 (Sharp)	5	0.04 to 0.16	GE Shock Tunnel	54-in. Diam (Nozzle Exit)	Maximum $\dot{q}$	None	156	0.25 $\approx 0.2$	$\delta$ Correlation, ( $L_T = 156$ in.)	0.3
*Present Study (see Figure VII-7)	$\blacktriangleright$	$\approx 7.5$		Sharp	10	0.6 to 2.75	AEDC-VKF F (Hotshot)	25-in. Diam		1.08	370	0.3 $\approx 0.3$	$\delta$ Correlation, see Figure B-8	
Reference (122)	$\diamond$	6.84	5.5	Sharp	10	0.4 to 0.5	NASA-Langley	11 by 11 in.	Maximum $\dot{q}$ Thin Skin	1.05	$\approx 65$	0.6 $\approx 0.52$	$\delta$ Correlation, see Figure B-7	0.7
Reference (26)	$\nabla$ $\diamond$ $\nabla$	8.0 6.21 5.0	7.24	Sharp	5 10 16	0.2 to 1.2	NASA-Langley	18.3-in. Diam	Maximum $\dot{q}$ Thin Skin Thin Film		112	$\approx 0.5$ $\approx 0.4$	$\delta$ Correlation, see Figure B-7	0.6
Reference (90)	$\diamond$	$\approx 21$ $\approx 16$		Sharp	2.87	0.53 to 1.67	NASA-Langley Helium	22-in. Diam	Maximum $\dot{q}$	None	$\approx 140$	1.0 $\approx 0.9$	Experimental Data Reference (90)	1.0

\*\* See Figure VI-12

\*Nitrogen Test Gas

$\dot{q}$  - Heat Transfer  
 $p_p$  - Peak In Surface Pilot Probe Pressure  
 $T_w$  - Maximum Surface Temperature

Symbols corresponding  
to data in Figure IX-9



It is well known that the model wall temperature ( $T_w/T_{aw}$ ) can have a significant effect on the location of transition at supersonic speeds (2,4,16). Consequently, all the transition data presented in Figure IX-8 were obtained at  $T_w/T_{aw} \approx 1$ , except the AEDC-VKF Tunnel F data ( $M_\infty \approx 8$ ) where  $T_w/T_{aw} \approx 0.3$ . For  $M_\infty \gtrsim 6$ , Deem et al. (63) and Rhudy (169) have shown that the location of transition on flat-plate models tested in wind tunnels was not dependent on  $T_w/T_{aw}$ . Therefore, all the transition data included in Figure IV-8 are assumed to represent adiabatic wall conditions.

The sharp-cone transition data obtained in the present research were also measured at adiabatic wall conditions,  $T_w/T_{aw} \approx 1$ . However, a large percentage of the transition data obtained from other sources for  $M_\infty \gtrsim 6$  were measured at nonadiabatic wall conditions ( $T_w < T_{aw}$ ). Table 6 provides a tabulation of the  $T_w/T_{aw}$  value for each data set. Based on the results of Deem et al. (63), Rhudy (169), and Kendall (14), it is assumed that the cone transition data are not a function of  $T_w/T_{aw}$  for  $M_\infty \gtrsim 6$ . Therefore, all the transition data included in Figure IX-9 are assumed to represent adiabatic wall values.

The correlation presented in Figures IX-8 and IX-9 and the digital computer program developed in Appendix C, page 326, will allow reasonably accurate predictions of transition Reynolds numbers and transition location on adiabatic wall, sharp flat plates and cones for  $M_\infty \geq 3$  and all size conventional supersonic-hypersonic wind tunnels.

The reader is reminded that the transition Reynolds number correlations cannot be applied to ballistic ranges, atmospheric free flight, or any test environment other than a conventional wind tunnel ( $M_\infty \gtrsim 3$ )

because of the obvious restrictions imposed by the aerodynamic-noise-dominance hypothesis and the correlating parameters  $C_F$ ,  $\delta^*$ , and  $C$ . Similarly, since the correlation was developed for finite size wind tunnels, the proper boundary conditions for free flight are not included. Conclusions relative to possible fundamental influences of Mach number and unit Reynolds number on  $Re_t$  in a disturbance-free environment cannot be drawn from these results.

It is felt that the results obtained in this research conclusively show that the fluctuating pressure field radiated by the tunnel wall turbulent boundary layer dominates the transition process on sharp flat plates and sharp cones at zero angle of attack in conventional supersonic and hypersonic wind tunnels ( $M_\infty \gtrsim 3$ ). It is concluded that the unit Reynolds number effect exhibited in supersonic-hypersonic wind tunnels is primarily the result of the radiated aerodynamic noise.<sup>19</sup> Furthermore these results show that it will be very difficult if not impossible to separate out "true" Mach number and unit Reynolds number trends (if they exist) from conventional wind tunnel  $Re_t$  data that are dominated by the radiated pressure field (aerodynamic noise).

---

<sup>19</sup>See Reference (23) for a detailed discussion of the unit Reynolds number effect in a "quiet" ballistic range environment.

## CHAPTER X

EFFECTS OF TUNNEL SIZE, UNIT REYNOLDS NUMBER, AND MACH NUMBER:  
COMPARISONS BETWEEN THEORY AND EXPERIMENTAL DATA

## I. INTRODUCTION

Presented in this chapter are experimental transition Reynolds number data obtained in wind tunnels varying in size (test section height) from 5 in. to 16 ft, for Mach numbers from 3 to 14, and over a unit Reynolds number range from  $0.1 \times 10^6$  to  $2.5 \times 10^6$  per in. Transition Reynolds number data for both sharp flat plates (and hollow cylinders) and sharp slender cones at zero incidence are presented.

A FORTRAN IV computer program was developed to predict  $(Re_t)_\delta$  and  $x_t$  values on zero bluntness, flat-plate, and cone models tested in conventional supersonic-hypersonic wind tunnels ( $M_\infty \gtrsim 3$ ). This model uses the aerodynamic-noise-transition empirical equations [Eqs. (10) and (11)] developed in Chapter IX. Details of the program are presented in Appendix C. In the following sections extensive comparisons are made between the experimental data and calculations from the math model.

## II. EFFECT OF TUNNEL SIZE

Experimental data illustrating the large variation of transition Reynolds numbers on sharp flat plates and sharp slender cones with tunnel size are presented in Figures X-1 and X-2, respectively, for a Mach number range from 3 to 16. The predicted variations of  $(Re_t)_\delta$  with

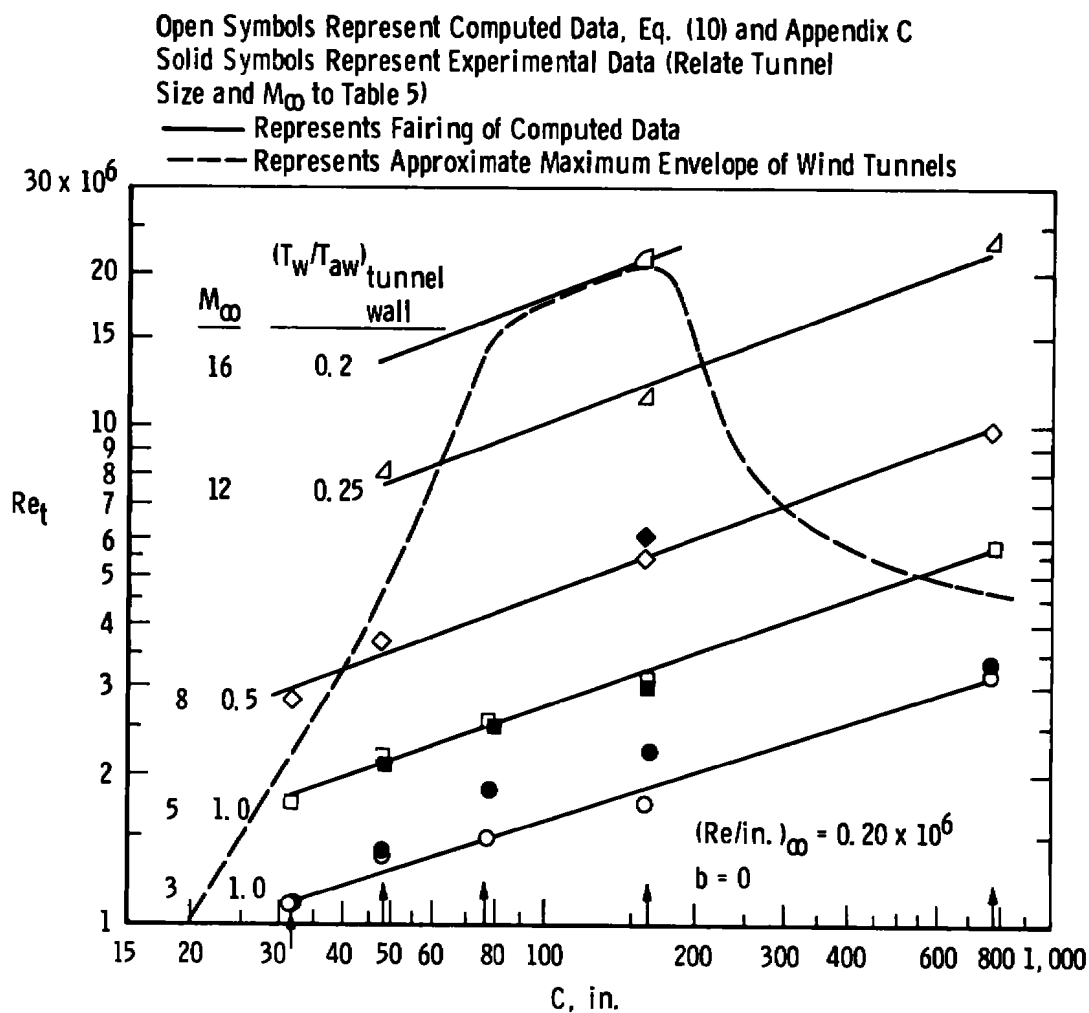


Figure X-1. Effect of wind tunnel size on planar model transition Reynolds numbers for various Mach numbers.

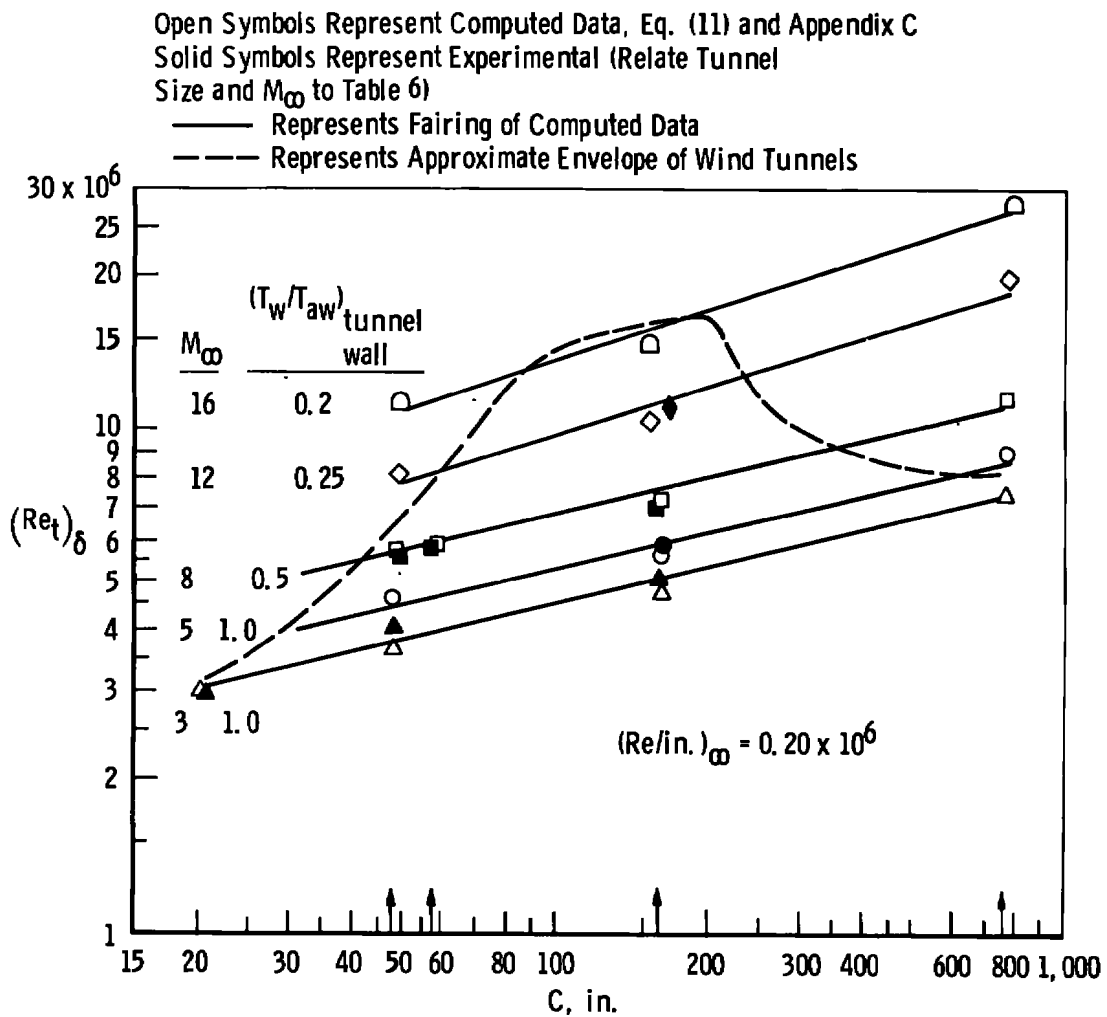


Figure X-2. Effect of wind tunnel size on sharp-cone transition Reynolds numbers for various Mach numbers.

tunnel size and  $(Re/in.)_{\infty} = 0.20 \times 10^6$  for a Mach number ranging from 3 to 16 are included in Figures X-1 and X-2.

The predicted values were computed for specific tunnel geometries and the calculated results were then faired to clearly illustrate the significant and monatomic increase in  $Re_t$  with increasing tunnel size. Experimental data have been included for comparative purposes, and in general, the agreement between the computed results and the experimental data is considered good. It should be noted that the computed data correspond to the correct tunnel wall temperature ratio  $(T_w/T_{aw})$  tunnel geometry and model location as indicated in Figures X-1 and X-2. Additional specific information can be obtained from Tables 5, page 234, and 6, page 237. It should be noted that the planar  $(Re_t)_{\delta}$  data (Figure X-1) is not as strongly Mach number dependent as the cone data (Figure X-2).

Included in Figures X-1 and X-2 are estimates of the available ranges of size and Mach number offered by today's wind tunnels. In general, the available experimental data confirm the predicted trends over about one-half of the envelope.

Results presented in Figures X-1 and X-2 show that the variation of  $(Re_t)_{\delta}$  with tunnel size is significant for all Mach numbers ( $M_{\infty} \gtrsim 3$ ). This variation must be considered when comparing  $(Re_t)_{\delta}$  data or transition-sensitive aerodynamic data from different facilities, developing new  $Re_t$  correlations, verifying  $(Re_t)_{\delta}$  theories, or planning wind tunnel test programs where the location of transition on the model could affect the data.

Figure X-3 shows the variation in  $Re_t$  data obtained on planar models in five  $M_\infty = 3$  wind tunnels having test section heights varying from 7.7 in. to 16 ft. The recent Russian data (53) have provided  $Re_t$  values at considerably higher unit Reynolds numbers than were obtained in the present research. It should be noted that the increase in  $Re_t$  with increasing  $Re/in.$  values appears to continue, at least up to  $Re/in. \approx 2 \times 10^6$ . The predicted results from the computer code are in good agreement with the experimental data and correctly predict the effects of tunnel size and unit Reynolds number.

Transition Reynolds numbers obtained in four  $M_\infty \approx 8$  wind tunnels are shown in Figure X-4. The  $M_\infty = 7.5$  data obtained in the present research are, to the author's knowledge, the highest unit Reynolds number wind tunnel  $Re_t$  data published. As was the case at  $M_\infty = 3$ , the values of  $(Re_t)_\delta$  continue to increase with increasing  $(Re/in.)$  values and increasing tunnel size. The computed values are in good agreement with the experimental data.

### III. VARIATION OF $Re_t$ WITH MODEL POSITION

It was shown in Figures X-1 through X-3 that a very large variation in  $Re_t$  occurred with increasing tunnel size. To gain further insight into tunnel size effects, an experimental study was conducted to determine whether a significant variation in  $Re_t$  occurred with fairly large changes in model axial locations in a specific tunnel. The 3.0-in.-diam hollow-cylinder model was tested in the AEDC-VKF Tunnels D and E at several axial locations as illustrated in Figure X-5 for the AEDC-VKF Tunnel E. The transition Reynolds number data obtained over a wide range of axial

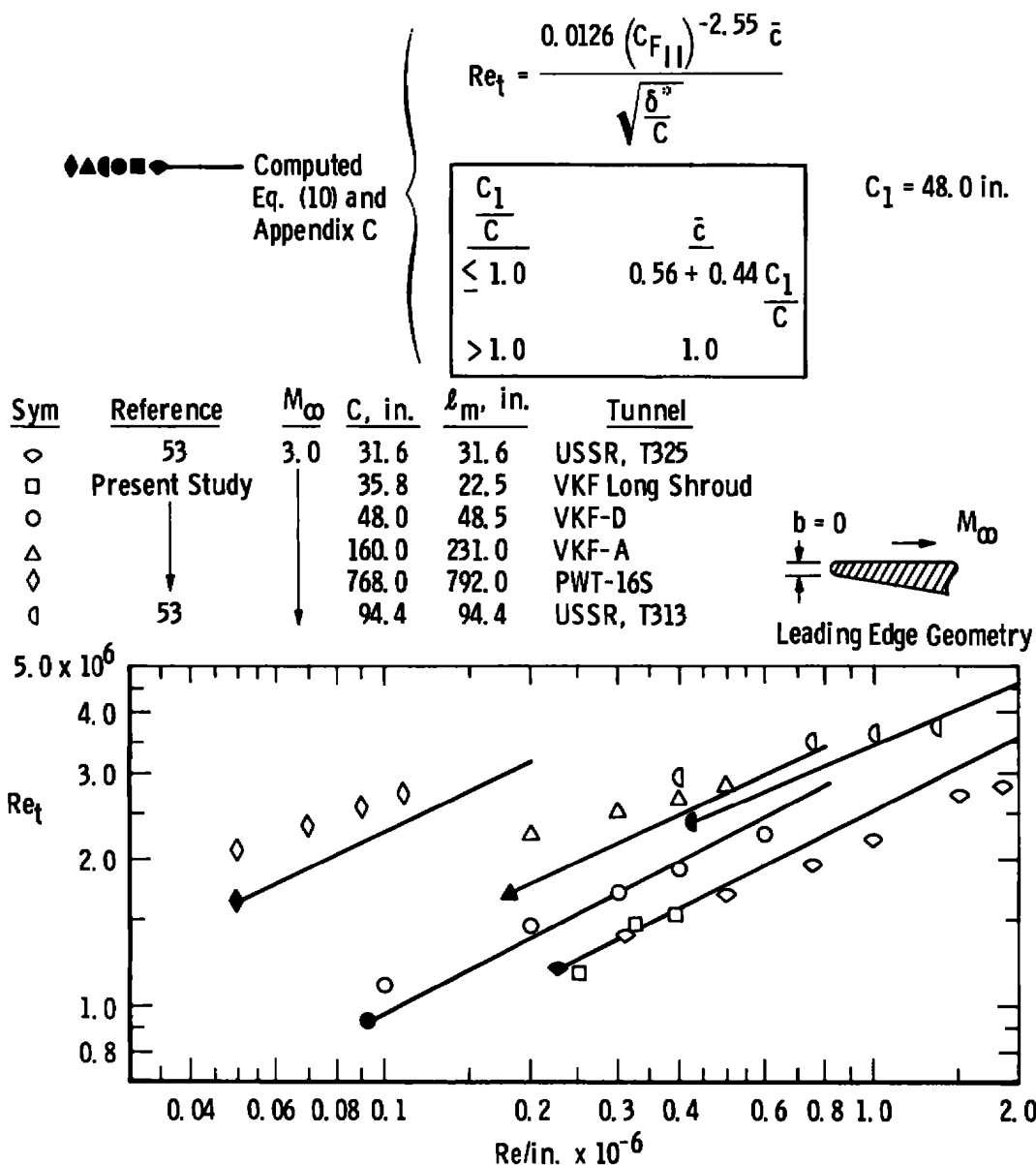


Figure X-3. Variation of transition Reynolds numbers with tunnel size and  $M_\infty = 3.0$ , sharp-leading-edge flat-plate/hollow-cylinder models.



Sym	Reference	$M_\infty$	$\theta_c$ , deg	Tunnel	$(T_w/T_{aw})_{\text{tunnel wall}}$
○	Present Invest.	$\approx 7.5$	10	AEDC VKF-F (25-in. Diam)	0.3
□	26	8.0	5, 10, 16	NASA-Langley (18.3-in. Diam)	0.6
△	137	8.0	10	AEDC VKF-E (12 by 12 in.)	0.6
◇	137	8.0	6, 9	AEDC VKF-B (50-in. Diam)	0.5

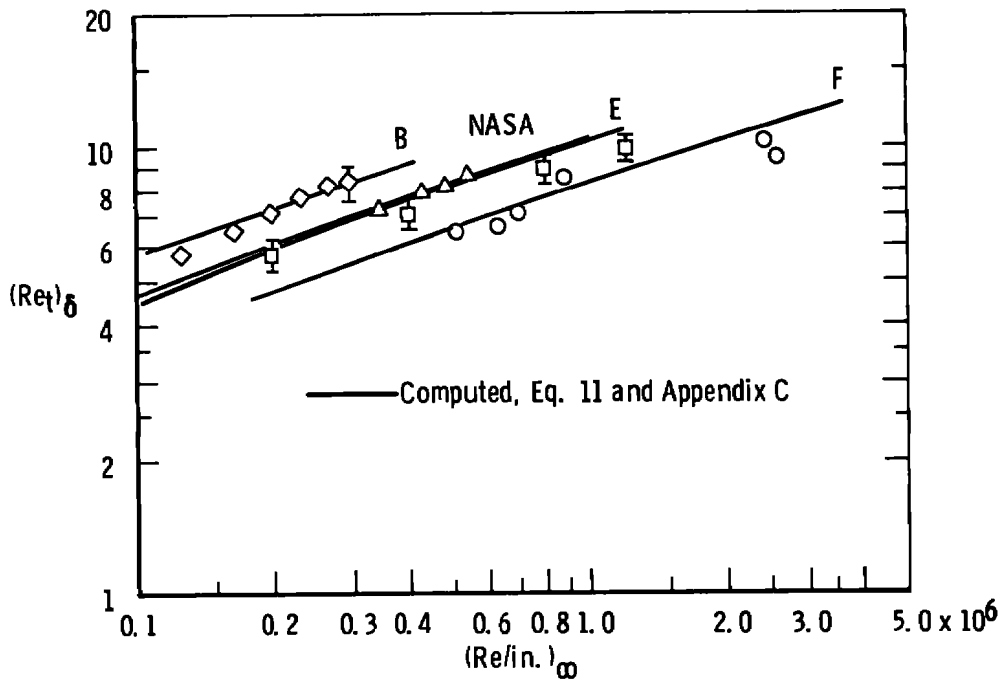


Figure X-4. Variation of sharp-cone transition Reynolds numbers with tunnel size at  $M_\infty \approx 8$ .

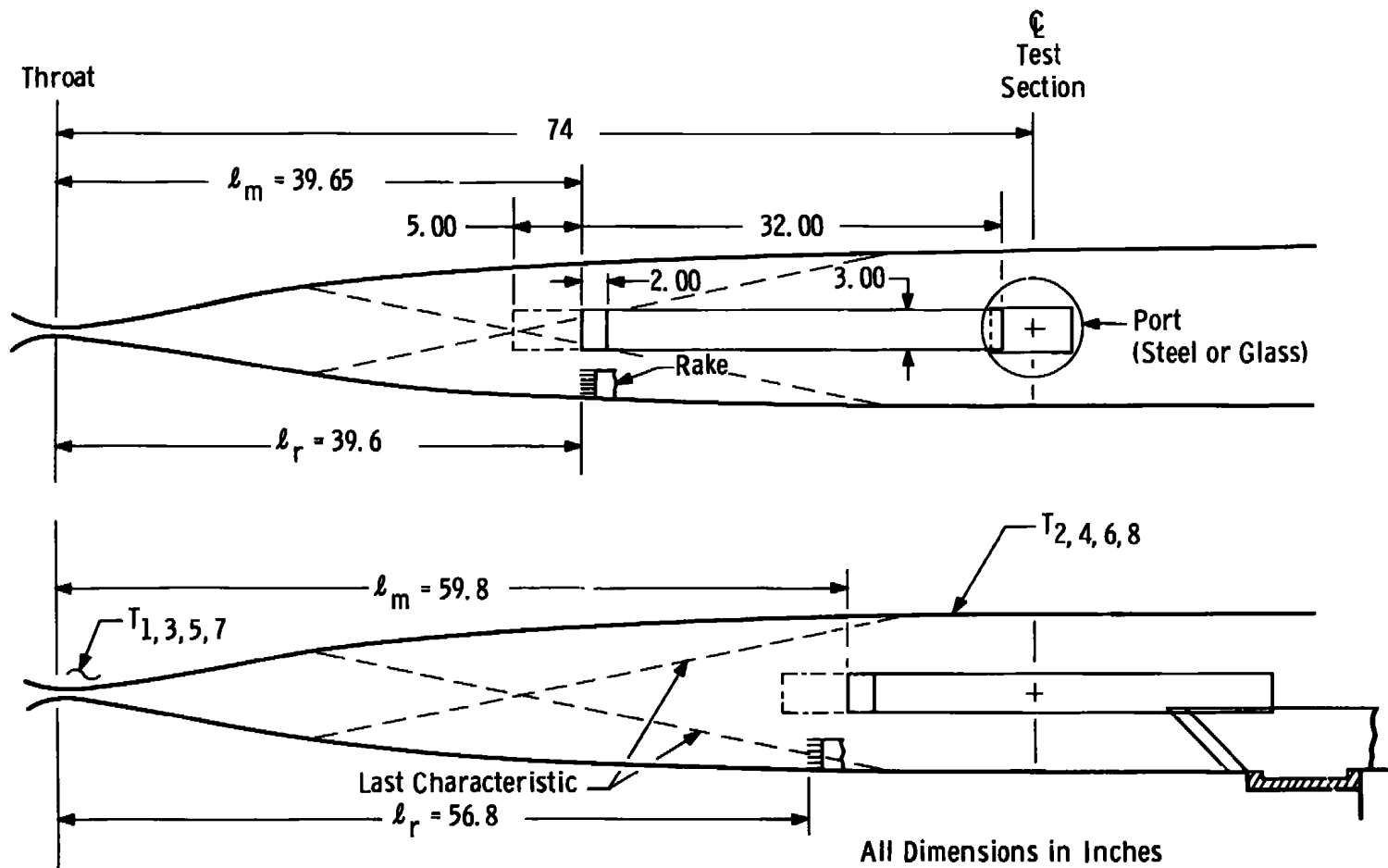


Figure X-5. AEDC-VKF Tunnel E transition model locations.

locations in Tunnels D and E for  $M_\infty = 4.5$  and  $5.0$ , respectively, are presented in Figure X-6. The data show a small, but systematic, increase in  $Re_t$  values as the model was moved closer to the throat section, i.e., decreasing  $x_m$ . However, the maximum change was only about  $\approx 15\%$  increase as the model was moved a maximum distance of 26.7 in. in Tunnel D and 20.2 in Tunnel E.

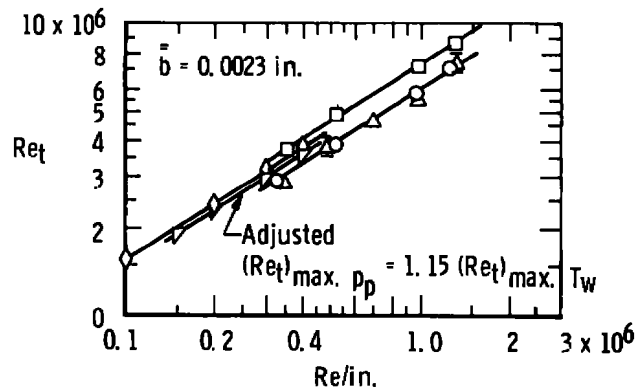
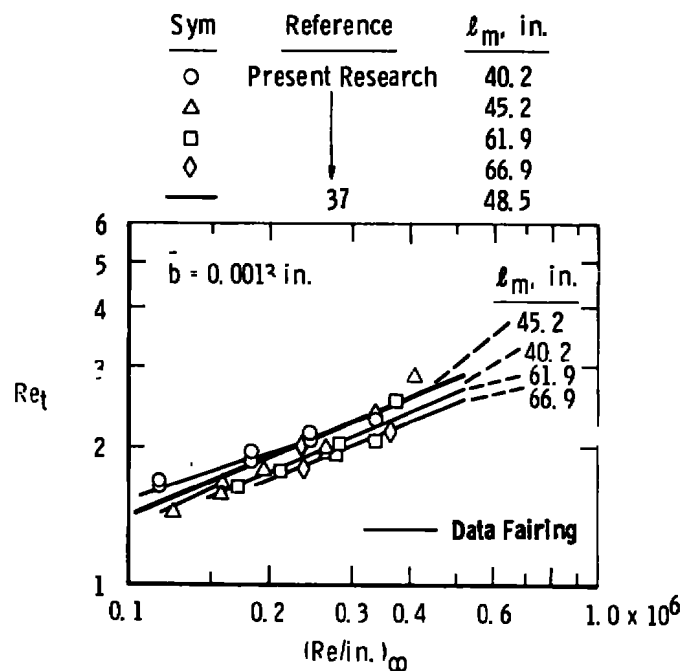
Estimated  $Re_t$  locations obtained from the computer program developed in Appendix D are shown in Figure X-7 for large axial locations in three different wind tunnels. It is seen that a negligible change in  $Re_t$  with changes in  $x_m$  were computed for the AEDC-VKF Tunnels D and E and Tunnel B and  $M_\infty = 4.5$ ,  $5.0$ , and  $8.0$ , respectively.

Therefore, it can be concluded from the results presented in Figures X-6 and X-7 that the variations of model axial positions within a test section will produce only small changes in model transition locations. It is of course assumed that the model will remain within the test rhombus and that uniform flow (that is, free from shock waves or compression or expansion waves) exists over the model.

#### IV. $Re_t$ TRENDS WITH MACH NUMBER AND UNIT REYNOLDS NUMBER

Presented in Figures X-8 and X-9 are plots of planar and cone model  $Re_t$  data as a function of unit Reynolds numbers  $(Re/in.)_\infty$  for a wide range of Mach numbers ( $M_\infty$ ). The  $Re_t$  data exhibit an increase with increasing unit Reynolds number. This trend is as expected and has been previously reported, e.g., see References (37) and (108). The data in Figures X-8 and X-9 show that the variation of  $Re_t$  with unit Reynolds number is not strongly dependent on Mach number and tunnel size. It

Sym	$l_m$ , in.	Source	Method-of-Detection
○	59.8	Present Study	Maximum $p_p$
△	54.8		
□	39.6	Figure VI-1 Ref. 119	Maximum $T_s$
◇	48.5		
▽	47.0		

a. AEDC-VKF Tunnel E,  $M_\infty = 5.0$ b. AEDC-VKF Tunnel D,  $M_\infty = 4.5$ Figure X-6. Effect of model axial locations on  $Re_t$  data (hollow-cylinder model).

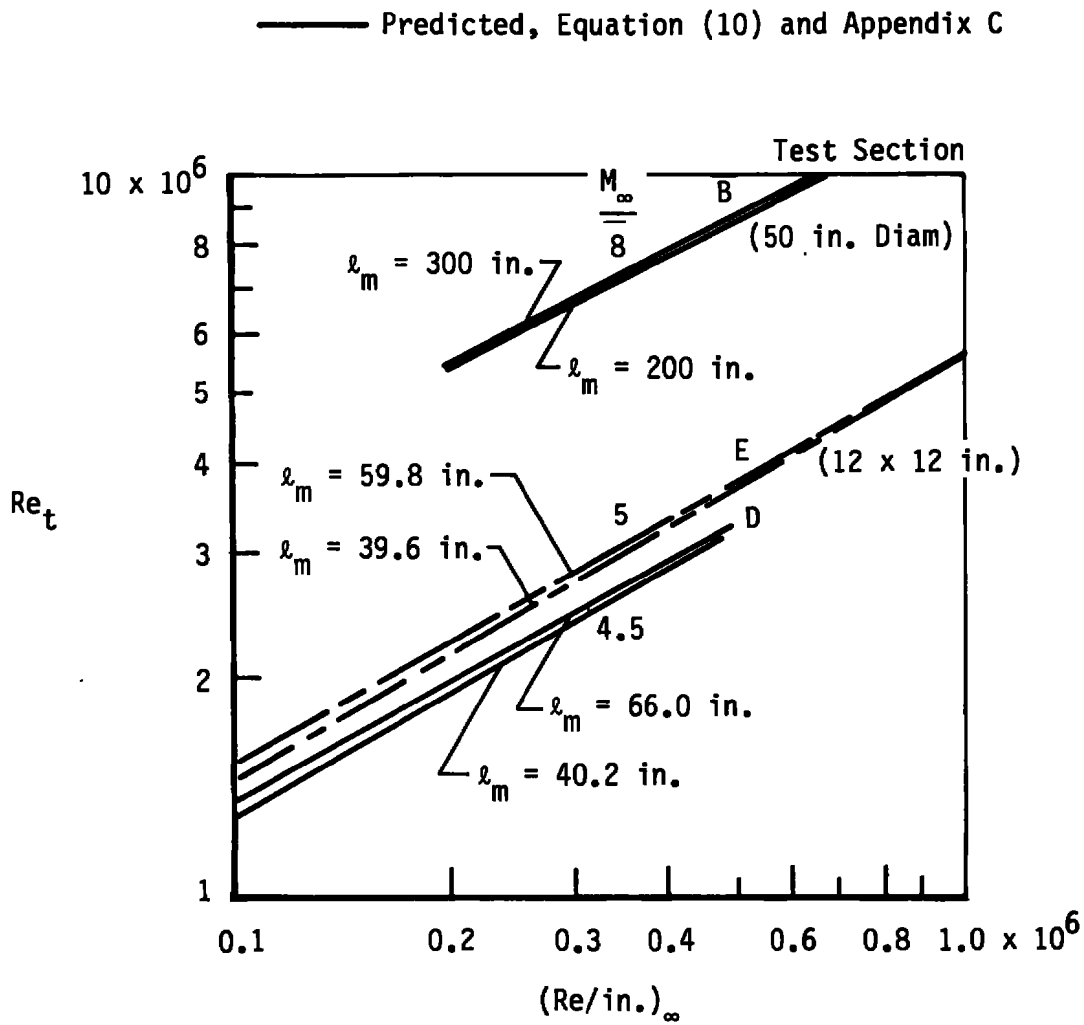
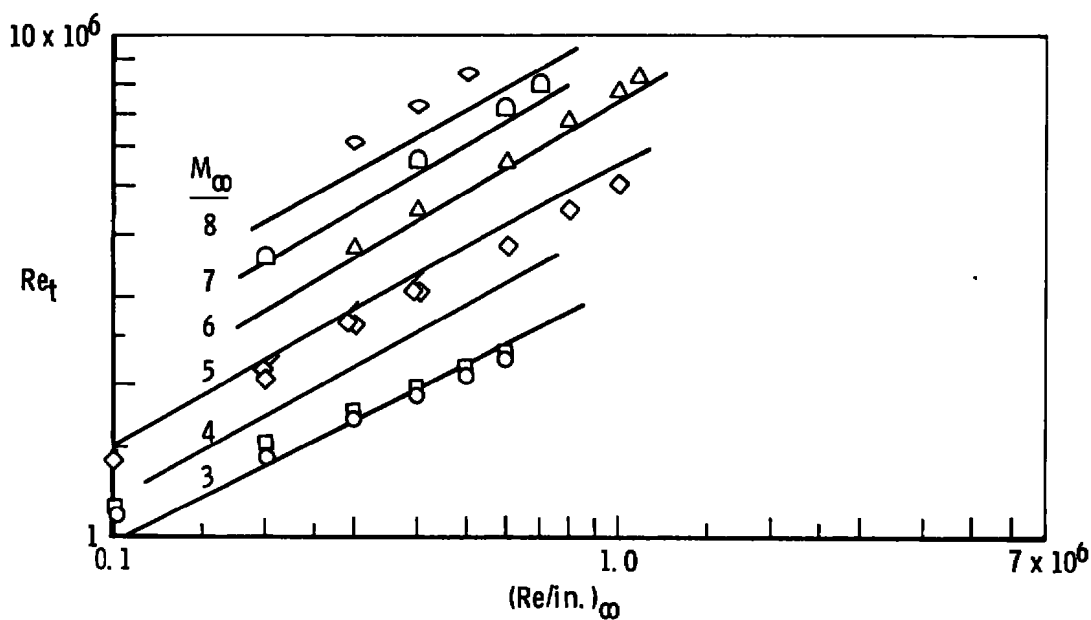


Figure X-7. Computed values of  $Re_t$  with varying model ( $l_m$ ) locations (planar models).

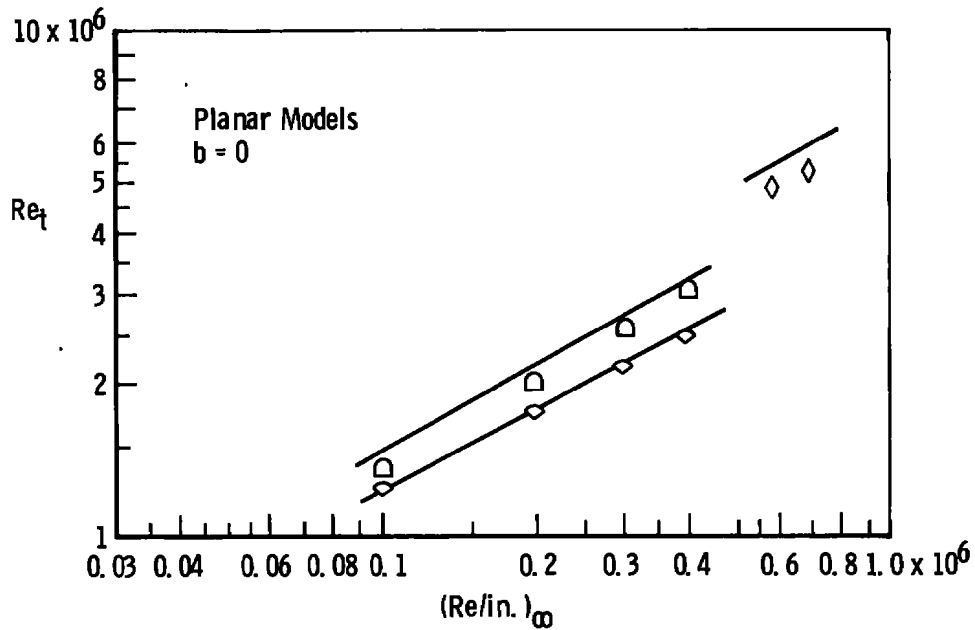
Sym	$M_\infty$	$(T_w/T_{aw})_{\text{tunnel wall}}$	Tunnel	Reference
○	3.0	1.0	AEDC-VKF-D (12 by 12 in.)	Present Investigation
□	4.0	↓	↓	↓
◇	5.0	↓	↓	↓
◊	5.0	↓	AEDC-VKF-E	↓
△	6.0	0.8	↓	169
◻	7.0	0.7	↓	↓
◊	8.0	0.6	↓	↓
— Computed, Eq. (10) and Appendix C				



#### a. Small Size Tunnels

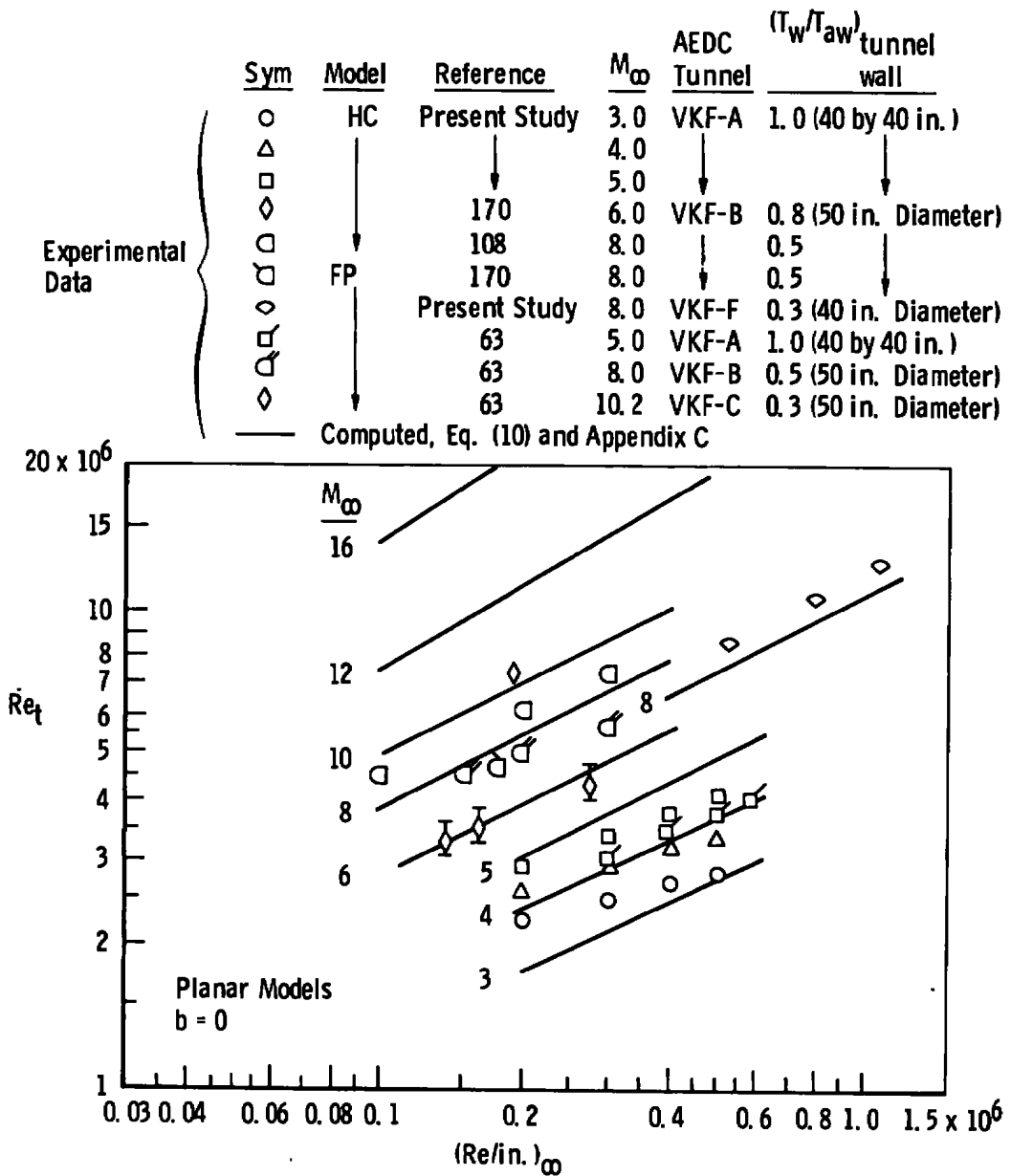
Figure X-8. Effect of Mach number and unit Reynolds number on planar model transition data.

Sym	Reference	$M_\infty$	Tunnel	$(T_w/T_{aw})_{\text{tunnel wall}}$
◇	123	3.7	JPL-SWT (18 by 20 in.)	1.0
□	123	4.6	JPL-SWT (18 by 20 in.)	1.0
◇	126	6.0	NASA Langley (20 by 20 in.)	0.8
— Computed, Eq. (10) and Appendix C				



## b. Medium Size Tunnels

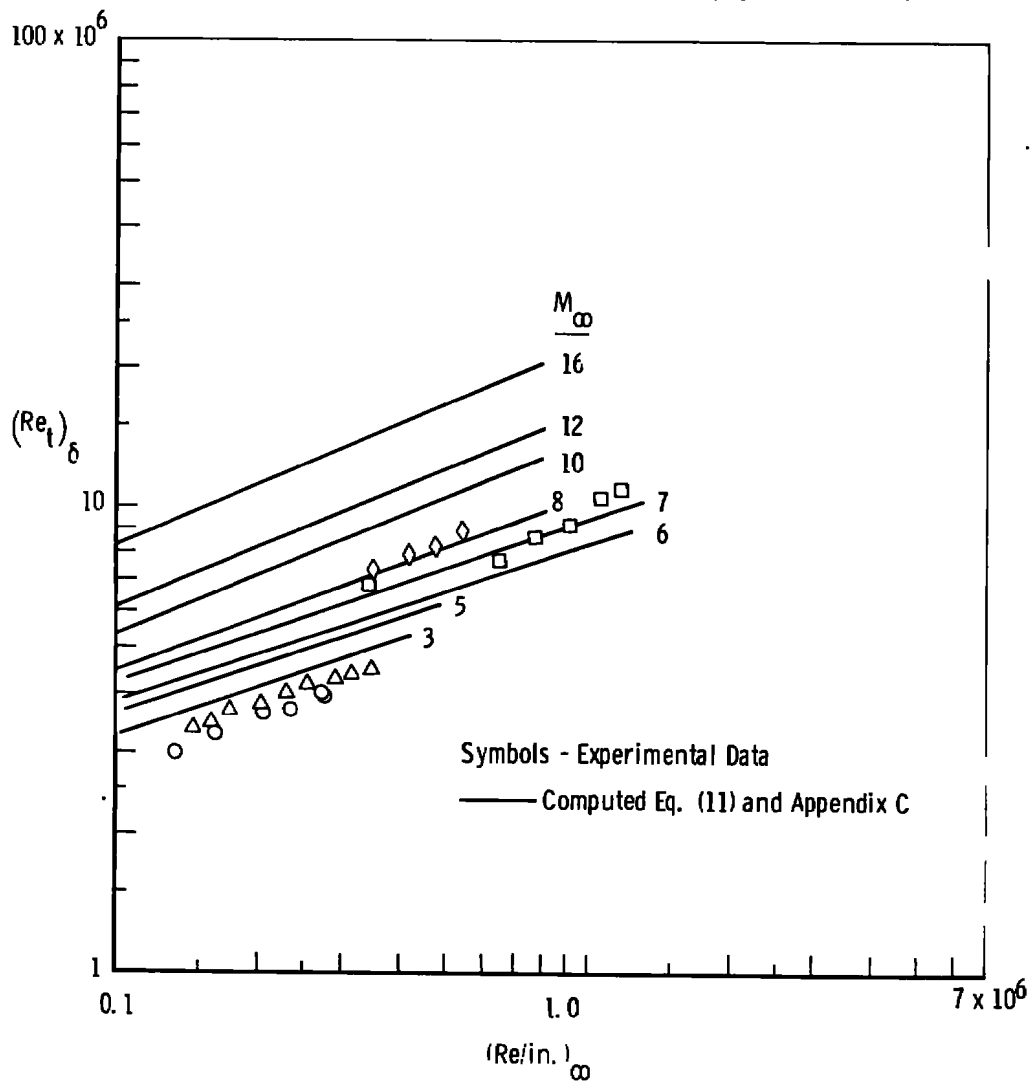
Figure X-8. (Continued).



c. Large Size Tunnels  
Figure X-8. (Continued).



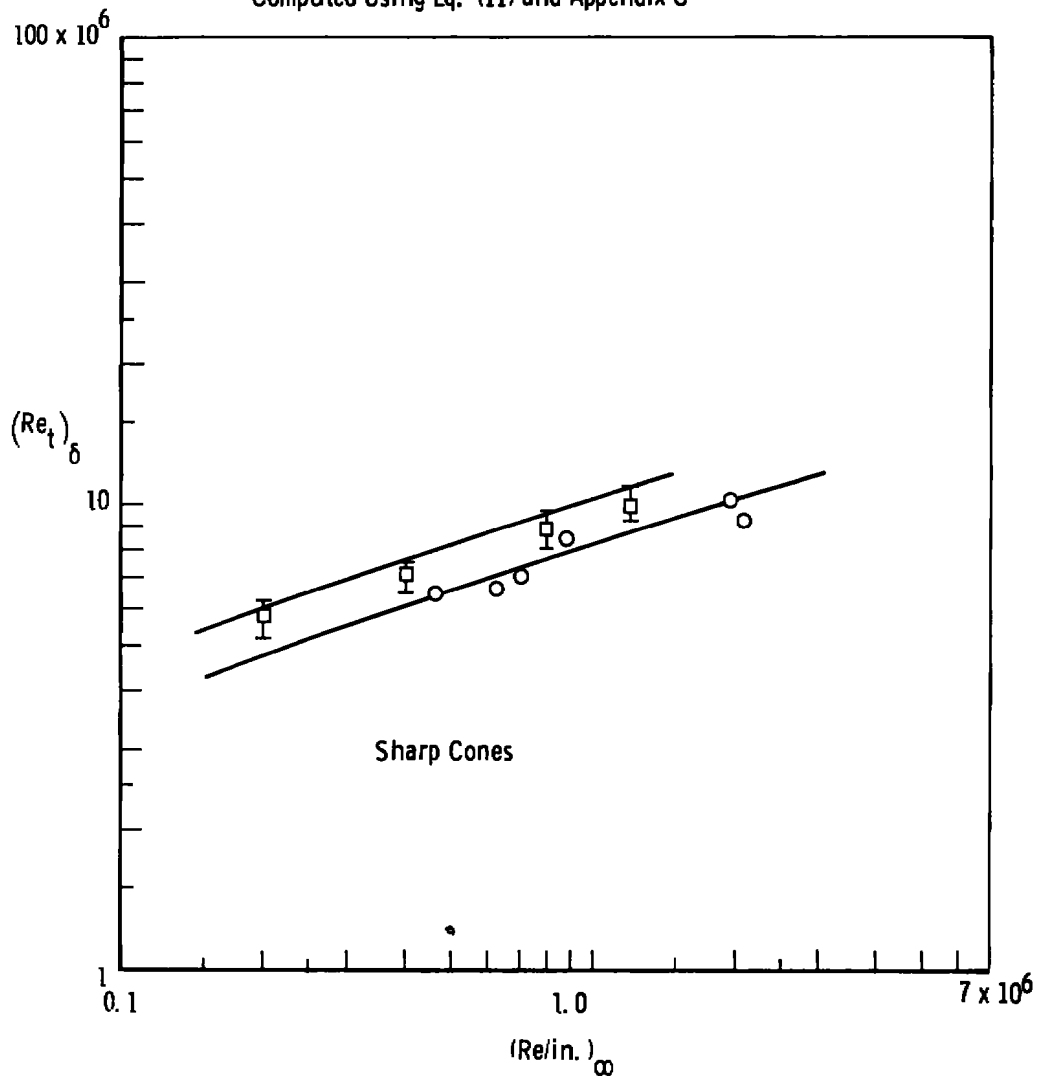
Sym	Reference	$M_\infty$	$\theta_c$ , deg	AEDC Tunnel	$(T_w/T_{aw})_{\text{tunnel wall}}$	Tunnel Test Section Size
○	Present Study	3.0	5.0	VKF-D	1.0	(12 by 12 in.)
△	Present Study	4.5	5.0	VKF-D	1.0	
□	137	6.0	10.0	VKF-E	0.8	
◇	137	8.0	10.0	VKF-E	0.6	
	Computed	10.0	---	---	0.35	
		12.0	---	---	0.25	
		16.0	---	---	0.20	



#### a. Small Size Tunnels

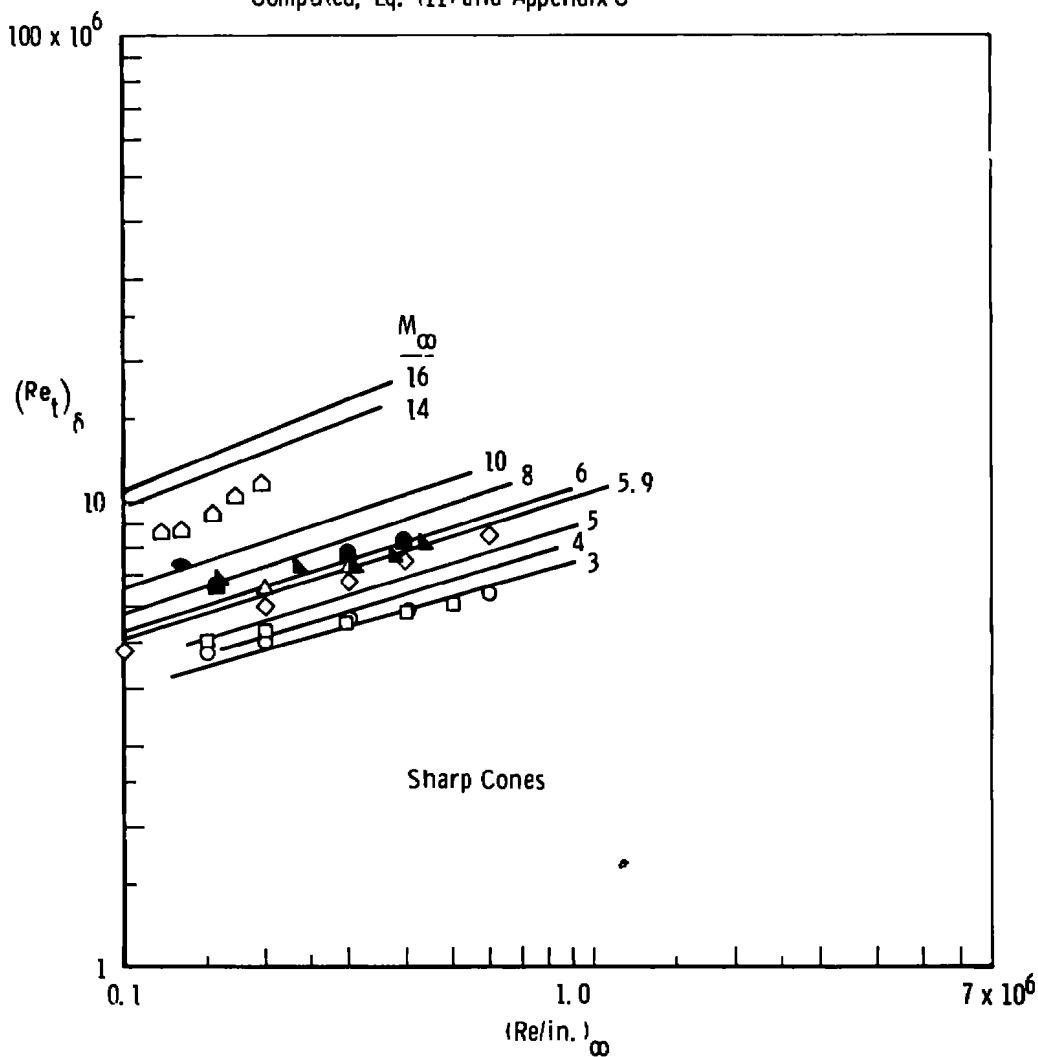
Figure X-9. Effect of Mach number and unit Reynolds number on sharp-cone transition data.

	Sym	Reference	$M_\infty$	$\theta_c$ , deg	Tunnel	$(T_w/T_{aw})_{\text{tunnel wall}}$
Experimental Data	○	Present Study	$\approx 7.5$	10	AEDC-VKF-F (40 in. Diameter)	0.3
	□	26	8.0	5, 10, 16	NASA Langley (18.3 in. Diameter)	0.6
— Computed Using Eq. (11) and Appendix C						



b. Medium Size Tunnels  
Figure X-9. (Continued).

	Sym	Reference	$M_\infty$	$\theta_c$ , deg	AEDC Tunnel	$(T_w/T_{aw})_{\text{tunnel wall}}$
Experimental Data	○	Present Study	3.0	5.0	VKF-A (40 by 40 in.)	1.0
	□		4.0	5.0		1.0
	◇		5.0	5.0		1.0
	△		5.9	5.0		0.9
	▲	137	6.0	6.0	VKF-B (50 in. Diameter)	0.8
	■	137	8.0	6.0	VKF-B (50 in. Diameter)	0.5
	◆	165	10.0	6.0	VKF-C (50 in. Diameter)	0.35
	◻	21	14.2	9.0	VKF-F (54 in. Diameter)	0.2
— Computed, Eq. (11) and Appendix C						



c. Large Size Tunnels  
Figure X-9. (Continued).

should be noted that the planar  $Re_t$  data presented in Figure X-8 have a slightly steeper slope compared to the cone data in Figure X-9.

The variations of  $Re_t$  data with Mach number for several different size tunnels are shown in Figures X-10 and X-11 for planar models and sharp cone models, respectively. Variation in  $Re_t$  with  $M_\infty$  is not strongly influenced by tunnel size for either planar or cone models. These data also indicate that the changes in  $Re_t$  data with changing  $M_\infty$  is significantly greater for planar models than sharp-cone models. The estimated values of  $Re_t$  obtained from the computer code are in good agreement with the experimental data as shown in Figures X-10 and X-11 except for the AEDC-VKF Tunnel D cone data at  $M_\infty \approx 4$ . A contributing factor to this discrepancy between the experimental data and computed values at  $M_\infty \approx 4$  is the disagreement between the measured tunnel wall  $\delta^*$  and the theoretical value of  $\delta^*$  used in the computer code (see Figure B-7 in Appendix B, page 339).

It is obvious from the results presented in Figures X-10 and X-11 that transition data from different sizes of supersonic-hypersonic wind tunnels cannot be used to establish "true" Mach number trends.

Figure X-12 presents  $(Re_t)_\delta$  data as a function of cone local Mach number for a free-stream Mach number of eight. The data for the 7.5- and 15.8-deg cones were published in Reference (130), and all the data shown in Figure X-12 were later published in Reference (121). For a given free-stream Mach number, there are two cone angles which will produce equivalent local unit Reynolds numbers, but significantly different local cone surface Mach numbers (see Figure D-2 in Appendix D, page 376). Figure X-12 shows that when the local Mach number was changed

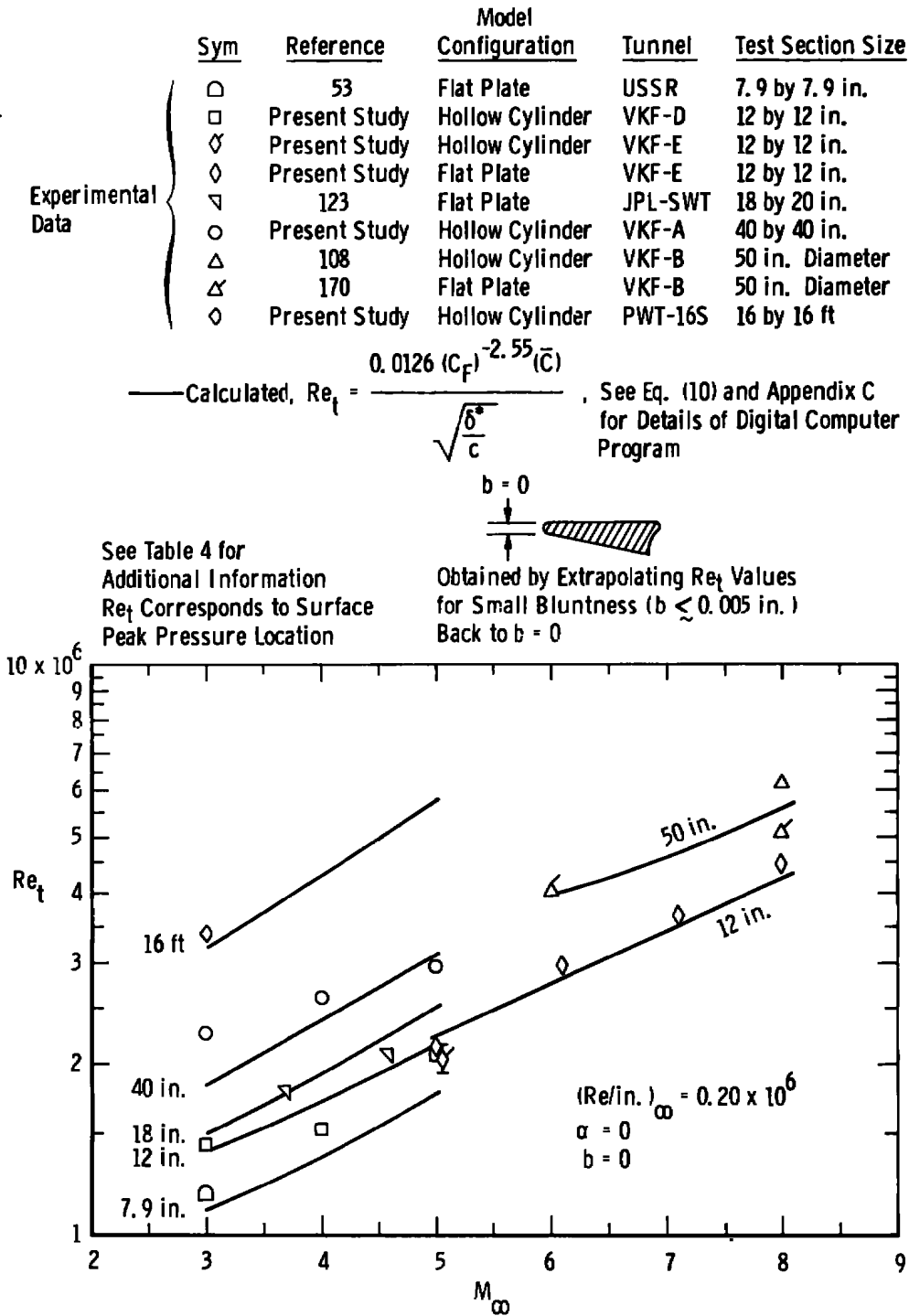


Figure X-10. Variation of planar model transition Reynolds numbers with tunnel size and Mach number.

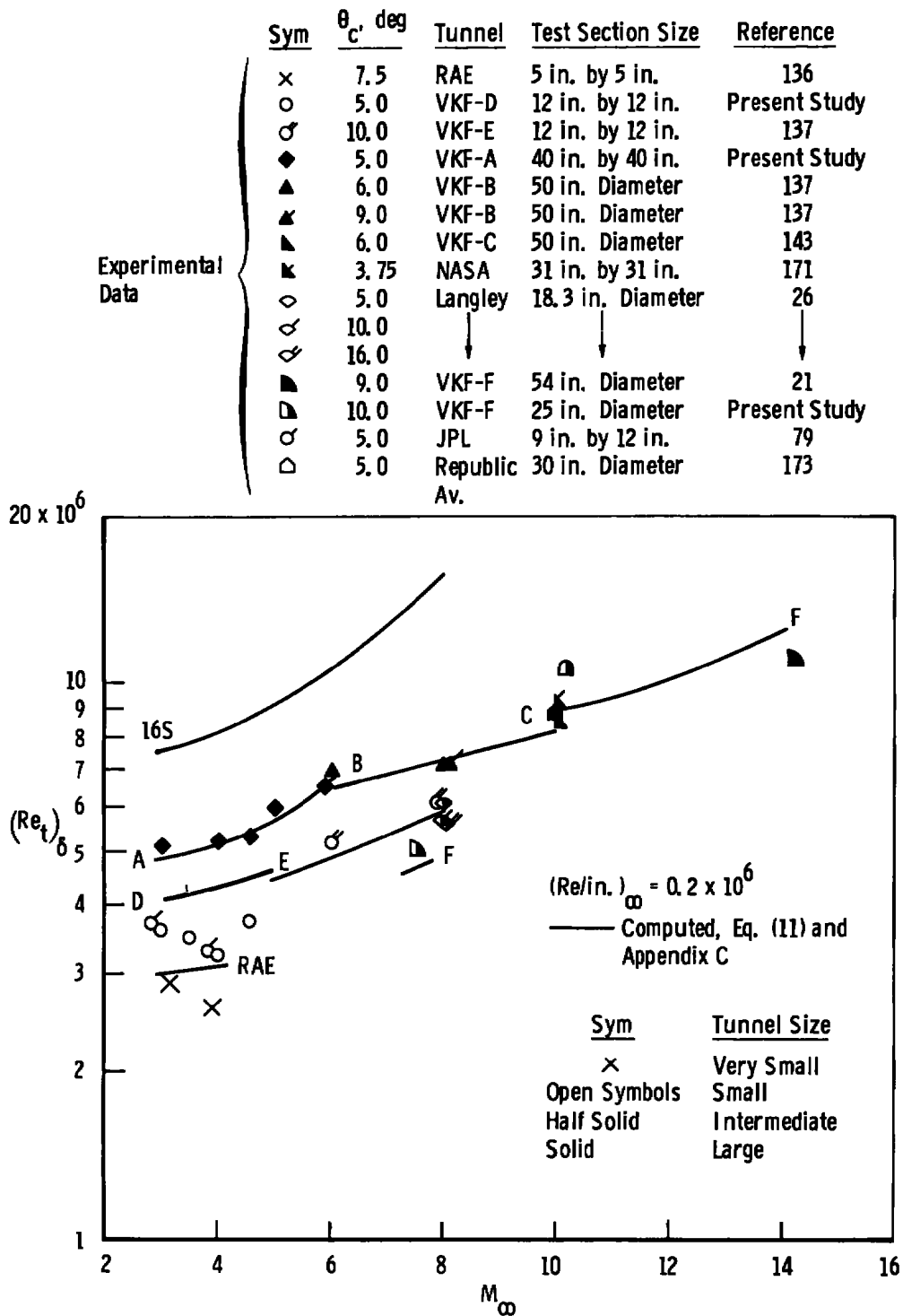
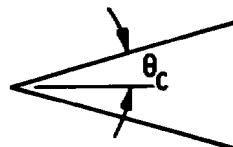


Figure X-11. Variation of sharp-cone transition Reynolds numbers with tunnel size and Mach number.

Sym	$(Re/in.)_{\delta}$ $\times 10^{-6}$	$\theta_c$ , deg	
		5, 20.1	7.5, 15.8
		$(Re/in.)_{\infty}$ $\times 10^{-6}$	$(Re/in.)_{\infty}$ $\times 10^{-6}$
○	0.116	0.092	0.082
■	0.224	0.18	0.16
◇	0.483	0.38	0.34
▲	1.17	0.93	0.83



$$(Re_t)_{\delta} = (Re/in.)_{\delta} x_t$$

$x_t$  determined from heat transfer data obtained using fusible paint.

Data from References 130 and 121

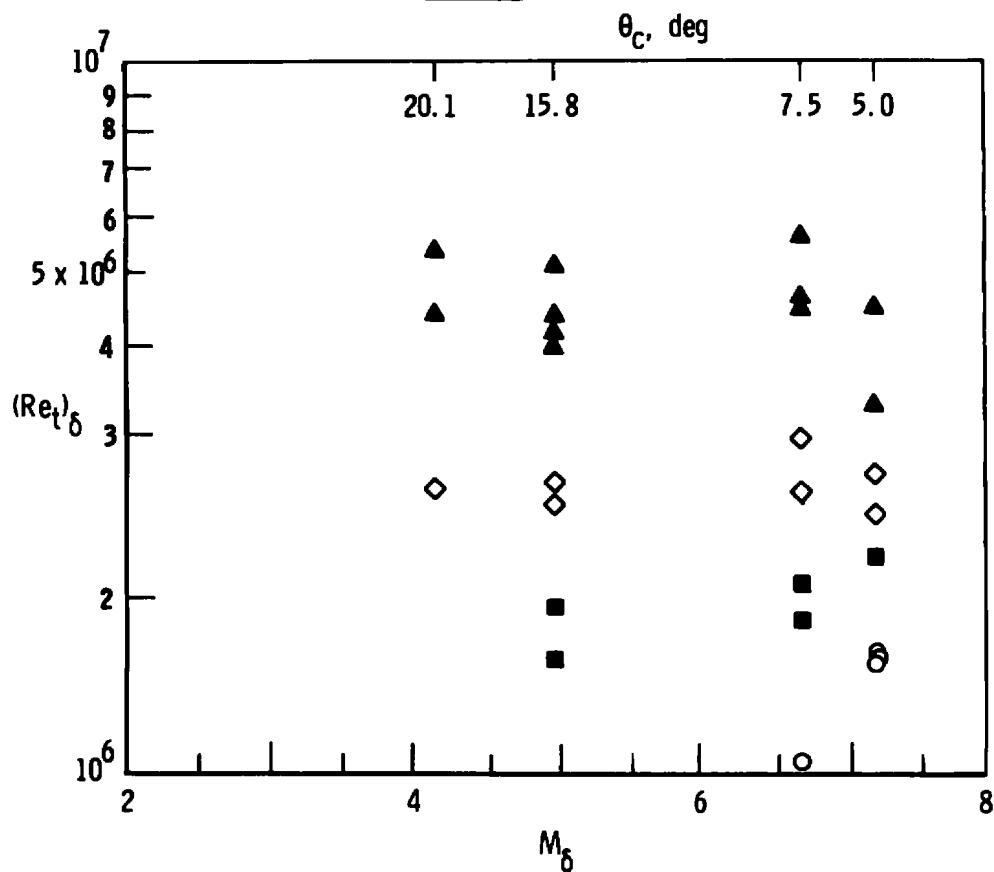


Figure X-12. Transition Reynolds numbers as a function of local Mach number for sharp cones,  $M_{\infty} = 8$ .

from approximately 4 to 7 for constant free-stream conditions [constant  $M_\infty$ , constant  $(Re/in.)_\infty$ ], there was no significant change (upward trend) with Mach number except at the lowest  $(Re/in.)_\infty$  value. Recent data published in Reference (26) using the same approach confirm the invariance of  $(Re_t)_\delta$  with  $M_\delta$  as shown in Figure X-13.

The experimental data presented in Figures X-12 and X-13 are particularly significant to the findings of the present research. The aerodynamic-noise-transition hypothesis formulated in this research and the resulting empirical equation developed [Eqs. (10) and (11)] predict no change in  $(Re_t)_\delta$  with changing  $M_\delta$ , provided the free-stream conditions  $M_\infty$  and  $(Re/in.)_\infty$  do not change. Predictions from the aerodynamic-noise-transition computer code [Eq. (11) and Appendix D] are presented in Figure X-13 and the agreement with the data is considered excellent. Note that the computer code predicted the slight increase in  $(Re_t)_\delta$  with increasing  $M_\infty$  that is evident in the data. This is a result of the  $\theta_c$  values not being selected to provide a constant  $(Re/in.)_\delta$  value as was the case for data shown in Figure X-12.

It should be pointed out that the 5- and 20-deg cone angles produce equivalent local unit Reynolds numbers as do the 7.5- and 15.8-deg cones for  $M_\infty = 8$  (see Figure X-12). However, for the local unit Reynolds number conditions to have been equivalent for both sets of cone data as listed in Figure X-12, there would necessarily have been a 10% to 15% difference in  $(Re/in.)_\infty$ . A 15% difference in  $(Re/in.)_\infty$  would produce a maximum change in  $Re_t$  of approximately 10%, and this is well within the scatter of the data shown in Figure X-12. Consequently, it seems justified to compare the four sets of data directly.



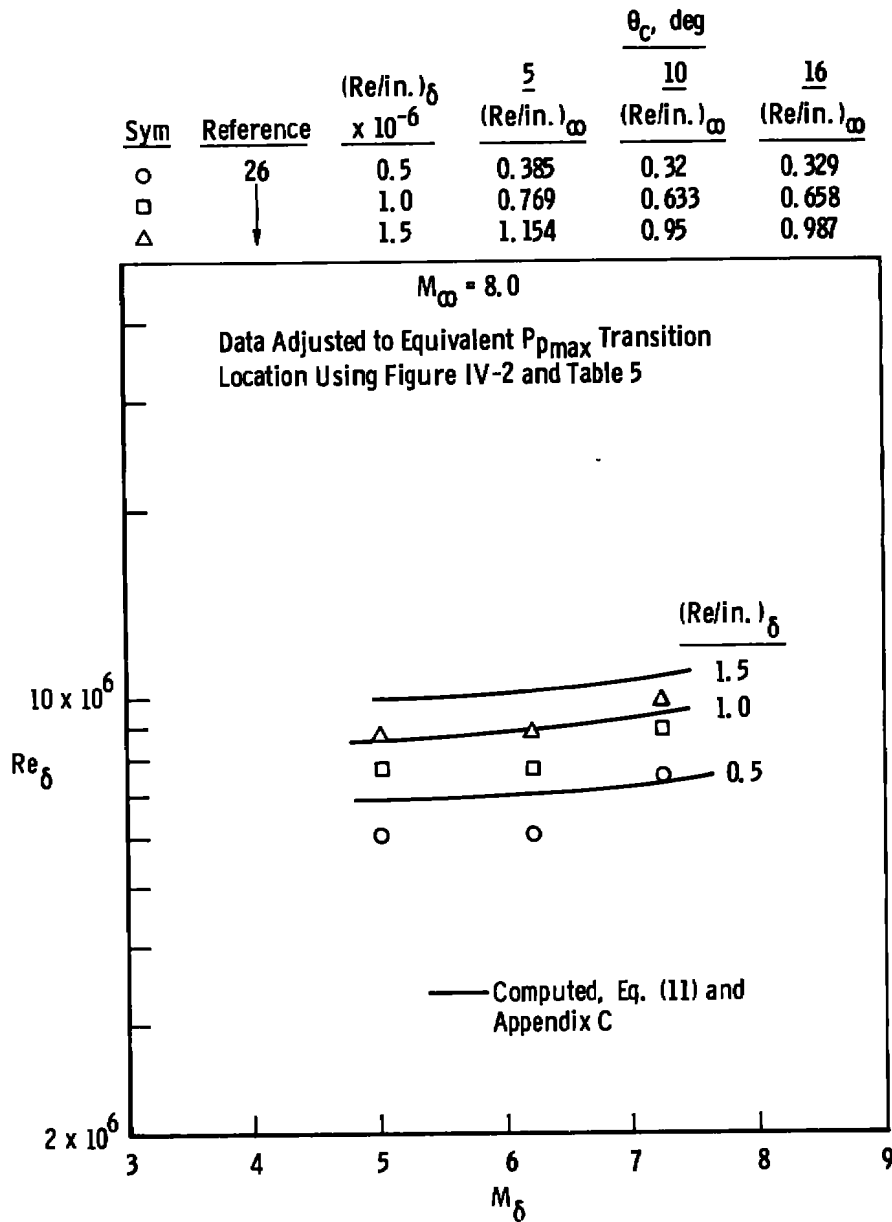


Figure X-13. Comparisons of predicted and measured  $(Re_t)_\delta$  values on sharp cones for various local Mach numbers,  $M_\infty = 8$ .

The results shown in Figures X-8 through X-13 strongly indicate a large, if not major, part of  $Re_t$  variation with Mach number in wind tunnels is related to the presence of free-stream aerodynamic noise disturbances. These results also indicate that transition data obtained in wind tunnels cannot be used to establish true Mach number effects.

The standard deviation ( $\sigma$ ) for the  $Re_t$  experimental data points and the computed values shown in Figs. X-1 through X-13 was determined. Based on these 262 data points, the standard deviation was found to be 11.6%. Figure X-14 presents a summary plot of the measured versus the computed  $Re_t$  values for the specified 262 data points. Two other transition studies have estimated standard deviation values for empirical prediction methods. Deem, et. al (Ref. 63), found a standard deviation of 33% (based on 291 data points as shown in Fig. II-10) and Beckwith and Bertran (Ref. 81) found  $\sigma \approx 35\%$  (see Fig. II-11) for empirical equations developed at NASA Langley.

Based on a direct comparison of the standard deviation values, it is seen that the current empirical equation provides a considerable improved method for predicting the location of boundary-layer transition.

Dougherty and Steinle indicated in Reference (52) that the aerodynamic-noise-transition correlation developed in this research (10) could be applied down to  $M_\infty = 2$ . As discussed in Chapter IX, the present aerodynamic-noise-transition correlation was restricted to  $M_\infty \gtrsim 3$  in the present research. This restriction was applied because of possible influences of velocity fluctuation disturbances (stilling chamber vorticity fluctuations) which can be present to a significant degree in the

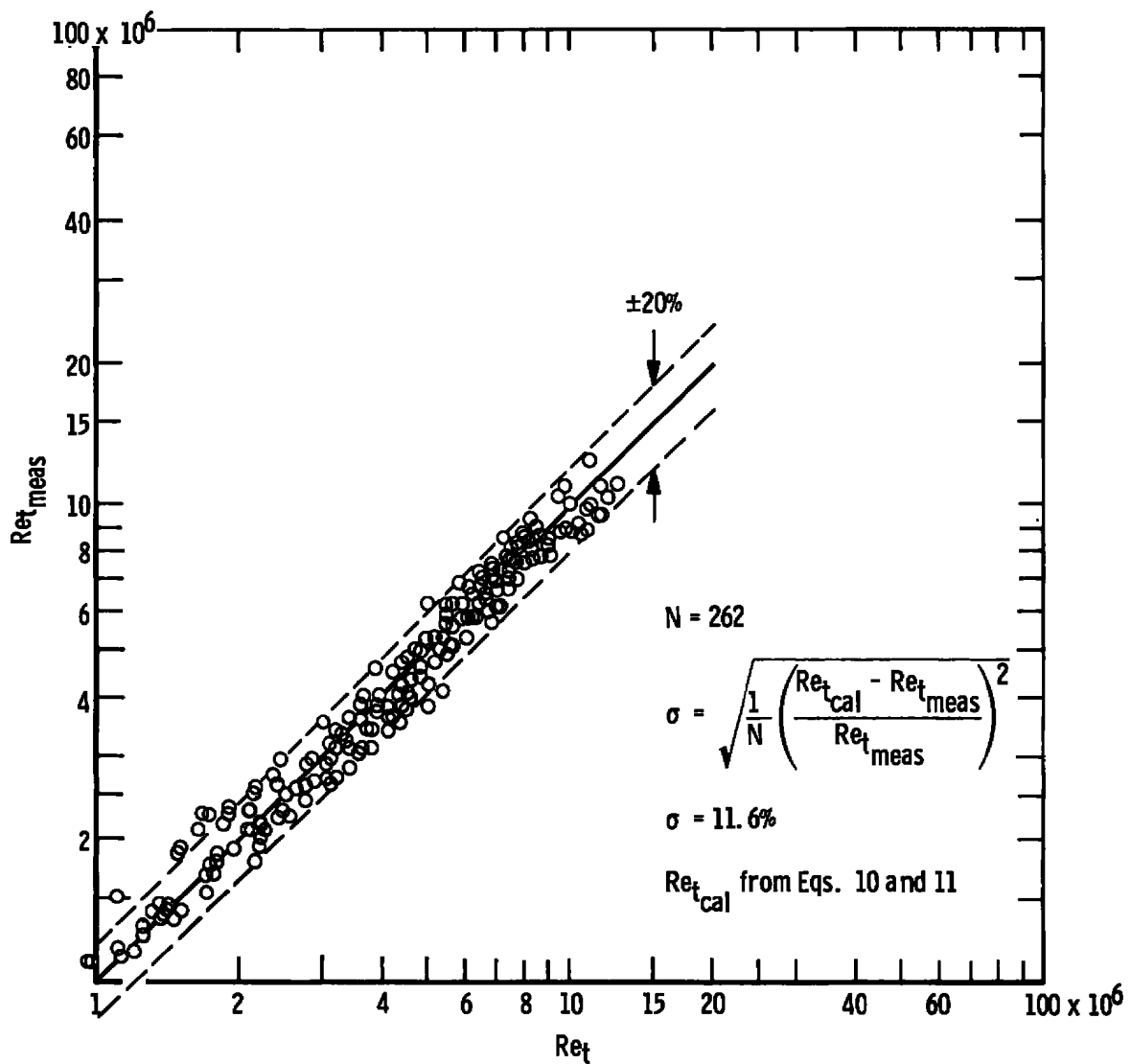
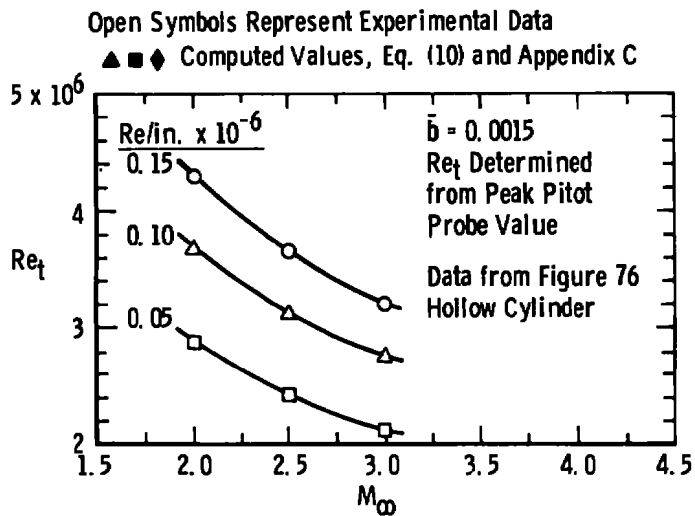
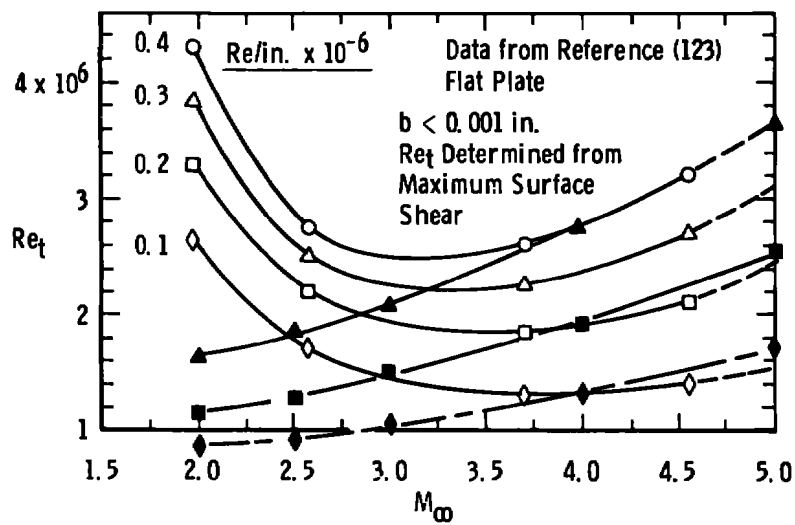


Fig. X-14 Comparison of Predicted and Measured Transition Reynolds Number from Current Method (Eqs. (10) and (11) and the Fortran Computer Program, Appendix C)



a. AEDC-PWT Tunnel 16S Transition Data



b. JPL Transition Data

Figure X-15. Variation of transition Reynolds numbers with tunnel Mach number.

tunnel free stream and which are not accounted for in the present correlation. Wind tunnel  $Re_t$  data also exhibit a reverse trend with Mach number for  $M_\infty \lesssim 3$ , as shown in Figure X-15. This trend is apparently present in all sizes of wind tunnels. This assumes, of course, that the data presented in Figure X-15 from the AEDC-PWT Tunnel 16S obtained in the present research and data from the JPL 18- by 20-in. tunnel published in Reference (123) are considered to be representative of all tunnels.

Included in Figure X-15b are the computed values of  $Re_t$  obtained from the computer code, Appendix C. It is seen from Figure X-15b that the aerodynamic-noise-transition correlation developed in the present research [Eq. (10) from Figure IX-8, page 249] and the resulting digital computer code developed in Appendix C is not valid for  $M_\infty \lesssim 3.0$ .

It is of interest to point out that Dougherty and Steinle (52) were able to correlate pressure fluctuation data ( $\tilde{p}/q_\infty$ ) from the AEDC-PWT Tunnel 16S directly with the parameter  $C_F \sqrt{\delta^*/C}$  for  $M_\infty = 1.7$  to 3.0. They also were able to correlate the measured  $(Re_t)_\delta$  data from the AEDC-PWT Tunnel 16S (Figure VII-3, page 186, and  $b = 0$ ) with the measured  $\tilde{p}/q_\infty$  values for  $M_\infty = 2.0, 2.5$ , and 3.0.

## V. COMPARISON OF TUNNEL AND BALLISTIC RANGE $Re_t$ DATA

Figure X-16 presents a direct and quantitative comparison of transition data from sharp slender cones obtained in wind tunnels and from an aeroballistic range at equivalent local Mach numbers using similar methods of transition detection. At a comparable  $(Re/in.)_\delta$  value,

Sym	Facility	$M_\delta$	$T_w/T_{aw}^\circ$	$\theta_c$ , deg	Source	Method of Detection
○	VKF Range K	4.3	$\approx 0.18$	10	Ref. 27	Shadowgraph - Schlieren
△	VKF Tunnel D (12 by 12 in.)	4.3	$\approx 1.0$	5	Present Study	Schlieren
□	VKF Tunnel A (40 by 40 in.)	4.3	$\approx 1.0$	5	Present Study	Surface Pitot Probe Maximum Value Adjusted to Schlieren Location ( $Re_t$ ) <sub>Schlieren</sub> $\approx 0.82$ ( $Re_t$ ) <sub>pmax</sub>
---	PWT-Tunnel 16S (16 by 16 ft)	4.3	$\approx 1.0$	5	Present Study	Estimated from Two-Dimensional Data Surface Probe Data

<sup>°</sup>Model Wall Temperature Ratio

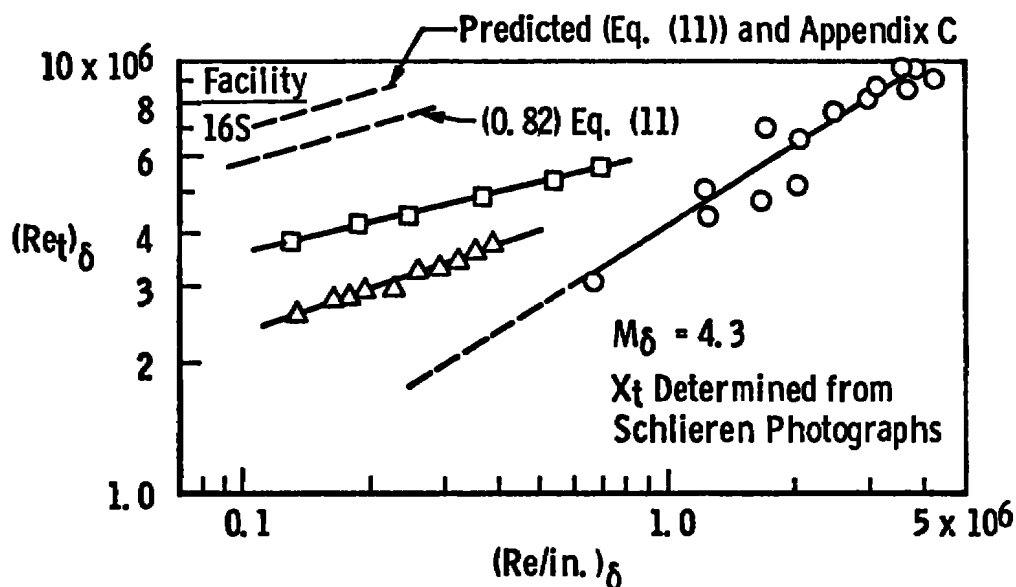


Figure X-16. Comparison of sharp-cone transition Reynolds numbers from wind tunnels and an aeroballistic range.

these data suggest that the range  $(Re_t)_\delta$  data are significantly lower than the tunnel results, even for the 12-in. tunnel.

One major nonsimilarity between the tunnel and range experimental conditions is in the surface temperature ratios. Transition reversals have been predicted theoretically (174) and verified experimentally (175,176), and possible transition reversals have been shown experimentally (176). However, to the author's knowledge, there are no experimental data that show transition Reynolds number to decrease below the adiabatic wall value for any degree of surface cooling. Therefore, if comparisons could be made where the model wall to free-stream temperature ratios were comparable, then a larger difference between tunnel and range  $(Re_t)_\delta$  data than suggested by Figure X-16 might exist.

One question that naturally arises is whether adverse environmental or model disturbances could be affecting the range results. It is also of interest to note that the data in Figure X-16 indicate a significant difference between the tunnel and range  $Re_t$  versus  $(Re/in.)_\delta$  slope. The significance of the unit Reynolds number effect evident in the range data and the results of preliminary investigations on range noise disturbances were reported by Potter (27).

Recently additional ballistic range transition data have been published by Potter (23). Potter conducted a thorough and systematic investigation of the possible effects of model nose-tip ablation, small changes in angle of attack, range disturbances, model vibrations, and model surface roughness. However, none of the above were identified as being the cause of the unit Reynolds number effect or the low  $(Re_t)_\delta$  values exhibited in Figure X-16. A particularly interesting result ob-

tained by Potter was that  $(Re_t)_\delta$  data obtained on 10-deg cone models at Mach numbers of  $M_\infty = 5.0$  ( $M_\delta = 4.3$ ) and  $M_\infty = 2.3$  ( $M_\delta = 2.1$ ) exhibited no Mach number effect. The range transition "anomaly" remains as one of the most baffling and challenging of ground testing transition phenomena.



## CHAPTER XI

## COMPARISONS OF PLANAR AND SHARP CONE TRANSITION REYNOLDS NUMBERS

Potter and Whitfield (137) made a qualitative comparison of  $(Re_t)_\delta$  data obtained on cones and planar bodies from several sources and observed that the ratio of  $(Re_t)_{\delta, \text{cone}} / (Re_t)_{\delta, \text{planar}}$  appeared to decrease from a value of approximately 3 at  $M_\infty \approx 3$  to a value of about 1.1 at  $M_\infty \approx 8$ . Based on the results of Pate and Schueler (10) and Pate (11), Whitfield and Iannuzzi (21) concluded that attempts at a comparison of  $(Re_t)_\delta$  data from various high-speed facilities as done in Reference (137) must now be viewed with reservation, and the relationship between cone and planar  $(Re_t)_\delta$  results could not be established from presently available data.

Therefore, one of the objectives of this research was to attempt to establish a quantitative correlation of sharp slender cones (axisymmetric) and flat-plate, hollow-cylinder (planar) transition Reynolds numbers at supersonic and hypersonic speeds.

Based on the results of the present investigation, it was concluded that a correlation was possible only if cone and flat-plate data were obtained in the same test facility, under identical test conditions, using equivalent methods of transition detection. There are no available investigations of the receptivity of a laminar boundary layer to radiated noise. Consequently, it was necessary to obtain  $(Re_t)_\delta$  data exposed to various intensity levels of radiated noise while continuing to maintain a constant free-stream unit Reynolds number and Mach number

if the cone-planar  $(Re_t)_\delta$  relation was to be determined. This was accomplished by obtaining test data in significantly different-sized tunnels (AEDC-VKF Tunnels A and D). The large variation of  $(Re_t)_\delta$  with tunnel size has been shown in Figures VIII-20, page 216, VIII-21, page 217, X-1, page 257, and X-2, page 258. The increase in cone  $(Re_t)_\delta$  values above flat-plate values was shown in the basic data presented in Figures VIII-20, page 216, VIII-21, page 217, VII-5, page 173, and VII-6, page 175.

Presented in Figure XI-1 is a correlation of cone and flat-plate  $(Re_t)_\delta$  data developed from the data obtained in this study (AEDC-VKF Tunnels A and D) and data from three other test facilities. It can be argued that various procedures are available for reducing this type of data. The three procedures used are outlined in the legend of Figure XI-1. The significant conclusions to be drawn from Figure XI-1 are: (a) the  $(Re_t)_\delta$  ratio appears to be about 2.2 to 2.5 at  $M_\infty = 3$ , (b) the trend decreases monotonically with increasing Mach number to a value of approximately 1.0 to 1.1 at  $M_\infty = 8$ , (c) close inspection of these results at a given Mach number ( $M_\infty = 3$  to 5) suggests a decrease in the  $(Re_t)_\delta$  ratio with increasing tunnel size, and (d) the  $(Re_t)_\delta$  ratio is also slightly dependent on the method of analysis.

An empirical equation for the cone-planar  $(Re_t)_\delta$  ratios can be obtained by ratioing Eqs. (10) and (11). Then

$$\frac{(Re_t)_{\delta, \text{ cone}}}{(Re_t)_{\delta, \text{ planar}}} = \frac{\text{Eq. (10)}}{\text{Eq. (11)}} = 3880 (C_F)^{1.15} \frac{(\bar{c})_{\text{cone}}}{(\bar{c})_{\text{flat plate}}} \quad (12)$$

Sym	Configuration	$\theta_c$ , deg	$M_\infty$	$M_\delta$	$(Re/in.)_\delta \times 10^{-6}$ Range	Facility	Method-of-Detection	Source	$f_m$ , in.
○	Sharp Cone	5	3 to 4.5	2.9 to 4.3	0.15 to 0.4	VKF-D (12 by 12 in.)	Maximum Pitot Pressure	Present Study and Reference (37)	44
	Hollow Cylinder ( $b = 0$ )		3 to 4.5	3 to 4.5					48.5
△	Sharp Cone	5	3 to 5	2.9 to 4.7	0.15 to 0.6	VKF-A (40 by 40 in.)	Maximum Pitot Pressure	Present Study	215
	Hollow Cylinder ( $b = 0$ )	---	3 to 5	3 to 5					231
□	Sharp Cone	5, 6	6	5.5	0.15 to 0.4	VKF-A	Shadowgraph	Present Study VKF	215
	Flat Plate ( $b \approx 0$ )		6	6		VKF-B (50-in. Diam)	$\dot{q}_{\text{maximum}}$	Reference (170)	232
◇	Sharp Cone	6, 9	8	7.0, 6.4	0.2, 0.3	VKF-B (50-in. Diam)	$\dot{q}_{\text{max}}$ and Shadowgraph	Reference (137) and VKF	245
	Hollow Cylinder ( $b = 0$ )		8	8			$(T_w)_{\text{max}}$ and Pitot Pressure	Reference (37)	232
▽	Sharp Cone	6, 9	8	7.0, 6.4	0.2	VKF-B (50-in. Diam)	$\dot{q}_{\text{max}}$ and Shadowgraph	Reference (137) and VKF	245
	Flat Plate ( $b \approx 0$ )		8	8			Pitot Pressure	Reference (63)	232
○	Sharp Cone	5	3.1	2.98	0.1 to 0.6	NACA-Lewis (12 by 12 in.)	$T_w$ max	Reference (120)	≈40
	Hollow Cylinder	---	3.1	3.1					40.5
○	Sharp Cone	2.5	5.0	4.90	0.15 to 0.5	NASA-Lewis (12 by 12 in.)	$T_w$ max	Reference (119)	47
	Hollow Cylinder	---	5.0	5.0					47

Flagged Symbols - Evaluated at Equivalent  $(Re/in.)_\delta$  and  $M_\delta$  Values ( $(Re/in.)_\delta = 0.2 \times 10^6$ )

Open Symbols - Evaluated at Equivalent  $(Re/in.)_\delta$  and  $M_\infty$  Values

Solid Symbols - Evaluated at Equivalent  $(Re/in.)_\infty$  and  $M_\delta$  Values (From Data Cross Plots)

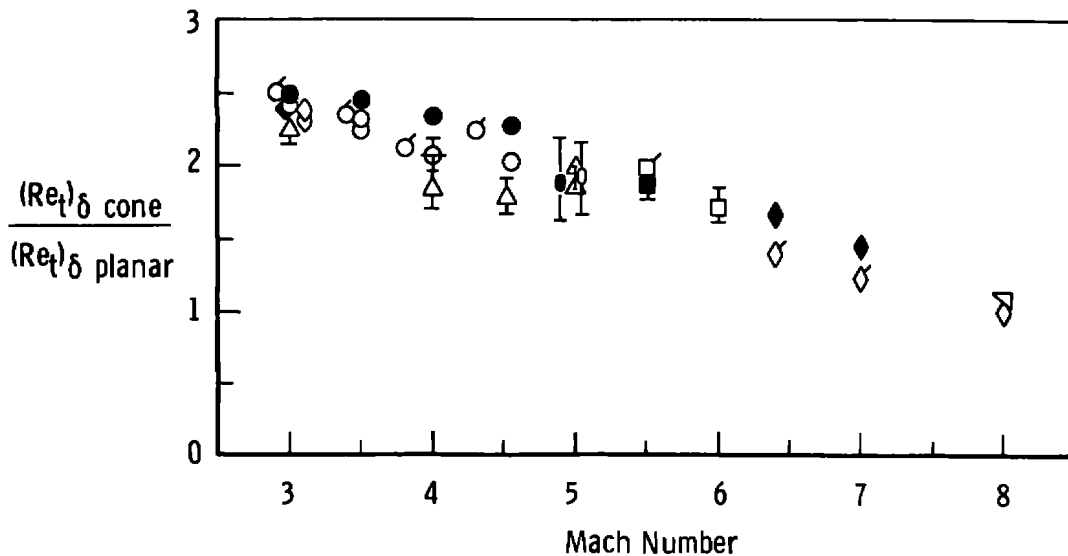


Figure XI-1. Correlation of axisymmetric and planar transition Reynolds number ratios.

Predicted transition ratios using Eq. (12) are presented in Figure XI-2 for a large range of tunnel sizes, Mach numbers, and  $(Re/in.)_{\infty}$  values. The experimental data for the 40- and 50-in. tunnels ( $3 \leq M_{\infty} \leq 8$ ) are in good agreement with the empirically predicted ratios. The data also indicate, qualitatively at least, a decrease in the transition ratio with an increase in tunnel size.

Many investigators have referenced the analytical analysis of Tetervin (138,139) and Battin and Lin (140) when attempting to explain the cone-planar  $(Re_t)_{\delta}$  ratios of approximately three that were observed experimentally.

Battin and Lin (140) concluded that the minimum critical Reynolds number  $(R_{x,cr})$  for a cone was three times greater than for a flat plate. However, the agreement between the ratio of approximately three exhibited by previously published transition data at moderate supersonic Mach numbers and the stability theory ratio of three is perhaps only fortuitous, as demonstrated by the data correlations presented in Figures XI-1 and XI-2.

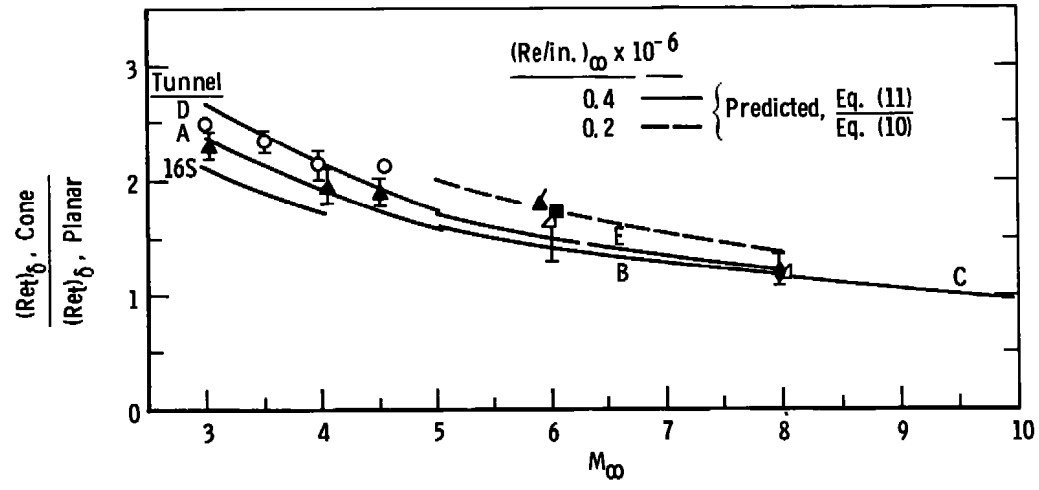
From Tetervin's theoretical analysis (138)

$$\frac{(Re_t)_{\delta, \text{ cone}}}{(Re_t)_{\delta, \text{ planar}}} = 1 + 2 \frac{(Re_t)_{\delta, \text{ planar-minimum}}}{(Re_t)_{\delta, \text{ planar}}} \quad (13)$$

The  $(Re_t)_{\delta, \text{ planar-minimum}}$  values represent the theoretical minimum transition Reynolds number that can occur on a flat plate, and these values are presented as a function of Mach number and model surface temperature in Reference (138).

▮ Variation of Experimental Data with  $Re/in.$

Symbols Are Identified in Figure XI-2b



a. Variation with Mach Number

Figure XI-2. Comparison of predicted and measured cone planar transition ratios.

Experimental Data Evaluated at Equivalent  $(Re/in.)_{\infty}$  and  $M_{\infty}$  Values

Sym	Configuration	$\theta_c$ , deg	$M_{\infty}$	$M_{\delta}$	$(Re/in.)_{\infty} \times 10^{-6}$ Range	Facility	Method of $x_t$ Detection	Source
○	Sharp Cone	5	3 to 4.5	2.9 to 4.3	0.15 to 0.5	VKF-D (12 by 12 in.)	Maximum Surface Pitot Probe Pressure	Present Study
	Hollow Cylinder (b = 0)	-	3 to 4.5	3 to 4.5	0.15 to 0.5			Present Study and Reference (37)
▲	Sharp Cone	5	3 to 5	2.9 to 4.7	0.15 to 0.5	VKF-A (40 by 40 in.)	Maximum Surface Pitot Probe Pressure	Present Study
	Hollow Cylinder (b = 0)	-	3 to 5	3 to 5	0.15 to 0.5			Reference (11)
◀	Sharp Cone	5	5.9	5.5	0.2	VKF-A (40 by 40 in.)	Schlieren	Present Study
	Hollow Cylinder (b = 0)	-	5.9	5.9	0.2		Schlieren	Present Study
■	Sharp Cone	6	6	5.5	0.2	VKF-B (50-in. Diam)	Adjusted Max. Heat Transfer (Adjusted by 1.08)	Reference (137 and VKF
	Flat Plate (b = 0)	-	6	6	0.2		Maximum Pitot Press.	Present Study and Reference (170)
◆	Sharp Cone	6, 9	8	7.0, 6.4	0.15 to 0.3	VKF-B (50-in. Diam)	Maximum Heat Trans. (No Adjustment)	Reference (137) and VKF
	Hollow Cylinder (b = 0)	-	8	8	0.15 to 0.3		Maximum Pitot Press.	Reference (108)
△	Sharp Cone	10	6, 8	5.0, 6.2	0.3 to 1.0, 0.35 to 0.55	VKF-E (12 by 12 in.)	Shadowgraph (Adjusted by 1.1)	Reference (137)
	Flat Plate (b = 0)	-	6, 8	6, 8	0.3 to 1.0, 0.35 to 0.55		Maximum Pitot Press.	Reference (169)

b. Specific Information

Figure XI-2. (Continued).

Tetervin's theoretical transition ratio [Eq. (12)] was derived using linear stability theory. As shown by Eq. (12) when  $(Re_t)_{\delta, \text{planar}}$  is near the minimum possible value, then the cone-planar ratio approaches a value of three. As  $(Re_t)_{\delta, \text{planar}}$  moves farther downstream then Eq. (12) approaches a value of unity. The assumptions that must be applied to Tetervin's analysis are: (a) free-stream disturbances are nonexistent, or (b) the disturbances affect only the laminar region of instability upstream of the respective  $(Re_t)_{\delta, \text{planar-minimum}}$  locations, or (c) the absorptivity characteristics of the laminar layers on both the cone and flat plate downstream of the  $(x_t)_{\text{planar-minimum}}$  locations are identical. There are no available experimental supersonic data that comply with assumption (a), and with disturbances present there is no evidence to support assumptions (b) and (c). Nevertheless, it appears to be of interest to use Eq. (12) and the theoretical  $(Re_t)_{\delta, \text{planar-minimum}}$  values of Reference (138) in conjunction with the experimental  $(Re_t)_{\delta, \text{planar}}$  values presented in Figure X-10, page 258, of this study to estimate a few cone-planar transition ratios. The results are listed in column six of Table 7.

An increased value for Eq. (12) can be obtained if experimentally measured minimum critical Reynolds number [Figure 3 of Reference (139), showing the stability data of Schubauer and Skramstad, Laufer and Vrebalovich, and Demetriades] is used instead of the theoretical estimates of Tetervin. Also the  $(Re_t)_{\delta}$  values presented in Figure X-10, page 258, [and used in the evaluation of Eq. (12), i.e., column 6] correspond to the maximum pitot probe pressure location which is on the order of a factor of two downstream of what one might consider as a

Table 7. Estimated cone-planar transition ratios.

1	2		3	4	5	6	7
						$1 + 2 \left( \frac{\textcircled{4}}{\textcircled{3}} \right)$	$1 + 2 \left( \frac{\textcircled{5}}{\textcircled{3}/2} \right)$
AEDC Tunnel	Free-Stream Conditions		Experimental (Figure X-10)	Theoretical [Reference (139)]	Critical Reynolds Number from Stability Experiments [Reference (139)]	Estimated, Eq. (13)	Estimated, Eq. (13) with Adjustments
	$M_\infty$	$(Re/n)_\infty \times 10^{-6}$	$(Re)_\delta, \text{Planar} \times 10^{-6}$	$Re)_\delta, \text{Planar-Minimum} \times 10^{-6}$		$\frac{(Re)_\delta, \text{Cone}}{(Re)_\delta, \text{Planar}}$	
D	3	0.2	1.42	0.016	$\approx 0.08$	1.022	1.23
A	3	0.2	2.25	0.016	$\approx 0.08$	1.014	1.14
16S	3	0.2	3.35	0.016	$\approx 0.08$	1.010	1.10
D	5	0.2	2.05	0.044	$\approx 0.5$	1.042	1.98
A	5	0.2	2.95	0.044	$\approx 0.5$	1.030	1.68
B	8	0.2	6.15	0.145	---	1.048	



"measurable" beginning of transition. Incorporating these adjustments into Eq. (12) produces the cone-planar ratios tabulated in column seven.

For a factor of three to exist in the estimated cone-planar transition ratio at  $M_\infty = 3$  would require, depending on the method of analysis, a two-dimensional  $(Re_t)_\delta, \text{planar}$  value of 16,000 to 80,000. To the author's knowledge, these values are on the order of a factor of 10 to 50 below any published data. Therefore, it would seem that the cone-to-flat-plate ratio of three quoted by many investigators as being theoretically predicted by Eq. (12) is perhaps without adequate foundation, and the apparent agreement with experimental data that appeared to exist is perhaps only fortuitous. Similarly, the decrease to approximately one exhibited by the experimental data in Figures XI-1 and XI-2 as the Mach number approaches eight does not appear, based on the results in Table 7, to be explained by Eq. (12). Based on the available information it is suggested that the absolute values produced by Eq. (12) are, at best, not adequate for accurate predictions or for laying a foundation for analyzing experimental transition results. However, it is of interest to note the trend predicted by Eq. (12) for a constant Mach number when the value of  $(Re_t)_{\delta, \text{planar-minimum}}$  is assumed constant. The cone-planar  $(Re_t)_\delta$  ratio as given by Eq. (13) is seen to decrease with increasing experimental  $(Re_t)_{\delta, \text{planar}}$  values--which will occur with increasing tunnel size or increasing  $(Re/in.)_\delta$ --and this trend is in agreement with the experimental results shown in Figures XI-1 and XI-2.

## CHAPTER XII

## CONCLUSIONS

Significant results obtained from this experimental research program, which was directed toward investigating the relationship between free-stream disturbances and boundary-layer transition on sharp flat plates and sharp slender cones in conventional supersonic-hypersonic wind tunnels, can be summarized as follows:

1. A set of unique experiments using a "shroud model" concept has demonstrated conclusively that radiated noise emanating from the turbulent boundary layer on wind tunnel walls can dominate the transition process.
2. Transition Reynolds numbers are strongly dependent on tunnel size. Boundary-layer transition data measured in supersonic wind tunnels ( $M_\infty \gtrsim 3$ ) having test section heights from 0.5 to 16 ft have demonstrated a significant and monotonic increase in transition Reynolds numbers with increasing tunnel size. Free-stream radiated noise measurements measured on a flat-plate microphone model have shown that the intensity levels decrease with increasing tunnel size.
3. Model transition Reynolds number data have been shown to correlate with the free-stream radiated noise intensities levels.
4. Correlations of transition Reynolds numbers as a function of the radiated noise parameters [tunnel wall  $C_f$  and  $\delta^*$  values and tunnel circumference ( $c$ )] have been developed.

- a. Sharp-flat-plate transition Reynolds number data from 13 different wind tunnels having test section sizes from 7.9 in. to 16 ft, for Mach numbers from 3 to 8, and a unit Reynolds number per inch range from  $0.1 \times 10^6$  to  $1.9 \times 10^6$  were successfully correlated and the following empirical equation developed:

$$Re_t = \frac{0.0126 (C_{FII})^{-2.55} (\bar{c})}{\sqrt{\frac{\delta^*}{c}}}$$

- b. Sharp-slender-cone transition Reynolds number data from 17 wind tunnels varying in size from 5 to 54 in. for a Mach number range from 3 to 14 and a unit Reynolds number per inch range from  $0.1 \times 10^6$  to  $2.75 \times 10^6$  were successfully correlated and the following empirical equation developed:

$$(Re_t)_{\text{cone}} = \frac{48.5 (C_{FII})^{-1.40} (\bar{c})}{\sqrt{\frac{\delta^*}{c}}}$$

5. A FORTRAN IV digital computer code that will accurately predict transition locations on sharp flat plates and cones in all sizes of conventional supersonic-hypersonic wind tunnels has been developed. Based on comparisons of standard deviations, the accuracy of this technique is considerable better than previously published methods. The standard deviation ( $\sigma$ ), based on the difference between the calculated and measured  $Re_t$  values for 262 data points, using the present

method was 11.6% whereas other published methods give values  $\sigma$  between 30 and 40%.

6. The ratio of cone transition Reynolds numbers to flat-plate values does not have a constant value of three, as often assumed. The ratio will vary from a value of near three at  $M_\infty = 3$  to near one at  $M_\infty = 8$ . The exact value is unit Reynolds number and tunnel size dependent. The aerodynamic-noise-transition empirical equations predict that for  $M_\infty \gtrsim 10$  and  $(Re/in.) \gtrsim 0.4 \times 10^6$ , the ratio will be less than one.
7. Radiated noise dominance of the transition process offers an explanation for the unit Reynolds number effect in conventional supersonic-hypersonic wind tunnels.
8. The effect of tunnel size on transition Reynolds numbers must be considered in the development of data correlations, in the evaluation of theoretical math models, and in the analysis of transition sensitive aerodynamic data.
9. If a true Mach number effect exists, it is doubtful that it can be determined from data obtained in conventional supersonic-hypersonic wind tunnels because of the adverse effect of radiated noise.
10. The boundary-layer trip correlation developed by van Driest and Blumer (wherein the effective transition location "knee" can be predicted) has been shown to be valid for different sizes of wind tunnels and not dependent on the free-stream

radiated noise levels (see Appendix E). The trip correlation developed by Potter and Whitfield remains valid if the effect of tunnel size on the smooth body transition location is taken into account (see Appendix E).

11. Wind tunnel transition Reynolds numbers have been shown to be significantly higher than ballistic range values.
12. Radiated noise intensities (pressure fluctuations) measured with a hot wire in the tunnel free stream will be significantly lower than pressure fluctuation levels measured by a microphone flush mounted in a flat plate. Caution should be exercised when comparing free-stream pressure fluctuations obtained from hot wires positioned in the free-stream and a plate-mounted microphone.

## REFERENCES

1. Schlichting, H. Boundary Layer Theory, 4th Edition, McGraw-Hill, New York, 1960.
2. White, Frank M. Viscous Fluid Flow, McGraw-Hill, New York, 1974.
3. Emmons, H. W. "The Laminar-Turbulent Transition in a Boundary Layer," Part I, Journal of the Aeronautical Sciences, Vol. 18, No. 7, July 18, 1951, pp. 490-498.
4. Morkovin, Mark V. "Critical Evaluation of Transition from Laminar to Turbulent Shear Layers with Emphasis on Hypervelocity Traveling Bodies," AFFDL-TR-68-149, March 1969.
5. Ward, L. K. "Influence of Boundary Layer Transition on Dynamic Stability at Hypersonic Speeds," Trans. of 2nd Technical Workshop on Dynamic Stability Testing, AEDC, Vol. II (AD472298), April 20-22, 1965.
6. Martellucci, A. "Asymmetric Transition Effects on the Static Stability and Motion History of a Slender Vehicle," Doc. 705 D451, SAMSO TR-70-141, January 1970, General Electric Company, Philadelphia, Pennsylvania. (Also AIAA Paper No. 70-987, August 1970.)
7. Ericsson, Lars E. "Transition Effects on Slender Vehicle Stability and Trim Characteristics," AIAA Paper No. 73-126, January 1973.
8. Fehrman, A. L. and Masek, R. U. "Study of Uncertainties of Predicting Space Shuttle Thermal Environment," MDC E0639, June 1972, McDonnell-Douglas Astronautics Company - East, St. Louis, Missouri.
9. Pate, S. R. and Eaves, R. H., Jr. "Sensitivity of Boundary-Layer Transition to Surface Irregularities for Space Shuttle Applications," Journal of Spacecraft and Rockets, Vol. 10, No. 12, December 1973, pp. 813-814.
10. Pate, S. R. and Schueler, C. J. "Radiated Aerodynamic Noise Effects on Boundary-Layer Transition in Supersonic and Hypersonic Wind Tunnels," AIAA Journal, Vol. 7, No. 3, March 1969, pp. 450-457.
11. Pate, S. R. "Measurements and Correlations of Transition Reynolds Numbers on Sharp Slender Cones at High Speeds," AIAA Journal, Vol. 9, No. 6, June 1971, pp. 1082-1090.
12. Reshotko, E. "Stability Theory as a Guide to the Evaluation of Transition Data," AIAA Journal, Vol. 7, No. 6, June 1969, pp. 1086-1091.

13. Mack, L. M. "Linear Stability Theory and the Problem of Supersonic Boundary-Layer Transition," AIAA Journal, Vol. 13, No. 3, March 1975, pp. 278-289.
14. Kendall, J. M. "Wind Tunnel Experiments Relating to Supersonic and Hypersonic Boundary-Layer Transition," AIAA Journal, Vol. 13, No. 3, March 1975, pp. 290-299.
15. Jaffe, N. A., Okamura, T. T., and Smith, A. M. O. "The Determination of Spatial Amplification Factors and Their Application to Predicting Transition," AIAA Paper No. 69-10, 7th Aerospace Sciences Meeting, January 1969.
16. van Driest, E. R. and Blumer, C. B. "Boundary-Layer Transition at Supersonic Speeds: Roughness Effects with Heat Transfer," AIAA Journal, Vol. 6, No. 4, April 1968, pp. 603-607.
17. van Driest, E. R. and Blumer, C. B. "Boundary Layer Transition on Blunt Bodies--Effects of Roughness," AIAA Journal, Vol. 5, No. 10, October 1967, pp. 1913-1915.
18. Pate, S. R. "Experimental and Analytical Investigation at Boundary Layer Transition on Swept Wings at Mach Numbers 2.5 to 5," Thesis Master of Science Degree, University of Tennessee Space Institute, Tullahoma, Tennessee, March 1965.
19. Pate, S. R. "Supersonic Boundary-Layer Transition - Effects of Roughness and Free-Stream Disturbances," AIAA Journal, Vol. 9, No. 5, May 1971, pp. 797-803.
20. Whitehead, Allen H., Jr. "Flow-Field and Drag Characteristics of Several Boundary-Layer Tripping Elements in Hypersonic Flow," NASA TN D-5454, October 1969.
21. Whitfield, J. D. and Iannuzzi, F. A. "Experiments on Roughness Effects on Cone Boundary-Layer Transition up to Mach 16," AIAA Journal, Vol. 7, No. 3, March 1969, pp. 465-470.
22. Hopkins, Edward J., Jillie, Don W., and Sorensen, Virginia L. "Charts for Estimating Boundary Layer Transition on Flat Plates," NASA TN-D-5846, June 1970.
23. Potter, J. Leith. "The Unit Reynolds Number Effect on Boundary Layer Transition," PhD Dissertation, Vanderbilt University, Nashville, Tennessee, May 1974.
24. Shamroth, S. J. and McDonald, H. "Assessment of a Transition Boundary Layer Theory at Low Hypersonic Mach Numbers," NASA CR-2131, Langley Research Center, United Aircraft Corporation, November 1972.

25. Reshotko, E. "A Program for Transition Research," AIAA Journal, Vol. 13, No. 3, March 1975, pp. 261-265.
26. Owen, F. K., Horstman, C. C., Stainback, P. C., and Wagner, R. D. "Comparison of Wind Tunnel Transition and Freestream Disturbance Measurements," AIAA Journal, Vol. 13, No. 3, March 1975, pp. 266-269. (Also NASA TN D-7453, 1976.)
27. Potter, J. L. "Boundary-Layer Transition on Supersonic Cones in an Aeroballistic Range," AIAA Journal, Vol. 13, No. 3, March 1975, pp. 270-277.
28. Beckwith, I. E. "Development of a High Reynolds Number Quiet Tunnel for Transition Research," AIAA Journal, Vol. 13, No. 3, March 1975, pp. 300-306.
29. Harvey, W. D., Stainback, P. C., Anders, J. B., and Cary, A. M. "Nozzle Wall Boundary-Layer Transition and Freestream Disturbances at Mach 5," AIAA Journal, Vol. 13, No. 3, pp. 307-314, March 1975.
30. Smith, A. M. O. Review of "The M & M Tapes," an AIAA Recorded Lecture Series Review: "High Speed Boundary Layer Stability and Transition," Astronautics and Aeronautics, April 1972.
31. Morkovin, M. V. and Mack, L. High Speed Boundary Layer Stability and Transition, AIAA Recorded Lecture Series, 1969.
32. Schubauer, G. B. and Skranstad, H. K. "Laminar-Boundary-Layer Oscillations and Transition on a Flat Plate," NACA Report 909, 1948.
33. Owen, P. R. and Randall, D. G. "Boundary Layer Transition on a Swept-Back Wing," RAE Tech. Memo Aero. 277, June 1952.
34. Chapman, Gary T. "Some Effects of Leading-Edge Sweep on Boundary-Layer Transition at Supersonic Speeds," NASA TN D-1075, September 1961.
35. Adams, J. C., Jr. "Three-Dimensional Laminar Boundary-Layer Analysis of Upwash Patterns on Sharp Cones at Angle of Attack," AEDC-TR-71-215 (AD736880), December 1971.
36. Adams, J. C., Jr. and Martindale, W. R. "Hypersonic Lifting Body Boundary-Layer Analysis at High Angles of Incidence," Journal of Spacecraft and Rockets, Vol. 11, No. 10, October 1974, pp. 721-727. (Also AEDC-TR-73-2, February 1973.)
37. Potter, J. L. and Whitfield, J. D. "Effects of Slight Nose Bluntness and Roughness on Boundary-Layer Transition in Supersonic Flow," Journal of Fluid Mechanics, Vol. 12, Pt. 4, April 1962,



pp. 501-535. (Also AEDC-TR-60-5, March 1960, Arnold Engineering Development Center, Tullahoma, Tennessee.)

38. Laufer, John. "Aerodynamic Noise in Supersonic Wind Tunnels," JPL Progress Report No. 20-378, February 1959, and Journal of the Aerospace Sciences, Vol. 28, No. 9, September 1961, pp. 685-692.
39. van Driest, E. R. and Blumer, C. B. "Boundary-Layer Transition: Free-stream Turbulence and Pressure Gradient Effects," AIAA Journal, Vol. 1, No. 6, June 1963, pp. 1303-1306.
40. Spangler, J. G. and Wells, C. S., Jr. "Effects of Freestream Disturbances on Boundary-Layer Transition," AIAA Journal, March 1968, pp. 543-545.
41. Michel, R. "Determination du Point de Transition de Calcul de la Trainee des Profils en Incompressible," La Recherche Aeronautique, No. 24, 1951.
42. Czarnecki, K. R. and Sinclair, Archibald R. "Factors Affecting Transition at Supersonic Speeds," NACA RM L53I18a, November 1953.
43. Kovasznay, Leslie, S. G. "Turbulence in Supersonic Flow," Journal of the Aeronautical Sciences, Vol. 20, No. 10, October 1953, pp. 657-674.
44. Morkovin, M. V. "On Transition Experiments at Moderate Supersonic Speeds," Journal of the Aeronautical Sciences, Vol. 24, No. 7, July 1957, pp. 480-486.
45. Morkovin, M. V. "On Supersonic Wind Tunnels with Low Free-Stream Disturbances," Journal of Applied Mechanics, Tran. ASME, Vol. 26, Series E, June 1959, pp. 319-324.
46. Laufer, John and Marte, Jack E. "Results and a Critical Discussion of Transition-Reynolds Numbers Measurements on Insulated Cones and Flat Plates in Supersonic Wind Tunnels," JPL Report No. 20-96, November 1955.
47. van Driest, E. R. and Boison, J. C. "Experiments on Boundary-Layer Transition at Supersonic Speeds," Journal of the Aeronautical Sciences, Vol. 24, No. 12, December 1957, pp. 885-899.
48. Brinich, P. F. "Effect of Leading-Edge Geometry on Boundary-Layer Transition at  $M_{\infty} = 3.1$ ," NACA TN 3659, 1956.
49. Ross, R. "Influence of Total Temperature on Transition in Supersonic Flow," AIAA Journal, Vol. 11, No. 4, April 1973, pp. 563-565.

50. Schueler, C. J. "Comparison of the Aerodynamic Characteristics of AGARD Model A from Tests in 12-in. and 40-in. Supersonic Wind Tunnels," AEDC-TN-61-8 (AD251477), February 1961.
51. Schueler, C. J. "A Comparison of Transition Reynolds Number from 12-in. and 40-in. Supersonic Tunnels," AEDC-TDR-63-57 (AD299290), March 1963.
52. Dougherty, N. S. and Steinle, F. W., Jr. "Transition Reynolds Number Comparisons in Several Major Transonic Tunnels," AIAA Paper No. 74-627, Bethesda, Maryland, 1974.
53. Struminskiy, V. V., Kharitonov, A. M., and Chernykh, V. V. "Experimental Study of the Transitions of a Laminar Boundary Layer into A Turbulent Layer at Supersonic Velocities," FTD-45-23-1793-72.
54. Kharitonov, A. M. and Chernykh, V. V. "Nature of the Influence of the Unit Reynolds Number on Supersonic Boundary Layer Transition," NASA Tech. Translation, NASA-TT-F-16,146, August 1974 (translated from Russian, January 1975).
55. Bergstrom, E. R., et al. "Flat Plate Boundary Layer Transition in the LUT Gun Tunnel: A Transition-Radiated Aerodynamic Noise Correlation for Gun Tunnel and Convention Wind Tunnel Data at Supersonic Hypersonic Mach Numbers," N72 12161, August 1971, Loughborough University of Technology, Leicestershire, England.
56. Charlton, E. "Boundary Layer Transition on a Hollow Cylinder Model in the B.E.D. Gun Tunnel," Rolls-Royce Ltd. Contract Report No. A.P. 5598, 1969.
57. LaGraff, John E. "Experimental Studies of Hypersonic Boundary Layer Transition," Oxford University, Prof. of Engr. Science, Rept. No. 1104/70, May 1970.
58. Ross, R. "A Simple Formula for Flat Plate Boundary-Layer Transition in Supersonic Wind Tunnels," AIAA Journal, Vol. 10, No. 3, March 1972, pp. 336-337.
59. Bergstrom, E. R. and Raghunathan, S. "Aerodynamic Noise and Boundary-Layer Transition Measurements in Supersonic Test Facilities," AIAA Journal, Vol. 10, No. 11, November 1972, pp. 1531-1532.
60. Ross, R. "Boundary Layer Transition on the Same Model in Two Supersonic Wind Tunnels," AIAA Journal, Vol. 12, No. 7, July 1974, pp. 992-993.
61. Michel, R. "Effects of Turbulence and Noise on Aerodynamic Phenomena and the Result of a Wind Tunnel Test," ONERA, Toulouse, France, November 1973.

62. Gazley, Carl, Jr. "Boundary-Layer Stability and Transition in Subsonic and Supersonic Flow," Journal of the Aeronautical Sciences, Vol. 20, No. 1, January 1953, pp. 19-28.
63. Deem, R. E., Erickson, C. R., and Murphy, J. S. "Flat-Plate Boundary-Layer Transition at Hypersonic Speeds," FDL-TDR-64-129, October 1964. (Also AIAA Paper No. 65-128, 1965.)
64. Granville, Paul S. "The Prediction of Transition from Laminar to Turbulent Flow in Boundary Layers on Bodies of Revolution," Naval Ship Research and Development Center, Bethesda, Maryland, September 1974, Report No. 3900 (AD787060).
65. Kistler, E. L. "Boundary-Layer Transition: A Review of Theory, Experiment and Related Phenomena," NASA-CR-128450, February 1971 (Lockheed Electronics Co1, Houston, Texas).
66. Tetervin, Neal. "An Empirical Equation for Predicting of Transition Location on Cones in Supersonic-Hypersonic Flight," NOL-TR-73-127, June 1973.
67. Hairston, David E. "Survey and Evaluation of Current Boundary Layer Transition Prediction Techniques," AIAA Paper No. 71-985, October 1971.
68. Smith, A.M.O. and Gamberoni, Nathalie. "Transition, Pressure Gradient and Stability Theory," Douglas Aircraft Report No. ES26388, August 1956.
69. Reshotko, E. L. "Boundary Layer Stability and Transition," Conference on Boundary Layer Concepts in Fluid Mechanics, University of Massachusetts, July 1969.
70. Hanner, O. Mark, Jr. and Schmitt, Durwin A. "A Review of Boundary-Layer Transition with Emphasis Upon Space Shuttle Design Considerations," In "Space Systems and Thermal Technology for the 70's," ASME 70 HT/SPT-18, June 1970.
71. Lees, L. and Lin, C. C. "Investigation of the Stability of the Laminar Boundary Layer in a Compressible Fluid," NACA TN 1115, September 1946.
72. Laufer, John and Vrebalovich, Thomas. "Stability and Transition of a Supersonic Laminar Boundary Layer on an Insulated Flat Plate," Journal of Fluid Mechanics, Vol. 9, 1960, pp. 257-299.
73. Mack, L. M. "Boundary Layer Stability Theory," JPL/CIT 900-277, Rev. A, Jet Propulsion Laboratory, Pasadena, California, November 1969.

74. Kendall, J. M., Jr. "Supersonic Boundary Layer Transition Studies," JPL Space Programs Summary 37-62, Vol. III, 1970.
75. Liepman, Hans W. "Investigation of Laminar Boundary-Layer Stability and Transition on Curved Boundaries," NACA ACR 3H30, August 1943.
76. Wells, C. Sinclair, Jr. "Effects of Free-Stream Turbulence on Boundary-Layer Transition," AIAA Journal, Vol. 5, No. 1, January 1967, pp. 172-174.
77. Benek, J. A. and High, M. D. "A Method for the Prediction of the Effects of Free-Stream Disturbances on Boundary-Layer Transition," AEDC-TR-73-158, October 1973. (Also AIAA Journal, Vol. 12, No. 10, pp. 1425-1427, October 1974.)
78. Dryden, Hugh L. "Review of Published Data on the Effect of Roughness on Transition from Laminar to Turbulent Flow," Journal of the Aeronautical Sciences, July 1953, pp. 477-482.
79. van Driest, E. R. and McCauley, W. D. "The Effect of Controlled Three-Dimensional Roughness on Boundary-Layer Transition at Supersonic Speeds," Journal of the Aeronautical Sciences, Vol. 27, No. 4, April 1960, pp. 261-271.
80. Stalmach, C. J., Jr. and Goodrich, W. D. "Aeroheating Model Advancements Featuring Electroless Metallic Plating," Proceedings of AIAA 9th Aerodynamic Testing Conference, Arlington, Texas, June 1976.
81. Beckwith, Ivan E. and Bertram, Mitchell H. "A Survey of NASA Langley Studies on High-Speed Transition and the Quiet Tunnel," NASA TM X-2566, July 1972, Langley Research Center, Hampton, Virginia.
82. Kipp, H. W. and Masek, R. O. "Aerodynamic Heating Constraints on Space Shuttle Vehicle Design," In "Space Systems and Thermal Technology for the 70's," ASME Paper 70-HI/SPI-45, June 1970.
83. Kovasznay, L. S. G. "The Hot-Wire Anemometer in Supersonic Flow," Journal of the Aeronautical Sciences, Vol. 17, No. 9, September 1950, pp. 565-572.
84. Morkovin, Mark V. "Fluctuations and Hot-Wire Anemometry in Compressible Flows," AGARDograph 24, North Atlantic Treaty Organization Advisory Group for Aeronautical Research and Development, Paris, France, November 1956.
85. Morkovin, Mark V. "Signal Interpretation in High-Speed Anemometry--A Review" in Advances in Hot Wire Anemometry, edited by Melnik, W. L. and Weske, J. R., AFOSR Report No. 68-1492 (AD676019), July 1968, pp. 38-51.

86. Laufer, J. "Sound Radiation from a Turbulent Boundary Layer," Jet Propulsion Laboratory Report JPL/CIT TR-32-119, November 1961.
87. Laufer, John. "Some Statistical Properties of the Pressure Field Radiated by a Turbulent Boundary," Physics of Fluids, Vol. 7, No. 8, August 1964, pp. 1191-1197.
88. Donaldson, J. C. and Wallace, J. P. "Flow Fluctuation Measurements at Mach Number 4 in the Test Section of the 12-inch Supersonic Tunnel D," AEDC-TR-71-143 (AD723630), August 1971.
89. Wagner, R. D., Maddalon, D. V., and Weinstein, L. M. "Influence of Measured Freestream Disturbances on Hypersonic Boundary-Layer Transition," AIAA Journal, Vol. 8, No. 9, September 1970, pp. 1664-1670. (Also AIAA Paper No. 69-704, 1969.)
90. Fischer, M. C. and Wagner, R. D. "Transition and Hot-Wire Measurements in Hypersonic Helium Flow," AIAA Journal, Vol. 10, No. 10, October 1972, pp. 1326-1332. (Also AIAA Paper No. 72-181, January 1972 by Stainback, Fischer, and Wagner.)
91. Stainback, P. C. and Wagner, R. D., Jr. "A Comparison of Measured Wind-Tunnel Disturbance Levels Measured with a Hot-Wire Anemometer and Pitot Pressure Probe," AIAA Paper No. 72-1003, September 1972.
92. Vrebalovich, Thomas. Discussion on "Supersonic Wind Tunnels with Low Free-Stream Disturbances," by M. V. Morkovin, Journal of Applied Mechanics, Trans. ASME, June 1960, pp. 362-364.
93. Jet Propulsion Laboratory Research Summary No. 36-6, Vol. II, January 1961.
94. Phillips, O. M. "On the Generation of Sound by Supersonic Turbulent Shear Layers," Journal of Fluid Mechanics, Vol. 9, Part 1, September 1960, pp. 1-28.
95. Kistler, A. L. and Chen, W. S. "Fluctuating Pressure Field in a Supersonic Turbulent Boundary Layer," Journal of Fluid Mechanics, Vol. 16, Part 1, May 1963, pp. 41-64.
96. Williams, J. E. F. and Maidanik, G. "The Mach Wave Field Radiated by Supersonic Turbulent Shear Flows," Journal of Fluid Mechanics, Vol. 21, Part 4, 1965, pp. 641-657.
97. Bell, D. R. "Boundary-Layer Characteristics at Mach Numbers 2 through 5 in the Test Section of the 12-inch Supersonic Tunnel (D)," AEDC-TDR-63-192 (AD418711), September 1963.

98. Demetriades, A. "Hydrodynamic Stability and Transition to Turbulence in the Hypersonic Boundary Layer over a Sharp Cone," AFOSR-TR-75-1435, July 1975.
99. Donaldson, J. C. "The Development of Hot-Wire Anemometry Test Capabilities for  $M = 8$  Applications," AEDC-TR-76-88 (AD-A029570), September 1976.
100. Schueler, C. J. and Strike, W. T. "Calibration of a 40-inch Continuous Flow Tunnel at Mach Numbers 1.5 to 6," AEDC-TN-59-136 (AD228776), November 1959.
101. Sivells, J. C. and Payne, R. G. "A Method of Calculating Turbulent-Boundary-Layer Growth at Hypersonic Mach Numbers." AEDC-TR-59-3 (AD208774), February 1959.
102. Matthews, R. K. and Trimmer, L. L. "Operating Conditions and Flow Parameters for the VKF Hypersonic Wind Tunnels," AEDC-TM-64-19, June 1964.
103. Pate, S. R. and Eaves, R. H., Jr. "Recent Advances in the Performance and Testing Capabilities of the AEDC-VKF Tunnel F (Hotshot) Hypersonic Facility," AIAA Paper No. 74-84, AIAA 12th Aerospace Sciences Meeting, January 1974.
104. Boudreau, A. H., Jr. "High Mach Number, High Reynolds Number Perfect Gas Wind Tunnels, and a Method of Comparison," AEDC-TR-69-268 (AD864392), January 1970.
105. Edenfield, Emmett E. "Design of a High Reynolds Number Mach Number 8 Contoured Nozzle for the Hypervelocity Wind Tunnel (F)," AEDC-TR-72-48 (AD746477), August 1972.
106. Nichols, J. H. "Supplemental Aerodynamic Calibration Results for the AEDC-PWT 16-ft Supersonic Tunnel," AEDC-TDR-64-76 (AD435732), April 1964.
107. Trimmer, L. L., Matthews, R. K., and Buchanan, T. D. "Measurement of Aerodynamic Heat Rates at the von Kármán Facility," ICIAASF 1973 Record, September 1973, pp. 35-44.
108. Whitfield, Jack D. and Potter, J. Leith. "The Influence of Slight Leading-Edge Bluntness on Boundary-Layer Transition at a Mach Number of Eight," AEDC-TDR-64-18 (AD431533), March 1964.
109. Adams, John C. "Implicit Finite-Difference Analysis of Compressible Laminar, Transitional, and Turbulent Boundary Layers along the Windward Streamline of a Sharp Slender Cone at Incidence," AEDC-TR-71-235 (AD734535), December 1971.

110. Lowson, M. V. "Prediction of Boundary Layer Pressure Fluctuations," AFFDL-TR-67-167, April 1968.
111. Speaker, W. V. and Ailman, C. M. "Spectra and Space-Time Correlations of the Fluctuating Pressures at a Wall Beneath a Supersonic Turbulent Boundary Layer Perturbed by Steps and Shock Waves," NASA CR-486, May 1966.
112. Owen, F. K. "Transition Experiments on a Flat Plate at Subsonic and Supersonic Speeds," AIAA Paper No. 69-9, presented at AIAA 7th Aerospace Sciences Meeting, January 1969.
113. Pate, S. R. and Brown, M. D. "Acoustic Measurements in Supersonic Transitional Boundary Layers," AEDC-TR-69-182 (AD694071), October 1969.
114. Hrubecky, Henry F. "Approximate Analysis for the Turbulent Boundary Layer Thickness on a Cone in Supersonic Flow," Applied Scientific Research, Section A, Vol. 11, No. 4, 1963, pp. 441-450.
115. Lewis, Thomas L. and Banner, Richard D. "Boundary-Layer Transition Detection on the X-15 Vertical Fin Using Surface Pressure Fluctuation Measurements," NASA TM-X-2466, December 1971.
116. Hanly, Richard D. "Effects of Transducer Flushness on Fluctuating Surface Pressure Measurements," AIAA Paper No. 75-534, March 1975.
117. White, Pritchard, H. "Effect of Transducer Size, Shape, and Surface Sensitivity on the Measurement of Boundary-Layer Pressures," The Journal of the Acoustical Society of America, Vol. 41, No. 5, May 1967, pp. 1358-1363.
118. Fellows, Mrs. K. A. "Pressure Fluctuations Caused by Transition at Supersonic Speeds," Aircraft Research Association Limited (ARA) Model Test Note M. 84/1, August 1974.
119. Brinich, Paul F. "Recovery Temperature, Transition and Heat-Transfer Measurements at Mach 5," NASA TN D-1047, August 1961.
120. Brinich, Paul F. and Sands, Norman. "Effect of Bluntness on Transition for a Cone and a Hollow Cylinder at Mach 3.1," NACA TN 3979, May 1957.
121. Stainback, Calvin P. "Effect of Unit Reynolds Number, Nose Bluntness, Angle of Attack, and Roughness on Transition on a 50° Half-Angle Cone at Mach 8," NASA TN D-4961, January 1969.

122. Fischer, Michael Carlton. "An Experimental Investigation on Unit Reynolds Number and Bluntness Effects on Boundary-Layer Transition for a  $10^\circ$  Half-Angle Cone at  $M_\infty = 7$ ," NASA TMX-61906 (N69-40204), June 1969.
123. Coles, Donald. "Measurements of Turbulent Friction on a Smooth Flat Plate in Supersonic Flow," Journal of the Aeronautical Sciences, Vol. 21, No. 7, July 1954, pp. 433-448.
124. Matthews, R. K., Eaves, R. H., Jr., and Martindale, W. R. "Heat-Transfer and Flow-Field Tests of the McDonnell Douglas-Martin Marietta Space Shuttle Configurations," AEDC-TR-73-53 (AD759176), April 1973.
125. Masaki, M. and Yakura, J. K. "Transitional Boundary-Layer Considerations for the Heating Analysis of Lifting Re-Entry Vehicles," Journal of Spacecraft and Rockets, Vol. 6, No. 9, September 1969, pp. 1048-1059.
126. Holloway, Paul F. and Sterrett, James R. "Effect on Controlled Surface Roughness on Boundary-Layer Transition and Heat Transfer at Mach Numbers 4.8 and 6.0," NASA TN D 2054, April 1964.
127. Mateer, George G. "A Comparison of Boundary-Layer Transition Data from Temperature Sensitive Paint and Thermocouple Techniques.," AIAA Journal, Vol. 8, No. 12, December 1970, pp. 2299-2300.
128. Kendall, James M., Jr. "Wind Tunnel Experiments Relating to Supersonic and Hypersonic Boundary-Layer Transition," AIAA Paper No. 74-143.
129. Miller, Charles G. and Maddalon, Del V. "Errors in Free-Stream Reynolds Number of Helium Wind Tunnels," AIAA Journal, Vol. 8, No. 5, May 1970, pp. 968-970.
130. Stainback, P. Calvin. "Some Effects of Roughness and Variable Entropy on Transition at a Mach Number of 8," AIAA Paper No. 67-132, January 1967.
131. Mateer, G. G. and Larsen, H. K. "Unusual Boundary-Layer Transition Results on Cones in Hypersonic Flow," AIAA Journal, Vol. 7, No. 4, April 1969, pp. 660-664.
132. Stainback, P. Calvin, Wagner, Richard D., Owen, F. Kevin, and Horstman, Clifford C. "Experimental Studies of Hypersonic Boundary-Layer Transition and Effects of Wind-Tunnel Disturbances," NASA TN D-7453, March 1974.
133. Richards, B. E. "Transitional and Turbulent Boundary Layers on a Cold Flat Plate in Hypersonic Flow," The Aeronautical Quarterly, Vol. XVIII, August 1967, pp. 237-258.



134. Taylor, G. I. "Statistical Theory of Turbulence. V. Effect of Turbulence on Boundary Layer," Proceedings of the Royal Society of London, Ser. A, Vol. 156, 1936, pp. 307-317.
135. van Driest, E. R. "Turbulent Boundary Layer in Compressible Fluids," Journal of the Aeronautical Sciences, Vol. 18, No. 3, March 1951, pp. 145-160.
136. Rogers, Ruth H. "Boundary Layer Development in Supersonic Shear Flow," AGARD Report 269, April 1960.
137. Potter, J. Leith and Whitfield, Jack D. "Boundary-Layer Transition under Hypersonic Conditions," AGARD Specialists Mtg. on Recent Developments in Boundary Layer Research, AGARDograph 97, Part III. (Also AEDC-TR-65-99 (AD462716), 1965.)
138. Tetervin, N. "A Discussion of Cone and Flat-Plate Reynolds Numbers for Equal Ratios of the Laminar Shear to the Shear Caused by Small Velocity Fluctuations in a Laminar Boundary Layer," NACA TN 4078, August 1957.
139. Tetervin, Neal. "An Estimate of the Minimum Reynolds Number for Transition from Laminar to Turbulent Flow by Means of Energy Considerations," Journal of the Aerospace Sciences, Vol. 28, No. 2, February 1961, pp. 160-161. (Also NAVORD Report 6854 (AD437345), January 1961.)
140. Battin, R. H. and Lin, C. C. "On the Stability of the Boundary Layer over a Cone," Journal of the Aeronautical Sciences, Vol. 17, No. 7, July 1950, pp. 453-454.
141. Spaulding, D. B. and Chi, S. W. "The Drag of a Compressible Turbulent Boundary Layer on a Smooth Flat Plate with and without Heat Transfer," Journal of Fluid Mechanics, Vol. 18, Pt. 1, January 1964, pp. 117-143.
142. van Driest, E. R. "The Problem of Aerodynamic Heating," Aeronautical Engineering Review, Vol. 15, No. 10, October 1956, pp. 26-41.
143. Komar, James J. "Skin-Friction Predictions in Turbulent Compressible Flow," AIAA Journal, Vol. 4, No. 7, July 1966, pp. 1307-1308.
144. Moore, D. R. and Harkness, J. "Experimental Investigations of the Compressible Turbulent Boundary Layer at Very High Reynolds Numbers," AIAA Journal, Vol. 3, No. 4, April 1965, pp 631-638.
145. Winter, K. G., Smith, K. G., and Gaudet, L. "Measurements of Turbulent Skin Friction at High Reynolds Numbers at Mach Numbers

of 0.2 and 2.2," AGARD Specialists Meeting on Recent Developments in Boundary Layer Research, Naples, Italy, 1965.

146. Cary, Aubrey, M., Jr. and Bertram, Mitchell H. "Engineering Prediction of Turbulent Skin Friction and Heat Transfer in High-Speed Flow," NASA TN D-7507, July 1974.
147. Hastings, R. C. and Sawyer, W. G. "Turbulent Boundary Layers on a Large Flat Plate at  $M = 4$ ," R&M No. 3678, Aeronautical Research Council, Aerodynamics Department, RAE Bedford, England, March 1970.
148. Harvey, W. D. and Clark, F. L. "Measurements of Skin Friction on the Wall of a Hypersonic Nozzle," AIAA Journal, Vol. 10, No. 9, September 1972, pp. 1256-1258.
149. Samuels, Richard D., Peterson, John B., Jr., and Adcock, Jerry B. "Experimental Investigation of the Turbulent Boundary Layer at a Mach Number of 6 with Heat Transfer at High Reynolds Numbers," NASA TN D-3858, March 1967.
150. Hopkins, E. J., Rubesin, Morris W., Inouye, M., Keener, Earl R., Mateer, G. C., and Polek, Thomas E. "Summary and Correlation of Skin-Friction and Heat-Transfer Data for a Hypersonic Turbulent Boundary Layer on Simple Shapes," NASA TN D-5089, June 1969.
151. Miles, John B. and Kim, Jong Hyun. "Evaluation of Coles' Turbulent Compressible Boundary-Layer Theory," AIAA Journal, Vol. 6, No. 6, June 1968, pp. 1187-1189.
152. Hopkins, Edward J. and Inouye, Mamoru. "An Evaluation of Theories for Predicting Turbulent Skin Friction and Heat Transfer on Flat Plates at Supersonic and Hypersonic Mach Numbers," AIAA Journal, Vol. 9, No. 6, June 1971, pp. 993-1003.
153. Coats, Jack D. "Flow Characteristics of a 40-inch Wind Tunnel at Mach Numbers 1.5 to 6," AEDC-TDR-62-130 (AD277289), June 1962.
154. Jones, J. H. "An Investigation of the Boundary-Layer Characteristics in the Test Section of a 40- by 40-inch Supersonic Tunnel," AEDC-TN-60-189 (AD245362), October 1960.
155. Ames Research Staff. "Equations, Tables, and Charts for Compressible Flow," NACA Report 1135, 1953.
156. Maxwell, H. and Jacocks, J. L. "Nondimensional Calculation of Turbulent Boundary-Layer Development in Two-Dimensional Nozzles of Supersonic Wind Tunnels," AEDC-TN-61-153 (AD270596), January 1962.

157. Tucker, Maurice. "Approximate Calculation of Turbulent Boundary-Layer Development in Compressible Flow," NACA TN 2337, April 1951.
158. Edenfield, E. E. "Contoured Nozzle Design and Evaluation for Hot-shot Wind Tunnels," AIAA Paper No. 68-369, presented at AIAA 3rd Testing Conference, April 1968.
159. Fiore, Anthony W. "Viscosity of Air," Journal of Spacecraft and Rockets, Vol. 3, No. 5, May 1966, pp. 756-758.
160. Rasmussen, M. L. "On Hypersonic Flow Past an Unyawed Cone," AIAA Journal, Vol. 5, No. 8, August 1967, pp. 1495-1497.
161. Jones, D. J. "Tables of Inviscid Supersonic Flow about Circular Cones of Incidence  $\gamma = 1.4$ ," AGARDograph 137, Parts I, II, 1969, Part III, 1971, North Atlantic Treaty Organization (NATO).
162. Sims, J. L. "Tables for Supersonic Flow around Right Circular Cones at Zero Angle of Attack," NASA SP-3004, 1964.
163. van Driest, E. R. and Blumer, C. B. "Boundary-Layer Transition at Supersonic Speeds--Three-Dimensional Roughness Effects (Spheres)," Journal of the Aeronautical Sciences, Vol. 29, No. 8, August 1962, pp. 909-916.
164. Nagamatsu, H. T., Sheer, R. E., Jr., and Graber, B. C. "Hypersonic Laminar Boundary-Layer Transition on 8-Foot-Long,  $10^\circ$  Cone,  $M_1 = 9.1 - 16$ ," AIAA Journal, Vol. 5, No. 7, July 1967, pp. 1245-1252.
165. McCauley, W. D., Saydah, A. R., and Bueche, J. F. "Effect of Spherical Roughness on Hypersonic Boundary-Layer Transition," AIAA Journal, Vol. 4, No. 12, December 1966, pp. 2142-2148.
166. Mack, Leslie, M. "Calculation of the Laminar Boundary Layer on an Insulated Flat Plate by the Klunker-McLeon Method," JPL/CIT-PR-20-352, July 1958.
167. Braslow, A. L. and Knox, E. C. "Simplified Method for Determination of Critical Height of Distributed Roughness Particles for Boundary-Layer Transition at Mach Numbers 0 to 5," NACA TN-4363, September 1958.
168. Dayman, Bain, Jr. "Comparison of Calculated with Measured Boundary-Layer Thickness on the Curved Walls of the JPL-20 in. Supersonic Wind Tunnel Two Dimensional Nozzle," JPL Technical Report No. 32-249, March 1963.
169. Rhudy, J. P. "Effect of Uncooled Leading-Edge on Cooled-Wall Hypersonic Flat Plate Boundary-Layer Transition," AIAA Journal, Vol. 8, No. 3, March 1970, pp. 576-577.

170. Nagel, A. L., Savage, R. T., and Wanner, R. "Investigation of Boundary Layer Transition in Hypersonic Flow at Angle of Attack," AFFDL-TR-66-122, August 1966.
171. Everhart, Philip E. and Hamilton, H. Harris. "Experimental Investigation of Boundary-Layer Transition on a Cooled  $7.5^\circ$  Total-Angle Cone at Mach 10," NASA TN-D-4188, October 1967.
172. Softley, E. J., Graber, B. C., and Zempel, R. E. "Experimental Observation of Transition of the Hypersonic Boundary Layer," AIAA Journal, Vol. 7, No. 2, February 1969, pp. 257-263.
173. Senator, R. J., DeCarlo, J. P., and Torrillo, D. T. "Hypersonic Boundary-Layer Transition Data for a Cold-Wall Slender Cone," AIAA Journal, Vol. 3, No. 4, April 1965, pp. 758-760.
174. Reshotko, E. "Transition Reversal and Tollmien-Schlichting Instability," The Physics of Fluids, Vol. 6, No. 3, March 1963, pp. 335-342.
175. Wisniewski, R. J. and Jack, J. R. "Recent Studies on the Effect of Cooling on Boundary Layer Transition at Mach 4," Journal of the Aeronautical Sciences, Vol. 28, No. 25, 1961.
176. Richards, B. E. and Stollery, J. L. "Further Experiments on Transition Reversal at Hypersonic Speeds," AIAA Journal, Vol. 4, No. 12, December 1966, pp. 2224-2226.
177. Shapiro, A. H. "The Dynamics and Thermodynamics of Compressible Fluid Flow," Ronald Press Co., New York, 1953-59.

## APPENDIX A

## TURBULENT BOUNDARY-LAYER SKIN FRICTION

In the initial phases of this research (10,11), the method of van Driest-I (135) was used to compute the mean, adiabatic, turbulent skin-friction coefficient for the boundary layer on supersonic-hypersonic wind tunnel walls. These skin-friction coefficients were then used in the aerodynamic-noise-transition empirical equations developed in Chapter IX [Eqs. (10) and (11), pages 248 and 252].

As a part of the present research effort, a review of available methods was conducted to establish if the method of van Driest-I (135) should be retained. This review included the evaluation of twelve survey papers, References (141 through 152) which in turn evaluated many different techniques. Based on this evaluation, the method of van Driest-II was selected as a suitable technique for computing tunnel wall, mean skin-friction values.

## I. REVIEW OF THEORETICAL METHODS

The now widely accepted and often referenced work of Spaulding and Chi (141) compared 20 different theoretical methods, including their own semi-empirical method, with existing experimental data. They concluded the best method was their own which gave a root-mean-square (rms) error of the difference in predicted and measured skin-friction data of 8.6% for adiabatic walls and 12.5% for flows with heat transfer with an overall error of 9.9%. The second best method was van Driest-II which gave a 9.7% error for adiabatic flow and a 13.6% error for flows with

heat transfer with an overall error of 11.0%. van Driest-I (135) had errors of 13.3% for adiabatic flow, 17.3% for heat transfer, and 14.7% overall error. Thus, there was not an extreme difference between van Driest-I and II, and van Driest-I finished fifth in the field of 21. The flat-plate data used by Spaulding and Chi for the evaluation covered a Mach number range from zero to 10 and a temperature range ( $T_w/T_\infty$ ) from 1.0 to  $\approx 18$ .

Komar (143) concluded that although the theoretical method of van Driest-II was in good agreement with the semi-empirical method of Spaulding and Chi, there was a significant difference (as much as 35%) at high heat-transfer rates. Consequently, Komar recommended the use of the Spaulding-Chi method as the preferred method and presented a monograph to assist in rapid calculations of local and/or mean skin-friction coefficients.

Moore and Harkness (144) investigated skin-friction data at  $M_\infty = 2.8$  for an adiabatic flow and high Reynolds numbers ( $2.3 \times 10^7 \leq Re_x \leq 1.4 \times 10^9$ ). The model geometry was a 10-ft-long flat plate and the floor of a supersonic wind tunnel. They compared the experimental data with three theoretical methods and found the best agreement with van Driest-II (142).

Winter, Smith, and Gaudet (145) used the sidewall of the R.A.E. 8- by 8-ft wind tunnel to provide experimental skin-friction data over the range  $0.2 \leq M_\infty \leq 2.2$  and Reynolds numbers up to  $Re_x = 200 \times 10^6$ . They found good agreement between the experimental data and the semi-empirical method of Spaulding and Chi.

Cary and Bertram (146) evaluated a large collection of experimental turbulent-skin friction and heat-transfer data for flat plates and cones to determine the most accurate of six popular prediction methods (Eckert, Spaulding and Chi, Coles, van Driest, White and Christoph and Moore). They concluded that for  $M_\infty < 10$ , Spaulding and Chi gave the best overall predictions. For  $M_\infty > 10$ , Coles' method was rated best.

An experimental study was conducted by Hastings and Sawyer (147) at  $M_\infty = 4$  using a flat-plate model with length Reynolds numbers up to  $Re_x = 34 \times 10^6$ . Measured skin-friction data were compared to five different prediction techniques (the reference temperature method of Sommer and Short, the semi-empirical method of Spaulding and Chi, the theory of van Driest-II, the theory of Coles, and the empirical method of Winter and Gaudet). They found that the method of Spaulding and Chi gave the best estimate. The predictions by van Driest-II (142) were high by about 10%.

Experimental skin-friction data measured on the wall of a  $M_\infty \approx 20$  wind tunnel was compared with eight different turbulent theories (Eckert, Spaulding-Chi, Sommer-Short, van Driest-II, Harkness, Baronti-Libby, Coles, and Moore) by Harvey and Clark (148). They concluded that the methods of Coles, Moore, and van Driest-II gave the best overall agreement with the experimental data. They also concluded that the turbulent boundary layer of a cold wall nozzle rapidly adjusts to local gradients and can be predicted by flat-plate theories such as van Driest-II (142).

Samuels, Peterson, and Adcock (149) compared experimental turbulent boundary-layer data taken on a hollow-cylinder model at  $M_\infty = 6$  with

heat transfer with five theories (van Driest, Monaghan, Johnson, Sommer and Short and Spaulding and Chi) and concluded that Spaulding and Chi (141) gave the best agreement which was judged as fair.

Hopkins, et al. (150) conducted experimental studies of turbulent skin friction on flat plates, cones, and a wind tunnel wall over the Mach number range from 5 to 7.4 and temperature ratios ( $T_w/T_{aw}$ ) from 0.1 to 0.6. They compared their experimental results with four theoretical methods (Sommer and Short, Spaulding and Chi, van Driest-II, and Coles) and concluded that Coles' theory underpredicts at the higher Reynolds numbers by 10%. At  $M_\infty > 6$  the method of Spaulding and Chi (141) under-predicted by 20% to 30%. The theory of van Driest-II (142) under-predicted the local skin-friction data by about 10% for nonadiabatic walls.

Miles and Kim (151) noted that Spaulding and Chi (141) had not included the method of Coles in their evaluation of 20 theories. Miles and Kim evaluated Coles' theory in a manner similar to the analysis of Spaulding and Chi and concluded that Coles' theory was competitive with the method of Spaulding and Chi.

Hopkins and Inouye (152) evaluated the ability of four theoretical methods (van Driest-II, Sommer-Short, Spaulding-Chi, and Coles) to predict the skin friction and heat transfer on adiabatic and non-adiabatic flat plates and wind tunnel walls. The experimental data covered a range of Mach numbers from 1.5 to 8.6 and  $T_w/T_{aw}$  from 0.14 to 1.0. Their conclusion was that the method of van Driest-II (142) was the best method for predicting turbulent skin friction at supersonic-hypersonic speeds.



Edenfield (105), based on his efforts to design a  $M_\infty = 8$  high Reynolds number axisymmetric nozzle, concluded that the theory of Coles (and others) would underpredict the wall skin friction. Although his work was done independently of the work by Hopkins and Inouye (152), Edenfield noted in his summary report (105) that the extensive studies by Hopkins and Inouye gave confirmation to his conclusions.

In summary, based on the results of References (141), (143), (145), (146), (147), and (149), it appears that the semi-empirical method of Spaulding and Chi is the best technique for predicting the skin friction on flat plates and wind tunnel walls, with the method of van Driest-II being a close second. However, if one accepts the results of References (142), (148), and (150) and the latest study by Hopkins and Inouye (152) then the order of preference would be reversed.

The method van Driest-II (142) was the method selected to compute the tunnel wall skin-friction coefficients used in the aerodynamic-noise-transition correlation developed in this dissertation. The method of van Driest-II was selected for three reasons:

1. It is among the best and perhaps the best method.
2. It is a "theoretical" method as opposed to an empirical or semi-empirical method, and the analytical expression, although implicit in  $C_F$ , can be programmed fairly easily for a digital computer, and
3. The author is more familiar with the method and personally likes it.

## II. METHOD OF VAN DRIEST-II

The method of van Driest-II was used to compute the wind tunnel wall mean turbulent skin-friction coefficients used in the aerodynamic-noise-transition correlations developed in Chapter IX, Figures IX-8, page 233, and IX-9, page 235.

Van Driest published in 1951 a theory for turbulent, compressible flow commonly referred to as van Driest-I (135). This theory was developed specifically for flat-plate flows and utilized the Prandtl mixing length hypothesis ( $\ell = ky$ ) as the principal assumption as discussed in Reference (135). In 1956, van Driest (142) published a second theory, commonly referred to as van Driest-II. In this theory the von Kármán mixing length hypothesis,  $\ell = k(du/dy)/(d^2u/dy^2)$ , was used. At certain flow conditions, particularly for  $M_\infty \gtrsim 5$ , there can be significant differences in  $C_F$ , as shown in Figure A-1, depending on which method is used. At the time the theories were published, van Driest saw no theoretical reasons to prefer one method over the other and stated that a preferred theory would have to wait for experimental verification. Based on comparisons with experimental data (as discussed in the last section), it is now generally accepted that van Driest-II (142) provides the best predictions.

Included in Figure A-1 are the experimental skin-friction coefficients obtained in this research on the walls of the AEDC-PWT Tunnel 16S. Experimental data from several other sources are also included. Reasonable agreement between the experimental data and the theory of van Driest-II exists.

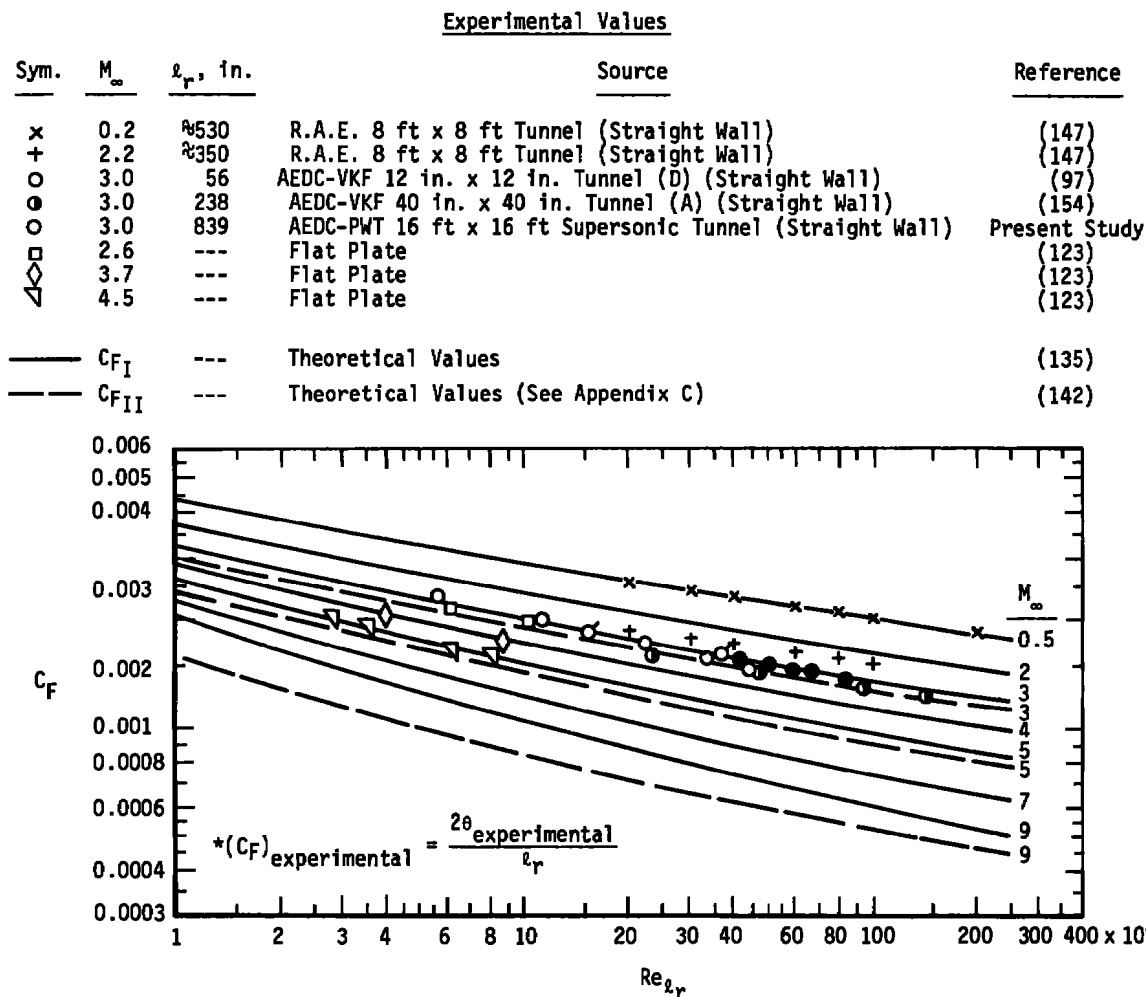


Figure A-1. Adiabatic, mean turbulent skin-friction coefficients as a function of Mach number and length Reynolds number.

Presented in Figure A-2 are calculations using the method of van Driest-II (as developed in Appendix C, page 343) to illustrate the significant effects of nonadiabatic wall conditions at high Mach numbers and/or high Reynolds numbers. The method of van Driest-II is discussed in detail in Appendix C, page 343.

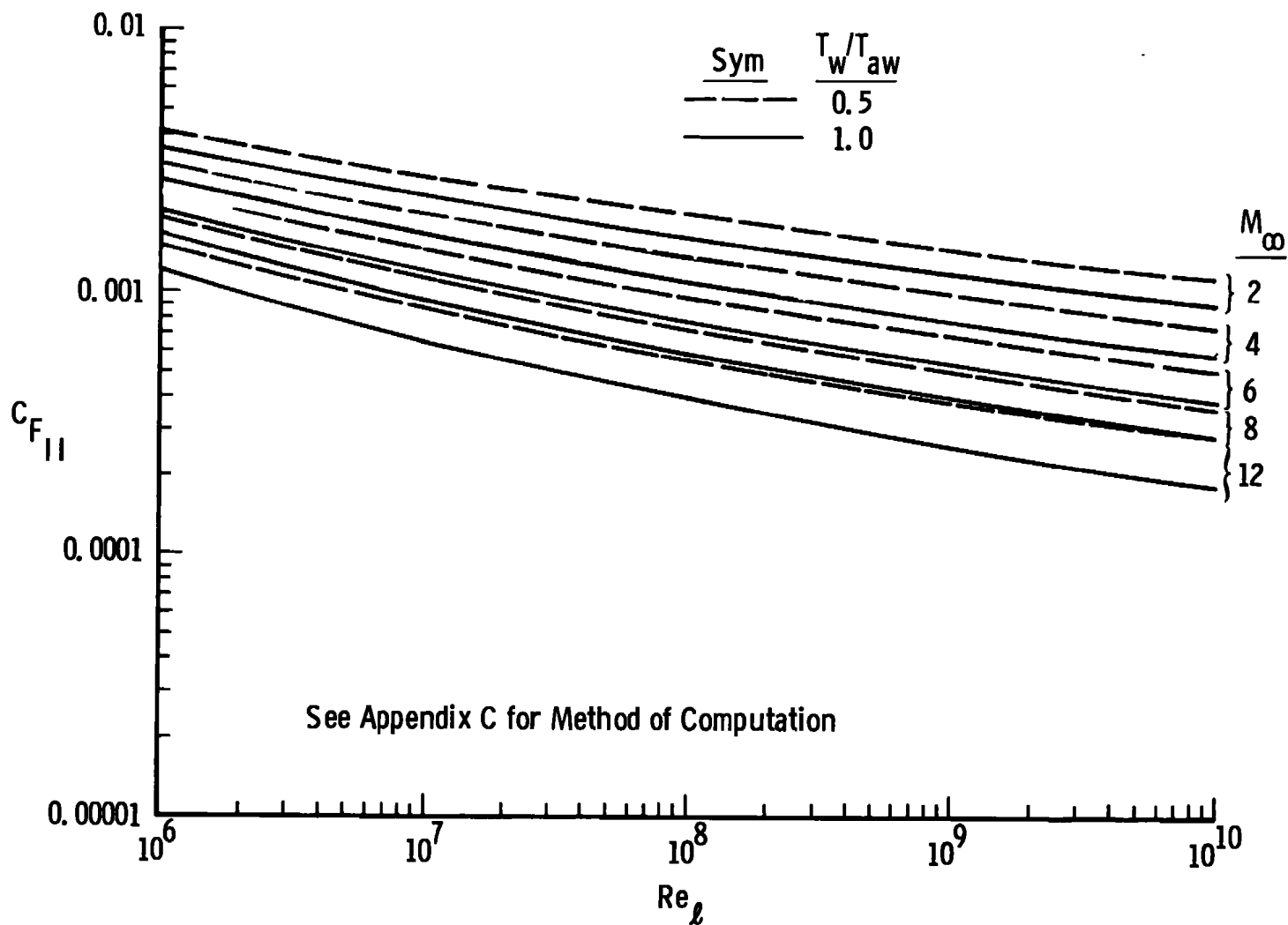


Figure A-2. Mean, turbulent skin-friction coefficient computed using the method of van Driest-II.

## APPENDIX B

## TUNNEL WALL BOUNDARY-LAYER CHARACTERISTICS

The aerodynamic-noise-transition correlations developed in Chapter IX [see Eq. (10), page 232, and Eq. (11), page 235] are dependent on the boundary-layer displacement thickness ( $\delta^*$ ) and the mean turbulent skin-friction coefficient ( $C_F$ ). Part of this research program included making boundary measurements in three of the AEDC wind tunnels (AEDC-VKF A, AEDC-VKF E, and AEDC-PWT 16S) to determine the values of  $\delta^*$ . The measurements in the AEDC-PWT 16S were the first boundary-layer data measured in that facility. The data from the AEDC-VKF Tunnel E was the first for  $M_\infty = 5$ . The AEDC-VKF Tunnel A test section boundary was re-surveyed in this research to establish if a modification to the tunnel wall flexible plates upstream of the throat region (153) that occurred after the tunnel was initially calibrated (154) affected the test section boundary layer.

This section presents the basic, experimental boundary-layer characteristics obtained in this research. Correlations that are adequate for predicting tunnel wall boundary-layer displacement thickness values for two-dimensional supersonic nozzles and axisymmetric hypersonic nozzles are presented.

## I. DATA REDUCTION PROCEDURES

The two-dimensional boundary-layer displacement thickness ( $\delta^*$ ) (mass defect) and momentum thickness ( $\theta$ ) (momentum defect) for a compressible flow are defined by Eqs. (B-1) and (B-2), respectively.

$$\delta^* = \int_0^\delta \left( 1 - \frac{\rho u}{\rho_e U_e} \right) dy \quad (B-1)$$

$$\theta = \int_0^\delta \frac{\rho u}{\rho_e U_e} \left( 1 - \frac{u}{U_e} \right) dy \quad (B-2)$$

Subscript e denotes values at edge of boundary layer.

Equations (B-1) and (B-2) were evaluated using the standard assumptions that the static pressure and the total temperature remain constant across the boundary layer. By employing a pitot pressure rake to measure the impact pressure across the boundary layer in conjunction with a measured wall static pressure at the rake location allows the local boundary-layer profile conditions to be determined. Writing Eqs. (B-1) and (B-2) in terms of local Mach number gives

$$\delta^* = \int_0^\delta \left[ 1 - \frac{M}{M_e} \left( \frac{1 + \frac{\gamma-1}{2} M^2}{1 + \frac{\gamma-1}{2} M_e^2} \right)^{\frac{1}{2}} \right] dy \quad (B-3)$$

$$\theta = \int_0^\delta \frac{M}{M_e} \left[ \left( \frac{1 + \frac{\gamma-1}{2} M^2}{1 + \frac{\gamma-1}{2} M_e^2} \right)^{\frac{1}{2}} - \frac{M}{M_e} \right] dy \quad (B-4)$$

For subsonic flow,  $p/p_0' \geq 0.528$ , Eq. (B-5) is used to compute the local Mach number:

$$M = \left\{ 5 \left[ \left( \frac{p_0'}{p} \right)^{\frac{\gamma-1}{\gamma}} - 1 \right] \right\}^{\frac{1}{2}} \quad (B-5)$$

For supersonic flow,  $p/p_0' < 0.528$ , the local Mach number was determined using the implicit Rayleigh-Pitot Formula (155).

$$\frac{p_0}{p} = \left[ \frac{(\gamma + 1)}{2} M^2 \right]^{\frac{\gamma}{\gamma-1}} \left[ \frac{\gamma + 1}{2\gamma - M^2 - (\gamma - 1)} \right]^{\frac{\gamma}{\gamma-1}} \quad (B-6)$$

where  $\gamma$  = ratio of specific heats = 1.4 for air or nitrogen.

The integrands of Eqs. (B-1) and (B-2) were plotted at the respective probe height ( $y$ ) and then  $\delta^*$  and  $\theta$  were determined from graphical integration using a planimeter.

If it is assumed that the boundary layer begins at the tunnel throat and that a uniform flow constant Mach number (i.e., zero pressure) flow exists over the full length of the nozzle, then the skin-friction coefficient is readily determined from the two-dimensional von Kármán momentum integral.

$$\frac{C_f}{2} = \frac{d\theta}{dx} + (2 + H - M^2) \frac{\theta}{U_e} \frac{dU_e}{dx} \quad (B-7)$$

where

$$H = \frac{\delta^*}{\theta} \equiv \text{shape parameter} \quad (B-8)$$

$x$  = axial distance

for uniform zero pressure gradient flow  $du/dx = 0$  and Eq. (B-7) becomes

$$\frac{C_f}{2} = \frac{d\theta}{dx} \quad (B-9)$$

Upon integrating Eq. (B-9) becomes

$$\int_0^x C_f dx = 2 \int_0^\theta d\theta \quad (B-10)$$

By definition

$$C_F = \frac{1}{x} \int_0^x C_f dx \quad (B-11)$$



then

$$C_F = \frac{2}{x} \int_0^\theta d\theta = \frac{2\theta}{x}$$

and

$$\boxed{C_F = \frac{2\theta}{x}} \quad (B-12)$$

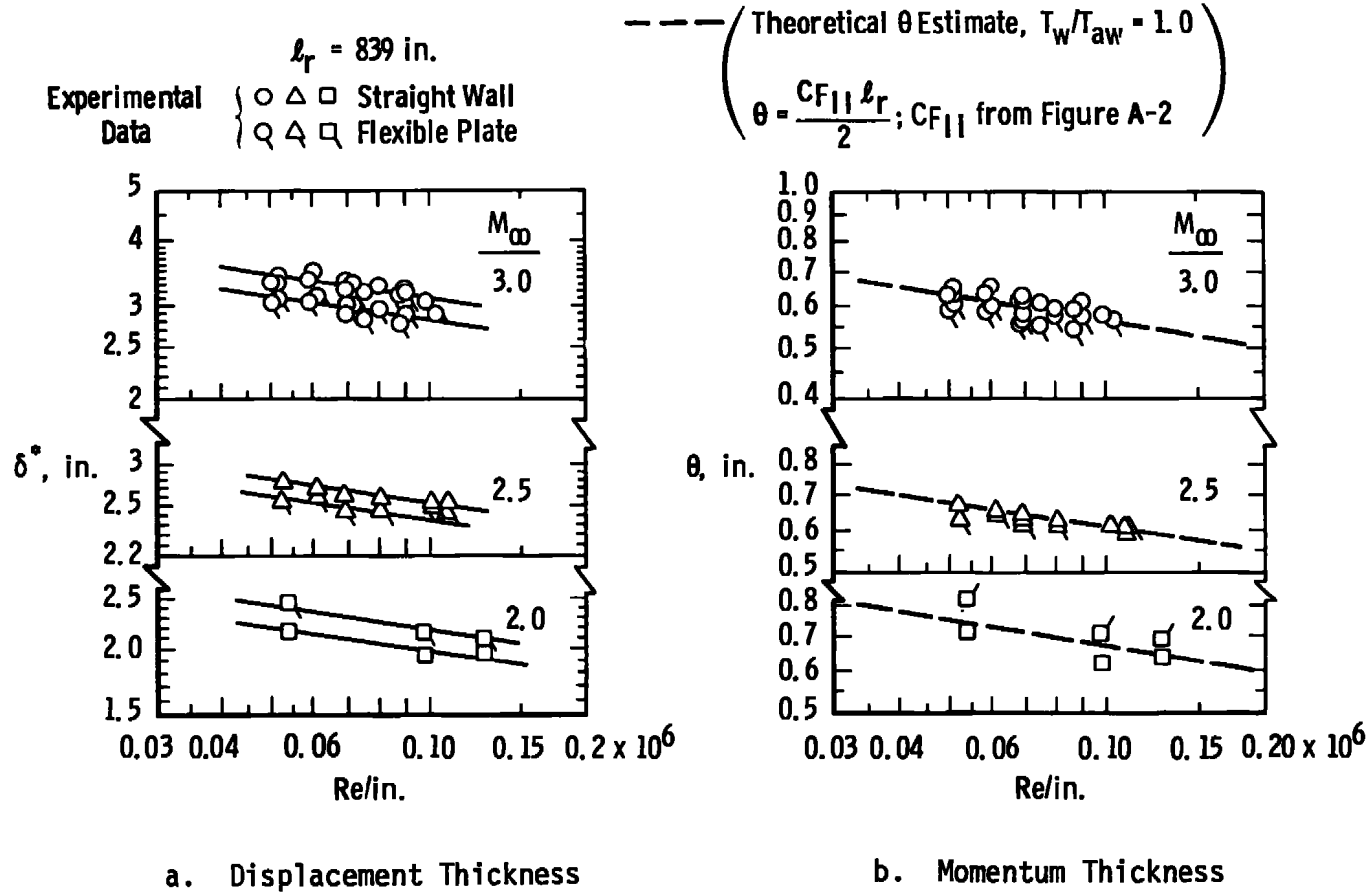
## II. AEDC-PWT TUNNEL 16S DATA

The displacement thickness ( $\delta^*$ ) and momentum thickness measured on the flexible plate in the 16- by 16-ft test section at  $M_\infty = 2.0, 2.5$ , and 3.0 are shown in Figure B-1. The geometry of the fourteen-probe boundary-layer rake used to obtain these data is shown in Figure B-2a. The rake location in the test section is shown in Chapter IV, Figure IV-11, page 90. There was a small difference in the straight wall and flexible plate data as evident in the data presented in Figure B-1.

The computed momentum thickness was determined from  $\theta = (C_F x)/2$  where  $C_F$  was determined using the theory of van Driest-II (see Appendix C). The agreement between the experimental  $\theta$  and the "flat plate" theoretical values for  $\theta$  is seen to be fairly good.

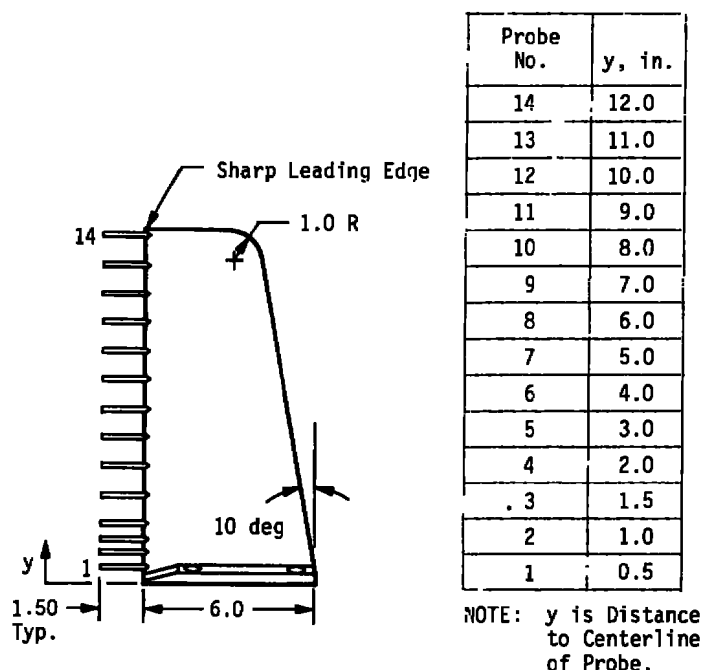
## III. AEDC-VKF TUNNEL A DATA

The flexible plate which forms the lower nozzle wall in the Tunnel A was damaged on October 10, 1961. The damage, Figure B-3, occurred in the converging region of the nozzle upstream of the throat where several of the lugs which connected the flexible plate to automatically controlled actuators were broken or cracked. Repair of the plate



--- ( Theoretical  $\theta$  Estimate,  $T_w/T_{aw} = 1.0$  )

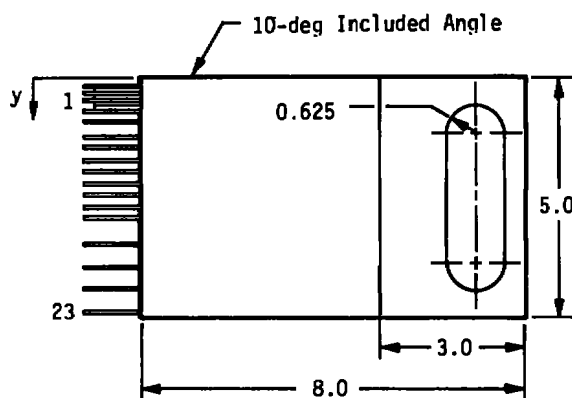
$$\theta = \frac{C_{F11} l_r}{2}; C_{F11} \text{ from Figure A-2}$$



a. AEDC-PWT Tunnel 16S Boundary-Layer Rake

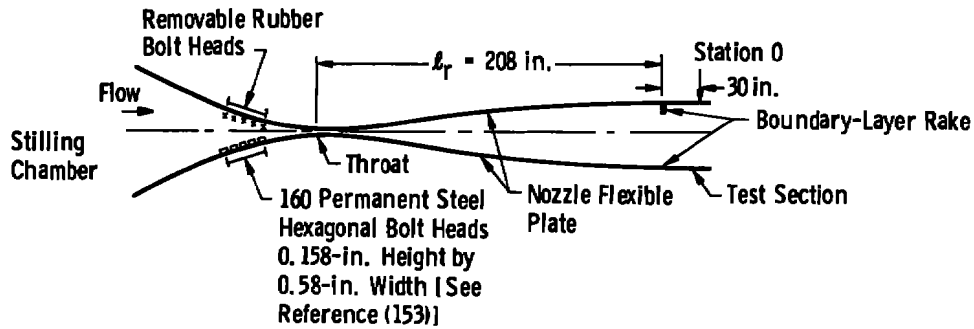
Probe No.	y, in.	Probe No.	y, in.
1	0.20	13	1.50
2	0.25	14	1.75
3	0.30	15	2.00
4	0.35	16	2.25
5	0.40	17	2.50
6	0.45	18	2.75
7	0.55	19	2.95
8	0.60	20	3.50
9	0.65	21	4.00
10	0.75	22	4.45
11	0.95	23	4.95
12	1.25		

NOTE: y is Nominal Distance to Centerline of Probe.  
Tube Size: 0.042 OD x 0.027 ID



b. AEDC-VKF Tunnel A Boundary-Layer Rake

Figure B-2. Boundary-layer rakes used in the AEDC-PWT 16S Tunnel and the AEDC-VKF Tunnel A to measure tunnel wall boundary-layer profiles.



AEDC-VKF Tunnel A Profile

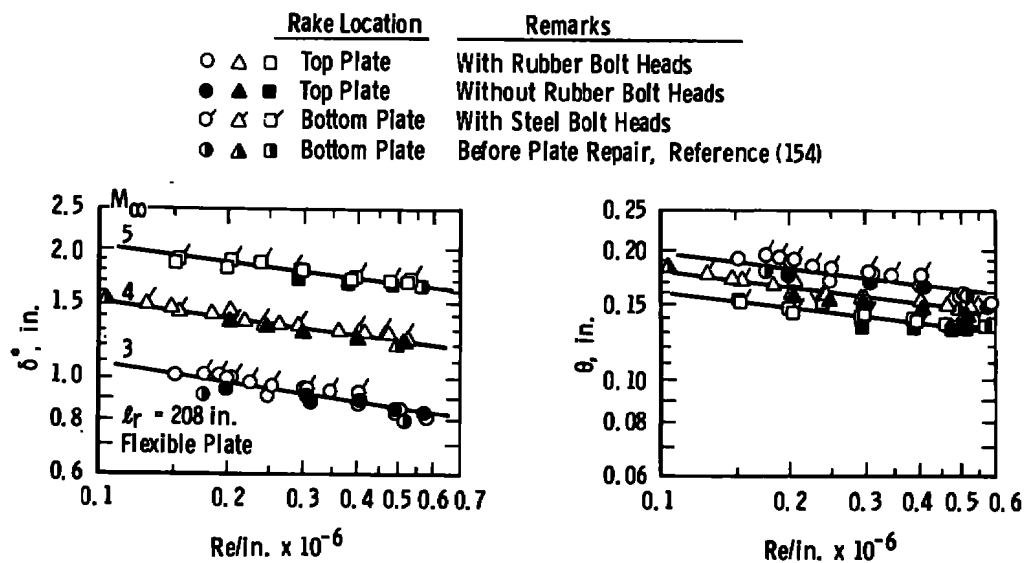


Figure B-3. AEDC-VKF Tunnel A boundary-layer characteristics.

required new lugs to be bolted to the plate. A total of 160 steel bolt heads, protruding 0.158-in. above the plate surface, was required (Figure B-3). Details of the replacement lugs, bolt heads, and plate damage can be found in Reference (153).

Test results presented in Reference (153) showed that the connecting bolt heads had no significant effect on the uniformity of the free-stream flow but increased the boundary-layer displacement thickness ( $\delta^*$ ) on the repaired plate by a factor of approximately 1.5 at a free-stream Mach number ( $M_\infty$ ) of 1.5 and had no effect on  $\delta^*$  at  $M_\infty = 5.0$ .

To obtain more information on the effects of the bolt heads on the bottom plate boundary-layer growth and to provide information on  $\delta^*$  to be used in the transition correlation (discussed in Chapter IX), additional boundary-layer profile measurements were made on the repaired bottom flexible plate using the rake shown in Figure B-2b. The experimental data are presented in Figure B-3 and confirm the results of Reference (153) which showed no bolt-head effects on the bottom plate at  $M_\infty = 5.0$ . Likewise, there was no effect at  $M_\infty = 4.0$  and only about a six-percent increase in  $\delta^*$  at  $M_\infty = 3.0$  when compared with the results from Reference (154).

Since this research was directed toward investigating the effects of radiated aerodynamic noise on transition, it was felt necessary to determine if the plate repair produced any noticeable differences on model transition. Therefore, duplicate rubber bolt heads were glued to the top flexible plate, and the boundary-layer characteristics on the top plate and the transition location on the 3.0-in.-diam hollow-cylinder model were measured with and without these rubber bolt heads. These results

were presented in Figure VII-2, page 170. The data presented in Figure B-3 show no significant effect of the plate repair and the upstream protuberances on the test section  $\delta^*$  and  $\theta$  for  $M_\infty = 3, 4, \text{ and } 5$ .

#### IV. AEDC-VKF TUNNEL E DATA

Studies were conducted in the AEDC-VKF Tunnel E (12- by 12-in. test section) to determine if the axial location of the model in the test section had a significant effect on the location of transition as discussed in Chapter X. An effort was also made to cool the walls of the tunnel using liquid nitrogen in an attempt to maintain laminar flow on the tunnel walls and thereby reduce (eliminate) the radiated aerodynamic noise. The boundary-layer profile was measured at the different model locations to establish if cooling was effective in producing laminar flow and to define the displacement thickness. Figure X-5, page 263, presented in Chapter X, shows the model and rake positions. An eighteen-probe rake was used to measure the pitot pressure distribution through the boundary layer on the bottom flexible plate. The static pressure was computed using the free-stream Mach number at the edge of the boundary (computed using the edge  $p'_0$  measurement) and the tunnel stilling chamber pressure.

Figure B-4 presents the pitot pressure profiles obtained at the two axial stations ( $x_r = 39.6 \text{ and } 56.0 \text{ in.}$ ) for several tunnel stagnation pressure levels. These data are for the uncooled tunnel wall condition and exhibit the mean value characteristics of a turbulent boundary layer. The profiles at  $x_r = 39.6 \text{ in.}$  exhibit a  $p/p'_0$  maximum value greater than 1.0 and also show a decrease in pitot pressure with increasing  $y$  distance

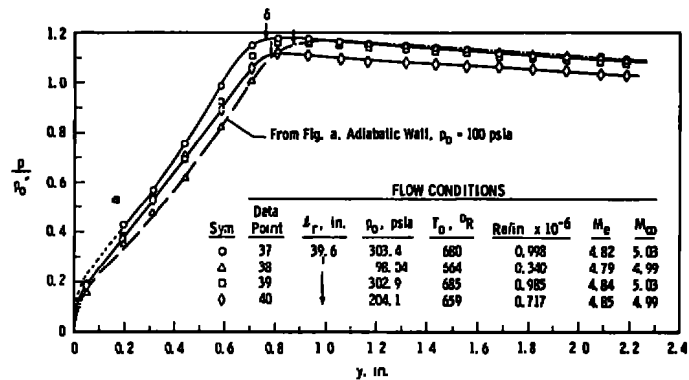
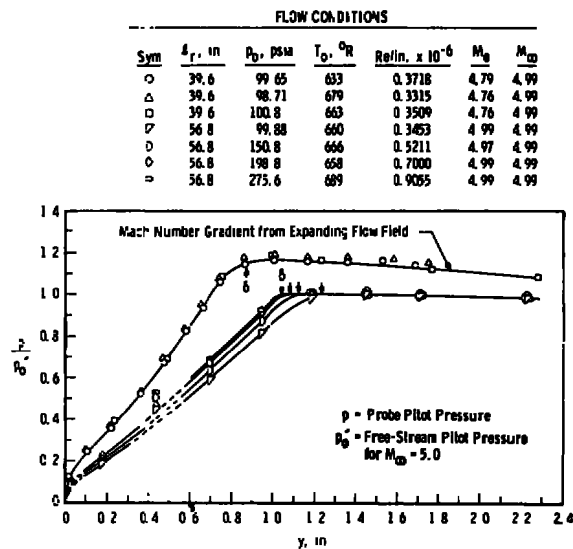


Figure B-4. Pilot pressure profiles from AEDC-VKF Tunnel E,  $M_\infty = 5.0$ .

outside the boundary layer. This is a direct result of the probe ( $x_r = 39.6$  in.) being located in the expanding flow field of the tunnel (see Figure X-5, page 263) where the boundary-layer-edge Mach number was approximately 4.8. The table included in Figure B-4 lists the flow conditions.

Figure B-4 allows a comparison between the cooled and uncooled wall pitot pressure profiles at station  $x_r = 39.6$  in. These data show that the wall cooling for these test conditions had a negligible effect on the development of the turbulent profile.

The boundary-layer displacement thickness ( $\delta^*$ ) values for stations  $x_r = 39.6$  and 56.8 are presented in Figure B-5 for both the cooled and uncooled wall case. These data again show no appreciable effect of cooling. Comparisons with the AEDC-VKF 12-in. Tunnel D data from Reference (97) and the theoretical values of  $\delta^*$  calculated using Reference (156) show good agreement.

It should be mentioned that the information necessary to provide an exact location of the last tunnel characteristic for  $M_\infty = 5$  in Tunnel E was not available. However, the rake data show a negligible Mach number gradient existing outside the boundary layer at station  $x_r = 56.8$  in., and this location is thought to be the approximate axial station for cancellation of the last characteristic for  $M_\infty = 5$ . Therefore, it is assumed that the last characteristic is cancelled at  $x_r = 56.8$  in., and this value is used with Reference (156) to calculate the theoretical  $\delta^*$  values. A knowledge of the last characteristic is also required to provide a meaningful analysis of the transition data.



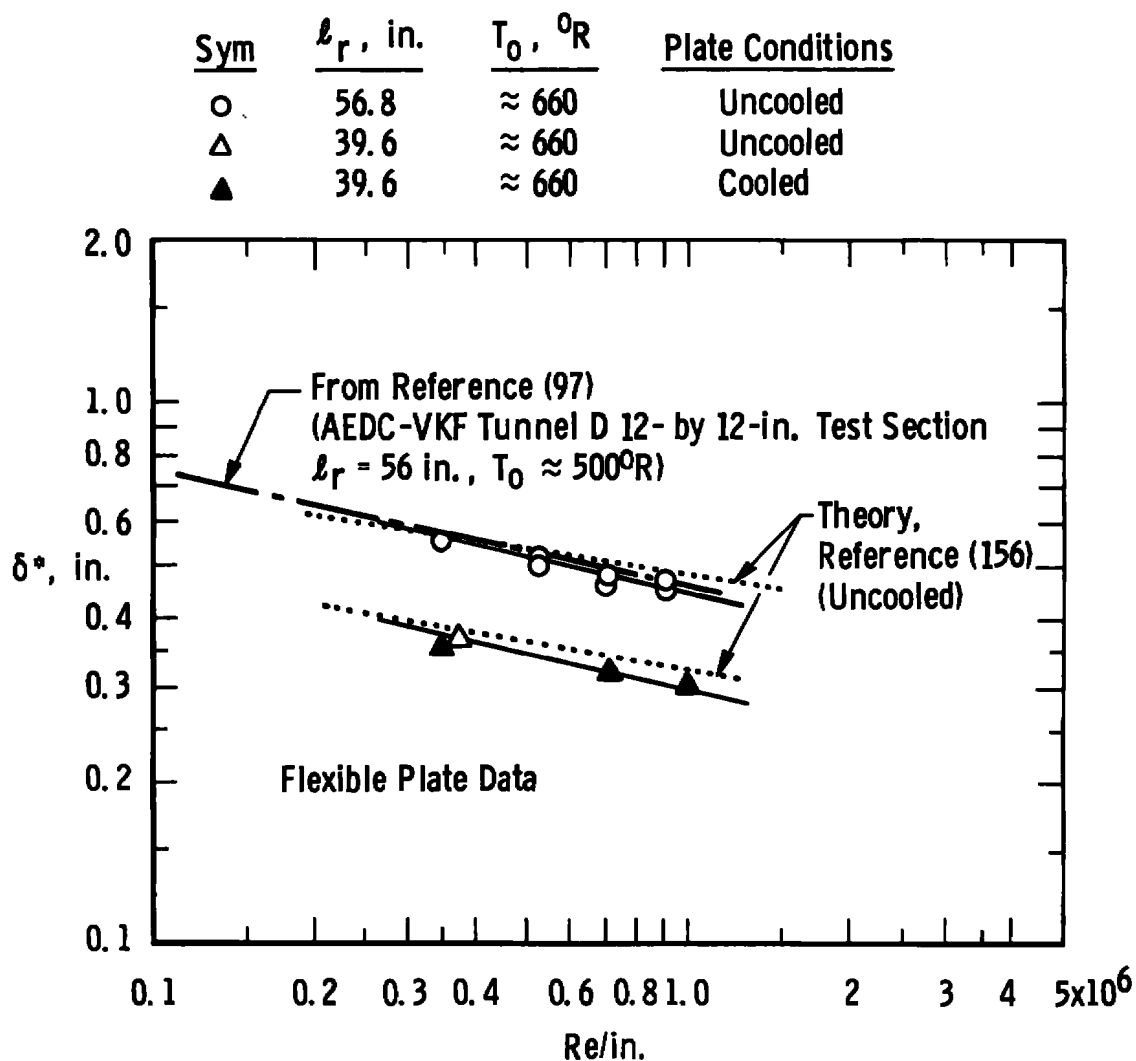


Figure B-5. AEDC-VKF Tunnel E turbulent boundary-layer displacement thickness ( $\delta^*$ ) for  $M_{\infty} = 5.0$ .

Presented in Figure B-6 is a summary of the  $\delta^*$  and  $\theta$  values determined from the experimental boundary-layer pitot pressure profiles measured in the AEDC-VKF Tunnels A and D and AEDC-PWT Tunnel 16S at  $M_\infty = 3.0$ .

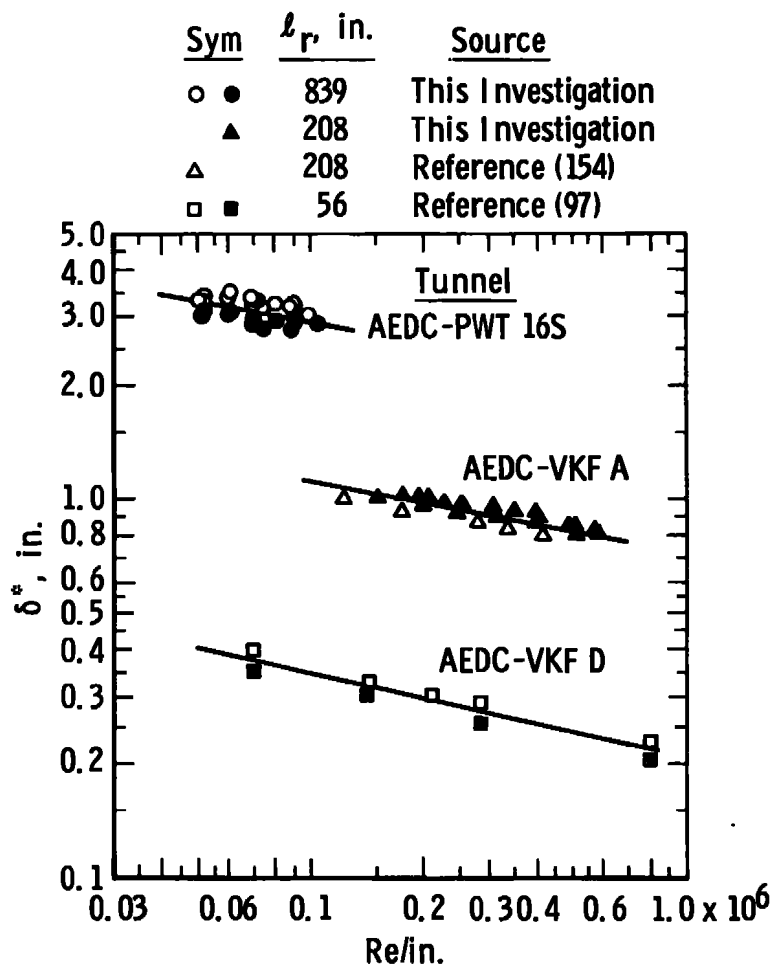
The experimental displacement thickness ( $\delta^*$ ) was evaluated employing the usual assumptions of constant total temperature and constant static pressure through the boundary layer at a particular station.

## V. CORRELATIONS OF BOUNDARY-LAYER DISPLACEMENT THICKNESS

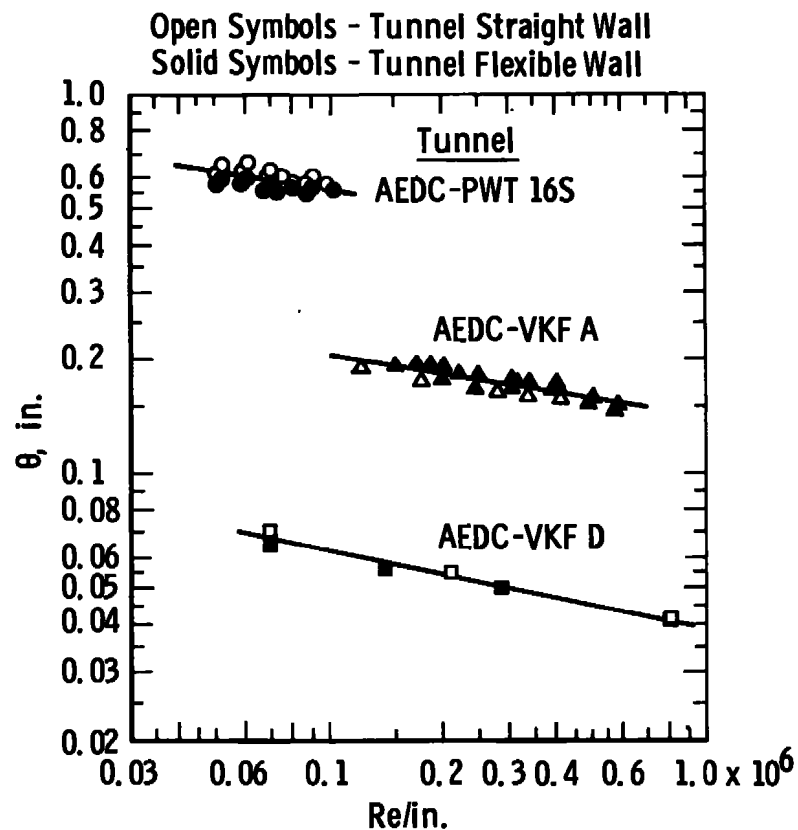
Some data sets used in verifying the aerodynamic-noise-transition correlation presented in Chapter IX required an estimate of  $\delta^*$ . Analytical relationships for  $\delta^*$  are also required in the FORTRAN Computer Program that will be developed in Appendix C for predicting the location of transition on sharp flat plates and sharp cones using the aerodynamic-noise-transition empirical equations [Eqs. (10) and (11)] that were developed in Chapter IX.

In this section the experimental values of  $\delta^*$  are compared with existing correlations to establish if applicable correlations exist, or can be developed, for a wide Mach number range ( $3 \leq M_\infty \leq 15$ ) for both two-dimensional and axisymmetric wind tunnel nozzles.

For  $1.5 \leq M_\infty \leq 5$  the theory developed by Maxwell and Jacocks (156) allows a good correlation of displacement thickness. The following non-dimensional correlating parameters were developed by Maxwell and Jacocks (156) by rearranging the theoretical equation presented by Tucker (157) [obtained by integrating the momentum integral equation].



a. Displacement Thickness



a. Displacement Thickness

Figure B-6. Turbulent boundary-layer characteristics at  $M_\infty = 3.0$  for AEDC Tunnels PWT-16S, VKF-A and VKF-D.

$$\overline{\delta^*} = \frac{\delta^*}{K(X_E)^{6/7}} \quad (\text{B-13})$$

where

$$K = 0.0131 \left( \frac{\mu_0}{\rho_0 a_0} \right)^{1/7} \quad (\text{B-13A})$$

and

$a_0$  = Speed of sound at stagnation conditions, ft/sec

$X_E$  = Longitudinal distance from tunnel throat to nozzle  
aerodynamic exit plane, ft

$\delta^*$  = Boundary-layer displacement thickness, ft

$\mu_0$  = Coefficient of viscosity at stagnation conditions,  
lb-sec/ft<sup>2</sup>

$\rho_0$  = Density at stagnation conditions, lb-sec<sup>2</sup>/ft<sup>4</sup>

Data from nine wind tunnels are presented in Figure B-7 for  $1.5 \leq M_\infty \leq 10$ . Up to  $M_\infty = 5$ , the experimental data are in good agreement with the theoretical estimate of Maxwell and Jacocks (156). One significant trend of the present data at  $M_\infty = 5$  is the dependence of  $\overline{\delta^*}$  on the  $Re/in.$  value. The AEDC-VKF Tunnel D (97) and Tunnel E data obtained in the present research show a decreasing value of  $\overline{\delta^*}$  with increasing  $Re/in.$  values over the range  $0.1 \times 10^6$  to  $1.3 \times 10^6$ . The theory of Reference (157) assumed a 1/7-power-law profile existed ( $u/U = (y/\delta)^{1/N}$ ,  $N = 7$ ), and the large  $Re/in.$  range of these data could reflect a variation in  $N$ . Although the correlation method developed by Maxwell and Jacocks is considered good, there can still be as much as a 10% difference in the predicted value using the mean correlation curve (theory curve) and the actual data value.

	Sym	Facility	Test Section Size	$\ell_r$ , in.	Source
	□	AEDC - VKF (A)	40 in. x 40 in.	---	Reference (156)
	△	AEDC - PWT (SMT)	12 in. x 12 in.	---	Reference (156)
	○	AEDC - VKF (D)	12 in. x 12 in.	56	Reference (97)
	▽	AEDC - PWT - 16S	16 ft x 16 ft	839	Present Invest.
	■	AEDC - VKF (A)	40 in. x 40 in.	208	Present Invest.
	x	JPL - 20-in. SWT	18 in. x 20 in.	66-118	Reference (93)
	⊕	JPL - 21-in. HWT	≈ 20 in. x 21 in.	159	Reference (93)
	◆	AEDC - VKF (E)	12 in. x 12 in.	64	Unpublished VKF Data
	◇	AEDC - VKF (B)	50-in. Diam	244	Figure B-8
	●	AEDC - VKF (E)	12 in. x 12 in.	57	Present Invest.
	⊙	AEDC-VKF (B)	50-in. Diam	242-302	Figure B-8

Cooled Walls

!  $\bar{\delta}^*$  Computed at Aerodynamic Exit Plane ( $\ell_E$ )  
 \*  $\bar{\delta}^*$  Computed at Rake Location ( $\ell_r$ )

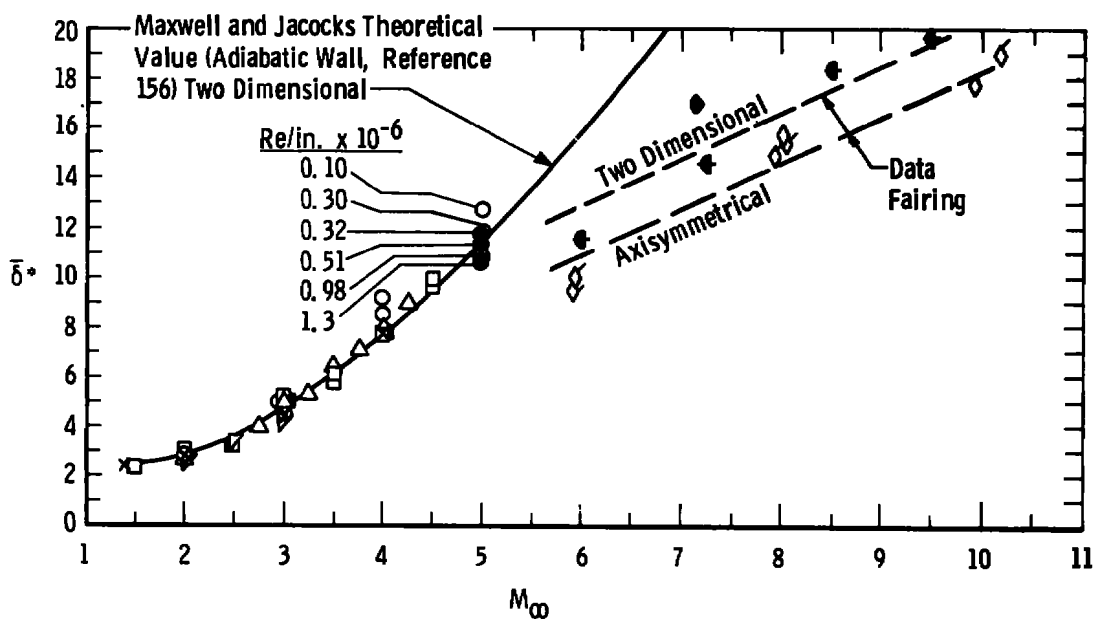


Figure B-7. Flexible plate displacement thickness correlations for  $M_\infty = 1$  to 10.

Data for Mach numbers greater than five do not follow the Maxwell-Jacocks curve as shown in Figure B-7. This is not unexpected since the power-law profile changes at higher Mach numbers ( $7 < N < 11$ ) [Edenfield (105)]; also there are cold wall effects. However, use of the parameter  $\overline{\delta^*}$  does allow a correlation for cold wall, contoured two-dimensional and axisymmetric nozzles to be developed in the range  $5 \leq M_\infty \leq 10$  as shown in Figure B-7. Note that two sets of data were available for the two-dimensional case and three sets for the axisymmetric case. Since axisymmetric (i.e., conical) boundary layers are thinner than two-dimensional boundary layers, it would be expected that the axisymmetric  $\delta^*$  data correlation would be lower than the two-dimensional data, and this is indeed the case as evident in Figure B-7. Empirical equations for the fairings of the  $\delta^*$  data shown in Figure B-7 are presented in Appendix C for use in the FORTRAN Computer Program.

Edenfield (105,158) reviewed different techniques for correlating and predicting  $\delta^*$  in hypersonic axisymmetric nozzles. This work showed that significant differences exist between the various methods, and no one method was clearly superior to the others over a large  $M_\infty$  and  $Re_\infty$  range. In order to select a method that was explicit in nature and produced consistent and reasonable results, the techniques discussed by Edenfield were reviewed and the method of Whitfield was selected as an acceptable method for hypersonic nozzles in the range  $M_\infty \gtrsim 10$ . Data from seven different hypersonic nozzles over a Mach number range from 6 to 16 and a large Reynolds number are presented in Figure B-8. The empirical equation of Whitfield is also presented and the agreement with the data is considered fairly good. The equation shown in Figure B-8 is the

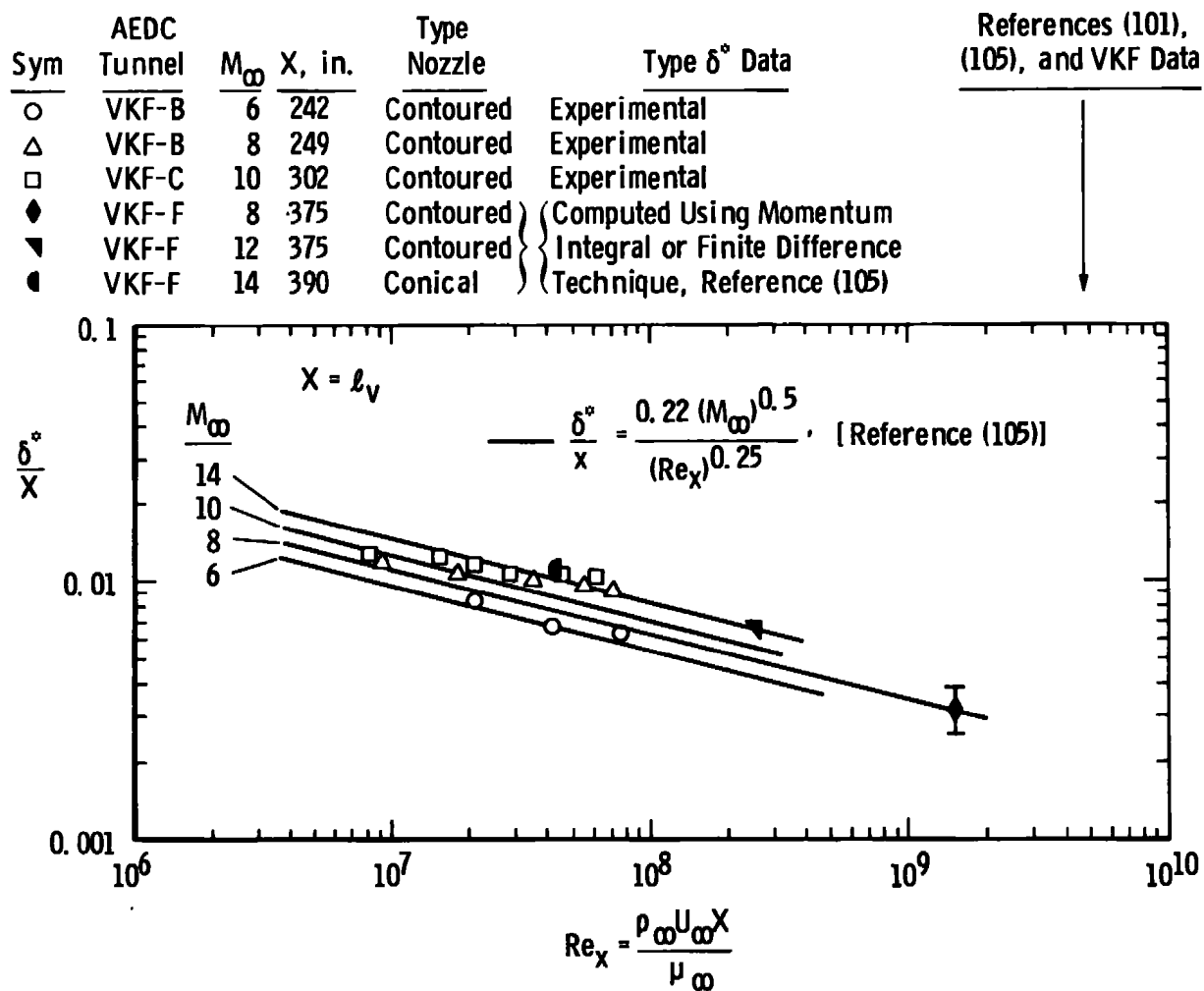


Figure B-8. Correlation of hypersonic wind tunnel wall displacement thickness ( $\delta^*$ ).

method used in the FORTRAN Computer Program developed in Appendix C for  $M_\infty > 10$  and/or  $M_\infty \gtrsim 8$  and  $Re_x \gtrsim 200 \times 10^6$ .



## APPENDIX C

DEVELOPMENT OF FORTRAN IV COMPUTER PROGRAM FOR  
PREDICTING TRANSITION LOCATIONS USING THE  
AERODYNAMIC-NOISE-TRANSITION CORRELATION

## I. METHOD OF APPROACH

The algorithm developed to solve the aerodynamic-noise-transition empirical equations for a sharp flat plate, Eq. (10), page 248, and sharp slender cone, Eq. (11), page 252, at zero angle of attack are presented and discussed in this section. At first glance, Eqs. (10) and (11) appear fairly simple;

Sharp Flat Plate at Zero Angle of Attack (Eq. (10), page 248)

$$(Re_t)_{FP} = \frac{0.0126 (C_{FII})^{-2.55} (\bar{c})}{\sqrt{\frac{\delta^*}{c}}} \quad (C-1)$$

Sharp Slender Cone at Zero Angle of Attack (Eq. (11), page 252)

$$(Re_t)_{cone} = \frac{48.5 (C_{FII})^{-1.40} (\bar{c})}{\sqrt{\frac{\delta^*}{c}}} \quad (C-2)$$

however, computation of the tunnel wall turbulent-boundary-layer displacement thickness ( $\delta^*$ ), tunnel wall skin-friction coefficient ( $C_F$ ), along with the tunnel free-stream unit Reynolds number and flow properties at the surface of an inviscid cone, become a fairly involved and lengthy process. In order to provide a systematic approach and to aide

persons who might be interested in the details of the computer program, the equations required to execute each individual program option are presented in this section. A special effort has been made to include many comment statements in the FORTRAN Program so that the program will be essentially self explanatory. A program listing is provided in Section IV.

There are four program options (KOPT). These options were developed in a manner considered most beneficial to potential users and are described in detail in the program listing. Only a brief description will be given here.

KOPT = 1 and 3

Calculations of transition Reynolds numbers and locations on sharp flat plates at zero angle of attack are provided.

KOPT = 1  $3 \leq M_{\infty} \leq 10$  (ideal gas flow)

KOPT = 3  $M_{\infty} \geq 10$  (real gas flow)

KOPT = 2 and 4

Calculations of transition Reynolds numbers and locations on sharp slender cones at zero angle of attack are provided.

KOPT = 2  $3 \leq M_{\infty} \leq 10$  (ideal gas flow)

KOPT = 4  $M_{\infty} \geq 10$  (real gas flow)

Required input data for all programs options are defined in the program listing (Section IV) and illustrated in the included check problems (Section V).

## II. BASIC EQUATIONS

The following equations were used in the development of KOPT = 1 and KOPT = 2.

### Tunnel Test Section Conditions (Free Stream)

The tunnel test section static temperature ( $T_\infty$ ) and pressure ( $P_\infty$ ) are computed using perfect gas, one-dimensional isentropic flow relationships (155) with  $\gamma = 1.4$ .

$$T_\infty = \frac{T_o}{1 + \frac{\gamma - 1}{2} M_\infty^2} = \frac{T_o}{1 + 0.2 M_\infty^2} \quad (C-3)$$

$$P_\infty = \frac{P_o}{\left(1 + \frac{\gamma - 1}{2} M_\infty^2\right)^{\frac{\gamma}{\gamma - 1}}} = \frac{P_o}{\left(1 + 0.2 M_\infty^2\right)^{3.5}} \quad (C-4)$$

and

$$U_\infty = M_\infty A_\infty = M_\infty \sqrt{\gamma R T_\infty} = (M_\infty)(49) \sqrt{T_\infty} \quad (C-5)$$

The value of the absolute viscosity ( $\mu$ ) is temperature dependent, and consequently two different viscosity laws (linear and Sutherland) are used to compute this parameter. A recent discussion of viscosity laws is given by Fiore in Reference (159).

For temperature below 216<sup>0</sup>R, the viscosity varies linearly with temperature:

### Linear Viscosity Law for Air

$$\mu = (0.0805)(T)(10^{-8}) \text{ lb-sec/ft}^2 \quad (C-6)$$

For temperature above 216<sup>0</sup>R and up to about 5,000<sup>0</sup>K, the Sutherland equation provides the best estimate:

Sutherland Viscosity Law for Air

$$\mu = \frac{(2.270)(T)^{1.5}}{198.6 + T} \times 10^{-8} \text{ lb-sec/ft}^2 \quad (\text{C-7})$$

The free-stream Reynolds number is computed using Eq. (C-8):

$$\text{Re}_\infty = \frac{\rho_\infty U_\infty}{\mu_\infty} = \frac{144 P_\infty U_\infty}{T_\infty \mu_\infty R} \quad (\text{C-8})$$

$$p_\infty \sim \text{lb/in.}^2$$

$$U_\infty \sim \text{ft/sec}$$

$$\mu_\infty \sim \text{lb-sec/ft}^2; \text{ Eqs. (C-6) or (C-7)}$$

$$T_\infty \sim ^\circ\text{R}$$

$$R \sim 1,716 \text{ ft}^2/\text{sec}^2\text{-}^\circ\text{R}$$

Length Reynolds Number

The Reynolds number based on tunnel free-stream conditions and the nozzle length is required in the computation of  $C_F$  and  $\delta^*$  and is computed using the free-stream unit Reynolds number and the tunnel length ( $\ell$ ):

$$\text{Re}_\ell = \text{Re}_{\infty, \ell} = (\text{Re}_\infty)(\ell)/(12) \quad (\text{C-9})$$

where

$$\text{Re}_\infty \sim \text{ft}^{-1}$$

$$\ell \sim \text{in.}$$

NOTE:

$$\ell = \ell_m$$

where  $\ell_m$  = model leading-edge location

Boundary-Layer Displacement Thickness

The turbulent boundary-layer displacement thickness used in Eqs. (C-1) and (C-2) is the tunnel wall value computed at the model leading-edge position ( $\ell_m$ ).

Four separate analytical expressions are required to provide adequate calculation of  $\delta^*$  for the Mach number range from 3 to 20 for two-dimensional, axisymmetric contoured nozzles and conical nozzles. The development of these correlations were discussed in Appendix B (see Figures B-7, page 339, and B-8, page 341).

For two-dimensional nozzles and  $2 \leq M_\infty \leq 5$ , the following empirical equation developed by Maxwell and Jacocks is applicable:

$$\delta^* = 0.0131 \left( \frac{\mu_0}{\rho_0 a_0} \right)^{1/7} (\ell)^{6/7} (\overline{\delta^*}); \text{ ft} \quad (\text{C-10})$$

where

$\mu_0 \sim$  computed from Eq. (C-7)

$\ell \sim$  nozzle length, ft

$$\rho_0 = \frac{144 P_0}{RT_0}, \frac{\text{lb-sec}^2}{\text{ft}^2} \quad (\text{C-10a})$$

$$a_0 = \sqrt{1.4 RT_0} = 49 \sqrt{T_0}, \text{ ft/sec}$$

$$P_0 \sim \text{lb/in.}^2$$

$$T_0 \sim ^\circ\text{R}$$

$$R = 1,717 \text{ ft}^2/\text{sec}^2\text{-}^\circ\text{R}$$

The value  $\delta^*$  is computed from a third-degree polynomial curve fit of the theoretical curve in Figure B-7, page 339:

$$\text{Two-Dimensional} \left\{ \overline{\delta^*} = 1.1408 M_\infty + 0.08813 M_\infty^2 + 0.02698 M_\infty^3; 2 \leq M_\infty \leq 5 \right\} \quad (\text{C-11})$$

Adiabatic  
Nozzles

Equation (C-11) matches the curve in Figure B-7, page 339, to within  $\pm 1.8\%$  for  $2 \leq M_\infty \leq 6$ .

For two-dimensional and axisymmetric nozzles and  $5 < M_\infty \leq 10$  (see Figure B-7, page 339) the following linear equations are used to compute  $\overline{\delta^*}$ :

$$5 < M_\infty \leq 10 \quad \left\{ \begin{array}{l} \overline{\delta^*} = 2.0 + 1.8333 M_\infty : \text{two-dimensional nozzle} \\ \overline{\delta^*} = 0.167 + 1.833 M_\infty : \text{axisymmetric nozzles} \end{array} \right\} \quad \begin{array}{l} \text{Cool Wall} \\ \text{Non-Adiabatic} \\ \text{Nozzles} \end{array} \quad \begin{array}{l} \text{(C-12a)} \\ \text{(C-12b)} \end{array}$$

For the following special conditions

1. Contoured or conical nozzle with  $10 < M_\infty \lesssim 15$
2. Very high Reynolds number flow,  $Re_\infty \geq 2.0 \times 10^6$ ,  
and  $7 < M_\infty < 10$

$\delta^*$  is computed using Whitfield's empirical formula. A discussion of this empirical equation is given in Reference (105) and compared with experimental data in Figure B-8, page 341. Whitfield's empirical equation is

$$\delta^* = \frac{(0.22)(\ell)(M_\infty)^{0.5}}{(Re_{\infty, \ell})^{0.25}} \quad \text{(C-13)}$$

### Turbulent Skin-Friction Coefficient

The method of van Driest-II (see Appendix B) was used to compute the turbulent flow mean-skin friction coefficient for the tunnel wall at the model location in the test section.

The van Driest-II mean skin-friction formula is

$$\frac{0.242}{A \sqrt{C_F} \sqrt{T_w/T_\infty}} (\sin^{-1} \alpha + \sin^{-1} \beta) = \log_{10}(Re_\ell C_F) + 1.5 \log_{10}(T_e/T_w) + \log_{10} \frac{198.6 + T_w}{198.6 + T_e} \quad \text{(C-14)}$$

$T_w$  = tunnel wall temperature

$Re_\ell \sim$  determined by Eq. (C-9)

$$A = \sqrt{\left(\frac{\gamma - 1}{2} r M_\infty^2\right) \frac{T_\infty}{T_w}} ; r = \text{recovery factor} = 0.9 \quad (\text{C-14a})$$

$$B = \left(1 + \frac{\gamma - 1}{2} r M_\infty^2\right) (T_\infty/T_w) - 1 \quad (\text{C-14b})$$

$$\alpha = (2A^2 - B)/\sqrt{B^2 + 4A^2} \quad (\text{C-14c})$$

$$\beta = B/\sqrt{B^2 + 4A^2} \quad (\text{C-14d})$$

$$\gamma = 1.4$$

Since Eq. (C-14) is implicit in  $C_F$ , the Newton-Raphson method was used to solve for  $C_F$  when  $M_\infty$ ,  $Re_\ell$ ,  $T_w$ , and an initial value of  $C_F$  are specified. Equation (C-14) can be rewritten as

$$FCF = \sqrt{C_F} (C_2 + C_3 + \log_{10} C_F) - C_4 \quad (\text{C-15})$$

where

$$C_4 = \frac{0.242 (\sin^{-1} \alpha + \sin^{-1} \beta)}{A \sqrt{T_w/T_\infty}} \quad (\text{C-15a})$$

$$C_2 = \log_{10} Re_\ell \quad (\text{C-15b})$$

$$C_3 = 1.5 \log_{10} \left(\frac{T_e}{T_w}\right) + \log_{10} \left(\frac{198.6 + T_w}{198.6 + T_e}\right) \quad (\text{C-15c})$$

Application of the Newtonian-Raphson method gives

$$C_{Fi} = C_{Fi-1} - FCF / \frac{dFCF}{dC_F} \quad (\text{C-16})$$

$\frac{dFCF}{dC_F}$  is the derivative of FCF with respect to  $C_F$ .

$$\frac{dFCF}{dC_F} = 0.5 (C_F)^{-\frac{1}{2}} [C_2 + C_3 + \log_{10} C_F + 0.8686] \quad (\text{C-17})$$

By computing an initial value of  $C_{FII}$  using  $C_{FII} = 0.0050/M_\infty$ , Eqs. (C-15) and (C-17) are solved and a new value of the  $C_F$  term ( $C_{Fi}$ ) is computed from Eq. (C-16)

This process is repeated using the newly computed  $C_F$  term in the right side of Eq. (C-16) until the difference in successive calculations of  $C_F$  are within the specified limit of 0.0000010:

$$(|C_{Fi} - C_{Fi-1}| \leq 0.0000010)$$

This value of  $C_F$  is then used along with the computed  $\delta^*$  value [Eqs. (C-12) or (C-13)] to calculate the transition Reynolds number from Eqs. (C-1) or (C-2).

#### Program Option 1 (Sharp Flat Plate at $\alpha = 0$ )

The location of transition on a flat plate is determined by

$$X_t = (Re_t/Re_\infty)(12); \text{ in.} \quad (C-18)$$

where  $Re_t$  is computed from Eq. (C-1) and  $Re_\infty$  from Eq. (C-8).

#### Program Option 2 (Sharp Slender Cone at $\alpha = 0$ )

The analytical expressions required to determine the transition location on a sharp cone are presented in this section.

The values for  $C_{FII}$  and  $\delta^*$  are computed exactly as in Program Option 1 [Eqs. (C-9) through (C-17)]. With known values of  $C_{FII}$ ,  $\delta^*$ , and the tunnel coordinates  $C$ ,  $\lambda$ , then the transition Reynolds number is computed using Eq. (C-2). However, what one usually wants to know is the location of transition on the cone surface and this requires knowing the cone surface inviscid Reynolds number, i.e., the local free-stream Reynolds number at the edge of the boundary layer on the cone surface.



For a flat plate at zero angle of attack, the plate surface inviscid parameters are assumed equal to the free-stream parameters, e.g., plate boundary-layer edge conditions equal  $M_\infty$ ,  $Re_\infty$ ,  $T_\infty$ ,  $p_\infty$ , etc. However, in order to determine the inviscid surface parameters for a sharp cone, relationships between the surface values and free-stream values are required.

### Cone Surface Static Pressure

The static pressure on the surface of a sharp cone at zero angle of attack is computed by the "approximate" analytical expression developed by Rasmussen (160). The cone surface pressure coefficient from Reference (160) is

$$\frac{C_{p_s}}{\sin^2 \delta} = 1 + \left\{ \left[ \frac{(\gamma + 1)K^2 + 2}{(\gamma - 1)K^2 + 2} \right] \ln \left( \frac{\gamma + 1}{2} + \frac{1}{K^2} \right) \right\} \quad (C-19)$$

where

$$K = M_\infty \sin \delta_c$$

$$\delta_c = \frac{1}{2} \text{ the cone included angle}$$

$$\gamma = \text{ratio of specific heats} = 1.4$$

and  $C_{p_s}$  is the pressure coefficient defined as

$$C_{p_s} = \frac{p_s - p_\infty}{q_\infty} = \frac{2(p_s - p_\infty)}{p_\infty M_\infty^2} \quad (C-20)$$

and

$$q_\infty = \frac{1}{2} \rho_\infty U_\infty^2 = \frac{1}{2} \frac{p_\infty}{RT_\infty} M_\infty^2 RT_\infty = \frac{1}{2} p_\infty \gamma M_\infty^2 \quad (C-21)$$

is defined as the free-stream dynamic pressure.

Using Eqs. (C-19), (C-20), and (C-21) the cone surface static pressure ( $p_s$ ) can be expressed as

$$\frac{p_s}{p_\infty} = 1 + \sin^2 \left( \frac{\gamma M_\infty^2}{2} \right) \left\{ 1 + \left[ \frac{(\gamma + 1) M_\infty^2 \sin^2 \delta + 2}{(\gamma - 1) M_\infty^2 \sin^2 \delta + 2} \right] \ln \left( \frac{\gamma + 1}{2} + \frac{1}{M_\infty^2 \sin^2 \delta} \right) \right\} \quad (C-22)$$

### Cone Shock Wave Angle

A formula for the bow shock angle ( $\phi$ ) as developed by Rasmussen (160) is

$$\frac{\sin \phi}{\sin \delta_c} = \left[ \frac{\gamma + 1}{2} + \frac{1}{K^2} \right]^{\frac{1}{2}} \quad (C-23)$$

### Cone Surface Velocities and Static Temperature

The velocity and temperature at the cone surface is found by using oblique shock wave theory and isentropic flow theory in conjunction with the known cone surface pressure and shock wave angle computed from Eqs. (C-22) and (C-23), respectively.

### Oblique Shock Wave Theory

The static pressure ( $p_2$ ) and temperature ( $T_2$ ) are computed using oblique shock wave equations (155). For  $\gamma = 1.4$ , these equations are

$$\frac{p_2}{p_\infty} = \frac{7 M_\infty^2 \sin^2 \phi - 1}{6} \quad (C-24)$$

$$\frac{T_2}{T_\infty} = \frac{(7 M_\infty^2 \sin^2 \phi - 1)(M_\infty^2 \sin^2 \phi + 5)}{36 M_\infty^2 \sin^2 \phi} \quad (C-25)$$

where  $P_2$  and  $T_2$  are the static pressure and temperature immediately downstream of the oblique shock wave.

Isentropic flow theory is valid between downstream of the bow shock wave and the cone surface since the flow field in this region is free from shock waves and consists of an isentropic compression process.

Using the isentropic flow relationship

$$\frac{p}{\rho^\gamma} = \text{constant} \quad (\text{C-26})$$

and the ideal gas equation of state

$$p = \rho RT \quad (\text{C-27})$$

one obtains

$$\frac{T_s}{T_2} = \left( \frac{p_2}{p_s} \right)^{\frac{\gamma-1}{\gamma}} \quad (\text{C-28})$$

$T_s$  can be computed directly from Eq. (C-28) since  $p_s$ ,  $p_2$ , and  $T_2$  are known quantities determined from Eqs. (C-20), (C-24), and (C-25), respectively, and  $\gamma = 1.4$  for air.

### Cone Surface Velocities

The velocity at the cone surface is computed using the equation for total enthalpy and the basic physical law that energy (total enthalpy) is conserved.

since

$$H_{0_\infty} = H_{02} = H_{0s} = h_s + \frac{U_s^2}{2} \quad (\text{C-29})$$

and

$$H_{0_\infty} = c_p T_o \quad (\text{C-30})$$

$$h_s = c_p T_s \quad (\text{C-31})$$

where for an ideal gas,  $C_p = \text{constant} = 6,006 \text{ ft}^2/\text{sec}^2\text{-OR}$ . Then from Eqs. (C-28), (C-29), (C-30, and (C-31), one gets

$$U_s = (2C_p)^{1/2} \left[ T_0 - T_2 \left( \frac{p_s}{p_2} \right)^{\frac{\gamma-1}{\gamma}} \right]^{1/2} \quad (\text{C-32})$$

and

$$M_s = \frac{U_s}{\sqrt{\gamma R T_s}} \quad (\text{C-33})$$

### Cone Surface Reynolds Number

The unit Reynolds number at the surface of an inviscid cone is computed from

$$\text{Re}_s = \frac{\rho_s U_s}{\mu_s} = \frac{p_s}{R T_s} \frac{U_s}{\mu_s} \quad (\text{C-34})$$

using Eqs. (C-22), (C-25), (C-28), and (C-32) with  $\mu_s$  computed from either Eqs. (C-6) or (C-7), depending on the value of  $T_s$ .

The location of transition on the cone surface is computed from

$$(X_t)_c = \frac{(\text{Re}_t)_c (12)}{\text{Re}_s}, \text{ in.} \quad (\text{C-35})$$

using Eqs. (C-2) and (C-34).

### Cone Surface Reynolds Number Ratios

Results obtained using the methods developed in the preceding section for computing inviscid cone surface flow properties and surface Reynolds number are compared in Figure C-1 with the "exact" numerical technique as developed by Jones (161) and used by Sims (162) to compute extensive tables of cone properties and by applying the appropriate

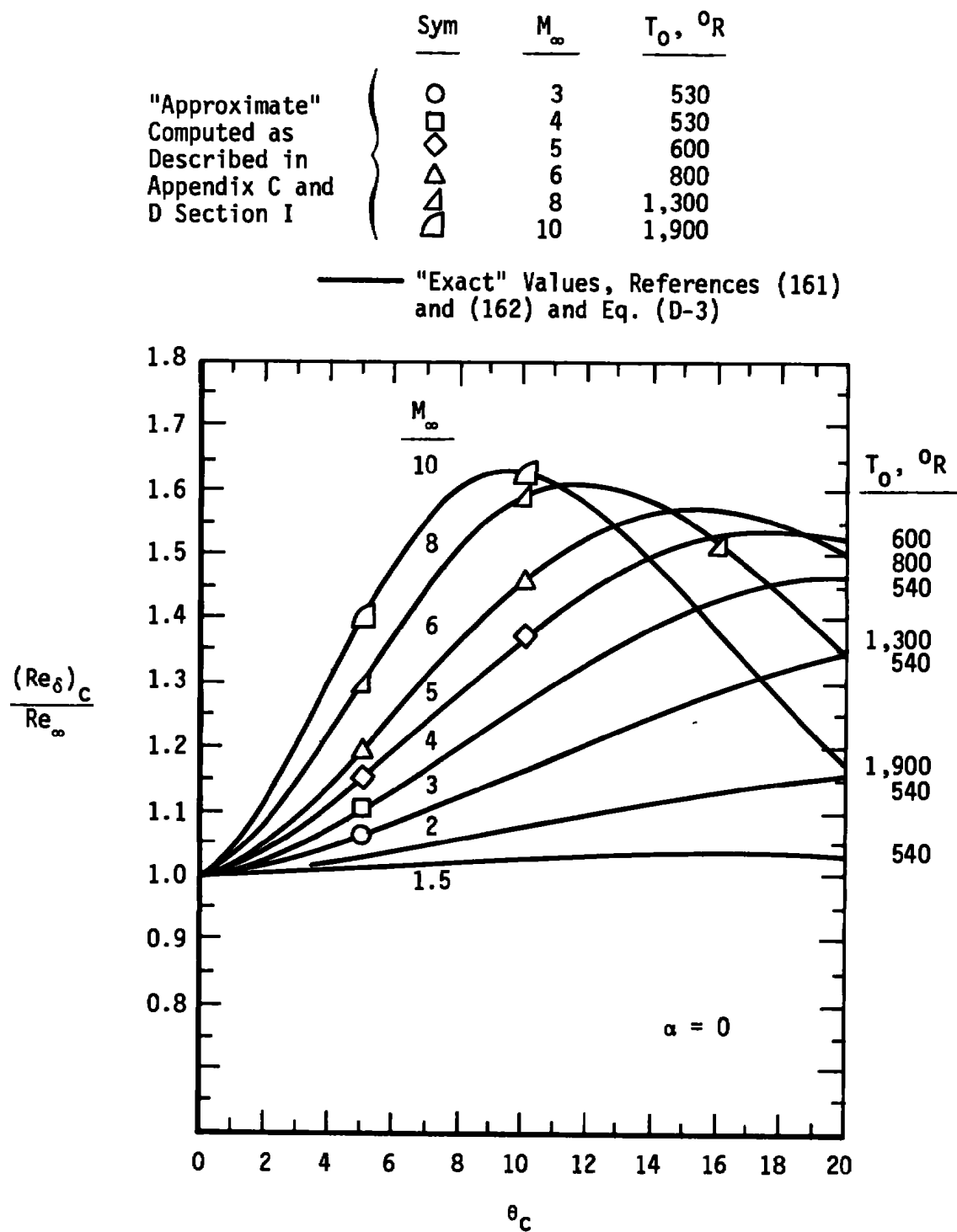


Figure C-1. Comparisons of approximate and exact cone surface Reynolds number ratios.

viscosity law [Eqs. (C-6) or (C-7)]. The results presented in Figure C-1 show that the approximate theories of Rasmussen (160) in conjunction with constant total enthalpy and isentropic flow theory as developed in the previous section adequately predicts the Reynolds number on the surface of inviscid cones for  $M_\infty \geq 3$  and  $\delta \geq 5$  deg.

#### Program Options 3 and 4

Transition Reynolds numbers are computed using Eqs. (C-1) or (C-2), page 326, in conjunction with Eqs. (C-13) and (C-14). The free-stream unit Reynolds number ( $Re_\infty = \rho_\infty U_\infty / \mu_\infty$ ) is a required manual input and not computed using the ideal gas equations [Eqs. (C-3) through (C-8)]. KOPTS 3 and 4 are designed to accommodate wind tunnels having a real gas nozzle expansion. Sharp cone surface Reynolds numbers are also a required manual input and can be obtained from Figure D-2, page 358.

Section IV provides a detailed description of Program Options 1, 2, 3, and 4 and specifies all required input data.

### III. COMPUTER CODE NOMENCLATURE

#### Symbols

<u>Computer</u>	<u>Conventional</u>	<u>Definition</u>	<u>Units</u>
A	---	Variable in Skin-Friction Formula, Eq. (C-14a)	---
AO	$a_0$	Tunnel Stilling Chamber Speed of Sound	ft/sec
ALPHA	$\alpha$	Variable in Skin-Friction Formula, Eq. (C-14c)	---
B	---	Variable in Skin-Friction Formula, Eq. (C-14b)	---

Symbols

<u>Computer</u>	<u>Conventional</u>	<u>Definition</u>	<u>Units</u>
BC	$\bar{C}$	Tunnel Size Parameter for Cones, Eq. (11)	---
BFP	$\bar{C}$	Tunnel Size Parameter for Flat Plates, Eq. (10)	---
BARDEL	$\bar{\delta}$	Tunnel Wall Boundary Displacement Thick- ness Parameter, Eq. (C-11)	---
BETA	$\beta$	Variable in Skin-Friction Formula, Eq. (C-14b)	---
C	C	Tunnel Test Section Circumference	in.
CC CFP	---	Aerodynamic-Noise-Transition Correlation Parameter, Eq. (10), $CC = \sqrt{\delta^*/C}$	---
CF	$C_F$	Mean Turbulent Skin-Friction Coefficient, Eq. (C-14), ( $C_F = C_{FII}$ )	---
CP	$C_p$	Specific Heat of Air at Constant Pres- sure, $C_p = 6,006 \text{ ft}^2/\text{sec}^2$ -OR	$\frac{\text{ft}^2}{\text{sec}^2}$ -OR
C1	$C_1$	Test Section Circumference of 12- by 12-in. Tunnel, $C_1 = 48 \text{ in.}$	in.
C2,C3, C4	$C_2, C_3, C_4$	Variables in Skin-Friction Formula, Eq. (C-15)	
DELS	$\delta^*$	Tunnel Wall Boundary-Layer Displacement Thickness	in.
DELTA	$\delta_c, \theta_c$	Cone Half-Angle	deg
FCF	$FC_F$	See Eq. (C-15)	---
FPRIME	$\frac{dFCF}{dC_F}$	See Eq. (C-17)	---

Symbols

<u>Computer</u>	<u>Conventional</u>	<u>Definition</u>	<u>Units</u>
GAMMA	$\gamma$	Ratio of Specific Heats ( $\gamma = 1.4$ for Air)	---
K	---	Counter in Number of Loops Used to Satisfy $C_F$ Convergence Criteria. If $K \geq 100$ Program Will Be Terminated.	---
KOPT	Option	Program Option	---
KGEOM	Geometry	Wind Tunnel Nozzle Geometry	---
		$K_{\text{geom}} = 1$ , Two-Dimensional Nozzle	---
		$K_{\text{geom}} = 2$ , Axisymmetric Nozzle	---
		$K_{\text{geom}} = 3$ , Conical Nozzle	---
OK	OK	Variable in $\delta^*$ Equation, Eq. (C-10), $OK = 0.0131 (\mu_\infty / \rho_0 a_0)^{1/7}$	(ft) <sup>1/7</sup>
PHI	$\phi$	Sharp Cone Bow Shock Angle, Eq. (C-23)	radians
P0	$p_0$	Tunnel Stilling Chamber Pressure	psia
PS1,PS2, PS3,PS4, PS5	--- --- ---	Variables in Cone Surface Static Pressure Equation, Eq. (C-22)	--- --- ---
P1	$p_\infty$	Free-Stream Static Pressure in Wind Tunnel Test Section, Eq. (C-4)	psia
R		Gas Constant, $R = 1,716 \text{ ft}^2/\text{sec}^2\text{-}^\circ\text{R}$	$\text{ft}^2/\text{sec}^2\text{-}^\circ\text{R}$
RT	$r, \eta_r$	Temperature Recovery Factor $r = (T_{aw} - T_\delta) / (T_0 - T_\delta)$	---
REL	$Re_{\ell_m}$	Reynolds Number Based on Distance to Model Leading-Edge Location, $Re_{\ell_m} = \rho_\infty U_\infty \ell_m / \mu_\infty$ , Eq. (C-9)	---



Symbols

<u>Computer</u>	<u>Conventional</u>	<u>Definition</u>	<u>Units</u>
RES, RESC	$(Re_\delta)_c$	Cone Surface Unit Reynolds Number $Re_s = \rho_s U_s / \mu_s$ , Eq. (C-34)	$(ft)^{-1}$
RHO	$\rho_0$	Tunnel Stilling Chamber Density, Eq. (C-10a)	$\frac{lb \cdot sec^2}{ft^2}$
RC1C	$\frac{C_1}{C}$	Ratio of Tunnel Circumference to Reference Value	---
RP21	$\frac{P_2}{P_\infty}$	Ratio of Static Pressure Immediately Behind Cone Bow Shock Wave to Free- Stream Static Pressure, Eq. (C-24)	---
RTS1	$\frac{T_s}{T_\infty}$	Ratio of Cone Surface Static Tempera- ture to Free-Stream Value	---
RT21	$\frac{T_2}{T_\infty}$	Ratio of Static Temperature Immediately Downstream of Cone Bow Shock Wave to Free-Stream Value, Eq. (C-25)	---
REINF	$Re_\infty$	Tunnel Test Section Free-Stream Unit Reynolds Number, Eq. (C-8)	$(ft)^{-1}$
RETFP	$Re_t$ $(Re_t)_{FP}$	Flat-Plate Transition Reynolds Number $Re_t = \rho_\infty U_\infty x_t / \mu_\infty$ , Eq. (C-1)	---
RETSC	$(Re_t)_c, (Re_t)_\delta$	Cone Transition Reynolds Number $(Re_t)_\delta = \rho_\delta U_\delta x_t / \mu_\delta$ , Eq. (C-2)	---
RMACH	$M_\infty$	Tunnel Test Section Free-Stream Mach Number	---
RMACHS	$M_\delta$	Cone Surface Reynolds Number, Eq. (C-33)	---

Symbols

<u>Computer</u>	<u>Conventional</u>	<u>Definition</u>	<u>Units</u>
RPSI	$\frac{p_s}{p_\infty}$	Ratio of Cone Surface Static Pressure to Tunnel Free-Stream Value, Eq. (C-22)	---
RRHOSI	$\frac{\rho_s}{\rho_\infty}$	Ratio of Cone Surface Static Density to Tunnel Test Section Free-Stream Value	---
RRESC RRES1	$\frac{Re_s}{Re_\infty}$	Ratio of Cone Surface Unit Reynolds Number to Tunnel-Stream Value	---
RTWTAW	$\frac{T_w}{T_{aw}}$	Ratio of Wall Temperature to Adiabatic Wall Temperature	---
T0	$T_o$	Tunnel Stilling Chamber Temperature	°R
TS	$T_s$	Cone Surface Static Temperature, Eq. (28)	°R
TW	$T_w$	Wall Temperature	°R
T1	$T_\infty$	Tunnel Test Section Free-Stream Static Temperature, Eq. (C-3)	°R
TAW	$T_{aw}$	Adiabatic Wall Temperature	
US	$U_s$	Flow Velocity at Cone Surface, Eq. (C-32)	ft/sec
U1	$U_\infty$	Tunnel Test Section Free-Stream Velocity, Eq. (C-5)	ft/sec
VISO	$\mu_o$	Tunnel Stilling Chamber Absolute Viscosity, Eq. (C-7)	$\frac{lb-sec}{ft^2}$
VISS		Cone Surface Absolute Viscosity Based on Linear Law, Eq. (C-6)	$\frac{lb-sec}{ft^2}$
VIS1		Tunnel Test Section Free-Stream Viscosity, Eqs. (C-6) or (C-7)	$\frac{lb-sec}{ft^2}$
XL	$X_\ell$	Distance from Tunnel Throat to Model Leading Edge	in.

Symbols

<u>Computer</u>	<u>Conventional</u>	<u>Definition</u>	<u>Units</u>
XTFP	$x_t$ $(x_t)_{FP}$	Transition Location on Flat Plate, Eq. (C-18)	in.
XTSC	$(x_t)_C$ $(x_t)_\delta$	Transition Location on Cone Surface, Eq. (C-35)	in.

## IV. COMPUTER PROGRAM LISTING

```

C *****
C *****PREDICTION OF BOUNDARY LAYER TRANSITION*****
C *****ON SHARP FLAT PLATES AND SHARP CONES USING *****
C *****PATE'S AERODYNAMIC-NOISE-TRANSITION CORRELATION*****
C *****
C ***** GENERAL COMMENTS *****
C **THIS COMPUTER CODE ALLOWS REASONABLY ACCURATE
C PREDICTIONS OF TRANSITION REYNOLDS NUMBERS AND
C LOCATIONS TO BE MADE ON SHARP FLAT PLATES AND
C SLENDER CONES AT ZERO INCIDENCE FOR ALL SIZE
C WIND TUNNELS AND  $3 < N < 20$ .
C
C **THIS COMPUTER CODE IS VALID FOR AIR OR NITROGEN
C
C **THE AERODYNAMIC-NOISE-TRANSITION CORRELATION AND
C CONSEQUENTLY ,THIS COMPUTER PROGRAM IS APPLICABLE
C ONLY TO CONVENTIONAL SUPERSONIC-HYPERSONIC WIND
C TUNNELS HAVING TURBULENT BOUNDARY LAYERS ON THE
C NOZZLE WALLS AND  $3 < M < 20$  .
C
C **THE PREDICTED LOCATION OF TRANSITION CORRESPONDS TO
C THE END OF TRANSITION AS DEFINED BY THE PEAK IN
C A SURFACE PITOT PROBE PRESSURE TRACE
C
C **THE VALUE OF THE TUNNEL WALL MEAN TURBULENT SKIN
C FRICTION COEFFICIENT USED IN THE AERODYNAMIC-NOISE
C TRANSITION CORRELATION IS COMPUTED USING THE METHOD
C OF VAN DRIEST-II ,INCLUDING NON-ADIABATIC WALL EFFECTS
C
C ** THE TUNNEL TEST SECTION WALL TURBULENT BOUNDARY
C LAYER DISPLACEMENT THICKNESS USED IN THE AERODYNAMIC-
C NOISE-TRANSITION CORRELATION IS COMPUTED USING
C CORRELATION DEVELOPED FROM 2-D AND 3-D NOZZLE DATA
C
C **FOUR PROGRAM OPTIONS ARE AVAILABLE
C *KOPT = 1 AND 2 ARE FOR IDEAL GASES,GAMMA=1.4
C *KOPT = 3 AND 4 ARE FOR REAL GAS NOZZLE EXPANSIONS
C
C *****
C PROGRAM OPTIONS
C *****
C
C KOPT = 1
C **TRANSITION REYNOLDS NUMBERS AND LOCATIONS ON SHARP
C FLAT PLATE OR HOLLOW CYLINDER AT ZERO INCIDENCE
C **IDEAL GAS, GAMMA = 1.4
C ** $3 < RMACH < 10$ 
C **** REQUIRED INPUT DATA ****
C * KOPT = 1
C * KGEUM = 1 OR 2
C * C=TUNNEL TEST SECTION CIRCUMFERENCE
C * XL= AXIAL DISTANCE FROM TUNNEL THROAT
C TO MODEL LEADING EDGE LOCATION,INCHES

```

```

C      * P0= TUNNEL STILLING CHAMBER PRESSURE,PSIA
C      * T0= TUNNEL STILLING CHAMBER TEMPERATURE ,DEG R
C      * RMACH= TUNNEL TEST SECTION MACH NUMBER
C      * TW=TUNNEL WALL TEMPERATURE, DEG R
C
C      KOPT = 2
C      **TRANSITION REYNOLDS NUMBERS AND LOCATIONS ON
C      SHARP SLENDER CONES AT ZERO INCIDENCE
C      **IDEAL GAS, GAMMA =1.4
C      **3 < RMACH < 10
C      **** REQUIRED INPUT DATA ****
C      * KOPT = 2
C      * KGEOM = 1 OR 2
C      * C=TUNNEL TEST SECTION CIRCUMFERENCE
C      * XL= AXIAL DISTANCE FROM TUNNEL THROAT
C      TO MODEL LEADING EDGE LOCATION,INCHES
C      * P0= TUNNEL STILLING CHAMBER PRESSURE,PSIA
C      * T0= TUNNEL STILLING CHAMBER TEMPERATURE ,DEG R
C      * RMACH= TUNNEL TEST SECTION MACH NUMBER
C      * DELTA = CONE HALF ANGLE ,DEG
C      * TW=TUNNEL WALL TEMPERATURE, DEG R
C
C      KOPT = 3
C      ** TRANSITION REYNOLDS NUMBERS AND LOCATIONS
C      ON SHARP FLAT PLATES AT ZERO INCIDENCE
C      ** REAL GAS EFFECTS CONSIDERED IN NOZZLE EXPANSION
C      PROCESS
C      ** 7 < RMACH < 20 , P0 > 5000 PSIA
C      ** FREE-STREAM STATIC TEMP. SET EQUAL TO 90 DEG R
C      **** REQUIRED INPUT DATA ****
C      * KOPT = 3
C      * KGEOM = 3
C      * C= TUNNEL TEST SECTION CIRCUMFERENCE
C      * XL=AXIAL DISTANCE FROM TUNNEL THROAT TO
C      MODEL LEADING EDGE LOCATION,INCHES
C      * RMACH
C      * REINF = TUNNEL TEST SECTION UNIT REYNOLDS
C      NUMBER ( OBTAIN FROM FIG )
C      * TW = TUNNEL WALL TEMPERATURE,DEG R
C
C      KOPT = 4
C      ** TRANSITION REYNOLDS NUMBERS AND LOCATIONS
C      ON SHARP SLENDER CONES AT ZERO INCIDENCE
C      ** REAL GAS EFFECTS CONSIDERED IN NOZZLE
C      EXPANSION PROCESS
C      ** 7 < RMACH < 20 , PP > 5000 PSIA
C      ** FREE-STREAM STATIC TEMPERATURE SET EQUAL
C      TO 90 DEG R
C      **** REQUIRED INPUT DATA ****
C      *KOPT = 4
C      *KGEOM = 3
C      * C= TUNNEL TEST SECTION CIRCUMFERENCE
C      * XL=AXIAL DISTANCE FROM TUNNEL THROAT TO
C      MODEL LEADING EDGE LOCATION,INCHES
C      * RMACH
C      * REINF = TUNNEL TEST SECTION UNIT REYNOLDS
C      NUMBER ( OBTAIN FROM FIG )
C      *RRESC = RATIO OF CONE SURFACE UNIT REYNOLDS

```

```

C                                     NUMBER TO FREE-STREAM VALUE
C                                     (USE FIG  )
C                                     * TW = TUNNEL WALL TEMPERATURE, DEG R
C                                     * DELTA = CONE HALF ANGLE DEG
C *****
C TUNNEL NOZZLE GEOMETRIES
C   KGEOM = 1
C     * FOR TWO-DIMENSIONAL CONTOURED NOZZLES
C     *  $1.5 < \text{RMACH} < 5$  ADIABATIC WALLS
C     *  $5 < \text{RMACH} < 10$  NON-ADIABATIC WALLS
C     * METHOD OF MAXWELL IS USED TO COMPUTE
C     * BOUNDARY LAYER DISPLACEMENT THICKNESS ON
C     * TUNNEL TEST SECTION WALL
C     * IDEAL GAS, GAMMA = 1.4
C     * USE WITH KOPT = 1 OR 2
C   KGEOM = 2
C     * FOR AXISYMMETRIC CONTOURED NOZZLES
C     *  $5 < \text{RMACH} < 10$ 
C     * NON-ADIABATIC WALL
C     *
C   KGEOM = 3
C     * FOR CONICAL AND CONTOURED AXISYMMETRIC NOZZLES
C     * NON-ADIABATIC WALL
C     *  $7 < \text{RMACH} < 20$ 
C     * USE WITH KOPT = 3 OR 4
C     * METHOD OF WHITFIELD USED TO COMPUTE BOUNDARY
C     * LAYER DISPLACEMENT THICKNESS ON TUNNEL TEST
C     * SECTION WALL
C *****
C     **FOR CONTINUOUS FLOW AND INTERMITTENT WIND-TUNNELS-
C     WITHOUT WALL COOLING ASSUME TW = TAW For  $M_\infty < 5$ 
C     TW =  $1.0 + 0.9 * (\text{GAMMA} - 1.0) * (\text{RMACH} ** 2.0) / 2.0$ 
C     TW =  $1.0 + 0.18 * \text{RMACH} ** 2.0$ 
C     **FOR FACILITIES WITH COMPLETE WATER COOLED NOZZLES
C     ASSUME TW = WATER TEMP. = 530 DEG R
C     **FOR IMPULSE FACILITIES ASSUME TW = AIR TEMP. = 530 DEG R
C *****
C 1 READ (5,2,END=8000) KOPT, KGEOM
C 2 FORMAT(11,11)
C 3 IF(KOPT=2) 4, 100, 200
C *****
C KOPT = 1
C WRITE COLUMN HEADINGS
C 4 WRITE (6,12) KOPT, KGEOM
C 12 FORMAT ( '1' , ' ESTIMATION OF BOUNDARY-LAYER TRANSITION ON SHARP
C FLAT PLATES' //
C 2,2X, 'IN CONVENTIONAL SUPERSONIC-HYPERSONIC WIND TUNNELS USING' //
C 3,1X, ' PATES AERODYNAMIC NOISE TRANSITION CORRELATION ' //
C 4,2X, 'KOPT=' ,12,3X, 'KGEOM=' ,12, //
C 5,4X, 'C,IN.' ,2X, 'XL,IN.' ,2X, 'RMACH' ,2X, 'PO,PSIA' ,3X, 'TO,R' ,4X, 'TW,R'
C 6,3X, 'REINF/FT' ,5X, 'REL' ,8X, 'CF' ,5X, 'DELS,IN.' ,3X, 'RETFP' ,4X,
C 7'XTFP,IN.' ,2X, 'TW/TAW' )
C 14 READ (5,16,END=1) C, XL,PO,TU,RMACH,TW
C 16 FORMAT ( 6F10.0)
C 18 CI = 48.0

```

```

      GAMMA = 1.4
      R = 1716
C     COMPUTE FREE-STREAM TEMPERATURE
      T1=TO/((1.0+0.2*(RMACH**2.0)))
C     COMPUTE FREE-STREAM VELOCITY
      U1=RMACH*SQRT(GAMMA*(R*T1))
C     COMPUTE FREE-STREAM ABSOLUTE VISCOSITY
C     USE SUTHERLANDS VISCOSITY LAW (T1<216 DEG R)
      IF(T1 .LE. 216) GO TO 30
      VIS1= 2.270*(T1**1.5)*(10.0**(-8.0))/(198.6+T1)
      GO TO 32
C     USE LINEAR VISCOSITY LAW (T1<216 DEG R)
30  VIS1=(0.0805*T1)*(10.0**(-8.0))
32  CONTINUE
C     COMPUTE FREE-STREAM STATIC PRESSURE
      P1=PO/((1.0+0.2*(RMACH**2.0))**3.5)
C     COMPUTE FREE-STREAM UNIT REYNOLDS NUMBER
      REINF=((144.0*P1)*U1)/((R*T1)*VIS1)
C     COMPUTE REYNOLDS NUMBER BASED ON TUNNEL NOZZLE LENGTH(XL)
34  REL = REINF * (XL/12.0)
      IF ( KGEOM-3) 35,90,8000
35  CONTINUE
C     COMPUTE TUNNEL TEST SECTION WALL TURBULENT BOUNDARY LAYER
C     DISPLACEMENT THICKNESS COMPUTED USING MAXWELL'S CORRELATION
C     ABSOLUTE VISCOSITY (VIS) COMPUTED USING SUTHERLAND'S LAW
C     VALID FOR 216<T< 5000 ,DEG R
36  VIS0=(2.270)*(TO**1.5)*(10.0**(-8.0))/(198.6+TO)
C     RHO IS STILLING CHAMBER DENSITY
38  RHO =(144 * PO)/(R* TO )
C     AO IS STILLING CHAMBER SPEED OF SOUND
40  AO = SQRT((GAMMA*R)* TO)
C     OK IS THE VARIABLE IN MAXWELL'S EQ.
42  OK = (0.0131)*((VIS0/(RHO* AO))**0.14286))
C     BARDEL IS MAXWELL CORRELATION PARAMETER
C     1BARDEL IS COMPUTED USING A THIRD DEGREE POLYNOMIAL CURVE FIT OF
C     1MAXWELL'S ORIGINAL CORRELATION FOR RMACH .LE. 6.0
      IF (RMACH = 5.0 ) 46, 46, 50
46  IF (KGEOM .GT. 1) GO TO 8000
48  BARDEL = 1.140824 * RMACH + 0.088132*((RMACH)**2.0)
      1+ 0.026978 *((RMACH)**3.0)
      GO TO 56
50  IF ( RMACH.GT. 10.0 ) GO TO 8000
      IF (KGEOM = 2 ) 52, 54, 8000
C     IF 5< RMACH<10 AND KGEOM = 1 THEN BARDEL = 2.0 + 1.8333*RMACH
52  BARDEL = 2.0 + 1.8333 * RMACH
      GO TO 56
54  BARDEL = 0.167 + 1.833*RMACH
C     DELS IS TUNNEL WALL DISPLACEMENT THICKNESS IN IN.
56  DELS=(OK)*(BARDEL)*((XL/12.0)**0.857143)*12.0
C     COMPUTE MEAN TURBULENT SKIN FRICTION(CF) USING VAN DRIEST-II WITH
C     TW IS INPUT DATA , DEG. RANKINE
C     RT IS THE RECOVERY FACTOR FOR A TURBULENT BOUNDARY LAYER
57  RT= 0.90
58  A=SQRT(((GAMMA-1.0)/2.0)*RT*(RMACH**2.0))*(T1/TW))
      B = (T1/TW) + (A**2.0)-1.0
      B1=B**2

```

```

      B=SQRT(B1)
      ALPHA=(2.0*(A**2.0)-B)/SQRT(B**2.0+4.0*(A**2.0))
      BETA = B/SQRT ((B**2.0)+4.0*(A**2.0))
      C4 = (0.242)*(ARSIN(ALPHA) + ARSIN(BETA))/(A * SQRT(TW/T1))
      C2 = ALOG10(REL)
      M = 0.76
      CJ = 1.5*ALOG10(T1/TW) + ALOG10((198.6*TW)/(198.6*T1))
C     STARTING VALUE OF CF IS 0.0050/RMACH
      CF=(0.0050)/RMACH
      K=0
70    FCF = SQRT(CF)*(C2+C3 + ALOG10(CF)) - C4
      K=K+1
      IF (K .GT. 100) GO TO 8000
C     FPRIME IS THE DERIVATIVE OF FCF WITH RESPECT TO CF
      FPRIME = (0.50 / SQRT(CF))*( C2+C3 + ALOG10(CF)+0.8686)
C     THE NEWTON-RAPHSON METHOD IS
      CF = CF - (FCF / FPRIME)
C     INTERATE UNTIL SUCCESSIVE APPROXIMATIONS OF ROOT IS LESS THAN
C     10.0000010
      ROOT = ABS( FCF/FPRIME)
      IF (ROOT .GT. 0.0000010) GO TO 70
      C1=48.0
      IF (KOPT .EQ. 2) GO TO 152
      IF (KOPT .EQ. 4) GO TO 222
      AFP=(CF)**(-2.55)
      RC1C = C1/C
      IF (RC1C - 1.0 ) 71, 71, 72
71    BFP = 0.56 + (0.44)* C1/C
      GO TO 73
72    BFP = 1.00
73    CFP = SQRT (DELS/ C )
      UFP=(0.0126)*AFP
      RETFP=(BFP*DFP)/CFP
      XTFP=(RETFP/RE1NF)*12.0
C     TAW= TUNNEL WALL RECOVERY TEMPERATURE
      TAW= T1*(1.0+ 0.18*(RMACH**2.0))
      RTWTAW= TW/TAW
      IF ( KOPT .EQ. 3) GO TO 210
80    WRITE (6,82) C,XL,RMACH,P0,T0,TW,HE1NF,REL,CF,DELS,RETFP,XTFP,
      IRTWTAW
82    FORMAT(1H,F8.1,F7.1,F8.1,F9.2,2F8.1,1PE11.4,1PE11.4,0PF10.6,
      1F9.4,1PE11.4,0PF8.2,F10.3)
      GO TO 14
C     COMPUTE DELS USING WHITFIELDS CORRELATION FOR CONICAL NOZZLES OR
C     REAL GAS AXISYMMETRIC NOZZLES
C     WHEN 7< RMACH <20
90    DELS=(0.22)*SQRT(RMACH)/SQRT(REL)
      GO TO 58
C     *****
C     KUPT = 2
100   WRITE (6,101) KOPT, KGEOM
101   FORMAT ( '1', 'ESTIMATION OF BOUNDARY LAYER TRANSITION ON SHARP SL
      1E=UWER CONES IN CONVENTIONAL SUPERSONIC-HYPERSONIC',//
      1,1X,'WIND TUNNELS USING THE AERODYNAMIC NOISE CORRELATIONS BY PATE
      1',//
      1,1X,'KOPT =' ,I2,3X,'KGEOM =' ,I2,1X,'

```

```

1,2X,'C,IN.',2X,'XL,IN.',2X,'RMACH',3X,'PO,PSIA',1X,'TO,R',4X,
2'TW,R',3X,'REINF/FT',3X,'DELTA,DEG',1X,'RTS',4X,'RPS',3X,'RMACHS'
3,1X,'RRESC',4X,'RETSC',3X,'XTSC,IN',2X,'TW/TAW')
102 READ(5,104,END= 1 ) C,XL, PO, TO, RMACH, DELTA, TW
104 FORMAT ( 7F10.0)
C   COMPUTE CONE SURFACE STATIC PRESSURE RATIO (RPS1 = PS/P1) USING
    DELTA = DELTA/ 57.296
C   1RASMUSSEN'S .EQ.
    PS1 = (SIN(DELTA)**2.0)*(1.4*(RMACH**2.0))/2.0
    PS2 = 2.4*(RMACH**2.0)*(SIN(DELTA)**2.0) + 2.0
    PS3 = 0.4*(RMACH**2.0)*(SIN(DELTA)**2.0) + 2.0
    PS4 = ALOG(1.20 + 1.0/((RMACH**2.0)*(SIN(DELTA)**2.0)))
    PS5 = (PS2/PS3)*PS4
    HPS1 = 1.0*PS1*(1.0*PS5)
    GAMMA = 1.40
    H=1716.0
C   COMPUTE CONE BOW SHOCK ANGLE (PHI)
110 PHI = ARSIN( SIN(DELTA)*((1.20 + 1.0/((RMACH*SIN(DELTA))**2.0))**
10.50))
C   COMPUTE STATIC PRESSURE AND TEMPERATURE BEHIND BOW SHOCK USING
C   2-D OBLIQUE SHOCK WAVE THEORY
C   RT21 = T2/T1
112 RT21 = (7.0*((RMACH*SIN(PHI))**2.0) - 1.0)*((RMACH*SIN(PHI))**2.0
1)*5.0)/(36.0*((RMACH*SIN(PHI))**2.0))
C   RP21 = P2/P1
114 RP21 = (7.0*((RMACH * SIN(PHI))**2.0)-1.0) /6.0
C   COMPUTE PRESSURE AND TEMPERATURE ON CONE SURFACE BY USING CONDITIO
C   BEHIND SHOCK WAVE AND ISENTROPIC COMPRESSION PROCESS
C   RTS1 = TS/T1
116 RTS1 = RT21 * ( (HPS1 / RP21)**0.285714 )
C   COMPUTE FREE-STREAM TEMPERATURE(T1)
118 T1 = TO/(1.0 + 0.2*(RMACH)**2.0)
120 TS=T1*RTS1
C   COMPUTE VELOCITY AT CONE SURFACE (US)
C   RATIO OF SPECIFIC HEAT IS CP=6006 FT.SQ./ SEC. SQ.-DEGR
    CP = 6006
122 US = (SQRT(2.0 * CP))*SQRT( TO - (T1*RT21)*((RPS1/RP21)**0.285714))
C   COMPUTE MACH NUMBER AT CONE SURFACE (RMACHS)
124 RMACHS = US / (49.0 * SQRT(TS))
C   COMPUTE DENSITY AT CONE SURFACE (RHOS)
    H=1716.0
C   COMPUTE FREE-STREAM STATIC PRESSURE (P1)
126 P1 = PO/ ((1.0 + 0.2*(RMACH**2.0))**3.5)
C   COMPUTE DENSITY RATIO AT CONE SURFACE (RRHOS1 = RHOS/RH01)
128 RRHOS1=(HPS1/RTS1)
C   COMPUTE REYNOLDS NUMBER AT CONE SURFACE (RRES1 = RES/RE1)
C   COMPUTE FREE-STREAM VELOCITY (U1)
130 U1 = (RMACH * 49.0)* SQRT(T1)
132 IF ( T1 .GE. 210) GO TO 138
C   COMPUTE FREE-STREAM ABSOLUTE VISCOSITY(VIS1) USING LINEAR LAW
    VIS1 = (0.0805 * T1)*(10.0)**(-8.0)
136 GO TO 140
C   COMPUTE FREE-STREAM ABSOLUTE VISCOSITY USING SUTHERLANDS LAW
138 VIS1 = (2.270*(T1**1.50))*(10.0**(-8.0))/(198.6 + T1)
C   RE1 = REINF = RH01 * U1/VIS1
C   COMPUTE FREE-STREAM-UNIT REYNOLDS NUMBER( RE1=REINF)

```



```

140 REINF=(U1*P1*144.0) / (R*T1 *V1S1)
142 IF (TS .GE. 216) GO TO 146
C   COMPUTE CONE SURFACE VISCOSITY VISS USING LINEAR LAW (TS) 216 DEGR
144 VISS = (0.0805 * TS)*(10.0**(-8.0))
    GO TO 148
C   COMPUTE CONE SURFACE VISCOSITY USING SUTHERLANDS LAW (TS>216 DEGR)
146 VISS = (2.270*(TS**1.50))*(10.0**(-8.0))/(198.6 + TS)
C   COMPUTE CONE SURFACE REYNOLDS NUMBER (RES)
148 RES=(RPS1*P1*144.0*US)/(R*TS*VISS)
C   COMPUTE REYNOLDS NUMBER RATIO(RRES1 = RES/REINF)
149 RRES1 = RES/REINF
150 GO TO 34
152 CONTINUE
    DELTA = DELTA * 5/.296
C   COMPUTE TRANSITION REYNOLDS NUMBER ON CONE SURFACE (RETSC)
153 AC = (CF)**(-1.40)
    RC1C = C1/ C
    IF (RC1C - 1.0 ) 154,154, 155
154 BC = 0.80 + 0.20*(C1/C)
    GO TO 156
155 BC = 1.00
156 CC = SQRT (DELS/C)
    RETSC=(48.5)*(AC * BC ) / CC
    XTSC =(RETSC / RES) * 12.0
C   TAW= TUNNEL WALL RECOVERY TEMPERATURE
    TAW= T1*(1.0+ 0.18*(RMACH**2.0))
    RTWTAW= TW/TAW
    WRITE (6,158) C,XL,RMACH,PO ,TO,TW ,REINF,DELTA,RTS1,RPS1,
    2,RMACHS,RRES1,RETSC,XTSC,RTWTAW
158 FORMAT ( 1H,F6.1,F7.1,F8.1,F9.1,F7.1,F7.1,1PE12.4,0PF8.2
    2,F8.3 ,F7.3,F7.2,F7.3,1PE12.4,0PF7.2,F8.3)
    GO TO 102
C   *****
C   KUPT = 3
C
200 IF (KUPT=4) 201, 214, 8000
201 IF (KGEOM - 3 ) 8000 , 202 , 8000
202 WRITE ( 6, 204) KUPT, KGEOM
204 FORMAT ( '1', 'PREDICTION OF BOUNDARY LAYER TRANSITION ON SHARP
    1FLAT PLATES'//
    1,2X,'FOR NON IDEAL GAS NOZZLE EXPANSION PROCESS'//
    1,2X,'RMACH > 10 OR RMACH > 8 , REINF > 15*10**6 ,SEE FIG '///
    1,2X,'USING PATES AERODYNAMIC NOISE TRANSITION CORRELATION'//
    1,2X,'KUPT = ',12,4X,'KGEOM= ',12,4X//
    1,4X,'C,IN,',5X,'XL,IN,',4X,'RMACH',5X,'TW',5X,'REINF',8X,'CF'
    1,3X,'DELS,IN.',8X,'RETFP',5X,'XIFP,IN.',5X,'TW/TAW')
206 READ(5, 208, END= 1 ) C, XL, RMACH, REINF, TW
208 FORMAT (5F10.0)
    REL = REINF*(XL/12.0)
C   COMPUTE DELS USING WHITFIELDS FORMULAS
    DELS = XL*(0.22)*SQRT(RMACH)/(REL**0.25)
C   COMPUTE TUNNEL WALL SKIN FRICTION USING VAN DRIEST-II
    GAMMA=1.40
C   SET FREE-STREAM STATIN TEMPERATURE EAUAL TO 90 DEG R
    T1 = 90.0
C   TAW= TUNNEL WALL RECOVERY TEMPERATURE

```

```

      TAW= T1*(1.0+ 0.18*(RMACH**2.0))
      RTWTAW= TW/TAW
      GO TO 57
210 CONTINUE
      WRITE (6,211) C,XL,RMACH,TW,REINF,CF,DELS,RETFP,XTFP,RTWTAW
211 FORMAT (1H,1F8.1,1F10.1,1F9.1,1F8.1,1PE12.4,0PF10.6,1F8.4,1PE16.4,
10PF10.2,F8.2)
212 GO TO 206
C *****
C      KOPT= 4
C
214 IF (KGEOM - 3 ) 8000 , 215 , 8000
215 WRITE ( 6, 216) KOPT, KGEOM
216 FORMAT ( '1', 'ESTIMATION OF BOUNDARY LAYER TRANSITION ON SHARP
1SLENDER CONES'//
1,2X, 'FOR MACH NUMBERS GREATER THAN 10 ON VERY HIGH REYNOLDS'//
1,2X, 'AT MACH NUMBER EQUAL APPROX 8(HEINF>10**7)'//
1,2X, 'USING PATES AERODYNAMIC NOISE TRANSITION CORRELATION'//
1,2X, 'KOPT = ',I2,4X, 'KGEOM= ',I2,//
1,1X,'C',IN,'5X,'XL',IN,'4X,'RMACH',3X,'TW',DEGR,'4X,'REINF/FT'
2,3X,'RESC/REINF',2X,'DELS',IN,'7X,'RETS',5X,'XTSC',IN,'3X,
3'DELTA,DEG',5X,'TW/TAW' )
218 READ(5,220,END= 1 ) C,XL,RMACH,REINF,RRESC,TW,DELTA
220 FORMAT (7F10.0)
      REL = REINF*(XL/12.0)
C      COMPUTE DELS USING WHITFIELD'S FORMULS
      DELS = XL*(0.22)*SQRT(RMACH)/(REL**0.25)
C      COMPUTE TUNNEL WALL SKIN FRICTION USING VAN DRIEST-II
      GAMMA=1.40
C      SET FREE-STREAM STATIC TEMPERATURE EQUAL TO 90 DEG R
      T1 = 90.0
C      TAW= TUNNEL WALL RECOVERY TEMPERATURE
      TAW= T1*(1.0+ 0.18*(RMACH**2.0))
      RTWTAW= TW/TAW
      GO TO 57
222 CONTINUE
C      COMPUTE TRANSITION REYNOLDS NUMBER ON CONE
      AC = (CF)**(-1.40)
      RC1C = C1 /C
      IF (RC1C - 1.0 ) 224, 224 , 225
224 BC = 0.80 + 0.20*(C1/C )
      GO TO 226
225 BC = 1.00
226 CC = SQRT (DELS/ C )
      RETSC =(48.5)*(AC * BC ) /CC
      RESC=RRESC*REINF
      XTSC=(RETSC/RESC)*12.0
      WRITE(6,230)C,XL,RMACH,TW,REINF,RRESC,DELS,RETS,XTSC,DELTA,RTWTAW
230 FORMAT(1H,F5.1,2F10.2,F10.2,1PE13.4,0PF9.3,F12.3,1PE16.4,0PF10.3,
1F10.3,F13.2 )
      GO TO 218
8000 CONTINUE
      STOP
      END

```



CARD	KOPT																																					
	KGEOM																																					
1	2	X																																				
2			C,IN.				XL,IN.					PO,PSIA				TO,R			OR				RMACH=M <sub>∞</sub>			DELTA,DEG				TW,R								
			X	X	X	.X						X	X	X	.X	X			X	X	X	.X			X	X	.X	X			X	X	X	.X				

ESTIMATION OF BOUNDARY LAYER TRANSITION ON SHARP SLENDER CONES IN CONVENTIONAL SUPERSONIC-HYPERSONIC WIND TUNNELS USING THE AERODYNAMIC NOISE CORRELATIONS BY PATE

KOPT = 2 KGEOM = 1

C,IN.	XL,IN.	RMACH	PO,PSIA	TO,R	TW,R	REINF/FT	DELTA,DEG	RTS	RPS	RMACHS	RRESC	RETSC	XTSC,IN.	TW/TAW
160.0	213.0	4.0	40.0	540.0	495.0	3.6921E 06	5.00	1.078	1.299	3.81	1.105	5.8567E 06	17.23	0.992

ESTIMATION OF BOUNDARY LAYER TRANSITION ON SHARP SLENDER CONES IN CONVENTIONAL SUPERSONIC-HYPERSONIC WIND TUNNELS USING THE AERODYNAMIC NOISE CORRELATIONS BY PATE

KOPT = 2 KGEOM = 1

C,IN.	XL,IN.	RMACH	PO,PSIA	TO,R	TW,R	REINF/FT	DELTA,DEG	RTS	RPS	RMACHS	RRESC	RETSC	XTSC,IN.	TW/TAW
157.0	300.0	8.0	450.0	1400.0	530.0	1.8433E 06	5.00	1.210	1.920	7.22	1.302	5.7956E 06	28.99	0.417

ESTIMATION OF BOUNDARY LAYER TRANSITION ON SHARP SLENDER CONES IN CONVENTIONAL SUPERSONIC-HYPERSONIC WIND TUNNELS USING THE AERODYNAMIC NOISE CORRELATIONS BY PATE

KOPT = 2 KGEOM = 2

C,IN.	XL,IN.	RMACH	PO,PSIA	TO,R	TW,R	REINF/FT	DELTA,DEG	RTS	RPS	RMACHS	RRESC	RETSC	XTSC,IN.	TW/TAW
157.0	300.0	8.0	450.0	1400.0	530.0	1.8433E 06	5.00	1.210	1.920	7.22	1.302	6.1437E 06	30.73	0.417

371

**AEDC-TR-77-107**

USING PATES AERODYNAMIC NOISE TRANSITION CORRELATION

C, IN.	XL, IN.	RMACH	TW	REINF	CF	DELS, IN.	RETFP	XTFP, IN.	TW/TAW
157.0	300.0	8.0	530.0	3.0000E 06	0.000771	2.0060	6.7141E 06	26.86	0.47

C, IN.	XL, IN.	RMACH	TW	REINF	CF	DELS, IN.	RETFP	XTFP, IN.	TW/TAW
157.0	300.0	8.0	530.0	3.0000E 06	0.000771	2.0060	6.7141E 06	26.86	0.47

[illegible]

	2	4	6	8	10	12	14	16	18	20	22	24	26	28	30	32	34	36	38	40	42	44	46	48	50	
2		C, IN.					XL, IN.				RMACH=M <sub>∞</sub>	REINF, FT-1									TW, OR					
		XXX.X					XXX.X				XX.XX					XXXXXXXXXX.X						XXXXX.X				

FOR MACH NUMBERS GREATER THAN 10 ON VERY HIGH REYNOLDS

### USING PATES AERODYNAMIC NOISE TRANSITION CORRELATION

KOPT = 4      KGEOM = 3

C, IN.	XL, IN.	RMACH	TW, DEGR	REINF/FT	RESC/REINF	DELS, IN.	REISC	XTSC, IN.	DELTA, DEG	TW/TAW
157.0	300.00	8.00	530.00	3.0000E 06	1.500	2.006	8.4295E 06	21.341	10.000	0.47

[illegible]

2	C, IN.	XL, IN.	RMACH	REINF, FT-1	RRESC.	TW, °R	DELTA, DEG.
	XXX.X	XXX.X	XX.XX	XXXXXXXXXX.X	XX.XX	XXXX.X	



## APPENDIX D

## EFFECTS OF DIFFERENT VISCOSITY LAWS ON INVISCID

## FLOW CONE SURFACE REYNOLDS NUMBER RATIOS

In reviewing published transition results, it became apparent that inconsistencies existed in the calculation of tunnel unit Reynolds number and more often for cone surface values. These differences were traceable primarily to different viscosity relationships used.\*

Using two different viscosity laws, Eqs. (C-6) and (C-7), pages 345 and 347, for air, three methods for computing the Reynolds number at the surface of unyawed cones were investigated.

1. Using the linear viscosity law ( $\mu \sim T$ ) which is valid in air and nitrogen for temperatures below approximately 2160K, then

$$\left[ \frac{(Re_\delta)_C}{Re_\infty} \right]_{\text{linear}} = \frac{p_C}{p_\infty} \frac{M_C}{M_\infty} \left( \frac{T_\infty}{T_C} \right)^{1.5} \quad (D-1)$$

2. Using Sutherland's viscosity law which is valid for temperatures above approximately 216°R, then

$$\left[ \frac{(Re_\delta)_C}{Re_\infty} \right]_{\text{Sutherland}} = \frac{p_C}{p_\infty} \frac{M_C}{M_\infty} \left( \frac{T_\infty}{T_C} \right)^2 \left( \frac{T_C + 198.6}{T_\infty + 198.6} \right) \quad (D-2)$$

3. Using a combination of the linear law and Sutherland's law, then

---

\*In addition to the linear law [Eq. (C-6)] and Sutherland's law [Eq. (C-7)], the power law  $\mu \sim (T)^w$ , when  $w \approx 0.76$ , is also often used.

$$\left[ \frac{(Re_{\delta})_c}{Re_{\infty}} \right]_{\text{linear and Sutherland}} = \frac{p_c}{p_{\infty}} \frac{M_c}{M_{\infty}} \left( \frac{T_{\infty}}{T_c} \right)^{\frac{1}{2}} \frac{\mu_{\infty}}{\mu_c} \quad (D-3)$$

where  $\mu_{\infty}$  and  $\mu_c$  are computed from Eqs. (C-6) or (C-7) depending on the value of  $T$ .

Equation (D-3) combines the two viscosity laws and therefore provides a more general method for calculating Reynolds number ratios. A combination of the viscosity laws allows the free-stream viscosity to be determined using the linear law and the cone surface value to be computed using Sutherland's law, which is often the condition existing in wind tunnels at high supersonic and hypersonic Mach numbers.

Presented in Figure D-1 are the Reynolds number ratios computed using cone surface pressure, temperature, and velocities from Reference (162) for  $M_{\infty} = 2, 5$ , and 12 and cone half-angles from 0 to 35 deg. It is evident from Figure D-2 that the two viscosity laws and the three methods can produce significant differences depending on the combined effects of cone angle and flow conditions.

A family of Reynolds number ratios calculated using Eq. (D-3) and the cone surface properties from Reference (162) are presented in Figure D-2. It should be noted that the ratios are temperature dependent at flow conditions where Sutherland's viscosity law was applicable. The range of temperatures ( $T_0$ ) was selected to represent the range of total temperatures usually available in wind tunnels.

All of the transition data generated in this research were calculated using Eq. (D-3). Data from other sources were corrected if it was established that a relationship other than Eq. (D-3) was used.

Note that Figure D-2 can be used to determine values for  $(Re_{\delta})_c / Re_{\infty}$  which is a required input for Program Options 3 and 4.



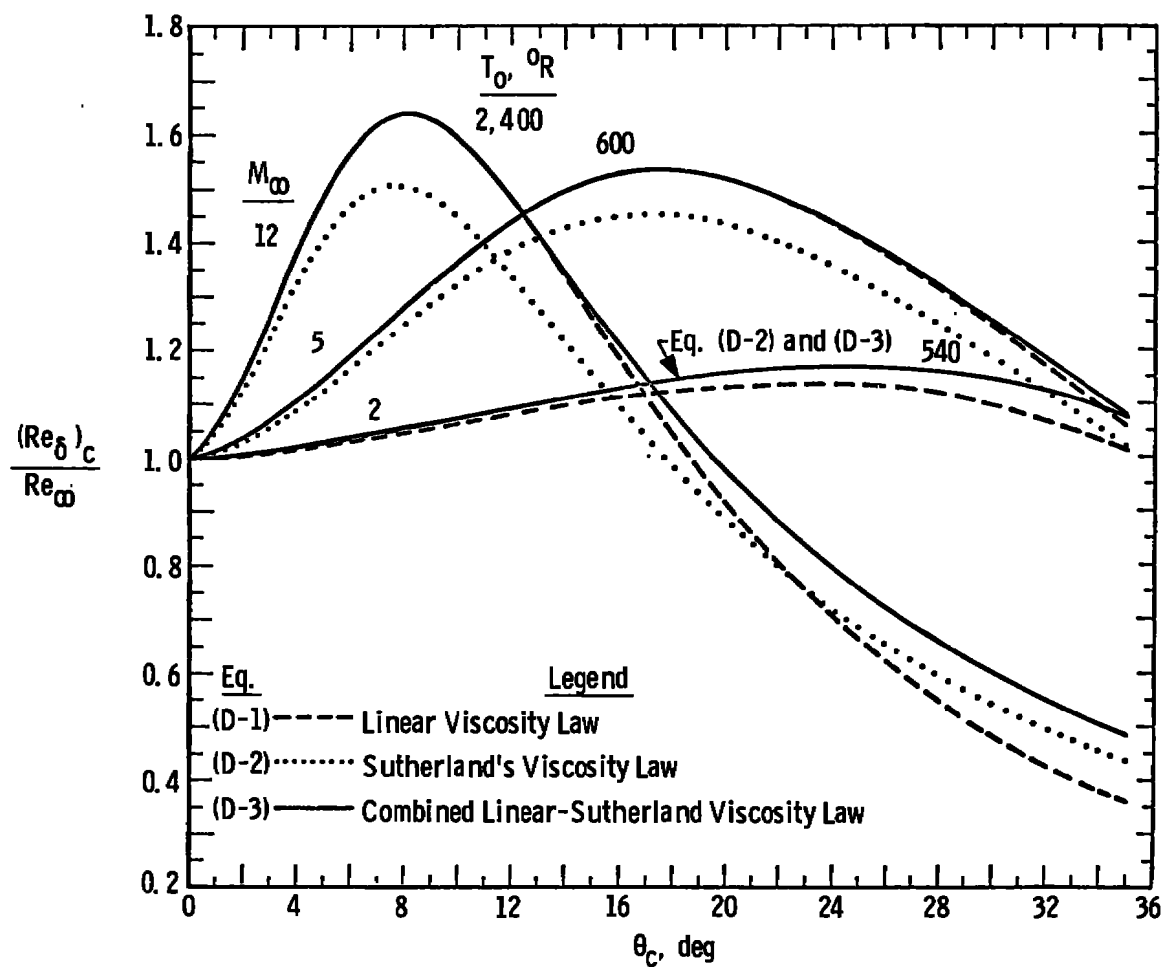


Figure D-1 Sensitivity of the Reynolds number ratio to various viscosity laws.

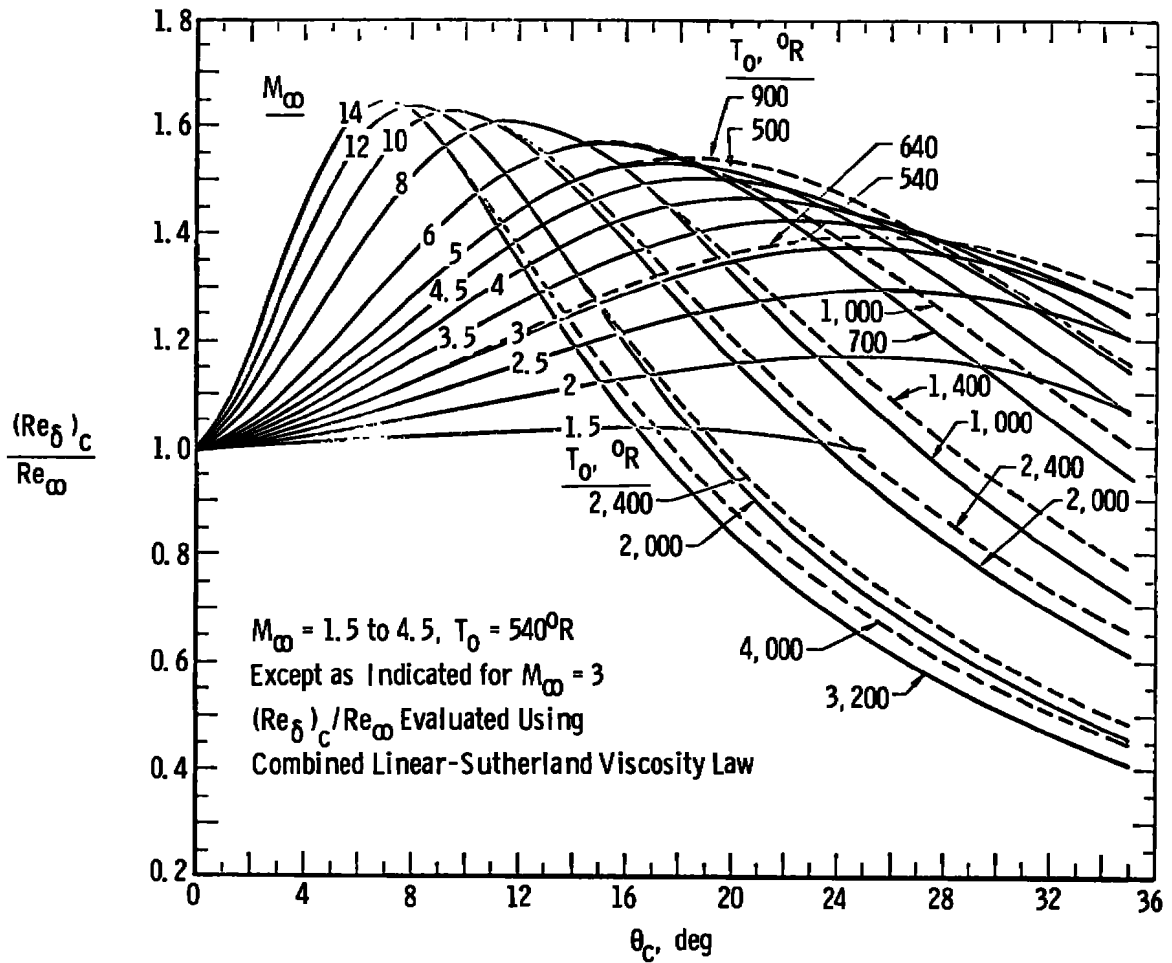


Figure D-2. Variation of Reynolds number ratio with cone half-angle, Mach number, and temperature.

## APPENDIX E

COMBINED EFFECTS OF AERODYNAMIC NOISE AND  
SURFACE ROUGHNESS ON TRANSITION

The literature provides abundant documentation for the necessity of providing effective boundary-layer tripping mechanisms for application in wind tunnel experiments. The effectiveness of surface roughness for inducing laminar boundary-layer transition on planar and conical bodies at supersonic and hypersonic speeds has been extensively reported in References (16), (17), (20), (21), (37), (47), (79), and (163) through (165). Although there may remain considerable doubt about the effectiveness of surface roughness in promoting "early" transition at hypersonic speeds (20, 21, 164, 165), the evidence to date would indicate that some confidence should be expected in estimating and predicting trip performance in the supersonic speed range (16, 17, 37, 141).

However, there may be some cause for concern when consideration is given to the absence of experimental data on the potential coupling between the radiated aerodynamic noise free-stream disturbances at supersonic speeds ( $M_\infty \gtrsim 3$ ), as discussed in Chapters III and VIII and the disturbance generated by the controlled surface roughness.

This section presents the experimental results of an investigation undertaken to determine if boundary-layer trip effectiveness is related to the tunnel size and the tunnel disturbance levels, per se. The studies were conducted in the AEDC-VKF 12- and 40-in. supersonic wind tunnels at  $M_\infty = 3$  and 4 on an adiabatic wall 10-deg total-angle sharp cone. Basic results are presented, analyzed, and compared with the two

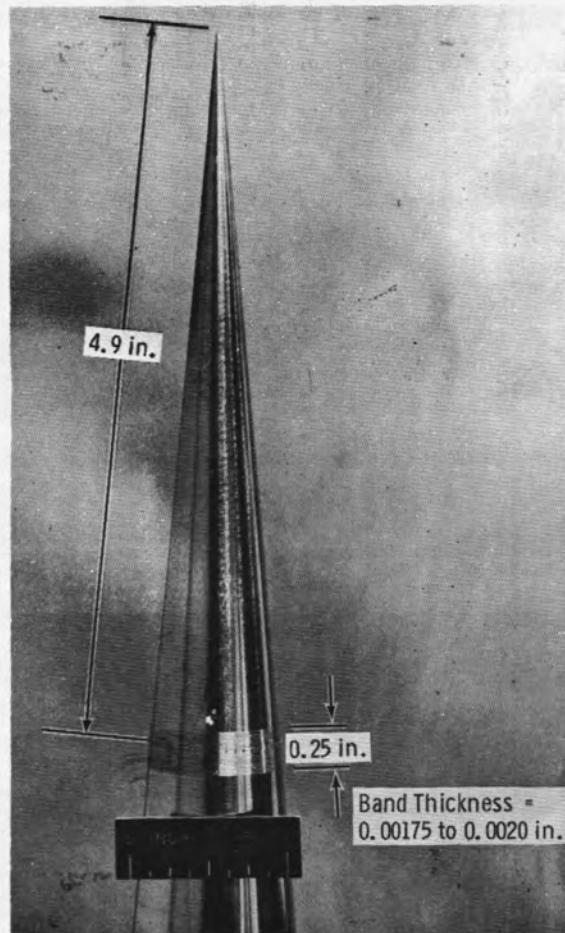
well-known and widely used trip correlations developed by van Driest-Blummer (163) and Potter-Whitfield (37).

### Transition Models and Apparatus

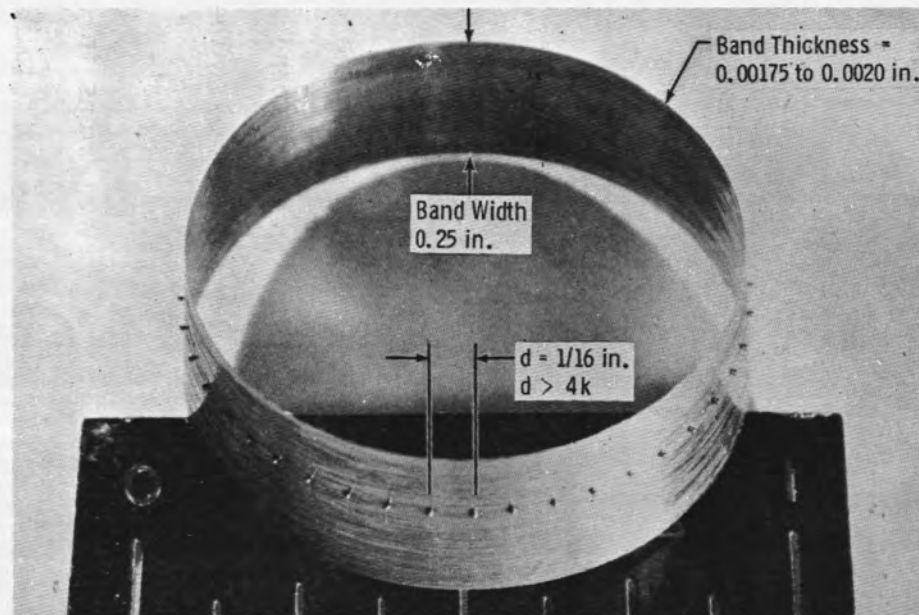
The transitional model was the 10-deg total-angle, stainless steel cone as described in Chapter IV and shown in Figure IV-14, page 112.

The boundary-layer trip mechanism consisted of a single row of precision steel balls having diameters of 0.010 and 0.015 in. and attached with epoxy resin to a  $\frac{1}{4}$ -in.-wide steel band having a thickness less than 0.002 in. as illustrated in Figure E-1. Ball spacing on the band was maintained constant at 1/16 in. between centers, and the band centerline was positioned approximately 4.9 in. from the cone apex. The trip bands were machined to match the cone surface angle and were attached to the surface using very small amounts of glue. Variations in the two sets of ball heights above the band were approximately  $\pm 2\%$  to  $\pm 3\%$ , and the average heights from the cone surface to the top of the 0.010- and 0.015-in.-diam spheres were 0.0117 and 0.0172 in., respectively.

Initially some difficulty was experienced in gluing the steel balls to the band because of an unacceptable accumulation of glue as determined by visual inspection with a ten-power eyeglass. However, satisfactory results were obtained with practice, as illustrated by the photograph in Figure E-1c. The spheres remained attached quite satisfactorily even after several hours of test time. Also the loss of several balls (provided they were not adjacent) did not noticeably affect the test



a. Trip Location



b. Trip Details



c. Enlarged View of Sphere Glued to Band

Figure E-1. Boundary-layer trip geometry.

data. It is probable that every other ball could have been lost without affecting the trip results since References (37) and (79) suggest that the allowable spacing could have been increased from 1/16 to 1/8 in. The minimum spacing as reported in References (16), (37), (39), and (163) has been established as about 4k.

It was demonstrated in Reference (163) that for test conditions similar to those of the present experiments a band height less than 0.002 in. had a negligible effect on the smooth wall transition data, and consequently the trip performance, provided the band was located 5 in. downstream of the cone trip.

A remotely controlled, electrically driven, surface pitot probe, as discussed in Chapter IV, provided a continuous trace of the probe pressure on an X-Y plotter from which the location of transition was determined. Tests in Tunnel A using different sizes of probes established that probe size effects on the location of transition ( $x_{t0}$ ) were negligible (see Chapter VI, Figure VI-5, page 151).

Schlieren photography was also utilized as a secondary method for detecting the location of transition in Tunnel D.

#### Transition Dependency on Tunnel Size

The purpose of this research was to determine if spherical roughness trips were equally effective in different sizes of supersonic ( $M_\infty \gtrsim 3$ ) wind tunnels where the differences in free-stream disturbances were sufficient to alter the smooth surface  $(Re_t)_\delta$  values. The relationship between free-stream disturbances which radiate from the tunnel wall boundary layer and their effect on the location of transition were shown

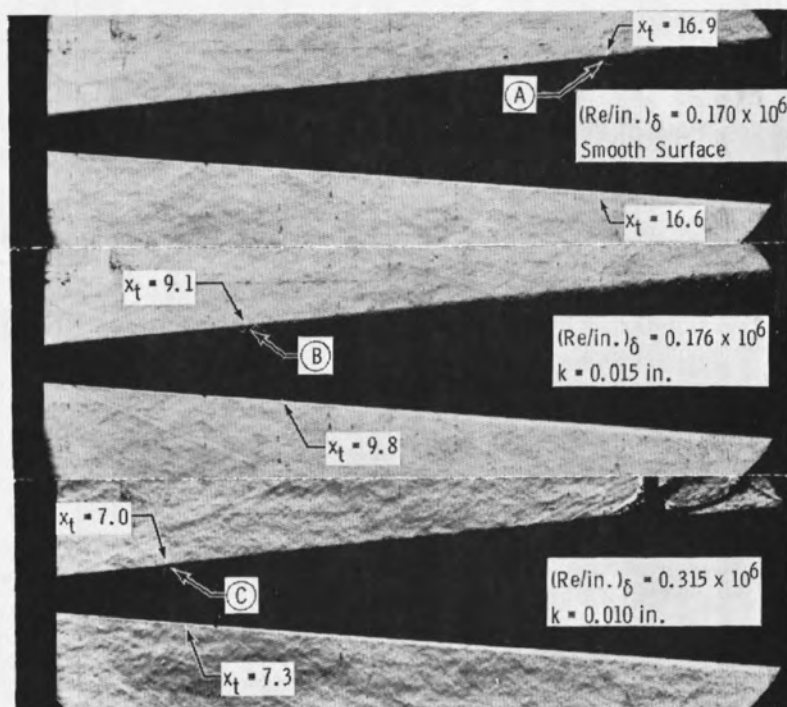
in Chapters VIII and X. Variations in  $(Re_t)_\delta$  with tunnel size as a result of these radiated noise effects are very significant, as exemplified by the data presented in Figure VIII-20, page 216, for both planar and sharp cones. The cone data presented in Figures VII-5, page 151, VII-6, page 175, and VIII-20, page 216, were obtained on the test model used for the current trip experiments, and these basic data will appear in different forms in later sections. It will be shown that the aerodynamic-noise-transition correlations presented in Figures IX-8, page 249, and IX-9, page 251, are useful for providing basic smooth wall  $(Re_t)_\delta$  values for application with the Potter-Whitfield trip correlation.

#### Transition Detection and Identification

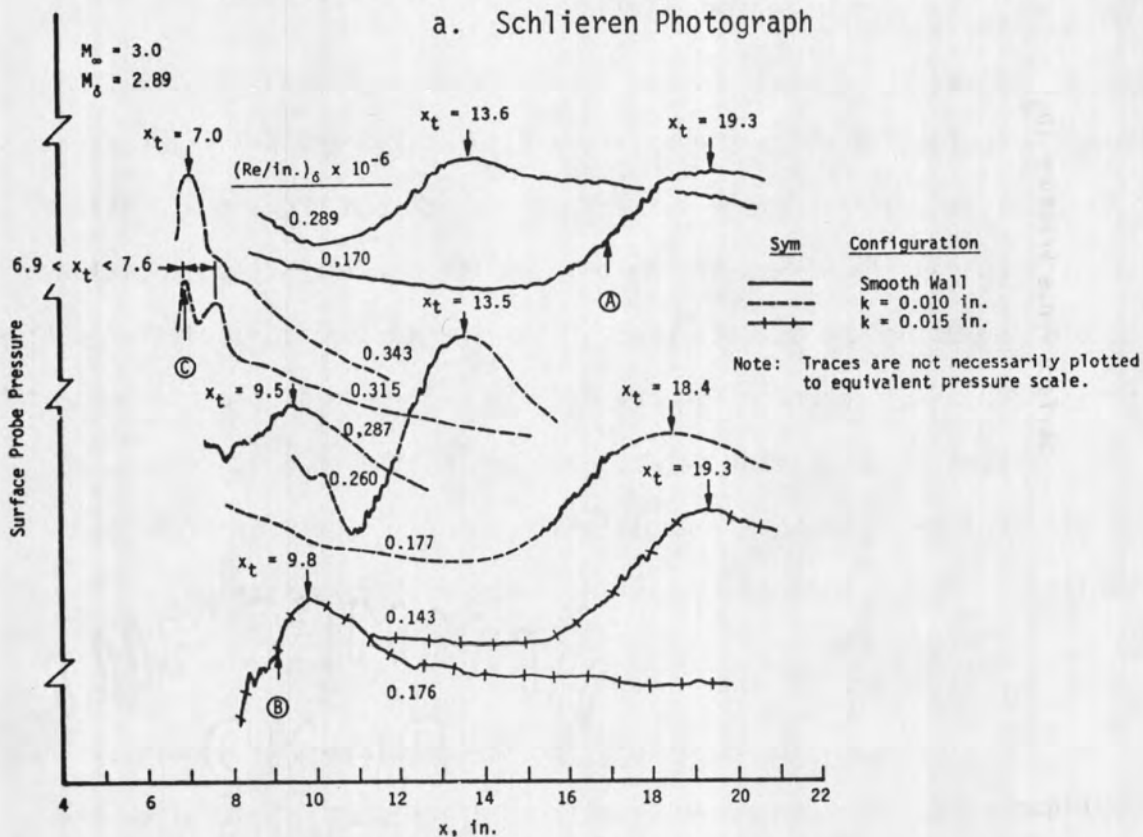
A series of basic transition profiles obtained with the traversing surface probe is presented in Figures E-2 and E-3. These data show that the surface probe was able to detect and provide a distinct transition profile very near the trip position. Transition locations determined using the surface probe (with the  $x_t$  location selected at the pressure peak as shown in Figures E-2 and E-3) were also consistent with the location of transition determined from schlieren photographs, as illustrated in Figure E-2. Additional comparison between probe and schlieren results will be presented in the following section.

#### Basic Results

Basic transition locations for the conditions of smooth surface and with spherical roughness elements positioned at 4.9 in. from the cone tip are presented in Figures E-4 through E-6 for  $M_\infty = 3$  and 4.



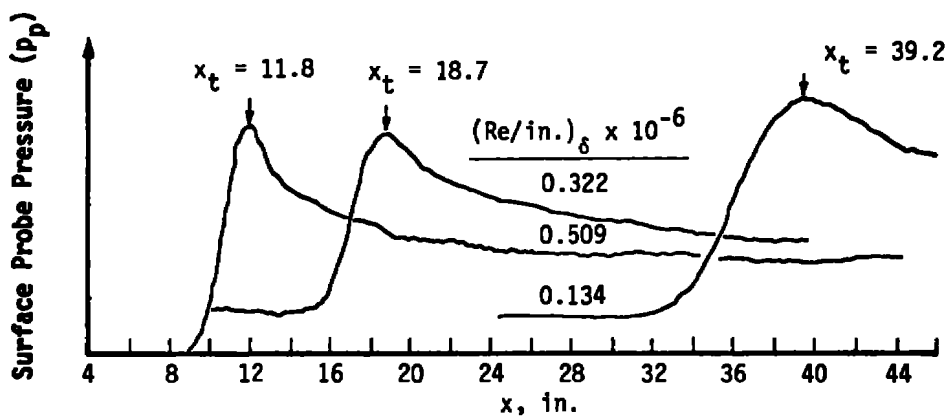
a. Schlieren Photograph



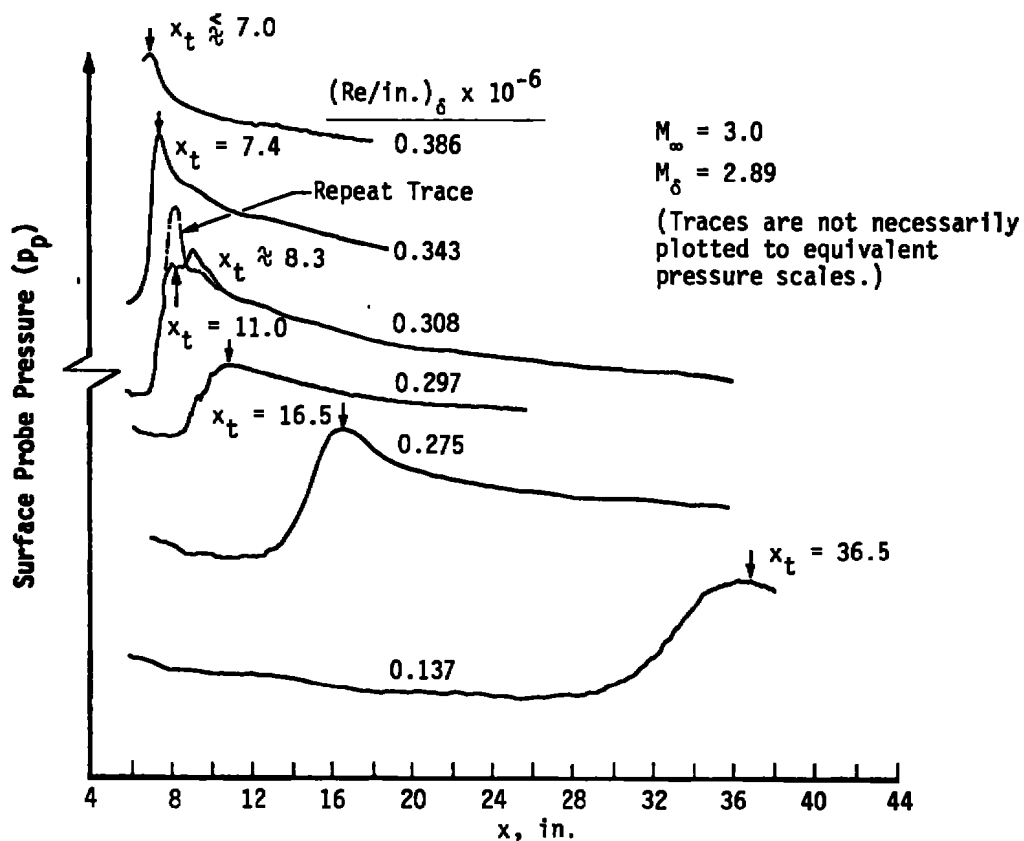
b. Surface Pitot Probe Traces

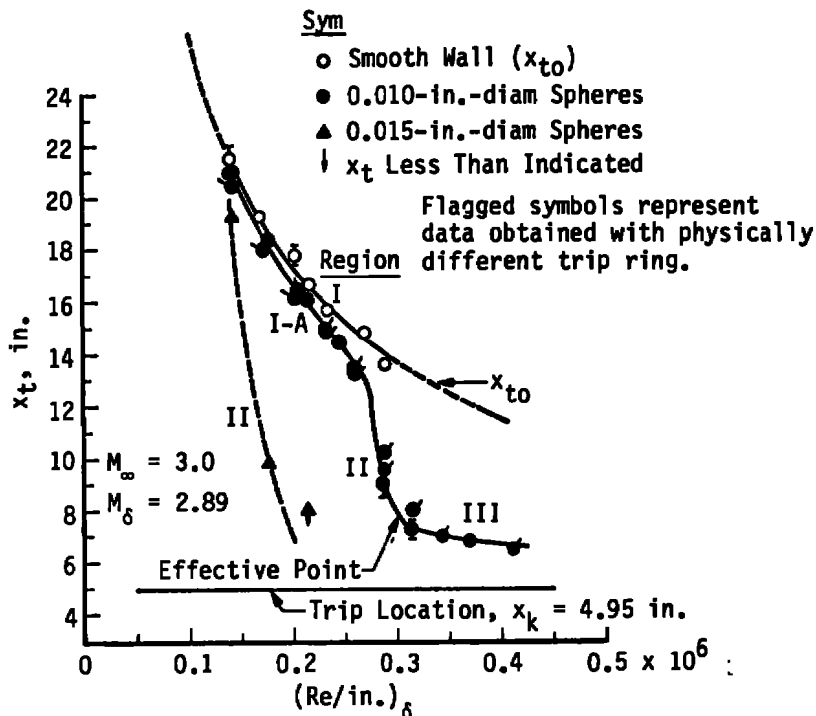
Figure E-2. Methods of transition detection,  $M_\infty = 3.0$ , AEDC-VKF Tunnel D.



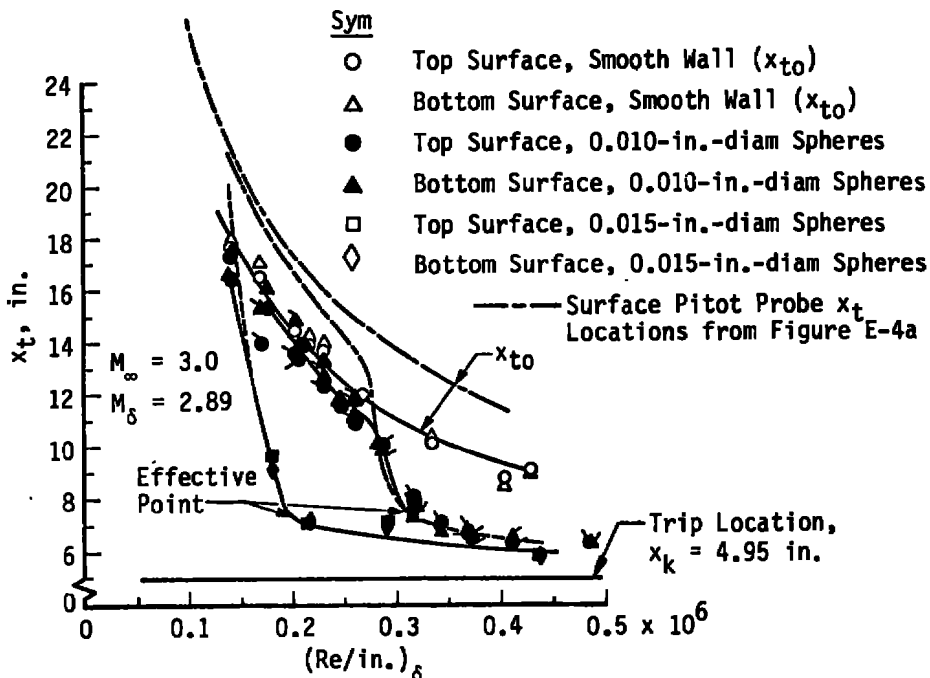


a. Smooth Surfaces

b. With Trip,  $k = 0.010$  in.Figure E-3. Surface probe transition profiles,  $M_\infty = 3.0$ , AEDC-VKF Tunnel A.



a. Surface Probe Results



b. Schlieren Results

Figure E-4. Effect of spherical roughness on transition location,  $M_\delta = 2.89$ , AEDC-VKF Tunnel D.

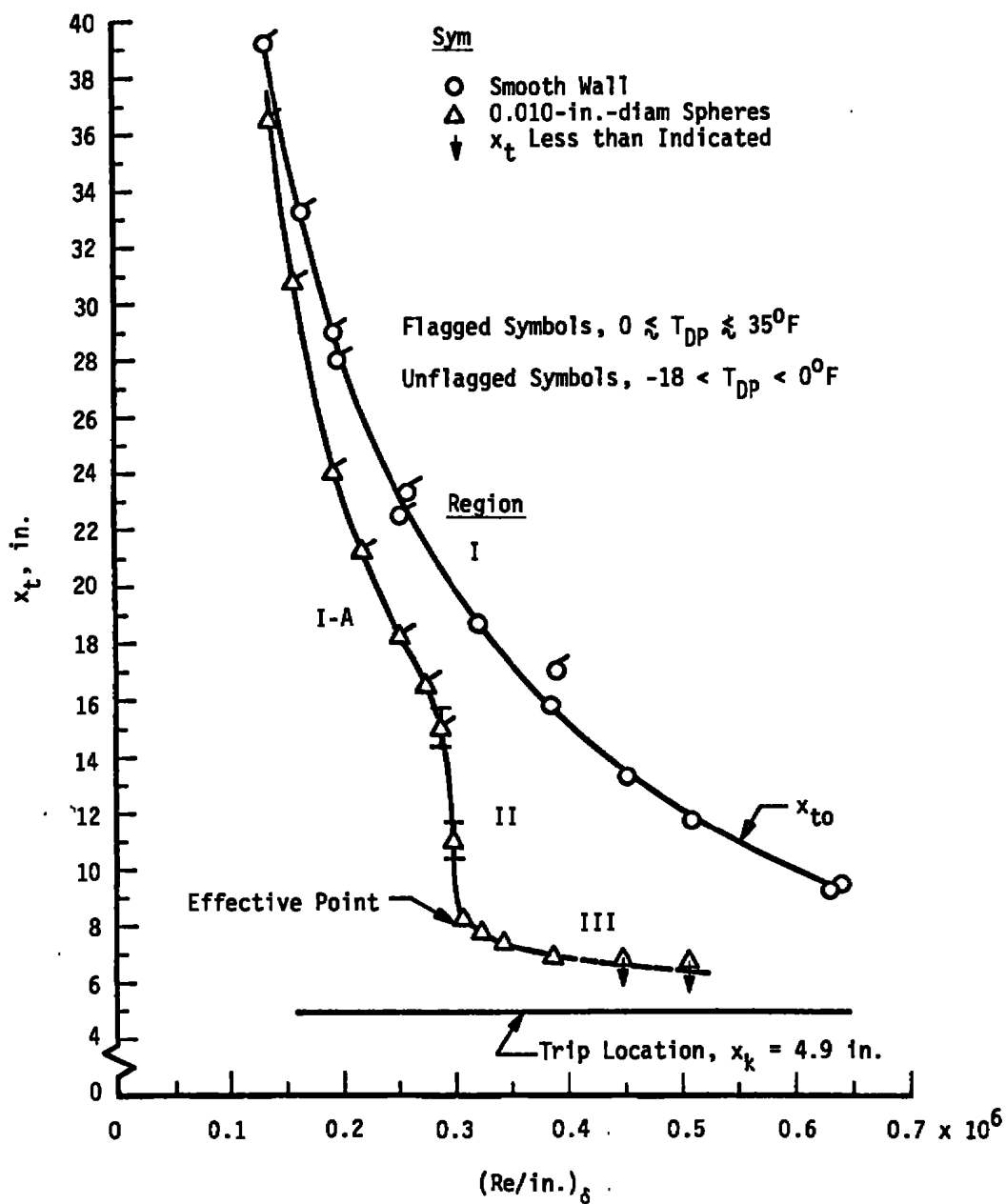
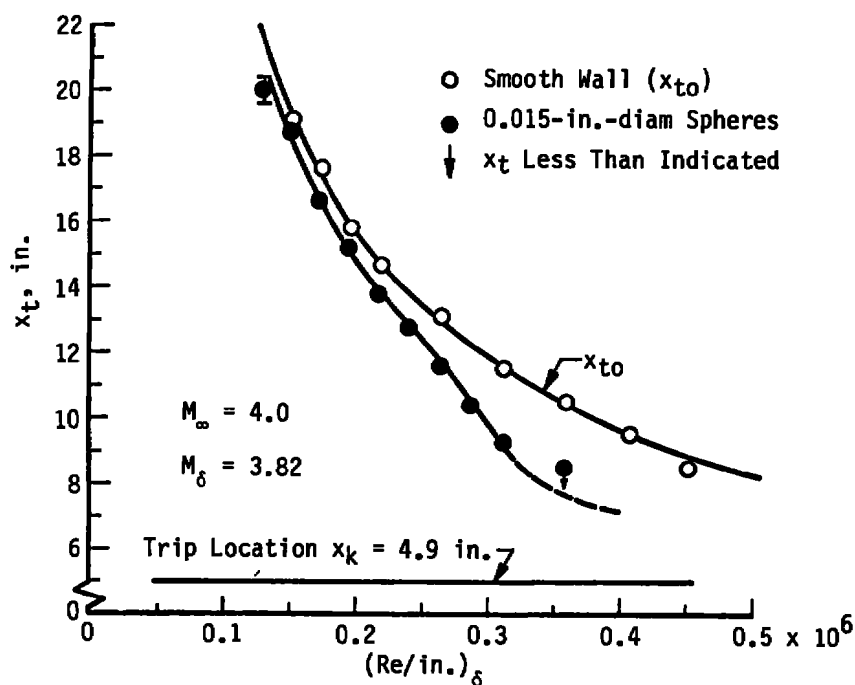
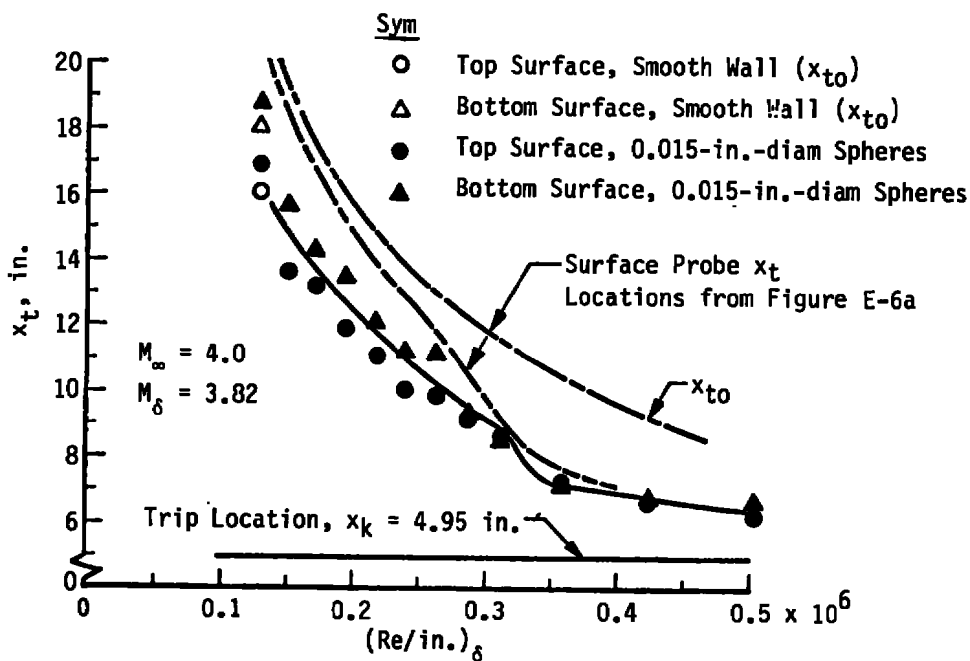


Figure E-5. Effect of spherical roughness on transition location,  $M_\delta = 2.89$ , AEDC-VKF Tunnel A.



a. Surface Probe Results



b. Schlieren Results

Figure E-6. Effect of spherical roughness on transition location,  $M_\delta = 3.82$ , AEDC-VKF Tunnel D.

These data were obtained in the AEDC-VKF 12-in. Tunnel D and 40-in. Tunnel A using sphere diameters of 0.010 and 0.015 in. attached to a 0.002-in.-thick band.

The various regions of interest which exist in a tripped-transition location profile are presented in Figures E-4a and E-5. Region I illustrates the variations in the smooth surface transition location as a function of the tunnel unit Reynolds number. A trend of this form is quite common (163), and the level has recently been shown to increase significantly with increasing tunnel size as discussed in the preceding section.

Region I-A is dominated by the free-stream disturbance levels, although trip disturbances are also being introduced into the transition process. Region II is a region of multiple dominance, and Region III (which represents the region between the "effective point" or "knee" and the trip) is dominated by the trip. The classification of the various parts of the tripped profile is taken from the definitions proposed by van Driest and Blumer (163). The "effective point" is by definition (163) the point where the transition Reynolds number is a minimum, as illustrated in Figure E-7. The author agrees with this interpretation of the phenomenon and chose to apply these criteria to the present study.

It is of interest to note that the schlieren transition location results presented in Figures E-4b and E-6b are about 10% to 20% lower than the probe locations in Region I, but as the tripped values of  $x_t$  approach  $x_k$  then the transition locations are about equal. One conclusion to be deduced from this observation is that the "effective

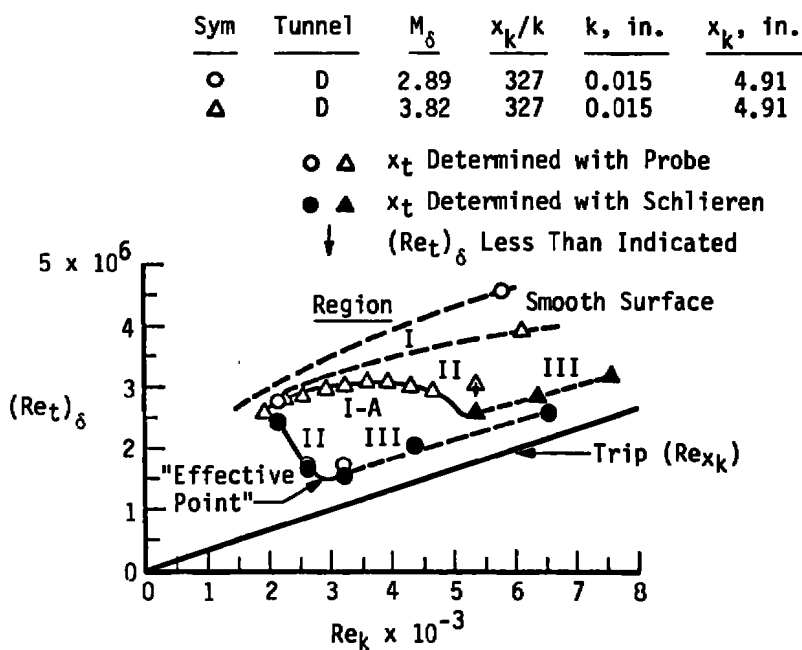
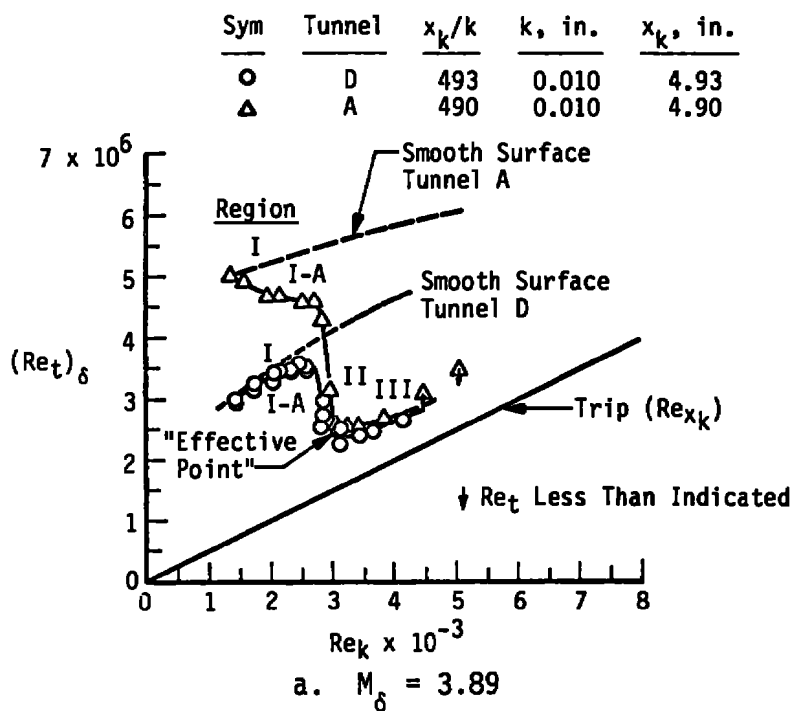


Figure E-7. Variation of transition Reynolds numbers with trip Reynolds number for  $M_\delta = 2.89$  and  $3.82$ , AEDC-VKF Tunnels D and A.

point" locations when determined from conventional schlieren photographs are not as distinguishable as the probe  $x_t$  locations.

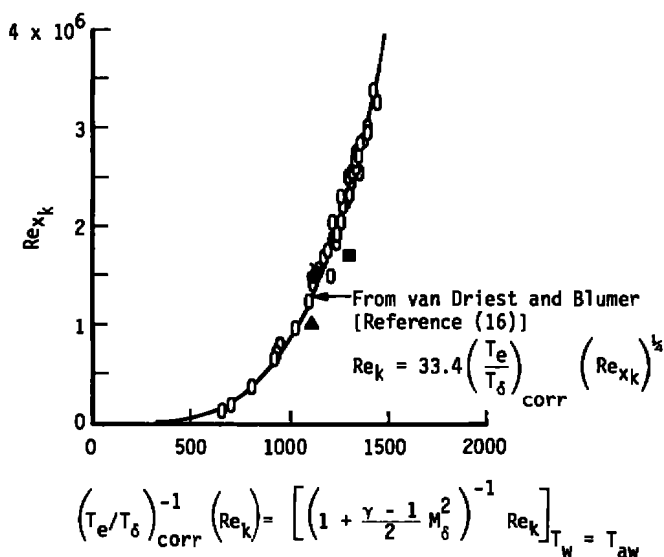
Composite plots of the tripped data from Tunnels A and D for  $M_\infty = 3$  and 4 are shown in Figure E-7 as a function of  $(Re_t)_\delta$  and the trip Reynolds number  $(Re_k)$ . Data presented in this form allow the Regions I-III to be illustrated in a different form. Also, data presented in this form are convenient for comparison with the results of van Driest (16,79,163). Once again the large variation of the smooth cone  $(Re_t)_\delta$  values with tunnel size is demonstrated. The data also show that a significant difference in trip effectiveness in Regions I-A and II exists. This avenue will be pursued in the following sections.

#### Van Driest, et al. Trip Correlation

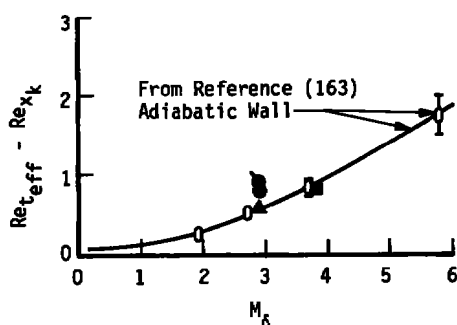
Van Driest, et al. (16,79,163) conducted a systematic experimental and analytical program that resulted in a spherical roughness correlation of "effective" point Reynolds numbers that is applicable to both planar models and sharp cones. This correlation incorporated the effects of surface Mach number from zero to approximately four and the effects of surface cooling.

Results from the present investigation are compared in Figure E-8 with results of van Driest and Blummer (16,163). The agreement is considered good, and the author feels these results provide additional confirmation to the conclusions of References (16) and (163). It should be specifically noted that all the data presented in Figure E-8 are based on the "effective point" concept. The "effective point" roughness criteria are based on the hypothesis that all  $x_t$  locations upstream of the

Facility	Sym	$M_\delta$	Source
JPL	○	1.90 to 3.67	Adiabatic and Wall Cooling References (16) and (163)
AEDC-VKF D	●	2.89	Present Study, Adiabatic Wall, $k = 0.010$
	▲	2.89	Present Study, Adiabatic Wall, $k = 0.015$
	■	3.82	Present Study, Adiabatic Wall, $k = 0.015$
AEDC-VKF A	●	2.89	Present Study, Adiabatic Wall, $k = 0.010$



#### a. Correlation of Effective Trip Location



#### b. Interval Between Effective Point and Trip Location Reynolds Numbers

Figure E-8. Correlation of tripped results using the methods of van Driest-Blumer.



"effective point" location are trip dominated and controlled, but downstream of this location the  $x_t$  values are significantly influenced by the combined effects of surface trip disturbances and free-stream disturbances (whatever the mode).

When evaluating the comparison between the two independent sets of data, it should be kept in mind that the test models, trip sizes, and general test conditions were nearly identical. Therefore, agreement would be expected provided the data were valid and all extraneous sources of error had been eliminated (or were identical) in both experiments. It is nevertheless reassuring to observe that different investigators can produce reproducible and repeatable results even in the very uncertain areas of boundary-layer tripping. In addition to the agreement exhibited in Figure E-8, direct comparison of the tripped transition locations [ $x_t$  versus  $(Re/in.)_\delta$ ] in the 12-in. Tunnel D data with the 12-in. JPL tunnel results in Reference (79) also show reasonable agreement. It was additionally encouraging to establish that the traversing probe produced results comparable in quality to the surface temperature and the magnified schlieren technique of References (16), (79), and (163).

#### Potter and Whitfield Trip Correlation

The trip correlation of Potter and Whitfield first appeared in References (37) and (137) and was further extended to include higher Mach numbers in Reference (21). To the author's knowledge, this correlation is without question the most comprehensive of any published to date. The correlation incorporates, as did the correlation of van Driest and Blumer, the effects of heat transfer and Mach number, and is applicable to both

planar models and sharp cones. However, the local Mach number range extends to approximately 10, and the correlation provides values of the trip size required to locate transition anywhere between the undisturbed smooth surface and trip location. The correlation also predicts the effectiveness of single two-dimensional surface wires in addition to single rows of spheres.

Data from the present investigation are presented in Figure E-9 using the correlation of Potter and Whitfield. The current data are seen to lie within the data band used in Reference (37) to establish a suggested curve. One observation is that the suggested correlation curve will not predict the "effective point" or "knee" location of the present data. However, the most significant result to note is that the correlating parameters provided a nearly identical collapse of the  $M_\delta = 2.89$ ,  $k = 0.010$ -in. data from the AEDC-VKF Tunnels A and D. It should be remembered that the only difference in these data (in terms of tunnel conditions and model and trip geometry) is the large difference in the smooth wall  $x_{to}$  locations. A tentative conclusion to be inferred from these results is that the  $x_{to}$  normalizing parameter in the Potter-Whitfield correlation will allow data from various sizes of supersonic-hypersonic tunnels to be successfully correlated.

Application of the Potter-Whitfield correlation parameters requires that the Mach number ( $M_k$ ) in undisturbed laminar flow at height  $\bar{k}$  be known. Values of  $M_k$  were obtained using the flat-plate similarity parameter  $[\eta = (y/x_k)(\sqrt{Re_{x_k}})]$  divided by the  $\sqrt{3}$  in conjunction with the results of Reference (144). Values of  $M_k$  for sharp cones can also be obtained directly from graphical results presented in Reference (145).

Sym	$M_\delta$	Roughness	AEDC Tunnel	Model	Reference
○	2.89	Spheres	D	Cone	Present Investigation
◐	3.82	Spheres	D	Cone	Present Investigation
●	2.89	Spheres	A	Cone	Present Investigation
▨	0-5	(Spheres) (Wires) (Grit)	-	(Cone, Cyl. Plate)	Reference (37)

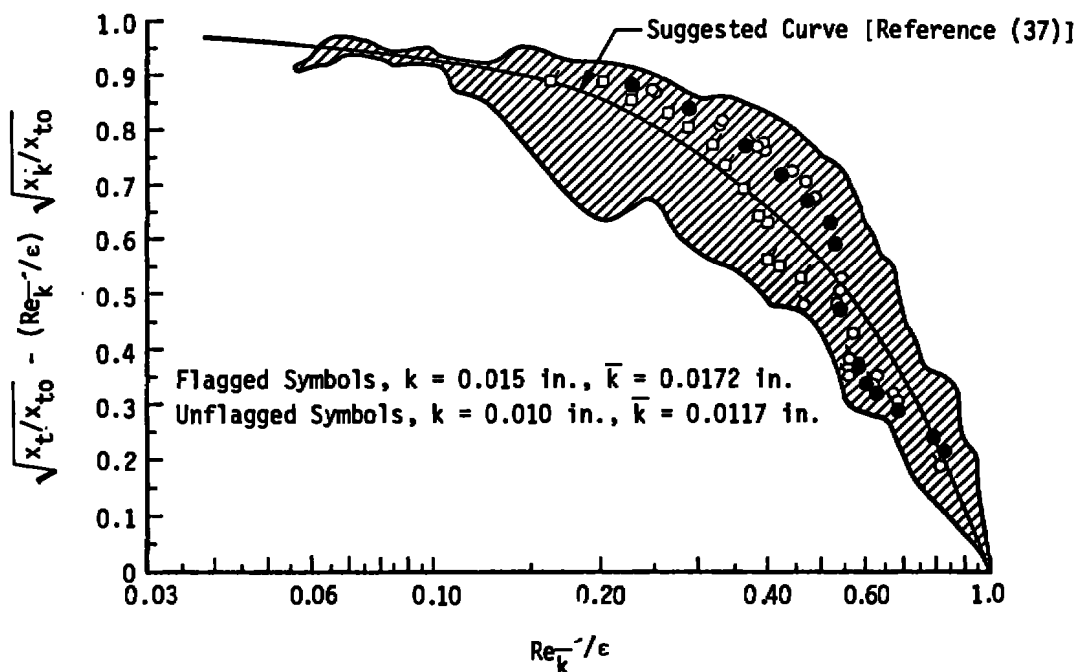


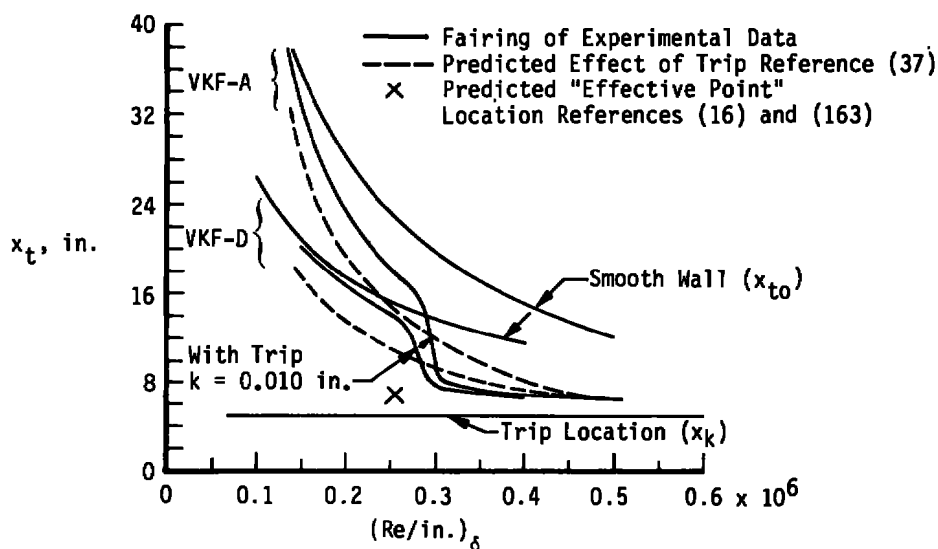
Figure E-9. Correlation of tripped results using the method of Potter-Whitfield.

In determining the boundary-layer thickness it has been assumed that the entropy layer generated by the bow shock has been "swallowed" by the boundary layer, and the cone acts as an "aerodynamically" sharp cone. This is a reasonable assumption, since the ratio at the trip location distance to the nose radius is approximately 2,000.

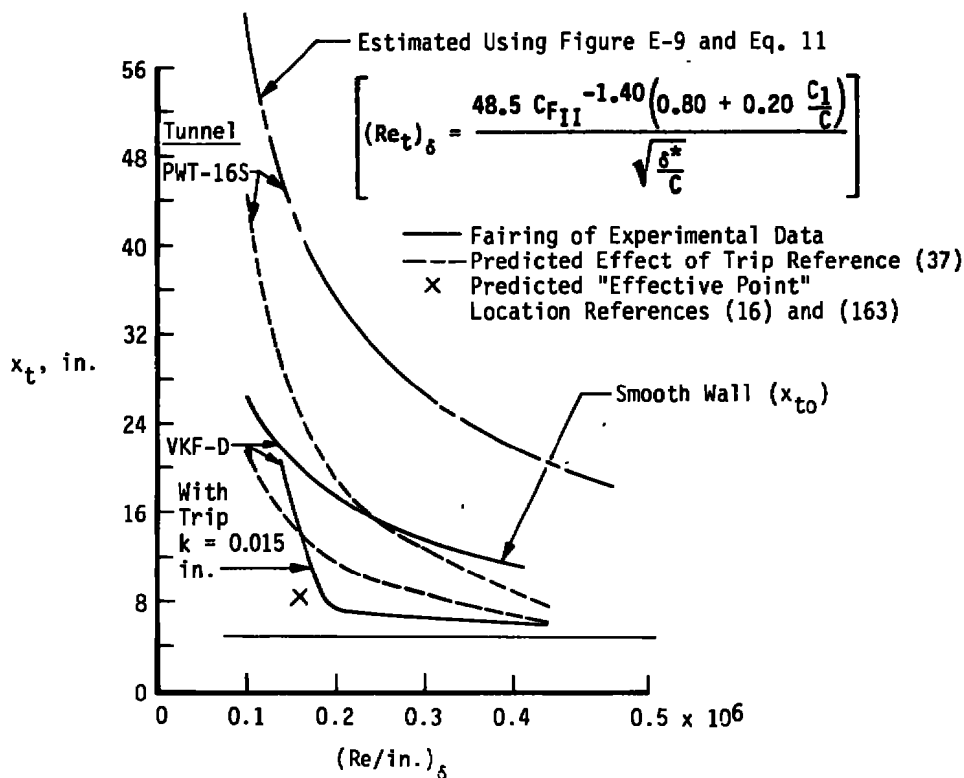
Inspection of the correlation parameters of Potter and Whitfield in Figure E-9 reveals that the smooth surface value of the transition location must be known. Therefore, when transition locations for  $M_\infty \gtrsim 3$  are desired for application in the Potter-Whitfield trip correlation, and measured values of  $x_{t0}$  from the facility under consideration are not available, the correlations presented in Figures IX-8, page 249, and IX-9, page 251, can be utilized to obtain estimated smooth wall  $(Re_t)_\delta$  values for either flat plates (or hollow cylinders) and sharp slender cones.

Direct comparisons between the experimental data and the estimated  $x_t$  locations using the correlation of Potter and Whitfield (37) for the specified spherical roughness heights of 0.0117 and 0.0172 in. for a local cone surface Mach number of 2.89 are provided in Figure E-10. The methods of van Driest and Blumer as presented in Figure E-8b, page 390, enabled the "effective point" location to be estimated. Estimates of tripped  $x_t$  locations to be expected in very large supersonic tunnels, such as the AEDC-PWT Tunnel 16S, are included in addition to the experimental data from the AEDC-VKF Tunnels D and A.

It is evident that when the Potter-Whitfield suggested curve from Figure E-9 is used, the "effective point" or "knee" location is not predicted. This deficiency could, of course, be eliminated if a



a.  $M_\delta = 2.89$ ,  $k = 0.010$  in.,  $\bar{k} = 0.0117$  in.,  $x_k = 4.9$  in.



b.  $M_\delta = 2.89$ ,  $k = 0.015$  in.,  $\bar{k} = 0.0172$  in.,  $x_k = 4.9$  in.

Figure E-10. Comparisons of correlation predictions with experimental results.

different "suggested curve" were used.<sup>20</sup> However, upon inspection of the data band in Figure E-9 it is not immediately evident that a different "suggested curve" would be justified. This disagreement in terms of physical distance (inches) also increases with tunnel size. The method of van Driest and Blumer predicts the "effective point"  $x_t$  location quite adequately, but misses the  $(Re/in.)_\delta$  value at which the knee occurs. However, the agreement between predictions and measurements using both methods is considered good and within the correlation scatter of the methods (e.g., see Figures E-8 and E-9).

Although perhaps somewhat limited in scope the present study has provided results which are considered to be significant. The model configuration was a sharp slender cone, but the results can also be expected to apply to spherical roughness on plates. The test Mach numbers of 3 and 4, although not covering a large Mach number range are Mach numbers of prime interest in many wind tunnel test programs. The data in Figures E-7 and E-10 indicate that the transition location between the trip and the "effective point" location is a function of the free-stream

---

<sup>20</sup>In a personal communication, J. L. Potter has told the author that he originally looked for evidence that the suggested curve in Figure E-9 should exhibit a "knee" or asymptotic approach to the abscissa in the region  $x_t \rightarrow x_k$ , but could not justify presenting the curve in that form [on the basis of the data used in Reference (37)] even though he thought some change in shape near the right side of the curve had plausibility.

disturbance level, but indicate that the Potter-Whitfield correlation through the use of the  $x_{t0}$  term successfully collapsed the tripped data. The present data support the "effective point" criteria proposed by van Driest and Blumer and suggest this location will be valid for all sizes of supersonic wind tunnels.

An observation which seems to merit mention is the absence of evidence of the "effective point" in the published hypersonic tripped data (21,137,164,165). If the hypersonic data represent the I-A and II regions, illustrated in Figures E-4, page 384, and E-5, page 385, then one might question whether the published results were trip dominated or whether the data could also have been significantly influenced by free-stream disturbance effects (either radiated noise or temperature spottiness).

It has been shown that the absolute effectiveness of spherical roughness can be influenced by the free-stream disturbances (aerodynamic noise) present. It is therefore concluded that to a significant degree the tripped transition location at supersonic speeds ( $M_\infty \gtrsim 3$ ) is dependent on the tunnel size or more precisely the free-stream disturbances. Thus, it appears appropriate to relate roughness effects to the smooth wall transition location ( $x_{t0}$ ), as done by Potter and Whitfield (37), when attempting to normalize tunnel flow effects. These results have further demonstrated that the trip correlation parameters developed by Potter and Whitfield successfully correlated the tripped transition data obtained in two significantly different sizes of supersonic tunnels having significantly different  $x_{t0}$  values. These studies also confirmed the

"effective point" criteria proposed by van Driest, et al. (163) and verified that the "effective point" is trip disturbance dominated and essentially independent of the tunnel disturbance levels ( $x_{to}$  location) at supersonic speeds.



## APPENDIX F

TABULATIONS OF BASIC EXPERIMENTAL TRANSITION DATA  
FROM THE AEDC SUPERSONIC-HYPERSOONIC WIND TUNNELS

Table F-1. AEDC-VKF Tunnel D transition Reynolds number data, 3.0-in.-diam hollow cylinder.

$M_\infty$	psia	$T_0$ , OR	$Re/in.$ $\times 10^{-6}$	$x_t^*$ , in.	$Re_t$ $\times 10^{-6}$	$b$ , in.	$\theta_{LE}$ , deg	Remarks
2.98	7.3	536	0.097	14.0	1.36	0.0036	6	Probe A (0.015 x 0.032 in.)
2.99	11.3	539	0.148	11.3	1.67			
2.99	14.4	540	0.188	10.0	1.88			
3.00	23.8	539	0.311	8.3	2.58			
3.00	30.7	537	0.402	7.0	2.81			
3.00	37.8	533	0.501	6.3	3.16			
3.00	44.5	528	0.598	5.5	3.29			
2.98	7.3	532	0.097	14.0	1.36			
2.99	11.4	535	0.151	11.0	1.66			
3.00	14.9	537	0.195	10.0	1.95			
3.00	22.8	536	0.300	8.25	2.47			
3.00	29.9	534	0.394	7.0	2.76			
3.00	37.8	526	0.511	6.1	3.12			
3.00	44.9	518	0.620	5.5	3.41			
2.98	7.6	529	0.102	11.7	1.19	0.0023	12	Probe A
3.00	23.0	533	0.305	6.8	2.07			
3.00	29.9	534	0.396	6.1	2.41			
3.00	37.9	530	0.507	5.4	2.74			
3.00	44.9	527	0.605	4.9	2.96			
2.98	7.5	523	0.103	13.2	1.36	0.0036	6	** Probe A
2.99	11.5	527	0.155	11.2	1.74			
2.99	15.0	529	0.201	9.8	1.97			
3.00	22.8	529	0.305	8.0	2.44			
3.00	31.1	523	0.423	6.8	2.87			
3.00	37.9	516	0.526	6.1	3.21			
3.00	45.0	510	0.636	5.4	3.44			
2.98	7.6	523	0.105	11.2	1.18	0.0021	6	Probe A
2.98	11.6	517	0.162	9.4	1.52			
2.99	15.1	512	0.213	8.3	1.77			
3.00	22.9	511	0.323	6.6	2.13			
3.00	30.0	515	0.419	5.9	2.47			
3.00	38.0	515	0.530	5.3	2.81			
3.00	44.9	514	0.626	4.9	3.07			
2.98	7.7	513	0.109	11.2	1.22			
2.98	11.6	511	0.165	9.8	1.62			
2.99	15.1	519	0.209	8.5	1.78			
3.00	23.0	527	0.309	7.0	2.16			
3.00	30.0	528	0.403	6.0	2.42			
3.00	38.0	526	0.513	5.3	2.72			
3.00	45.0	520	0.620	4.7	2.91			
2.98	11.7	511	0.165	9.6	1.58	0.0021	6	Probe B (0.007 x 0.0037 in.)
2.99	15.1	517	0.211	8.5	1.79			
3.00	23.0	529	0.308	7.0	2.16			
3.00	30.0	529	0.401	6.0	2.41			
3.00	38.1	526	0.514	5.2	2.67			
3.00	45.2	515	0.630	4.7	2.96			
3.0	---	530	0.1	---	1.10	0	---	Extrapolated Values of $Re_t$ from Figure VI-1
			0.2		1.43			
			0.3		1.70			
			0.4		1.93			
			0.5		2.09			
			0.6		2.24			
4.0		540	0.1		1.12			Extrapolated Values of $Re_t$ from Figure VI-1
			0.2		1.51			
			0.3		1.76			
			0.4		1.96			
			0.5		2.15			
			0.6		2.31			
5.0			0.1		1.40			
			0.2		2.06			
			0.3		2.65			
			0.4		3.10			

\* $x_t$  Determined with a Surface Pitot Probe Peak Value

\*\*Boundary-Layer Trip Located on Inside Bevel Angle 1/8-in. from Hollow-Cylinder Leading Edge.

Table F-2. AEDC-VKF Tunnel E 3.0-in.-diam hollow-cylinder transition data.

Data Point	$M_\infty$	$P_{0^*}$ , psia	$P_{\infty^*}$ , psia	$T_{0^*}$ , °R	$Re/in.$ $\times 10^{-6}$	$*(X_t)_{min.}$ in. $p_p$	$(Re_t)_{min.}$ $\times 10^{-6}$ $p_p$	$*(X_t)_{max.}$ in. $p_p$	$(Re_t)_{max.}$ $\times 10^{-6}$ $p_p$	$l_m$ , in.	Wall Condition	$\bar{b}$ , in.
1	4.99	101.1	0.193	666	0.349	---	---	8.1	2.83	54.8	Uncooled	0.0023
2	5.00	200.2	0.378	665	0.690	3.4	2.34	6.7	4.63	↓		
3	5.03	303.5	0.554	681	0.996	3.1	3.09	5.4	5.38	↓		
4	5.00	142.9	0.270	680	0.477	4.0	1.91	$8.0 \pm 0.3$	$3.81 \pm 0.14$	↓		
5	5.04	399.1	0.720	672	1.329	---	---	$5.5 \pm 0.3$	$7.30 \pm 0.4$	↓		
6	4.99	94.2	0.180	668	0.324	4.0	1.30	9.0	2.92	59.8		
7	5.03	296.5	0.541	680	0.975	---	---	5.9	5.75	↓		
8	5.00	147.1	0.278	662	0.511	3.5	1.79	7.6	3.88	↓		
9	5.04	398.1	0.718	692	1.270	---	---	5.5	6.99	↓		
10	4.99	137.9	0.264	660	0.483	---	---	---	---	39.6		
11	4.99	101.2	0.194	660	0.355	$4.75 \pm 0.75$	$1.69 \pm 0.27$	$10.5 \pm 0.2$	3.73	↓		
12	5.03	300	0.55	680	0.98	4.0	3.92	7.2	7.1	↓		
13	4.99	150.4	0.288	664	0.522	4.5	2.35	9.3	4.86	↓		
14	5.04	399.5	0.721	676	1.319	---	5.28	6.5	8.58	↓		
15	4.99	97.4	0.186	664	0.338	---	---	12.3	4.16	34.6		
16	5.03	300.2	0.548	677	0.994	---	---	7.8	7.75	↓		
17	4.99	154.4	0.295	658	0.543	$5.5 \pm 0.5$	$2.98 \pm 0.27$	10.5	5.71	↓		
18	5.04	409.8	0.739	690	1.312	---	---	---	---	↓		
41	5	101.8	0.19	658	0.36	---	---	13.0	4.66	34.6	Cooled	
42	5	305.3	0.56	686	0.99	3.0	2.97	$5.25 \pm 0.25$	$5.20 \pm 0.25$	↓		
43	5	54.6	0.10	495	0.29	---	---	$14.5 \pm 0.5$	$4.20 \pm 0.14$	↓		

\* $X_t$  Determined with a Surface Pitot Probe;  $p_p$  = Pitot Probe.

Table F-3. AEDC-VKF Tunnel A transition Reynolds number data, 3.0-in.-diam hollow cylinder.

$M_\infty$	$P_0$ , psia	$T_0$ , °R	$Re/in.$ $\times 10^{-6}$	$x_t$ , in.	$Re_t$ $\times 10^{-6}$	$\delta$ , in.	$\theta_{LE}$ , deg	Remarks
2.98	16.6	560	0.206	13.3	2.74	0.0021	6	
2.99	20.5	560	0.253	11.5	2.91			
2.99	24.8	564	0.303	10.5	3.18			
2.99	32.8	565	0.400	8.6	3.44			
3.00	40.7	566	0.493	7.5	3.69			
4.02	28.0	565	0.200	14.6	2.92			
4.02	34.1	563	0.244	12.6	3.08			
4.02	41.0	565	0.292	11.0	3.22			
4.02	56.5	562	0.405	9.1	3.69			
4.02	64.5	565	0.459	8.4	3.85			
5.04	50.95	603	0.200	17.0	3.40			
5.04	81.96	640	0.294	13.6	4.00			
5.06	136.7	644	0.484	10.9	5.26			
2.98	16.2	572	0.195	16.0	3.12	0.0036	6	
2.99	20.5	571	0.246	13.5	3.32			
2.99	25.6	570	0.308	11.7	3.60			
2.99	33.3	571	0.400	10.0	4.00			
2.99	41.4	573	0.494	9.0	4.45			
3.00	49.2	575	0.581	8.3	4.82			
4.02	28.4	563	0.203	15.0	3.04			
4.02	34.3	561	0.246	14.0	3.44			
4.02	41.5	561	0.298	13.5	4.02			
4.02	56.3	562	0.404	11.3	4.56			
4.02	73.4	567	0.518	10.0	5.18			
5.05	81.5	638	0.292	16.0	4.67			
5.06	109.9	645	0.386	14.5	5.60			
5.06	137.1	647	0.478	14.0	6.69			
5.05	150.5	649	0.526	13.8	7.26			
3.00	41.0	563	0.503	6.5	3.27	0.0013	12	
2.99	32.9	563	0.403	7.6	3.06			
2.99	24.8	562	0.305	9.2	2.81			
2.98	16.7	562	0.206	12.5	2.58			
5.06	136.4	642	0.483	9.9	4.78			
5.04	82.3	640	0.296	12.7	3.76			
2.98	16.5	565	0.203	13.4	2.72	0.0023	12	
2.99	32.7	563	0.401	8.4	3.37			
2.99	24.7	562	0.304	10.0	3.04			
2.98	16.2	566	0.198	15.0	2.97	0.0030	12	
2.99	25.4	566	0.309	10.7	3.31			
2.99	33.6	568	0.407	9.2	3.74			
2.99	40.9	571	0.491	8.0	3.93			
3.00	48.7	573	0.578	7.3	4.22			
2.99	33.1	564	0.404	9.3	3.76			
2.99	25.0	565	0.305	10.6	3.24			
3.0	---	560	0.15	---	2.10	0	---	Extrapolated Value of $Re_t$ From Figure V1-2
			0.2	---	2.25			
			0.3	---	2.49			
			0.4	---	2.68			
			0.5	---	2.82			
			0.6	---	2.96			
4.0	---	560	0.15	---	2.37			
			0.20	---	2.60			
			0.30	---	2.92			
			0.40	---	3.20			
			0.50	---	3.41			
			0.60	---	3.60			
5.0	---	---	0.15	---	2.64			
			0.20	---	2.91			
			0.30	---	3.38			
			0.40	---	3.60			
			0.50	---	4.12			
			0.60	---	4.40			

\* $x_t$  Determined from Surface Pitot Probe Peak Value.

Table F-4. AEDC-PWT-16S Tunnel basic transition Reynolds number data, 12.0-in.-diam hollow cylinder.

$M_\infty$	$P_{O_2}$ psia	$T_{O_2}$ °R	$Re/in.$ $\times 10^{-6}$	** $Re_{t1}$ $\times 10^{-6}$	** $Re_{t2}$ $\times 10^{-6}$	** $Re_{t3}$ $\times 10^{-6}$	** $Re_{t4}$ $\times 10^{-6}$	Average ** $Re_t$ $\times 10^{-6}$	Average $\delta$ , in.	Dew Point Referenced to Atmospheric Pressure, °F
3.00	5.23	647	0.0516	2.16	2.16	---	2.12	2.15	0.0015	0
3.00	6.21	666	0.0591	2.26	2.26	---	2.26	2.26	↓	-13
3.01	7.09	656	0.0686	2.42	2.40	2.47	2.32	2.40		-18
3.01	7.06	653	0.0689	2.48	2.43	2.46	2.34	2.43		-18
3.00	7.93	669	0.0748	2.43	2.42	2.54	2.40	2.45		-13
3.00	9.27	671	0.0873	2.57	2.59	2.62	2.53	2.58		-14
3.00	9.27	669	0.0876	2.59	2.63	2.72	2.54	2.62	↓	-14
3.00	10.92	667	0.104	2.85	2.88	2.91	2.68	2.83		-2
3.00	5.09	645	0.0517	---	2.30	2.36	2.32	2.33	0.0050	+25
3.00	7.12	649	0.0701	2.64	---	2.64	2.54	2.61	0.0042	0
3.00	7.17	655	0.0700	---	2.82	---	2.88	2.85	0.0050	+12
3.00	9.28	664	0.0888	---	2.81	2.84	2.77	2.81	0.0050	+7
3.00	6.22	658	0.0603	2.53	2.63	2.77	2.63	2.64	0.0090	-4
3.00	7.05	657	0.0686	2.75	2.81	---	2.75	2.77	↓	+1
3.03	8.36	659	0.0794	2.94	3.05	3.08	2.91	2.99		-8
3.00	9.20	644	0.0920	3.26	3.36	3.40	3.18	3.27		+1
3.03	10.52	659	0.0998	3.19	3.39	3.36	3.23	3.29		-9
2.50	4.06	641	0.0535	2.52	2.52	---	---	2.52	0.0015	+5
2.51	4.62	642	0.0605	2.54	2.60	2.64	---	2.59	↓	-4
2.50	5.34	654	0.0685	2.71	2.81	2.81	2.81	2.78		+7
2.50	5.46	655	0.0694	2.66	2.70	2.77	---	2.71		-16
2.50	6.31	657	0.0798	2.76	2.71	2.87	---	2.78		-16
2.50	7.82	654	0.1003	3.18	3.08	3.29	3.12	3.16		+11
2.50	8.57	658	0.1089	3.32	3.16	3.38	3.16	3.25	↓	+7
2.50	5.38	658	0.0684	2.82	2.93	2.93	2.98	2.91	0.0050	+6
2.50	6.26	655	0.0799	3.04	3.14	3.12	2.98	3.07	+6	
2.50	8.65	656	0.1105	3.68	3.65	3.80	3.76	3.72	↓	+6
2.00	5.62	632	0.0970	3.68	3.40	3.83	3.64	3.64	0.0015	+13
2.00	7.45	631	0.1286	4.12	3.73	4.38	4.12	4.09	0.0015	+13
3.0	---	---	0.050	---	---	---	---	2.09	0*	---
↓	↓	↓	0.070	↓	↓	↓	↓	2.32	↓	↓
			0.090					2.54		
			0.11					2.71		
			0.050					2.38		
2.5	↓	↓	0.070	↓	↓	↓	↓	2.64	↓	↓
↓	↓	↓	0.090					2.89		
			0.11					3.09		
			0.090					3.40		
2.0	↓	↓	0.11	↓	↓	↓	↓	3.65	↓	↓
↓	↓	↓	0.13					3.86		

\*Extrapolated Values of  $Re_t$  from Figure VI-4.\*\*1, 2, 3, 4 Correspond to the Four Surface Probes;  $x_t$  Determined from Surface Pitot Probe Peak Value.

Table F-5. AEDC-VKF Tunnel D transition Reynolds number, 10-deg total-angle sharp cone.

$M_\infty$	$M_c = M_\delta$	$p_o$ , psia	$T_o$ , °R	$(Re/in.)_\infty \times 10^{-6}$	$(Re/in.)_\delta \times 10^{-6}$	$x_t$ ,* in.	$(Re_t)_\delta \times 10^{-6}$
2.98	2.87	9.93	533	0.133	0.141	~21	~2.97
2.99	2.88	14.9	524	0.204	0.217	16.7	3.62
3.00	2.89	20.0	523	0.272	0.289	13.6	3.93
2.98	2.87	9.86	532	0.133	0.141	~21	~2.96
2.99	2.88	12.4	544	0.160	0.170	19.3	3.28
2.99	2.88	14.9	548	0.191	0.203	17.8	3.61
3.00	2.89	17.4	549	0.220	0.234	15.7	3.67
3.00	2.89	20.0	549	0.253	0.269	14.8	3.98
3.48	3.34	15.0	520	0.160	0.172	18.5	3.18
3.48	3.34	20.0	516	0.215	0.232	15.3	3.54
3.48	3.34	24.8	514	0.269	0.289	13.2	3.82
3.48	3.34	30.0	513	0.326	0.350	12.0	4.20
3.99	3.81	17.5	580	0.139	0.152	19.1	2.91
4.00	3.82	20.0	528	0.159	0.174	17.6	3.07
4.00	3.82	22.5	526	0.180	0.197	15.8	3.12
4.00	3.82	24.9	523	0.201	0.220	14.7	3.24
4.00	3.82	29.9	521	0.242	0.265	13.1	3.47
4.00	3.82	34.9	518	0.286	0.313	11.5	3.60
3.99	3.81	39.9	518	0.328	0.359	10.5	3.77
3.99	3.81	45.0	517	0.371	0.407	9.4	3.83
3.99	3.81	50.0	518	0.411	0.451	8.4	3.78
4.55	4.32	24.9	539	0.146	0.163	~20.5	3.34
4.56	4.33	27.4	540	0.159	0.177	19.5	3.46
4.56	4.33	29.9	542	0.173	0.193	18.9	3.65
4.56	4.33	34.9	543	0.202	0.225	16.6	3.74
4.56	4.33	39.9	544	0.229	0.255	15.6	3.98
4.56	4.33	45.0	546	0.258	0.288	14.5	4.17
4.56	4.33	49.9	547	0.285	0.318	13.5	4.29
4.56	4.33	55.0	548	0.312	0.348	12.6	4.38
4.55	4.32	60.0	546	0.345	0.385	11.7	4.50

\* $x_t$  Determined from Surface Probe Peak Pressure.

Table F-6. AEDC-VKF Tunnel A transition Reynolds number, 10-deg total-angle sharp cone.

$M_\infty$	$M_c = M_\delta$	$p_o$ , psia	$T_o$ , °R	$(Re/in.)_\infty \times 10^{-6}$	$(Re/in.)_\delta \times 10^{-6}$	$x_t$ ,* in.	$(Re_t)_\delta \times 10^{-6}$	Dew Point Referenced to Atmospheric Pressure, °F
2.99	2.88	19.8	562	0.243	0.258	23.2	6.01	14.5
2.99	2.88	29.7	562	0.364	0.387	17.0	6.57	5.5
2.99	2.88	14.8	565	0.181	0.192	29.0	5.57	14.0
2.98	2.88	10.1	561	0.126	0.134	39.2	5.25	35
3.00	2.89	49.9	566	0.603	0.640	9.5	6.08	- 1.5
3.00	2.89	49.6	569	0.596	0.633	9.3	5.89	- 1
3.00	2.89	39.8	568	0.479	0.509	11.8	6.00	-18
3.00	2.89	35.0	566	0.424	0.450	13.3	5.99	-11
2.99	2.88	29.6	565	0.362	0.384	15.8	6.07	- 9.5
2.99	2.88	24.7	563	0.303	0.322	18.7	6.02	- 2.5
2.99	2.88	19.7	568	0.238	0.253	22.5	5.69	2.5
2.99	2.88	15.1	562	0.186	0.198	28.0	5.53	13
2.98	2.87	12.6	561	0.156	0.166	33.2	5.51	19
4.02	3.84	69.9	569	0.493	0.540	10.5	5.67	-10.5
4.02	3.84	50.0	562	0.359	0.394	14.6	5.75	-10
4.02	3.84	34.6	565	0.246	0.269	20.0	5.38	- 4.5
4.01	3.83	24.7	563	0.178	0.195	27.0	5.25	8.0
4.00	3.82	19.8	564	0.143	0.157	31.6	4.95	12
4.54	4.31	116	573	0.623	0.695	10.0	6.95	-19.5
4.53	4.30	89.6	573	0.483	0.539	12.2	6.57	-23
4.53	4.30	59.7	568	0.327	0.365	16.4	5.98	-19
4.53	4.30	39.6	565	0.218	0.243	22.3	5.42	-12
4.52	4.29	29.8	564	0.166	0.185	28	5.2	- 3.5
4.50	4.27	19.7	563	0.111	0.124	38	4.7	8.0
5.04	4.75	150	646	0.532	0.612	13.8	8.44	-18
5.06	4.77	120	644	0.420	0.483	15.8	7.63	-14
5.05	4.76	101	645	0.354	0.407	17.5	7.12	-17
5.05	4.76	79.9	646	0.281	0.323	20.2	6.53	-13.5
5.04	4.75	59.9	645	0.212	0.244	25.2	6.14	-12
5.02	4.73	40.2	616	0.154	0.177	31.2	5.53	- 2.5
5.00	4.71	29.9	600	0.120	0.138	37.0	5.11	6.5
5.00	4.71	24.9	602	0.100	0.115	44	5.06	14.5

\* $x_t$  Determined from Surface Pitot Probe Peak Pressure

Table F-7. AEDC-VKF Tunnel A long- and short-shroud transition results.

$M_\infty$	Configuration	$P_{01}$ psia	$T_{01}$ °R	$Re/in.$ $\times 10^{-6}$	$x_t^{**}$ , in.	$Re_t$ $\times 10^{-6}$	$\bar{b}$ , in.	$\theta$ , deg
2.98	Long Shroud	16.6	563	0.203	12.7	2.58	0.0021	6
2.99		20.4	562	0.252	10.2	2.57		
2.99		24.7	562	0.304	8.0	2.43		
2.99		32.7	563	0.401	5.5	2.21		
2.99		28.1	562	0.345	6.6	2.28		
2.99		18.2	561	0.225	11.5	2.59		
2.98		14.2	562	0.176	14.5	2.55		
2.98		15.3	561	0.191	13.5	2.58		
4.02		28.4	566	0.202	9.5	1.92		
4.00		21.3	564	0.154	14.0	2.16		
3.99		17.7	564	0.128	*---	---		
4.02		34.0	564	0.243	8.0	1.94		
4.02		41.1	564	0.293	6.7	1.96		
4.02		56.3	564	0.403	5.2	2.09		
4.02		64.5	562	0.463	4.7	2.17		
4.02		73.4	563	0.525	4.4	2.31		
5.04	Long Shroud with Trip	50.9	601	0.201	12.5	2.51	0.0013	12
5.04		82.0	638	0.296	9.0	2.66		
5.06		110.1	639	0.392	7.2	2.82		
5.06		136.5	645	0.480	6.2	2.98		
5.05		150.0	644	0.531	6.0	3.19		
5.04		66.6	641	0.238	10.5	2.50		
5.04		39.2	606	0.153	16.1	2.46		
5.04		39.1	604	0.153	15.5	2.37		
5.04		50.6	603	0.199	11.5	2.29		
5.04		82.0	638	0.296	8.2	2.43		
5.06		136.9	638	0.490	5.7	2.79		
5.04		39.4	603	0.155	16.0	2.48		
5.04		50.8	601	0.200	12.0	2.40		
5.04		82.2	639	0.296	9.0	2.66		
2.98	Short Shroud	14.3	564	0.176	9.0	1.58	0.0021	6
2.98		16.6	563	0.205	6.6	1.35		
2.99		20.5	565	0.250	5.5	1.37		
2.99		26.1	563	0.324	5.3	1.72		
2.99		32.8	564	0.39	4.8	1.87		
3.0	Short Shroud	---	---	---	*---	---	0.0021	6
4.02		28.2	564	0.202	*---	---		
4.02		34.4	564	0.245	*---	---		
4.02		41.3	562	0.296	11.2	3.31		
4.02		56.4	565	0.401	9.5	3.81		
4.02		64.7	569	0.457	8.7	3.98		
4.02		73.5	565	0.524	8.0	4.19		
5.05		150.6	643	0.532	10.8	5.75		
5.06		136.9	643	0.484	11.1	5.37		
5.06		109.9	643	0.389	11.7	4.55		
5.05		82.4	645	0.292	14.0	4.09		

\*Shroud Lip Shock Wave Interference.

\*\* $x_t$  Measured on 3.0-in.-diam Hollow-Cylinder Transition Model Using Surface Pitot Probe Peak Value.

Table F-8. AEDC-VKF Tunnel F transition Reynolds number data.

Flat Plate,  $\alpha = 0$ 

$M_\infty$	$T_0$ , °R	$(Re/in.)_\infty \times 10^{-6}$	$x_t$ ,* in.	$Re_t \times 10^{-6}$	$\bar{b}$ , in.	Remarks
$\approx 8.0$	$\approx 1900$	0.54	16.0	8.6	0.0005	40-in. Diam Contoured Nozzle
↓	↓	0.80	13.3	10.6	↓	
		1.07	11.7	12.5		

Sharp 10-deg Half-Angle Cone,  $\alpha = 0$ 

$M_\infty$	$T_0$ , °R	$(Re/in.)_\infty \times 10^{-6}$	$x_t$ ,* in.	$(Re_t)_\delta \times 10^{-6}$	Remarks
$\approx 7.5$	$\approx 1800$	0.51	7.5	5.9	25-in. Diam Contoured Nozzle
↓	↓	0.62	6.3	6.1	
		0.70	6.0	6.5	
		0.88	5.6	7.7	
		2.56	2.2	8.6	
		2.42	2.5	9.4	

\* $x_t$  Determined from Maximum  $\dot{q}$  Value.



## NOMENCLATURE

$A$	Amplitude of boundary-layer disturbance fluctuations
$A_0$	Amplitude of disturbance at the neutral stability point
$A_r$	Reference amplitude for boundary-layer disturbance (determined at $M_\infty = 1.3$ )
$a_{ij}$	Coefficients in Eq. (1)
$b$	Model leading-edge thickness at a specific location
$\bar{b}$	Average value of model leading-edge thickness
$C$	Tunnel test section circumference
$C_1$	Tunnel test section circumference of 12- x 12-in. tunnel ( $C_1 = 48$ in.)
$C_F$	Mean turbulent skin-friction coefficient
$C_{FI}$	Mean turbulent skin-friction coefficient calculated using method of van Driest-I
$C_{FII}$	Mean turbulent skin-friction coefficient calculated using method of van Driest-II
$C_f$	Local skin-friction coefficient, $C_f = \tau_w/q_\infty$
$C_h$	Heat-transfer coefficient, $C_h = \dot{q}/(T_0 - T_w)$
$\bar{c}$	Aerodynamic-noise-transition correlation size parameter [see Eq. (10)]
$\tilde{e}$	Root-mean-square of the hot-wire voltage fluctuation
$e'$	Instantaneous value of hot-wire fluctuation voltage
$F(w)$	Power spectral density (psia) <sup>2</sup> /radian/sec
$f$	Frequency, cycles/sec
$H, h$	Enthalpy
$k$	Diameter of roughness element (sphere diameter)
$\bar{k}$	Total height of roughness element above model surface (sphere diameter plus band thickness)

$\ell$	Reference length
$\ell_m$	Axial distance from tunnel throat to model nose
$\ell_r$	Axial distance from tunnel throat to wall boundary-layer rake
$M$	Mach number
$M_\delta$	Local Mach number outside boundary layer
$\tilde{m}$	Root-mean-square of the mass flow fluctuation
$\overline{m}$	Mean mass flow value
$m'$	Instantaneous mass flow fluctuation value
$Pr$	Prandtl number, $Pr = C_p \mu / k$
$p$	Static pressure
$\tilde{p}, \tilde{p}_{RMS}$	Root-mean-square value of radiated pressure fluctuation
$p'$	Instantaneous fluctuating pressure
$p_c$	Cone surface static pressure
$p_o$	Tunnel stilling chamber total pressure
$p_o'$	Total pressure downstream of a normal shock wave (free-stream)
$p_p$	Surface probe pitot pressure
$p_s$	Model surface static pressure
$p_\infty$	Free-stream static pressure
$\dot{q}$	Heat-transfer rate
$\dot{q}_o$	Stagnation heat-transfer rate on a 1.0-in.-diam hemisphere probe
$q_\delta$	Dynamic pressure based on local condition at edge of boundary layer, $q_\delta = \frac{1}{2} \rho_\delta U_\delta^2$
$q_\infty$	Free-stream dynamic pressure, psia $q_\infty = \frac{1}{2} \rho_\infty U_\infty^2 = \frac{\gamma}{2} p_\infty M_\infty^2$
$R$	Shroud internal radius, in. ( $R = 5.72$ in.)

$Re$	Reynolds number
$Re/in., Re_{\infty}, (Re/in.)_{\infty}$	Free-stream Reynolds number, per in. ( $\rho_{\infty} U_{\infty}/\mu_{\infty}$ )
$Re_{e,\theta}$	Reynolds number based on edge conditions and momentum thickness at the transition location, $x_t$
$Re_k$	Trip Reynolds number $\left( Re_k = \frac{\rho_{\infty} U_{\infty} k}{\mu_{\infty}} \right)$
$Re_k'$	Potter-Whitfield trip correlation Reynolds number $Re_k' = \left( \frac{U_k \bar{k}}{\nu_k} \frac{T_k}{T_e} \right)^{0.5+\omega}$ <p>For adiabatic wall</p> $Re_k' = \bar{k} \left( \frac{U_{\delta}}{\nu_{\delta}} \right) \left( \frac{M_k}{M_{\delta}} \right) \left[ 1 + \frac{1}{2} (\gamma - 1) \eta_r M_{\delta}^2 \right]^{-1.26}$
$Re_l, Re_{\infty,l}$	Length Reynolds number $Re_{\infty,l} = \frac{\rho_{\infty} U_{\infty} l}{\mu_{\infty}}$
$Re_{l_m}$	Length Reynolds number $\left( Re_{l_m} = \frac{\rho_{\infty} U_{\infty} l_m}{\mu_{\infty}} \right)$
$Re_{l_r}$	Length Reynolds number $\left( Re_{l_r} = \frac{\rho_{\infty} U_{\infty} l_r}{\mu_{\infty}} \right)$
$Re_t$	Flat plate or hollow-cylinder transition Reynolds number based on free-stream conditions, $Re_t = (Re/in.)_{\infty} (X_t) = \frac{U_{\infty} X_t}{\nu_{\infty}}$
$Re_{t_{eff}}$	Effective point transition Reynolds number ( $\rho_{\delta} U_{\delta} X_{t_{eff}}/\mu_{\delta}$ )
$(Re_t)_{\delta}$	Cone transition Reynolds number (based on local conditions), $(Re_t)_{\delta} = (Re/in.)_{\delta} (X_t) = \frac{U_{\delta} X_t}{\nu_{\delta}}$
$Re_x$	Length Reynolds number ( $Re_x = \rho_{\delta} U_{\delta} x/\mu_{\delta}$ )

$Re_{x_k}$	Trip position Reynolds number, $Re_{x_k} = \rho_\delta U_\delta x_k / \mu_\delta$
$Re_\delta, (Re/in.)_\delta$	Inviscid flow local surface unit Reynolds number per in. $(\rho_\delta U_\delta / \mu_\delta)$
$Re_{\delta^*,t}$	Reynolds number based on the boundary-layer displacement thickness at the transition location, $x_t$
$S_T, S_{T_\infty}$	Stanton number $[(\dot{q} / \rho_\infty U_\infty) (H_o - H_w)]$
$T$	Temperature
$T_{aw}$	Adiabatic wall temperature, $T_{aw} = T_\infty \left(1 + \frac{\gamma - 1}{2} r M_\infty^2\right)$
$\tilde{T}$	Root-mean-square of the temperature fluctuation
$T_{DP}$	Dewpoint temperature at atmospheric pressure
$(T_e/T_\delta)_{corr}$	Corrected effective temperature ratio as defined in Reference (163)
$T'_T$	Instantaneous value of the total temperature fluctuation
$\bar{T}_T$	Mean total temperature value
$U$	Velocity outside the boundary layer
$U_c$	Source convection velocity
$U_L$	Local velocity outside the long shroud inner wall boundary layer
$U_\infty$	Free-stream velocity
$u$	Velocity in the boundary layer
$\tilde{u}$	Root-mean-square velocity fluctuation
$u'$	Instantaneous velocity fluctuation
$x_s$	Shroud lip shock impingement location
$x_t$	Surface distance location of boundary-layer transition
$x_{teff}$	Effective point transition location
$x_{t_0}$	Transition location on smooth body
$x$	Surface distance from model nose

$x_k$	Distance from cone tip to center-of-roughness sphere
$y$	Distance normal to model surface
$\gamma$	Ratio of specific heats
$\Delta C_p, \Delta C_{p_{rms}}$	Dynamic pressure coefficient, $\Delta C_p = \tilde{p}/q_\infty$
$\Delta e_T, \Delta e_m$	Hot-wire sensitivity coefficients
$\alpha$	Speed of sound
$\delta$	Boundary-layer thickness
$\delta^*$	Boundary-layer displacement thickness
$\overline{\delta^*}$	Boundary-layer displacement thickness parameter (Eq. B-13)
$\delta_c$	Cone half angle
$\delta_k^*$	Boundary-layer displacement thickness at $k$ location
$\epsilon$	Value of $Re_k^-$ where $X_t = X_k$ ; $\epsilon = f(M_k^-)$ as shown in Reference (37)
$\eta_r, r$	Temperature recovery factor ( $T_{aw} - T_\delta/T_0 - T_\delta$ )
$\theta$	Boundary-layer momentum thickness
$\theta_c$	Cone half-angle
$\theta_{LE}$	Planar model leading-edge bevel angle
$\mu$	Absolute viscosity
$\nu$	Kinematic viscosity, $\nu = \mu/\rho$
$\rho$	Density
$\rho'$	Instantaneous fluctuating density
$\tau_w$	Wall local shear stress
$\phi$	Cone bow shock wave angle
$\Phi$	Power spectral density, $\tilde{p}^2 = \int_0^\infty \Phi df$ , $\text{psia}^2/\text{Hz}$
$\omega$	Angular frequency (radians/sec) and exponent in viscosity-temperature relation ( $\omega = 0.76$ )

Subscripts

2	Conditions immediately downstream of an oblique shock wave
AW, aw	Adiabatic wall
Beg.	Beginning of transition location
c	Cone configuration
End	End of transition location
e	Boundary-layer edge conditions
FP	Flat plate
K	At height k in undisturbed laminar boundary layer
k	Trip location
$\bar{K}$	At total height $\bar{k}$ in undisturbed laminar boundary layer
L	Local conditions at edge of boundary layer
max	Peak value
min	Minimum value
o	Stagnation conditions
planar	Two-dimensional configuration, either hollow cylinder or flat plate
s	Cone surface inviscid values
t	Transition
w	Wall
x	Surface distance
$\delta$	Local inviscid flow properties at edge of boundary layer
$\theta$	Momentum thickness
$\infty$	Free stream